



HAL
open science

Star-disk interactions in young stars: dippers as seen with K2

Noemi Roggero

► **To cite this version:**

Noemi Roggero. Star-disk interactions in young stars: dippers as seen with K2. Astrophysics [astro-ph]. Université Grenoble Alpes [2020-..], 2021. English. NNT : 2021GRALY058 . tel-03577104

HAL Id: tel-03577104

<https://theses.hal.science/tel-03577104>

Submitted on 16 Feb 2022

HAL is a multi-disciplinary open access archive for the deposit and dissemination of scientific research documents, whether they are published or not. The documents may come from teaching and research institutions in France or abroad, or from public or private research centers.

L'archive ouverte pluridisciplinaire **HAL**, est destinée au dépôt et à la diffusion de documents scientifiques de niveau recherche, publiés ou non, émanant des établissements d'enseignement et de recherche français ou étrangers, des laboratoires publics ou privés.

THÈSE

Pour obtenir le grade de

DOCTEUR DE L'UNIVERSITÉ GRENOBLE ALPES

Spécialité : Astrophysique et Milieux Dilués

Arrêté ministériel : 25 mai 2016

Présentée par

Noemi ROGGERO

Thèse dirigée par **Jérôme BOUVIER**

et codirigée par **François MENARD**, Université Grenoble Alpes

préparée au sein du **Laboratoire Institut de Planetologie et dAstrophysique de Grenoble**
dans l'**École Doctorale Physique**

Interactions étoile-disque dans les étoiles jeunes : dippers observés avec K2

Star-disk interactions in young stars: dippers as seen with K2

Thèse soutenue publiquement le **11 octobre 2021**,
devant le jury composé de :

Madame SILVIA HELENA PAIXAO ALENCAR

PROFESSEUR ASSISTANT, Universidade Federal de Minas Gerais,
Rapporteure

Monsieur LAURENT EYER

MAITRE DE CONFERENCES, Université de Genève, Rapporteur

Madame CATHERINE DOUGADOS

DIRECTEUR DE RECHERCHE, CNRS DELEGATION ALPES,
Examinatrice

Monsieur JONATHAN FERREIRA

PROFESSEUR DES UNIVERSITES, UNIVERSITE GRENOBLE ALPES,
Président

Monsieur JEAN-FRANÇOIS DONATI

DIRECTEUR DE RECHERCHE, CNRS DELEGATION OCCITANIE
OUEST, Examinateur



E quando miro in cielo arder le stelle;
dico fra me pensando:
– A che tante facelle?
[. . .] ed io che sono? –

G. LEOPARDI, *XXIII. Canto notturno di un pastore errante dell'Asia*

Ich habe fertig!

— G. Trapattoni

ACKNOWLEDGMENTS

My path to a PhD in astrophysics has been a bit tortuous, since in the beginning of my studies it was the only thing I was sure not to do. I would not have expected to end up doing it here in Grenoble either and I wish to thank my supervisor, Jérôme Bouvier, for offering me this opportunity. I could learn a lot of things from you during the ups and downs of this long marathon. I learned not only about science, but also a lot about myself. I also want to thank François Ménard, with whom I worked during my last year, who allowed me to embrace quite a different topic.

I am also grateful to the members of the jury, Catherine Dougados, Jonathan Ferreira, Laurent Eyer, Silvia Alencar and Jean-François Donati for having taken the time of reading my manuscript and giving helpful comments, and having come from very far for my defense, which cannot be taken for granted in these days.

A big thanks goes also to the members of the SPIDI team (aka the SPIDI mafia of the 2nd floor), who helped me adjust in Grenoble in and out of the lab. I am grateful to George for his patience in explaining me his complicated simulations, to Benjamin and Christophe for all their help on MCFOST and radiative transfer, to Kim for spending so much time on the phone with French service providers, and to William and Alana for the time spent together. I am happy to have taught you the basics of body language and the importance of good coffee. I will miss those moments around a warm mug in the morning.

I will not forget in this place all the good moments spent with the other PhD students at IPAG who came and left during my time here. Not only discussing about python in the lab (thanks Clément and Aloïs), but also skiing, hiking and partying around Grenoble. Thank you Flo, Oriane, Thomas, Cyprien, both Marions, Antoine, Jon, Benjamin, both Guillaumes, Arthur, and sorry if I forgot more names, I am bad at it.

Thank you Catherine, Sébastien and the Odyssey team for the time together. I really appreciated your prompt feedback on my work, whenever I was stuck on something. I wish to thank Didier not only for the helpful scientific discussions, but also for believing in me, when I was not able to do it myself. Even though you think you did not do much, it meant a lot to me.

There are many people who have helped me find my way to research, from a little town in Italy throughout Europe, and there is no space to name them all. Thank you for having listened to me and helping me understand what do I want, and how I can achieve it. I am grateful to my family, who always supported me through my studies, even though it meant to be so far from home. I will not forget here my extended family of friends, without whom I would have never managed to complete my studies so successfully. Despite the distance, you stayed by my side even when I was complaining (a lot!) about the tough moments in my PhD. I wish you all the best for your future, too. And, of course, thank you Dev, for bringing into my life the light that I searched for so long.

ABSTRACT

After more than fifty years of research on star formation, we know that low-mass stars build a protoplanetary disk during their early stages of evolution. From this, planetary systems are formed. While the large-scale properties and behaviors of such disks are nowadays observable, most of the physical star-disk interactions that occur at scales of a few stellar radii are challenging to resolve with the most powerful interferometers. Among others, models of magnetosphere-driven accretion can be probed indirectly by means of photometry and spectroscopy. Dusty accretion streams can produce, under certain conditions, an episodic fading of the stellar brightness. Such stars are called ‘dippers’. This thesis aims to study dipper stars in the Taurus star forming region, using extremely precise light curves as provided by the space mission *K2*.

First, I build the dipper sample among all light curves that are provided for the Taurus region. I then study the dippers’ periodicity with different techniques and the dips’ morphology. Combining the *K2* data with data from the literature and several archives, I provide stellar parameters in order to probe several explanations that have been proposed for the dipper phenomenon, first of all magnetospheric accretion. Confirming the results of previous surveys in different clusters, dippers in Taurus are very common, with a lower limit of their occurrence of $\sim 20\text{-}30\%$. Given the constraints on their observability and short lifetime, the mechanisms at their origin are relevant for a majority of classical T Tauri stars. Most of the dippers that show dips as predominant variability are quasi-periodic, with periods of a few days that support corotation of the dusty inner disk material and star. Magnetospheric accretion can account for most, but not all of the light curves in this dipper sample.

Finally, I apply radiative transfer modeling with the MCFOST code to JH 223, which is a prototypical dipper of the sample. Relevant information such as dust density, temperature, size of the occulting structure and its optical depth is degenerate in the observed light curves. The model of an optically thick, dusty sinusoidal wall is able to reproduce the observations of different irregular dips, with a variation of the dust content which is consistent with a moderate mass-accretion rate. Further improvements in the modeling of dusty accretion columns and the coupling with magnetohydrodynamical simulations will contribute to provide a full picture of this phenomenon in the near future.

RESUMÉ

Après plus de cinquante ans de recherche sur la formation des étoiles, nous savons que les étoiles de faible masse forment un disque protoplanétaire au cours des premiers stades de leur évolution. C'est à partir de ce disque que se forment les systèmes planétaires. Si les propriétés et les comportements à grande échelle de ces disques sont aujourd'hui observables, la plupart des interactions physiques étoile-disque qui se produisent à des échelles de quelques rayons stellaires sont difficiles à résoudre avec les interféromètres les plus puissants. Entre autres, les modèles d'accrétion induite par la magnétosphère peuvent être sondés indirectement au moyen de la photométrie et de la spectroscopie. Sous certaines conditions, les courants d'accrétion composés de gaz et poussière peuvent produire une diminution épisodique de la brillance de l'étoile. De telles étoiles sont appelées 'dippers'. Cette thèse a pour but d'étudier les étoiles de type dipper dans la région de formation d'étoiles du Taureau, en utilisant des courbes de lumière extrêmement précises fournies par la mission spatiale *K2*.

Tout d'abord, je construis l'échantillon de dippers parmi toutes les courbes de lumière qui sont fournies pour la région du Taureau. J'étudie ensuite la périodicité des creux avec différentes techniques ainsi que leur morphologie. En combinant les données *K2* avec les données de la littérature et de plusieurs archives, je fournis des paramètres stellaires afin de sonder plusieurs explications qui ont été proposées pour le phénomène des dippers, en premier lieu l'accrétion magnétosphérique. Confirmant les résultats des études précédentes dans différents amas, les dippers dans la région du Taureau sont très communs, avec une limite inférieure de leur occurrence de $\sim 20\text{-}30\%$. Étant donné les contraintes sur leur observabilité et leur courte durée de vie, les mécanismes à leur origine sont significatifs pour une majorité d'étoiles T Tauri classiques. La plupart des dippers qui présentent des creux comme variabilité prédominante sont quasi-périodiques, avec des périodes de quelques jours qui soutiennent l'hypothèse que le matériau du disque interne contenant de la poussière et l'étoile soient en corotation. L'accrétion magnétosphérique peut expliquer la plupart, mais pas la totalité, des courbes de lumière de cet échantillon de dippers.

Enfin, j'applique un modèle de transfert radiatif avec le code MCFOST à JH 223, qui est un dipper prototypique de l'échantillon. Des informations importantes telles que la densité de poussière, la température, la taille de la structure occultante et sa profondeur optique sont dégénérées dans les courbes de lumière observées. Le modèle d'un mur de forme sinusoïdale contenant de la poussière et optiquement épais est capable de reproduire les observations de différents creux irréguliers, avec une variation de la teneur en poussière qui est cohérente avec un taux d'accrétion de masse modéré. De prochaines améliorations dans la modélisation des colonnes d'accrétion contenant de la poussière et le couplage avec les simulations magnétohydrodynamiques contribueront à fournir une image complète de ce phénomène dans un futur proche.

CONTENTS

SYNTHÈSE EN FRANÇAIS / FRENCH SYNOPSIS	xiii
1 INTRODUCTION	1
1.1 Low-mass star formation	2
1.2 Photometric variability of young stars	6
1.3 Protoplanetary disks and their inner region	8
1.4 Accretion on T Tauri stars	10
1.5 Star-inner-disk interactions: dippers	13
1.6 Aim of the thesis	18
2 TECHNIQUES	21
2.1 Wavelet Analysis	22
2.2 Application to YSOs in Taurus	25
2.3 The MCFOST code	34
3 K2 LIGHT CURVES OF TAURUS DIPPERS	39
3.1 K2 Photometry	40
3.2 Periodicity Analysis	48
3.3 Light Curve Morphology	50
3.4 Stellar Parameters	60
3.5 Detailed notes on individual objects	68
3.6 What can we infer from dippers?	73
3.7 Summary	78
4 RADIATIVE TRANSFER MODELING WITH MCFOST	81
4.1 Testing a basic disk	82
4.2 Modeling JH 223 with an inner disk wall	86
5 CONCLUSION AND OUTLOOK	101
A APPENDIX	105
A.1 Additional figures - dipper light curves	105
A.2 MCFOST parameter files	113
B PUBLICATIONS	119
B.1 First-author publications	119
B.2 Co-authored publication	156
 BIBLIOGRAPHY	 187

LIST OF FIGURES

Figure 1.1	A portion of the Taurus molecular cloud as observed with LABOCA on the APEX telescope.	3
Figure 1.2	Pre-main sequence evolution from pre-stellar core to weak-line T Tauri star. . . .	6
Figure 1.3	Hertzsprung-Russel diagram of the Taurus region.	7
Figure 1.4	Disk structure and observational signatures of a Herbig Ae/Be star (Dullemond, 2010).	10
Figure 1.5	MHD simulation of magnetospheric accretion in a stable accretion regime. . . .	12
Figure 1.6	Magnetospheric accretion model developed for AA Tau (Bouvier et al., 1999). . .	14
Figure 1.7	Generalized magnetospheric accretion model (Bodman et al., 2017).	17
Figure 2.1	Principle of the Windowed Fourier Transform (WFT).	23
Figure 2.2	The complex Morlet wavelet.	24
Figure 2.3	Example of Fourier and wavelet power spectrum of the chirp signal.	26
Figure 2.4	Variation of the parameters of the complex Morlet wavelet applied to the chirp signal.	26
Figure 2.5	Wavelet Power Spectrum of DQ Tau computed using different parameters of the Morlet wavelet.	28
Figure 2.6	Examples of WPS of different variable stars in Taurus.	30
Figure 2.6	Examples of WPS of different variable stars in Taurus (cont.).	31
Figure 2.6	Examples of WPS of different variable stars in Taurus (cont.).	32
Figure 2.6	Examples of WPS of different variable stars in Taurus (cont.).	33
Figure 3.1	From top to bottom: example of an aperiodic dipper (HD 285893); a quasi-periodic dipper (JH 223); a dipper with a complex light curve (DK Tau).	42
Figure 3.2	From top to bottom: a spot-dominated light curve with aperiodic dips (EPIC246859790); a burst-dominated light curve with dips (CI Tau); a low-quality dipper candidate (IQ Tau).	43
Figure 3.3	Light curves for the dipper sample studied.	44
Figure 3.3	Light curves for the dipper sample studied (cont.).	45
Figure 3.4	Light curves of additional dippers dominated by another type of variability. . .	46
Figure 3.5	Light curves of potential dipper candidates that do not fulfill all selection criteria. .	47
Figure 3.6	Different examples of WPS for a time-resolved changing period (DK Tau) and a periodic dipper (GM Tau).	51
Figure 3.7	Periodogram and sinusoidal fit subtraction applied to the light curve of EPIC247885481. .	52
Figure 3.8	Fitting with periodic Gaussian pulses of the residual light curve of EPIC247885481 curve after the removal of the sinusoidal variability.	53
Figure 3.9	A few cycles of the light curve of JH 223.	54
Figure 3.10	Light curves of the double-peaked periodic dippers.	55
Figure 3.11	Example of the multi-peaked light curve of LkCa 15, color-coded for each rotation cycle.	56
Figure 3.12	Determination of the dips' amplitude with the example of HP Tau.	57
Figure 3.13	Dip width measured as FWHM of the binned light curve.	59
Figure 3.14	Temperature and bolometric correction conversion as in Pecaut and Mamajek (2013).	61
Figure 3.15	Left: comparison between V from the literature and the $\langle V \rangle$ from the SDSS. Right: comparison between V from the literature and from <i>Gaia</i>	61
Figure 3.16	Comparison between the A_V derived here from the $(V - J)$ colors compared to the literature values derived also from the optical.	63
Figure 3.17	JHK color-color diagram of the underreddened dipper sample.	64

Figure 3.18	HR diagram of the dipper sample with evolutionary tracks and isochrones from Baraffe et al. (2015).	66
Figure 3.19	Period of the dippers in comparison to the minimal rotation period required for a temperature ≤ 1500 K at corotation.	75
Figure 3.20	Dependence of dip width in phase units and period of the quasi-periodic stars in the dipper sample.	76
Figure 3.21	Dependence between dip width in units of phase and the corotation radius.	77
Figure 4.1	Temperature structure of a simple disk.	82
Figure 4.2	SEDs for three different disk inclinations.	83
Figure 4.3	Monochromatic images at different wavelengths and inclinations.	84
Figure 4.4	Dust density of the disk.	84
Figure 4.5	Optical depth map in four different directions.	85
Figure 4.6	Light curve obtained from the standard disk seen under 60°	86
Figure 4.7	<i>K2</i> light curve of JH 223.	87
Figure 4.8	Dips with smaller amplitude modeled with run 4.	89
Figure 4.9	Dips with larger amplitude modeled with run 5.	90
Figure 4.10	Monochromatic maps at 575 nm of run 4 at six different snapshots.	91
Figure 4.11	Monochromatic maps at 575 nm of run 5 at six different snapshots.	91
Figure 4.12	Light curves generated from all the runs.	92
Figure 4.13	Qualitative comparison of the optical depth variation of the wall.	92
Figure 4.14	Phase-folded light curve of JH 223 as observed in 2019 in the V , R_c , I_c bands by the LCOGT and the LT.	93
Figure 4.15	Color variation as $(V - I_c)$ and $(V - R_c)$ for the light curves from run 4, 5 and ground-based observations.	94
Figure 4.16	Color variation (a), synthetic light curve compared to dip 5 (b) and snapshot at 575 nm of run 14.	96
Figure 4.17	Color variation of run 17 (a), observed color variation for comparison (b) and synthetic light curve compared to dip 4 (c).	97
Figure 4.18	Optical depth map of the inner-disk wall for run 14 (a) and for run 17 (b).	97
Figure 4.19	SED of JH 223 as computed with MCFOST and observed with different surveys.	98

LIST OF TABLES

Table 3.1	Additional dippers that exhibit dips in their light curves as secondary variability.	43
Table 3.2	Variable YSOs that are dipper candidates of lower quality.	48
Table 3.3	Periods of the dipper sample.	49
Table 3.4	Morphological properties of the dips.	58
Table 3.5	Spectral types, effective temperatures and $VJHK$ photometry for the presented sample of 22 best dippers. JHK measurements are from <i>2MASS</i>	62
Table 3.6	A_V as measured with $V-J$ compared to the literature.	64
Table 3.7	Stellar properties of the dipper sample.	67
Table 3.8	Inclination of the star axis i_* from this study compared to observations of the outer disk i_{disk} from the literature.	69
Table 4.1	Stellar parameters of JH 223.	87
Table 4.2	Parameters and results from the different MCFOST runs.	88
Table 4.3	Variation of the slope s of the $(V - I_c)$ and $(V - R_c)$ colors depending on the maximal grain size a_{max} and the dust mass of the wall $M_{\text{d,w}}$	95

INTRODUCTION

Cette thèse étudie les étoiles situées dans la région de formation stellaire du Taureau, située ~ 140 pc de nous. Historiquement, cette région est l'une des plus étudiées, principalement en raison de sa proximité. C'est dans ces types de nuages moléculaires que la formation des étoiles a lieu. La théorie qui recueille le plus large consensus stipule que les régions plus denses du nuage peuvent induire un effondrement lorsqu'elles remplissent le critère de Jeans d'une masse critique. Le gaz qui s'effondre crée un noyau (protoétoile de classe 0), puis un disque d'accrétion épais (classe I). A un âge de $\sim 10^5$ ans, la jeune étoile entre dans la phase T Tauri classique (CTT, Classe II). Ce sont les objets d'intérêt de cette thèse. Les CTTs sont âgées de quelques millions d'années, montrent une forte activité stellaire, et sont entourés d'un disque protoplanétaire composé de gaz et de poussière (100:1) à partir duquel ils accrètent encore du gaz, et dans lequel les premières planètes se forment. Les TTs à lignes faibles (WTTs, classe III) ne présentent plus de signature d'accrétion. Leur disque se dissipe alors qu'elles se déplacent vers l'âge zéro de leur séquence principale.

Pour en revenir aux CTTs, elles peuvent être étudiées dans différentes régions de leur disque et à différentes longueurs d'onde : depuis la gamme des mm dans le disque externe froid avec, par exemple, ALMA, jusqu'à l'IR proche du disque interne, où la poussière chaude réémet à des longueurs d'onde plus courtes. Cette région en particulier est très difficile à observer, même avec des interféromètres puissants comme GRAVITY, car elle nécessite une résolution angulaire élevée et les cibles de très faible masse sont également peu lumineuses. Cependant, c'est dans cette région que l'interaction étoile-disque et l'accrétion ont lieu. De plus, il a été observé que plusieurs systèmes exoplanétaires présentent des planètes qui sont regroupées dans l'orbite de Mercure. Cela suggère que les planètes pourraient se former dans cette région, au niveau du bord interne du disque. Une façon d'étudier indirectement cette région est d'observer l'étoile centrale. Comme mentionné ci-dessus, les CTTs sont très actives et présentent plusieurs types de variabilité photométrique et spectroscopique, due aux taches stellaires froides, aux sursauts d'accrétion, à la binarité, aux transits planétaires et à l'extinction circumstellaire.

Cette dernière variabilité est d'un intérêt particulier pour cette thèse. Il a été observé que certaines étoiles présentent des creux dans leurs courbes de lumière, très probablement dus à la présence de poussière au niveau du disque interne occultant l'étoile. Ces étoiles sont appelées dippers. Les signatures spectroscopiques ont permis de les qualifier d'accréteurs modérés ou faibles. Les dippers ont été observés à ce jour dans de nombreuses régions de formation stellaire, ce qui en fait une population significative parmi les étoiles jeunes et variables. Leur occurrence varie entre 20% et 30% des étoiles entourées d'un disque. Différents scénarios ont été proposés pour expliquer l'origine de ce phénomène. Le scénario le plus souvent invoqué est celui de l'accrétion magnétosphérique. Le fort champ magnétique des CTTs est capable de tronquer le disque interne, où la pression magnétique est égale à la pression du disque. La matière s'accumule à ce rayon de truncation et est ensuite accrétée le long des lignes du champ magnétique. Les simulations magnéto-hydrodynamiques (MHD) prévoient deux flux de matière en forme d'entonnoir à symétrie centrale qui se terminent par une tache stellaire chaude à la surface de l'étoile en cas d'accrétion stable, sinon des langues de matière irrégulières qui frappent l'étoile plutôt autour de l'équateur. La poussière, présente dans le disque, est soulevée au-dessus du plan médian du disque et est capable d'obscurcir l'étoile lorsqu'elle croise la ligne de visée de l'observateur. Cependant, cela nécessite des températures inférieures à la température de sublimation de la poussière de 1500K . Cette condition ne peut être donnée qu'à la base de tels courants de matière ou gauchissements, et seulement pour les étoiles de type spectral tardif, qui sont suffisamment froides à leur rayon de truncation. Ceci contraint certains angles de vue pour l'observateur.

L'objectif de cette thèse est d'utiliser les courbes de lumière fournies par la mission spatiale *Kepler2* pour identifier la population de dippers dans la région de formation stellaire du Taureau et étudier leurs propriétés. Une autre partie est l'application du code de transfert radiatif MCFOST pour modéliser les propriétés de la poussière et du disque capables d'induire de telles courbes de lumière.

TECHNIQUES

L'une des premières étapes de l'analyse de l'échantillon du Taureau a été l'étude des périodicités. L'outil le plus couramment utilisé en astronomie à cette fin est l'algorithme de Lomb-Scargle, une approche basée sur la méthode de Fourier qui permet de détecter des fréquences dans des données échantillonnées de manière irrégulière. L'une des principales limites de cette méthode est l'absence de résolution temporelle dans son spectre de puissance. Cela signifie que l'observateur ne peut pas savoir si une certaine fréquence ou période est constamment présente dans le signal, et si ce n'est pas le cas, quand elle apparaît dans la série temporelle. L'analyse par ondelettes est une solution robuste à ce problème. Une ondelette est une onde sinusoïdale confinée dans le temps, qui permet de retrouver la résolution temporelle lorsqu'elle est transformée dans le domaine des fréquences.

J'ai appliqué cet algorithme aux 200 courbes de lumière des membres certains et supposés de l'amas du Taureau afin de connaître leurs périodes, et de savoir si des périodicités plus complexes apparaissent dans les données. Il en résulte que $\sim 80\%$ des étoiles sont périodiques, dont 20% présentent des périodes multiples. La grande majorité des périodes (95%) est compatible avec une tache froide à la surface stellaire. Les résultats soutiennent l'hypothèse que le disque interne est verrouillé en rotation avec l'étoile, et que les étoiles jeunes de type spectral M précoce sont les rotateurs les plus lents. Ces résultats ont été publiés dans Rebull et al. (2020).

Les observations indirectes de l'interaction étoile-disque à travers les dippers donnent un aperçu de la structure poussiéreuse qui occulte l'étoile, mais sont complètement dégénérées pour les propriétés de la poussière dans le disque interne. Pour cette raison, j'applique le code de transfert radiatif MCFOST afin de reproduire les courbes de lumière avec un modèle paramétrique.

Le code utilise une grille 3D cylindrique ou sphérique, et les propriétés de la poussière peuvent varier sur toute la grille en fonction de (r, z) , bien qu'elles soient considérées comme constantes dans une cellule donnée. Compte tenu de la structure du disque et des propriétés de la poussière, le code peut calculer la structure de température, la distribution d'énergie spectrale (SED), les images monochromatiques, l'émission de raies moléculaires et des propriétés telles que la profondeur optique et la distribution des grains de poussière. La structure du disque peut être paramétrique (cette thèse), ou peut être le résultat de simulations MHD, comme ce sera le cas dans les travaux futurs. Le code calcule la température dans chaque cellule de la grille en résolvant l'équation d'équilibre radiatif. Il utilise ce résultat pour résoudre l'équation de transfert radiatif le long de chaque rayon et pour générer des images monochromatiques.

COURBES DE LUMIÈRE K2 DES DIPPERS DE TAUREAU

J'ai cherché des dippers dans un échantillon de 179 membres certains et supposés du Taureau. J'ai identifié un total de 34 dippers, dont 22 sont des dippers non dominés par un autre type de variabilité. Cela représente $\sim 20\%$ des membres certains et supposés du Taureau et $\sim 30\%$ des membres du Taureau porteurs de disques. Les observations du Taureau mettent en évidence le caractère éphémère des dippers. Un exemple frappant est le prototype de dipper AA Tau, qui est devenu moins brillant et ne serait plus classé comme dipper à première vue. Les courbes de lumière des dippers peuvent persister sur des échelles de temps de quelques années ou même de quelques jours. Cela suggère fortement que les taux d'occurrence observés sont une limite inférieure à leur véritable occurrence parmi les CTTSs.

Le rapport entre les dippers périodiques et apériodiques est de 1:1, bien que la plupart des dippers étudiés en détail soient périodiques. La grande majorité des dippers apériodiques observés dans le Taureau est en fait dominée par un autre type de variabilité, principalement celle due aux taches froides.

Comme il a été observé dans d'autres études, les étoiles dippers sont de type spectral tardif K ou M, car la température de surface plus basse permet à la poussière de survivre dans le disque interne et de créer les dippers. Presque tous les dippers de l'échantillon sont des étoiles de faible masse ($< 1 M_{\odot}$) entièrement convectives, jusqu'à la limite des naines brunes. En accord avec les études précédentes, les périodes observées sont dans la gamme des périodes de rotation des CTTs de faible masse. Une des étoiles présente une courbe de lumière périodique avec des creux qui ne persistent que pendant quelques cycles de rotation ; une autre présente dans son spectre à ondelettes une période croissante au cours des observations K2. Les creux observés avec une tache froide chez EPIC 247885481 corroborent l'hypothèse que la matière poussiéreuse est située au rayon de corotation. Les températures dérivées à la corotation sont également compatibles avec la survie de la poussière et les taux d'accrétion sont dans la moyenne des CTTs. La plupart des dippers pour lesquels il a été possible de dériver une inclinaison stellaire sont vus sous un angle d'inclinaison modéré à élevé. Ceci est compatible avec le modèle d'accrétion magnétosphérique généralisé (Bodman et al., 2017), mais suggère que l'axe du champ magnétique stellaire est fortement incliné par rapport à l'axe de rotation ou que la poussière peut être optiquement épaisse plus haut que la base de la colonne d'accrétion (Nagel and Bouvier, 2020). D'autres mécanismes, comme les vents de disque poussiéreux et les instabilités d'ondes de Rossby, ne semblent pas convaincants pour expliquer les dippers observés sous faible inclinaison dans cet échantillon.

Une fraction des dippers périodiques présente des creux doubles ou de forme complexe, dont la structure varie avec le temps et dont les minima sont décalés d'un cycle à l'autre. Ces exemples méritent d'être explorés dans une analyse dynamique plus précise à l'avenir. Cela pourrait fournir plus d'indices sur l'origine de cette variabilité, qui pourrait être liée à des variations du taux d'accrétion, par exemple. Je trouve également une corrélation entre la largeur du creux en unités de phase (c'est-à-dire l'équivalent de l'extension angulaire de la structure occultante) et la période de rotation des dippers. Une possible explication est que les colonnes d'accrétion des étoiles à rotation plus lente ont une base plus large, reflétant peut-être une topologie différente du champ magnétique. Cette dépendance doit être vérifiée pour les dippers dans d'autres amas dans des travaux futurs.

MODÈLES DE TRANSFER RADIATIF AVEC MCFOST

La photométrie est capable de fournir des informations utiles sur la région du disque interne. Cependant, l'information sur les propriétés de la poussière est complètement dégénérée dans les observations. Pour cette raison, il est pertinent d'appliquer la modélisation du transfert radiatif pour tester des propriétés telles que la masse de la poussière, la taille et la forme de la structure occultante, et sa profondeur optique. MCFOST est capable de fournir des SEDs, des structures de température, des images monochromatiques et des cartes de profondeur optique. Dans cette section, je présente les résultats préliminaires.

J'utilise la courbe de lumière de JH 223 comme l'une des plus claires de l'échantillon. La courbe de lumière est quasi-périodique, présente une luminosité maximale constante et n'est pas affectée par un autre type de variabilité. Je choisis comme modèle le mur du disque interne proposé par Bouvier et al. (1999). Là où le disque est tronqué par le champ magnétique stellaire, un mur mince et poussiéreux varie sa hauteur entre 0 et h_{\max} suivant une fonction sinusoïdale. En tournant devant l'étoile, il est capable de produire des occultations périodiques. Ce modèle simplifié n'est pas en mesure, bien sûr, de reproduire la structure 3D complète des gauchissements et des colonnes d'accrétion. Cependant, c'est un bon début pour reproduire les creux.

Je produis des images monochromatiques dans la bande K2 et les intègre pour différents azimuts afin de générer des points synthétiques d'une série temporelle photométrique. Je choisis des paramètres standards pour le disque externe et un mélange de silicates astrophysiques pour les grains de poussière, et je fais varier l'inclinaison, la taille des grains et la masse de poussière dans le mur. Je suis capable de reproduire les creux avec une inclinaison de 70° , ce qui est compatible avec le modèle d'accrétion magnétosphérique. Le choix de ce modèle contraint fortement les inclinaisons autorisées autour de cette valeur. Différentes amplitudes des creux peuvent être modélisées avec une masse de poussière

variable. Cela change également la profondeur optique du mur, entre 1 et 6. Je peux également reproduire la pente de la variation de couleur de JH 223 telle que mesurée lors des observations de suivi depuis le sol. La variation de la masse de poussière nécessaire pour reproduire les petits et grands creux peut être utilisée pour estimer un taux d'accrétion pour l'étoile. Je dérive une valeur de l'ordre de $10^{-10} M_{\odot} \text{ yr}^{-1}$, ce qui est cohérent avec une naine M qui accrète modérément. Je compare également la SED du modèle avec les données de la littérature. La comparaison montre que les paramètres globaux choisis pour l'étoile et le disque ne correspondent pas bien aux observations. Cependant, cet aspect n'affecte pas la production de courbes de lumière synthétiques et peut être perfectionné dans un travail futur.

CONCLUSION ET PERSPECTIVES

L'interaction étoile-disque est un phénomène complexe, qui nécessite une approche multidisciplinaire pour démêler ses différents produits qui en résultent. La rotation stellaire, la topologie du champ magnétique, les processus d'accrétion et l'interaction des lignes de champ magnétique avec le disque interne sont autant de propriétés qui doivent être étudiées en détail pour obtenir une image complète. Dans ce contexte, les dippers peuvent aider à répondre à la question de savoir comment le disque interne est déformé près du rayon de truncation, en conséquence de l'interaction du champ magnétique stellaire avec la matière du disque.

Pour la partie principale de ma thèse, j'ai étudié les courbes de lumière de haute précision fournies par la mission spatiale K2 pour la région de formation stellaire du Taureau. Tout d'abord, j'ai identifié les dippers dans l'échantillon. L'occurrence des dippers que je trouve dans le Taureau, qui varie entre 20% et 30% selon le critère, est en accord avec les études précédentes. Ceci, combiné avec les durées de vie relativement courtes des dippers et les contraintes observationnelles pour la photométrie - principalement l'angle d'observation - souligne une fois de plus que l'occurrence que nous observons est une limite inférieure, et que ce phénomène est probablement pertinent pour une majorité d'étoiles à un moment de leur phase T Tauri.

Parmi leurs propriétés, j'ai étudié en premier lieu leur périodicité. Dans le but de démêler les nombreuses et complexes sources de variabilité, j'ai appliqué l'analyse par ondelettes aux courbes de lumière. Cette technique commence à être appliquée plus largement en astronomie seulement récemment (par exemple, Bravo et al., 2014; Sicilia-Aguilar et al., 2020). Les périodes des dippers sont, conformément aux enquêtes précédentes, dans la gamme des périodes de rotation stellaire, soutenant l'hypothèse que la matière poussiéreuse est située au rayon de corotation.

J'ai également combiné les données photométriques, astrométriques et spectroscopiques de la littérature pour dériver de manière cohérente et robuste les paramètres stellaires de l'échantillon étudié, afin de sonder les modèles proposés. L'inclinaison stellaire est le paramètre le plus important pour tester le modèle d'accrétion magnétosphérique, puisque la présence d'un dipper dépend de l'angle de vue des systèmes. Le modèle est capable d'expliquer la plupart, mais pas la totalité, des courbes de lumière observées, qui sont principalement vues sous une inclinaison modérée à élevée, avec de grandes incertitudes.

L'étude de la morphologie des creux confirme que de nombreuses questions sur ces colonnes d'accrétions poussiéreuses et les déformations du disque interne restent ouvertes, ce qui nécessitera un travail approfondi. La présence de plusieurs pics dans les creux soulève la question de savoir s'ils sont produits par différents éléments poussiéreux ou par un seul complexe, fortement instable. De plus, bien qu'ils aient une occurrence périodique, de nombreux dippers présentent des déphasages des minima entre les cycles de rotation. Une analyse plus détaillée sera nécessaire à l'avenir pour comprendre si ces décalages sont corrélés les uns aux autres, et quels mécanismes physiques du disque interne induisent cette perturbation. Enfin, je trouve que les creux larges et complexes sont corrélés avec une période de rotation plus grande, ce qui suggère que les étoiles en rotation lente produisent des colonnes d'accrétion ou des déformations du disque interne avec une plus grande extension angulaire. Il sera intéressant de vérifier si ces structures poussiéreuses plus grandes sont influencées par une topologie différente du champ magnétique.

Afin de surmonter la dégénérescence de l'information contenue dans les courbes de lumière, j'utilise le code MCFOST pour modéliser le transfert radiatif d'une des courbes de lumière. Je trouve qu'il est possible de modéliser les différents creux de JH 223 au moyen d'un mur de disque interne poussiéreux comme dans (Bouvier et al., 1999), avec les différentes amplitudes des creux induites par une teneur en poussière variable. Cette variation est compatible avec un taux d'accrétion raisonnable pour une étoile de faible masse. Le modèle est également capable de reproduire la pente de la variation de couleur telle que fournie par les observations au sol. Cependant, le mur du disque interne est un modèle simple et symétrique qui doit être amélioré pour être capable de reproduire des creux plus complexes, comme le montre l'absence de corrélations géométriques dans les observations des dippers.

Ces résultats sont préliminaires et, en tant que tels, nécessitent une analyse plus approfondie pour une modélisation plus robuste. Dans l'immédiat et dans la mesure du possible, l'espace des paramètres devrait être élargi afin de permettre plus de géométries du mur et différentes populations de poussière. Dans le cadre du projet SPIDI, il sera possible dans un futur proche de coupler les résultats de simulations MHD réalistes, qui fournissent la structure de densité du disque, avec MCFOST. Les modèles MHD seuls ne prennent pas en compte la profondeur optique et l'absorption par la poussière, ce qui est crucial pour simuler correctement les courbes de lumière des dippers. Cela permettra de produire un modèle réaliste au lieu d'un modèle paramétrique simplifié, ce qui conduira à une compréhension beaucoup plus complète du phénomène des dippers dans les systèmes d'interaction étoile-disque.

Les observations photométriques de suivi idéales seront multi-bandes et couplées à des données spectroscopiques et spectropolarimétriques simultanées. Elles permettront de mieux comprendre les durées de vie du phénomène des dippers et les échelles de temps de variation du taux d'accrétion. La spectropolarimétrie fournit, par le biais de l'analyse Zeeman-Doppler, un aperçu de la topologie du champ magnétique, qui influence la façon dont la matière du disque interne est accrétée sur la surface stellaire. Depuis la fin de la mission *K2*, *TESS* est capable de fournir des observations à haute cadence pour des cibles plus brillantes que celles observées avec *K2*. Les données optiques, combinées avec les données infrarouges, permettent d'étudier les variations de couleur de ces systèmes. Des lignes spectroscopiques choisies dans l'infrarouge et dans l'optique permettent de tracer le choc d'accrétion et de sonder le processus d'accrétion, en traçant le matériel d'accrétion, qui est supposé obscurcir l'étoile pendant les creux photométriques. CHFT/SPIRou est un instrument sensible ($H \sim 10$ mag) qui observe dans l'IR en complément de CHFT/ESPaDonS dans l'optique et fournit déjà des résultats intéressants. Le développement d'instruments interférométriques contribuera également à mettre en lumière l'interaction étoile-disque à quelques rayons stellaires de l'étoile. VLT/GRAVITY a déjà fourni d'excellentes observations dans cette direction. Pour l'instant, l'instrument est limité dans sa sensibilité à $K \sim 10$ mag, ce qui signifie que les objets très faibles ne peuvent pas encore être observés avec cette résolution. GRAVITY+ vise à augmenter la sensibilité de 4 à 5 mag, ainsi que la couverture du ciel.

INTRODUCTION

Summary

1.1	Low-mass star formation	2
1.1.1	The Taurus star forming region and the milestones of star formation	2
1.1.2	From molecular clouds to the zero-age main sequence	3
1.2	Photometric variability of young stars	6
1.3	Protoplanetary disks and their inner region	8
1.3.1	Historical remarks	9
1.3.2	Disk structure	9
1.4	Accretion on T Tauri stars	10
1.4.1	Theory and simulations	11
1.4.2	Observational signatures	13
1.5	Star-inner-disk interactions: dippers	13
1.5.1	The first dipper: AA Tau	13
1.5.2	Dipper stars	15
1.6	Aim of the thesis	18

The way how our Solar system was formed is an ancestral question for mankind. In a way, it is a quest for our own origins. Astronomy and astrophysics have provided exciting, yet still incomplete, answers to how and where stars similar to our Sun are formed, where the elements of our world come from, how other planetary systems look like and how planets are formed around young stars. We know that young stars are surrounded by a disk of gas and dust, which in part is accreted onto the star, in part condenses locally in the disk and grows to the size of planets. Both the processes of accretion and planet formation are the object of active research. This thesis represents a step towards the understanding of the interaction between the young star and the inner part of its protoplanetary disk. Although big improvements are being made in the interferometric techniques required to directly resolve this region, most of the information is still inferred indirectly, through photometry, spectroscopy and spectropolarimetry of the central star. The so-gathered knowledge will allow for a better understanding not only of the early stages of stellar evolution, but also of the physical processes which influence both the star and the inner part of the disk. This will provide also a base to determine how tight planetary systems within the orbit of Mercury form. They might sound exotic compared to our Solar system, but they seem to be fairly common in our stellar neighborhood. The following chapter resumes some of the topics which are relevant for this thesis, such as low-mass star formation, photometric variability of young stars, the structure of protoplanetary disks, accretion and, of course, dippers, which are the objects studied throughout this work.

1.1 LOW-MASS STAR FORMATION

Low mass, pre-main sequence stars are called T Tauri stars, from the star with the same name located in the Taurus star-forming region. Nowadays, we know that star formation takes place in molecular clouds, which are almost ubiquitous in the spiral arms of the Milky Way.

1.1.1 *The Taurus star forming region and the milestones of star formation*

Taurus, which is the region of interest for this thesis, is also one of the closest star forming regions, located at a distance of ~ 140 pc (e.g. Fleming et al., 2019; Galli et al., 2018). Its age is estimated to be $\lesssim 3$ Myr (e.g., Kraus and Hillenbrand, 2009; White and Ghez, 2001) and it hosts ~ 400 known members (Kenyon et al., 2008). The stars form along the filaments and clumps of the cloud (Fig. 1.1).

Historically, it is one of the most studied regions for star formation, partly due to its proximity. From the observations of Taurus over the last 80 years it became more and more clear when and how stars form, how they evolve and where planetary systems come from. For a review, see, e.g., Kenyon et al. (2008) and Kenyon and Hartmann (1995). Variable stars in Taurus were first spectroscopically characterized and linked to the molecular cloud by A. Joy (Joy, 1945, 1949). They were of late spectral type, variable in the optical and showed emission in the H I and Ca II spectral lines. Later on, it was discovered that they were up to 3 mag brighter than stars lying on the main sequence of the Hertzsprung-Russell diagram¹ (Herbig, 1952; Kholopov, 1951). Ambartsumian (1947) realized that T Tauri stars form also in OB associations. Since massive O-type stars have very short lifetimes (~ 50 Myr), he concluded that T Tauri variables had to be younger than 10 Myr. This fact marks the beginning of the research on star formation.

In the 1960's, it was observed that T Tauri stars were affected by UV excess (Smak, 1964; Varsavsky, 1960) and a strong IR excess, even after reddening correction (Cohen, 1973; Mendoza V., 1966, 1968; Rydgren et al., 1976, 1982). The former is a tracer of accretion (Sec. 1.4), the latter delivered evidence for the existence of protoplanetary disks, presented in Sec. 1.3. This young population has been extensively used to test evolutionary models (e.g. Baraffe et al., 2015; Chabrier et al., 2000; Feiden, 2016; Siess et al., 2000), as well as accretion (e.g. Calvet and Gullbring, 1998; Koenigl, 1991; Lamzin, 1995; Stahler et al., 1980) and planet formation (e.g., Currie et al., 2019; Dipierro et al., 2015; Keppler et al., 2018; Pinte

¹ The Hertzsprung-Russell represents the stars' luminosity as a function of their temperature. Most of the stars are distributed along the so-called main sequence. Stars that strongly deviate from this locus are either in their early or in their late stages of evolution.



Figure 1.1 – A portion of the Taurus molecular cloud (Barnard 211 and Barnard 213 filaments). On a background observed in the visible, the dust glows at $\lambda \sim 1$ mm as observed with LABOCA on the APEX telescope, while it appears as a dark cloud in the optical. Credit: ESO/APEX (MPIfR/ESO/OSO)/A. Hacar et al./Digitized Sky Survey 2. Acknowledgment: Davide De Martin.

et al., 2019; Sallum et al., 2015; Thalmann et al., 2016) in several star-forming regions. The following sections give an overview of low-mass star formation (see e.g., Stahler and Palla, 2004).

1.1.2 From molecular clouds to the zero-age main sequence

The first evidence for the existence of interstellar matter dates back to 1904 (Hartmann, 1904). By observing the spectrum of the binary star δ Orionis, Hartmann realized that a very narrow calcium line was not being periodically shifted according to the Doppler effect, as expected for spectroscopic binaries. He proposed that this line was not produced by the star, but by a cloud between the observer and the star, composed of calcium vapor.

Nowadays we know that interstellar matter is ubiquitous, in general cold with temperatures ~ 50 - 300 K, and made mainly of atomic hydrogen (HI) and helium. Hydrogen makes up around 90% of the mass of the interstellar matter and is mostly concentrated in the galactic plane of the Milky Way. Stars can form in large number in giant molecular clouds; individual stars can also form in Bok globuli, which are smaller, isolated dark clouds. In regions of higher density the interstellar medium (ISM) can appear in different forms: cold molecular clouds, dark clouds/globuli, hot HII regions.

It is in molecular clouds that star formation takes place. These are composed of molecular hydrogen ($\approx 63\%$), Helium ($\approx 36\%$), other molecules, free atoms and dust ($\approx 1\%$). It is still not fully understood

how these clouds form, although there is consensus that dust and molecules are produced by stars and ejected into the ISM via winds, jets, outflows and supernova explosions (feedback mechanisms). It seems that molecular clouds are dominated by turbulence. In general, molecular clouds are in equilibrium and stable. However, instabilities can be induced by strong winds or supernova explosions of nearby massive stars, or density waves in the spiral arms of the galaxy. These can lead locally to higher densities and a gravitational collapse.

JEANS CRITERION AND CLOUD COLLAPSE Let us consider a gas in hydrostatic equilibrium at rest, with constant density ρ , gravitational potential Φ , pressure P and a velocity $v_0 = 0$. The gas obeys to hydrodynamical motion, the continuity equation, the Poisson's equation and the equation of state of an ideal gas. By introducing a perturbation of the form

$$\rho = \rho_0 + \rho_1, \quad P = P_0 + P_1, \quad \Phi = \Phi_0 + \Phi_1, \quad v = v_1 \quad (1.1)$$

the solution of the equations is, for an isothermal perturbation that does not influence v , a wave of the form $\exp[i(kx + \omega t)]$, where k is the wave number, x the distance, ω the angular frequency and t the time, with

$$\omega^2 = k^2 v_s^2 - 4\pi G \rho_0, \quad (1.2)$$

where G is the gravitational constant. Hence, the perturbation propagates with the sound speed v_s . If only a small amount of mass is compressed ($k \rightarrow \infty$), the pressure of the gas will overcome the gravitational force and the system will go back to equilibrium. In fact, it takes a time t_s for a sound wave to travel to a distance R , $t_s = \frac{R}{v_s}$ and come back to re-establish the equilibrium, and a time t_{ff} for free fall due to the gravitational pull: $t_{ff} = \frac{1}{\sqrt{G\rho}}$. In this case, $t_s < t_{ff}$. For $k^2 < \frac{4\pi G \rho_0}{v_s^2}$ in Eq. 1.2, the solution for ω gives $\pm i\zeta$ and the perturbation grows exponentially, $\propto \exp(\pm \zeta t)$. The gravitational pull of the mass overcomes pressure and the molecular cloud starts collapsing. This defines the Jeans limit (1902):

$$k_J^2 := \frac{4\pi G \rho_0}{v_s^2} \quad (1.3)$$

and the Jeans length scale ($\lambda > \lambda_J$) of the molecular cloud for collapse:

$$\lambda_J := \sqrt{\frac{\pi}{G\rho_0}} v_s. \quad (1.4)$$

The Jeans mass is contained in a sphere of radius $R_J = \frac{1}{2}\lambda_J$ with an average density $\bar{\rho}$ and writes:

$$M_J = \frac{4}{3}\pi \bar{\rho} R_J^3. \quad (1.5)$$

The Jeans mass M_J can also be expressed with observables. First, let us introduce the speed of sound of an isothermal, ideal gas

$$c_s = \sqrt{\frac{\mathcal{R}T}{\mu}}, \quad (1.6)$$

where \mathcal{R} is the ideal gas constant, T its temperature and μ its molecular weight, and substitute in Eqs. 1.4 and 1.5. Further, for a clump in the molecular cloud that originates a star, with typical values $T \sim 10$ K, $\rho_0 = 10^{-19}$ g cm $^{-3}$ and molecular and neutral hydrogen and helium (molecular weight $\mu \sim 2.3$), Eq. 1.5 can be also written as:

$$M_J = 1.1 M_\odot \left(\frac{T}{10 \text{ K}}\right)^{\frac{3}{2}} \left(\frac{\rho}{10^{-19} \text{ g cm}^{-3}}\right)^{-\frac{1}{2}} \left(\frac{\mu}{2.3}\right)^{-\frac{3}{2}}, \quad (1.7)$$

under the assumption of a marginally stable sphere. The numerical factors of this equation can vary slightly depending on the different possible assumptions in the derivation. In general, the Jeans mass for a molecular cloud is on the order of $10^5 M_{\odot}$, thus close to its mass. The Jeans mass depends on density and temperature, hence it decreases for cooler and denser regions. These conditions facilitate the instability in regions of lower mass in the cloud. For a more complete and detailed derivation of the above formulae, see Kippenhahn et al. (2012).

Hoyle (1953) speculated that star formation in large molecular clouds is driven by the fragmentation of the cloud in smaller clumps, and not by gravitational contraction alone. The cores exist on average ~ 1 Myr before they collapse. During the collapse, the free-fall time t_{ff} is smaller than the sound timescale t_s . This means that only the inner core included in a sphere of radius $r = v_s t$ collapses, since the ‘information’ of the collapse does not have time to reach the outer layers.

The dynamical collapse of the dense core gives origin to a protostar. During its pre-main sequence evolution, a low-mass protostar goes through different phases, from class 0 to class III. A relevant issue of pre-main sequence evolution is how to transport the angular momentum of the rotating material of the cloud after it contracts. Its most visible effect is that the infalling material flattens forming a disk. A main difference between low-mass and high-mass star formation is the ignition of hydrogen burning already during the pre-main sequence phase in the high-mass case; this process heavily influences the development of a young, massive star. The following paragraphs and Fig. 1.2 summarize the evolutionary stages of low-mass stars.

CLASS 0: ACCRETING, EMBEDDED PROTOSTAR At this stage, the prestellar core is hidden in its molecular cloud and accretes from a gas envelope (e.g., Andre et al., 2000; Evans et al., 2009). A hint to the existence of an embedded source can be given by collimated outflows, a compact radio source or extended mm-emission. This phase is considered to be quite short ($\sim 10^4$ yr). The gravitational collapse drags the magnetic field lines in an hourglass shape and exerts a torque (magnetic braking). This allows to transport angular momentum from the inner to the outer part of the envelope (Galli et al., 2006). Both Class 0 and Class I objects eject mass in form of outflows and jets (Cabrit, 2002).

CLASS I: ACCRETING PROTOSTAR Due to the conservation of angular momentum, the accreting material around the star flattens and forms a thick disk. The contraction spins up the protostar and the dynamo effect induces a strong magnetic field. The star also ejects matter from the disk in form of jets, as well as a consequence of the star-disk interaction (e.g., Ferreira et al., 2006; Ray and Ferreira, 2021). This process allows to remove angular momentum from the disk. At this stage, the protostar has accreted most of the mass of the surrounding envelope. Class I objects (Adams et al., 1987; Lada and Wilking, 1984) are warmer than class 0 objects (a few ~ 100 K), therefore they can be observed in the mid- ($5 < \lambda < 40 \mu\text{m}$) and far-IR ($40 < \lambda < 250 \mu\text{m}$). The age of such an object, in general, does not exceed 10^5 yr.

CLASS II: CLASSICAL T TAURI STAR After the dissipation of the envelope, low-mass (i.e., $M < 2M_{\odot}$) stars enter the T Tauri phase. The star is still accreting from a protoplanetary disk made of gas and dust, with a dust to gas ratio $\sim 1 : 100$. In the disk, planets can already start to form, causing gaps, rings (ALMA Partnership et al., 2015; Huang et al., 2018a; Long et al., 2018) and spirals (Benisty et al., 2015; Huang et al., 2018b; Stolker et al., 2016) in the disk. The star can exhibit molecular outflows, launched in the inner region (e.g. Ray et al., 2007). The mass ejection is driven by the disk accretion (Cabrit et al., 1990) and allows to remove angular momentum from the disk (e.g. Zanni and Ferreira, 2013). The spectral energy distribution (SED) shows the stellar radiation, with a strong IR-excess due to the presence of circumstellar dust. The emission in the near-IR is a sign of the presence of warm dust in the inner disk, while the weak far-IR emission hints to the fact that the outer disk is cold. The spectrum of a T Tauri star is characterized by accretion signatures, mainly $H\alpha$ emission and UV excess (Bertout et al., 1988, and see Sec. 1.4). The star is fully convective and on its Hayashi track (Hayashi, 1961) in the HR diagram (Fig. 1.3). Depending on their mass, T Tauri stars spend 1-10 Myr in this stage. This thesis focuses on classical T Tauri stars (CTTSs).

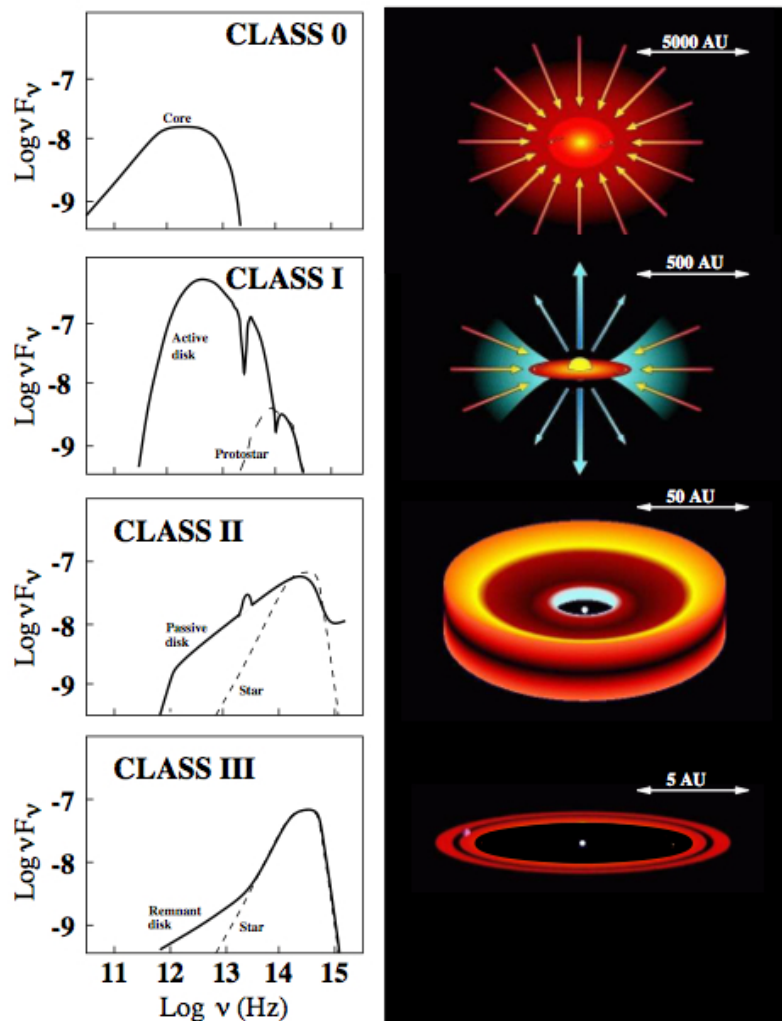


Figure 1.2 – Pre-main sequence evolution from pre-stellar core to weak-line T Tauri star. Left: SED during the different stages. Source: Andrea Isella's PhD Thesis (2006).

CLASS III: WEAK LINE T TAURI STAR When the star has accreted the matter from its inner disk, the IR excess almost disappears due to dust depletion. Now most of the stellar radiation is observable in the optical. Their names comes from the strongly reduced accretion signatures. The forming planetesimals start to clean up their orbits, and the disk is now called debris disk. The star still shows a strong stellar activity (e.g. stellar spots, x-ray emission). The star moves away from the Hayashi track to the zero-age main sequence (ZAMS), where hydrogen burning is ignited. The age of a low-mass star when it reaches the ZAMS is on the order of 30-40 Myr for stars of $1 M_{\odot}$.

1.2 PHOTOMETRIC VARIABILITY OF YOUNG STARS

From their youth until their latest stages, stars display a number of types of photometric variability. The variability can be intrinsic, i.e. driven by stellar activity (pulsation, eruptions, cold stellar spots...) or extrinsic (eclipsing binaries, accretion disks, planetary transits...). This section will focus on types of photometric variability commonly observed in young, low-mass stars.

The interest for variable stars in the western world was re-awakened after the observations of a supernova with the bare eye by Tycho Brahe in 1572, who believed it to be a newborn star. It was in

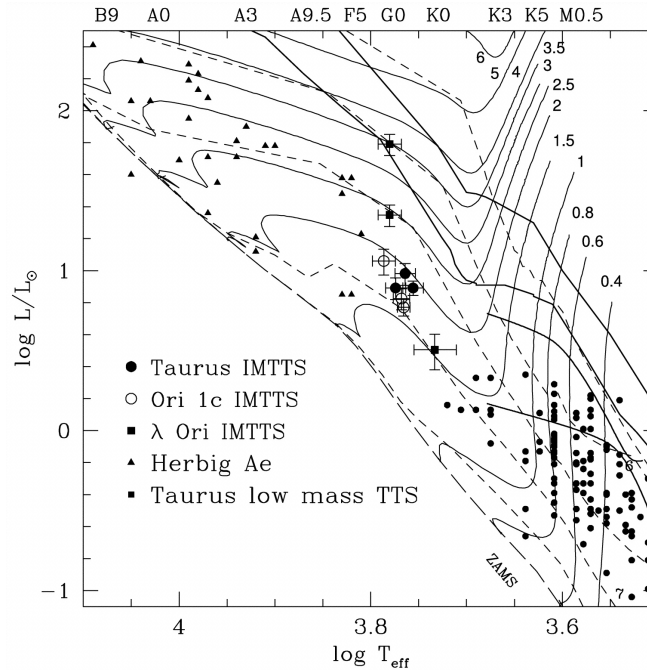


Figure 1.3 – HR diagram of the Taurus region and a few stars in Orion (Calvet et al., 2004), with evolutionary tracks by Siess et al. (2000). Each track describes the evolution of a star for a given mass. The isochrones (dashed lines) mark the positions on the HR diagram where all stars have the same age. The zero-age main sequence (ZAMS) is reached with hydrogen ignition. The solid lines indicate birth lines as predicted from different theoretical models. Low-mass TTSs (small black points) are fully convective before the turning point of their evolutionary track.

the XVII century, with Galilei’s development of the telescope, that astronomic observations could reach a new precision. A second revolution of astronomical observation was the application of the spreading technique of photography to telescopes in the late XIX century. Long exposure times allowed to unveil fainter objects and the plates kept a permanent record of the observations, besides the possibility of measuring the brightness of many stars at once. The beginning of the XX. century was marked by the introduction of photoelectric photometry, which is at the base of the modern CCD and allows much more precise measurements. Radio-astronomy was initiated by the study of the interference in phone calls of the Bell Phone Laboratories by Karl Jansky. With the company’s antenna, he was actually capturing the emission of Sagittarius A*, which is nowadays identified as the black hole in the center of the Milky Way. Modern radio astronomy makes use of large interferometers such as *ALMA* in Chile, *VLA* in the USA, and the international network *VLBI*. Also in the early 1920’s, photometric observations in the IR began. A major issue for these observations is the Earth’s atmosphere, which absorbs and blocks the radiation from space in broad bands, allowing to perform observations in absorption-free ‘windows’ (the *JHKLM* photometric system). Space observatories have revolutioned the field and have provided extensive IR surveys (e.g. *IRAS*, *Spitzer*), UV and x-ray observations impossible to obtain from ground (e.g. *IUE*, *EUVE*, *FUSE* in the UV and *ROSAT*, *XMM-Newton* and *Chandra* for x-rays) as well as continuous, extremely precise optical light curves (e.g., *MOST*, *CoRoT*, *Kepler*, *TESS*), which have allowed not only to detect thousands of exoplanets², but also to study stellar variability at much shorter timescales and amplitudes. This section mentions some of the variability types that can be observed in low-mass, young stars. For a more comprehensive review, see, e.g., Percy (2007).

COLD STELLAR SPOTS Cold stellar spots (e.g. Herbst et al., 1994) are region of the photosphere colder than the rest, that appear to be darker on the Sun and reduce the total brightness of the star. These are induced by a strong magnetic activity; on the spots, the magnetic field lines are normal with respect to the stellar surface. The magnetic field of the Sun of ~ 1 G gives origin to many, small spots

² The *Kepler* satellite found around 4400 confirmed planets, <https://exoplanets.nasa.gov/> (Visited on June 20, 2021).

(with a local field strength of some kG) that do not significantly reduce the total stellar brightness. For young stars, the situation is very different: the globally very strong magnetic fields in the order of ~ 1 kG generate giant spots that can cover almost half of the stellar surface. On the observational point of view, they produce a sinusoidal pattern in the light curve, as the spot appears on the line of sight and is driven away as the star rotates. Due to the star's differential rotation, their period is either equal or very close to that of the star, depending whether the spot is located at the equator or at higher latitude.

ACCRETION BURSTS AND HOTSPOTS For young stars sudden and irregular increases in the stellar brightness are considered to be driven by accretion (e.g., Bouvier et al., 1995; Calvet and Gullbring, 1998; Herbst et al., 1994; Koenigl, 1991). The accreted gas generates a shock on the stellar surface, visible in the UV and as variable veiling (see Sec. 1.4). These bursts have a duration of ~ 1 d and are mostly not periodic. However, some of them seem to be long-lived hotspots which correlate with stellar rotation (Stauffer et al., 2014).

PLANETARY TRANSITS AND ECLIPSING BINARIES In a binary or planetary system, the stellar brightness is periodically dimmed if the orbit of the companion star or planet crosses the observer's line of sight. When an object passes in front of the primary or central star, it produces a dip in the light curve, whose period and shape are constant. For binary stars, the amplitude of the variability can be on the order of $\sim 50\%$ for similar stars seen along the orbital plane. Although binaries are much more common among high-mass stars (Chini et al., 2012; Sana et al., 2014; Sota et al., 2014), they represent an important fraction of low-mass stars as well (e.g. Duchêne and Kraus, 2013). Exoplanets can be detected thanks to their transit, but the large contrast between the planet's and star's diameter requires very precise instruments installed on space telescopes. Recent space missions, such as *Kepler*, *CoRoT*, *TESS* have allowed a breakthrough in exoplanetary science, passing from a few hundreds massive planets in the early 2000's to thousands of known exoplanets. The amplitudes are extremely small and the dips are mostly flat, since the time to cross the stellar edge is much smaller than the transit time, during which the stellar brightness remains constant. The *Kepler* mission is responsible for most of the findings with the transit method up to date, allowing to reveal entire planetary systems (e.g., the Kepler-9 system as in Holman et al., 2010) and planets that are likely still in formation (e.g., V1289 Tau as in David et al., 2019).

CIRCUMSTELLAR EXTINCTION Class II and Class III objects are observable in the visible and are still surrounded by a disk, which is mostly made of debris in the later stages of evolution. If seen edge-on, the disk can completely absorb the light emitted by the star. In CTTs, the dust irradiated by the central star re-emits the light in the IR, causing a moderate to strong IR excess (e.g., Bertout et al., 1988; Cohen and Kuhl, 1979; Mendoza V., 1968). Instabilities in the disk can lift up material that can obscure the star. Forming planets might build clumps that induce a photometric variability. Accretion onto the star and tilts of the magnetic field axis are also believed to create warps or funnels in the inner disk, which occult the star and can be quasi-periodic in phases of stable accretion (dippers). Dipper stars are extensively presented in Sec. 1.5. Recently, another possible source of circumstellar extinction has been proposed in the form of dusty disk winds (for a more detailed discussion, see Sec. 1.5). Dust, dragged away with gas, is able to survive in a wind of temperatures of several 10^3 K (Tambovtseva and Grinin, 2008). The so floating dust in the disk is able to produce optical fading events and NIR brightening (Miyake et al., 2016).

1.3 PROTOPLANETARY DISKS AND THEIR INNER REGION

A major issue in a molecular cloud collapsing and forming a compact star is the conservation of angular momentum. The most efficient way to dissipate it is forming a circumstellar accretion disk. During the phases of pre-main sequence evolution, the disk is depleted of gas and dust and leaves behind a planetary system.

1.3.1 *Historical remarks*

Accretion disks surround not only pre-main sequence stars, but also extreme objects such as close binaries and black holes. It is for black holes that accretion disk properties were constrained in the first place (Shakura and Sunyaev, 1973). Accretion was proposed as a consequence of angular momentum loss in particles of a Keplerian disk. The friction in the viscous disk would lead particles to spiral inward. The idea of a viscous gas disk from which a young star can accrete was later explored by Lynden-Bell and Pringle (1974). This first model implied a flat and thin disk, whose radiation could be represented by a succession of blackbodies. This allowed to explain the observed SEDs for young stars. Adams and Shu (1986) showed in their calculations that protostars must be rotating in order to get an SED which matches the observations. Rotation would allow the presence of a flat accretion disk. For Kenyon and Hartmann (1987), a disk like that proposed by Lynden-Bell and Pringle (1974) did not have to be massive and thin: a flared shape could deliver the same observables with a much lower mass. The concept of flared disk was further developed by Chiang and Goldreich (1997). Bertout et al. (1988) proposed that T Tauri stars might also accrete from a circumstellar disk, and that this fact would both explain the observed IR excess (due to the re-processed stellar light) and UV excess at the boundary layer. Further studies on intermediate-mass Herbig Ae/Be stars, which are the T Tauri equivalent for masses between 2 and $8 M_{\odot}$ and spectral types earlier than F0, led to the proposition of high mass-accretion rates and a truncated disk, optically thin in the inner part, to account for the near-IR bump observed in the SED (Hillenbrand et al., 1992). This implied the evaporation of dust in the inner disk. The near-IR bump is evident rather in Ae/Be stars, but it is also present in the spectrum of CTTSs after the subtraction of the stellar spectrum (Muzerolle et al., 2003). Dullemond et al. (2001) proposed that, at least for Herbig Ae stars, the bump is associated with a puffed-up inner disk dim, located at the dust sublimation radius, that would cast a shadow on the rest of the disk.

All above models imply a viscous disk, which is dominated by turbulence and allows to transport angular momentum mainly through MRI (magneto-rotational instability). Observations of the so-called 'dead zone', a large region at the core of the disk where the MRI is suppressed, lead to prefer, as for today, the scenario of magnetised disk winds to transport angular momentum out of the disk (Blandford and Payne, 1982). The comparison of the disk occurrence among clusters of different ages (Haisch et al., 2001) revealed that the disk fraction decreases with age. Hence, the derived average disk lifetime is of ~ 6 Myr.

1.3.2 *Disk structure*

Disks of solar-type stars have a lifetime of 1-10 Myr, with a median of 3 Myr. The median ratio of disk to star mass is 0.9%, thus self-gravity in the disk is negligible (Williams and Cieza, 2011). Both gas and dust are present in a protoplanetary disk, with a ratio that can be assumed to be $\sim 100:1$. It is from this material that planets are formed during the disk evolution. These increase the complexity of the disk structure, by interacting with the surrounding material and building spiral arms in the disk, or by cleaning up their orbit and forming gaps. With increasing distance from the central star, the dust and gas in the disk become colder and colder and emit light from the near IR towards mm wavelengths. Fig. 1.4 shows how different disk regions impact the observations and mark the presence of a disk in the SED.

The size and mass of a circumstellar disk can strongly vary among pre-main sequence stars. In general, magnetospheric accretion (see Sec. 1.4) truncates the inner disk at a few stellar radii. The outer disk can extend to tens or more than 1000 AU. This huge difference in distance from the central star implies that the temperature of the disk strongly varies from the inner to the outer disk. A low-mass CTTS can present an outer disk as cold as a few 10 K, while towards the inner disk rim temperatures can increase to $\sim 10^3$ K, close to the dust sublimation temperature. At this point it should be remarked that the star presented in Fig. 1.4 is hotter than an average CTTS and sublimates dust at a larger distance.

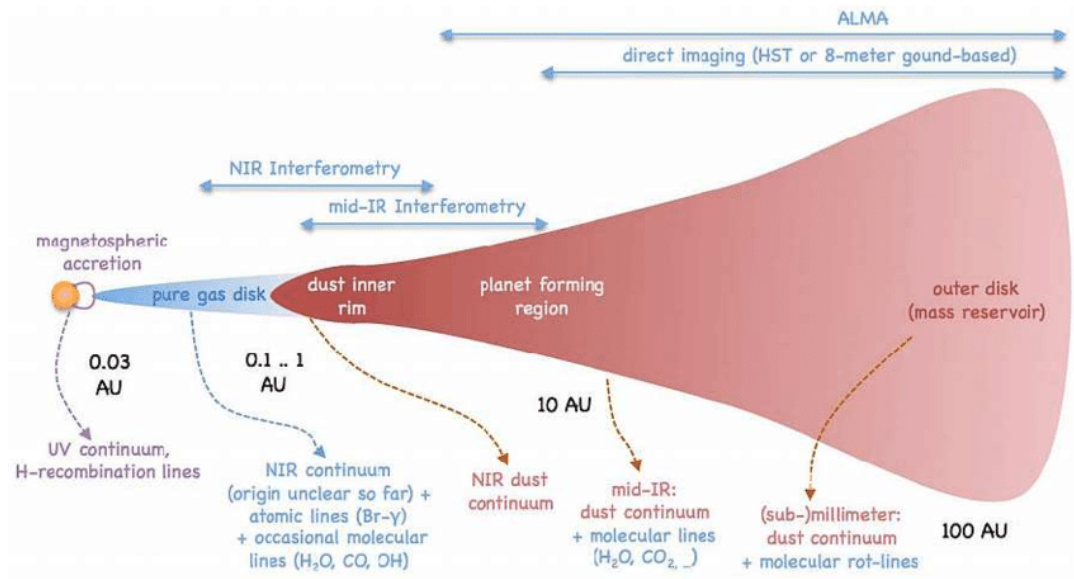


Figure 1.4 – Disk structure and observational signatures of a Herbig Ae/Be star (Dullemond, 2010).

The different temperatures at which dust emits delimit the instruments that can be used to probe each region. The cold, outer region emits in the sub-mm range and can be best observed with instruments such as ALMA. Mid-IR interferometry can probe the warm dust emitting in the mid-IR, in a region < 10 AU. Inner disk observations of CTTS with near-IR interferometry are currently a challenge, since at the same time the stars of low mass are relatively faint compared to Herbig stars and a high resolution is required. Currently, the inner disk region can be, in some circumstances, observed indirectly from the stellar photometry (see dippers in Sec. 1.5).

The region of interest of this thesis goes from ~ 0.02 AU (a few stellar radii) to ~ 1 AU. Due to the stellar proximity, the dust is warm and re-emits in the near-infrared. A huge leap forward has been made in the required instrumentation in the past few years, with instruments such as the Keck interferometer (10 m aperture and 85 m baseline), which allowed to measure the size of the inner disk in T Tauri stars (e.g. Colavita et al., 2003; Eisner et al., 2007; Eisner et al., 2010), VLTI/AMBER (e.g. Vural et al., 2012), VLTI/PIONIER (baseline up to ~ 100 m) (e.g. Anthonioz et al., 2015), with an improved resolution of up to 3 mas, and finally VLTI/GRAVITY (Gravity Collaboration et al., 2017), which can observe even fainter stars. The two main issues of interferometry for the inner disks of T Tauri stars are the required resolution of milliarcseconds or less, and their faintness, since for interferometers a high spatial resolution goes along with a lower sensitivity. GRAVITY has provided very encouraging results in this direction (see, e.g. Bouvier et al., 2020; Gravity Collaboration et al., 2020; Liu et al., 2019). The exact inner disk structure of low-mass CTTSs is at the current time still object of research. The stellar magnetic field is strong enough to truncate the inner disk at the magnetospheric truncation radius, and the structure of the inner disk rim is directly influenced by the accretion process.

1.4 ACCRETION ON T TAURI STARS

During the core collapse in the molecular cloud, gravitation and conservation of the angular momentum are the main ingredients of accretion. In the earliest stages of protostellar evolution, the infalling matter

of the envelope tends to flatten to an accretion disk, while some matter is ejected in form of jets. The magnetosphere of the star drives at this point the accretion from the inner disk rim. This phenomenon is observed in nearly all CTTSs. The energy of the accreting gas is then radiated at the accretion shock on the stellar surface. Interferometry shows that for some T Tauri stars the accretion luminosity is even comparable to the star's luminosity (Dullemond, 2010). During the CTTS phase, a low-mass star accretes $\sim 10^{-8} M_{\odot} \text{ yr}^{-1}$ for 2-3 Myr. In this section, it is briefly presented how accretion is driven from the circumstellar disk on a T Tauri star from a theoretical and observational point of view. For a review, see Hartmann et al. (2016).

1.4.1 Theory and simulations

The stellar magnetic field is a vector of accretion for the star. First studies on the interaction between magnetic field and viscous disk of neutron stars showed that the magnetic field B cuts off the disk where the magnetic pressure is equal to the pressure of the infalling gas. Moreover, the coupling of the magnetic field lines with the Keplerian disk exerts a torque and is able to spin up and down the star (Ghosh and Lamb, 1978, 1979a,b). The possibility that CTTSs are still accreting from a circumstellar disk was first proposed by Bertout et al. (1988). The magnetic properties of CTTSs were constrained later on. A rotating magnetosphere of a star with a strong magnetic field (in the order of kG) disrupts the inner disk at a few stellar radii from the star and accretes the material along the closed field lines; the open field lines induce a strong disk wind (Camenzind, 1990; Collier Cameron and Campbell, 1993; Koenigl, 1991; Shu et al., 1994). Low-mass, pre-main sequence stars are fully convective in their Class II phase. The most common magnetic field configuration for T Tauri stars is a strong dipole. Depending on the evolutionary status, other magnetic field topologies are possible, but the dipole remains the dominant component further away from the star in most cases; moreover, a misalignment between the dipole axis and the stellar rotation axis seems to be very common (Gregory et al., 2012). Even when an octupole component is present, it decays much faster than the dipole. Therefore, in general the dipole dominates the star-disk interaction.

The matter from the inner disk can be accreted when the thermal pressure and ram pressure of the disk equal the magnetic pressure of the stellar magnetic field. At this point, the magnetosphere is able to truncate the disk at the so defined truncation radius R_{T} . Different physical criteria have been considered in the literature to derive the truncation radius (e.g., Pantolmos et al., 2020; Romanova and Owocki, 2015; Zanni and Ferreira, 2009), which all converge to a similar expression and merely differ by a numerical factor (for a more detailed discussion on the scaling, see Bessolaz et al., 2008). In the following, I assume $P_{\text{ram}} = 0.5\rho v^2 = P_{\text{B}} = B^2/8\pi$, where ρ is the gas density, v its velocity, and B the magnetic field strength. In spherical accretion, the magnetic field is: $B^2 = \dot{M}v/r^2$, where \dot{M} is the mass accretion rate and r the distance from the star (Bouvier et al., 2007a). By considering the energy conservation of the infalling gas, the free fall velocity can be expressed as $v_{\text{ff}} = \sqrt{2GM_*/R_{\text{T}}}$, which corresponds to the escape velocity. A magnetic field dipole decays as $B = B_*(R_*/r)^3$. Combining the two approximations, the truncation radius writes (Bouvier et al., 2007a):

$$\frac{R_{\text{T}}}{R_*} = \left(\frac{B_*^4 R_*^5}{2\dot{M}^2 GM_*} \right)^{\frac{1}{7}}, \quad (1.8)$$

which corresponds here to the Alfvén radius. Moreover, when there is such a misalignment between spin and dipole axis, the rotation of the disk provokes a twist in the magnetic field lines, which are dragged in the rotation. The magnetic pressure is not the same in the upper and lower part of the disk and the normal vector of the inner disk becomes tilted with respect to the rotation axis. This induces a disk warp (Lai, 1999; Terquem and Papaloizou, 2000).

Magneto-hydrodynamical (MHD) simulations confirm the possibility of magnetospheric accretion warping the disk (e.g. Romanova et al., 2013; Romanova and Owocki, 2015; Romanova et al., 2008). One of the main features of magnetospheric accretion is the locking of star and disk rotation through the magnetic field lines (Long et al., 2005). If there is no equilibrium, the magnetic field lines exert a torque and spin up or down the star. In every scenario, accretion can occur in a stable or unstable

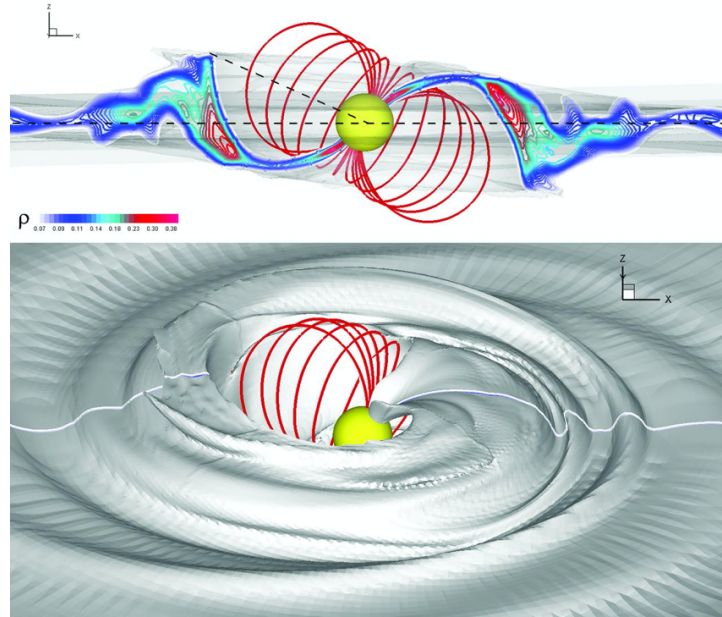


Figure 1.5 – MHD simulation of magnetospheric accretion in a stable accretion regime. Two symmetric accretion streams reach the stellar photosphere close to the magnetic poles. From Romanova et al. (2013).

accretion regime, where the boundary is given by the ratio between stellar rotation Ω_* and Keplerian disk rotation ω_K (Blinova et al., 2016). In a Keplerian disk in equilibrium, the gravitational pull equals the centrifugal force and the rotation is determined as $\omega(r) = \sqrt{GM/r^3}$.

In a stable configuration (stable accretion regime), two broad, stable and symmetric matter streams form from the disk and are accreted as funnel flows on the stellar surface, producing a hotspot on each hemisphere. In this scenario, the magnetosphere truncates the disk at a few stellar radii close to corotation, where the disk material rotates with $\omega \sim \Omega_*$. The most favorable magnetic field configuration for a stable accretion regime is a tilted dipole (Romanova et al., 2013). The base of the accretion column can host warm dust and be optically thick. The observer can see the star obscured either by the dusty warp or even by the funnel flow itself, where its density is at its lowest. In this case, the extent of the magnetosphere nearly coincides with the corotation radius, $R_T \approx R_{\text{cor}}$. Depending on the misalignment θ of the magnetic dipole axis with respect to the stellar spin axis, the height of this dusty warp h_w might reach to up to 30% of the distance between the warp and the star. According to MHD simulations (Romanova et al., 2013), a maximum warp height is reached for $\theta = 30^\circ$, but $\theta \lesssim 20^\circ$ still produces a warp able to occult the star. Stars that exhibit this kind of occultations in their photometry are called dippers (Sec. 1.5).

The extent of the magnetosphere does not necessarily coincide with the corotation radius. In case of $R_{\text{cor}} < R_T$, the inner region of the disk rotates with $\omega > \Omega_K$ (where Ω_K is the Keplerian velocity at corotation) and the star is in the propeller regime. The magneto-centrifugal forces lead to the ejection of disk material into an outflow (Romanova and Owocki, 2015).

During phases of enhanced mass accretion, in which the dipole component of the magnetic field decreases, the disk compresses the magnetosphere and reduces R_T (Romanova et al., 2013). For $R_T < R_{\text{cor}}$ the star is in the accretion regime and the magnetosphere rotates slower than the inner disk ($\omega < \Omega_K$). In case of a small or no misalignment θ between the stellar spin axis and the magnetic moment, the matter of the inner disk accumulates at R_T and the accretion rather occurs via unstable accretion tongues (Romanova et al., 2013), taller and thinner than funnel flows, that rather reach the stellar surface close to equator. They can be observable as irregular hotspots in the UV. As a result, the light curve will be rather stochastic and bursting.

The extent of the corotation radius directly depends on the stellar rotation period. For slow rotators, the corotation radius is located at a larger distance from the star and the inner disk so rotates faster

than the star. This facilitates the accretion via instabilities (Kulkarni and Romanova, 2008; Romanova et al., 2013). A misalignment between the magnetic moment and the rotation axis $\theta \gtrsim 30^\circ$ or a very strong magnetic field stops the instability.

1.4.2 *Observational signatures*

Spectra of CTTSs exhibit a range of characteristic features: beyond the photospheric absorption lines, chromospheric activity, emission lines and continuum emission (optical and UV excess). The strong emission lines have been attributed to accretion, rather than winds (Hartmann et al., 1994). The lines most sensitive to accretion are hydrogen Balmer lines and HeI lines. Radiative transfer modeling has provided observational predictions for these signatures (e.g. Hartmann et al., 1994; Kurosawa et al., 2006, 2011; Lima et al., 2010; Muzerolle et al., 2001). Infalling material can be traced with red-shifted absorption components of emission lines such as H β or the NaI doublet. Despite being a tracer of accretion, the H α line has a complex structure and does not always show signs of matter infall.

The hotspots generated on the photosphere by infalling material are mainly detectable through continuum excess flux in the UV. It is also in the UV that most of the accretion energy escapes (Hartmann et al., 2016). Another tracer of hotspots is veiling (optical flux excess). As a result, a ‘blue’ continuum flux is added to the stellar spectrum and absorption lines shallow. In practice, the variation of the veiling related to the rotation of the hotspot can be estimated by measuring the equivalent width of affected lines or computing the ratio between continuum excess flux and photospheric flux. During the accretion process, the infalling material generates a shock and heats the photosphere below it; around half of the energy heats the post-shock region and the other half is sent back to the pre-shock region. The matter in the post-shock region cools down and is compressed to higher densities, while the pre-shock region re-emits the energy at longer wavelengths. In the spectrum, the heated photosphere contributes to the continuum at short wavelengths, the transition at the post-shock region emits in the Balmer jump and as a consequence, it contributes to the stellar continuum at shorter wavelengths. The same happens for the pre-shock region, which in addition contributes to the FUV continuum (Hartmann et al., 2016). Hotspots have larger densities ($10^{11} - 10^{12} \text{ g cm}^{-3}$) than cool spots. Zeeman-Doppler imaging shows that a few percent of the stellar surface are covered by hotspots (e.g. Donati et al., 2011).

1.5 STAR-INNER-DISK INTERACTIONS: DIPPERS

1.5.1 *The first dipper: AA Tau*

T Tauri stars display a wide range of variability, as presented in Sec. 1.2. At the end of the 90’s, the interest rose for AA Tau, a classic CTTS of late spectral type, with moderate IR excess and emission lines in its spectrum. The star was observed photometrically and spectroscopically (Bouvier et al., 1999). The light curve was dominated by broad, irregular dips, with a quasi-periodic occurrence. A striking characteristic was that the variability had almost the same amplitude in all optical bands. This implied that there was nearly no color variation in the optical bands during these fading events, with a tendency of the system to be bluer ($\Delta m \simeq 0.1 \text{ mag}$) when fainter. The very common variability due to hot or cold spots on the photosphere is, instead, associated with a color variation. Moreover, the same variability was observed in the infrared (*JHK* bands), but with a significantly smaller amplitude. The SED showed that an IR-excess was present during the whole cycle. The spectra hinted to the equivalent widths of the H α and H β Balmer lines being anticorrelated with the brightness variation. The radial velocities and the achromatic variability excluded the possibilities of a hot/cold stellar spot and of an eclipsing binary, while the correlation with the IR variability suggested that variable extinction due to circumstellar dust might play a role in the phenomenon. The period of the photometric variability was in accordance with the previously observed rotation period.

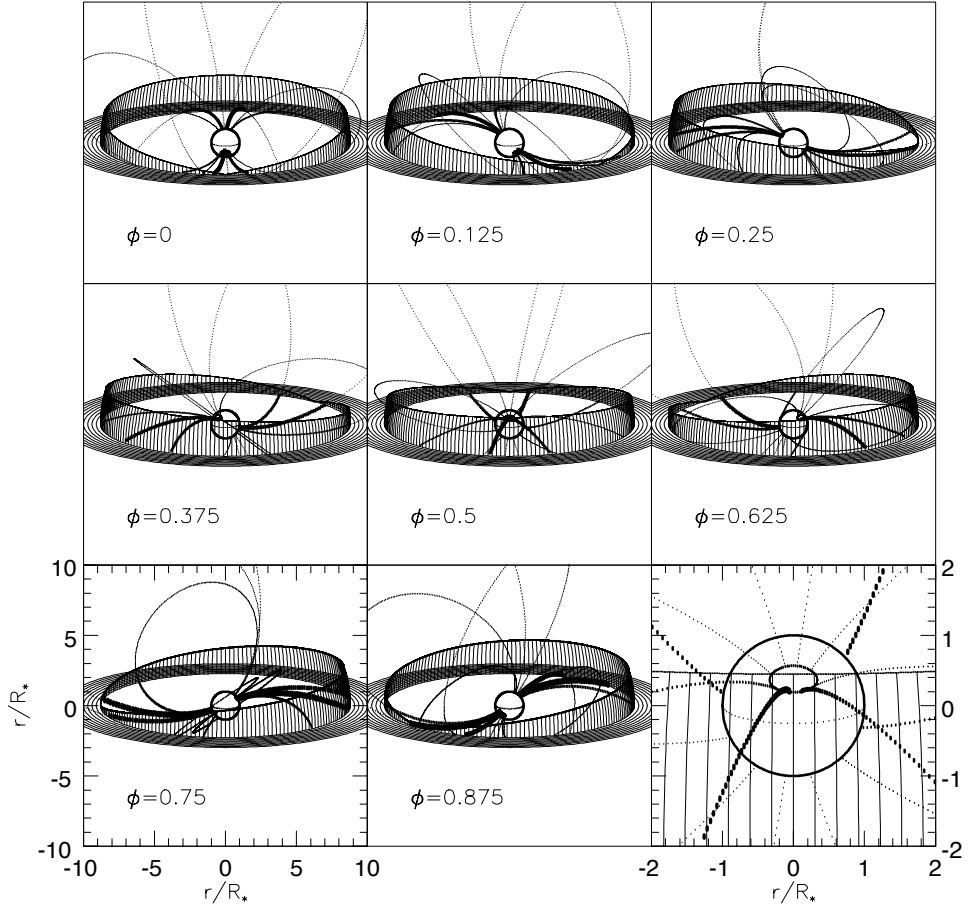


Figure 1.6 – Magnetospheric accretion model developed for AA Tau (Bouvier et al., 1999). The inclined dipole truncates the disk at $8.8R_*$. The figure shows the inner disk wall built by this interaction at different rotational phases ϕ . The star is mostly obscured at $\phi = 0.5$. The lower-right panel zooms in onto the star at $\phi = 0.5$.

All of these clues led to the proposition of an arched dusty disk warp, located at the inner disk and locked in corotation with the star, azimuthally more extended than π , that is seen under high inclination and has a height h which varies according to:

$$h(\phi) = h_{\max} \left| \cos \left(\frac{\phi - \phi_0}{2} \right) \right| \quad (1.9)$$

where ϕ is the azimuthal position and ϕ_0 the center of the brightness dip, associated with the (optically) thickest part of the warp. When, due to the disk rotation, the optically thick material crosses the line of sight of the observer, it obscures the central star and causes a dimming of the stellar brightness. This model is shown in Fig. 1.6. This kind of variability was later on called ‘dipper’, coming from the characteristic dips in the light curve. AA Tau later came into a dimmed state of ~ 15 mag and the global shape of the light curve is not dipping anymore (Bouvier et al., 2013; Roggero et al., 2021).

A later survey (Bouvier et al., 2003) studied the spectroscopic behaviour of AA Tau in more detail. For AA Tau, no strong veiling could be detected, although it was correlated with $(B-V)$ color and the He I line, with a time lag for the latter. The magnetospheric accretion model implies that the He I emission line forms at the base of the accretion column. The variation of the veiling was in accordance with the rotation period of AA Tau (Bouvier et al., 2007b). The $H\alpha$ and $H\beta$ lines were in emission and displayed a red- and a blue-shifted absorption, which were clearer in the $H\alpha$ profile. In general, blue-shifted absorption is linked to a wind that moves towards the observer, red-shifted absorption to accretion that moves away from the observer to the stellar surface. The tight correlation of the

red-shifted and blue-shifted absorption, the first related to accretion, the latter to a cool wind, was explained with the inflation of the magnetic field lines. This is induced by the different rotation velocity of the magnetic field lines and the inner disk (Bouvier et al., 2003). High-velocity red-shifted absorption appeared in both H α and H β during the photometric minimum (Bouvier et al., 2007b). This observation, along with the reddening experienced during the eclipses, sustained the hypothesis of magnetospheric accretion that produces a dusty disk warp.

1.5.2 Dipper stars

Since the identification of AA Tau as a dipper star, many surveys have tried to identify and characterize dippers in all possible styles and regions.

Observations

NGC 2264 The young stellar cluster NGC 2264 was observed with *CoRoT* in several campaigns (Alencar et al., 2010; Cody et al., 2014; McGinnis et al., 2015; Stauffer et al., 2015). The region is about ~ 3 Myr old and is located at a distance of ~ 760 pc (Dahm, 2008). The mean rotational periods of CTTSs in that region is of 3-4 d. Alencar et al. (2010) found AA Tau-like light curves to be widely present among CTTSs, with an occurrence rate of 30%-40% for disked stars and of 0% for naked photospheres, thus corroborating the hypothesis that the dipper variability is generated in the inner disk. The photometric period were in agreement with the rotational period, with the only remark that the fastest rotators in the cluster only showed a spotted light curve.

ORION The ~ 2 Myr old region, at around ~ 400 pc from us (Reggiani et al., 2011), was observed with *Spitzer* and other ground-based optical instruments by Morales-Calderón et al. (2011). The occurrence of dippers in Orion was of the order of only 5%, but the survey was also not designed to detect this kind of variability. Around one third of the identified dippers were periodic, while half of them displayed the same variability 10 years before, therefore suggesting a stable physical mechanism at their origin. AA Tau-like stars were associated with Class II objects, rather than Class I.

ρ OPHIUCUS AND UPPER SCO The two regions have a quite different age ~ 1 Myr (Andrews and Williams, 2007) and 10 Myr (Pecaut et al., 2012), respectively— and are relative close to our Solar system, with distances ~ 120 pc (Loinard et al., 2008) and ~ 140 pc (de Zeeuw et al., 1999), respectively. The region has been observed with *K2* (Ansdell et al., 2016b; Cody and Hillenbrand, 2018; Hedges et al., 2018). Hedges et al. (2018) find a dipper fraction of 20%, brought to 30% by Cody and Hillenbrand (2018). They point out that in the older Upper Sco a higher dipper fraction is observed in disk-bearing stars.

TAURUS Taurus has an age of about $\lesssim 3$ Myr (e.g. Kraus and Hillenbrand, 2009; White and Ghez, 2001) and is located at ~ 140 pc (e.g. Galli et al., 2018). The star-forming region hosts two differently spatially distributed populations (Fleming et al., 2019). Among the Taurus members observed with *K2*, Rebull et al., 2020, over 80% are periodic and around 60% exhibit IR-excess, an indicator of youth. Around 10% of all members and 20% of disked stars are classified as dippers.

Spectroscopy

As mentioned above, veiling is a tracer of accretion in form of hotspots on the stellar surface. McGinnis et al. (2015) investigated if veiling has some correlation with the dippers' photometric variability, since both are related to accretion. For the studied stars in NGC 2264, it turned out that indeed the brightness of bursters was directly correlated with veiling—the brightness increases due to the accretion shock—, while it was anticorrelated with the dippers' brightness, indicating that the star was obscured—probably by the base of the accretion column— while the hotspot was passing on the line of sight. When the veiling was not considerably varying, the photometric variability was either attributed to

a superposition of cold spots or a dusty base of an accretion column, with an accretion too small to generate an UV excess.

Pa γ emission is linked like H α to magnetospheric accretion, while HeI absorption at 1.803 μm is a tracer of the inner disk: red-shifted for infalling material, blue-shifted for inner disk winds. Br γ is a line used to probe directly the accretion column. Depending on the accretion tracers used in the inquiry, dippers are found to be moderate to faint accretors (e.g., Ansdell et al., 2016b; Venuti et al., 2014).

IR variability

Pre-transition disks, which host some optically thick dust at the dust sublimation radius, can show ‘see-saw’ variability in the mid-IR (anticorrelation of flux between short/long wavelengths). This is linked to changes in the height of the inner disk wall (e.g. Flaherty et al., 2012) and can be linked to dippers if it happens in the inner disk. This variability was observed in a few dippers in Upper Sco/ ρ Oph (Ansdell et al., 2016b). Ansdell et al., 2016b found a correlation in Upper Sco/ ρ Oph between the excess $E(K_s - W2)$ band at 4.6 μm and the dip depth. At that wavelength warm dust of 400-600 K can be observed; no correlation was found for W3 and W4, tracers of cooler dust in the outer disk.

Dipper models

The magnetospheric accretion model for AA Tau was generalized for dippers by Bodman et al. (2017) and remains the model that gains the largest consensus. The increasing number of surveys and collected data about dippers, however, challenge this model as unique physical explanation of the phenomenon. A major issue is the more and more common detection of dippers associated with almost face-on disks. In the following paragraphs, other alternatives are presented.

DUSTY DISK WARPS AND THE UNIFIED MAGNETOSPHERIC ACCRETION MODEL This is the model first attributed to AA Tau. For low-mass, pre-main sequence stars, the most common magnetic field configuration is the dipole, which dominates on the octupole far away from the stellar surface. Moreover, it seems that in most cases the dipole axis is inclined with respect to the the spin axis (Gregory et al., 2012). When there is such a misalignment, the rotation of the disk provokes a twist in the magnetic field lines, which are dragged in the rotation. The magnetic pressure is not the same in the upper and lower part of the disk and the normal vector of the inner disk becomes tilted with respect to the rotation axis. This induces a disk warp (Lai, 1999; Terquem and Papaloizou, 2000). The matter from the inner disk is then accreted onto the star following the field lines (Fig. 1.7). For accretion to be stable, the magnetospheric truncation radius R_T has to be close to corotation and $R_T < R_{\text{cor}}$ must apply (Bodman et al., 2017). If it is not the case, the material of the inner disk rotates with a different velocity with respect to the magnetosphere; this exerts a torque and spins up or down the rotation until a stable state is reached (Romanova and Owocki, 2015). The corotation radius is defined as the distance at which a Keplerian disk rotates with the same angular velocity ω as that of the star, ω_* . By considering in a stable orbit the gravitational pull equal to the centrifugal force,

$$\frac{GM_*}{r^2} = \frac{v^2}{r}, \quad v = \omega_* r, \quad (1.10)$$

the corotation radius is defined as:

$$R_{\text{cor}} := \left(\frac{P}{2\pi} \right)^{\frac{2}{3}} (GM_*)^{\frac{1}{3}} \quad (1.11)$$

where P is the rotation period of the star. For dippers, it is assumed that the warp occulting the star is located at corotation and that the photometric period of the dips is equal, or very close, to the stellar period (e.g. Alencar et al., 2018; Stauffer et al., 2015).

With the basic approximation that a dust grain located at corotation does not interact with the rest of the disk, the irradiation received by the star is reduced by a factor 4 (see, e.g. Bouvier et al., 1999).

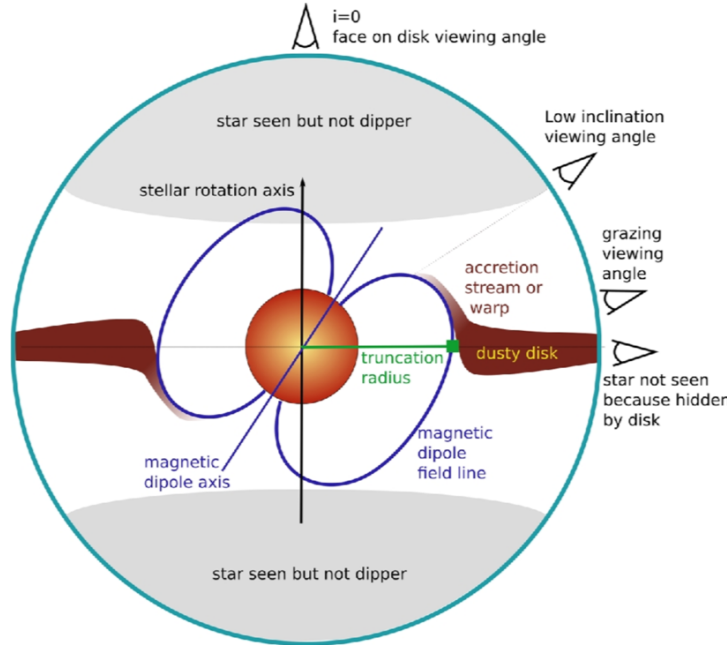


Figure 1.7 – Generalized magnetospheric accretion model. Depending on the viewing angle, the observer will see either the disk warp or the base of the funnel flow. For inclinations close to edge-on, the star will be hidden by its disk. Figure: Bodman et al. (2017).

Thus, considering the stellar luminosity $L_* = 4\pi\sigma R_*^2 T_{\text{eff}}^4$ (with σ as the Stefan-Boltzmann constant), the temperature at corotation writes:

$$T_{\text{cor}} = 2^{-\frac{1}{2}} T_{\text{eff}} \left(\frac{R_*}{R_{\text{cor}}} \right)^{\frac{1}{2}}. \quad (1.12)$$

For dust to survive at corotation, it must be given that $T_{\text{cor}} < T_{\text{subl}}$. To explain the high occurrence of dippers, Bodman et al. (2017) proposed a unified magnetospheric accretion model. Dust and gas pile up at the truncation radius before being accreted. If the magnetic dipole axis is tilted in comparison to the spin axis, this induces a warp at the inner edge of the disk. Dust is not supposed to survive in the hot accretion stream. Nevertheless, a sufficiently cold environment and low mass accretion rates could allow dust to survive at the base of funnel flow. This would be rather optically thin and could be compatible with a broader range of dip amplitudes and widths, and with lower viewing angles as well. The model is thus able to explain the occurrence of dippers down to moderate inclination angles of 50° . Still, warps and accretion funnel flows cannot account for dippers seen under low inclination. Moreover, dippers are sometimes associated with low mass-accretion rates, making it difficult to explain how enough material to produce observable dips can be accreted (e.g., McGinnis et al., 2015).

ACCRETION FUNNEL FLOW In addition to accretion-induced disk warps, Stauffer et al. (2015) invoke the accretion funnel itself for obscuring the star in certain cases. If the gas mixed with dust is lifted beyond the corotation radius at $\omega < \Omega_*$, the dust might spiral above the midplane before approaching the star and sublimate (Romanova et al., 2013). Nagel and Bouvier (2020) also propose that dust high in the accretion column becomes optically thick right before sublimation. If sufficient to obscure the star to observe dips, this might allow lower inclination angles to observe a dipper.

ROSSBY WAVE, MRI INSTABILITIES Small dips could be explained by instabilities in the disk, which create vortices that either enhance the surface density in a region or lift some material above the disk midplane (e.g. Lyra and Lin, 2013; Lyra and Mac Low, 2012). However, the amplitude of the dip caused

by such a vortex can reach up a few percent at best, thus being able only to explain few of the dippers with small amplitude. Ansdell et al. (2016b) claim that vortices induced by RWI can in some cases reach up to 1 rad of extension. Nevertheless, these are stable over hundreds of orbits and are not able to explain quasi-periodic or aperiodic dimming events. These should also be formed in areas too cold for the gas to become conductive and allow for MRI instabilities.

DUSTY DISK WINDS Another way of lifting dust away from the disk midplane is through dusty disk winds. These are spatially more extended than the base of accretion funnel flows and might shield the star's brightness at lower viewing angles (Ansdell et al., 2020). Magnetic field lines inclined with respect to the disk symmetry axis ($\theta \geq 30^\circ$) are able to accelerate matter away from the disk. Dust, dragged away with gas, is able to survive in a disk-driven wind at temperatures of several 10^3 K, due to the high inefficiency in heating the dust through collisions with gas particles and sputtering (Tambovtseva and Grinin, 2008). A mass accretion rate $\dot{M}_{\text{acc}} \geq 10^{-8} M_\odot \text{ yr}^{-1}$ is needed for intermediate-mass H Ae stars, so that the optically thick dust component can significantly reabsorb the star's radiation. Only the small dust grains are dragged by the disk wind, while the large-size grains remain in the disk mid-plane (Miyake et al., 2016). The so-floating dust in the wind is able to produce optical fading events and NIR brightening. Bans and Königl (2012) model the NIR $3 \mu\text{m}$ bump as produced by absorbed stellar radiation in a dusty wind. The launching position r_0 of this wind lies beyond the dust sublimation radius r_{sub} and can be close to the magnetospheric truncation radius r_T . A strong magnetic field (kG) is required to launch such a disk wind (Labdon et al., 2019). The model could be successfully applied to SU Aur in order to explain the NIR excess in the SED and the observed visibilities, with the constraint of a mass outflow rate feeding the disk wind of at least $10^{-7} M_\odot \text{ yr}^{-1}$ (Labdon et al., 2019). However, it seems that the dust present in the dusty disk wind can be seen in the optical only under high inclination (Vinković and Čemeljić, 2020). This would rule out dusty disk winds as explanation for low-inclination dippers.

INNER DISK MISALIGNMENT Ansdell et al. (2020) pointed out that dippers seem, in some cases, to have an inner disk misaligned with respect to the outer disk. Simulations have shown that a disk misalignment can be indeed induced by binarity (e.g., Facchini et al., 2013) and substellar companions (e.g., Facchini et al., 2018). Also a detailed study of the single star LkCa 15 (Alencar et al., 2018) finds that the inner disk is tilted with respect to the outer disk. This feature might be more common than previously expected among CTTs (e.g., Bouvier et al., 2020; Mayama et al., 2018).

PLANETS IN THE INNER DISK? Stauffer et al. (2015) investigated whether a planet located at the inner disk rim could form a spiral arm in the disk large enough to produce dips in the light curve. A massive planet can produce in some configurations a bump in the inner disk; nevertheless, it is not large enough to be detectable in most of the configurations.

OLD DIPPERS Recently, some 'old' dipper stars have been observed (Gaidos et al., 2019; Tajiri et al., 2020). These exhibit optical extinction events like normal dippers, have IR excess, but are older than 10 Myr. They might host 'extreme' dust-rich debris disks, which occur in 1% of the cases and have a strong IR excess (Balog et al., 2009; Kennedy and Wyatt, 2013). Hence, this event is quite rare. Gaidos et al. (2019) claimed that the variability was induced by disrupting planetesimals that form a clumped cloud that passes in front of the central star. Tajiri et al. (2020) suggest that aperiodic dippers are induced by randomly distributed dust clumps, from which planetesimals can form.

1.6 AIM OF THE THESIS

As discussed above, there is still much to learn about the most inner region of protoplanetary disks, where most of the stellar accretion physics takes place. A number of techniques and wavelength ranges are required to probe the processes at a few ~ 0.01 AU from the central star, going from IR interferometry, to UV, optical and IR photometry, spectroscopy and spectropolarimetry.

In this context, dippers offer a relatively easy way to indirectly observe the star-disk interaction. High-precision, high-cadency light curves of the *K2* space mission represent a powerful resource to study the physical mechanisms which induce the quasi-periodic occultations. Moreover, the discovery of exoplanetary systems with several, tightly packed planets with orbits close to the star suggest that they might form in or close to the region of interest for dippers. Since it is not possible at this moment in time to directly detect forming planets close to the inner disk rim, their possible interaction with the base of inner disk warps and accretion columns could open a way for their detection.

We are still not that far. To reach there, we first need to understand in more depth how dippers are generated, in order to disentangle the dipper signal from other stellar, disk or planet activity. This is challenging, since accretion processes are always to some extent stochastic and a generic model cannot reproduce the observations in detail. This thesis focuses on the dipper population of Taurus with two different approaches. First, the *K2* light curves will be studied to learn more about the hosting population and to assess the physical mechanisms compatible with the observations of dippers. In a second part, the radiative transfer code MCFOST will be applied to stars with similar features, in order to learn which dust and disk properties allow to produce a light curve as observed in nature.

TECHNIQUES

Summary

2.1	Wavelet Analysis	22
2.1.1	The Fourier transform and its limits	22
2.1.2	The wavelet transform	23
2.2	Application to YSOs in Taurus	25
2.2.1	The wavelet power spectrum for K2 observations	27
2.2.2	WPS of different types of variability	27
2.2.3	Results: periodicities of the Taurus sample	29
2.3	The MCFOST code	34
2.3.1	Radiative transfer	34
2.3.2	Disk parameters and code output	35

2.1 WAVELET ANALYSIS

With the aim of studying the periodicities of the stars in the Taurus sample, we chose to move towards time-resolved period analysis. The usage of such algorithms is more complex in comparison to traditional periodograms (for a review about the Lomb-Scargle periodogram see, e.g., VanderPlas, 2018), but it allows to determine not only the frequencies present in a signal, but also their occurrence in time and their variation, if present. Periodicities in YSOs can be caused by all types of variability presented in Sec. 1.2. Most of them are phenomena that are transient on different timescales, as stellar spots can disappear, circumstellar material can be depleted, stochastic accretion bursts might persist over several rotation cycles. In case of multiple periodicities present at the same time, some of them might not be persistent for the entire duration of the observation epoch, independently of the peak strength in the periodogram. For this reason, time-resolved time-series analysis is able to deliver more information. In the following section, an overview of wavelet analysis is presented.

2.1.1 The Fourier transform and its limits

The most used technique for time-series analysis is the Fourier transform (FT). It allows representing a variable signal in the time domain as a sum of frequencies in the frequency domain. The Fourier transform (FT) is an extension of the Fourier series, which expresses periodic functions as sums of sinusoids. The FT of a function $f(t)$ in the frequency domain writes:

$$\mathcal{F}f(\omega) = \hat{f}(\omega) := \frac{1}{\sqrt{2\pi}} \int_{-\infty}^{\infty} f(t)e^{-i\omega t} dt. \quad (2.1)$$

It decomposes the signal in the frequency domain and its power spectrum allows to recognize each frequency present in the original signal. As an example, the FT of a simple signal with a single frequency such as $f(t) = \sin(t)$ delivers a delta function $i\sqrt{\frac{\pi}{2}}\delta(\omega - 1)$ for $\omega > 0$. Its power spectrum is defined as:

$$S_{ff}(\omega) = |\hat{f}(\omega)|^2 \quad (2.2)$$

which would correspond to a thin peak at a frequency of 1 in this example. Fourier analysis requires evenly sampled data as a condition to decompose the signal. Gaps in the time series result in noise and distortions in the frequency spectrum. Moreover, sometimes frequencies in the signal might change over time, which the Fourier analysis in its simplest form cannot detect, because S_{ff} is a function of the frequency only, and not of time. This is due to the fact that the complex sinusoids employed to transform the signal are infinite in time. The windowed Fourier transform (WFT) can help in solving this issue by considering a ‘window’ (i.e., a slice) of the signal f and transforming only that section, translating the window along the signal (see Fig. 2.1). This allows to study whether the signal changes between different windows. Given the window $g(t)$, the windowed signal is defined as

$$f_t(s) \equiv g(s - t)f(s) \quad (2.3)$$

Its Fourier transform becomes

$$\mathcal{F}f(\omega, t) = \hat{f}_t(\omega) = \int_{-\infty}^{\infty} f_t(s)e^{-i\omega s} ds = \int_{-\infty}^{\infty} f(s)g(s - t)e^{-i\omega s} ds. \quad (2.4)$$

In physics, $g(t)$ is commonly chosen to be a Gaussian. The window is multiplied with a chop of the signal, transformed separately and then shifted along the signal. If g is centered in time and frequency, $\hat{f}_t(\omega)$ corresponds to the information of f around time t and frequency ω . The WFT underlies the uncertainty principle: the lower bound for the product of time and frequency resolution is

$$\Delta f \cdot \Delta \tau \geq \frac{1}{4\pi}. \quad (2.5)$$

For this method, the quality of the resulting analysis strongly depends on the chosen size τ of the window function. This determines the time and the frequency resolution a priori and might be inconvenient if both a good time and good frequency resolution are required.

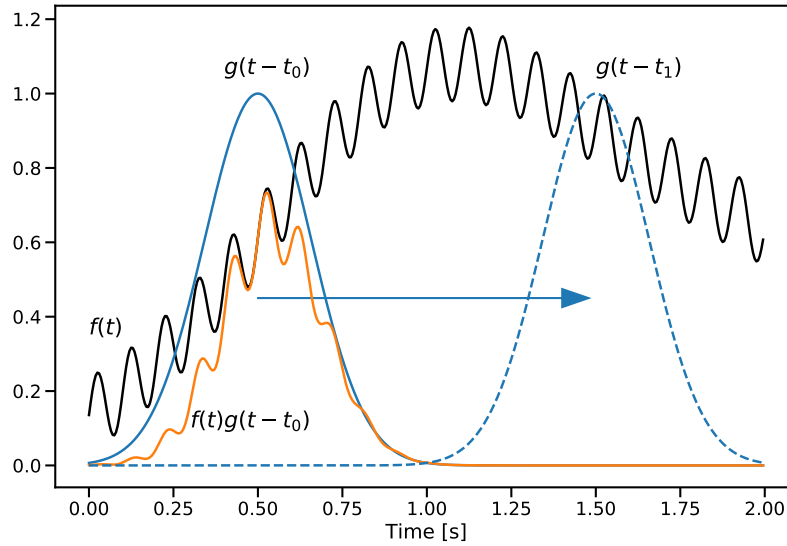


Figure 2.1 – Principle of the WFT. A Gaussian window $g(t)$ is multiplied with the function $f(t)$ before computing the FT. Then the window is shifted along the signal and the procedure is repeated.

2.1.2 The wavelet transform

The methods described in the previous section have major issues. The windowed Fourier transform has the issue of the fixed size of the window, and the Fourier transform delivers no time resolution at all. This issue can be solved by wavelets. The wavelet transform is similar in spirit to the WFT: one confined function is convolved with signal and Fourier-transformed, shifted with a certain time step and convolved again until the end of the signal. The power of the resulting spectrum is a measure of the correlation between the window and the chop of the signal. There are two main differences with the WFT: first, the wavelet is, in general, a sinusoidal function that is confined in time, which can have different shapes (e.g., Morlet, Mexican Hat, Daubechies...). Second, the wavelet can not only be shifted along the signal, but also stretched and compressed. This is the striking property of the wavelet transform (WT). The fact of stretching the wavelet increases its correlation with the shape of the signal at both high and low frequencies. As a result, the resolution in the frequency domain is not fixed as in the WFT, but variable and adapted to the frequency domain. In Fig. 2.3 this is exemplary analyzed for a chirp signal. For references and further readings, see Aguiar-Conraria and Soares (2010), Chun-Lin (2010), Daubechies (1992), Daubechies (1990), Farge (1992), Gao and Yan (2011), Kaiser (2011), Liner (2010), Torrence and Compo (1998), and Yakovlev (2005). Just as the Fourier transform, the WT can be continuous or discrete, depending on the applications. In this thesis, the continuous wavelet transform (CWT) has been used:

$$\text{CWT}_f(s, \tau) = \frac{1}{\sqrt{s}} \int_{-\infty}^{\infty} f(t) \psi^* \left(\frac{t - \tau}{s} \right) dt. \quad (2.6)$$

The *mother wavelet* $\psi(t)$ (and its complex conjugate ψ^*) is the wave confined in time, stretched and compressed according to the *scale* s and shifted with a *time step* τ along the time series. The normalization factor $\frac{1}{\sqrt{s}}$ ensures that the transformed signal has the same energy at each scale. The 2-dimensional wavelet power spectrum (WPS) is produced by a convolution between the wavelet and the signal, which is recomputed for each scale along all the time series. As for the WFT, also wavelets are subject to the uncertainty principle. Based on its shape, a certain wavelet has either a higher time or frequency resolution. The fact of being confined in the time domain results in a broader peak in the

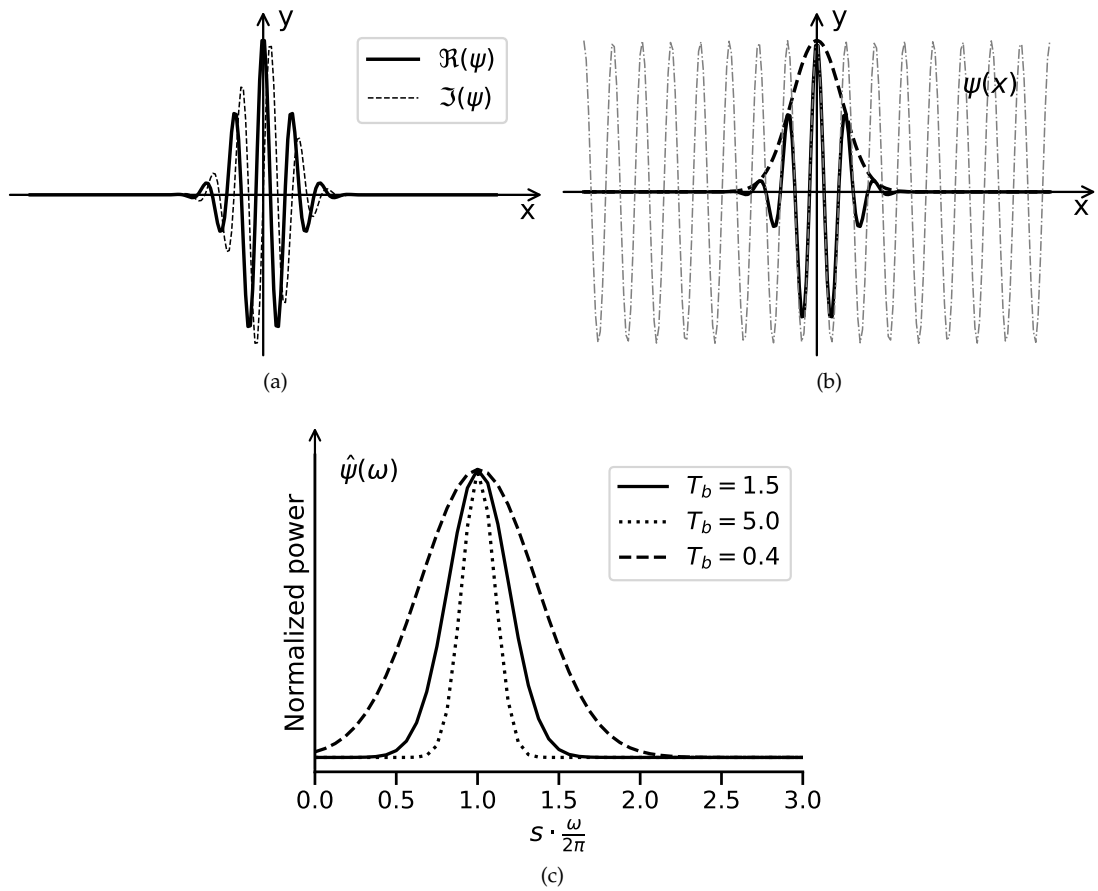


Figure 2.2 – The complex Morlet wavelet (a) contains a real and an imaginary component. It is defined (b) as complex wave (grey dashed line, real part) multiplied by a Gaussian (black dashed line). The variance of the Gaussian ($\propto T_b$) influences the wavelet’s time and frequency resolution: a Gaussian broader in time results in a narrower, more precise peak in the frequency domain (c).

frequency domain, which would be a δ -function in the case of the sinusoid of the FT. The complex Morlet wavelet is a good compromise in this aspect; moreover, its shape is close to the light curve variability we are interested in (see Fig. 2.2). The complex Morlet wavelet (e.g., Grossmann and Morlet, 1984) used in this work is defined as a superposition of a complex wave and a Gaussian, such as:

$$\psi(x) = \frac{1}{\sqrt{\pi T_b}} e^{-\frac{x^2}{T_b}} e^{i2\pi F_c x} \quad (2.7)$$

where the parameters F_c and T_b are the central frequency and the bandwidth parameter, respectively and x is a unitless time parameter (python package pywt, Lee et al., 2019). This is a time parameter due to the fact that the wavelet in the CWT takes as argument a time-shifted and stretched signal, and not the original signal itself (Eq. 2.6). The scales s are also unitless. The above formulation of the Morlet wavelet differs from the one in Torrence and Compo (1998), as they assume a Gaussian with unit variance – that can be varied here – and a frequency $\omega_0 = 6$. The advantage of freely setting the bandwidth and the central frequency is that one can customize the time and frequency resolution of the resulting wavelet plot, in order to highlight the position of a periodicity or to focus on the frequencies. This can be explained by the fact that a broader Gaussian in the time domain -thus a lower time resolution- is represented by a narrower peak in the frequency domain, which means higher frequency resolution. Changing the variance of the Gaussian modifies the wavelet's normalization and thus affects the signal reconstruction. However, this application is not relevant for the simple study of the signal's periodicities. Increasing the bandwidth T_b , i.e., the width of the Gaussian, in the time domain decreases the bandwidth in the Fourier domain, i.e., delivers a higher frequency resolution by losing time resolution. In the limit case of $T_b \rightarrow \infty$ the Morlet wavelet becomes a Fourier kernel. The central frequency should be near to the frequency of the signal of interest. Fig. 2.3 and Fig. 2.4 illustrate these properties with the example of the chirp signal, which has a steadily increasing frequency .

In the wavelet power spectrum (WPS), a certain scale s corresponds to a frequency F_s as:

$$F_s = \frac{F_c}{s \cdot dt} \quad (2.8)$$

The set of scales of the wavelet transform is equivalent to the custom frequency resolution of a periodogram. They can be set linearly going from s_0 to s_{\max} , where s_{\max} corresponds to the longest period of interest following Eq. 2.8. For a faster and more efficient computation of the WPS, it is better to choose the set of scales according to a power law:

$$s = s_0 2^{j\delta j}, \quad j = 0, 1, \dots, J, \quad \delta j = \frac{\log_2 \left(\frac{s_{\max}}{s_0} \right)}{J} \quad (2.9)$$

Where J is the total number of scales and δj is a measure of the resolution. The smaller δj , the higher the resolution.

Similar to the FT, the WT is also affected by edge effects, where the stretched or compressed wavelet is cut at the beginning and at the end of the time series, for the first (last) time steps. The cone of influence (COI) defines the range from which the WPS is affected by edge effects, which grow with the scale, as the wavelet is more and more stretched in time. The power spectrum contained in this region should not be considered as significant. Considering that for the Morlet wavelet the Fourier period λ is almost equivalent to the scale, as $\lambda = 1.03s$ (Torrence and Compo, 1998), the COI is plotted as $\sqrt{2}p$, where p is the period corresponding to a frequency. A central frequency different than 1.0 affects the COI as $\sqrt{2}pF_c$. Examples are provided in the next section.

2.2 APPLICATION TO YSOS IN TAURUS

An aim of this thesis is to characterize the variable stars in the sample of Taurus observed with the space mission K2 and to define a subsample of dipper stars. While the more detailed analysis of dippers is presented in the next chapter, I present here the application of wavelets to study the periodicities of all the stars of the sample. In Sec. 2.2.3 I provide a summary of the results published in Rebull et al. (2020).

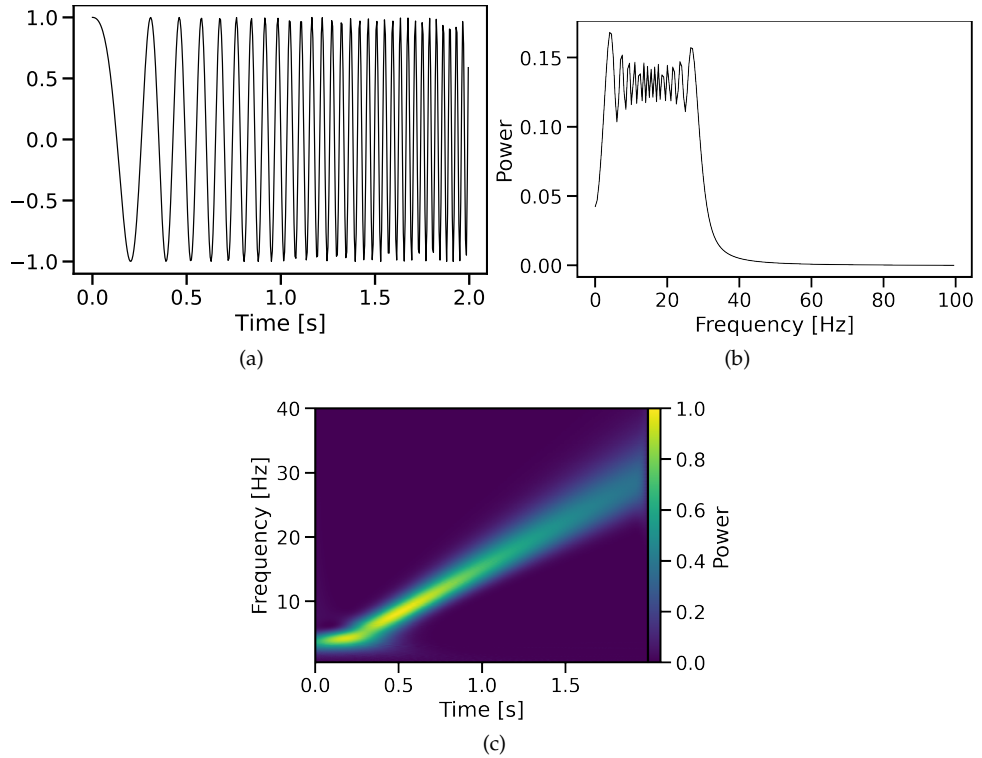


Figure 2.3 – Example of a signal (a) with constantly increasing frequency (chirp). The FT is not able to retrieve the frequencies present in the signal (b). The WPS (c) retrieves not only the frequencies but also their time evolution. For this example, the parameters are $F_c = 1.0; T_b = 1.5; s_0 = 5; s_{max} = 400$. The frequency of the wavelet does not vary; for each scale s the Morlet wavelet is stretched or compressed. The scale s corresponds to a pseudo-frequency F_s as in Eq. 2.8, which for this wavelet is practically equal to the physical frequencies (y-axes), but has, in general, to be first transformed to f . The wavelet is convolved with the signal for each time step τ and the resulting power is a measure of its correlation with the chop of the signal. Widely stretched wavelets cover the low-frequency range and vice-versa.

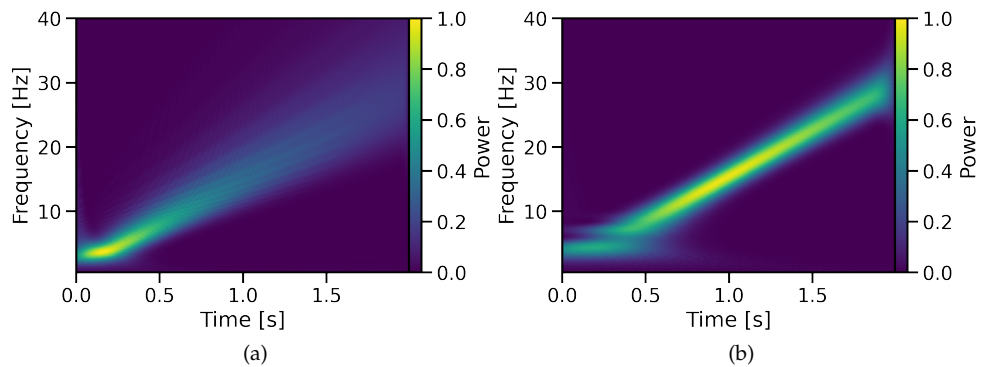


Figure 2.4 – The chirp signal is the same as in the previous figure and T_b is the parameter that has been varied. In (a) T_b is set to 0.4, which means a narrower Gaussian in the time domain –higher time resolution– and a broader Gaussian in the frequency domain –lower frequency resolution. A better frequency resolution than in Fig. 2.3 can be achieved for $T_b = 5$. However, the relevant time-localized information in the first chop of the signal gets lost. All three representations of the WPS are ‘correct’. They just enhance different features of the time series and the focus on time or frequency resolution depends on the purpose of the analysis.

2.2.1 *The wavelet power spectrum for K2 observations*

The *Kepler* satellite provided during the *K2* mission (Chapter 3) and over 2 observation campaigns around 800 light curves for stars located in a field that includes the Taurus star-forming region. An initial subsample of ~ 200 possible cluster members has been studied in the beginning and was refined later with more stringent criteria (see Chapter 3 and Rebull et al., 2020).

Space observations provide for the first time almost continuous observations, in which the only gaps are due to flagged out values. This improvement has encouraged astronomers to apply the WT to photometric observations. Although relatively new in this field, wavelets are already a very common method for biomedical signal processing and denoising in electrical engineering. Wavelet analysis has been applied to *K2* data to study the stellar rotation in asteroseismology (Bravo et al., 2014; García et al., 2014; Mathur et al., 2014), white dwarfs (Bravo et al., 2014; de Lira et al., 2019), dippers (Sicilia-Aguilar et al., 2020), planetary transits, stellar variability, pulsation, and binaries (Bravo et al., 2014). Elsewhere in the literature, it has been applied to the interstellar medium (Robitaille et al., 2014) and the observations of the solar corona (Auchère et al., 2016).

Since the WT requires evenly spaced data, the few missing points can be linearly interpolated. The cadence of ~ 29.5 min provides a very good time resolution for most of the variability types presented in Sec. 1.2. To observe the periodicity, a default value of $F_c = 1.0$ is a good starting point for timescales in the order of a few days. Given the length of the observations of ~ 70 d, the longest detectable period is of ~ 35 d, and still this would be indistinguishable from a pattern that recurs twice by chance. Following Eq. 2.8, the scales adapted for this purpose go thus from ~ 1 to ~ 1700 .

An example of the resulting WPS is shown in Fig. 2.5. A logarithmic representation on the y-axis is better to avoid a large smearing of the frequency resolution at longer periods. The uncertainty principle becomes clear when one looks at the periodicity ‘band’, far less precise than a periodogram’s peak. The power is saturated at the 99th and 3rd percentiles of its value to increase the contrast of the figure. The COI is represented as crossed lines and grows following the stretching of the Morlet wavelet.

In general, a 1D representation of the WPS can be achieved by averaging the WPS over time. The result is something similar to a periodogram. However, the frequency resolution of the WT is per definition lower than any Fourier-based method and for the purpose to merely identify the periods, a ‘classic’ periodogram is a better choice.

2.2.2 *WPS of different types of variability*

In the Taurus sample, all stars are variable. This is due to their stellar activity, which decreases during the main-sequence phase, and their protoplanetary disk. Fig. 2.6 illustrates the variability of a few of the Taurus stars and is explanatory to learn how to interpret the WPS.

For the morphological classification of the different types of variability, a few criteria are very useful: spots or spot groups induce a sinusoidal shape of the light curve, which can be complex for a large number of spots, but constant in shape and amplitude. Moreover, the light curves presented in this thesis are normalized to the flux median. Accretion bursts increase the stellar brightness, which goes above the median for the duration of the burst. Bursts are strongly irregular from timescales of around a week, down to hours or minutes. This adds apparent noise to the light curve. On the opposite, dippers are occulted by circumstellar material, thus the stellar brightness decreases compared to the ‘normal’ state. Their shape is also strongly irregular, but not down to as short timescales as bursters, thus the light curves are not, in general, as ‘noisy’. In a region such as Taurus, the stars are young and of low mass. Hence, eclipsing binaries are likely to be well detached and of Algol type, which means that they alternate sharp eclipses of the primary and secondary star to the normal brightness level. They are easy to distinguish from dippers, since their eclipses are regular and periodic. Planetary transits produce occultations with an amplitude of a few percent or less. Without pre-processing of the data, they are unlikely to be seen by the eye or by a periodogram. Finally, long-term variations or trends can be produced by the evolution of the stellar activity and of the disk. The length of the *K2* campaigns does not allow to infer much about them. These criteria are straightforward in case of only

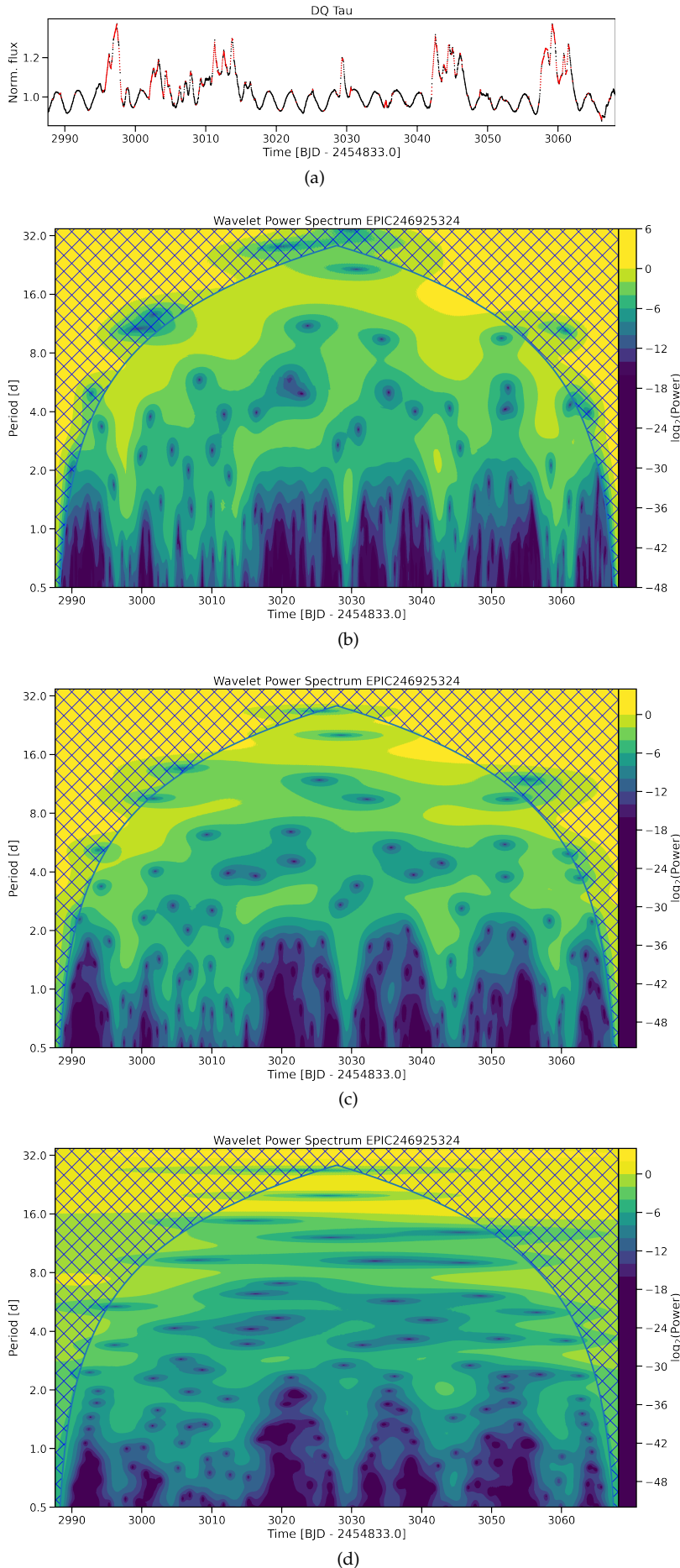


Figure 2.5 – WPS of DQ Tau computed using different parameters of the Morlet wavelet. (a) The light curve is linearly interpolated to be continuous (red points) and presents a periodic cold spot ($P \sim 3$ d) superimposed on accretion bursts, which occur every two weeks. (b) For a low value $T_b = 0.7$ the frequency resolution is strongly reduced and the time resolution enhanced. In the lower part of the plot, the punctual bursts produce spikes in the WPS. (c) WPS with $T_b = 1.5$, which is in general a good compromise between the two. The periodicity of the spot is perturbed by the bursts, which produce low-power regions in the ~ 3 d periodicity stripe and spikes at the bottom of the plot. The alias of the bursts' timescale at 8 d becomes visible as well. (d) For a high $T_b = 5.0$, the time resolution is almost completely lost and the spot's periodicity appears as an almost constant stripe. For all the power spectra the central frequency is set to 1.0. The COI which marks the region of the WPS that might be affected by edge effects. It is represented as blue crosses.

one variability present in the light curve. However, nature is often more complex than that and the classification can be more controversial. Cody et al. (2014) provide an overview on the morphological classification of the light curves of young stars as observed by space observatories.

All plots in Fig. 2.6 show on top the light curve, with the interpolated points in red, at the bottom the WPS with default values $F_c = 1.0$ and $T_b = 1.5$, on the right the CLEAN periodogram (Roberts et al., 1987). The two methods can be efficiently used in a complementary way, as the better frequency resolution of the periodogram can be used to estimate the exact period. In the upper right corner the common name –where available– is listed, along with the highest peak of the periodogram, the *Kepler* and *Gaia* magnitudes.

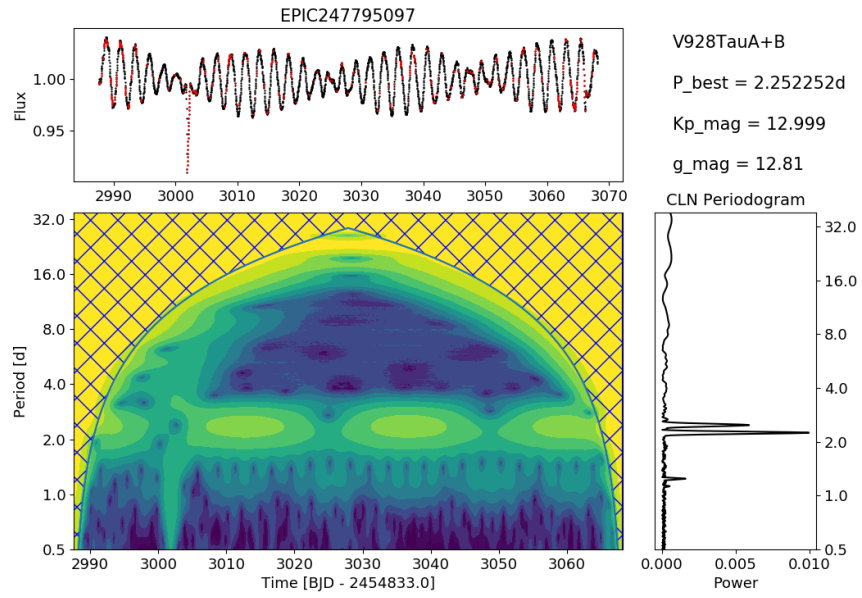
Panel (a) shows a star with a beat in its period. This indicates that the two frequencies in the signal are very close to each other, which leads to an amplitude modulation that varies following $\frac{f_1 - f_2}{2}$. Young stars can show this variation when two spots or spot groups are present at different latitudes, which rotate at slightly different periods due to the differential rotation of the stellar surface; another explanation for this can be nearly synchronized binaries. The WPS cannot resolve the peaks and its power varies periodically following the beat frequency. The stripe below (small peak in the periodogram) is the corresponding alias frequency. The star is also an eclipsing binary, as it can be seen in the sharp eclipse at $t \sim 3002$ d. The period of the binary is larger than the *K2* epoch. This ‘pulse’ with large amplitude provokes a spike in the WPS. The star in panel (b) shows a complex periodogram, which can be interpreted as 3 real periodicities being present at different moments in time. The morphology of the light curve is also complex, but it suggests cold stellar spots (sinusoidal pattern) superimposed to bursts. Panel (c) shows a star with two clear and distant peaks in the periodogram. We probably see the periods of each component of a non-resolved binary star. Two sudden brightness increases induce a spike in the WPS. DQ Tau –panel (d)– is a spotted and bursting star. It is presented in more detail in the previous section. The light curve in panel (e) is dominated by a long-term trend. A regular spot-like pattern has very low power in both WPS and periodogram, due to its amplitude. The star in panel (f) superimposes a long-term trend, a spot-like sinusoidal variation and binary eclipses. The second peak of the periodogram is an alias. Finally, a transient dipper is presented in panel (g). The dips only occur between $t = 3000$ and $t = 3030$ d, which is confirmed by the WPS. As long as they are present, they are quasi-periodic. The dipper stars of this sample are extensively discussed in the next chapter. The peak around ~ 18 d seems to be related to a repeating pattern in the light curve, rather than something physical.

2.2.3 Results: periodicities of the Taurus sample

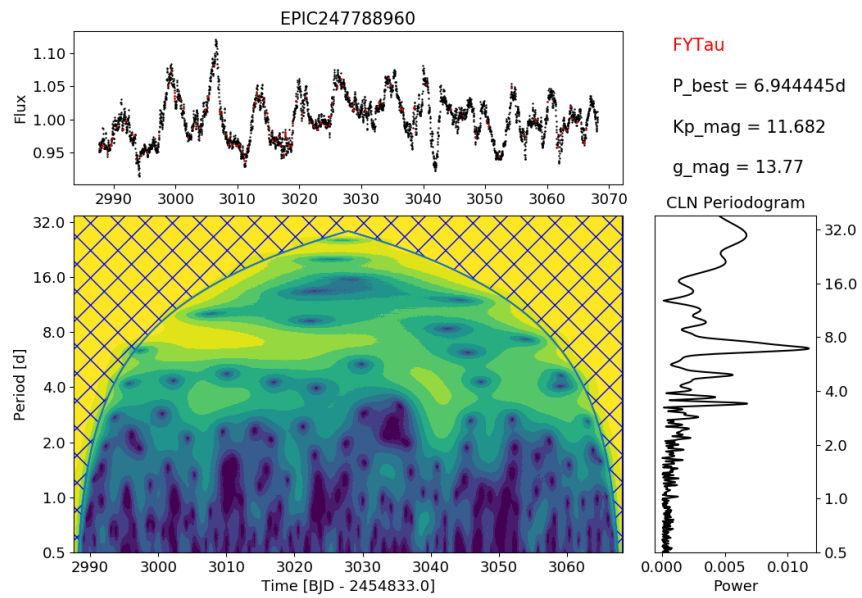
I made the study of the periodicities among *K2* Taurus members in the frame of a larger study on stellar rotation in the Taurus cluster (Rebull et al., 2020). This section summarizes its main results. Among all 851 light curves delivered by *K2*, 156 are considered high-quality members, and 23 are possible members. 38 of them are older (> 30 Myr) foreground stars, likely members of an independent association, Group 29 (Rebull et al., 2020, and references therein). The rest of the light curves is considered to be of non-members of Taurus. A more detailed discussion on membership is provided in Chapter 3.

We assessed the periodicities of the sample comparing the CLEAN periodogram (Roberts et al., 1987) (see Chapter 3), the Lomb-Scargle periodogram (Lomb, 1976; Scargle, 1982) and the WPS. Interestingly, the CLEAN periodogram was more performing than the Lomb-Scargle in resolving close peaks (beats). The WPS was helpful for its time-localization of the periods. For example, a sudden sinusoidal pulse with high amplitude in the light curve can produce a peak in a complex periodogram. This also increases the power of the WPS, but it becomes easily evident that this is not a real period. The WPS also helps to assess which period is related to the stellar rotation. Normally, stellar spots are used for this purpose and their period should be constant in the WPS.

Around $\sim 80\%$ of the members are periodic and 20% among them present multiple periods. Distant peaks in the periodogram can be often related to unresolved binaries, where each component has its own period. It is important to determine the amount of disked stars, the main indicator of stellar youth.

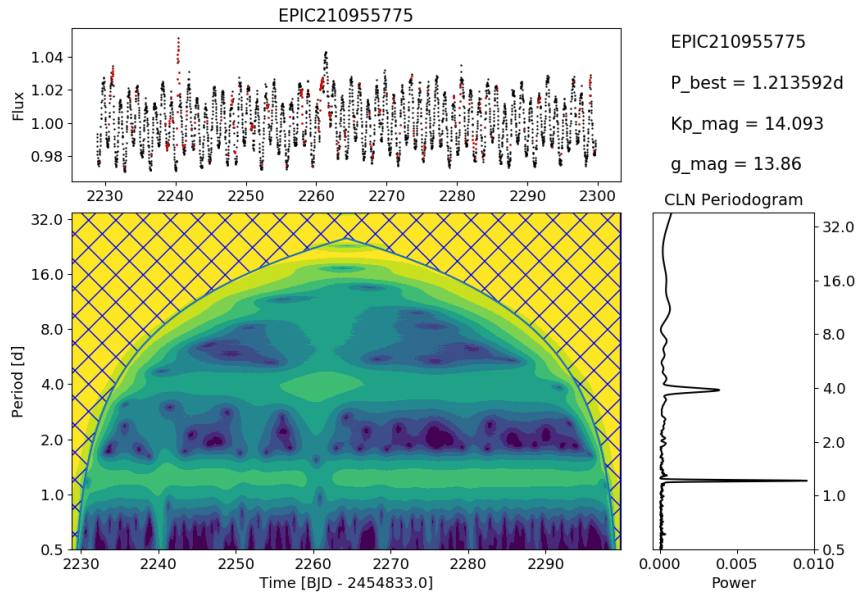


(a)

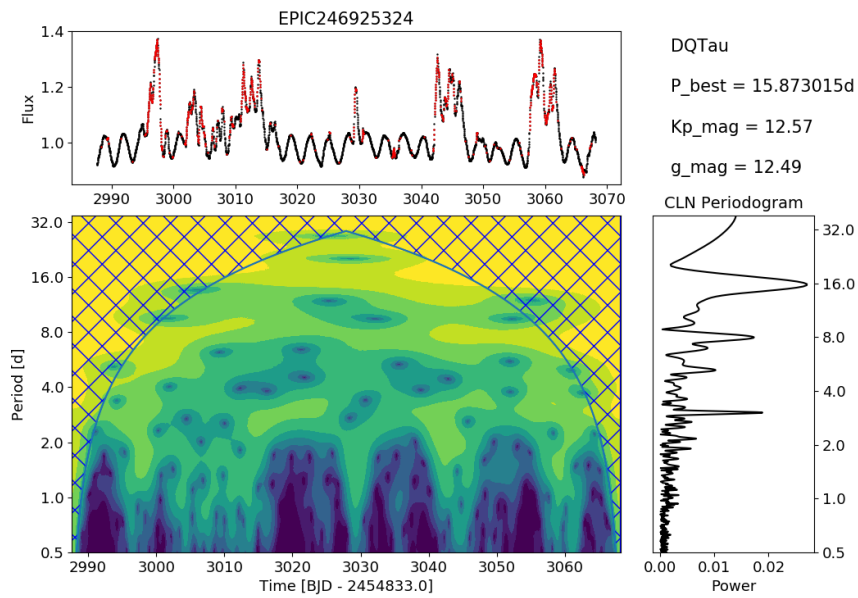


(b)

Figure 2.6 – Examples of WPS of different variable stars in Taurus.

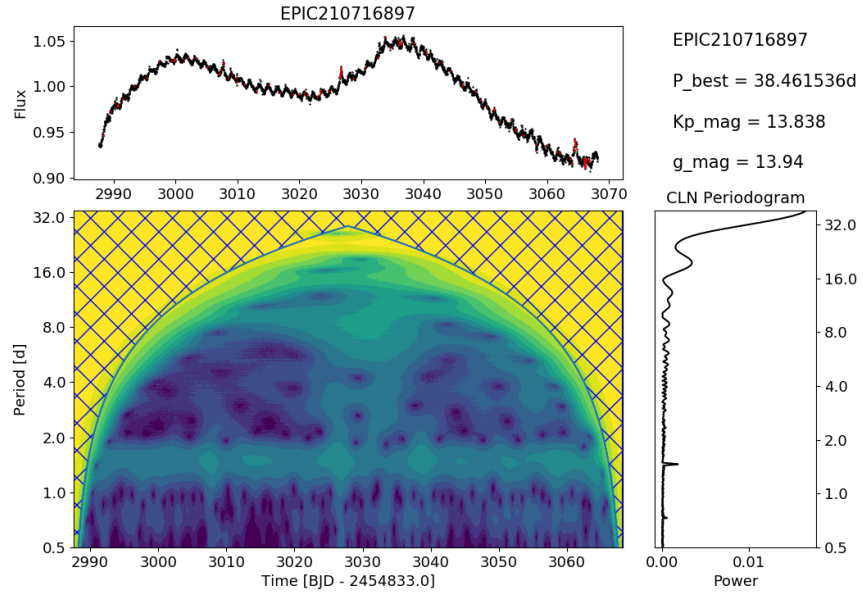


(c)

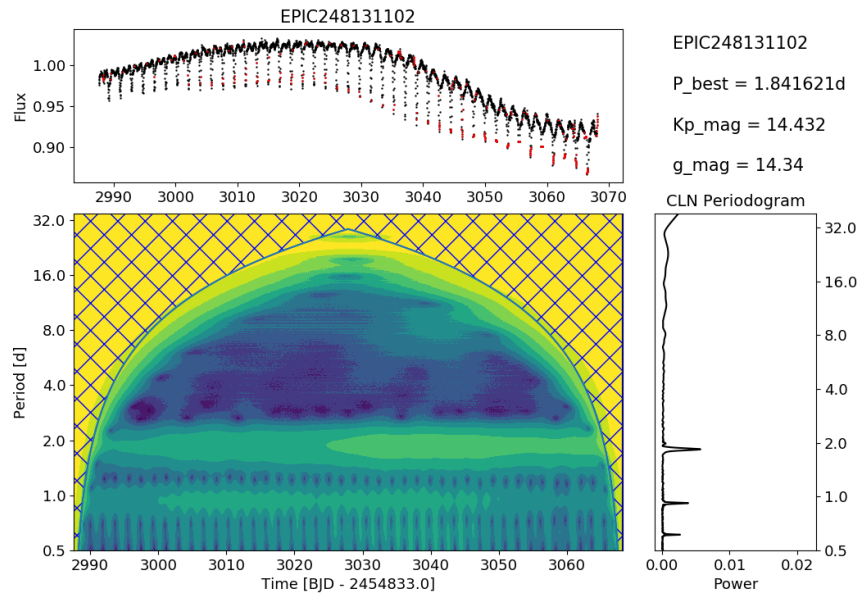


(d)

Figure 2.6 – Examples of WPS of different variable stars in Taurus (cont.).



(e)



(f)

Figure 2.6 – Examples of WPS of different variable stars in Taurus (cont.).

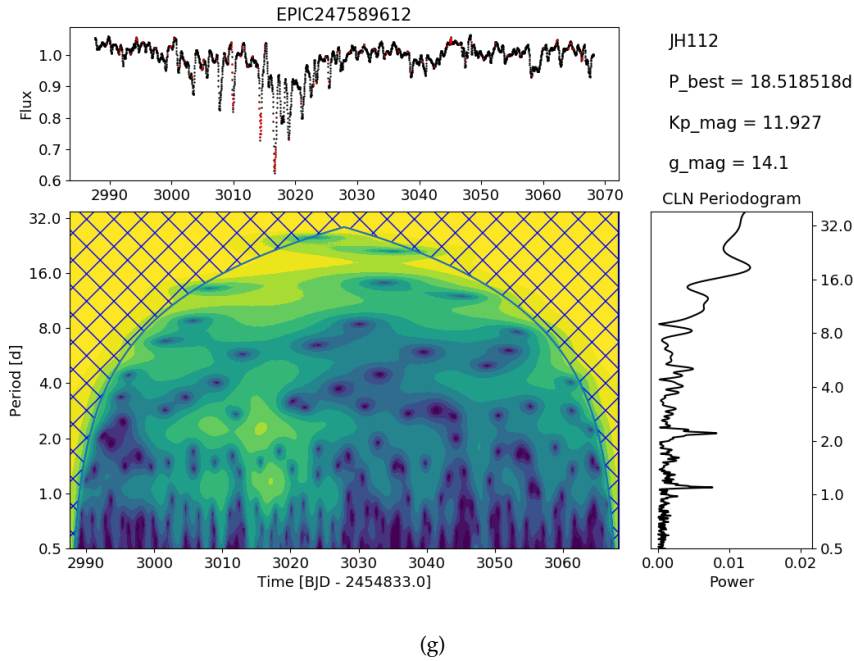


Figure 2.6 – Examples of WPS of different variable stars in Taurus (cont.).

The IR excess is used for this purpose. As a result, $\sim 70\%$ of members and possible members hints at the presence of a disk. Around two-thirds of disked members are periodic. In general, the fraction of periodic stars in Taurus is lower than, e.g., Praesepe, Upper Sco and the Pleiades clusters (Rebull et al., 2016a,b, 2017, 2018). A probable bias is the presence of non-members, which are likely not periodic. However, the Taurus membership was determined carefully and this lower fraction of periodic stars is probably rather due to stochastic disk emission, which contaminates the light curve. Older clusters also host a larger number of WTTs, whose light curve is mainly affected by periodic, cold spots.

More than 95% of the periodicities (148 periodic stars out of 179 members and possible members) are compatible with a cold surface spot. Around 20 stars show stochastic bursts in their light curve. Another 18 stars are classified as dippers. The latter classification slightly differs from what has been retained in this thesis and this is explained in detail in Chapter 3. All of these variable stars have disks, in accordance to the hypothesis that these phenomena are related to accretion from the circumstellar disk.

The Taurus sample supports the idea that the inner disk is rotationally locked to the star, as periods larger than a few days are pretty rare among disked stars. Faster rotators have in general no disk and are in a later stage of stellar evolution. Another important conclusion is that, in accordance with other clusters, early M stars are the slowest rotators, while both more and less massive stars are rather fast rotators (e.g., Rebull et al., 2017, 2018; Stauffer et al., 2016).

2.3 THE MCFOST CODE

Before reaching the observer on Earth, the photons emitted by a young star interact with the gas and dust present in the disk. Depending on the particle size and composition, photons can be absorbed, re-emitted or scattered. Solving the radiative transfer equation allows to reconstruct the temperature and the emitted flux in the different regions of the disk. The solution of the equation depends on the local properties of the dust, which in turn depend on the radiation field. For this reason, the problem has to be solved numerically. Indirect observations of dippers such as light curves deliver constraints on some parameters of the inner disk region, such as inclination or azimuthal extension of the dusty occulting structure. However, they are degenerate for everything else: dust density, composition, grain size, height of the structure and optical depth. For this reason and to go beyond the limits of photometric observations, I use MCFOST to model one of the most ‘prototypical’ dippers of the sample. MCFOST (Pinte et al., 2006, 2009) is a Monte-Carlo based 3D radiative transfer code built on the first version of Ménard (1989), developed to model scattered light in dusty environments. The code uses a 3D cylindrical or spherical grid, and dust properties can be varied throughout the grid as a function of (r, z) , although they are considered constant in a given cell. Given a disk structure and dust properties, the code can compute the temperature structure, the SED, monochromatic images, molecular line emission and properties such as the optical depth and dust grain distribution. The disk structure can be parametric (this thesis), or can be the output of MHD simulations, as it will be the case in future work.

2.3.1 Radiative transfer

The goal of a radiative transfer code is to find the intensity I at a wavelength λ , expressed in its generic form as

$$\frac{dI_\lambda(\vec{r}, \vec{n})}{ds} = -\kappa_\lambda^{\text{ext}}(\vec{r})I_\lambda(\vec{r}, \vec{n}) + j_\lambda(\vec{r}) \quad (2.10)$$

where $\kappa_\lambda^{\text{ext}}(\vec{r})$ describes the extinction (= absorption + scattering) term, $j_\lambda(\vec{r})$ is the emission term and \vec{r} the distance following the propagation. The emission term depends on the thermal emission, thus on the temperature at distance \vec{r} , and the scattered light. The full equation, which considers anisotropic scattering in dust, writes:

$$\frac{dI_\lambda(\vec{r}, \vec{n})}{ds} = -\kappa_\lambda^{\text{ext}}(\vec{r})I_\lambda(\vec{r}, \vec{n}) + \kappa_\lambda^{\text{abs}}(\vec{r})B_\lambda(T(\vec{r})) + \kappa_\lambda^{\text{sca}} \frac{1}{4\pi} \iint_{\Omega} \psi_\lambda(\vec{r}, \vec{n}, \vec{n}')I_\lambda(\vec{r}, \vec{n}')d\Omega' \quad (2.11)$$

where $\kappa_\lambda^{\text{abs}}(\vec{r})/\kappa_\lambda^{\text{sca}}(\vec{r})$ are the absorption and scattering opacities, $B_\lambda(T(\vec{r}))$ is the Planck function, and $\psi_\lambda(\vec{r}, \vec{n}, \vec{n}')$ the scattering phase function, which delivers the probability for a photon located at position \vec{r} traveling in direction \vec{n} to be scattered in direction \vec{n}' in a solid angle Ω . In order to solve the radiative transfer equation, MCFOST propagates ‘photon packets’ through the disk, by using the Monte Carlo method. The sources of radiation are the emission from the stellar photosphere and the thermal emission from the disk. Each photon packet reaches the outer end of the grid by traveling from one interaction site to another. In each cell, the dust follows the distribution $f(a, \vec{r})$ based on the grain size a and its composition, if wished by the user. The dust optical properties can be derived by either following the Mie theory (this thesis), which assumes homogeneous and spherical grains, or a hollow spheres distribution (DHS). The extinction and scattering opacities are computed following

$$\kappa^{\text{ext/sca}}(\lambda, \vec{r}) = \int_{a_{\text{min}}}^{a_{\text{max}}} \pi a^2 Q_{\text{ext/sca}}(\lambda, a) f(a, \vec{r}) da \quad (2.12)$$

where $Q_{\text{ext/sca}}(\lambda, a)$ is the extinction (scattering) cross section of a grain of size a at the wavelength λ . From this, it is possible to derive the optical depth between two interaction sites as:

$$\tau_\lambda = \int_0^l \kappa^{\text{ext}}(\lambda, \vec{r}) \rho(\vec{r}) ds, \quad (2.13)$$

where ρ is the local density. In order to solve the radiative transfer problem, also the temperature of the dust grains has to be computed. In the case of local thermal equilibrium (LTE), the gas is thermally coupled to the dust. The temperature T_i in each cell can be computed by solving the radiative equilibrium equation:

$$4\pi \int_0^\infty \kappa_i^{\text{abs}}(\lambda) B_\lambda(T_i) d\lambda = \Gamma_i^{\text{abs}}, \quad (2.14)$$

where κ_i^{abs} is the absorption opacity, $B_\lambda(T_i)$ is the Planck function and Γ_i^{abs} is the energy absorption rate. In practice, MCFOST solves

$$\int_0^\infty \kappa_i^{\text{abs}} B_\lambda(T_i) d\lambda = \frac{L_*}{4\pi V_i N_\gamma} N_{\gamma \text{ abs},i}, \quad (2.15)$$

where L_* is the stellar luminosity, V_i the volume of the cell, N_γ the number of photon packets and $N_{\gamma \text{ abs},i}$ the current number of absorbed photons in cell i . Once all photons have been propagated, the temperature structure is refined following the method of Lucy (1999), which computes the mean intensity J_γ as:

$$J_\gamma = \frac{1}{4\pi V_i} \sum_\gamma \epsilon \Delta l_\gamma = \frac{1}{4\pi V_i} \sum_\gamma \frac{L_*}{N_\gamma} \Delta l_\gamma \quad (2.16)$$

where ϵ is the luminosity of the photon packet and Δl_γ the distance traveled in the cell.

Once the temperature is computed for each cell, MCFOST can produce an SED. These data can be produced by the code either via Monte-Carlo or with ray-tracing, the latter being the default. In the first case, the number of photon packets is kept constant for all wavelengths in order to reduce the convergence time. Moreover, photon packets that reach regions with high optical depth are not propagated through the entire grid. For ray-tracing, the code makes use of the computed temperature structure and computes the solution of the radiative transfer equation along each ray, finally integrating the light over the grid. The same principle of ray-tracing is used to produce monochromatic images.

2.3.2 Disk parameters and code output

MCFOST runs with a user-set parameter file. First of all, the user can set the specifications of the grid (cylindrical, spherical, number of cells in each direction), as well as the number of photon packages to propagate for each output. The grid is logarithmic in radial direction. This allows to better sample the photon mean free path in the inner disk, where the density is higher if the disk density follows a power law in radial direction. The computation time can be reduced by suppressing the production of maps for each component (i.e., for each Stokes parameter) and/or by indicating symmetries of the system. The other properties of the system can be set up as follows:

- Disk structure and physics: it is possible to define a dust settling (not the case here). Several independent zones with different independent properties can be defined in the disk. The disk is modeled as a flared disk that follows

$$\rho(r, z) = \rho_0(r) \exp\left(-\frac{z^2}{2h(r)^2}\right) \quad (2.17)$$

in cylindrical z and r directions. The scale height of the disk is defined as

$$h(r) = h_0 (r/r_0)^\beta, \quad (2.18)$$

where β is the flaring exponent, here set to 9/8. The parameter h_0 defines the scale height at the reference radius r_0 . The surface density of the disk is described by

$$\Sigma(r) = \Sigma_0 (r/r_0)^\alpha, \quad (2.19)$$

with α set to -0.5.

- Grain properties: the gas-to-dust ratio is set to 100:1. It is possible to freely set M_{dust} . The standard dust grains of MCFOST are silicates. However, one can set another type of dust and mix different dust populations in the same disk. The user can set the minimal and maximal size of the grains a_{min} and a_{max} and the grain size distribution follows

$$\frac{N(a)}{da} = a^{-a_{\text{exp}}}. \quad (2.20)$$

The exponent is set here to $a_{\text{exp}} = 3.5$.

- Global disk properties: inner and outer disk radius (R_{in} and R_{out}), disk inclination, distance, position angle.
- Stellar properties: M_* , R_* , T_{eff} . MCFOST assumes a certain stellar spectrum from the indicated properties. It is possible to choose a specific one.

MCFOST is also able to model molecular line emission and enables coupling with other codes, such as ProDiMo and Phantom. These features are not used in this thesis. The output files that are useful to model dippers in the first place and to compare with photometric observations are the temperature structure of the disk, the SED, monochromatic images and optical depth maps. The code is able to produce a wealth of files that allow to understand the modeled system in depth. Among others, dust properties such as albedo, opacity, scattering phase function, polarizability; disk properties such as gas, dust and dust particle density maps, the used grids; column densities.

K2 LIGHT CURVES OF TAURUS DIPPERS

Summary

3.1	K2 Photometry	40
3.1.1	Light curve extraction	40
3.1.2	Membership assessment and sample selection	41
3.2	Periodicity Analysis	48
3.2.1	A different period for spots and dips?	50
3.3	Light Curve Morphology	50
3.3.1	Ideal dippers	50
3.3.2	Transient dippers	50
3.3.3	Double- and multi-peaked dippers	53
3.3.4	Dip amplitude and dip width	57
3.4	Stellar Parameters	60
3.4.1	Effective temperatures and spectral types	60
3.4.2	<i>VJHK</i> photometry	60
3.4.3	Visual extinction	62
3.4.4	Luminosities	63
3.4.5	Masses and radii	65
3.4.6	Radius and temperature at corotation	66
3.4.7	Inclinations	67
3.4.8	Mass accretion rates and accretion regime	68
3.5	Detailed notes on individual objects	68
3.6	What can we infer from dippers?	73
3.6.1	Dippers in Taurus and in other clusters	73
3.6.2	Star and outer disk inclination	74
3.6.3	Temperature at corotation and dust survival	75
3.6.4	Dip width and period	76
3.7	Summary	78

This chapter is dedicated to the analysis of dipper light curves as delivered by the *K2* mission. First, I selected dippers by visual inspection among the rich variable star sample of the Taurus field (Sec. 3.1.2). Secondly, I studied their periodicity implementing a customized wavelet transform routine. This task is more time-consuming than the application of period-finding algorithms, but is justified by the quasi-periodicity and complex morphology of dippers (Sec. 3.2). In order to assess whether the current models can account for these dippers, stellar parameters such as mass and radius are needed. These can be derived indirectly from stellar luminosity and effective temperature. Again, these are not directly observable. The observables are the spectral type, the parallax and the stellar apparent magnitude in different filters, which can be converted to visual extinction, absolute magnitude, effective temperature, etc. For each of the dippers of interest, I compiled the full parameter list available in the literature, in order to have measurements as precise as possible and compensate a high systematic uncertainty due to the use of a large number of conversions (Sec. 3.4). I also derived the dip's morphological properties from the light curve, which motivate a more consistent and quantitative analysis in future (Sec. 3.3). The end of this chapter provides a discussion on possible dipper mechanisms, the implications and outlook for future work.

3.1 K2 PHOTOMETRY

3.1.1 *Light curve extraction*

The *Kepler* satellite (Borucki et al., 2010; Haas et al., 2010) was launched in 2009 with the main aim of detecting Earth-like exoplanets and observed over 170,000 targets simultaneously in its long-cadence mode of 29.4 min, with an extremely high precision up to sub-mmag. The space mission allowed to detect more than 2500 exoplanets. Originally, *Kepler* was meant to observe a fixed field of view out of the ecliptic plane, in order to avoid interference with the Sun's light. The chosen constellations of Cygnus and Lyra were both out of the ecliptic plane and rich in stars. The failure of two reaction wheels in 2013 led to a substantial change in the observing strategy and renaming of the mission as *K2* (Howell et al., 2014). The spacecraft used its two remaining reaction wheels in tandem with the solar radiation pressure (plus compensatory periodic thruster firings) to control movement in the third dimension. Instead of staring at one field as the original *Kepler* mission had done, *K2* was constrained to view fields in the ecliptic plane for about 80 days at a time (Howell et al., 2014), in order to avoid the Sun's irradiation. This allowed to prolong the science mission until October 2018, when the satellite went out of fuel. Within the framework of the *K2* mission (2014 - 2018), 19 fields of 100 square degrees were observed (Howell et al., 2014). In the context of this work, for the purpose of reducing the data, the two most important artifacts to keep in mind are the periodic thruster firings and the relatively low spatial resolution, limited by pixels of $\sim 4 \times 4''$ and the 95% encircled energy diameter of up to 7.5 px. The thruster firings happen every 0.245 days, and so apparent astrophysical periods near that must be scrutinized carefully to assure that they are not affected by the spacecraft. The low spatial resolution means that source confusion can be an issue, and each source (and light curve) must be inspected individually to assess confusion, and customized apertures are sometimes needed to attempt to mitigate it. The effective observed range of *K2* lies between $6 \text{ mag} < K_s < 16 \text{ mag}$ (e.g., Rebull et al., 2016a). Saturation is not a relevant detection bias in Taurus, which does not host a massive star population. However, deeply embedded low-mass stars are likely to remain undetected with *K2*.

A few Taurus members were observed in *K2* C4 (2015 Feb 15 - 2015 Apr 24), but most of the Taurus members were observed during C13 from the (2017 Mar 8 - 2017 May 27)¹. This work builds on the analysis presented in Rebull et al. (2020). First, *K2* LCs were only downloaded for targets submitted in advance, so completeness is limited by the submitted list of targets. The *K2* fields do not cover the entire Taurus cluster; however, the stellar properties of the cluster are not supposed to vary based

¹ https://archive.stsci.edu/files/live/sites/mast/files/home/missions-and-data/k2/_documents/KSCI-19116-003.pdf

on the spatial distribution (see, e.g., Fig. 1 in Rebull et al., 2020). We used light curves from several different data reduction pipelines (also see Rebull et al., 2017):

- pre-search data conditioning (PDC) version from MAST (Mikulski Archive for Space Telescopes);
- a position-detrended version with moving apertures as in Cody and Hillenbrand (2018);
- the ‘self-flat-fielding’ approach by Vanderburg and Johnson (2014) and the K2SFF pipeline as obtained from MAST;
- the EVEREST2 pipeline, based on pixel level decorrelation Luger et al. (2016), as downloaded from MAST.

A comparison of all these light curve versions allows us to constrain the periodicity (or periodicities) and select the ‘best available’ (see Rebull et al., 2020, and references therein) to represent that star’s light curve. If the light curve does not present particular issues, the version with moving aperture as in Cody and Hillenbrand (2018) was used by default for consistency. This version was also the one used for the dipper sample presented in this paper.

3.1.2 Membership assessment and sample selection

The *K2* campaigns 4 and 13 deliver ~ 850 light curves, most of which are from C13. Until *Gaia* DR2, the largest collection of precise parallaxes and distances for the Milky Way (now updated and expanded by DR3), membership assessment for open clusters has been a complicated and imprecise task. Taurus is no exception. In order to assess the membership of the observed stars, these are divided in different categories: high-confidence members, lower-confidence members, non-members (Rebull et al., 2020). Another additional category are older (~ 30 Myr), foreground stars most of which are likely related to the so-called Group 29 (Luhman, 2018; Oh et al., 2017). Esplin and Luhman (2019), building on Luhman (2018), extensively studied the proper motions, optical and IR data to select a sample that can be reasonably considered as composed of certain Taurus members. The stars that overlap with *K2* C4 or C13 are thus considered high-quality members. Additionally, some stars which are not included in that sample, but which have *Gaia* data compatible with Taurus membership and some references in the literature are considered possible members, with lower confidence. The final Taurus sample consists of 156 high-confidence members and 23 possible members.

Among the light curves of the high-confidence and possible members, I identified dippers based on a visual inspection of the light curve. The way in which different types of variability affect the light curves has been mentioned in Sec. 2.2.2 and in Sec. 1.2. To resume again, the almost ubiquitous cold spots produce sinusoidal patterns. Irregular, aperiodic increases in the star’s brightness (bursts) are linked to accretion shocks for T Tauri stars. Planetary transits and eclipsing binaries do produce dips, but these are strictly periodic. Moreover, the former have a very small amplitude in flux. The criteria to select dippers are thus the following:

- The dips are sharp and have an irregular shape;
- The dip duration is up to a few days;
- The dip amplitude is of at least $\sim 10\%$ and up to $\sim 60\%$ of the flux.

As a result, 22 stars are retained as dippers (Table 3.3, some examples in Fig. 3.1). Moreover, another 12 objects are dominated by another type of variability –mostly spots– and exhibit also a few –mostly aperiodic– dips in their light curves (Table 3.1, some examples in Fig. 3.2). These objects are not further studied in this thesis, since the corresponding light curves are rather complex, but are still counted as dippers for the statistics. Table 3.2 lists some additional light curves which might look like dippers, but do not fulfill all of the selection criteria.

Several statistical light curve classification criteria have been proposed in the literature, one of which is the Q/M metric (Cody et al., 2014). Q is a measure of the periodicity of the light curve, and compares

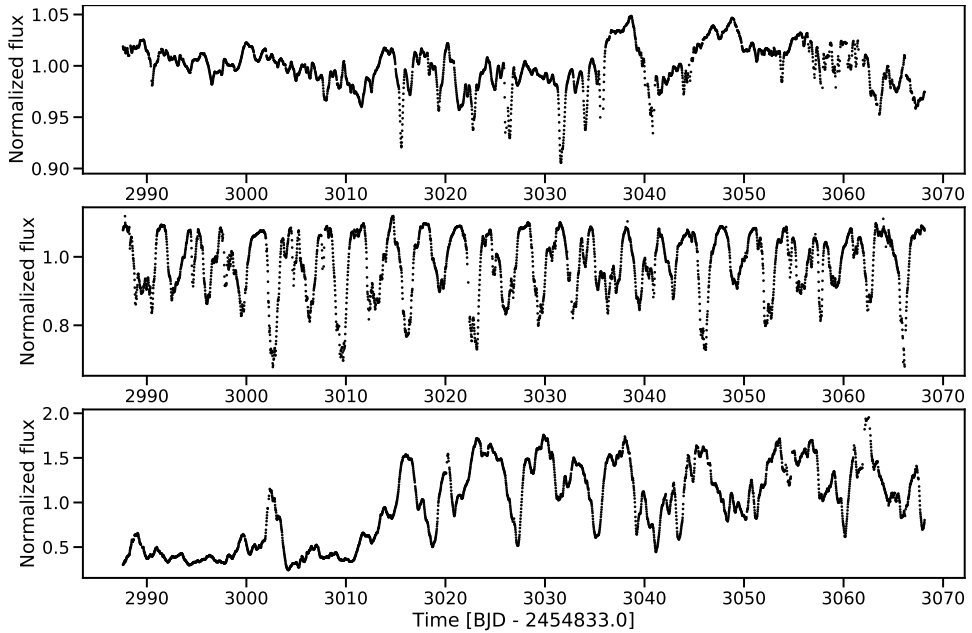


Figure 3.1 – From top to bottom: example of an aperiodic dipper (HD 285893); a quasi-periodic dipper (JH 223); a dipper with a complex light curve (DK Tau). Dipper light curves are characterized by irregularly shaped fading events, which can last to up to a few days.

the boxcar smoothed and folded light curve to the original one. This metric classifies stars between periodic, quasi-periodic and stochastic. The M metric is a measure of the light curve flux asymmetry. It compares the mean of the top and bottom 10% flux percentile and the median, divided by the overall root mean square (rms) of the flux. This operation allows to discriminate between light curves that tend to episodically increase their brightness (bursters) and those that undergo episodic fading (dippers). The metric works well for dipper stars that have a constant continuum flux interrupted by the dips, and have thus a high bright/faint flux asymmetry. Although appropriate for an automatic classification in a large sample, the M metric tends to classify as QPS (quasi-periodic symmetric) light curves with irregular dips which do not have a constant brightness continuum. On a physical point of view, this should not be the striking selection criterium and I prefer a manual classification instead.

Dippers with an irregular brightness continuum are CFHT Tau 12 and ITG 34. More symmetric are HK Tau, GH Tau, GM Tau and EPIC 247820821 (2MASS J04295950+2433078). The last two are more ambiguous and I differentiate them from spots because of the sharp shape of their dips. It cannot be excluded that the dips are superimposed on spots. GI Tau is contaminated by the neighbour GK Tau and its light curve is complex. However, its own periodicity can be retrieved and clear dips are visible in the light curve. DK Tau also exhibits a complex light curve. After ~ 25 d of quiescent state, the star becomes a clear dipper. All dipper light curves are shown in Fig. 3.3. The other light curves of dippers not further considered and of discarded dippers are shown in Fig. 3.4 and Fig. 3.5, respectively.

The manual classification I apply is more generous than that of Rebull et al. (2020), who classify 21 stars as dippers. Some of those dippers are listed here in Table 3.1 as stars dominated by another variability. One further light curve (EPIC 247078342) indicated as dipper in Rebull et al. (2020) is discarded in this study, since its shape strongly depends on the reduction pipeline.

To conclude, 34 stars in the Taurus sample are dippers. They represent the 19% of high-confidence and possible Taurus members (156 + 23 as in Rebull et al., 2020) and 31% of the disked stars (94 + 7 as in Rebull et al., 2020) in this sample.

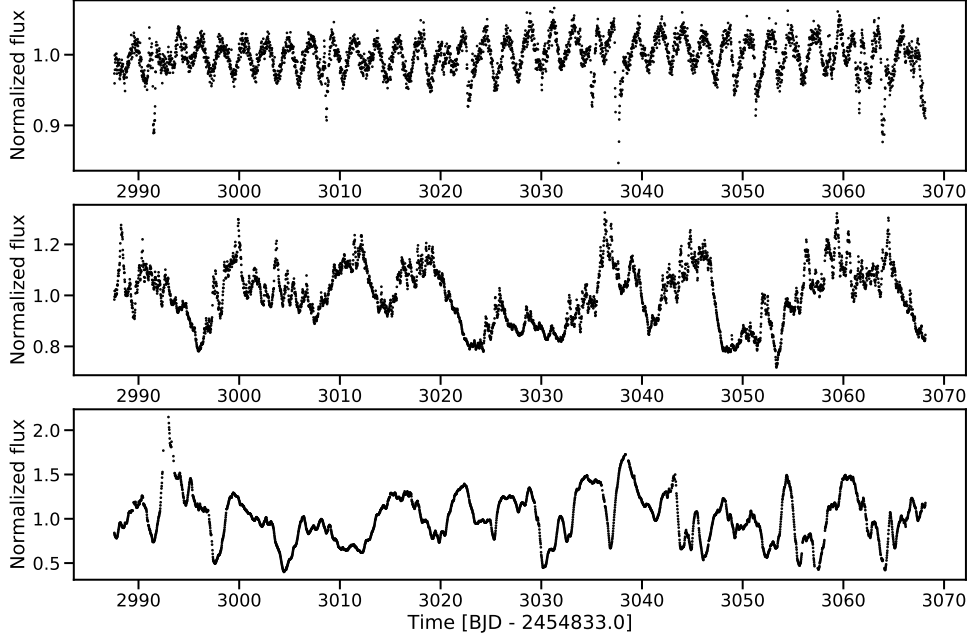


Figure 3.2 – From top to bottom: a spot-dominated light curve with aperiodic dips (EPIC246859790); a burst-dominated light curve with dips (CI Tau); a low-quality dipper candidate (IQ Tau). Although some dips are present, the light curve is dominated by another type of variability.

Table 3.1 – Additional dippers that exhibit dips in their light curves as secondary variability.

EPIC	2MASS	Name	Type	Period [d]	G [mag]
210725857	J04285053+1844361	...	Sd	2.06	15.19
246859790*	J04440164+1621324	...	Sd	2.16	17.30
247575425	J04331907+2246342	IRAS 04303+2240	Td	7.5	16.09
247584113	J04335200+2250301	CI Tau	db	8.5;	12.15
247585465	J04322415+2251083	...	Bd?	2.48	15.25
247788960	J04323058+2419572	FY Tau	B?d	6.94;	13.77
247810494	J04345542+2428531	AA Tau	d?	...	14.49
247827638*	J04293606+2435556	XEST 13-010	Sd	3.9	14.85
247915927	J04442713+2512164	IRAS 04414+2506	S?d	4.42	15.48
248009353	J04324282+2552314	UZ Tau	Bd	...	12.39
248018164*	J04413882+2556267	Haro 6-33	Td?	...	15.94
248030407*	J04394488+2601527	ITG 15	S?d	3.45	15.00

The variability type has to be interpreted as: capital letter = dominant variability; d = dipper; s = spot; b = burster; t = long term trend. The periods are derived with the CLEAN periodogram and the listed value is the dominant period of the light curve, i.e., of the spot, when present. Only CI Tau and EPIC 247585465 exhibit quasi-periodic dips. The brightness is obtained from the *Gaia* G band.

* Star reported as dipper by Rebull et al. (2020).

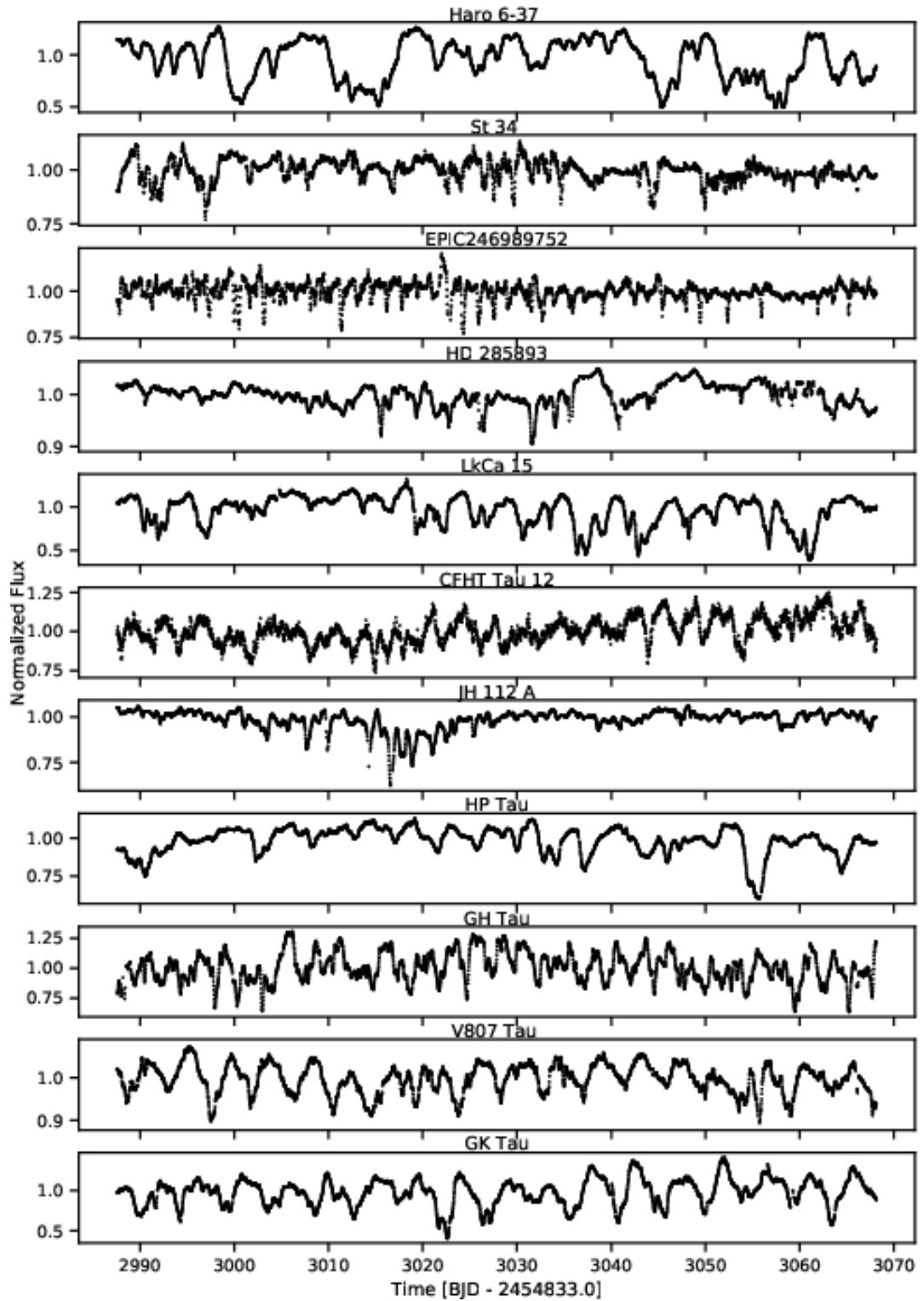


Figure 3.3 – Light curves for the dipper sample studied.

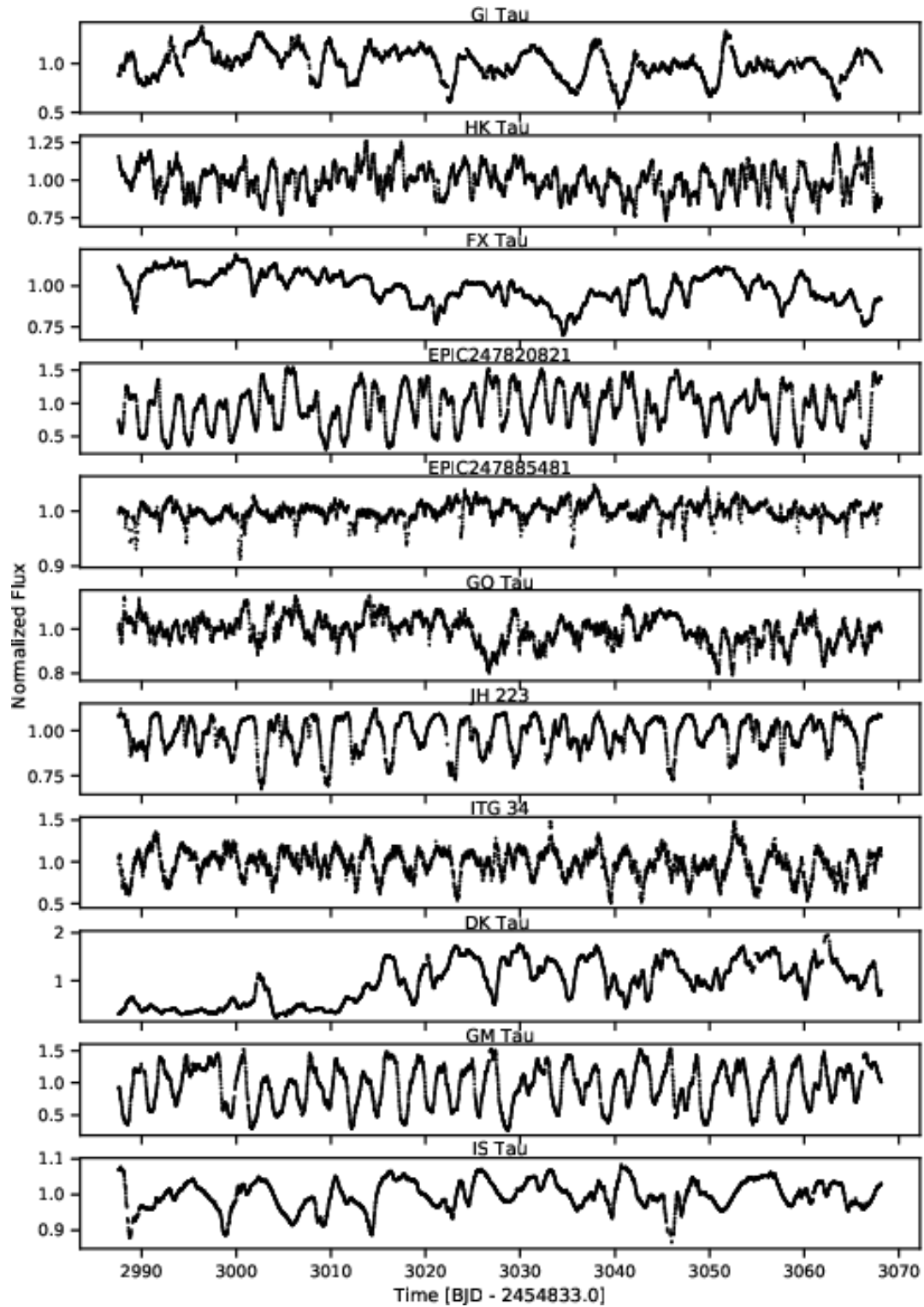


Figure 3.3 – Light curves for the dipper sample studied (cont.).

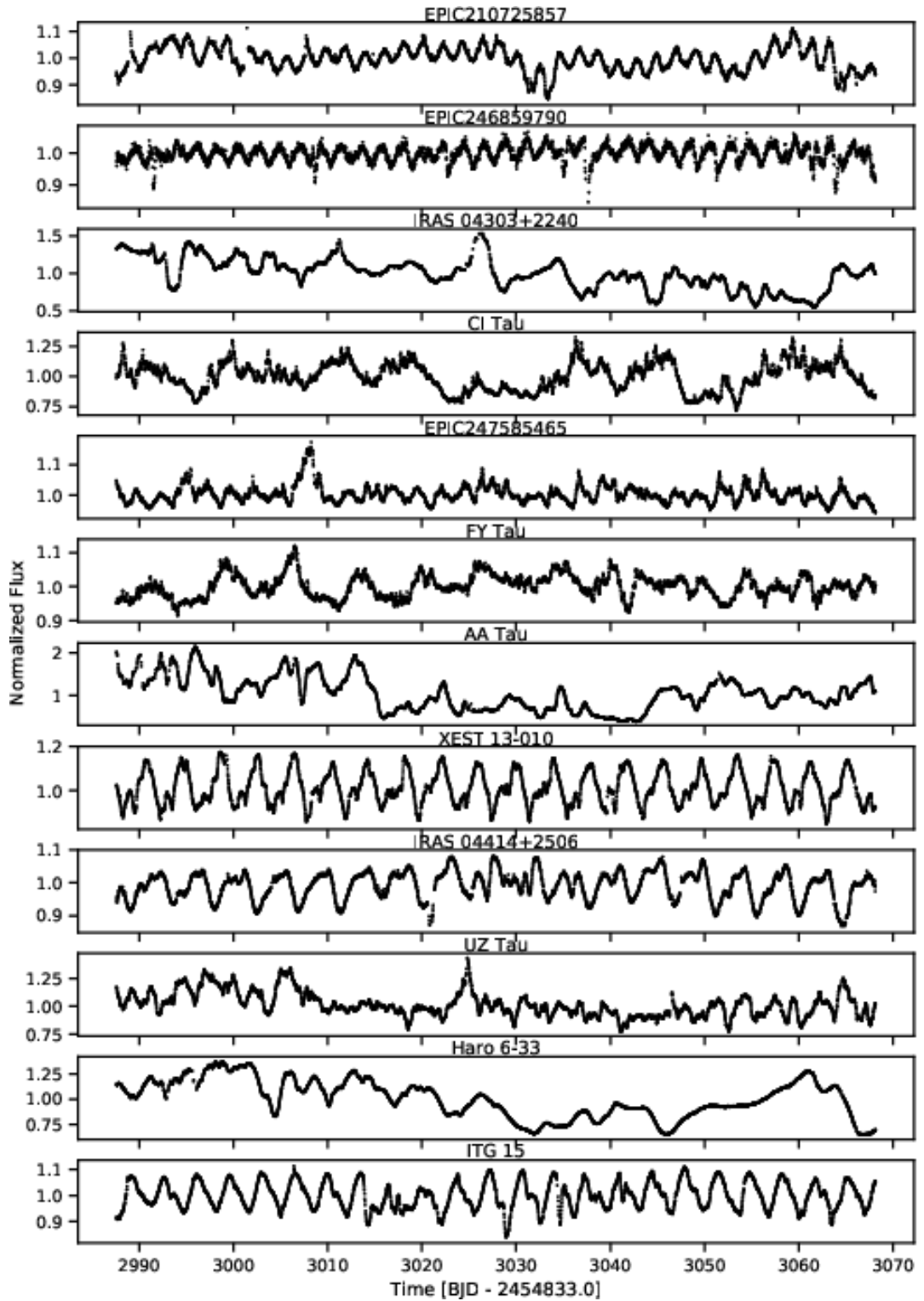


Figure 3.4 – Light curves of additional dippers dominated by another type of variability.

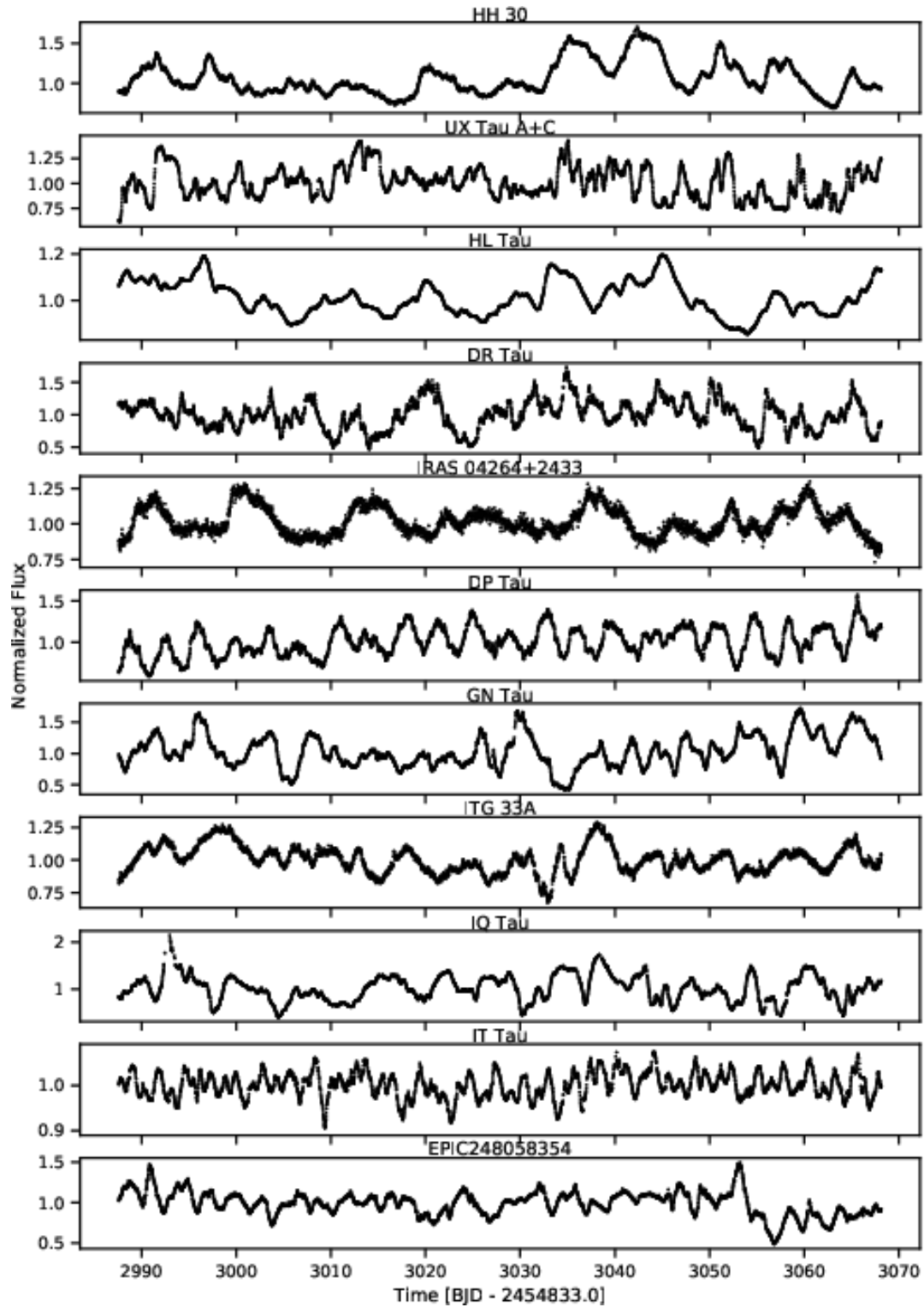


Figure 3.5 – Light curves of potential dipper candidates that do not fulfill all selection criteria.

Table 3.2 – Variable YSOs that are dipper candidates of lower quality.

EPIC	2MASS	Name	Type	Period [d]	G [mag]
210689083	J04313747+1812244	HH 30	t	7.51	...
210690735	J04300399+1813493	UX Tau A+C	t?	3.6;	11.29
210690913	J04313843+1813576	HL Tau	t?
246923113	J04470620+1658428	DR Tau	Bd?	14.71	11.65
247837468	J04293008+2439550	IRAS 04264+2433	?	11.9	...
247923794	J04423769+2515374	DP Tau	t	3.66;	13.51
247992574	J04392090+2545021	GN Tau	t	5.75;	14.56
248017479	J04410826+2556074	ITG 33A	t	6.6;	17.60
248040905	J04295156+2606448	IQ Tau	t	...	13.24
248055184	J04335470+2613275	IT Tau	t	2.74	...
248058354	J04334465+2615005	...	?	...	16.50

The variability type has to be interpreted as: capital letter = dominant variability; d = dipper; s = spot; b = burster; t = long term trend. The periods are derived with the CLEAN periodogram and the listed value is the dominant period of the light curve. Most objects in this list are dominated by a long term trend. The brightness is obtained from the *Gaia* G band.

3.2 PERIODICITY ANALYSIS

Dippers often appear to be quasi-periodic. Following the disk warp model (e.g., Bouvier et al., 2007b), the dusty material obscuring the star must be located close to corotation, which is per definition the region where circumstellar material rotates with the same angular velocity as the star. Stauffer et al. (2015) and Rebull et al. (2018) identified some light curves which showed both spots and dips. The overlapping periods of both phenomena strongly supported the scenario of an inner disk rotationally locked to the star, since stellar spots follow the stellar rotation. It is thus of interest to discuss the periodicities of dippers compared to stellar rotation.

To study the periodicities of dippers, both the WPS (Sec. 2.1) and the CLEAN periodogram (Roberts et al., 1987) are used.

In this sample, 8 stars exhibit a single, clear periodicity (JH 223, EPIC 246989752, CFHT Tau 12, V807 Tau, GK Tau, HK Tau, GM Tau, IS Tau); 3 are aperiodic (HD 285893, FX Tau, GO Tau); for 3 stars, the periodicity is unclear (Haro 6-37, St 34, DK Tau). Two stars are transient, quasi-periodic dippers (JH 112 A and DK Tau). The last 7 dippers are quasi-periodic, but their light curve/periodogram are more complex than the other dippers: LkCa 15, EPIC 247885481, HP Tau, GH Tau, GI Tau, EPIC 247820821, ITG 34. The periods are listed in Table 3.3; those that are uncertain are flagged with a semicolon.

The periods coincide with those published by Rebull et al. (2020), with the exception of DK Tau (7.84 d vs. 7.69 d derived here); this small difference is due to the complex periodogram and the usage of two different algorithms. The WPS (Fig. 3.6 shows that the period increases during the *K2* campaign. The periodogram exhibits two peaks at ~ 8 and ~ 10 d. By means of the WPS, they can be interpreted as a single, changing period. This could explain why the period of DK Tau is never constrained precisely in the literature (see Sec. 3.5 for more details). The stars ITG 34 and GH Tau have a second reported period (Rebull et al., 2020), which is confirmed here. For GH Tau, a possible third period at 5.09 d is present. An interesting case is EPIC 247885481 (see the following section for a detailed discussion), where the main periodicity of 2.99 d is most probably caused by a spot, while the dips can be folded in phase with a period of 2.90 d. Rebull et al. (2020) report 2.99 d for the main periodicity, while the dipper period is unresolved in both the periodogram here and in Rebull et al. (2020). In the

Table 3.3 – Periods of the dipper sample.

EPIC	2MASS	Name [d]	P [d]	σ_P
246929818	J04465897+1702381	Haro 6-37	10.63;	0.72
246942563	J04542368+1709534	St 34	5.23;	0.20
246989752	J04384725+1737260	...	1.62	0.03
247103541	J04363081+1842153	HD 285893
247520207	J04391779+2221034	LkCa 15	5.78	0.20
247575958	J04330945+2246487	CFHT Tau 12	3.48	0.07
247589612	J04324911+2253027	JH 112 A	2.21	0.07
247592463	J04355277+2254231	HP Tau	4.33	0.17
247763883	J04330622+2409339	GH Tau	2.49	0.06
247764745	J04330664+2409549	V807 Tau	4.39	0.12
247791801	J04333456+2421058	GK Tau	4.61	0.15
247792225	J04333405+2421170	GI Tau	7.13	0.40
247799571	J04315056+2424180	HK Tau	3.3	0.07
247805410	J04302961+2426450	FX Tau
247820821	J04295950+2433078	...	2.38	0.04
247885481	J05023985+2459337	...	2.90*	0.08
247935061	J04430309+2520187	GO Tau
248006676	J04404950+2551191	JH 223	3.31	0.09
248015397	J04411078+2555116	ITG 34	3.91	0.17
248029373	J04304425+2601244	DK Tau	7.69;	0.45
248046139	J04382134+2609137	GM Tau	2.67	0.05
248047443	J04333678+2609492	IS Tau	7.58	0.41

Columns: the photometric period P and the uncertainty estimated from the Gaussian fitting of the periodogram peak σ_P .

* The peak of the periodogram is at 2.99 d and is linked to a cold spot. A more thorough analysis is needed to retrieve the dipper period at 2.90 d.

case of GI Tau, the light curve is contaminated by the neighboring GK Tau and the dominant peak in the periodogram is the period of GK Tau. Thus, only the second period is reported as being of GI Tau. EPIC 247820821 shows a second periodicity on the WPS at 7.00 d that does not appear on the periodogram. When folded in phase, the pattern seems to be related to a shift of the minimum of the dip. ITG 34's periodogram exhibits several, double-peaked periods, which cannot be harmonics of each other. It is difficult to recognize a dominant structure in the folded light curve. All the folded light curves and WPS plots are presented in App. B (Roggero et al., 2021, see App. E and F).

The motions of the *Kepler* satellite might create spurious periods at 0.22, 1.75 and 1.97 d. None of them has been observed here.

3.2.1 A different period for spots and dips?

The light curve for EPIC 247885481 (2MASS J05023985+2459337) shows narrow dips superimposed on a sinusoidal variability. The periodogram shows a clear peak at 2.99 d with $\sigma = 0.08$ d, but the folded light curve shows that the period actually refers to the sinusoidal variation (Fig. 3.7). The dips can be folded in phase around $P - \sigma$ at ~ 2.90 d, with a certain scatter in phase. The peak in the periodogram does not seem to have any complex structure.

In order to better study the periodicity, the spot was fitted with a sinusoidal wave with a period of 2.99 d (Fig. 3.7), which was then subtracted from the light curve (Fig. 3.8). The periodogram before and after the subtraction shows that the main contribution to the periodicity is given by the spot; no substructure appears after the spot subtraction. This can be explained by the fact that the amplitude of the eclipses is very small compared to the noise and that the dip is not clearly present in every period. The dips' shape is nearly Gaussian and the dip width small compared to the period. The residual was fitted with a periodic Gaussian pulse such as $f(t) = c + A \sum_{n=-\infty}^{\infty} \exp -\frac{(t-nT-\delta)^2}{2\sigma^2}$, with the period T as a free parameter. The retrieved period is thus 2.90 d for the dips, still very close to $P - \sigma$ and it cannot be confirmed that they are significantly different. Similar conclusions about other stars were reached by Stauffer et al. (2015); nevertheless, the fact that the dips cannot be folded in phase with the period of the spot is a clear hint that they must be different. The difference between the two periods could be explained by the differential rotation of the stellar surface, assuming that the co-rotating material is aligned with the equator and the spot is at higher latitude.

3.3 LIGHT CURVE MORPHOLOGY

3.3.1 Ideal dippers

A good example for a quasi-periodic dipper is JH 223 (Fig. 3.1): the occurrence of the dips is periodic, their shape irregular and their amplitude can almost double in two neighbouring dips. No other types of variability in form of bursts or other patterns affect the classification and the brightness continuum is stable. Its period of 3.31 d and the dip duration of ~ 2 d are in range of both rotation periods of CTTs and observed dip properties. A zoom-in on the single dips is shown in Fig. 3.9. Aperiodic dippers tend to present either very narrow dips whose shape is rather simple (e.g., Stauffer et al., 2015), which is the case of HD 285893 (Fig. 3.1), or broad and complex dips.

3.3.2 Transient dippers

The only clear example of quasi-periodic and transient dipper in the sample is JH 112 A (Fig. 3.3). The dips have a period of 2.21 d and, if directly linked to the stellar rotation, they are present for a timescale of ~ 10 full rotations. Interestingly, the continuum's brightness decreases only as long as the eclipses occur. DK Tau (Fig. 3.1) also changes from a fade state to a dipper with a higher brightness continuum, but its light curve is complex and a strong overall variability has already been observed in former campaigns. The dipper status of quasi-periodic dippers is known to be transient over a few years (e.g.,

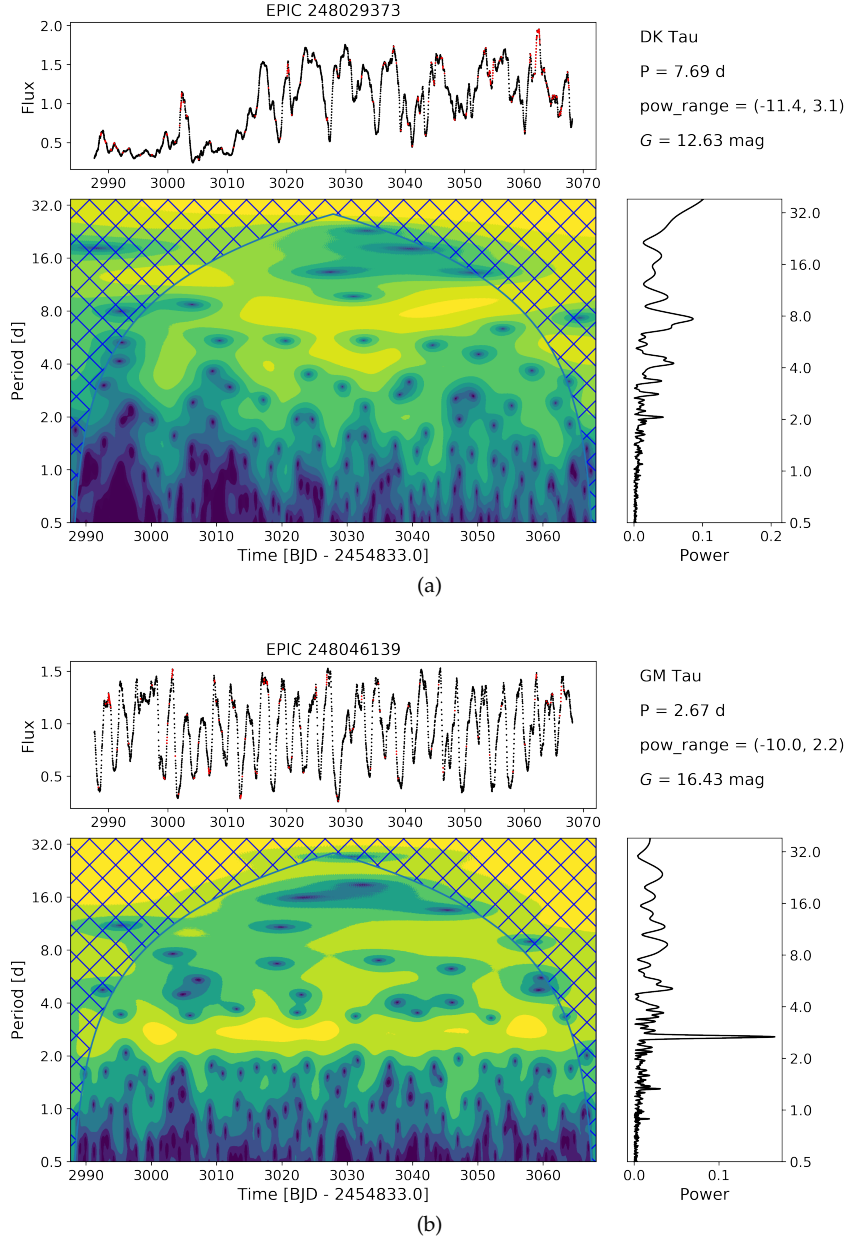


Figure 3.6 – Different examples of WPS for a time-resolved changing period (DK Tau) and a periodic dipper (GM Tau). Top panel: light curves with interpolated points marked in red. Left panel: 2-dimensional WPS. The crossed lines mark the COI, where edge effects of the wavelet transform become relevant. The power contours go from low (blue) to high (yellow). The power range and the *Gaia* magnitude are annotated on the upper right corner. Right panel: CLEAN periodogram. The logarithmic y-axis with the periods is the same as for the WPS. In the case of DK Tau (left), the two peaks in the periodogram at ~ 8 and ~ 10 d can be interpreted as a single period that changes during the observations by means of the WPS. GM Tau displays only one clear period in both the WPS and the periodogram. The green stripe at ~ 10 d is just a recurrent pattern in the light curve: a deeper dip at $t = 3030, 3040, 3050$ d. This is not a relevant periodicity and also does not appear in the periodogram.

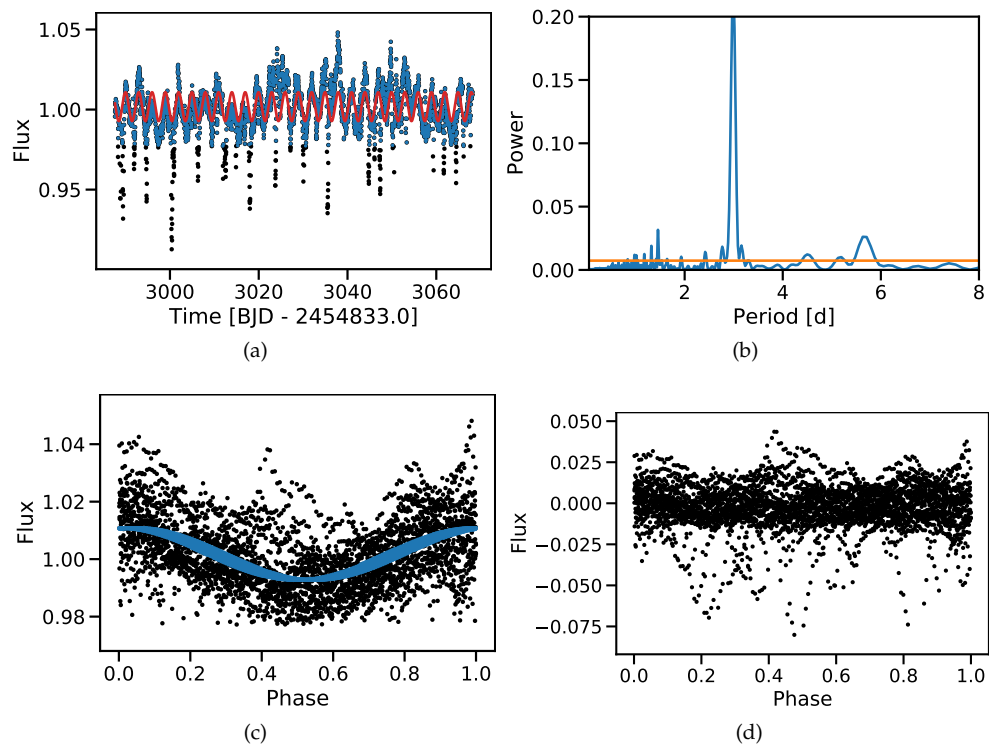


Figure 3.7 – (a) Light curve of EPIC247885481. Red: sinusoidal fit of the flux above the 5th percentile (blue). (b) Periodogram of the star with FAP level at 0.05 (orange). (c) Light curve above the 5th percentile folded at 2.99 d and sinusoidal fit (blue). (d) Residual light curve after subtraction of the fit as in (a) and (c), folded at 2.99 d. The noise is high compared to the dips, but no evident pattern is present.

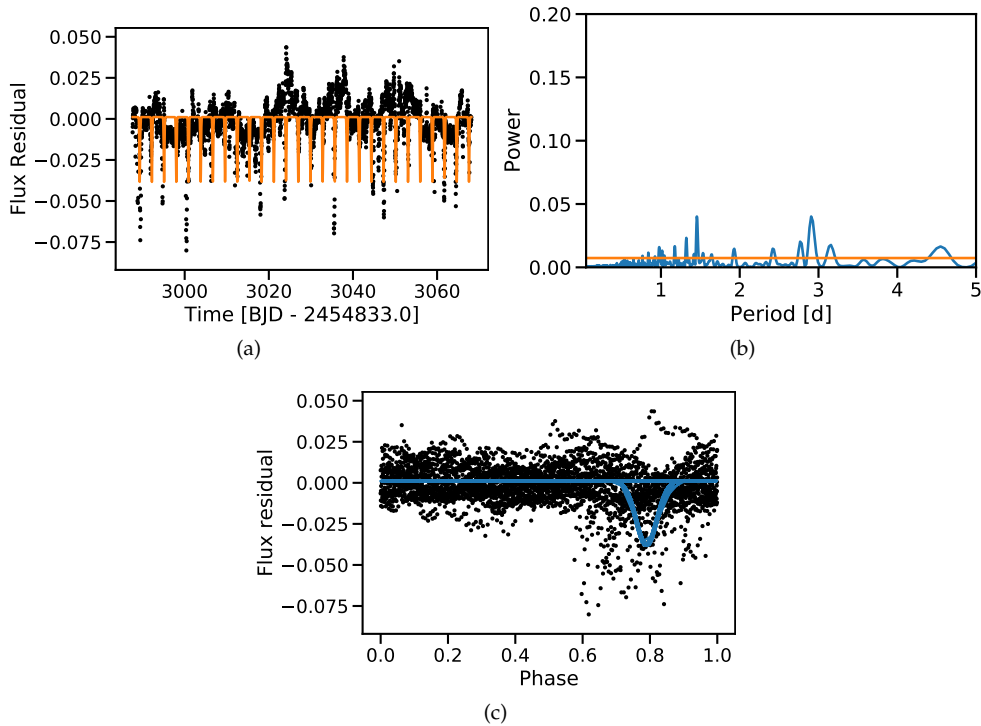


Figure 3.8 – Fitting with periodic Gaussian pulses (a) of the residual light curve of EPIC247885481 after the removal of the sinusoidal variability. (b) Periodogram of the residual light curve. The peak is far less evident, but still significant. (c) Residual light curve folded at 2.90 d with the fitted Gaussian pulses (blue).

AA Tau), but it is rare to observe a quasi-periodic one on such a short timescale. The explanation of a disk warp would imply that the warp significantly changes its height and becomes not visible for the observer after a few rotations, or that the dust in it is completely dissipated on a short timescale.

3.3.3 Double- and multi-peaked dippers

In the sample studied, 6 periodic dippers exhibit clear double-peaked dips in their light curve: LkCa 15, JH 112 A, HP Tau, GI Tau, HK Tau, IS Tau (Fig. 3.10). The here presented double- or multiple-peaked dippers exhibit at least two well-detached dips in the folded light curve (see App. A.1). It should be noted that the dips themselves are in general not Gaussian and have a complex shape. The determination of the dip width for these sources depends on the desired information (the width of the primary peak/the total width of the multi-peaked dip) and is handled in the following section. In the scenario of a dusty warp occulting the star, the constant presence (or not) of a double dip delivers a hint about the stability and the shape of the warp.

LKCA 15 At least two clear peaks with variable depth and occurrence (i.e. position in phase) are always present in the light curve (Fig. 3.11). A third peak appears on the right in some of the panels, but due to the complexity of the light curve, it is difficult to affirm that the number of dips is variable, or that they just so faint that they are not visible in some of the cycles.

JH 112 A In a few periods, two well-detached peaks are present (App. A.1). In general the main peak seems Gaussian, but in certain phases it should be rather modeled by a double Gaussian. The primary peak is always present, while the secondary is strongly variable and sometimes clearly double-peaked.

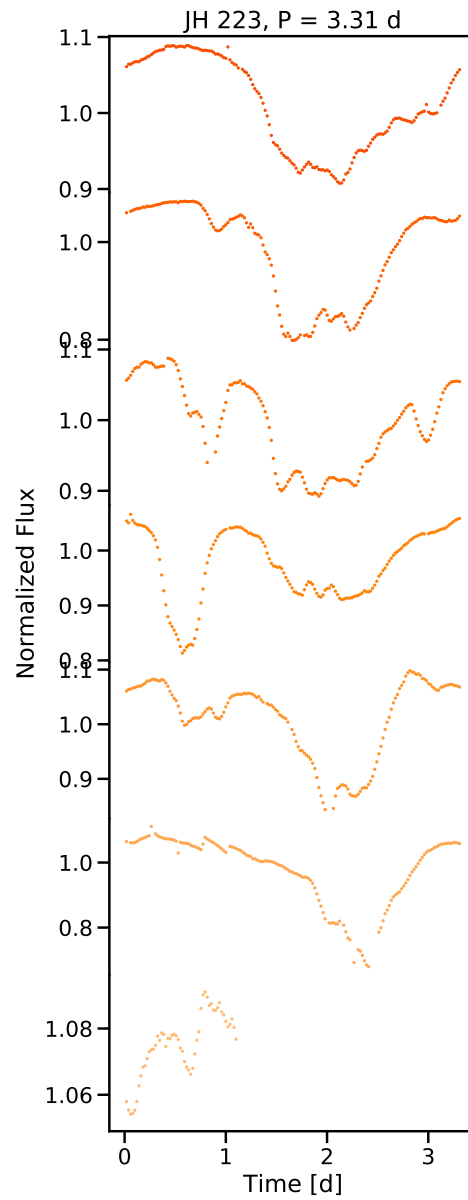


Figure 3.9 – A few cycles of the light curve of JH 223. The dip is irregular in shape, but its occurrence periodic. On its left, another small dip appears and disappears over a few rotation periods.

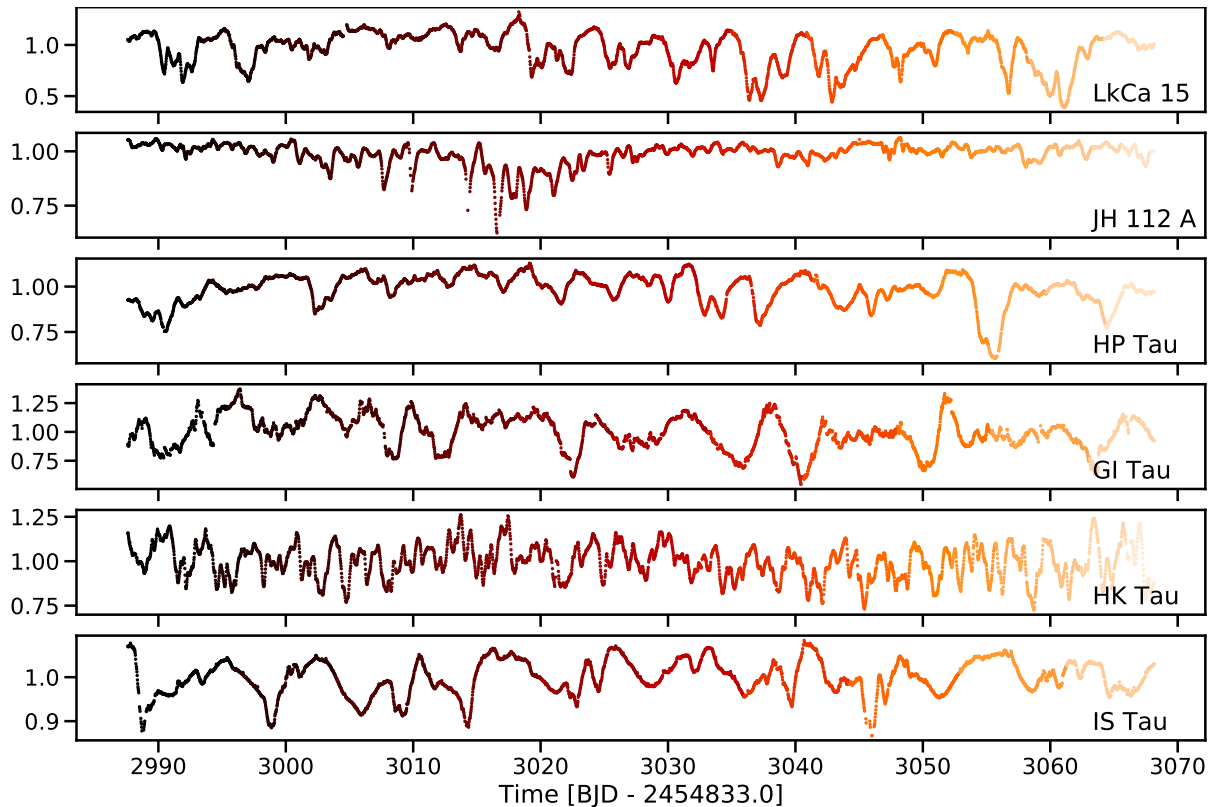


Figure 3.10 – Light curves of the double-peaked periodic dippers. Top to bottom: LkCa 15, JH 112 A, HP Tau, GI Tau, HK Tau, IS Tau. Color code normalized to the length of the observations, one color per phase.

HP TAU The dips are strongly variable (App. A.1), but a clear single Gaussian dip is never present. Towards the end of the light curve, the amplitude of both strongly increases. The shape of the dips is not always related to the precedent pattern.

GI TAU The light curve is contaminated by GK Tau, although the real periodicity of GI Tau can still be retrieved (App. A.1). A comparison with the light curve of GK Tau (not shown here), split in each phase according to GI Tau’s period, shows that the dips are heavily influenced by the neighbour star. Although GI Tau’s intrinsic variability emerges well, it is difficult to describe the behaviour of its different dips, if there are any.

HK TAU Rather than a double-peaked dipper, the star can be considered as multi-peaked (App. A.1). The different dips are always present, with a strongly varying amplitude that seems uncorrelated between different dips. The Gaussian-shaped tip of the dips is constant, while the dips’ shape strongly varies, suggesting that multiple stellar spots might contribute to the photometric variability.

IS TAU Both dips are always present, with the primary (the left one in App. A.1) having a larger, quite constant amplitude, with only one exception (fore-last phase, bottom left). For this star, the phase shift of the single dips is larger than for the other double-peaked dippers.

In general, it can be remarked that the eclipses, although periodic, do not occur exactly at the same phase. For HP Tau, the WPS shows how the periodicity slightly varies around the period of 4.33 d. The shift of the eclipse can be easily seen in App. A.1. Moreover, the variation of the different dips’ amplitudes do not seem correlated to each other. This suggests that either smaller and independent dusty warps occult the star, or that the dusty structure’s shape is highly unstable.

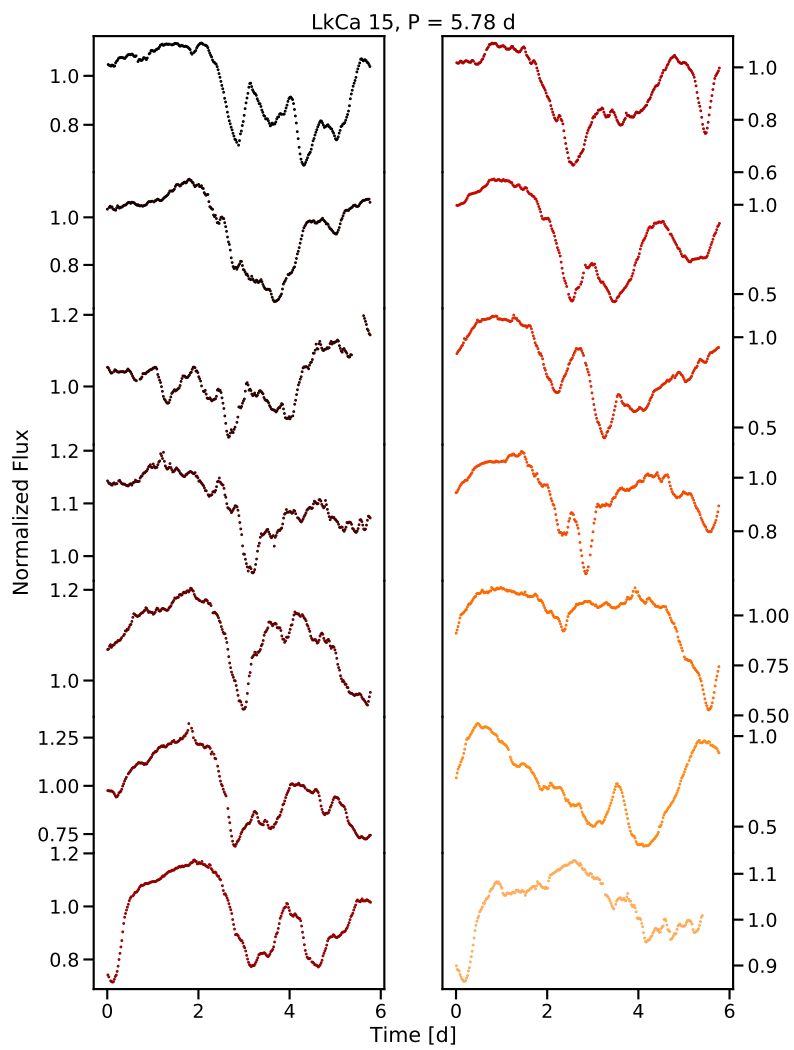


Figure 3.11 – Example of the multi-peaked light curve of LkCa 15, color-coded for each rotation cycle.

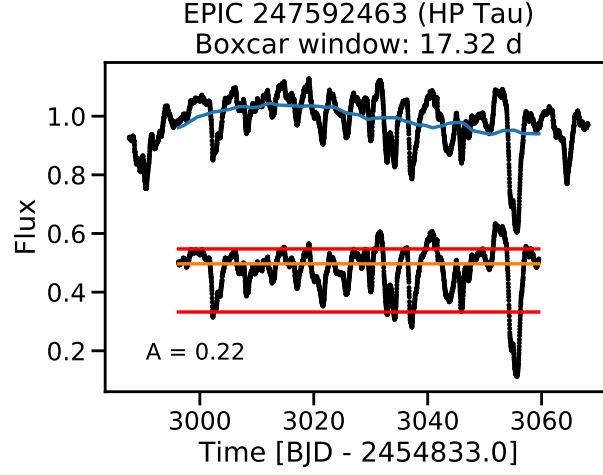


Figure 3.12 – Determination of the dips’ amplitude with the example of HP Tau. Top: light curve detrending of the original data (black) with a boxcar of size $4 \cdot P$. The blue line is the trend. Bottom: detrended light curve. The convolution with a boxcar removes a small part of the data at the edges. Orange line: flux median. Red lines: 90th and 5th percentiles of flux. The usage of flux percentiles allows us to consider the global variability of the light curve.

3.3.4 Dip amplitude and dip width

Among all other sources of variability for young stellar objects (YSOs), the long-term trends particularly affect the determination of the dips’ amplitude, due to the unstable continuum brightness. Thus, for the determination of the dips’ amplitudes, the light curves are detrended. For this aim, I apply a boxcar filter such as

$$\bar{x}[i] = \frac{1}{2M+1} \sum_{j=-M}^M x[i+j] \quad (3.1)$$

where $x[i+j]$ are the data points around $x[i]$ and $2M$ is the window width. This is chosen to be 4 times the period, in order to remove the long term variability and without interfering with the dips (Fig. 3.12). For non-periodic dippers, I choose a standard window of 7 d. In practice, I compute the convolution of the flux with a window that contains M times $\frac{1}{M}$. The detrending cuts off the data at the edges at $t_0 + \frac{M}{2}$ and $t_{\text{end}} - \frac{M}{2}$. The amplitudes are computed as the difference between the 90th and 5th percentile and peak-to-peak and are listed in Table 3.4. The light curves of Haro 6-37, JH 223, IS Tau and DK Tau (for this star, the faint state of the first ~ 30 d has not been included for this and the following analysis) do not need detrending, thanks to a stable continuum brightness. The detrending is not applied for the study of the periodicity, as it might influence the result and interfere with the physical phenomena that cause variability. It is only used in a pragmatic approach to study the dips’ morphology, without the influence of other stellar variability.

To define an eclipse width, it is useful to bin the phase-folded and detrended light curve (purple line in the upper panel of Fig. 3.13). This means that for each phase bin the flux of the different cycles is averaged. The dip width (black horizontal line in the upper panel of Fig. 3.13) is then defined at the full width of half maximum (FWHM) of the resulting binned curve. The results are listed in Table 3.4 and shown in App. B (Roggero et al., 2021, see App. F). In general, the dip width is around half of the period. The largest dip widths are linked to double- or multi-peaked dippers, with the exception of JH 112 A and HK Tau, which both exhibit a relatively small dip width ($\lesssim 0.5 P$) and the shortest periods in this group (2.21 and 3.3 d, respectively). The discussion about the correlation between dip width and period is presented in Sec. 3.6.4.

I estimate an uncertainty on the dip width as follows. First, for each phase bin, the standard deviation $\sigma(\text{phase})$ of the flux between the different cycles is computed (purple line in the upper panel of Fig. 3.13). Then, for every point of the binned light curve, the standard deviation of the phase bin is

Table 3.4 – Morphological properties of the dips.

EPIC	Name	P [d]	σ_P [d]	W [P]	$W_{-\sigma}$ [P]	$W_{+\sigma}$ [P]	A [mag]	$p2p$ [mag]
246929818 ^a	Haro 6-37	10.63;	0.72	0.59	0.65	0.50	0.75	1.03
246942563	St 34	5.23;	0.20	0.65 ^b	0.59	0.76	0.14	0.33
246989752	...	1.62	0.03	0.22	0.18	0.37	0.16	0.46
247103541	HD 285893	0.05	0.13
247520207	LkCa 15	5.78	0.20	0.64 ^c	0.47	0.62	0.54	1.05
247575958	CFHT Tau 12	3.48	0.07	0.59	0.60	0.70	0.23	0.50
247589612	JH 112 A	2.21	0.07	0.20 ^c	0.18	0.34	0.11	0.53
247592463	HP Tau	4.33	0.17	0.55 ^c	0.51	0.64	0.24	0.65
247763883	GH Tau	2.49	0.06	0.44	0.54	0.48	0.37	0.74
247764745	V807 Tau	4.39	0.12	0.39	0.40	0.35	0.11	0.18
247791801	GK Tau	4.61	0.15	0.43	0.41	0.48	0.62	1.28
247792225	GI Tau	7.13	0.40	0.67 ^c	0.34	0.68	0.49	0.97
247799571	HK Tau	3.3	0.07	0.50	0.53	0.44	0.29	0.55
247805410	FX Tau	0.18	0.36
247820821	...	2.38	0.04	0.41	0.43	0.36	1.18	1.77
247885481	...	2.90 ^d	0.08	0.60 ^b	0.32	0.89	0.05	0.14
247935061	GO Tau	0.17	0.36
248006676 ^a	JH 223	3.31	0.09	0.36	0.36	0.39	0.32	0.54
248015397	ITG 34	3.91	0.17	0.51	0.46	0.58	0.53	1.22
248029373 ^a	DK Tau	7.69;	0.45	0.57	0.65	0.35	1.08	1.91
248046139	GM Tau	2.67	0.05	0.44	0.49	0.40	1.30	2.00
248047443	IS Tau	7.58	0.41	0.54 ^c	0.68	0.43	0.13	0.24

Columns: the photometric period P , the uncertainty estimated from the Gaussian fitting of the periodogram peak σ_P , the dip width W measured as FWHM of the folded and binned light curve in units of phase, the dip width estimated considering the binned light curve $\pm\sigma$ of the flux ($W_{-\sigma}$, $W_{+\sigma}$), the dip amplitude with the 90th and 5th flux percentiles A , the peak-to-peak amplitude $p2p$.

^(a) The stars are detrended before determining the width with the exception of those marked with ^(a).

^b Value discarded because not representative of the real dip width.

^c Double-peaked dip.

^d The peak of the periodogram is at 2.99 d and is linked to a cold spot. A more thorough analysis is needed to retrieve the dipper period at 2.90 d.

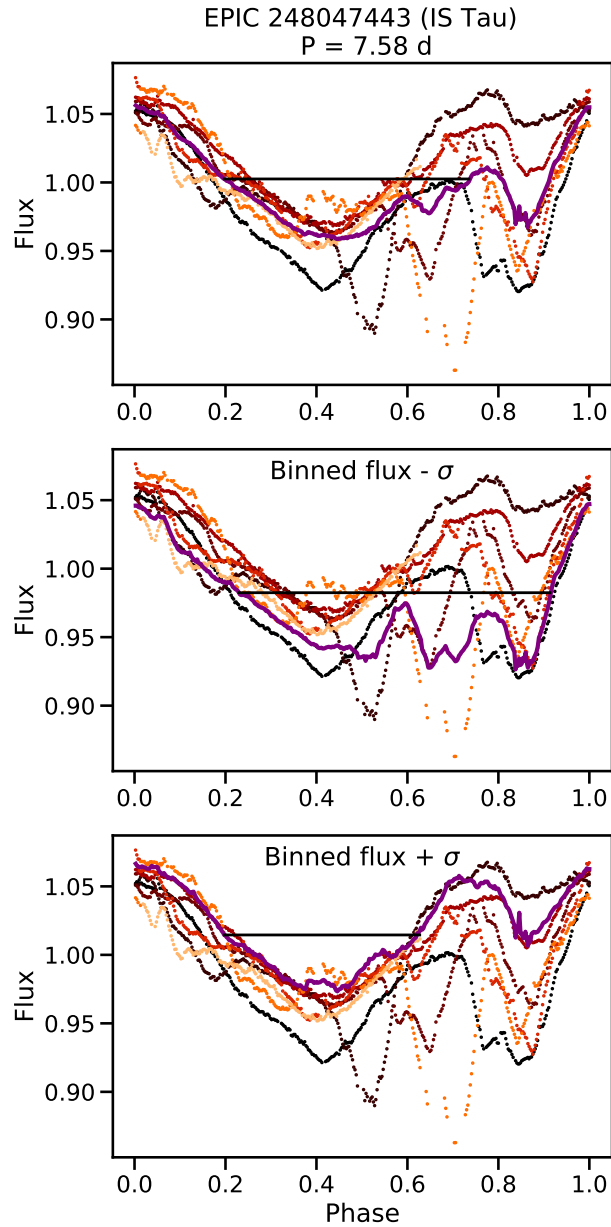


Figure 3.13 – Dip width measured as FWHM of the binned light curve (purple line, top). For the folded light curve, each color represents a different cycle. By adding or subtracting the flux' standard deviation for each phase bin, it is possible to distinguish between the width of the main dip (bottom) and the double peak (center).

in one case added, in the other subtracted (purple line on center and bottom panel in Fig. 3.13). Finally, the dip width is computed again as FWHM of these modified binned light curves. Upper and lower error bars are defined as difference between the dip width of the modified binned light curves and the original one. Since the shape of the dips may strongly vary after this operation, these error bars can be large.

For double-peaked dippers, the line drawn at FWHM can cross the binned light curve in more than two points: the error bars $w + \sigma$ and $w - \sigma$ are then chosen to represent both the primary peak's width and the total width of the dip, which is in these cases very large. This can result in strongly asymmetric error bars (see Sec. 3.6.4). In Table 3.4, some width values are flagged for not being reliable. This can happen when the folded light curve is very noisy and the binned light curve does not show the dips as they can be seen by eye. These plots appear in App. B (Roggero et al., 2021, see App. F).

Another possible representation of the uncertainty on the dip width would be to compute the dip width at different thresholds of the same binned light curve, e.g., at 0.3, 0.5 (FWHM), 0.7 of the flux maximum. However, the information about the width of the main dip and the total dip in double-peaked dips (see e.g., IS Tau) would be lost.

3.4 STELLAR PARAMETERS

Dipper stars are most commonly low-mass T Tauri stars. Their periods of a few days are consistent with the range of rotational periods found in general for young, low-mass stars. There is consensus that the dips in the light curve are caused by dust; in the dusty disk warp scenario, the inner disk warp is located at the corotation radius. Moreover, whatever the position of the occulting dusty structure is, the temperature must be low enough for dust to be able to be present, i.e., not to sublimate.

In the following section, the derivation of the different stellar parameters for dipper stars is discussed. In order to verify the conditions and to compute the radius and temperature at corotation, the masses and radii of the star are required. The discussion about each parameter follows in the next subsections.

3.4.1 *Effective temperatures and spectral types*

Effective temperatures are listed in Table 3.5 and were derived according to the SpT- T_{eff} conversions of Pecaut and Mamajek (2013). The main sources for the spectral types are Esplin and Luhman (2019) and Herczeg and Hillenbrand (2014), which agree for almost all objects. In case of spectral subclasses not explicitly listed in the conversion tables, the value of T_{eff} was linearly interpolated between the two closest subclasses. For spectral types later than M5, the temperature conversions by Herczeg and Hillenbrand (2014) are used. This is more consistent than a simple linear extrapolation (Fig. 3.14), which would assign to spectral types later than M5 a T_{eff} significantly higher than for the earlier types M3 and M4.

The uncertainty on T_{eff} follows the uncertainty on the spectral type: for spectral types up to K9, the uncertainty is one spectral subclass; for spectral types between M0 and M4, 0.4 subclasses; for spectral types later than M4, 0.25 subclasses (Herczeg and Hillenbrand, 2014). As a consequence, asymmetric error bars are computed from Pecaut and Mamajek (2013) for an earlier and later spectral type, respectively. If the later spectral type is missing at the end of the table, a symmetric error bar is produced. The systematic uncertainty linked to the choice of the models of up to 150 K is not taken into account here. A discussion of the consequences on the derived stellar parameters is given in Sec. 3.4.7.

3.4.2 *VJHK photometry*

The light curves of young, accreting stars might be affected by contamination (e.g., by hotspots) in the blue band. Thus, photometry in the V and JHK bands is preferred. The dipper list was cross-matched with the Two Micron All-Sky Survey (2MASS, Skrutskie et al., 2006) to obtain JHK photometry.

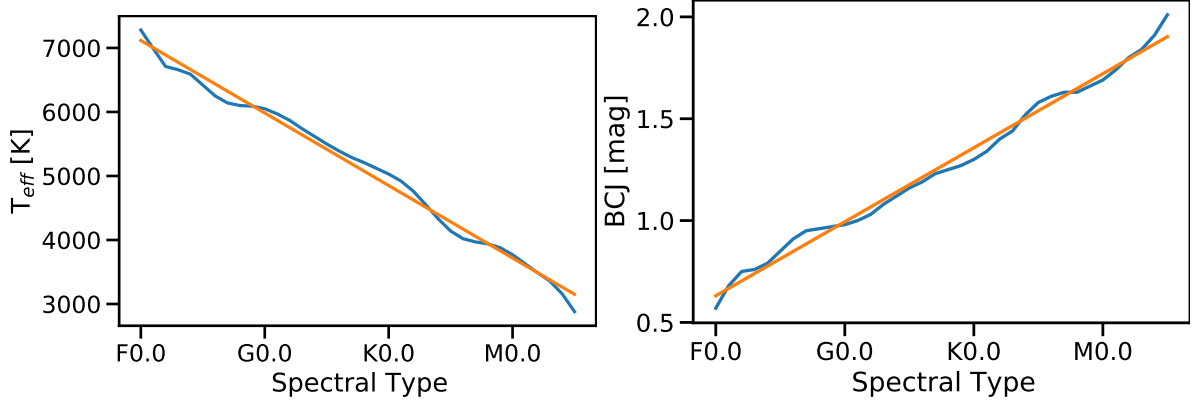


Figure 3.14 – Temperature and bolometric correction conversion as in Pecaut and Mamajek (2013). Orange line: linear fit. The trend is not linear towards the end and the value of T_{eff} would be more affected by a simple extrapolation.

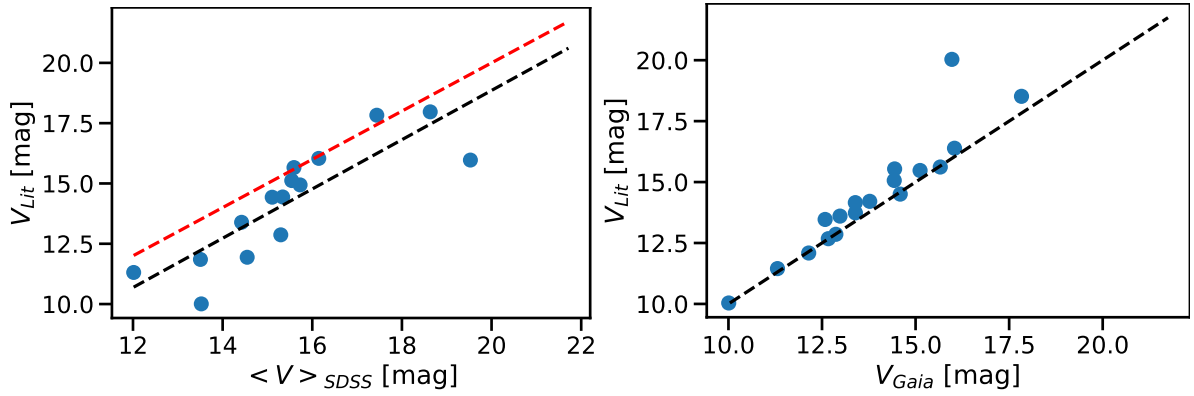


Figure 3.15 – Left: comparison between V from the literature and the $\langle V \rangle$ from the SDSS, averaged from different conversion formulae. Black line: linear fit. Red line: $V_{\text{Lit}} = \langle V \rangle_{\text{SDSS}}$. Right: comparison between measurement from other catalogs and $GaiaG$ converted to V from its components $G_{\text{BP}}, G_{\text{RP}}$. Black line: $V_{\text{Lit}} = V_{\text{Gaia}}$.

As for the V band, since a photometric monitoring is the best way to determine the magnitude of variable stars, values reported in the photometric monitoring by Grankin et al. (2007) are preferred, where available. An inspection of the light curves presented for the objects studied here leads to the choice of their \bar{V}_m as best estimation for the brightness continuum. However, many of the dipper stars are not present in that collection and other sources have to be included as well. The photometric catalogs including V common to most sources are three: GSC2.3.2 (Lasker et al., 2008), NOMAD-1 (Zacharias et al., 2005), APASS (Henden et al., 2016), SDSS. The entries in NOMAD are from the YB6 catalog, which consists of scanned plates and is thus considered as lower-quality source. The SDSS is discarded because an offset of ~ 1 mag is present in the converted V band, compared with the other catalogs (Fig. 3.15). For individual stars, other extra measurements could be retrieved from the literature. All available values for each star were inspected to verify if there were any strong inconsistencies between the collections. More entries are available in the GSC catalog than in any other collection. If the star was not already reported in Grankin et al. (2007) and there were not particular problems with the photometry, the entry of the GSC catalog is set as V value in Table 3.5, when available.

In the few cases where these single measurements were highly discordant ($\Delta V > 1$ mag) between the catalogs, due to the intrinsic variability of young stars, special attention was given to those stars. One way to assess the plausibility of a V band measurement is to verify that it does not lead to a strongly negative extinction.

In order to verify that the individually picked visual magnitudes from different sources were self-consistent, the values of V were compared with the *Gaia* G (Gaia Collaboration et al., 2016, 2018) converted to V as²:

$$G - V = -0.0176 - 0.006860(G_{\text{BP}} - G_{\text{RP}}) - 0.1732(G_{\text{BP}} - G_{\text{RP}})^2. \quad (3.2)$$

No offset could be found (Fig. 3.15). I could also have used the converted G_{BP} and G_{RP} , thus preferring an homogeneous source for all values. However, dippers are affected by a strong variability, thus making a single measurement (as from *Gaia*) less reliable. This exercise allows to exclude that the strong stellar variability influenced the single *Gaia* measurements and makes the values used for V more robust.

Table 3.5 – Spectral types, effective temperatures and $VJHK$ photometry for the presented sample of 22 best dippers. JHK measurements are from 2MASS.

EPIC	2MASS	Name	SpT	Refs.	T_{eff} [K]	A_V [mag]	V	Refs.	J	H	K
246929818	J04465897+1702381	Haro 6-37	K8	1,2	3940	2.1	12.98	7	9.24	7.99	7.31
246942563	J04542368+1709534	St 34	M3	3	3360	0.5	14.59	7	10.69	10.08	9.79
246989752	J04384725+1737260	...	M5.5	1,2	2920**	0.0	12.75	12.11	11.75
247103541	J04363081+1842153	HD 285893	F8	4	6100	0.3	10.01	8	8.76	8.37	7.99
247520207	J04391779+2221034	LkCa 15	K4	5	4492***	0.4	12.14	9	9.42	8.60	8.16
247575958	J04330945+2246487	CFHT Tau 12	M6	1	2860**	3.0	13.15	12.14	11.54
247589612	J04324911+2253027	JH 112 A	K5.5	1,2	4080	2.9	14.44	7	10.24	8.99	8.17
247592463	J04355277+2254231	HP Tau	K4	1,2	4330	3.2	13.78	9	9.55	8.47	7.62
247763883	J04330622+2409339	GH Tau	M2	1,2	3490	0.4	12.87	7	9.11	8.23	7.79
247764745	J04330664+2409549	V807 Tau	K7*	1,2	3970	0.4	11.31	7	8.15	7.36	6.96
247791801	J04333456+2421058	GK Tau	K6.5	1,2	3995	1.0	12.67	9	9.05	8.11	7.47
247792225	J04333405+2421170	GI Tau	Mo.4	1,2	3714	1.3	13.39	9	9.34	8.42	7.89
247799571	J04315056+2424180	HK Tau	M1*	1,2	3630	2.4	15.12	7	10.45	9.25	8.59
247805410	J04302961+2426450	FX Tau	M2.2	1,2	3464	1.0	13.39	7	9.39	8.40	7.92
247820821	J04295950+2433078	...	M5	1	2880	0.0	15.97****	10	11.68	10.54	9.81
247885481	J05023985+2459337	...	M4.25	6	3090	0.0	16.04	7	11.78	11.09	10.78
247935061	J04430309+2520187	GO Tau	M2.3	1,2	3451	1.6	14.43	7	10.71	9.78	9.33
248006676	J04404950+2551191	JH 223	M2.8	1,2	3386	1.4	15.66	7	10.75	9.92	9.49
248015397	J04411078+2555116	ITG 34	M5.5	1	2920**	2.2	13.19	12.12	11.45
248029373	J04304425+2601244	DK Tau	K8.5	1,2	3910	0.7	12.58	9	8.72	7.76	7.10
248046139	J04382134+2609137	GM Tau	M5	1,2	2880	2.1	17.83	7	12.80	11.59	10.63
248047443	J04333678+2609492	IS Tau	Mo*	1,2	3770	2.4	14.94	7	10.32	9.29	8.64

* Spectral type by Esplin and Luhman (2019) differs of 0.5 subclasses or more in comparison with Herczeg and Hillenbrand (2014).

** For spectral types later than M5, the temperature conversion by Herczeg and Hillenbrand (2014) is used. The extrapolation for M6 in Pecaut and Mamajek (2013) would deliver 3038 K.

*** T_{eff} derived spectroscopically by Alencar et al. (2018).

**** The provided amplitude and $\langle V \rangle$ were combined to derive a more representative V_{min} .

References. (1) Esplin and Luhman (2019); (2) Herczeg and Hillenbrand (2014); (3) Dahm and Lyke (2011); (4) Nesterov et al. (1995); (5) Alencar et al. (2018); (6) Esplin et al. (2014); (7) Lasker et al. (2008); (8) Henden et al. (2016); (9) Grankin et al. (2007); (10) Drake et al. (2014).

3.4.3 Visual extinction

Most stars in Taurus are subject to at least some reddening. Many stars have moderate/strong infrared excesses, which can affect even the near-IR bands. At the same time, the fainter stars are harder to

² https://gea.esac.esa.int/archive/documentation/GDR2/Data_processing/chap_cu5pho/sec_cu5pho_calibr/ssec_cu5pho_PhotTransf.html. Visited on July 12, 2021.

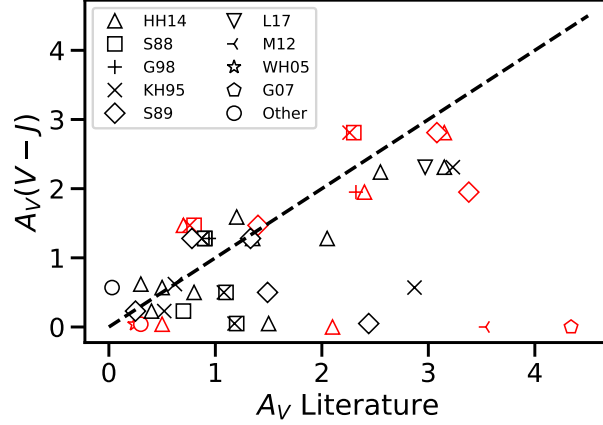


Figure 3.16 – Comparison between the A_V derived here from the $(V - J)$ colors compared to the literature values derived also from the optical. References appear in Table 3.6. Red points: stars with high veiling. For these, the spectroscopic measurement by Herczeg and Hillenbrand (2014) is preferred. The dashed line represents $A_V(V - J) = A_V(\text{lit})$. For GO Tau (4 black symbols at the bottom, close to $A_V(V - J) = 0$) the $A_V(V - J)$ value is discarded because it is inconsistent with the literature. Another outlier is the A_V of V807 Tau as measured by KH95; this value is discarded for the same reason. The stars with the largest scatter are strongly veiled and the extinction measured with photometry is less reliable.

detect at shorter wavelengths. Hence, I calculate visual extinction by comparing the $(V - J)$ colors as observed to those for the corresponding spectral type in Pecaut and Mamajek (2013). Herczeg and Hillenbrand (2014) measured a quite high veiling at 7510 \AA for some objects in this sample. For those with high veiling, extinction derived with photometry will not be as accurate as with spectroscopy. For the stars with $r > 0.1$, the A_V computed by Herczeg and Hillenbrand (2014) from spectroscopy is preferred.

I wanted to minimize the risk of inconsistent values that goes along with very few, or just one, photometric measurement. For this reason, the available measurements of A_V in the optical in the literature were collected and compared (see Table 3.6). This could allow to filter out a couple of clear outliers, flagged in Table 3.6. For stars with lower veiling, the final A_V is an average of the extinction computed here using $(V - J)$ and the other values in the literature (a comparison between the here derived values and the literature is shown in Fig. 3.16). The usage of $(J - K)$ leads to an increase of A_V up to a factor 5, due to the infrared excess, and is therefore not applied here. For measurements of $A_V < 0$, A_V is set to 0 in order to be physical, as well as the uncertainty if $A_V \ll 0$. The uncertainty on A_V is set as the root-mean-square (rms) of the A_V derived in this study compared with the literature. A minimum reasonable uncertainty of 0.3 mag is applied. Empirically, the uncertainty does not grow with extinction. Fig. 3.16 shows how veiling impacts the derivation of the extinction from photometry. For stars not affected by veiling, the A_V computed from $(V - J)$ is consistent with optical measurements in the literature.

The distribution of the dipper stars in the JHK color diagram is represented in Fig. 3.17. Stars right of the main sequence and its extinction vector have an intrinsic IR excess, as it is the case for a fraction of dippers. The region left of the plot is forbidden for CTTSs. The outlier at the bottom of the plot is HD 285893, which is a more massive and probably older star (see Sec. 3.5).

3.4.4 Luminosities

The stellar luminosity is computed from the bolometric magnitude M_{bol} as in:

$$L_*/L_\odot = 10^{-\frac{M_{bol} - M_{bol,\odot}}{2.5}} \quad (3.3)$$

Table 3.6 – A_V as measured with V - J compared to the literature.

EPIC	Name	A_V	r_{7510}^a	A_V^d	A_V^b	A_V^c	A_V^e	A_V^f	A_V^g	A_V^h	A_V^i	A_V^j	σ_{A_V}	
246929818	Haro 6-37	...	0.33	2.05	1.8	...	2.12	2.44	2.1	0.3
246942563	St 34	0.04	0.14	0.5	0.24	0.3^1	0.5	0.3
246989752	0.0	0.0	0.3
247103541	HD 285893	0.32	0.3	0.3
247520207	LkCa 15	0.62	0.04	0.3	0.62	0.5	0.3
247575958	CFHT Tau 12	2.64	...	3.44^2	...	3.0	0.6
247589612	JH 112 A	2.31	0.0	3.15	3.23	...	2.97	2.9	0.4
247592463	HP Tau	2.81	0.16	3.15	2.3	...	2.26	3.08	3.2	0.3
247763883	GH Tau	0.23	0.0	0.4	0.7	...	0.52	0.25	0.4	0.2
247764745	V807 Tau	0.57	0.05	0.5	2.87^*	0.03^3	0.4	0.3
247791801	GK Tau	1.28	0.08	1.35	0.9	0.94	0.87	0.78	1.0	0.2
247792225	GI Tau	1.28	0.04	2.05	0.9	1.34	0.87	1.33	1.3	0.4
247799571	HK Tau	1.95	0.1	2.4	...	2.32	...	3.38	2.4	0.3
247805410	FX Tau	0.50	0.06	0.8	1.1	...	1.08	1.49	1.0	0.4
247820821	...	-1.35	0.0	0.0
247885481	...	-0.43	0.0	0.0	0.0
247935061	GO Tau	0.05^*	0.09	1.5	1.2	...	1.18	2.44	1.6	0.9
248006676	JH 223	1.59	0.0	1.2	1.4	0.3
248015397	ITG 34	2.6	...	1.77^2	2.2	0.6
248029373	DK Tau	1.47	0.27	0.7	0.8	1.42	0.76	1.4	0.7	0.3
248046139	GM Tau	-0.28	0.26	2.1	3.54	...	4.34^2	2.1	0.3
248047443	IS Tau	2.24	0.02	2.55	2.4	0.3

Only the extinction measured by Luhman et al. (2017) with optical or CTTS methods are reported here. The veiling is measured at 7510 Å by Herczeg and Hillenbrand (2014).

* Value discarded because inconsistent with the literature.

References. (a) Herczeg and Hillenbrand (2014); (b) Strom et al. (1988); (c) Gullbring et al. (1998); (d) Kenyon and Hartmann (1995); (e) Strom et al. (1989); (f) Luhman et al. (2017); (g) Mayne et al. (2012); (h) White and Hillenbrand (2005); (i) other refs; (j) this work; (1) Hartmann et al. (2005); (2) Guieu et al. (2007); (3) Schaefer et al. (2012).

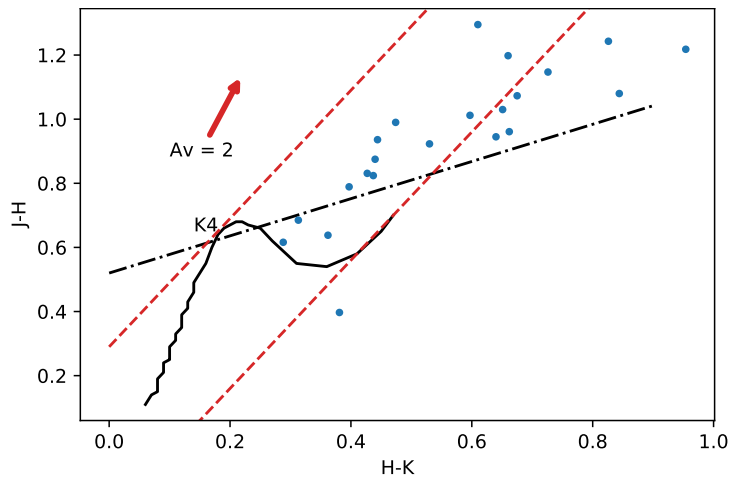


Figure 3.17 – JHK color-color diagram of the underreddened dipper sample. Solid black line: unreddened main sequence going from spectral type F0 to M5. The red dashed lines are parallel to the extinction vector A_V . The black dashed line is the T Tauri locus according to Meyer et al. (1997).

where $M_{bol,\odot} = 4.25$ mag. Since the brightness and bolometric corrections are mostly available for the J band, the bolometric magnitude is derived according to:

$$M_{bol} = m_J - 5 \log(p^{-1}) + 5 - A_J + BC_J \quad (3.4)$$

where m_J is the J -band magnitude, p is the parallax (here from *Gaia*), A_J the extinction in the J -band and BC_J the bolometric correction for the J -band. The bolometric corrections were retrieved from Pecaut and Mamajek (2013) and interpolated for intermediate spectral types. In case of spectral types later than M5 (not present in the tables), the BC_J was extrapolated. The computation of A_J from $(J - K)$ is affected by IR excess. Thus, it is preferred to convert A_V to A_J as $\frac{A_J}{A_V} = 0.282$ (Cardelli et al., 1989).

The *Gaia* parallax from DR2 was not available for three objects (GH Tau, IS Tau, FX Tau). For those, the distance distributions in Taurus by Fleming et al. (2019) were used. FX Tau and GH Tau are located in the B18 cloud, which contains members of the ‘near’ population at 127.4 ± 3.8 pc. A standard deviation of 7.9 pc is applied as uncertainty for unknown parallaxes. IS Tau lies on the filament L1495, which contains members of both populations. Its luminosity is computed for both mean distances and shown with an arrow in Fig. 3.18. It seems that IS Tau is more likely a member of the far population at 150-180 pc, if one assumes it has the same age as the other dippers. In the case of Haro 6-37, the 2MASS measurement in the J band is corrupted and no other measurements are available. The visual magnitude and the corresponding BC_V are considered instead.

The procedure for deriving uncertainties on the bolometric correction is the same as for the effective temperature. A major issue for the determination of the luminosity uncertainty is the intrinsic photometric variability of dipper stars, which cannot be included here in absence of an extensive observation campaign. Nevertheless, for stars on their Hayashi tracks, the derivation of the mass depends much more on a precise spectral type, rather than on luminosity (see Fig. 3.18). The uncertainty on the luminosity affects much more the derivation of age; hence, the isochrones in Fig. 3.18 are approximations.

3.4.5 Masses and radii

In order to derive the mass of the dipper stars in this sample, evolutionary models that go to the lowest end of stellar formation are needed. Thus, the tracks of Baraffe et al. (2015) are preferred (Fig. 3.18), as they include M-dwarfs.

The aim here is to be self-consistent; therefore, all masses are derived from the same model. The effective temperature is the dominant term for identifying the corresponding track for this sample. Thus, an identification of the corresponding tracks along the x-axis is the most efficient, with the only exception of the latest M-dwarfs, for which the luminosity also plays an important role. Since the tracks are quantized –with a resolution of $0.1 M_{\odot}$ down to $m = 0.2 M_{\odot}$, $0.02 M_{\odot}$ for $0.1 < m \leq 0.2 M_{\odot}$, $0.01 M_{\odot}$ for $m \leq 0.1 M_{\odot}$ –, the error bars represent the distance between the upper/lower values of the data point and the closest track. The small error bars on the masses listed in Table 3.7 reflect the small error bars on the effective temperatures.

The Hertzsprung-Russell diagram with some of the evolutionary tracks and isochrones is shown in Fig. 3.18. The dippers are uniformly distributed around 1 Myr. With the exception of LkCa 15 and HD 285893, the stars identified as dippers have a mass less than $1 M_{\odot}$, with a few M-dwarfs close to the brown dwarf limit of $\sim 0.072 M_{\odot}$. The stars in Herczeg and Hillenbrand (2014) are cross-matched with the members and possible members of Taurus in Rebull et al. (2020) and appear as grey points on the HR diagram. The spectral types are converted to temperatures with the same conversion that we apply to dippers. For spectral types later than K4, the conversion provided by Herczeg and Hillenbrand (2014) exhibits a systematic temperature offset of around +60 K and up to +130 K, while for earlier spectral types, the temperatures proposed by Pecaut and Mamajek (2013) are higher. For the case that several luminosities are provided for a star, the values are averaged in the HR diagram. Since dippers are associated with circumstellar extinction events and their V measurement might have been taken in the fainter state, one might expect that they are less luminous than non-dipper stars, which does not seem to be the case here. Interestingly, many stars with a mass between 0.1 and $0.3 M_{\odot}$ with

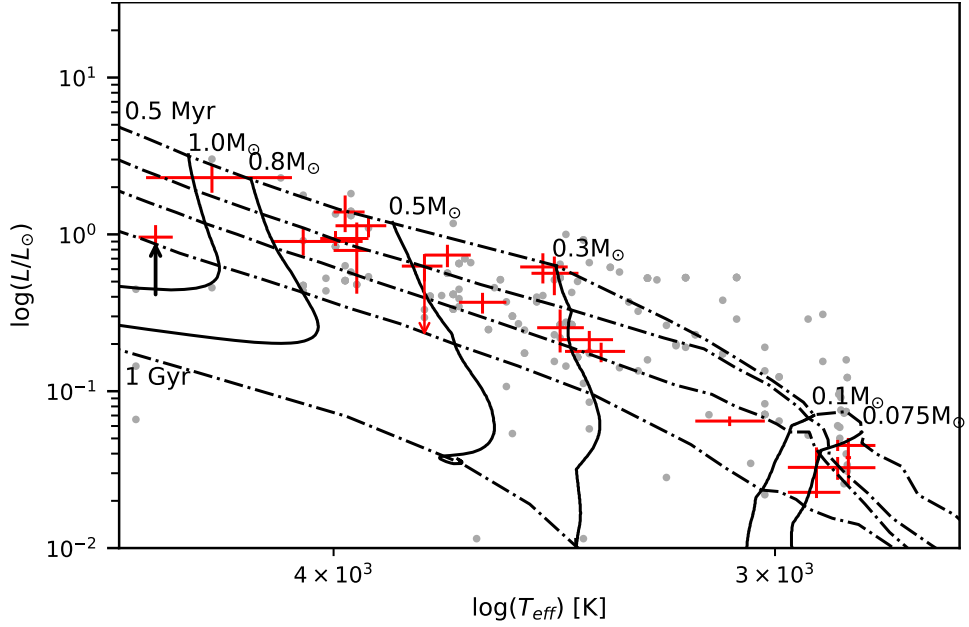


Figure 3.18 – HR diagram of the dipper sample with evolutionary tracks (solid lines) and isochrones (dashed lines) from Baraffe et al. (2015). The brown dwarf limit lies at $0.073 M_{\odot}$. Isochrones from top to bottom: 0.5, 1, 2, 5 Myr, 1 Gyr. The red points are the Taurus members classified as dippers, while the gray points (without error bars) are Taurus members as in Herzig and Hillenbrand (2014). HD 285893 (SpT F8) does not appear on this plot for the sake of readability, since its derived T_{eff} is much higher than the rest of the sample. The stars’ age scatters around 1 Myr and, with the exception of LkCa15 (marked with a black arrow) and HD 285893, they are on their Hayashi tracks and still fully convective.

parameters derived by Herzig and Hillenbrand (2014) lie well above the youngest isochrone. On one hand, this might be a hint to the difficulty of providing precise evolutionary models for stars with a very low mass. On the other hand, for faint and accreting brown dwarfs, the accretion luminosity might be dominant compared to the faint stellar luminosity. At the other extreme, with a $T_{\text{eff}} = 6100$ K and $L = 1.99 L_{\odot}$, HD 285893 almost lies on the ZAMS on the HR diagram. A more detailed discussion is given in the individual notes in Sec. 3.5; this ‘old’ dipper might belong to a recently identified class of debris disk dippers (Gaidos et al., 2019; Tajiri et al., 2020), for which aperiodic extinction events have been attributed to the disruption of planetesimals.

The stellar radii are derived according to the Stefan-Boltzmann law as

$$\frac{R}{R_{\odot}} = \left(\frac{L}{L_{\odot}} \right)^{\frac{1}{2}} \left(\frac{T_{\odot}}{T_{\text{eff}}} \right)^2 \quad (3.5)$$

and are presented along with the masses in Table 3.7. The uncertainties on T_{eff} and the luminosity are propagated to the stellar radius.

3.4.6 Radius and temperature at corotation

In the magnetospheric accretion scenario, the dusty warp that obscures the star is located at corotation. The corotation radius defines the distance from the star at which the Keplerian disk’s material rotates with the same angular velocity as the star. Given that, in a stable orbit, the gravitational potential of the star is equal to the centrifugal force, the corotation radius is derived as:

$$R_{\text{cor}} = \left(\frac{P}{2\pi} \right)^{\frac{2}{3}} (GM_{*})^{\frac{1}{3}} \quad (3.6)$$

where P is the stellar period. Considering the simple approximation of no energy transfer between a dust grain situated at R_{cor} and the rest of the disk, which reduces the effective irradiation by a factor 4 as in Bouvier et al. (1999), it is possible to derive the temperature at corotation as:

$$T_{\text{cor}} = 2^{-\frac{1}{2}} T_{\text{eff}} \left(\frac{R_*}{R_{\text{cor}}} \right)^{\frac{1}{2}} \quad (3.7)$$

The so computed corotation radii and temperatures are listed in Table 3.7. The corotation radii extend to a few stellar radii, between 2.5 and $9 R_*$. The temperatures at corotation are around ~ 1000 K, with a few stars that reach up to ~ 1500 K. The error bars on this quantity are large, because the uncertainties on the stellar radii are of the order of 10%-20% for young stars.

Table 3.7 – Stellar properties of the dipper sample.

EPIC	Name	L_* [L_\odot]	M_* [M_\odot]	R_* [R_\odot]	R_{cor} [R_*]	T_{cor} [K]	$v \sin i$ [km s^{-1}]	Ref.	i_* [$^\circ$]	$\log \dot{M}_{\text{acc}}$ [$M_\odot \text{ yr}^{-1}$]	Refs.
246929818	Haro 6-37	$0.79^{+0.40}_{-0.37}$	$0.60^{+0.05}_{-0.05}$	$1.91^{+0.54}_{-0.48}$	8.98	930^{+179}_{-158}	12.1 ± 1.2	1	> 47	-7.00/-8.12	6,7,8
246942563	St 34	$0.18^{+0.02}_{-0.03}$	$0.25^{+0.05}_{-0.05}$	$1.25^{+0.14}_{-0.13}$	6.38	941^{+118}_{-107}
246989752	...	$0.023^{+0.004}_{-0.002}$	$0.071^{+0.014}_{-0.011}$	$0.59^{+0.08}_{-0.04}$	4.08	1022^{+122}_{-91}
247103541	HD 285893	$1.99^{+0.25}_{-0.25}$	$1.15^{+0.02}_{-0.02}$	$1.26^{+0.08}_{-0.10}$
247520207	LkCa 15	$0.96^{+0.19}_{-0.17}$	$1.12^{+0.01}_{-0.01}$	$1.62^{+0.19}_{-0.18}$	8.69	1077^{+99}_{-95}	13.9 ± 1.2	1	79^{+11}_{-24}	-8.83/-8.87/-9.17	8,6,9
247575958	CFHT Tau 12	$0.038^{+0.013}_{-0.013}$	$0.065^{+0.010}_{-0.005}$	$0.79^{+0.14}_{-0.14}$	4.90	913^{+100}_{-112}
247589612	JH 112 A	$0.90^{+0.19}_{-0.17}$	$0.700^{+0.020}_{-0.015}$	$1.90^{+0.28}_{-0.32}$	3:33	1581^{+172}_{-217}
247592463	HP Tau	$2.30^{+0.50}_{-0.46}$	$0.9^{+0.3}_{-0.2}$	$2.70^{+0.53}_{-0.54}$	4.00	1531^{+294}_{-336}	15.4 ± 1.6	2	29^{+11}_{-11}
247763883	GH Tau	$0.62^{+0.14}_{-0.13}$	$0.325^{+0.025}_{-0.025}$	$2.16^{+0.30}_{-0.30}$	2.46	1572^{+166}_{-168}	30.3 ± 0.7	1	44^{+10}_{-10}	-7.92/-8.02/-8.90	7,10,6,8
247764745	V807 Tau	$1.39^{+0.38}_{-0.36}$	$0.60^{+0.05}_{-0.05}$	$2.50^{+0.38}_{-0.38}$	3.81	1437^{+154}_{-161}	13.6 ± 0.7	1	28^{+7}_{-7}	-8.40/<-8.68	8,10
247791801	GK Tau	$0.94^{+0.11}_{-0.10}$	$0.65^{+0.05}_{-0.05}$	$2.03^{+0.16}_{-0.19}$	4.98	1266^{+93}_{-117}	18.7 ± 3.5	2	57^{+23}_{-22}	-8.19	6,7,8,11
247792225	GI Tau	$0.74^{+0.12}_{-0.12}$	$0.45^{+0.05}_{-0.05}$	$2.08^{+0.23}_{-0.23}$	5.75	1095^{+118}_{-118}	12.7 ± 1.9	1	59^{+24}_{-24}	-8.00/-8.02/-8.08	11,6,7,8
247799571	HK Tau	$0.37^{+0.05}_{-0.06}$	$0.40^{+0.05}_{-0.05}$	$1.54^{+0.16}_{-0.16}$	4.47	1214^{+115}_{-115}	21.8 ± 2.5	3	68^{+21}_{-21}	-7.65	12
247805410	FX Tau	$0.56^{+0.16}_{-0.16}$	$0.300^{+0.050}_{-0.025}$	$2.09^{+0.35}_{-0.35}$	9.61 ± 0.19	1	...	-8.65	6,7
247820821	...	$0.045^{+0.004}_{-0.004}$	$0.075^{+0.015}_{-0.003}$	$0.85^{+0.04}_{-0.07}$	3:70	1058^{+39}_{-110}	18.4 ± 1.0	4	> 64
247885481	...	$0.065^{+0.005}_{-0.005}$	$0.15^{+0.03}_{-0.03}$	$0.89^{+0.07}_{-0.07}$	5:23	956^{+100}_{-100}
247935061	GO Tau	$0.25^{+0.08}_{-0.08}$	$0.300^{+0.050}_{-0.025}$	$1.41^{+0.26}_{-0.26}$	17.5 ± 9.7	2	...	-7.93/-8.33/-8.42	6,9,8
248006676	JH 223	$0.21^{+0.03}_{-0.03}$	$0.275^{+0.025}_{-0.025}$	$1.34^{+0.14}_{-0.14}$	4:52	1126^{+107}_{-103}
248015397	ITG 34	$0.033^{+0.011}_{-0.010}$	$0.075^{+0.015}_{-0.015}$	$0.71^{+0.15}_{-0.13}$	6.23	827^{+143}_{-128}
248029373	DK Tau	$1.14^{+0.16}_{-0.18}$	$0.55^{+0.05}_{-0.05}$	$2.33^{+0.27}_{-0.24}$	5:78	1150^{+131}_{-112}	17.5 ± 1.2	1	> 60	-7.42	6,7,11
248046139	GM Tau	$0.033^{+0.006}_{-0.005}$	$0.065^{+0.015}_{-0.005}$	$0.73^{+0.06}_{-0.09}$	4.49	961^{+60}_{-126}	9.0 ± 2.0	5	41^{+17}_{-15}	-8.60/-8.70	13,14
248047443	IS Tau	$0.63^{+0.12}_{-0.13}$	$0.50^{+0.05}_{-0.05}$	$1.86^{+0.24}_{-0.23}$	6.93	1013^{+116}_{-110}	-7.91/-8.01	10,8

Stellar inclinations reported as lower limits have $\sin i > 1$.

(1) Nguyen et al. (2012); (2) Güdel et al. (2007); (3) Hartmann et al. (1986); (4) Kraus et al. (2017); (5) Mohanty et al. (2005); (6) Hartmann et al. (1998); (7) Muzerolle et al. (1998); (8) White and Ghez (2001); (9) Isella et al. (2009); (10) Hartigan and Kenyon (2003); (11) Gullbring et al. (1998); (12) White and Hillenbrand (2004); (13) White and Basri (2003); (14) Herczeg and Hillenbrand (2008).

3.4.7 Inclinations

In order to probe the capacity of the magnetospheric accretion model to account for dippers, the angle under which we observe the system is required, as dippers cannot be seen close to face-on, if the dusty part of the accretion column has to cross the observer's line of sight to produce dips in the light curve (e.g., Bodman et al., 2017; McGinnis et al., 2015). A more detailed discussion on this point is provided in Sec. 3.6.2. The stellar inclination is derived according to the formula:

$$v \sin i = \sin i \frac{2\pi R_*}{P} \quad (3.8)$$

Here, the convention used to define the inclination is 0° for the star seen pole-on and 90° for edge-on. The $v \sin i$ values are retrieved from the literature (see Table 3.7): main sources are Nguyen et al. (2012) and Güdel et al. (2007), who retrieve their values for this sample from Rebull et al. (2004).

The uncertainty on i grows with $\sin i$, thus higher inclination angles have larger uncertainties. Some stars (Haro 6-37, EPIC 247820821, DK Tau) exhibit a $\sin i > 1$, which probably hints that something went wrong with the stellar parameters. In these cases, the minimal inclination angle is indicated as a lower limit. The results are listed in Table 3.7. For Haro 6-37, the period is uncertain. It is possible that the observed period is not correct or not directly related to the rotation period. For DK Tau, different periods have been reported in the literature due to the complexity of the light curve, and the WPS (Roggero et al., 2021, App. F) shows an increasing period during the $K2$ observations. Since the stellar rotation period is not supposed to vary much, physical phenomena other than rotation might influence the dips and their apparent periodicity. Moreover, Grankin et al. (2007) report for this star a long-term variability amplitude of $\Delta V \sim 1.8$ mag, which propagates from luminosity and stellar radius to any inclination angle between 30° and 90° , if taken into account for the uncertainty on V_{mag} .

3.4.8 Mass accretion rates and accretion regime

The mass accretion rates of the dippers are collected from the literature and are, when available, in the order of magnitude of $10^{-8} M_\odot \text{yr}^{-1}$ (Table 3.7). This is in agreement with the observed mass accretion ranges for T Tauri stars (Gregory et al., 2006). Exceptions are Haro 6-37, HK Tau, and DK Tau, which are stronger accretors of the order of $10^{-7} M_\odot \text{yr}^{-1}$. LkCa 15 has a very small mass accretion rate for its mass, but it is also a transition object and a lower mass accretion rate is expected at this stage. In general, quasi-periodic dippers are expected to be generated in a stable accretion regime and aperiodic dippers instead in an unstable regime (McGinnis et al., 2015), which could be provoked by a phase of enhanced mass accretion. The complex light curve of DK Tau, one of the strongest accretors, might be an example of unstable accretion. However, for the dipper sample presented in this paper, no correlation between mass accretion rate and periodicity could be found.

3.5 DETAILED NOTES ON INDIVIDUAL OBJECTS

In the following section, remarks about individual objects are presented. Three stars (St 34, HD 285893, 2MASSJ05023985+2459337) are possible Taurus members (Rebull et al., 2020).

HARO 6-37 is a triple system. The close binary AB ($0.3''$ Duchêne et al., 1999) is separated from C by $2.6''$ (White and Ghez, 2001). The light curve presents unusually broad dips for a dipper with high amplitude (0.5 mag). The periodicity is unclear in both WPS and periodogram. The luminosity derived is highly discordant with Herczeg and Hillenbrand (2014), who derive luminosities by fitting the spectra (here $0.8L_\odot$, there $0.07L_\odot$). The derived inclination suggests that the period is either wrong, or that the occultations have another origin.

ST 34 is a multiple system (Aab+B) with separation $1.18''$, surrounded by a circumbinary, transitional disk (Rigliaco et al., 2015). The star is reported as an SB2 by Akeson et al. (2019). The inner disk seems to be depleted, although some dust is still present (Hartmann et al., 2005). Its membership to the Taurus association is controversial (Dahm and Lyke, 2011; Hartmann et al., 2005; White and Hillenbrand, 2005). Dahm and Lyke (2011) find an age for St 34 of ~ 10 Myr. Its lithium depletion (White and Hillenbrand, 2005) would lead to an age of 25 Myr, thus the authors must assume a distance of only 90 pc. In the H-R diagram of the present study (Fig. 3.18), the star seems to have an age of 1-2 Myr, given the limitations on the luminosity due to photometric variability. The *Gaia* parallax reports a distance of 143 pc, thus showing that St 34 cannot be a foreground star. It seems, thus, that the age-derivation via the lithium depletion timescale does not apply to this star. The light curve is irregular and a period forest is present in both the periodogram and WPS. The presented period is uncertain. Some contamination might arise from multiplicity.

Table 3.8 – Inclination of the star axis i_* from this study compared to observations of the outer disk i_{disk} from the literature.

EPIC	Name	i_*	i_{disk}	
		[°]	(1)	(Other)
246929818	Haro 6-37	> 47
246942563	St 34
246989752
247103541	HD 285893
247520207	LkCa 15	79^{+11}_{-24}	...	55 (2); 50^{+4}_{-6} (3)
247575958	CFHT Tau 12
247589612	JH 112 A
247589803	JH 112 B
247592463	HP Tau	29^{+11}_{-11}	$18.3^{+1.2}_{-1.4}$...
247763883	GH Tau	44^{+10}_{-10}
247764745	V807 Tau	28^{+7}_{-7}
247791801	GK Tau	57^{+23}_{-22}	$40.2^{+5.9}_{-6.2}$	73.0^{+59}_{-59} (4); 71^{+5}_{-5} (5)
247792225	GI Tau	59^{+24}_{-24}	$44.0^{+2.0}_{-2.0}$...
247799571	HK Tau	68^{+21}_{-21}	$56.9^{+0.5}_{-0.5}$	46.0^{+29}_{-29} (4); 51^{+2}_{-2} (5); 57.0^{+4}_{-4} (6)
247805410	FX Tau	40^{+4}_{-4} (5)
247820821	...	> 64
247885481
247935061	GO Tau	...	$53.9^{+0.5}_{-0.5}$...
248006676	JH 223
248015397	ITG 34
248029373	DK Tau	> 60	$12.8^{+2.5}_{-2.8}$	41.0^{+11}_{-11} (4); 20^{+5}_{-5} (5); 27.0^{+9}_{-9} (6)
248046139	GM Tau	41^{+17}_{-15}
248047443	IS Tau

References. (1) Long et al. (2019); (2) van der Marel et al. (2015); (3) Thalmann et al. (2014); (4) Akesson and Jensen (2014); (5) Simon et al. (2017); (6) Harris et al. (2012).

2MASSJ04384725+1737260 No companion is known in the literature. The star never clearly reaches the continuum; the periodicity is pretty clear, but some dips seem to be aperiodic (Roggero et al., 2021, see folded light curve in App. F). Possibly there are also one or more spots.

HD 285893 According to the HR diagram, the star lies almost on the ZAMS, thus being much older than the Taurus population. There are several possibilities to explain this: the star might not be a Taurus member (it is considered a possible member); the spectral type might not be correctly estimated; and/or the star might be seen edge-on, thus its luminosity would be strongly underestimated. The star shows a clear dipper behaviour in the light curve, which is unexpected for a spectral type F8, since the higher temperature of the star depletes the inner disk of dust at distances much larger than corotation. The object is not well-studied in the literature and does not appear in more recent spectroscopic surveys. Its behaviour seems related to the so-called ‘old’ dippers, which can host a debris disk and whose occultations might be caused by disrupting planetesimals (Gaidos et al., 2019; Tajiri et al., 2020). The dips are narrow, as it is commonly the case for aperiodic dippers. The light curve continuum is unstable and aperiodic.

LKCA15 is a single star (Akeson et al., 2019) which hosts a transition disk. Donati et al. (2019) and Alencar et al. (2018) studied the star in detail. Alencar et al. (2018) confirm it as a dipper, with a light curve that does not show large changes in its variability over the years (see also Grankin et al., 2007). The *K2* light curve shows a variability amplitude of 0.4 mag, in accordance with previous literature. The derived inner disk inclination suggests an inner disk misaligned with the outer disk ($\sim 50^\circ$, see Thalmann et al., 2014; van der Marel et al., 2015). The photometric period is very close to the period derived from radial velocity and veiling (Alencar et al., 2018), thus supporting the scenario of an inclined warp located at the corotation radius. Donati et al. (2019) find a slightly lower $v \sin i$ in comparison to Alencar et al. (2018). The here-derived luminosity ($0.96 \pm 0.18L_\odot$) agrees with theirs ($0.8 \pm 0.15L_\odot$) within the error bars. Nevertheless, the spectroscopically measured T_{eff} is 450 K higher than the conversion by Pecaut and Mamajek (2013). In this analysis, the directly derived temperature by Alencar et al. (2018) is preferred.

CFHT TAU 12 No binarity information has been reported for this star. The star is quasi-periodic (its period agrees with Scholz et al., 2018), but there are no measurements of $v \sin i$ from which we can derive an inclination. The light curve never reaches a continuum, and no periodicity for the long term trend can be derived within the time window of the observations. The shape of the dips clearly distinguishes the dipper phenomenon from spots. The folded light curve is noisy.

JH 112 A is separated from its companion JH 112 B by $6.56''$. JH 112 A is itself a close binary Aa+Ab with a separation of $1.65''$ (Kraus et al., 2011). The star is a transient, quasi-periodic dipper, with dips occurring with a period of 2.21 d. The dips are accompanied by a general decrease in brightness; it is not clear if the phenomenon is physical or instrumental. The estimated luminosity is discordant with Herczeg and Hillenbrand (2014). The temperature at corotation is close to 1600 K, thus requiring higher gas densities for dust to survive (Pollack et al., 1994).

HP TAU The star does not have a companion (Akeson et al., 2019). Its light curve is quasi-periodic, with strong variations in shape and brightness (up to 0.4 mag). The dips are strongly variable and never appear to be single. The structure of the dips varies from double-peaked to a broad, single peak. Güdel et al. (2007) and Rebull et al. (2004) found in the literature a period of 5.90 d, not in agreement with the *K2* period of 4.33 d. The light curve is strongly variable and the periodicity complex; thus, the period might change over time. The luminosity is discordant with that derived by Herczeg and Hillenbrand (2014) and lies with $2.3L_\odot$ above the average of a CTTS. The resulting stellar inclination is low and it might be that for some reason the luminosity is overestimated. It is possible that due to the high amplitude of the variability (3 mag in the *V* band for different surveys) the stellar parameters cannot be constrained correctly.

GH TAU is separated from its companion by $0.3''$ (Akeson et al., 2019). The light curve is irregular and it is unclear whether there are two kinds of eclipses, or if the star is bursting or if there is a long-term variation. The folded light curve is very noisy. Two main periodicities at 2.49 d and 2.94 d are present, although the latter does not show any significant structure. Güdel et al. (2007) indicate a period ≤ 3.57 d derived from $v \sin i$. No *Gaia* parallax was available for this object, but it is located in the B18 group of Taurus (Fleming et al., 2019), with an average distance of 127.4 pc. The star is the fastest rotator in this sample ($v \sin i = 30 \text{ km s}^{-1}$).

V807 TAU is a multiple system (A + Bab) and a separation of $0.3''$ for the wide components, $0.04''$ for the secondary (Schaefer et al., 2012). The *Gaia* distance of V807 Tau is 113 pc, thus it is maybe underestimated. The system is multiple, which means that there might be an issue with the *Gaia* parallax. Nevertheless, the star is located in the B18 region of Taurus (Fleming et al., 2019), which has a distance of 110-150 pc. This value has to be considered with caution, but it is not an outlier for this region. Rodriguez et al. (2017) find a period of 0.809 d, inconsistent with *K2* data. Schaefer et al. (2012) decompose the brightness of the individual components and get a primary star 0.5 mag fainter than the *2MASS J* measurement. This leads to a much smaller stellar radius and higher, more plausible stellar inclination. Pouilly et al. (2021) derive stellar parameters by means of spectroscopy and propose an inclination of $41 \pm 10^\circ$, which seems also more plausible, but still low for a dipper. The light curve presents an apparently sinusoidal long-term modulation; moreover, it is unclear whether the star reaches its maximum brightness at all. The modulation does not seem to be related to binarity, because the binary system has a period of 12 yr. There is only one clear periodicity and the shape of the dips does not suggest stellar spots.

GK TAU is separated from GI Tau by $13.1''$ (Akeson et al., 2019). It is debated in the literature whether these two stars are physically bound or not. The star is a clear dipper with high amplitude (0.5 mag), although no constant brightness continuum can be seen on the light curve. The periodicity is clear and no other physical phenomena seem to influence the light curve. The period is in agreement with previous data (Artemenko et al., 2012; Güdel et al., 2007; Percy et al., 2010; Rebull et al., 2004). Percy et al. (2010) find for this object a long-term variability with a time scale of 2500 d.

GI TAU Guo et al. (2018) report an uncertain spectral type K5-M0 for this star. In this study, a spectral type of M0.4 is adopted. The inclination of 60° agrees with the one derived here. Guo et al. (2018) link the 7 d period, also found here, to a spot. In their optical monitoring from 2014 to 2016, the folded light curve is clearly sinusoidal, which is far from the observed behaviour in the *K2* light curve. Guo et al. (2018) observed quasi-periodic dips on timescales which are a multiple of the rotation period. The folded *K2* light curve is highly irregular and contaminated by GK Tau. The first peak in the periodogram is a periodicity related to GK Tau and not to GI Tau. The 7.1 d period agrees with previous data (Artemenko et al., 2012; Güdel et al., 2007; Percy et al., 2010; Rebull et al., 2004). Our observed amplitude of 0.4 mag is lower than the variability observed by Guo et al. (2018). The folded light curve suggests the presence of small bursts occurring during the *K2* campaign. The star was already classified as dipper, although aperiodic, by Rodriguez et al. (2017). A comparison with the light curve of GK Tau (not shown here), split in each phase according to GI Tau's period, shows that the dips are heavily influenced by the neighbour star. Although GI Tau's intrinsic variability emerges well, it is difficult to describe the behaviour of its multiple dips, if there are any. The complexity of the *K2* light curve does not allow us to clearly distinguish between contamination and GI Tau's signal.

HK TAU is a wide binary with a separation of $2.3''$ (Akeson and Jensen, 2014). Both components have disks misaligned with the orbital motion. The light curve does not show a stable continuum. The periodicity is very clear, but the folded light curve is noisy. It seems that some other phenomenon takes place at the stellar surface. Güdel et al. (2007) report a $v \sin i = 10 \text{ km s}^{-1}$, measured by Hartmann and Stauffer (1989), which would lead to a very low inclination inconsistent with both a dipper and the outer disk. We consider this value less reliable than the measurement by Hartmann et al. (1986) (Table 3.7), because 10 km s^{-1} is the detection limit for $v \sin i$.

FX TAU is binary with a separation $0.9''$. Each component hosts a disk (Akeson et al., 2019). This aperiodic dipper alternates wide and narrow dips. A long term-trend is present in the light curve.

2MASSJ04295950+2433078 No binarity known (Davies et al., 2014). It has a high variability amplitude (0.66 mag). The sinusoidal pattern of the light curve looks rather spot-like, but the star is classified as dipper due to the irregular shape of the dips. The WPS shows a significant periodicity at ~ 7.5 d, which is much weaker in the periodogram. This might be due to the shape of the light curve, which is well-matched to the Morlet Wavelet and is therefore highly correlated. Folded at 7 d, a periodic pattern of several dips appears. An harmonic is excluded.

2MASSJ05023985+2459337 No companion is known in the literature. The light curve exhibits both a spot and a dipper pattern. A dedicated discussion is presented in Sec. 3.2.1.

GO TAU The light curve shows an active star, where bursts also occur. This makes it difficult to define a brightness continuum. The period forest in the periodogram results in no clear periodicity in the WPS. This aperiodic dipper includes both very narrow and wider dips. Güdel et al. (2007) derive from $v \sin i$ an upper limit for the rotation period ≤ 3.96 d.

JH 223 is the best example of a quasi-periodic dipper in the sample. The star is a binary with a separation of $2''$. It seems that both components have a disk (Itoh et al., 2015). The star is reported in Kraus et al. (2012) as having a disk, but without evidence for accretion.

ITG 34 is known to be single (Akeson et al., 2019; Davies et al., 2014). The amplitude of the dips is large (0.39 mag). According to the light curve, the star either almost never reaches the continuum level or a few bursts occur during the *K2* campaign. The periodogram shows 2 double-peaked periodicities, with the main one being also more stable over time according to the WPS. The second periodicity cannot be an harmonic of the first. The folded light curve is noisy and no new features become visible if it is folded at a different period. The apparent beat cannot be explained with binarity.

DK TAU is a binary star with a separation of $2.4''$, where both stars have disks (Akeson and Jensen, 2014; Akeson et al., 2019). The light curve exhibits strong variations over long timescales (see Grankin et al., 2007; Rebull et al., 2020, and references therein) and the period varies from one survey to the other. The WPS shows how DK Tau's period increases from 7.69 d to ~ 10 d during *K2* C13, after a fading state in lower brightness. This explains the two different, broad peaks in the periodogram. Percy et al. (2010) and Artemenko et al. (2012) find a period of 8.18 d, while (Rebull et al., 2020) find 7.84 d. The difference can be easily explained for the first with the complexity of the light curve, and for the second, by the use of a different period-finding algorithm in presence of a broad peak. Xiao et al. (2012) find 4.14 d, which is not consistent with the *K2* data. Percy et al. (2010) also find a long-term time scale of 2000 d for the variability of DK Tau. Excluding the fading state, the amplitude of the occultations is 0.6 mag.

GM TAU is a single brown dwarf (Akeson et al., 2019) with a transitional disk. The star is a strong accretor and is highly veiled (Herczeg and Hillenbrand, 2008, 2014). The light curve has a sinusoidal shape and does not show a constant brightness continuum; the star is considered a dipper because of the irregularity of the dips.

IS TAU is a binary with $0.2''$ separation (Schaefer et al., 2014). It is not known which (or if both) component hosts a disk. Watson et al. (2009) find a very high mass fraction (80%-100%) of crystalline silicates in the inner disk. The light curve is characterized by a combination of broad and narrow eclipses. The strongest periodicity is given by the broad dips. The *Gaia* parallax is not available. The star is also located on the L1495 filament of Taurus, which contains members of both the close and the far population (Fleming et al., 2019). In the HR diagram in Fig. 3.18, the possible luminosity of IS Tau

is plotted according to mean distances of 130.6 and 160.2 pc (Fleming et al., 2019). The age is more consistent with the rest of the sample if IS Tau is a member of the far population.

3.6 WHAT CAN WE INFER FROM DIPPERS?

As presented in Chapter 1, the dipper phenomenon is the result of the interaction between the star and the inner disk. There is consensus that dust is at the origin of the optical fading events. However, several mechanisms are able, in principle, to cause asymmetries in the dust distribution close to the star (Sec. 1.5.2). A few conditions are required for a dusty structure to be able to occult the star. First, the viewing angle of the observer, which is constrained differently depending on the mechanism. Second, since the periodicities suggest that these structures corotate with the star, the environment at corotation must be cold enough to avoid dust evaporation. Other important, but difficult to derive, parameters are the mass accretion rate and the magnetic field strength and topology. The first is important to determine whether the star is actively accreting or not. Enhanced mass accretion phases are more likely to produce stochastic accretion tongues (e.g., Romanova and Owocki, 2015). The magnetic field strength determines the size of the magnetosphere, and its topology the accretion funnels. Other parameters not directly constrainable from photometry are the dust properties such as the optical depth.

In the following section, the results are set in context with previous dipper surveys in other regions. Then the inclinations of inner and outer disk are compared and possible mechanisms constrained. Other parameters and existing correlations are discussed in the final part.

3.6.1 *Dippers in Taurus and in other clusters*

The star-forming regions so far known to host dippers include NGC 2264, Orion, ρ Oph, Upper Sco, Taurus (see Sec. 1.5.2). A feature common to all of these regions is the late spectral type, K to M, of the identified dippers. A common explanation for this is the longer pre-main sequence phase of late-type stars, which allows the disk to be present for a longer time, thus increasing the probability of observing a dipper. Moreover, the lower surface temperature makes it possible for dust to be present close to the star's magnetosphere. In Taurus, as in ρ Oph and Upper Sco, the occurrence of M-type dippers is higher than of K-type, since stars of lower mass always exist in a larger number.

As for the fractional rate at which dippers are found among YSOs, the statistics differ from region to region. The main reasons for this are the different counting methods (i.e., fraction of disk-bearing stars vs. all members of the cluster), the different selection techniques, and the target selection process of the survey, not necessarily optimized to find dippers. On average, surveys find an occurrence rate of 20%-30% for dippers. An exception is Orion, where only 5% of the stars are classified as dippers. This might be due to the photometric accuracy of the survey (lower cadence) and a biased target selection (Morales-Calderón et al., 2011), as well as the fact of not considering a disked-star sample. Moreover, they use *Spitzer* data in the IR, where the dips have a smaller amplitude and the disk contribution complexifies the light curve. In Taurus, considering the additional 12 dippers in Table 3.1, the occurrence rate is of 19% of all the members observed with *K2*, and 31% of the members hosting a disk.

The ratio of quasi-periodic to aperiodic dippers lies around 1:1 for NGC 2264, ρ Oph, and Upper Sco. In Orion, only one third of the dippers is quasi-periodic. In contrast, it seems that in Taurus, most dippers are quasi-periodic. The sample analyzed in this study might be unusual in this sense (only 3 aperiodic and 3 uncertain dippers out of 22 in Table 3.3); it must be noted that of the 12 additional dippers in Table 3.1, only two of the reported periods are most probably linked to quasi-periodic dips. As for the rest, the predominant periodicity in the light curve is caused by cold stellar spots, while the extinction events are stochastic. This said, only 17 out of the 34 presented dippers are strictly quasi-periodic, bringing the ratio to about 1:1. The periods marked as uncertain in Table 3.4 are not counted as quasi-periodic here.

3.6.2 *Star and outer disk inclination*

In this section, I investigate whether the stellar inclination agrees with the outer disk inclination, and if this is compatible with an AA Tau-like star. For most of the objects considered here, a moderate to high inclination is clear despite the large error bars. GH Tau and GM Tau are compatible with an inclination of $\sim 50^\circ$, close to the minimal inclination required for the magnetospheric accretion scenario. This suggests that the magnetic field axis is highly tilted with respect to the stellar spin axis. In the case of HP Tau and V807 Tau, the proposed dusty warp scenario for the production of dippers fails to explain fading events seen at such a low inclination. I tested whether the photometric variability might significantly influence the estimation of the luminosity and propagate up to the derived stellar inclination. None of these stars shows an amplitude in the *K2* light curve large enough to explain the discrepancy. Nevertheless, for HP Tau, a long-term amplitude variation of $\Delta V \sim 1$ mag was reported by Grankin et al. (2007). This could be roughly converted into an upper limit of $i \sim 50^\circ$, at the lower limit for the magnetospheric accretion model. For V807 Tau, which is a triple system, an overestimation of the brightness of the primary is possible. Schaefer et al. (2012) estimate that V807 A could be 0.5 mag fainter than the total system in the *J* band and fit to the system an extinction of 0. From these parameters, a higher stellar inclination of 40° can be derived, which is more plausible. Pouilly et al. (2021) also derive a similar inclination by using spectroscopic measurements. Still, this is not sufficient to explain the discrepancy. A stellar radius of $\sim 1.5 R_\odot$ would be required to reach an inclination angle of at least 50° .

It is thus more probable that some other phenomenon contributes to the quasi-periodic extinction events for these stars that are inconsistent with a sufficiently high inclination. Dusty disk winds also need high inclination angles to be observable (Vinković and Čemeljić, 2020), and the mass accretion rate of V807 Tau is too low (Table 3.7). The small amplitude of ~ 0.1 mag might hint at vortices caused by Rossby wave instabilities. However, given the clear periodicity of the light curve, this mechanism can be discarded. Also given the almost constant shape of the dips, the structure occulting the star is probably stable, not very large, optically thick, and it might be that just a small fraction of it is seen by the observer under this low inclination. One more possibility would be, in the magnetospheric accretion scenario, that the dust high in the accretion column increases its optical depth right before sublimation, since evaporation and free-fall timescales are similar (Nagel and Bouvier, 2020). This could imply that an optically thick part of the accretion column could cross the observer's line of sight, thus requiring a lower inclination to see dips.

I compared the stellar inclinations of this dipper sample to outer disk inclinations directly measured at mm wavelengths (Table 3.8). Akesson and Jensen (2014) derive the disk inclination in the image plane by fitting the clean continuum maps with 2D Gaussians. This results in larger error bars than with the methods used by other authors, as the continuum map is reconstructed from the visibilities. In general, the outer disk inclination is slightly lower than the inclination derived for the inner region, with the exception of DK Tau, which seems strongly misaligned with the outer disk, although this value has to be considered with caution (see Sec. 3.4).

Appenzeller and Bertout (2013) point out how the inclination of CTTs derived from $v \sin i$ as in Eq. 3.8 are imprecise for $i > 30^\circ$, due to the uncertainty growing with i . The inclination might also be overestimated if all line broadening effects are not properly considered. For a sample of known CTTs in different regions, i_* and i_{disk} are correlated, but the inclination derived from rotation is on average 19° higher (Appenzeller and Bertout, 2013). This trend is also observed in Taurus for HP Tau, GK Tau, GI Tau, and HK Tau. Nevertheless, the recent observations of misaligned inner disks support the possibility that this systematic also has a physical basis. Another systematic uncertainty on the stellar inclination is produced by the use of conversion tables between spectral type and effective temperature, which are still imprecise for young stars. The use of different conversions can lead to discrepancies of the order of 150 K, which for a late-type star with $T_{\text{eff}} \sim 3000\text{-}3500$ K mean an additional uncertainty of $\sim 5\%$. Propagated to R_* and $\sin i$, this final uncertainty of $\sim 10\%$ corresponds to about 5° for $i_* < 30^\circ$ or 10° for $i_* > 30^\circ$. Thus, the stellar inclinations could be in the order of 10° higher than derived.

No extreme cases of face-on dippers, as reported by Ansdell et al. (2016a), are observed in this sample. The stellar inclination has been derived for 11 dippers (50%) and outer disk inclinations are

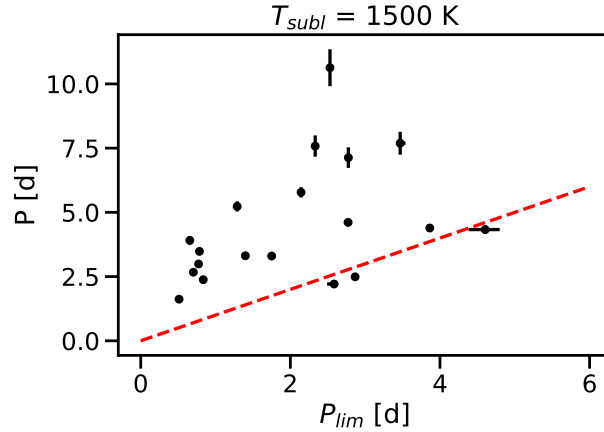


Figure 3.19 – Period of the dippers in comparison to the minimal rotation period (red line) required for a temperature ≤ 1500 K at corotation. If the star rotates faster, the inner disk will be purely gaseous at corotation.

available for 8 (36%) dippers. The dippers for which it was possible to derive a stellar inclination are compatible with the disk warp scenario (thus 9/11), with the exception of HP Tau, whose stellar parameters might be heavily influenced by a strong overall photometric variability, and V807 Tau, for which a different scenario is required, even after decomposition of the system’s primary and secondary brightness. In general, the stellar inclinations of Taurus dippers are lower than the ones, e.g., of dippers in NGC 2264 (McGinnis et al., 2015).

3.6.3 Temperature at corotation and dust survival

Given the assumption that dusty material at corotation causes the dips, it is interesting to compare the temperature at corotation with dust sublimation temperatures, in order to confirm or exclude certain characteristics of the dust grains. The sublimation temperature, T_{sub} , of the grains depends on the gas pressure, latent heat, and molecular weight, more than on the stellar parameters (Kobayashi et al., 2011). The full range of T_{cor} in Table 3.7 goes from 800 K to 1600 K, with error bars of the order of 100 K. The only materials able to withstand these temperatures are olivine, pyroxene, and iron (Pollack et al., 1994, see their Table 3). Moreover, the sublimation temperature increases with the gas density – stars with $T_{\text{cor}} > 1400$ K exclude gas densities $< 10^{-8}$ g cm $^{-3}$. The stars with the highest temperatures at corotation in Tab. 3.7 can only host dust for even higher gas densities $> 10^{-6}$ g cm $^{-3}$. Due to the current difficulties in resolving the inner disk rim for low-mass YSOs, models for this region have only been developed for intermediate-mass stars (e.g., Isella and Natta, 2005; Tannirkulam et al., 2007). It is thus of interest to better constrain these properties for CTTSs in future studies to verify the conditions for dust survival.

Setting a critical temperature for dust $T_{\text{subl}} = 1500$ K, it is possible to derive from Eq. 3.7 and Eq. 3.6 the minimal stellar rotation period, for given mass and radius, that permits a sufficiently cold environment for dust to survive at corotation as:

$$P_{\text{lim}} = 2^{-\frac{1}{2}} \pi \left(\frac{T_{\text{eff}}}{T_{\text{subl}}} \right)^3 R_*^{\frac{3}{2}} (GM_*)^{-\frac{1}{2}} \quad (3.9)$$

Fig. 3.19 shows how all periods of dipper stars are well above this limit. For the few stars close to the limit, the condition is satisfied if a $T_{\text{subl}} = 1600$ K is assumed. Previous observations of dippers in ρ Oph and Upper Sco (Bodman et al., 2017) also indicate that it is possible for dust to survive at the corotation radius of dipper stars.

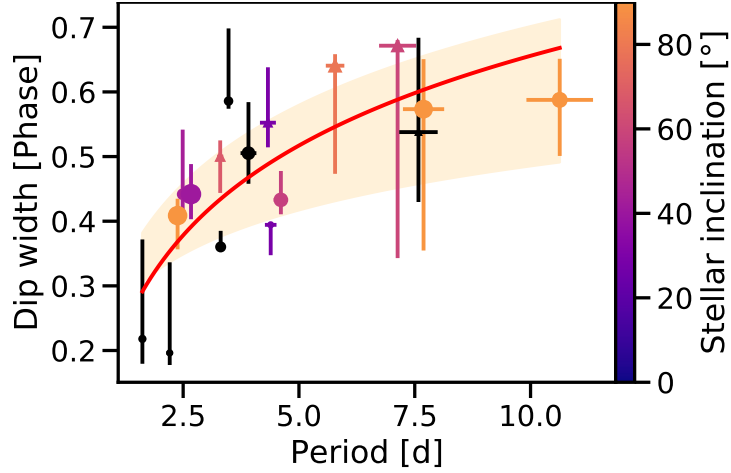


Figure 3.20 – Dependence of dip width in phase units and period of the quasi-periodic stars in the dipper sample. The error bars on dip width and period correspond to those listed in Table 3.4. A logarithmic fit $a \log x + b$ is performed just on the data points (red line), and for upper and lower limits of the dip width (orange interval). The double-dipped stars are represented as triangles. The size of the markers is proportional to the square root of the dips' amplitude (between 0.05 and 1.3 mag). Two stars for which the so derived dip width is not reliable are not represented in this plot. The stellar inclination in degrees is coded as colors of the data points, when available. Although the exact coefficients of the fitting function cannot be constrained from this small sample, W correlates with $\ln P$ with a Pearson's $r = 0.77$. No significant correlation with the dips' amplitude can be measured.

3.6.4 Dip width and period

Previous studies investigated whether dip width, dip amplitude and/or dip width are correlated for dippers. Until now, no such correlations could be found (e.g., Bodman et al., 2017), besides the class of short-period narrow dips presented by Stauffer et al. (2015). As for dip width and amplitude, a dependency would be a constraint on the geometrical properties of the dusty warp as presented by Bouvier et al. (1999). The amplitude of the eclipses depends not only on the viewing angle, but also on the vertical extent of the dusty material occulting the star; on the other hand, the dip width delivers an estimate of its azimuthal extent.

For this sample of Taurus dippers, the quasi-periodic dippers for which it was possible to derive a reliable width are shown in Fig. 3.20. The data suggest a logarithmic trend between the dip width and the period, with a high scatter due to the intrinsic variability of dippers. It is remarkable that many dippers are obscured $\gtrsim 50\%$ of the time, suggesting that the azimuthal extent of the dusty structure must be larger than 180° around the star. According to the geometrical constraints of a dusty warp, the observed dip width should grow with the inclination. The inclination values listed in Table 3.8 are represented in Fig. 3.20 as color code of the data points. The amplitude of the dips is proportional to the size of the data points as $2\sqrt{\frac{A}{A_{min}}}$, where A_{min} is the smallest amplitude of the sample. No correlation is observed within the inclination and the dip width, nor between inclination and dip amplitude. Towards the higher end of the widths, the 'dip' is often double- or multi-peaked, and its shape and position vary from phase to phase. This is the case for HP Tau, LkCa 15, GI Tau, JH 112 A, HK Tau, and IS Tau (see Sec. 3.3.3). The large error bars on the dip width for these double- or multi-peaked stars reflect the difference between considering the width of the full occultation and the width of the main dip.

Although the dependency can be described at best with a logarithmic curve, the size of the sample is too small to draw a solid conclusion on the nature of the best-fitting curve. It is also possible that two different regimes are present, such as a linear trend for short periods, followed by a plateau for longer periods. The two quantities dip width (W) and the natural logarithm of the period ($\ln P$) are correlated with a Pearson's correlation coefficient $r = 0.77$ and a p-value of $2.8 \cdot 10^{-4}$. A logarithmic, rather than linear, trend is expected, since the star cannot be eclipsing close to 100% of the time, thus

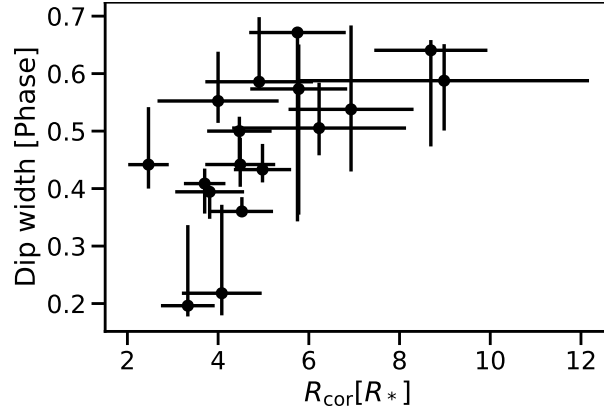


Figure 3.21 – Dependency between dip width in units of phase and the corotation radius. Although weaker (Pearson’s $r = 0.63$), a correlation between W and $\ln R_{\text{cor}}$ is also evident here. The lower correlation can be explained by the fact that R_{cor} is a function of both P and M_* .

flattening the curve for longer periods. The two lower-left stars are, though, crucial for this correlation. EPIC246989752 and JH 112 A (Roggero et al., 2021, App. F for the dip width) fall under the category of short-duration quasi-periodic dips (Stauffer et al., 2015), with the interesting case of JH 112 A being a transient dipper. The derived dip width describes well the dip as observed in the folded light curve. Moreover, the upper error bar is very generous, since the binned light curve $+\sigma$ is almost flat. Therefore, it can be excluded that the dip width for these two stars is overestimated. Stauffer et al. (2015) identified a particular class of Gaussian-shaped, narrow and short-periodic dips. The definition of “narrow” is set where the ratio of the FWHM of the fitted Gaussian and the period is less than 0.25, while on average the narrow dips in NGC 2264 have a FWHM/period ratio of 0.15. In Taurus, EPIC 246989752 and JH 112 A would correspond to this category, with a FWHM/period ratio of 0.22 and 0.20, respectively. Both exhibit a Gaussian shape. The short-period dippers in NGC 2264 tend to have narrow eclipses for later spectral types (Stauffer et al., 2015). Here, this is true for EPIC 246989752, which is an M-dwarf, while JH 112 A has a spectral type of K5.5. We searched for a correlation between dip width and spectral type in the dipper sample and could not find any. Another star that can be associated with the population defined by Stauffer et al. (2015) is EPIC 247885481 (Sec. 3.2.1). It does not appear on Fig. 3.20, since the width of the dips cannot be constrained reliably in a standardized way. The amplitude is very small compared to the noise and the dips do not clearly appear in each phase (see Sec. 3.2.1). The star is a M-dwarf, so compatible with the group identified in NGC 2264.

A correlation between R_{cor} and the dip width in units of phase is presented in Fig. 3.21. Although weaker (Pearson’s $r = 0.63$), a behaviour similar to that of Fig. 3.20 is evident. This is not surprising, since the corotation radius as derived in Eq. 3.6 is a function of the stellar period. In this case, the correlation is evident even without considering the two data points in the lower-left corner, which only argue for a logarithmic instead of a linear dependency.

It is of interest to verify if this dip width-period correlation is an implication of existing models and if the observed dip widths are compatible with the mechanisms thus far proposed to explain dippers. In the framework of magnetospheric accretion, in order to generate a quasi-periodic dipper, the most stable configuration of the magnetic field seems to be an inclined dipole (Romanova et al., 2013). Two broad, stable and symmetric matter streams form from the disk and are accreted as funnel flow on the stellar surface, producing a hotspot on each hemisphere. The observer can see the star obscured either by the dusty warp or even by the funnel flow itself. In this case, the extent of the magnetosphere nearly coincides with the corotation radius, $R_T \approx R_{\text{cor}}$. In case of $R_{\text{cor}} < R_T$, the inner region of the disk rotates with $\omega > \Omega_K$ (where Ω_K is the Keplerian velocity at corotation) and the star is in the propeller regime. The magneto-centrifugal forces lead to the ejection of disk material into an outflow (Romanova and Owocki, 2015). During phases of enhanced accretion, in which the mass accretion rate increases, the disk compresses the magnetosphere and reduces R_T (Romanova et al., 2013). For $R_T < R_{\text{cor}}$, the star is in the accretion regime and the magnetosphere rotates slower than the inner disk ($\omega < \Omega_K$). In

case of a small or no misalignment between the stellar spin axis and the magnetic moment, the matter from the inner disk accumulates at R_T and the accretion instead occurs via unstable accretion tongues (Romanova et al., 2013), taller and thinner than funnel flows, that reach the stellar surface close to equator. They can be observable as irregular hotspots in the *UV*. As a result, the light curve will be rather stochastic and bursting. An unstable accretion regime has been invoked to explain aperiodic dippers (e.g., McGinnis et al., 2015). The extent of the corotation radius directly depends on the stellar rotation period. For slow rotators, the corotation radius is located at a higher distance from the star, and the inner disk therefore rotates faster than the star. This facilitates the accretion via instabilities (Kulkarni and Romanova, 2008; Romanova et al., 2013).

An observer would expect broad dips to be quasi-periodic, since the unstable accretion tongues are rather narrow and tall and would not be able to obscure the star for a significant fraction of time (Romanova et al., 2008). The aperiodic dippers observed in Taurus exhibit, indeed, rather narrow dips in their light curves. The quasi-periods observed in dippers might also be linked to a configuration in the accretion regime. In this case, trapped density waves in the inner disk can produce a warp that rotates slower than the star and beyond the corotation radius, with a period that might vary over time. In this case, the simulations show that the inner disk is tilted and also rotates more slowly (Romanova et al., 2013). This could explain the changing, rather long period observed in the WPS of the K2 light curve of DK Tau, which is associated with an outer disk seen at low inclination. However, that would not suffice to explain why the star is obscured in the first part of the light curve. The slow rotating warp should also have a smaller height than a fast rotating warp and DK Tau has an amplitude of 1 mag. A correlation between period and dip width thus suggests that slow rotators are more probably occulted by more azimuthally extended dusty structures. This aspect has not been directly predicted in simulations to date. In the scenario of magnetospheric accretion, this might imply a broader funnel flow for slow rotators.

For T Tauri stars of late spectral type, the internal structure is either fully convective or with small radiative cores (Gregory et al., 2012). The HR diagram of Taurus dippers shows that, with the exception of LkCa 15, all stars are on their Hayashi tracks and fully convective. In this case, the magnetic field is expected to be axisymmetric and the dipole component dominates, as it is the case for AA Tau. Vidotto et al. (2014) found a correlation between magnetic flux and rotation period for accreting PMS stars. This implies that stars with a simple magnetic field (i.e., dipole) and with the strongest magnetic fields are also the slowest rotators and truncate the disk at larger distances R_T . Hence, the star-disk interaction impacts the magnetic fields, which in turn influences the stellar rotation. We speculate that the large-scale magnetic field topology might be at the origin of the correlation between dip width and period. A stronger magnetic field might have a stabilizing effect on a large warp.

3.7 SUMMARY

We have studied a sample of 179 YSOs in Taurus, which are members or possible members of the cluster (Rebull et al., 2020). I identify a total of 34 dippers, of which 22 are dippers not dominated by another kind of variability. This makes up $\sim 20\%$ of the high-confidence and possible Taurus members and $\sim 30\%$ of the disk-bearing Taurus members. The observations of Taurus highlight again how ephemeral dippers are. A striking example is the dipper prototype AA Tau, which came to a fainter state and would not be classified as dipper at first glance anymore. Fig. 3.4 illustrates how only a few dips occur on AA Tau's otherwise complex light curve. Dipper light curves can persist over timescales of a few years or even a few days. This strongly suggests that the observed occurrence rates are a lower limit to their true occurrence among CTTSs.

The ratio of periodic to aperiodic dippers is 1:1, although most of the dippers studied in detail are periodic. The large majority of aperiodic dippers observed in Taurus is actually dominated by another type of variability, mainly of the kind due to cold spots. As it was observed in other surveys, dipper stars are of late spectral type K or M, since the lower surface temperature allows dust to survive in the inner disk and create the dips. The dipper stars of the sample are fully convective, low-mass ($< 1 M_\odot$) stars down to the brown dwarf limit. One exception is LkCa 15, which hosts a transition disk,

and the other is HD 285893, with a spectral type F8 and close to the ZAMS on the HR diagram. This source might be an interesting case of ‘old’ dipper, which can be produced by rare, dust-rich debris disks or disrupting planetesimals (Gaidos et al., 2019; Tajiri et al., 2020). In accordance with previous surveys, the observed periods are in the range of the rotation periods of low-mass CTTs. One star (JH 112 A) exhibits a periodic dipper light curve that persists for only few rotation cycles; DK Tau is found to have an increasing period over the K2 epoch through wavelet analysis. The dips observed along with a spot in EPIC 247885481 corroborate the assumption that the dusty material is located at corotation (e.g., Stauffer et al., 2015). The temperatures derived at corotation also are compatible with dust survival and the mass accretion rates are on average for CTTs. Many of the dippers for which it was possible to derive a stellar inclination are seen under a moderate to high inclination angle. This is compatible with the generalized magnetospheric accretion model (Bodman et al., 2017), but it would suggest that the magnetic field axis is highly tilted with respect to the spin axis or that dust can be optically thick further up than just the base of the accretion column (Nagel and Bouvier, 2020). Nevertheless, a systematic uncertainty on the stellar radius, due to the use of conversions between spectral type and temperature, can increase the stellar inclination on the order of 10° . The nature of the systematic of a stellar inclination higher than the outer disk inclination cannot be constrained accurately in this small sample, but it might be put in the frame of recently observed stars with a tilted inner disk (e.g., Ansdell et al., 2020). LkCa 15 has been studied in more detail in this context (Alencar et al., 2018). Other mechanisms, such as dusty disk winds and Rossby wave instabilities, do not seem convincing to explain the dippers seen under low inclination in this sample.

A fraction of the periodic dippers exhibits double or complex-shaped dips, whose structure varies with time and whose minima are shifted from one cycle to the next. These examples are worth exploring in a more precise dynamical analysis in future. This might provide more hints about the origin of this variability, which might be linked to variations in the mass-accretion rate, for example. I also find a correlation between the dip width in units of phase (i.e., the equivalent of the angular extension of the occulting structure) and the rotational period of the dippers. We speculate that this would suggest that the accretion columns of slower rotating stars have a larger base, possibly reflecting a different magnetic field topology. This dependency needs to be verified for dippers in other clusters in future work.

RADIATIVE TRANSFER MODELING WITH MCFOST

Summary

4.1	Testing a basic disk	82
4.1.1	Basic disk outputs	82
4.1.2	Derivation of the light curve	86
4.2	Modeling JH 223 with an inner disk wall	86
4.2.1	Inner disk wall: model parameters	87
4.2.2	Inner disk wall: results	88
4.2.3	Influence of the parameters on the result	88
4.2.4	Color variation	92
4.2.5	Model adjustment with interstellar dust grains	95
4.2.6	Spectral Energy Distribution	98
4.2.7	Discussion	98

This chapter presents the preliminary results of the modeling of the prototypical dipper of the sample, JH 223. The first step was to model a basic disk to get familiar with the code and understand its outputs for known conditions. After trying a geometry with a tilted inner disk which adds an asymmetry to the disk, an inner disk wall $\propto \cos \frac{\phi - \phi_0}{2}$ as defined in Bouvier et al. (1999) is the best choice to model the light curve of JH 223.

4.1 TESTING A BASIC DISK

The default disk of MCFOST (Sec. 2.3) surrounds a $1 M_{\odot}$ star with $T_{\text{eff}} = 4000 \text{ K}$, is symmetric and homogeneous and extends from 1 to 300 AU. The dust mass M_{dust} is of $10^{-3} M_{\odot}$ and the scale height is of $h = 10 \text{ AU}$ at $r_0 = 100 \text{ AU}$. Here and in the rest of this chapter, the flaring exponent and the surface density exponent are set to $\beta = 1.125$ and $\alpha = -0.5$, respectively. The dust grains are silicates that follow the Mie theory, with sizes from 0.03 to $1000 \mu\text{m}$. In the following sections, the main outputs for different inclinations are presented, i.e., monochromatic images, temperature structure, SEDs and optical depth maps.

4.1.1 Basic disk outputs

The code runs in 2D in cylindrical coordinates for a symmetric disk. As a first step, MCFOST computes the temperature structure of the disk (Fig. 4.1). The grid in cylindrical coordinates follows the flared shape of the disk, which means that for given distances from the star, the cells with the same number in z direction have different physical heights. As expected, the temperature in Fig. 4.1 is highest at the inner disk edge, and is higher at the disk surface than in the disk midplane. The code uses the thermal emission and scattered light to compute an SED (Fig. 4.2). For this aim, three different inclinations are tested, face-on ($i = 0^\circ$), moderate inclination ($i = 60^\circ$), edge-on ($i = 90^\circ$). Four different components are combined to compute the total flux: the direct light from the star, the stellar light scattered at the disk surface, and then thermal emission and scattered thermal emission from the disk. The shape of the resulting SED is typical for a CTTS: although the stellar spectrum dominates at short wavelengths, the presence of a circumstellar disk induces a strong IR excess. The thermal emission is also used as

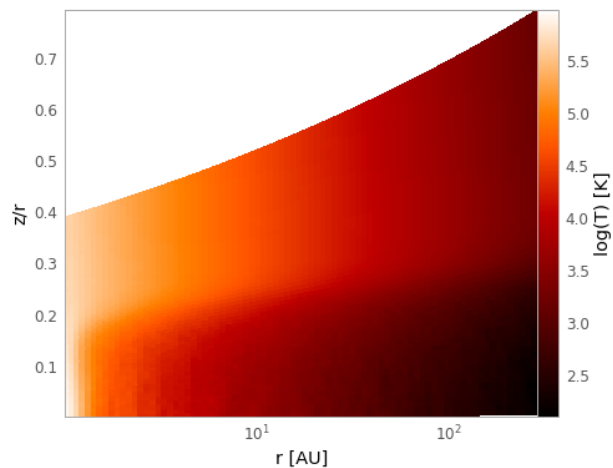


Figure 4.1 – Temperature structure of a simple disk. The temperature at the inner disk rim has the highest temperature $\sim 400 \text{ K}$.

base to produce a monochromatic image. Fig. 4.3 shows the monochromatic images of this disk, which includes the total flux of all contributions, for different inclination angles and wavelengths. In the

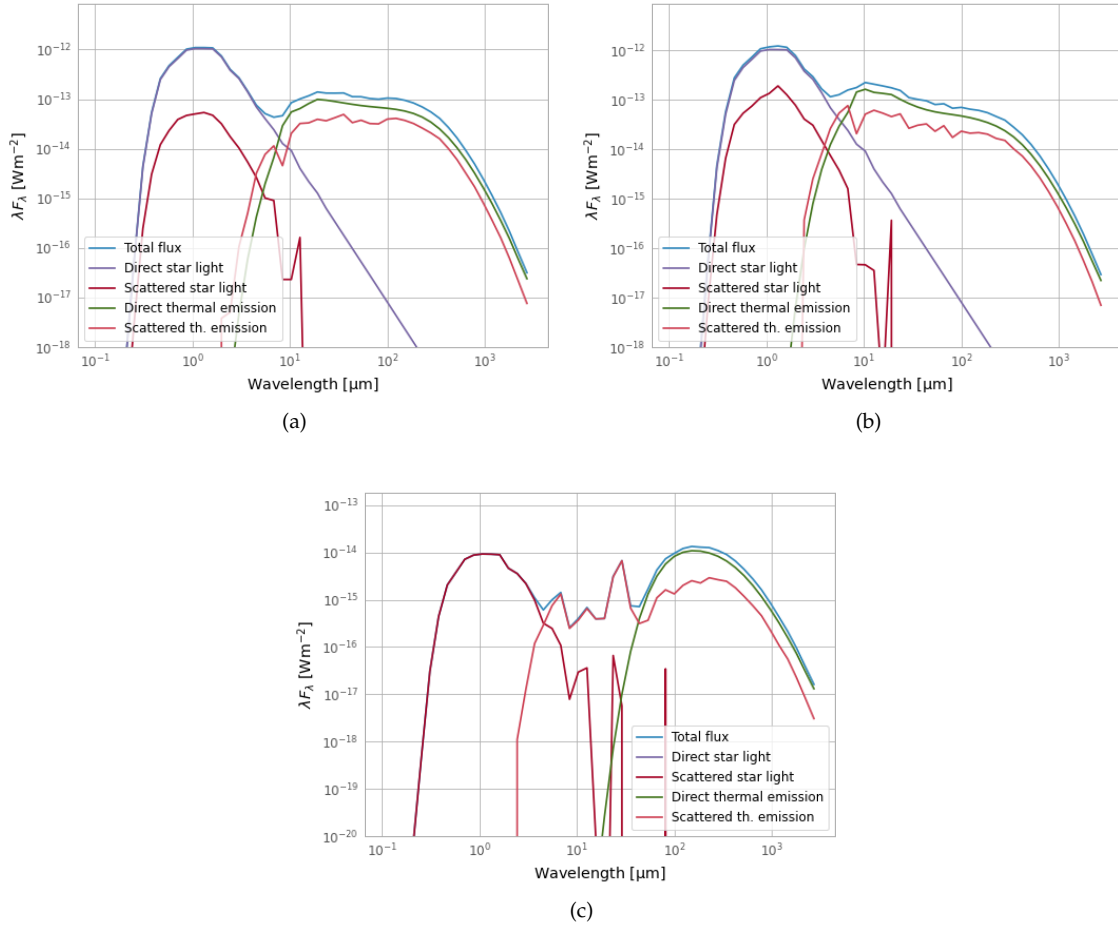


Figure 4.2 – SEDs for three different disk inclinations (left to right, top to bottom): $i = 0^\circ$, $i = 60^\circ$, $i = 90^\circ$. The contribution of the disk becomes dominant when the star is seen at higher inclination. For the star seen edge-on, no direct flux is visible and only the scattered star light reaches the observer. Both the scattered star light and scattered thermal emission curve are derived with Monte Carlo and are more heavily affected by noise.

optical, the scattered star light dominates. When the disk is seen face-on, it appears as faint compared to the direct star light. When seen edge-on, the star remains embedded in the disk and the total flux decreases by several orders of magnitude.

As for the disk structure, the dust is concentrated in the inner part of the disk midplane (Fig. 4.4). The larger dust grains are rather confined in the midplane, while the lighter grains float at higher z . From the dust properties it is possible to derive the optical depth as in Sec. 2.3. For a value of $\tau \lesssim 1$, the disk is considered optically thin, while for $\tau \gtrsim 1$ it is considered optically thick. This property is important to understand whether a part of the disk is able to block the stellar light and reduce its brightness. MCFOST can produce optical depth maps for a given wavelength, integrating in different directions (Fig. 4.5). The map which will be used here is the one which is integrated towards the star. For a given cell, its optical depth value corresponds to the integrated path from that cell to the star. For this reason, the value of τ increases with the distance from the star. It is possible to derive the optical depth as seen by an observer under different angles, by picking at a given r the cell of the map which corresponds to the height z which crosses the line of sight. The parameter file used to produce these data can be found in App. A.2.

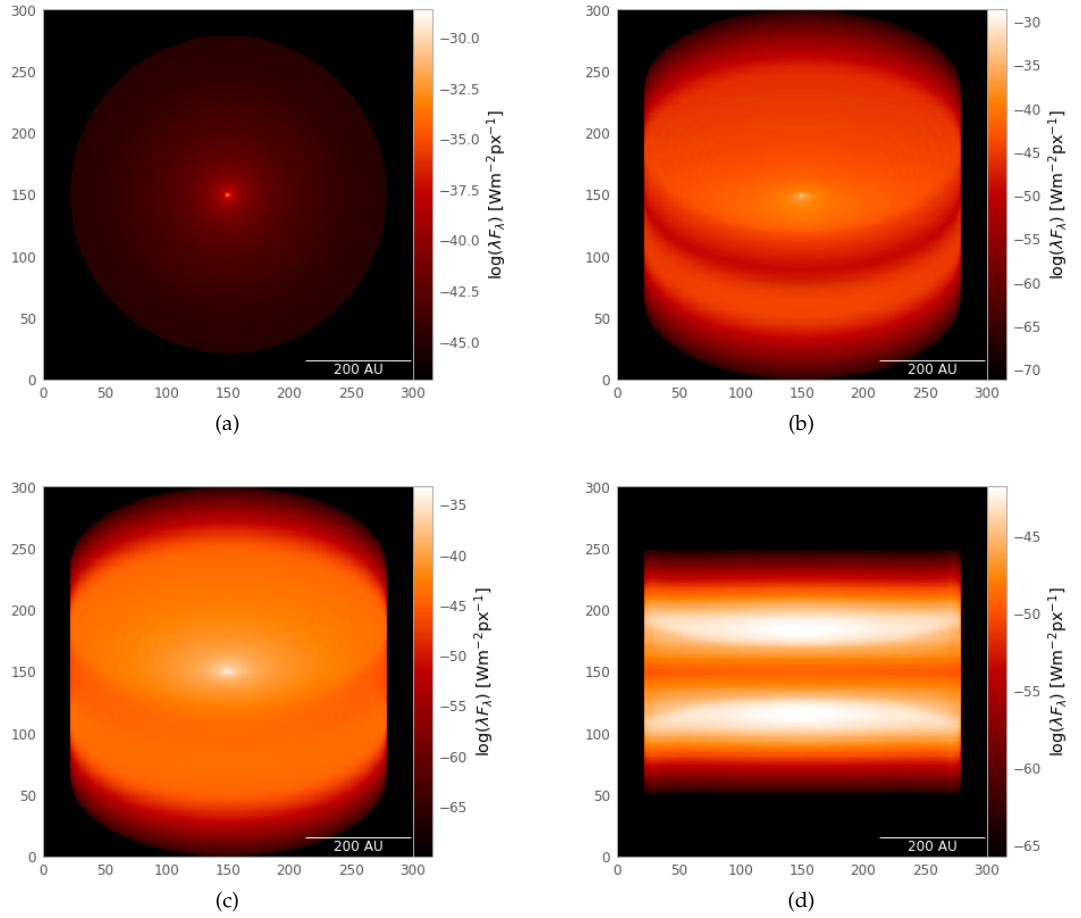


Figure 4.3 – Monochromatic images at 575 nm for (a) the disk seen face-on; (b) an inclination of 60°; (d) the disk seen edge-on. (c) Image at 100 μm for an inclination of 60°. In the IR, the star is less bright and the dust thermal emission becomes visible.

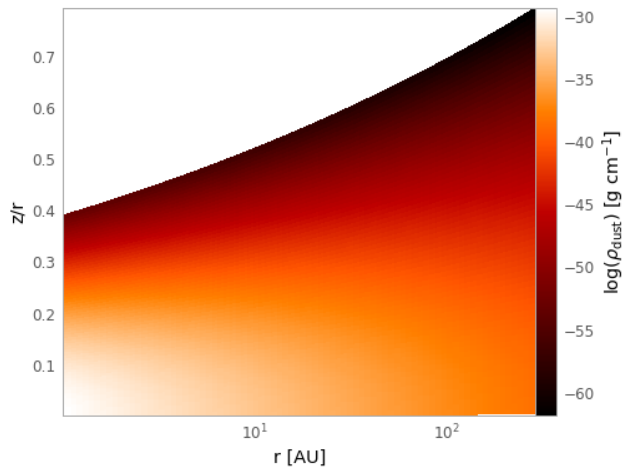


Figure 4.4 – Dust density of the disk.

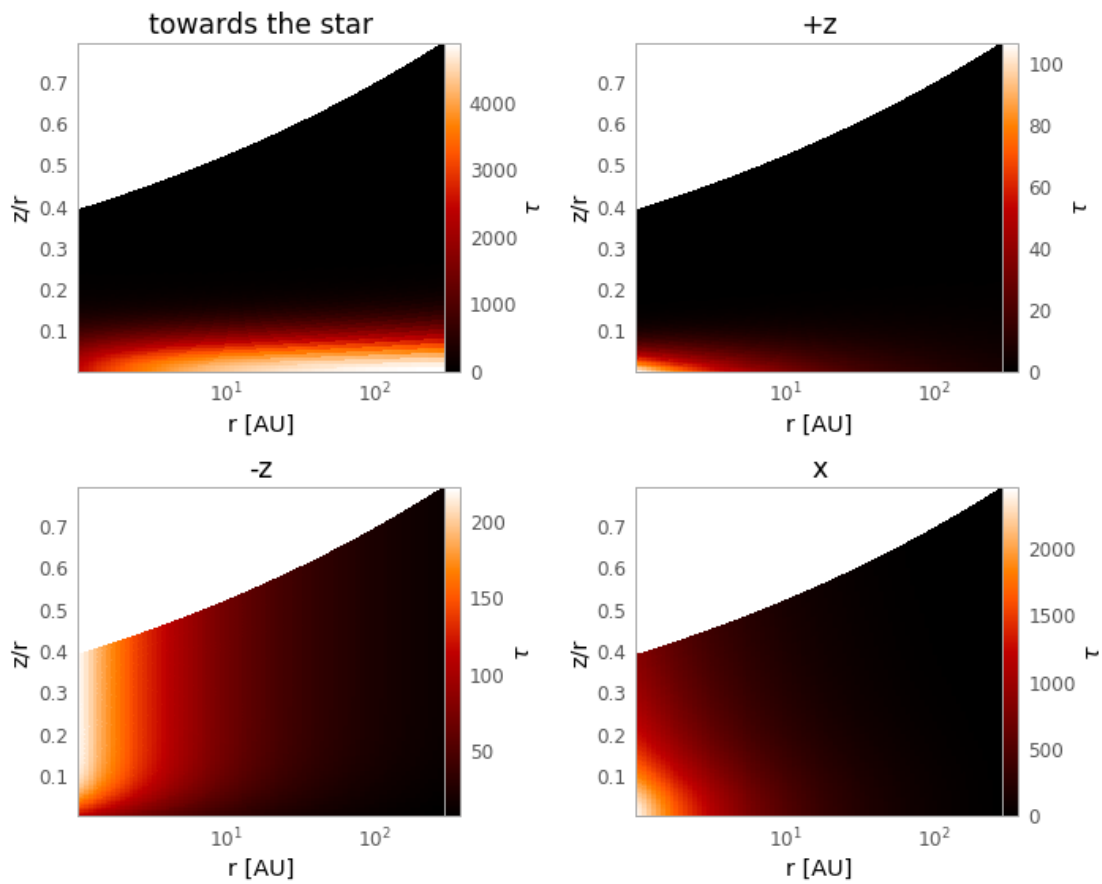


Figure 4.5 – Optical depth map in four different directions. Towards the star: see text. +z direction: For each cell τ is integrated vertically going out of the disk. -z direction: τ is integrated from each cell towards the disk midplane. For this reason, the value is high and constant over the inner disk (with higher dust density) and decreases in the disk midplane. x direction: for each cell τ is integrated between the cell and the outer disk in Cartesian x direction.

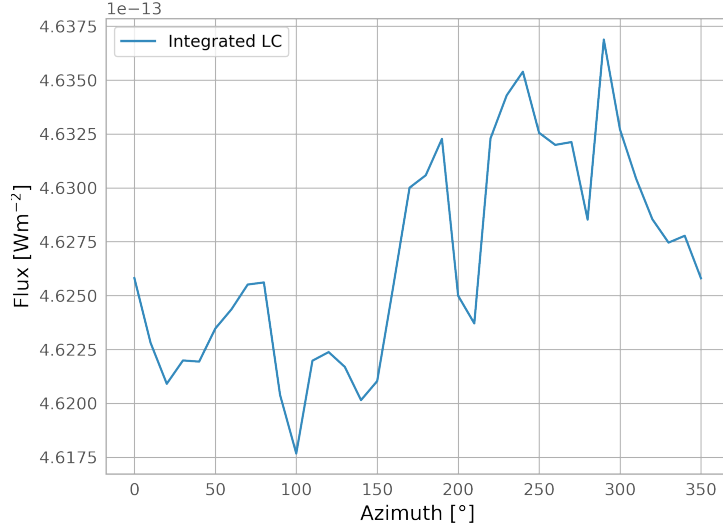


Figure 4.6 – Light curve obtained from the standard disk seen under 60° .

4.1.2 Derivation of the light curve

MCFOST does not produce light curves automatically. However, this can be easily achieved by using the monochromatic images. For this aim, I compute a 3D model with, in general, 36 azimuth values, i.e., one snapshot every 10° . This is equivalent to observe the system in rotation. I produce data points for the light curve by integrating high-resolution images of the inner disk for the later part of this chapter. It is possible to produce 1 pixel images which are already integrated by MCFOST; however, the size of the grid used to produce images is not well sampled close to the star and the resulting light curve does not always correspond to the integrated one (either it presents a flux offset or the shape is slightly different). Moreover, we are interested at the innermost region of the disk, and a good resolution around the star is crucial to model the variability. This leads to a small loss in the total flux from the disk. However, taking as example the disk seen under 60° of Fig. 4.3, the integrated flux from the image is of $4.36 \cdot 10^{-13} \text{ W m}^{-2}$. The contributions of direct star light and scattered star light are of $3.90 \cdot 10^{-13} \text{ W m}^{-2}$ and $4.59 \cdot 10^{-14} \text{ W m}^{-2}$, respectively, with most of the star scattered light concentrated at the inner disk rim. Thus, using images of the inner disk only does not affect heavily the total flux. The thermal emission from the disk is negligible at optical wavelengths. For the images in the rest of this chapter, I choose a wavelength of 575 nm, which is the maximum of the photometric spectral response of the *Kepler* instrument¹, and a map of 301×301 px that covers 0.3 AU.

Fig. 4.6 provides an example of the so computed light curve for a symmetric disk. For this aim, 36 data points are derived from as many monochromatic images with $0^\circ < \phi < 360^\circ$. The data points correspond to a light curve folded in phase according to its rotation period. As expected, the light curve is nearly constant and shows only some numerical noise. The sinusoidal trend with small amplitude seems to be related to a numerical issue of the grid at the inner disk. In order to produce light curves as observed for dippers, some asymmetric structure at the inner disk has to be added to the system.

4.2 MODELING JH 223 WITH AN INNER DISK WALL

The dipper from the Taurus sample which is best suited for detailed modeling is JH 223. The star only shows quasi-periodic dips on an otherwise stable continuum. This suggests that no other variability affects the light curve, and that the accretion process, if it is at the origin of the dips, remains pretty stable over the rotation cycles observed with K2. Fig. 4.7 shows again the light curve to be modeled

¹ <https://archive.stsci.edu/kepler/manuals/KSCI-19033-002.pdf>

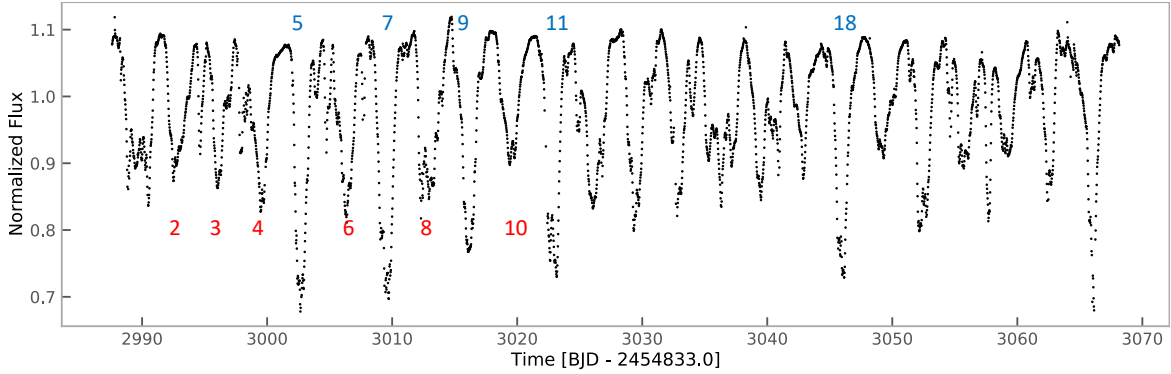


Figure 4.7 – K2 light curve of JH 223. Red numbers, bottom: faint dips to be modeled. Blue numbers, top: Deeper dips to be modeled.

Table 4.1 – Stellar parameters of JH 223.

P	W_{dip}	V	T_{eff}	L_*	M_*	R_*	R_{cor}	T_{cor}	i_*	\dot{M}_{acc}
[d]	[P]	[mag]	[K]	[L_{\odot}]	[M_{\odot}]	[R_{\odot}]	[R_*]	[K]	[$^{\circ}$]	[$M_{\odot} \text{ yr}^{-1}$]
3.31	0.36	15.66	3386	0.21	0.275	1.34	4.52	1126

with MCFOST. In general, two different amplitudes are present: one of $\sim 20\%$, one of $\sim 40\%$ (0.3 mag on average). Table 4.1 summarizes the properties of the star as derived in Chapter 3.

4.2.1 Inner disk wall: model parameters

After some trials of adding asymmetry via a tilted inner disk, the physical model chosen to reproduce the light curve is an inner disk wall with variable height $h_w = h_{\text{max}} \cos \frac{\phi - \phi_0}{2}$ and thickness Δr_w , which has been proposed to model AA Tau (Bouvier et al., 1999, 2007b). The density ρ_w is constant in the wall. The depth of the dips is mainly determined by two factors. First, the optical depth of the wall occulting the star. This quantity is degenerate, since it depends on both size and dust density of the wall. Δr_w will be kept constant to 0.01 AU and wall height and mass will be varied. Second, the geometry of the system, which depends on the height of the wall and the inclination of the system. For a given height h_w of the wall, the higher the inclination, the more likely it will be for the observer to cross the wall on his line of sight. This model excludes inclinations close to edge-on ($i \sim 90^{\circ}$), because the disk midplane is optically thick and would occult the star completely. McGinnis et al. (2015) were able to fit dips in NGC 2264 with this geometrical model and constrained inclinations of $i \sim 70^{\circ}$. Another possible constraint on the properties of the wall originates in the assumption that this wall is accretion-driven. Accretion columns are supposed to not deviate much from the closed magnetic field lines. Thus, the maximum height of the wall should not significantly exceed R_* .

Other relevant properties are the size, the shape and density of the disk; however, these are strongly degenerate. A strong flaring of the disk and a high dust density would prevent the observer from seeing the star at inclinations close to edge-on, but would not cause in itself a variability of the light curve as it is observed for dippers. Thus, I set for the surface density exponent and the flaring exponent typical values such as $\alpha = -0.5$ and $\beta = 1.125$. As for the disk geometry, I choose a scale height of $h_0 = 5 \text{ AU}$ at $r_0 = 100 \text{ AU}$. This relatively thin disk allows to focus on the inner region. R_{out} is kept at 300 AU and I assume that the inner disk is truncated close to the corotation radius at $\sim 0.03 \text{ AU}$. For a star of mass much lower than that presented in Sec. 4.1, the disk mass is scaled down to $2 \cdot 10^{-4} M_{\odot}$.

Finally, the nature of the dust grain is also relevant for the result, since it influences directly the opacity and the optical depth. As a first step, I keep a standard mixture of spherical and compact silicate grains that follow the Mie theory for opacity and scattering properties, and are distributed

Table 4.2 – Parameters and results from the different MCFOST runs.

Run	i [°]	$M_{d,w}$ [M_{\odot}]	h_w [AU]	A_d	W_d [P]
1	75	1.00E-12	0.02	0.75	0.53
2	75	1.00E-12	0.01	0.57	0.39
3	75	5.00E-13	0.01	0.45	0.33
4	70	5.00E-13	0.01	0.22	0.28
5	70	1.00E-12	0.01	0.31	0.28
6	70	5.00E-12	0.01	0.42	0.28
7	70	1.00E-11	0.01	0.42	0.28
8	65	5.00E-13	0.01	0.04	0.17

from $a_{\min} = 0.03 \mu\text{m}$ to $a_{\max} = 1000 \mu\text{m}$. In forthcoming studies, the impact of these properties should be further considered, by varying, for example, the chemical dust composition and the size and distribution of the grains.

4.2.2 Inner disk wall: results

One issue in modeling the wall in cylindrical coordinates is the limitation of grid, which follows closely the scale height of the disk. At the inner disk rim of 0.03 AU, the height of the disk is of $5.44 \cdot 10^{-4}$ AU for the chosen scale height. A large asymmetry located at the inner disk rim results in the wall being cut off at its base. The issue can be solved using the option `-cutoff n` in the MCFOST command line. The command cuts the grid at n times the height of the disk. Otherwise, a spherical grid delivers equivalent results. I increase the resolution of the grid to 120 cells in z (θ) direction and to 120 in ϕ direction.

After some trials that lead to clearly nonphysical results, like too massive walls that do not allow the propagation of the star light in the disk, the inclination is varied between 65° and 75° , the dust mass of the wall between 10^{-11} and $10^{-13} M_{\odot}$, and its height h_w between 0.01 and 0.02 AU. Table 4.2 summarizes the parameter space that has been explored and one of the parameter files is shown in App. A.2. For each set of parameters, the full 3D model is run and the light curve built from 36 data points. The fainter dips can be fitted with run 4 (Fig. 4.8 and Fig. 4.10). An amplitude close to 20% can be achieved; however, the dip structure is asymmetric and complex and suggests that in reality several accretion columns or otherwise dusty structures contribute to the light curve. The dip width is congruent with the main dip when the different components are clearly detached (Fig. 4.8, dip 3). The wall has an optical depth $1 < \tau < 2$. The deeper dips with amplitudes $\sim 30\%$ can be reproduced with run 5 (Fig. 4.9 and Fig. 4.11). In this case, their structure is less complex and both amplitude and dip width are closer to each other. The wall has a higher optical depth $2.5 < \tau < 4.5$.

4.2.3 Influence of the parameters on the result

From the limited parameter space explored here, it appears that the geometry of the system plays the major role in the light curve production. The results from all runs are compared in Fig. 4.12. Small variations in the inclination strongly influence the amplitude of the dips. As a consequence, from 75° to 70° the dip amplitude decreases from $\sim 50\%$ (run 1 and 2) to 30% for the same parameters. For $i = 65^\circ$ (run 8) the light curve remains almost constant and is not able to account for dipper light curves anymore. The height of the wall h_w is set to 0.01 AU for all runs but the first. For $h_w = 0.02$ AU, the wall is so large that it covers the star completely for a significant fraction of time, thus flattening the bottom part of the dip. For runs 4-7, the amplitude of the dips is influenced by the amount of dust

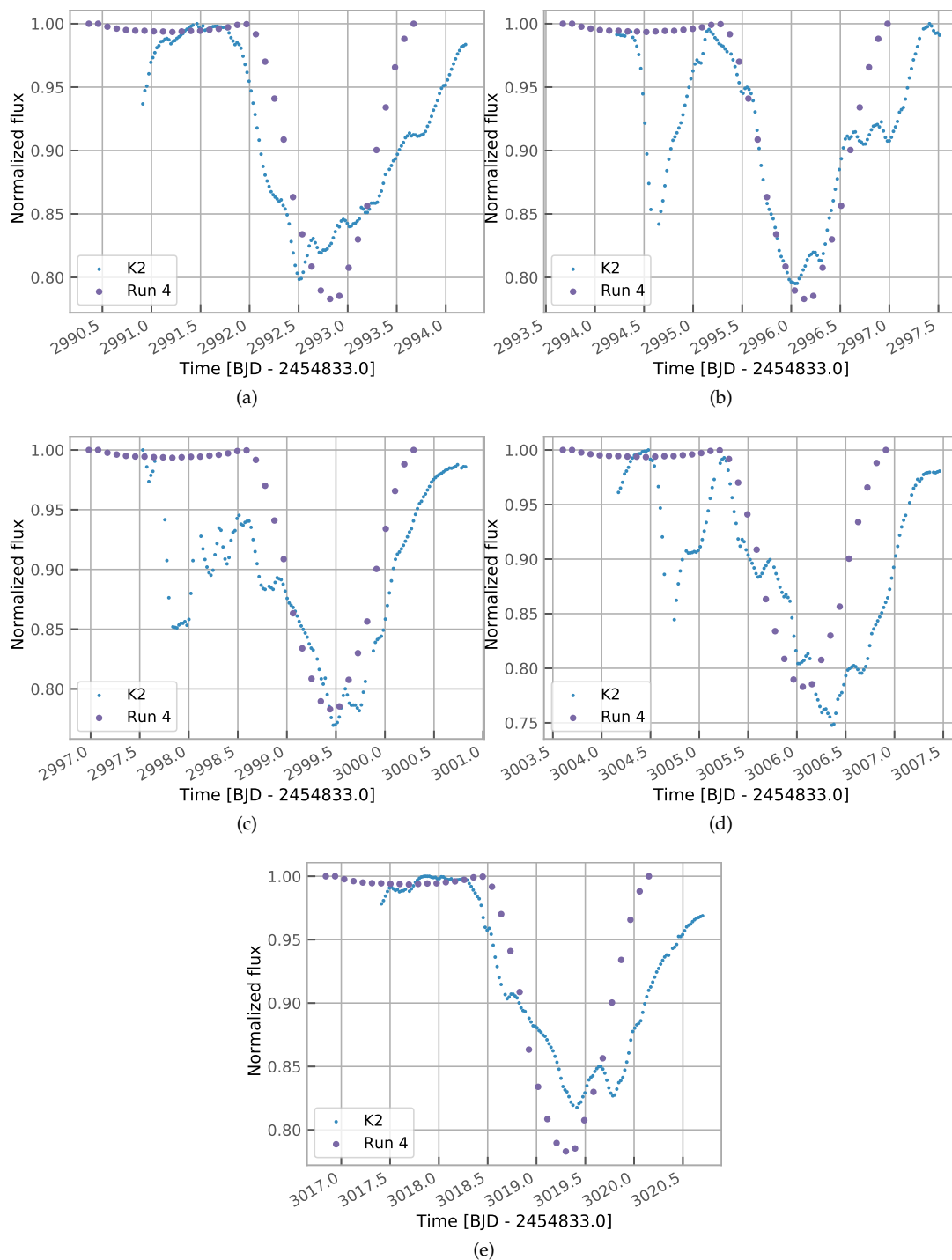


Figure 4.8 – Dips with smaller amplitude modeled with run 4. They are marked in red on Fig. 4.7. The synthetic light curve is shifted back in phase by 0.55 d for all plots.

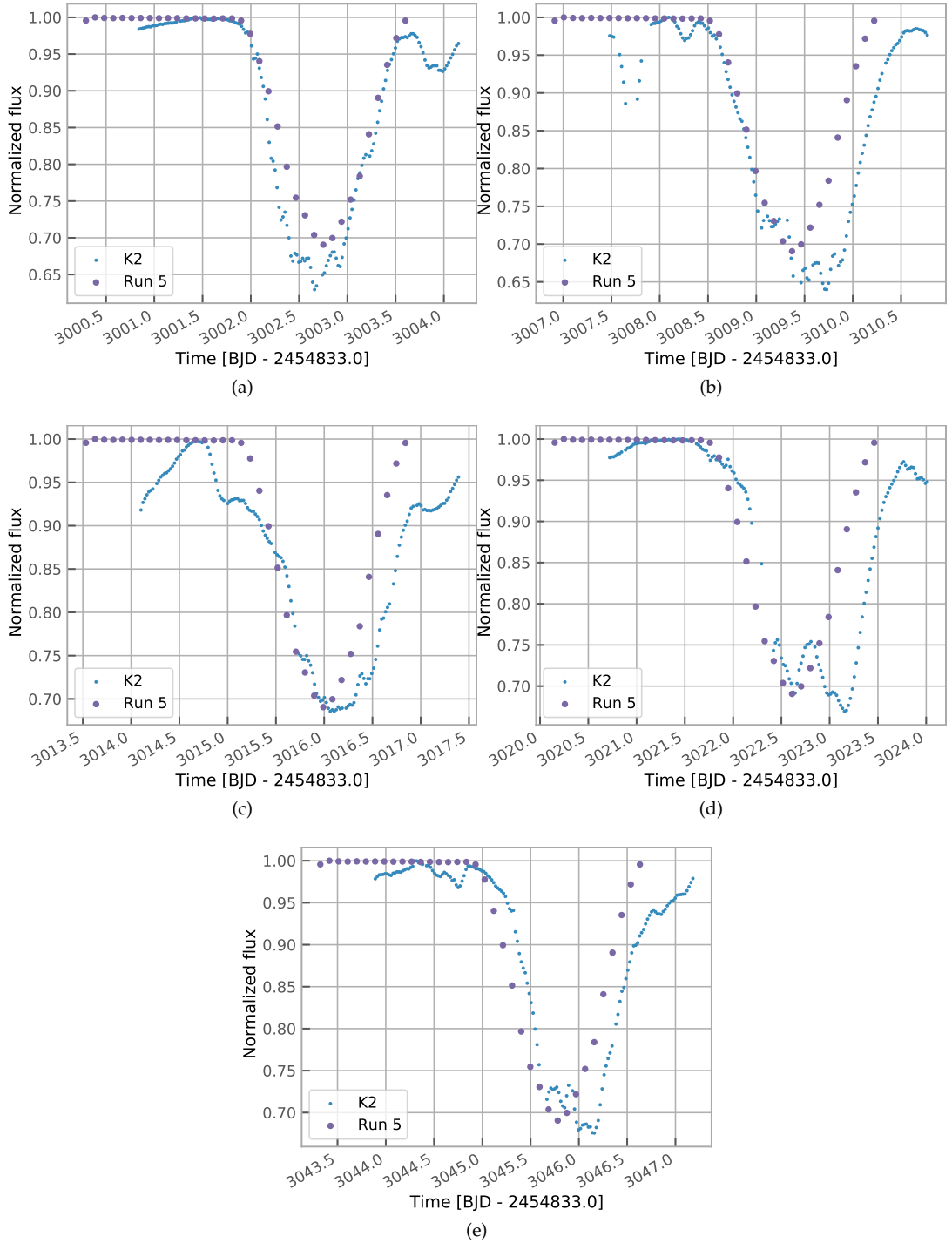


Figure 4.9 – Dips with larger amplitude modeled with run 5. They are marked in blue on Fig. 4.7. The synthetic light curve is shifted back in phase by 0.55 d for all plots.

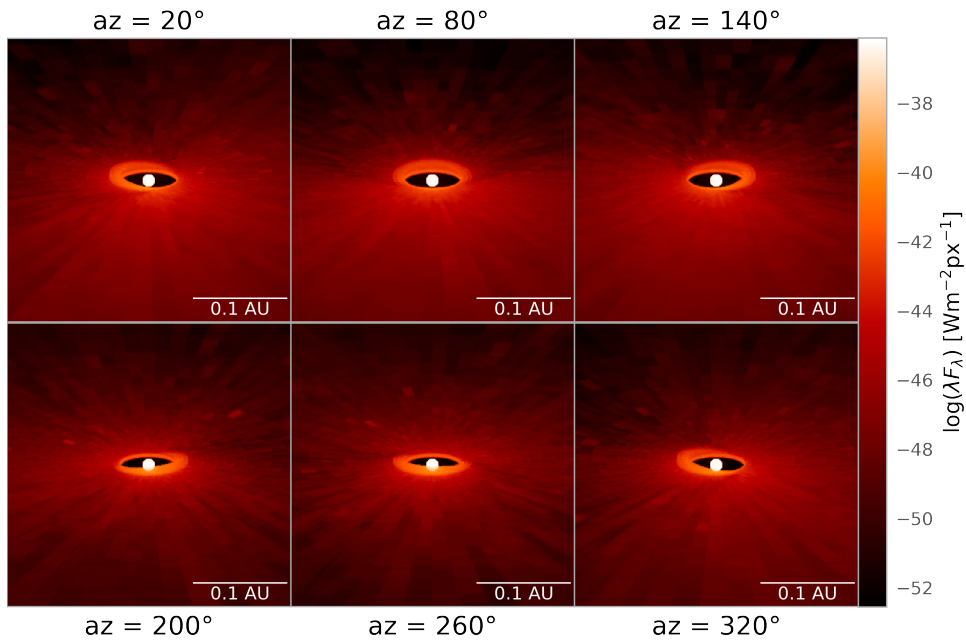


Figure 4.10 – Monochromatic maps at 575 nm of run 4 at six different snapshots. This model is able to (partially) account for the smaller dips of JH 223.

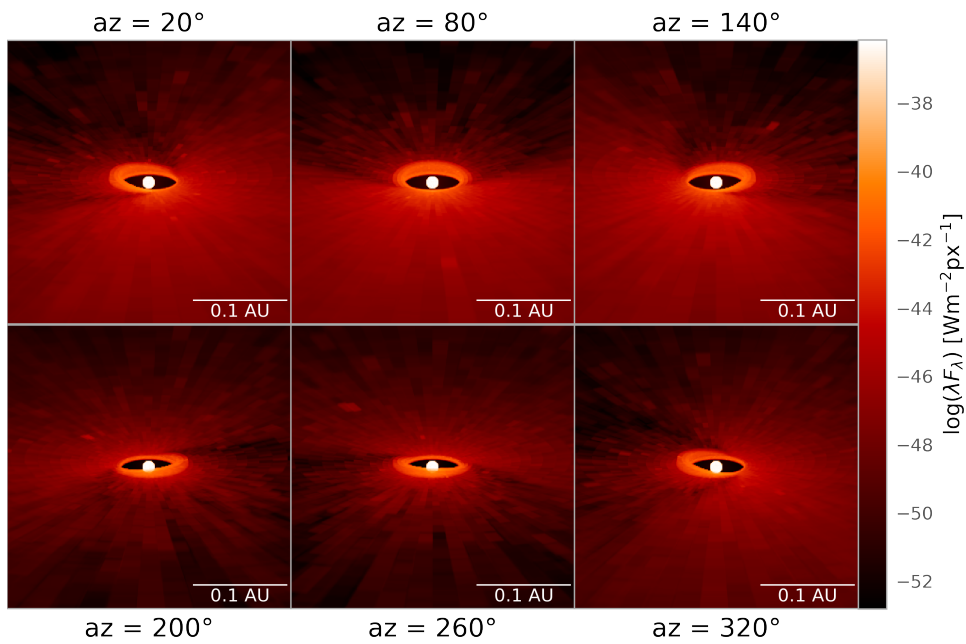


Figure 4.11 – Monochromatic maps at 575 nm of run 5 at six different snapshots. This model is able to account for the larger dips of JH 223.

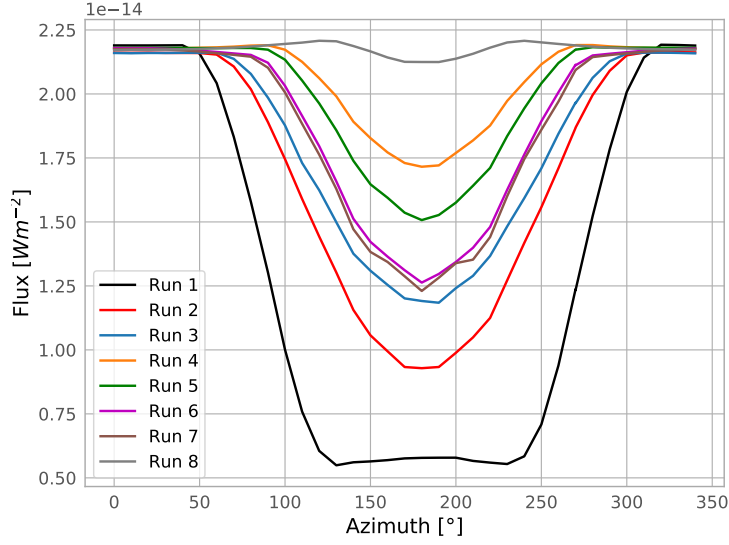


Figure 4.12 – Light curves generated from all the runs. The dips are re-centered in phase and shifted by 80° in comparison with the monochromatic images.

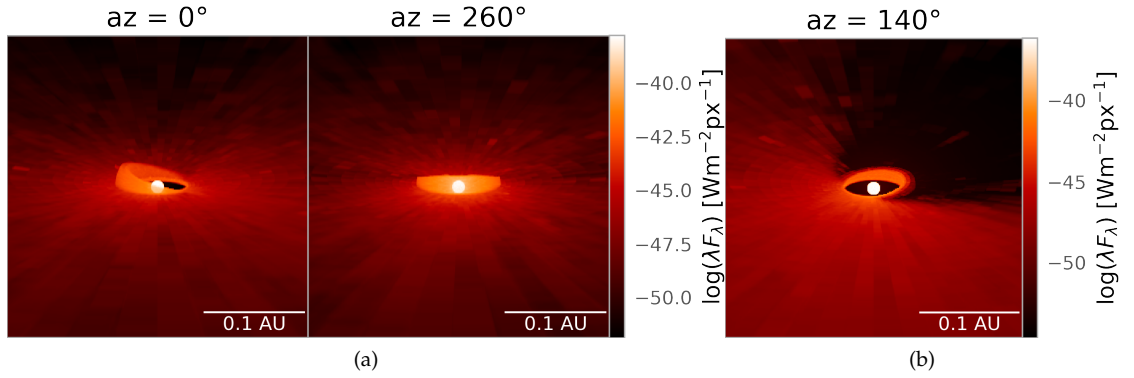


Figure 4.13 – Qualitative comparison of the optical depth variation of the wall. (a) Optically thin wall from run 1. For a constant inclination and h_w of later runs, the optical depth increases gradually as in Fig. 4.10 and Fig. 4.11 ($M_{d,w} = 5 \cdot 10^{-13}$ and $10^{-12} M_\odot$, respectively) and the wall casts a darker shadow on the disk. (b) Optically thick wall from run 6 with $M_{d,w} = 5 \cdot 10^{-12} M_\odot$.

present in the wall, while the dip width defined at FWHM as in Chap. 3 does not vary. Increasing the dust mass of the wall directly influences the optical depth, as it can be seen in Fig. 4.13, Fig. 4.10 and Fig. 4.11, in which a wall with a higher optical depth casts a darker shadow on the disk. Shadows cast by asymmetric structures located at the inner disk have indeed been observed with *SPHERE* in other young stars (e.g., Thalmann et al., 2016). Once the wall has reached a high optical depth, the amplitude of the dips does not significantly increase, and is only determined by the geometry.

4.2.4 Color variation

The dipper phenomenon is associated with a slight color variation in the optical during the dips, when the system becomes redder as the brightness in the *V* band decreases (Bouvier et al., 1999, 2003). This supports the hypothesis of a dusty structure at the origin of the dips, since dust produces a larger extinction at shorter wavelengths. It is difficult to observe faint, young stars in the *U* band, so the preferred ground-based observations take place in the *V*, *I*, *R* bands. Simultaneous follow-up

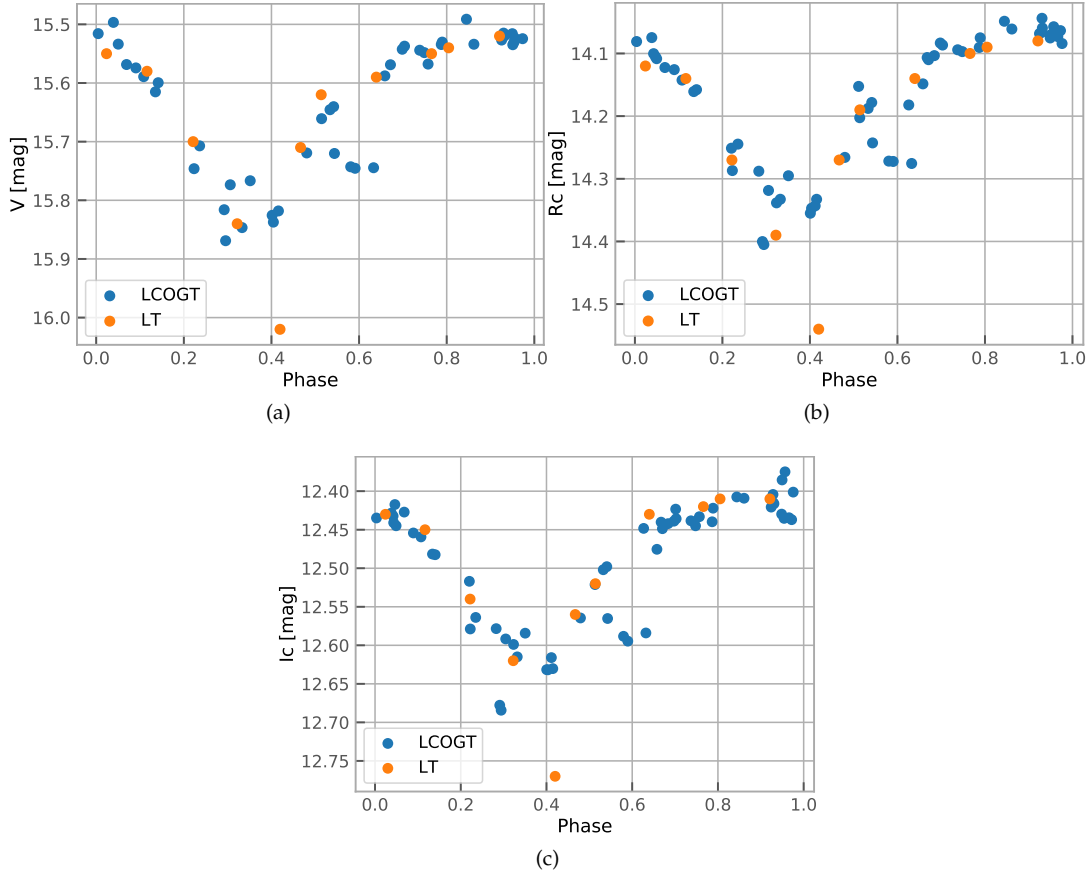


Figure 4.14 – Phase-folded light curve of JH 223 as observed in 2019 in the V (a), R_c (b), I_c (c) bands by the LCOGT (blue points) and the LT (orange points).

observations of JH 223 were mainly provided in 2019 by the LCOGT in Gran Canaria, and a few data points by the LT in La Palma (Fig. 4.14).

The corresponding color variation is shown in Fig. 4.15. I computed synthetic light curves at 545, 640 and 798 nm, which are the central wavelengths of the corresponding V , R_c , I_c filters in the Johnson-Cousins photometric system. In order to compare with the synthetic light curves provided by MCFOST, the synthetic flux has to be converted into magnitudes. For this purpose, I first convert the MCFOST flux into F_ν by dividing it by c/λ and then apply:

$$m_1 - m_0 = -2.5 \log_{10} \frac{F_{\nu,1}}{F_{\nu,0}} \quad (4.1)$$

where m_1 is the magnitude of the star, $m_0 = 0$, $F_{\nu,1}$ the converted flux from MCFOST, and $F_{\nu,0}$ the absolute flux density for $m = 0$ as in Bessell (1979). The resulting comparison between observed and modeled color variation is shown in Fig. 4.15. It is clear that, although there is a color variation, the slope is not large enough compared to the observations (see Table 4.3 for the exact values). This can be due to either a too high optical depth, or too large dust grains, since the scattering properties of dust change with a large grain size (from Rayleigh to Mie scattering). In the next section, I present the model of an inner-disk wall with the same geometrical properties as run 4 and 5, but with interstellar dust grains, i.e., $0.01 \mu\text{m} < a < 0.25 \mu\text{m}$.

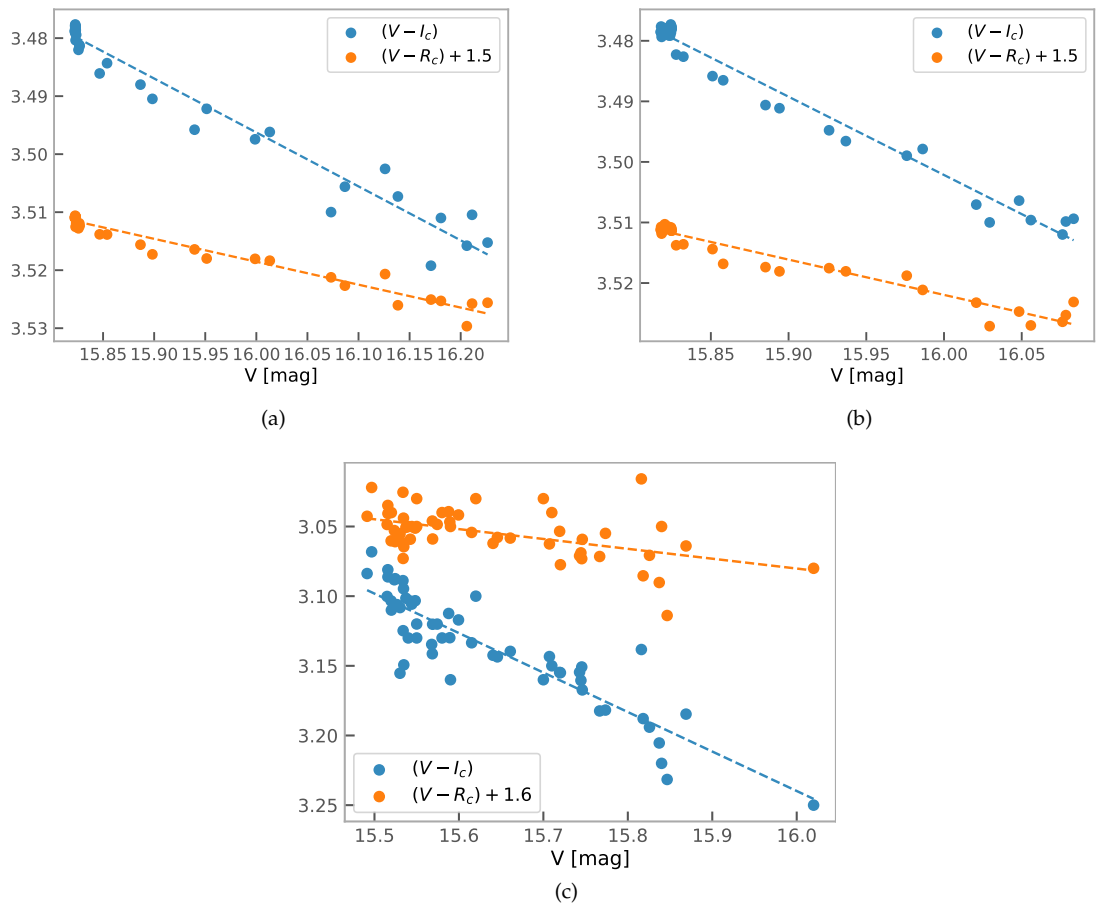


Figure 4.15 – Color variation as $(V - I_c)$ and $(V - R_c)$ for the light curves from run 5 (a), run 4 (b), and from the ground-based observations (c). An offset of the order of ~ 0.4 mag is evident on the y-axis. At the same time, the slope of the color variation cannot be reproduced well with the synthetic data.

Table 4.3 – Variation of the slope s of the $(V - I_c)$ and $(V - R_c)$ colors depending on the maximal grain size a_{\max} and the dust mass of the wall $M_{d,w}$.

Run	a_{\max} [μm]	$M_{d,w}$ [M_{\odot}]	$s(V - I_c)$	$s(V - R_c)$
4	1000	5.00E-13	0.129	0.058
5	1000	1.00E-12	0.093	0.039
9	1	1.00E-12	-0.009	0.003
10	0.25	5.00E-13	0.034	0.013
11	0.25	1.00E-13	0.128	0.034
12	0.25	5.00E-12	0.128	0.034
13	0.25	5.00E-14	0.237	0.084
14	0.25	4.00E-14	0.272	0.091
15	0.25	3.50E-14	0.301	0.111
16	0.25	2.50E-14	0.348	0.131
17	0.25	1.50E-14	0.416	0.184
18	0.25	1.00E-14	0.452	0.201
Obs.			0.283	0.071

4.2.5 Model adjustment with interstellar dust grains

Besides decreasing the maximal grain size a_{\max} , it is also necessary to adjust the total mass of the wall. Using the same mass and this modified grain-size distribution implies that there will be more small dust grains than before and the optical depth will increase significantly. Table 4.3 lists the parameters explored in order to reproduce the slope of the color variation. Runs 9 and 10 illustrate the necessity of reducing the dust mass of the wall: the slope is nearly 0, meaning that the structure is completely optically thick and the color variation is suppressed.

The color variation can be reproduced best by run 14 (Fig. 4.16). The corresponding parameter file is shown in App. A.2. The offset of 0.3-0.4 mag on the absolute value of the colors might be due to different factors. On one hand, the MCFOST code includes the circumstellar, but not the interstellar extinction, which in revenge affects the observations ($A_V = 1.4$ mag for this star). On the other hand, the intrinsic colors of M dwarfs vary more strongly with their spectral type (e.g., Pecaut and Mamajek, 2013). An uncertainty on the spectral type M2.8 of JH 223 will be noticeable when considering the colors.

Run 14 can also reproduce well the large dips. However, with these constraints on the parameters, it is not possible to reproduce both the observed color variation and the amplitude of the small dips. Run 17 can fit them well (Fig. 4.17), but with a slope for the $(V - I_c)$ color which is much larger than observed. One possibility would be different dust properties or grain sizes. Nevertheless, it is unclear why they should change from one rotation cycle to the other, when switching between large and small dips. It is more likely that the geometry, and maybe even the position of the dusty wall change due to fluctuations in the mass-accretion process. The complexity of the small dips shows that a symmetric wall alone cannot account for the full light curve.

The optical depth maps of the wall for these two runs are presented in Fig. 4.18. Similarly to the former parameter set with larger dust grains, it varies between $1 < \tau < 2.25$ and $3 < \tau < 6$ for the small dips (run 17) and the large dips (run 14), respectively.

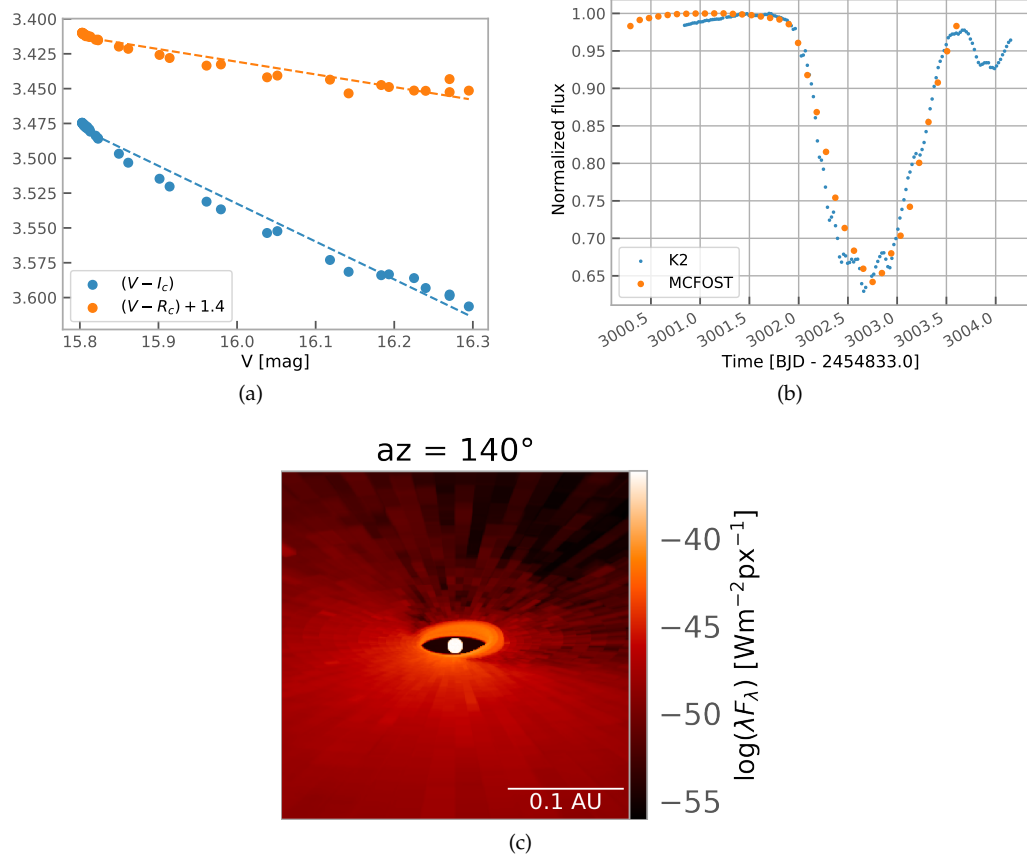


Figure 4.16 – Color variation (a), synthetic light curve compared to dip 5 (b) and snapshot at 575 nm of run 14.

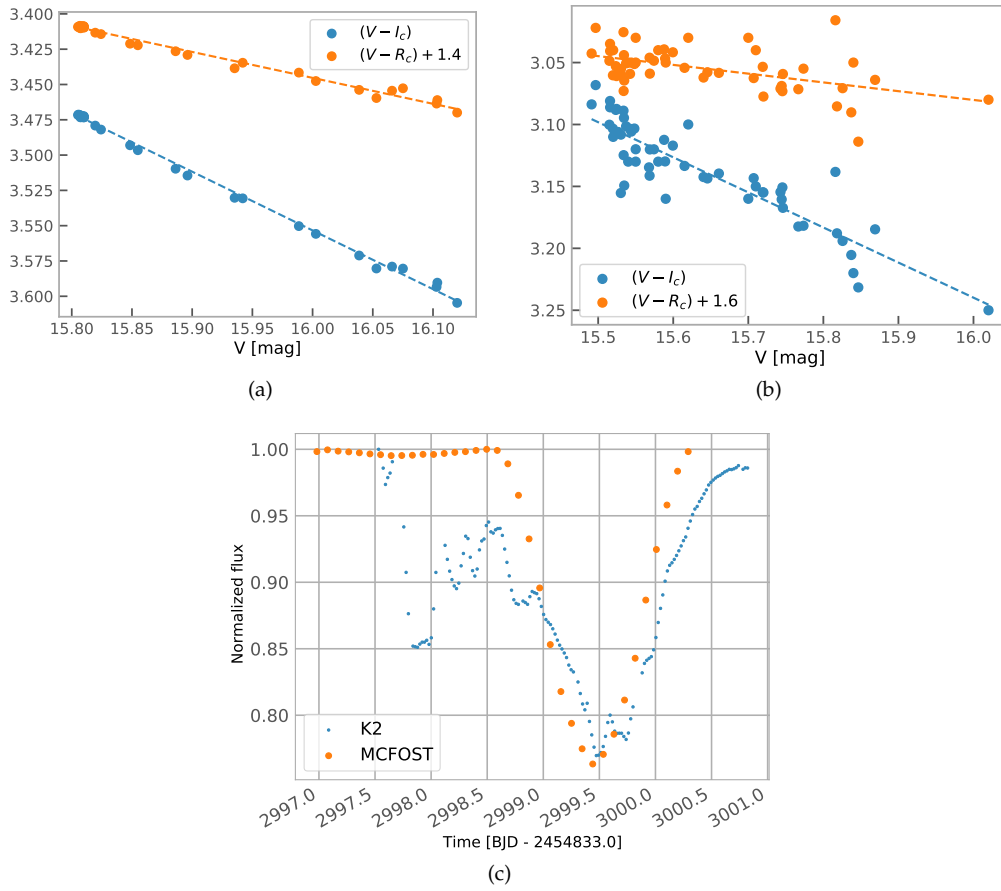


Figure 4.17 – Color variation of run 17 (a), observed color variation for comparison (b) and synthetic light curve compared to dip 4 (c).

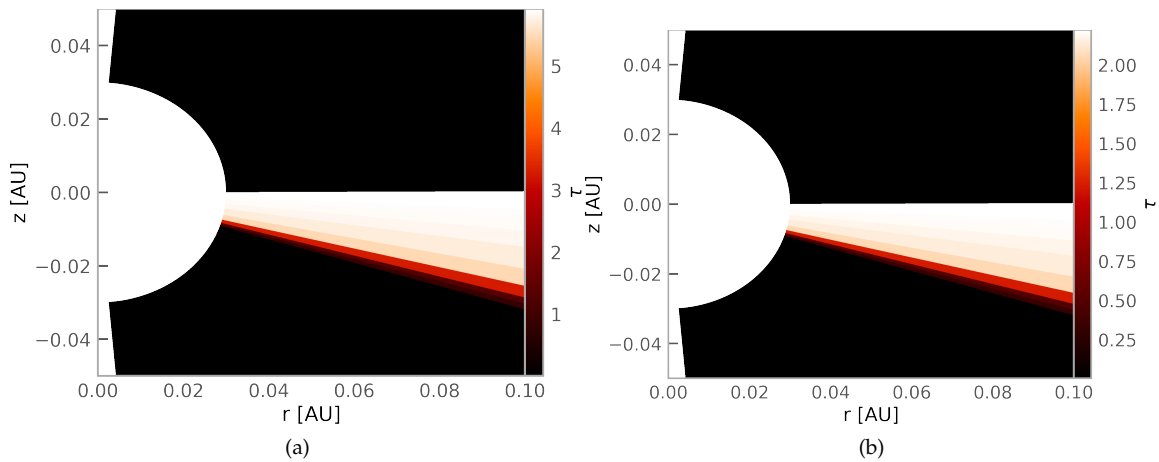


Figure 4.18 – Optical depth map at 575 nm of the inner-disk wall for run 14 (a) and for run 17 (b). The optical depth map of the disk alone has been subtracted from the map that includes both disk and wall.

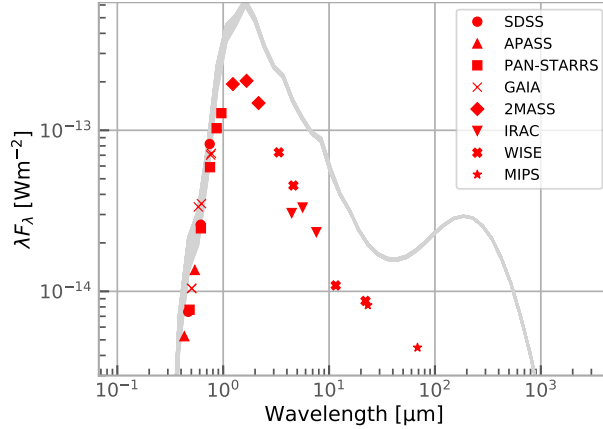


Figure 4.19 – SED of JH 223 (run 13) for 36 azimuths (grey contour). Red points: measurements from the different surveys.

4.2.6 Spectral Energy Distribution

With a model that is converging for the reproduction of both the dips’ morphology and the color variation, the next step is to probe the SED. I searched through the measurements available in the literature with the tool VOSA (Bayo et al., 2008). The SED for all azimuths is computed with MCFOST for run 13 (Fig. 4.19). The IR-excess starts after 3.3 μm . It is evident that the luminosity of the star is overestimated with MCFOST, as well as the outer disk contribution. This suggests that either the effective temperature or the stellar radius (derived in Sec. 3.4), used as input in the parameter file, are overestimated. The distance of the star in MCFOST is set to 140 pc, as measured by *Gaia*. The outer disk is likely much smaller than assumed, or has a much lower mass. However, the color and the light-curve variability induced by the rotation of the star and the inner-disk wall are not directly affected by these properties.

4.2.7 Discussion

The results presented here are preliminary, but promising. The model originally developed for AA Tau is able to account for the light curve of JH 223 as well, with strict constraints on the viewing angle. The synthetic light curves can reproduce closely the symmetric dips with a simple geometry, but fail to reproduce the width of dips that are asymmetric or clearly present several components. This suggests as a first hypothesis that more than one structure, with properties similar to those proposed here, occult the star. Another possibility is that one warp is present, which is stable, but regularly depleted and refilled by dust, while other stochastic and short-lived accretion streams form during the observations (e.g., Blinova et al., 2016).

The difference in dust content for the deeper and fainter dips in the first set of parameters with $a_{\text{max}} = 1000 \mu\text{m}$ is on the order of $5 \cdot 10^{-13} M_{\odot}$, which means that the star has likely accreted $\sim 1.5 \cdot 10^{-13} M_{\odot} \text{d}^{-1}$ of dust, and 100 times more of gas. This gives a lower limit to the accretion rate of $\sim 5 \cdot 10^{-9} M_{\odot} \text{yr}^{-1}$. For interstellar dust grains, the so-estimated mass-accretion rate is $\sim 2.7 \cdot 10^{-10} M_{\odot} \text{yr}^{-1}$.

The main caveat of these results is the limited parameter space that has been explored. In general, the outer disk parameters can be kept constant with standard values due to their strong degeneracy, although the SED shows that they are far from reproducing the real disk of JH 223. The dust properties should be taken into account in more depth to properly model the dips. Different dust mixtures and grain sizes might influence the optical depth of the wall. Moreover, not all types of dust sublimate at the same temperature, and dust grains might change their opacity right before sublimation (Nagel and Bouvier, 2020). Of course, more combinations of inclination, height of the wall and dust mass of the wall would deliver a more complete picture of these variations, and it cannot be excluded that

the light curve of JH 223 could be modeled with a different parameter set. Another limitation is the chosen model in itself: the dusty structure occulting the star might have a different shape than the one defined by the wall. Moreover, in this simplified case the wall is superimposed to the disk without continuity in the density. A determinant future development will be the coupling of the disk density, as obtained from MHD simulations of accreting stars, with MCFOST.

5

CONCLUSION AND OUTLOOK

The star-disk interaction is a complex phenomenon, which requires a multidisciplinary approach to disentangle its different outcomes. Stellar rotation, magnetic field topology, accretion processes and the interaction of the magnetic field lines with the inner disk are all properties that need to be studied in detail to get a complete picture. In this context, dippers can help answer the question of how the inner disk is deformed close to the truncation radius, as a consequence of the interaction of the stellar magnetic field with the matter from the disk.

For the main part of my PhD, I have studied the high-precision light curves provided by the space mission *K2* for the Taurus star-forming region. Among a sample of 179 cluster members, I classify 34 of them as dippers, 22 of which do not display another dominant variability. The dipper phenomenon is intrinsically ephemeral on scales from a few years down to a few days, as shown by long-term observations of former dipper stars such as AA Tau, and transient dippers observed in this campaign. The occurrence of dippers that I find in Taurus, which is on the order of 20% for the observed members and up to 30% for disk-bearing stars, is in accordance with previous surveys. This, combined with the relatively short lifetimes of dippers and the observational constraints for the photometry –mainly the viewing angle– stresses once more that the occurrence we observe is a lower limit, and that this phenomenon is probably relevant for a majority of stars at some point of their T Tauri phase.

Among their properties, I have studied their periodicity in the first place. All explanations given for dippers converge on the fact that the dusty, occulting structure is located at the inner disk. Therefore, their periodicity should be similar to the stellar rotation. Moreover, the different periodic and aperiodic dipper light curves might be linked to differences in the accretion regime of the star. With the aim of disentangling the numerous and complex sources of variability, I applied wavelet analysis to the light curves. This technique starts to be applied more widely in astronomy only recently (e.g., Bravo et al., 2014; Sicilia-Aguilar et al., 2020). Although complex, these algorithms provide a custom time-resolved frequency analysis, which helps in understanding the nature of multiple periodicities, transient phenomena and also changing periods. I found a similar number of periodic and aperiodic dippers, the latter being more often superimposed to other types of stellar variability. The dipper periods are, in accordance with previous surveys, in the range of the stellar rotation periods, supporting the hypothesis that the dusty material is located at the corotation radius.

I also combined photometric, astrometric and spectroscopic data from the literature to derive in a consistent and robust way the stellar parameters of the studied sample, in order to prove the proposed models. The observed dippers are in general of late spectral type (K to M), fully convective, and have low masses ($< 1 M_{\odot}$) down to the brown dwarf limit. In agreement with theoretical calculations, the corotation radii are located at a few stellar radii. The temperatures at corotation derived with simple approximations are consistent with the presence of dust at that distance. The stellar inclination is the most important parameter to test the magnetospheric accretion model, since the presence of a dipper depends on the viewing angle of the systems. The model is able to explain most, but not all, of the observed dipper light curves that are mostly seen under moderate to high inclination, with large uncertainties. While two of them are seen under low inclination, one is an older star of early spectral type, for which the dipper phenomenon might rather be explained by disrupting planetesimals than accretion (Gaidos et al., 2019; Tajiri et al., 2020). Another additional phenomenon that might explain the high occurrence rate of dippers, despite the geometrical constraints, are inner disks misaligned with their outer disk. These seem to be pretty common among young stars (e.g., Alencar et al., 2018; Bouvier et al., 2020). The stellar inclinations often larger than outer disk inclinations observed in this sample corroborate this possibility.

The study of the dip morphology confirms that many questions on these dusty accretions columns and inner disk warps remain open, which will require further in-depth work. The proposed possible features able to partially occult the star would require some correlation between dip width and amplitude, as proxies of the viewing angle, height and angular extension of this structure, which could not be found until now. The presence of several peaks in the dips raises the question whether they are produced by different dusty features or by a complex, strongly unstable one. Several open questions persist on the nature of accretion columns in stable and unstable accretion regimes. Especially for the unstable regime, which has been invoked to explain aperiodic dippers, it is unclear how dust behaves when accretion tongues form at the stellar equator, and within the truncation radius (Romanova et al.,

2008). Since dippers require the presence of dust, radiative transfer modeling is essential to verify whether dust is able to survive in that environment, as it seems to be the case under certain conditions (Nagel and Bouvier, 2020). Moreover, although they have a periodic occurrence, many dippers exhibit phase shifts of the minima between rotation cycles. More detailed analysis will be necessary in future to understand whether these shifts are correlated to each other, and what physical mechanisms at the inner disk induce this perturbation. Finally, I find that broad and complex dips correlate with a larger rotation period, suggesting that slowly rotating stars produce accretion columns or inner disk warps with a larger angular extension. It will be interesting to verify whether these larger dusty structures are influenced by a different magnetic field topology.

Although helpful to indirectly observe the inner disk region, photometric observations are strongly degenerate. One can recover some constraints on upper and lower limits, but it is impossible to tell whether the obscuring structure is large and optically thin or small and optically thick, and the exact geometry cannot be retrieved due to the projection effects. Moreover, it is not possible to derive precise dust properties and composition just from the light curves. For this reason, I use the MCFOST code for radiative transfer modeling of one of the light curves. I find that it is possible to model the different dips of JH 223 by means of a dusty inner-disk wall as in Bouvier et al. (2007b), with the different dip depth induced by a varying dust content. This variation is compatible with a reasonable mass accretion rate of a low-mass star. The model is also able to reproduce the slope of the color variation as provided by follow-up, ground-based observations, which is an expected behavior for dippers. However, the inner-disk wall is a simple, symmetric model which has to be upgraded to be able to reproduce more complex dips, as shown by the absence of geometrical correlations in the observations of dips.

These results are preliminary, and as such require more analysis for a more robust modeling. As immediate and feasible steps, the parameter space should be expanded in order to allow more wall geometries and different dust populations. In the frame of the SPIDI project, it will be possible to couple in the near future the output of realistic MHD simulations, which provide the disk density structure, with MCFOST. MHD models alone do not take into account the optical depth and absorption through dust, which is crucial to simulate correctly dipper light curves. This will allow to produce a ‘real-life’ model instead of a simplified, parametric one, leading towards a much more comprehensive understanding of the dipper phenomenon in star-disk interaction systems.

Ideal follow-up photometric observations will be multi-band and coupled to simultaneous spectroscopic and spectropolarimetric data. These will allow to better understand the lifetimes of the dipper phenomenon and the timescales of variation of the mass-accretion rate. Spectropolarimetry provides, by means of Zeeman-Doppler analysis, insights on the magnetic field topology, which influences the way the material of the inner disk is accreted onto the stellar surface. Since the end of the *K2* mission, *TESS* is able to provide high-cadence observations for targets brighter than those observed with *K2*. Optical data, combined with infrared data, allow to study the color variations of dipper systems. Spectroscopic lines in the infrared and in the optical, such as Pa β , He I at 1083 nm, H α and H β , allow to probe accretion. Their red-shifted component traces infalling material, which is supposed to be obscuring the star during the photometric dips. The He I line at 587.6 nm traces the accretion shock and allows to recover the rotational modulation due to the star. CHFT/SPIRou is a sensitive instrument ($H \sim 10$ mag) that observes in the IR as a complement to CHFT/ESPaDonS in the optical and is already providing interesting results (e.g., Sousa et al., 2021).

The development of interferometric instruments will also contribute to shed light on the star-disk interaction at a few stellar radii from the star. VLTI/GRAVITY has already provided excellent observations in this direction. While the spatial resolution can go down to ~ 2 mas, equivalent to ~ 0.2 AU for the distance of the Taurus cluster, the differential observation of the photocenter phase shift of the Br γ line can locate the source of emission at ~ 0.05 AU (Bouvier et al., 2020). As for now, the instrument is limited in its sensitivity at $K \sim 10$ mag, which means that very faint objects cannot be observed with this resolution yet. GRAVITY+ aims to increase the sensitivity by 4-5 mag, and the sky coverage as well (Eisenhauer, 2019)¹.

¹ https://www.mpe.mpg.de/7480772/GRAVITYplus_WhitePaper.pdf

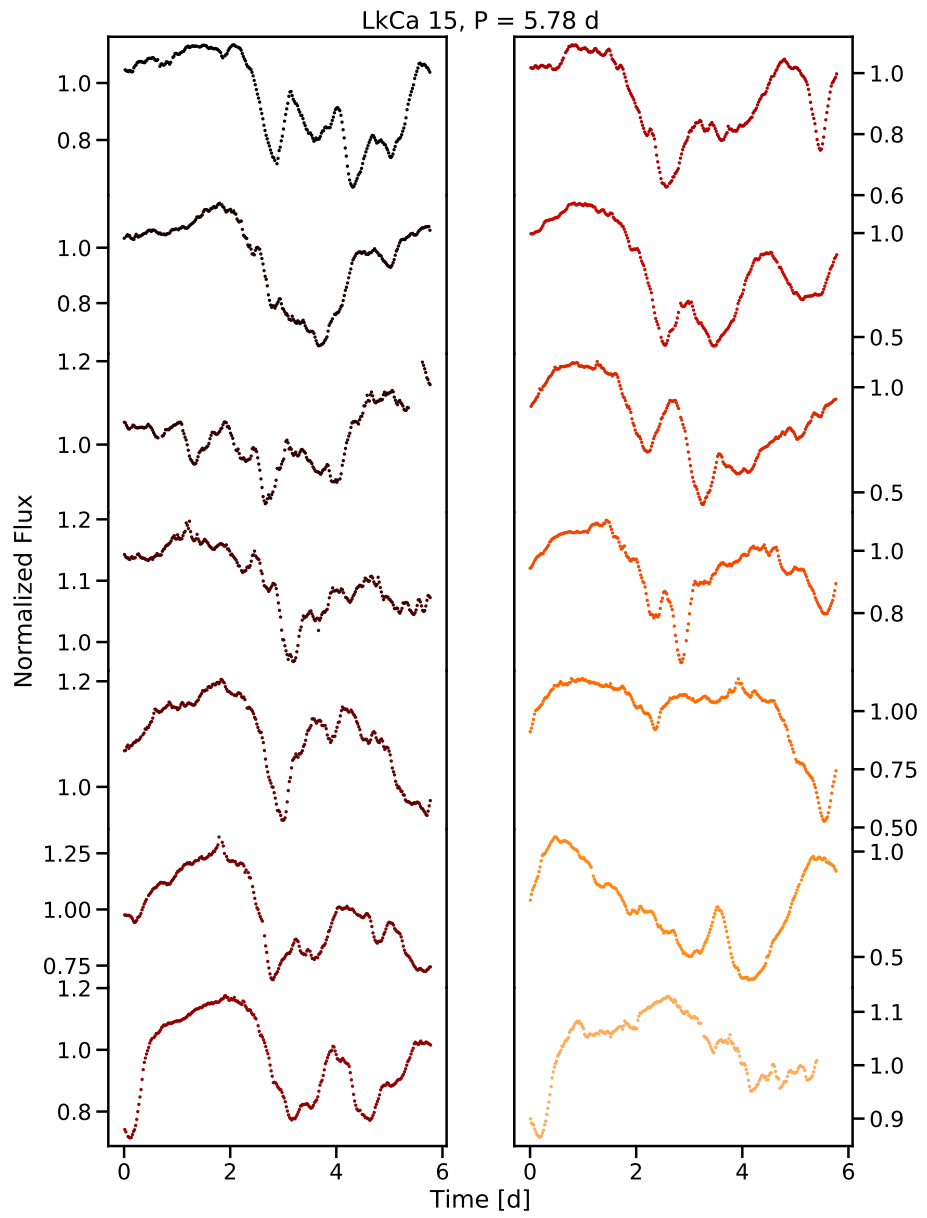
A

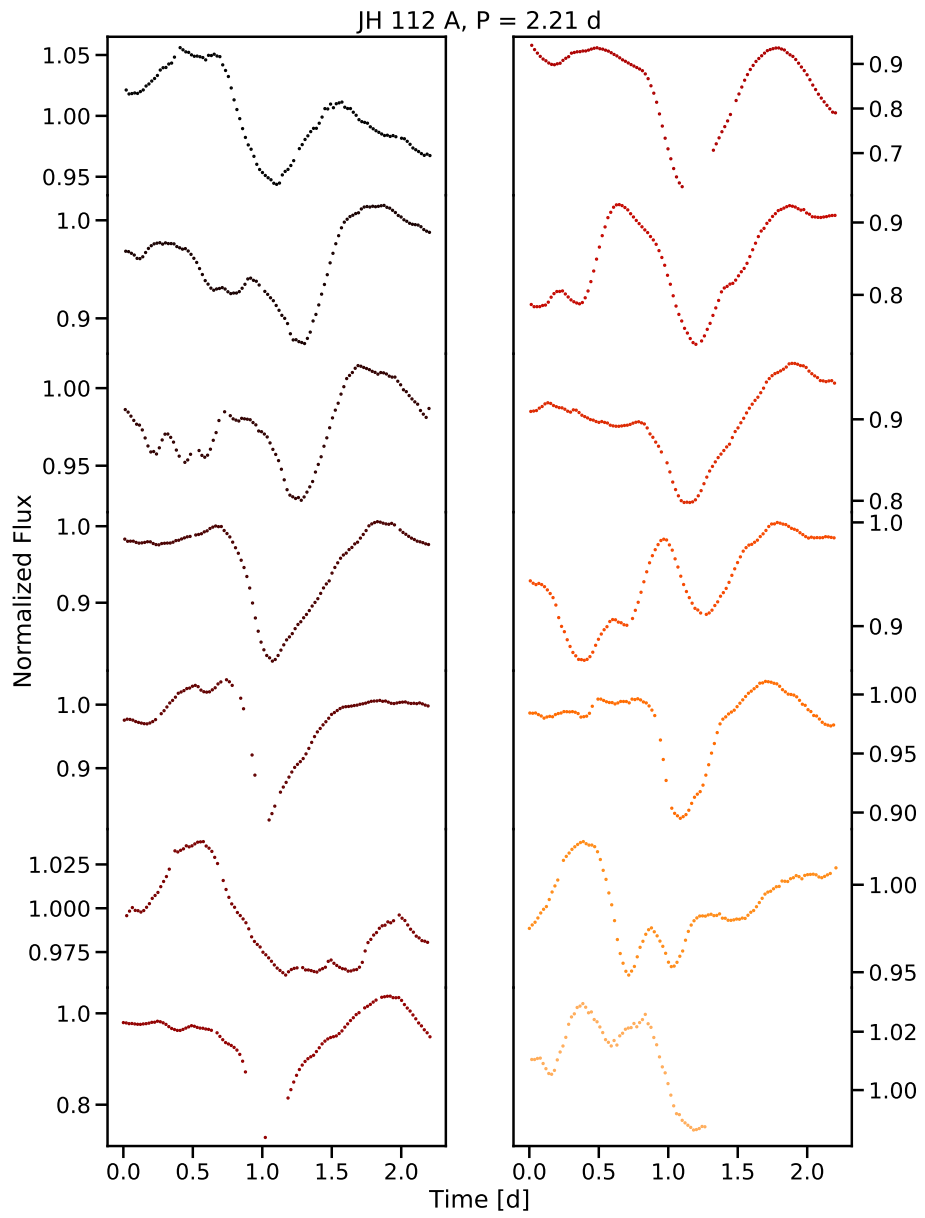
APPENDIX

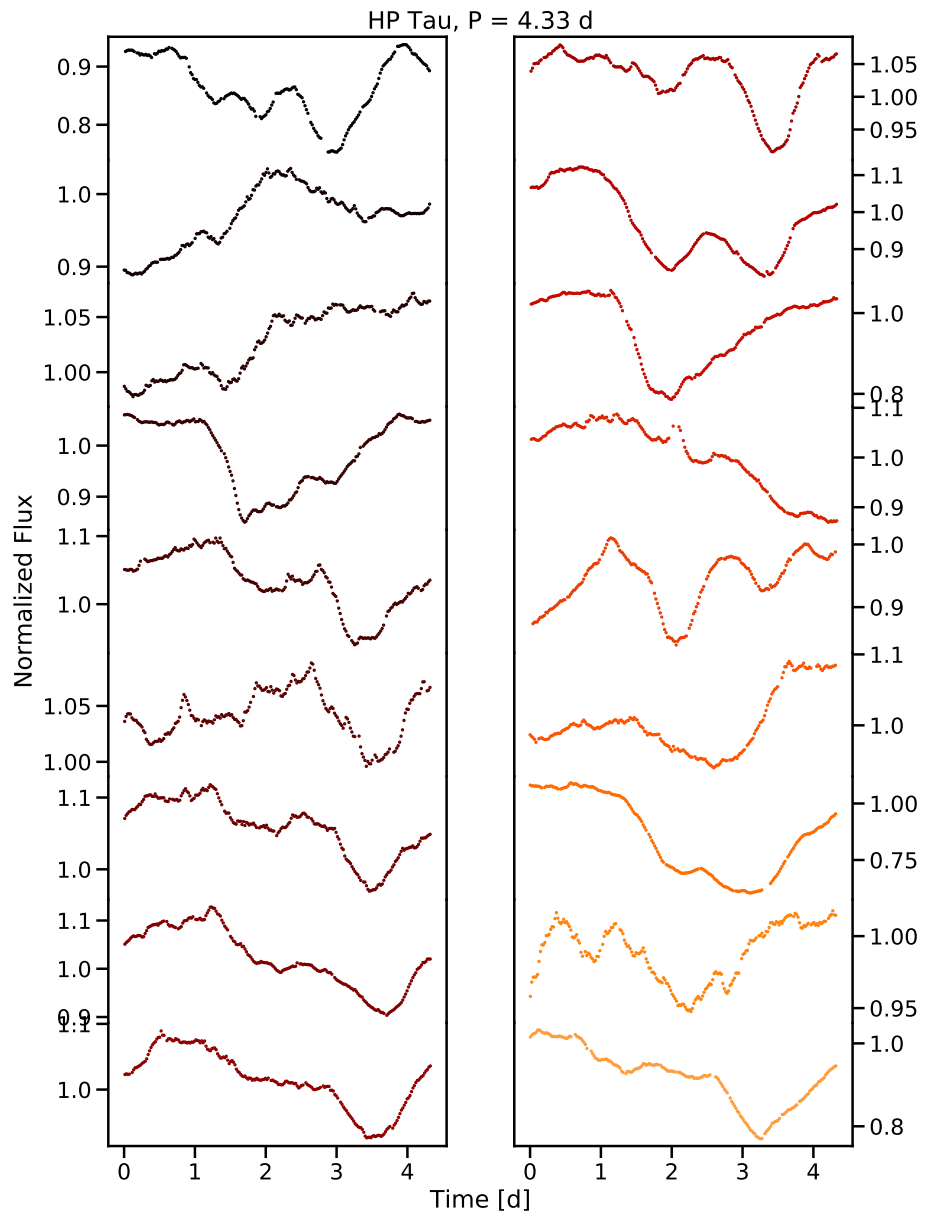
A.1	Additional figures - dipper light curves	105
A.2	MCFOST parameter files	113
A.2.1	Parameter file of the basic disk of MCFOST	113
A.2.2	Parameter file to model the dips of JH 223 using large dust grains	114
A.2.3	Parameter file to model the color variation of JH 223	116

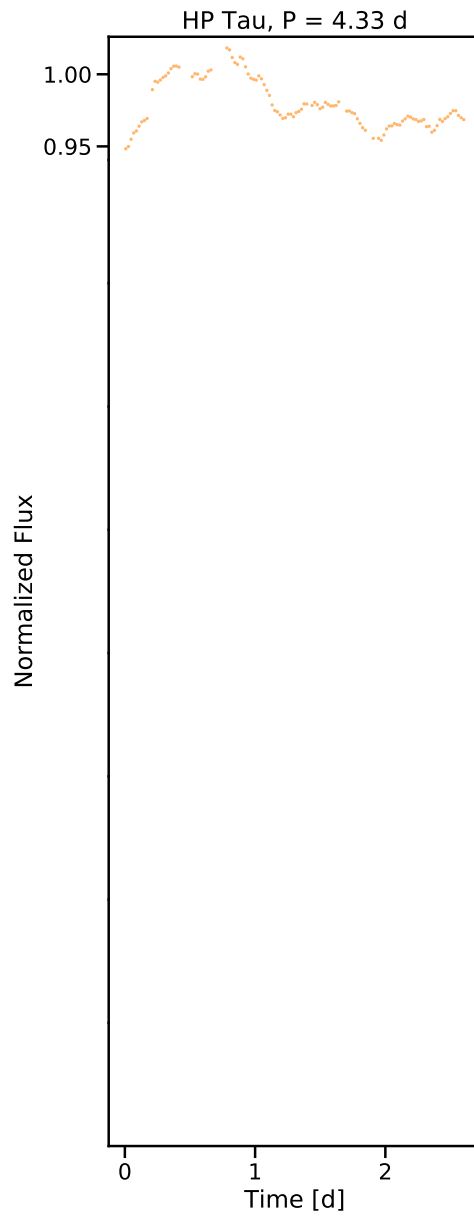
A.1 ADDITIONAL FIGURES - DIPPER LIGHT CURVES

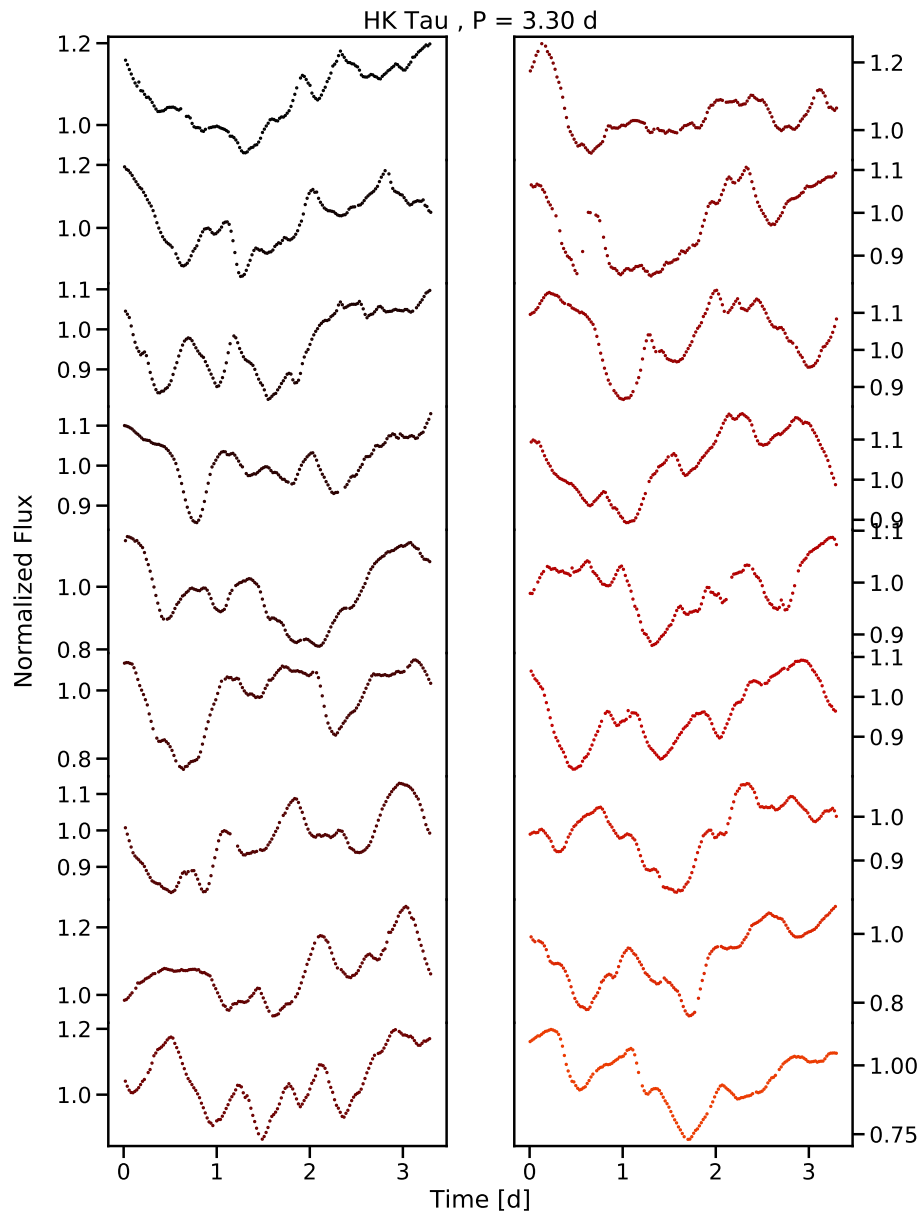
This section contains the detailed light curve of double- or multi-peaked dippers split for each period (one color per phase, from top to bottom and left to right).

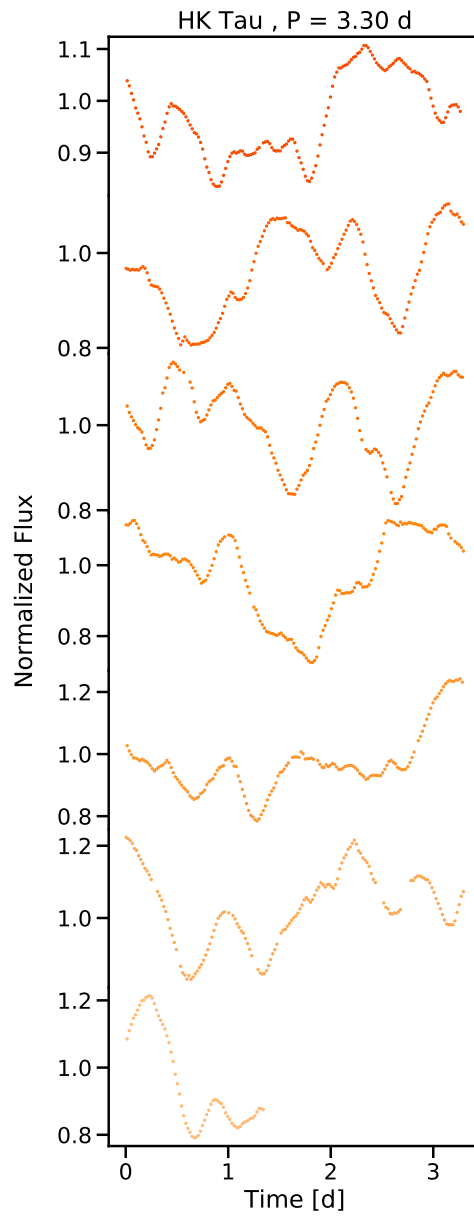


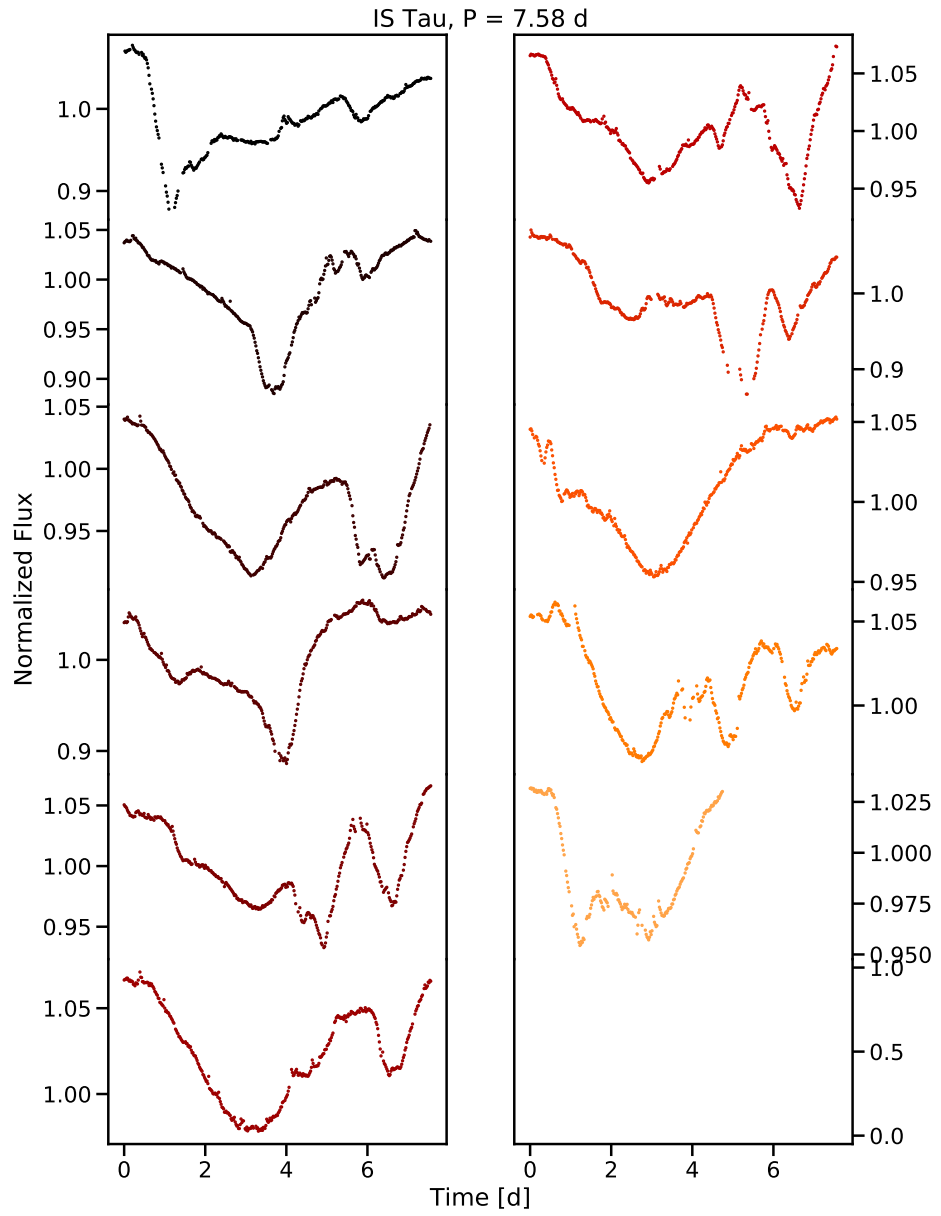












A.2 MCFOST PARAMETER FILES

a.2.1 *Parameter file of the basic disk of MCFOST*

```

3.0                                mcfost version

#Number of photon packages
1.28e5                             nbr_photons_eq_th  : T computation
1.28e4                             nbr_photons_lambda : SED computation
1.28e6                             nbr_photons_image  : images computation

#Wavelength
50 0.1 3000.0                      n_lambda, lambda_min, lambda_max [mum] Do not change this line unless
you know what you are doing
T T T   compute temperature?, compute sed?, use default wavelength grid for output ?
IMLup.lambda  wavelength file (if previous parameter is F)
T T   separation of different contributions?, stokes parameters?

#Grid geometry and size
1 1 = cylindrical, 2 = spherical (a Voronoi mesh is selected automatically with -phantom)
100 70 1 20                        n_rad (log distribution), nz (or n_theta), n_az, n_rad_in

#Maps
301 301 700.                       grid (nx,ny), size [AU]
0. 0. 1 F                          RT: imin, imax, n_incl, centered ?
0 0. 1                               RT: az_min, az_max, n_az angles
140.0  distance (pc)
0.  disk PA

#Scattering method
0 0=auto, 1=grain prop, 2=cell prop
1 1=exact phase function, 2=hg function with same g (2 implies the loss
of polarizarion)

#Symmetries
T image symmetry
T central symmetry
T axial symmetry (important only if N_phi > 1)

#Disk physics
0 0.50 1.0  dust_settling (0=no settling, 1=parametric, 2=Dubrulle, 3=Fromang),
exp_strat, a_strat (for parametric settling)
F dust radial migration
F sublimate dust
F hydrostatic equilibrium
F 1e-5  viscous heating, alpha_viscosity

#Number of zones : 1 zone = 1 density structure + corresponding grain properties
1 needs to be 1 if you read a density file (phantom or fits file)

#Density structure
1 zone type : 1 = disk, 2 = tapered-edge disk, 3 = envelope,

```

```

4 = debris disk, 5 = wall
1.e-3 100. dust mass, gas-to-dust mass ratio
10. 100.0 2 scale height, reference radius (AU), unused for envelope,
vertical profile exponent (only for debris disk)
1.0 0.0 300. 100. Rin, edge, Rout, Rc (AU) Rc is only used for tapered-edge
& debris disks (Rout set to 8*Rc if Rout==0)
1.125 flaring exponent, unused for envelope
-0.5 0.0 surface density exponent (or -gamma for tapered-edge disk or
volume density for envelope), usually < 0, -gamma_exp (or alpha_in & alpha_out for
debris disk)

#Grain properties
1 Number of species
Mie 1 2 0.0 1.0 0.9 Grain type (Mie or DHS), N_components, mixing rule (1 = EMT
or 2 = coating), porosity, mass fraction, Vmax (for DHS)
Draine_Si_sUV.dat 1.0 Optical indices file, volume fraction
1 Heating method : 1 = RE + LTE, 2 = RE + NLTE, 3 = NRE
0.03 1000.0 3.5 100 amin, amax [mum], aexp, n_grains (log distribution)

#Molecular RT settings
T T T 15. lpop, laccurate_pop, LTE, profile width [km/s]
0.05 Turbulence velocity [km/s]
1 Number of molecules
co.dat 6 molecular data filename, level max up to which NLTE
populations are calculated
10.0 20 vmax [km/s], number of velocity bins between 0 and vmax
T 1.e-4 abundance.fits.gz cst molecule abundance ?, abundance, abundance file
T 2 ray tracing ?, number of lines in ray-tracing
2 3 transition numbers

#Star properties
1 Number of stars
4000.0 2.0 1.0 0.0 0.0 0.0 T Temp, radius (solar radius),M (solar mass),x,y,z (AU),
automatic spectrum?
lte4000-3.5.NextGen.fits.gz
0.0 2.2 fUV, slope_fUV

a.2.2 Parameter file to model the dips of JH 223 using large dust grains

3.0 mcfost version

#Number of photon packages
1.28e7 nbr_photons_eq_th : T computation
1.28e3 nbr_photons_lambda : SED computation
1.28e6 nbr_photons_image : images computation

#Wavelength
50 0.1 3000.0 n_lambda, lambda_min, lambda_max [mum] Do not change this line
unless you know what you are doing
T F T compute temperature?, compute sed?, use default wavelength grid for output ?
IMLup.lambda wavelength file (if previous parameter is F)
T F separation of different contributions?, stokes parameters?

```

```

#Grid geometry and size
  2  1 = cylindrical, 2 = spherical (a Voronoi mesh is selected automatically with -phantom)
100 140 120 20          n_rad (log distribution), nz (or n_theta), n_az, n_rad_in

#Maps
  301 301 0.3          grid (nx,ny), size [AU]
  70.  70.  1  F      RT: imin, imax, n_incl, centered ?
  0   360.   36      RT: az_min, az_max, n_az angles
  140.0  distance (pc)
  0.   disk PA

#Scattering method
  0          0=auto, 1=grain prop, 2=cell prop
  1          1=exact phase function, 2=hg function with same g (2 implies the loss
of polarizarion)

#Symmetries
  F          image symmetry
  F          central symmetry
  F          axial symmetry (important only if N_phi > 1)

#Disk physics
  0   0.50  1.0  dust_settling (0=no settling, 1=parametric, 2=Dubrulle, 3=Fromang),
exp_strat, a_strat (for parametric settling)
  F          dust radial migration
  F   sublimates dust
  F          hydrostatic equilibrium
  F  1e-5  viscous heating, alpha_viscosity

#Number of zones : 1 zone = 1 density structure + corresponding grain properties
  2          needs to be 1 if you read a density file (phantom or fits file)

#Density structure
  1          zone type : 1 = disk, 2 = tapered-edge disk, 3 = envelope,
4 = debris disk, 5 = wall
  2.e-4  100.  dust mass, gas-to-dust mass ratio
  5.  100.0  2          scale height, reference radius (AU), unused for envelope, vertical
profile exponent (only for debris disk)
  0.03  0.0   300.  100.  Rin, edge, Rout, Rc (AU) Rc is only used for tapered-edge &
debris disks (Rout set to 8*Rc if Rout==0)
  1.125          flaring exponent, unused for envelope
  -0.5  0.0          surface density exponent (or -gamma for tapered-edge disk or
volume density for envelope), usually < 0, -gamma_exp (or alpha_in & alpha_out for debris disk)

  5          zone type : 1 = disk, 2 = tapered-edge disk, 3 = envelope,
4 = debris disk, 5 = wall
  5.e-13  100.  dust mass, gas-to-dust mass ratio
  0.01  100.  2          scale height, reference radius (AU), unused for envelope,
vertical profile exponent (only for debris disk)
  0.03  0.0   0.04  100.  Rin, edge, Rout, Rc (AU) Rc is only used for tapered-edge &
debris disks (Rout set to 8*Rc if Rout==0)
  1.125          flaring exponent, unused for envelope
  -0.5  0.0          surface density exponent (or -gamma for tapered-edge disk or volume

```



```

density for envelope), usually < 0, -gamma_exp (or alpha_in & alpha_out for debris disk)

#Grain properties
1 Number of species
Mie 1 2 0.0 1.0 0.9 Grain type (Mie or DHS), N_components, mixing rule (1 = EMT
or 2 = coating), porosity, mass fraction, Vmax (for DHS)
Draine_Si_UV.dat 1.0 Optical indices file, volume fraction
1 Heating method : 1 = RE + LTE, 2 = RE + NLTE, 3 = NRE
0.03 1000.0 3.5 100 amin, amax [mum], aexp, n_grains (log distribution)

1 Number of species
Mie 1 2 0.0 1.0 0.9 Grain type (Mie or DHS), N_components, mixing rule (1 = EMT
or 2 = coating), porosity, mass fraction, Vmax (for DHS)
Draine_Si_UV.dat 1.0 Optical indices file, volume fraction
1 Heating method : 1 = RE + LTE, 2 = RE + NLTE, 3 = NRE
0.03 1000.0 3.5 100 amin, amax [mum], aexp, n_grains (log distribution)

#Molecular RT settings
T T T 15. lpop, laccurate_pop, LTE, profile width [km/s]
0.05 Turbulence velocity [km/s]
1 Number of molecules
co.dat 6 molecular data filename, level max up to which NLTE
populations are calculated
10.0 20 vmax [km/s], number of velocity bins between 0 and vmax
T 1.e-4 abundance.fits.gz cst molecule abundance ?, abundance, abundance file
T 2 ray tracing ?, number of lines in ray-tracing
2 3 transition numbers

#Star properties
1 Number of stars
3386.0 1.34 0.275 0.0 0.0 0.0 T Temp, radius (solar radius),M (solar mass),x,y,z (AU),
automatic spectrum?
lte4000-3.5.NextGen.fits.gz
0.0 2.2 fUV, slope_fUV

a.2.3 Parameter file to model the color variation of JH 223

3.0 mcfost version

#Number of photon packages
1.28e7 nbr_photons_eq_th : T computation
1.28e3 nbr_photons_lambda : SED computation
1.28e6 nbr_photons_image : images computation

#Wavelength
50 0.1 3000.0 n_lambda, lambda_min, lambda_max [mum] Do not change this line
unless you know what you are doing
T F T compute temperature?, compute sed?, use default wavelength grid for output ?
IMLup.lambda wavelength file (if previous parameter is F)
T F separation of different contributions?, stokes parameters?

#Grid geometry and size
2 1 = cylindrical, 2 = spherical (a Voronoi mesh is selected automatically with

```

```

-phantom)
100 140 120 20          n_rad (log distribution), nz (or n_theta), n_az, n_rad_in

#Maps
301 301 0.3          grid (nx,ny), size [AU]
70. 70. 1 F          RT: imin, imax, n_incl, centered ?
0 360. 36           RT: az_min, az_max, n_az angles
140.0 distance (pc)
0. disk PA

#Scattering method
0 0=auto, 1=grain prop, 2=cell prop
1 1=exact phase function, 2=hg function with same g (2 implies the loss
of polarizarion)

#Symmetries
F image symmetry
F central symmetry
F axial symmetry (important only if N_phi > 1)

#Disk physics
0 0.50 1.0 dust_settling (0=no settling, 1=parametric, 2=Dubrulle, 3=Fromang),
exp_strat, a_strat (for parametric settling)
F dust radial migration
F sublimate dust
F hydrostatic equilibrium
F 1e-5 viscous heating, alpha_viscosity

#Number of zones : 1 zone = 1 density structure + corresponding grain properties
2 needs to be 1 if you read a density file (phantom or fits file)

#Density structure
1 zone type : 1 = disk, 2 = tapered-edge disk, 3 = envelope, 4 = debris
disk, 5 = wall
2.e-4 100. dust mass, gas-to-dust mass ratio
5. 100.0 2 scale height, reference radius (AU), unused for envelope, vertical
profile exponent (only for debris disk)
0.03 0.0 300. 100. Rin, edge, Rout, Rc (AU) Rc is only used for tapered-edge & debris
disks (Rout set to 8*Rc if Rout==0)
1.125 flaring exponent, unused for envelope
-0.5 0.0 surface density exponent (or -gamma for tapered-edge disk or volume
density for envelope), usually < 0, -gamma_exp (or alpha_in & alpha_out for debris disk)

5 zone type : 1 = disk, 2 = tapered-edge disk, 3 = envelope, 4 = debris
disk, 5 = wall
4.0e-14 100. dust mass, gas-to-dust mass ratio
0.01 100. 2 scale height, reference radius (AU), unused for envelope, vertical
profile exponent (only for debris disk)
0.03 0.0 0.04 100. Rin, edge, Rout, Rc (AU) Rc is only used for tapered-edge &
debris disks (Rout set to 8*Rc if Rout==0)
1.125 flaring exponent, unused for envelope
-0.5 0.0 surface density exponent (or -gamma for tapered-edge disk or volume
density for envelope), usually < 0, -gamma_exp (or alpha_in & alpha_out for debris disk)

```

#Grain properties

```

1 Number of species
Mie 1 2 0.0 1.0 0.9 Grain type (Mie or DHS), N_components, mixing rule (1 = EMT or
2 = coating), porosity, mass fraction, Vmax (for DHS)
Draine_Si_sUV.dat 1.0 Optical indices file, volume fraction
1 Heating method : 1 = RE + LTE, 2 = RE + NLTE, 3 = NRE
0.03 1000.0 3.5 100 amin, amax [mum], aexp, n_grains (log distribution)

```

```

1 Number of species
Mie 1 2 0.0 1.0 0.9 Grain type (Mie or DHS), N_components, mixing rule (1 = EMT or
2 = coating), porosity, mass fraction, Vmax (for DHS)
Draine_Si_sUV.dat 1.0 Optical indices file, volume fraction
1 Heating method : 1 = RE + LTE, 2 = RE + NLTE, 3 = NRE
0.03 0.25 3.5 100 amin, amax [mum], aexp, n_grains (log distribution)

```

#Molecular RT settings

```

T T T 15. lpop, laccurate_pop, LTE, profile width [km/s]
0.05 Turbulence velocity [km/s]
1 Number of molecules
co.dat 6 molecular data filename, level max up to which NLTE populations
are calculated
10.0 20 vmax [km/s], number of velocity bins between 0 and vmax
T 1.e-4 abundance.fits.gz cst molecule abundance ?, abundance, abundance file
T 2 ray tracing ?, number of lines in ray-tracing
2 3 transition numbers

```

#Star properties

```

1 Number of stars
3386.0 1.34 0.275 0.0 0.0 0.0 T Temp, radius (solar radius),M (solar mass),
x,y,z (AU), automatic spectrum?
lte4000-3.5.NextGen.fits.gz
0.0 2.2 fUV, slope_fUV

```

B

PUBLICATIONS

B.1	First-author publications	119
B.2	Co-authored publication	156

B.1 FIRST-AUTHOR PUBLICATIONS

WAVELET ANALYSIS OF TAURUS K2 DIPPER LIGHT CURVES

N. Roggero¹, J. Bouvier¹, A.M. Cody² and L. Rebull³

Abstract. During the evolution of T Tauri stars and the formation of their planetary systems, accretion processes play a key role. However, the more complex interaction at the rim of the inner region of the disk is still not fully understood. The SPIDI (Star-Planet-Inner Disk-Interactions) project aims to further investigate this phenomenon and its influence on forming planets in the inner disk.

The magnetic field of a young star truncates the disk where the magnetic field pressure is equal to the ram pressure of the accreting material. Thus, the dust and the gas present in the disk are lifted above the plane along the magnetic field lines. If the temperature is low enough for dust to survive, this accretion warp obscures the star and causes eclipses observable with photometry, i.e. the dipper phenomenon. The periodicity of a dipper star depends on the stability of the dusty warp.

In this work, wavelet analysis of the K2 light curves from the Taurus region allows us to study the time-resolved periodicity of the dippers and other signals present in the light curves. This information, together with further fitting with an occultation model, dust survival models, and radiative transfer modelling, will allow us to isolate a possible planetary signal embedded in accretion-driven photometric variability.

Keywords: stars: variables: T Tauri, protoplanetary disks, techniques: photometric

1 Introduction

Classical T Tauri stars (CTTSs) are low-mass, pre-main sequence stars which are still accreting from their circumstellar disks. They are Class II protostars, which means that the main contribution to the SED is given by stellar radiation, while a significant infrared excess from the disk is present.

The disk itself might extend up to hundreds AU. We will focus on the very inner part of the disk –at a scale of a few stellar radii, i.e. ~ 0.02 AU–, where dust evaporates and the accretion takes place onto the star. This region is very challenging to observe, as it is at the limit of the resolution of interferometry. Light curves allow an indirect observation of the phenomena occurring at the inner disk rim.

In recent years, it was noticed that a significant percentage of T Tauri stars –around 30% of the disk-bearing stars– display eclipses in their light curves that cannot be traced back to binarity. It was supposed that these ”dipper” light curves are caused by dusty material from the disk, that occults the star during its rotation (e.g. , Cody et al. (2014), Alencar et al. (2010)).

The occurrence of dippers might be explained by the magnetospheric accretion model (Bouvier et al. 1999). The inner disk is truncated when it reaches the magnetosphere of the star, as its material is accreted onto the star following the magnetic field lines. If the temperature in this region is cool enough for dust to survive, dust might be lifted above the disk plane in form of an accretion stream or warp. An observer at a high inclination angle will thus be able to observe a dipper light curve (Bodman et al. 2017).

Photometric observations can thus deliver information about the position and the temperature at the truncation radius, which is of vital importance for understanding the interaction between the star and the inner disk.

¹ Univ. Grenoble Alpes, CNRS, IPAG, 38000 Grenoble, France

² NASA Ames Research Center, Moffett Field, CA 94035, USA ; Bay Area Environmental Research Institute, 625 2nd St., Suite 209, Petaluma, CA 94952, USA

³ Caltech-IPAC/IRSA, Pasadena, CA, United States

2 Observations and Data Reduction

The Taurus region was observed nearly continuously with the *Kepler* satellite within the framework of the K2 mission, with a cadence of 29.4 min and a duration of 80 days. The observation campaigns C13 (Mar - May 2017) and C4 (Feb - Apr 2015) delivered light curves for about 900 potential members.

K2 data are challenging to reduce and several pipelines are available for this purpose. If the light curve does not present particular issues, we used the version with moving aperture as in Cody & Hillenbrand (2018) as default and performed a more careful inspection on dipper candidates.

The process to assess the membership of each star to the cluster is explained by Rebull et al. (in prep.). We attribute higher confidence membership to candidates which already appear as members in Luhman (2018). Finally, we produce a sample of 225 Taurus members with K2 light curves and use it as basis to search for dippers.

3 Wavelet analysis of dippers

Detailed information on the periodicity of dippers is necessary to derive a number of parameters, among them the location of the dusty warp that obscures the star.

The exact configuration of the inner disk changes from cycle to cycle; dippers are thus either aperiodic or quasi-periodic phenomena. This distinction is important, as aperiodic dippers seem to be generated by different mechanisms than quasi-periodic ones (Ansdell et al. 2016; Stauffer et al. 2015). In some cases, the occultations are transient, making it difficult for classic period-finding algorithms to determine the correct period. It is also interesting to find out if the period evolves over time.

The wavelet transform is an efficient tool to analyze the frequency spectrum of a signal and to gain time resolution (see Torrence & Compo (1998)). Lately, the tool has found application in light curve analysis (e.g., Hedges et al. (2018), Bravo et al. (2014) and García et al. (2014) for *Kepler* light curves).

It can be viewed as a time-resolved Windowed Fourier Transform (WFT) with variable window width, that reveals both high and low frequency features. The wavelet, which is a finite wave in the time domain –instead of an infinite sinusoid as in the Fourier transform– is convolved with the signal at each position with a given time step. To gain time resolution, the wavelet is scaled in the time domain (i.e. stretched or compressed) and again convolved and shifted along the signal. A high correlation between the wavelet and the time series results in high power in the Wavelet Power Spectrum (WPS).

In this work, the complex Morlet wavelet is used, as it is a good compromise between time and frequency resolution and allows for adjustment of these two parameters according to one’s needs.

4 Results

The dippers are identified among the Taurus members from a visual inspection of the light curve. We classified by eye 35 young stars as either dippers or variable stars that show dips in their light curves as secondary variability. Among the 23 stars classified as dippers, 12 are periodic and the rest are either aperiodic or show complex periodicities. The period range varies between 2 and 11 days and most of the stars have a period shorter than 5 d.

An example of a periodic dipper (JH 223) is shown in Fig. 1. The star displays a constant brightness and periodic dips, which vary in shape and depth. The Wavelet Power Spectrum (WPS) shows the power at different periods (y-axis) at different positions in time (x-axis). The comparison with the CLEAN periodogram (Roberts et al. 1987) illustrates the loss of frequency resolution in the wavelet transform. The exact values of the period are, where possible, retrieved from the periodogram.

GH Tau is a good example where wavelet analysis is beneficial to interpret a complex periodogram (Fig. 2, left panel). By looking at the WPS, it becomes clear that most of the peaks seen on the periodogram are local periodicities, while only the two highest peaks might be real periods. At the same time, the double peak illustrates well the uncertainty principle of time and frequency resolution, since it is not resolved on the WPS.

JH 112 is a transient, periodic dipper. The mostly constant brightness makes it difficult for the periodogram analysis to reach a high detection significance (Fig. 2, right panel). The WPS shows how the local periodicity

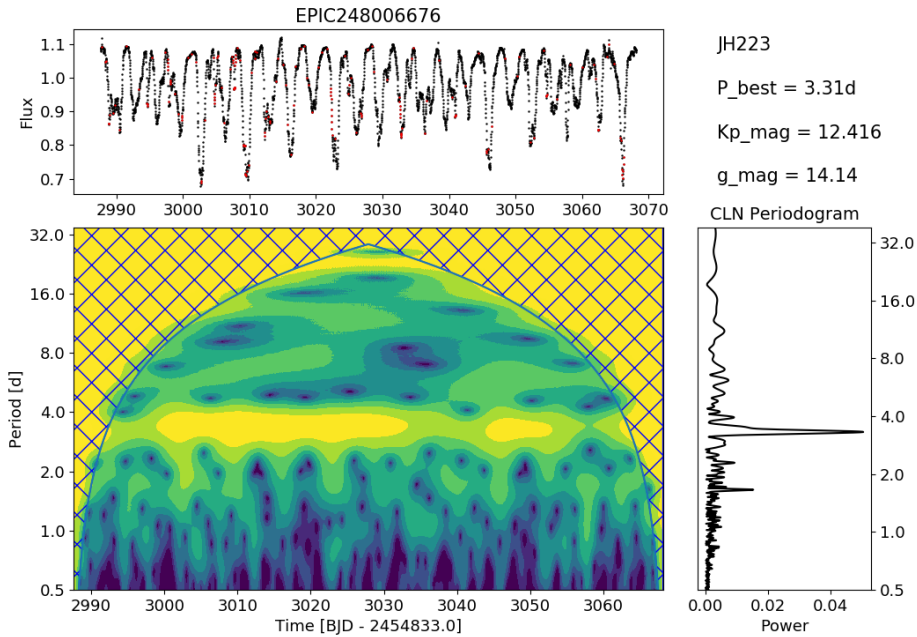


Fig. 1. In order to perform the wavelet transform, the K2 light curve (top) is linearly interpolated at the missing values (red dots). The Wavelet Power Spectrum shows the time-resolved frequency spectrum (bottom). The contours indicate the power of a certain period at a certain point in time; yellow contours have the highest power, blue ones the lowest. In order to obtain a better contrast, the contours are saturated at the 3 and 99 percentile. The Cone of Influence (crosses) delimits the area where the WPS is affected by edge effects; a high power in this region is not significant. The WPS is compared to a CLEAN periodogram (right).

corresponds to the visually detectable dipping.

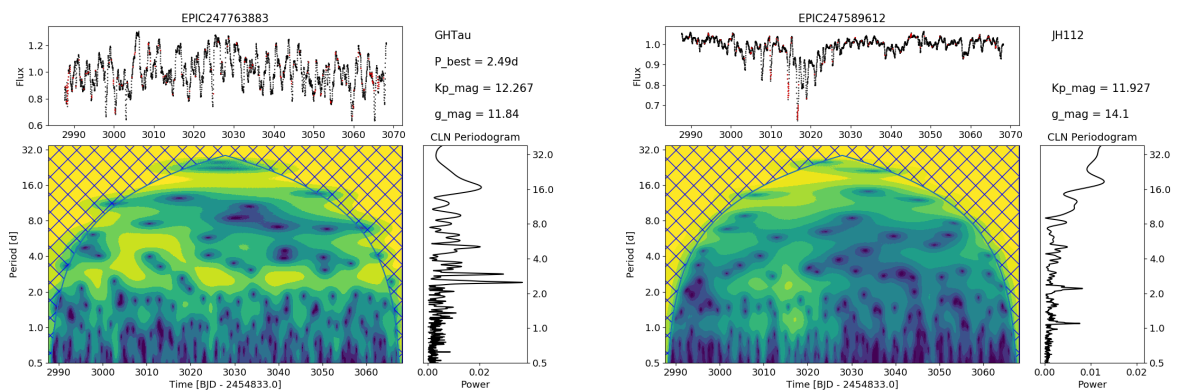


Fig. 2. **Left:** Light curve, periodogram and WPS of GH Tau. **Right:** Light curve, periodogram and WPS of JH 112.

5 Conclusions and Outlook

The application of wavelet analysis to dipper light curves allows us to more thoroughly study their periodicity. Among the 225 Taurus members, 35 show dipping events in their light curves. Of the 23 dippers with no other




evident variability, about 50% are periodic with periods between 2 and 11 d. This information allows us to compute the location of the dusty warp. Furthermore, a simple occultation model makes it possible to derive the geometry of the system, i.e. the inclination, the warp's maximum height and its azimuthal extension. In upcoming work, a full modeling will be attempted using the MCFOST radiative transfer code (Pinte et al. 2006), to hopefully reach beyond the simple detection of the main periodicity.

This project has received funding from the European Research Council (ERC) under the European Union's Horizon 2020 research and innovation programme (grant agreement No 742095; *SPIDI*: Star-Planets-Inner Disk-Interactions). <http://spidi-eu.org/>
This paper includes data collected by the K2 mission. Funding for the K2 mission is provided by the NASA Science Mission directorate.

References

- Alencar, S. H. P., Teixeira, P. S., Guimarães, M. M., et al. 2010, *A&A*, 519, A88
Ansdell, M., Gaidos, E., Rappaport, S. A., et al. 2016, *ApJ*, 816, 69
Bodman, E. H. L., Quillen, A. C., Ansdell, M., et al. 2017, *MNRAS*, 470, 202
Bouvier, J., Chelli, A., Allain, S., et al. 1999, *A&A*, 349, 619
Bravo, J. P., Roque, S., Estrela, R., Leão, I. C., & De Medeiros, J. R. 2014, *A&A*, 568, A34
Cody, A. M. & Hillenbrand, L. A. 2018, *AJ*, 156, 71
Cody, A. M., Stauffer, J., Baglin, A., et al. 2014, *AJ*, 147, 82
García, R. A., Ceillier, T., Salabert, D., et al. 2014, *A&A*, 572, A34
Hedges, C., Hodgkin, S., & Kennedy, G. 2018, *MNRAS*, 476, 2968
Luhman, K. L. 2018, *AJ*, 156, 271
Pinte, C., Ménard, F., Duchêne, G., & Bastien, P. 2006, *Astronomy and Astrophysics*, 459, 797
Rebull, L. R., Stauffer, J. R., Cody, A. M., & Bouvier, J. in prep.
Roberts, D. H., Lehar, J., & Dreher, J. W. 1987, *AJ*, 93, 968
Stauffer, J., Cody, A. M., McGinnis, P., et al. 2015, *AJ*, 149, 130
Torrence, C. & Compo, G. P. 1998, *Bulletin of the American Meteorological Society*, 79, 61

The dipper population of Taurus seen with K2

Noemi Roggero¹ , Jérôme Bouvier¹, Luisa M. Rebull² , and Ann Marie Cody³ 

¹ Univ. Grenoble Alpes, CNRS, IPAG, 38000 Grenoble, France
e-mail: noemi.roggero@univ-grenoble-alpes.fr

² Infrared Science Archive (IRSA), IPAC, 1200 E. California Blvd., California Institute of Technology, Pasadena, CA 91125, USA

³ SETI Institute, 189 N Bernardo Ave. Suite 200, Mountain View, CA 94043 USA

Received 23 February 2021 / Accepted 10 May 2021

ABSTRACT

Context. Dippers are typically low-mass, pre-main-sequence stars that display dips in their light curves. These dips have been attributed to dusty warps that form in the inner part of the disk.

Aims. Our goal is to derive the characteristics of dipper stars in Taurus to assess the physical mechanisms that induce dipper light curves.

Methods. We used the light curves of the fourth and thirteenth campaigns of K2 to select a dipper sample among 179 members and possible members of the Taurus star-forming region based on the light-curve morphology. We studied the periodicities by combining periodograms with wavelet analysis and derived the stellar parameters of the sample from the photometry. We also studied the morphology of the photometric dips.

Results. We find a dipper occurrence of $\sim 30\%$ in disk-bearing stars observed with K2 that were identified visually by us. This represents a lower limit to their true occurrence, on the one hand because they are ephemeral, and on the other because there are detection limits. About half of the dippers are aperiodic, and most of these are dominated by another type of variability. The chosen sample is of late spectral type (K/M), low mass (mostly $< 1 M_{\odot}$), and moderate mass accretion rates and has periods of a few days. We observed a transient dipper over a few rotation cycles and observed a dipper with a changing period. The structure of the dips can be complex and varies strongly over timescales of down to one stellar rotation. The corotation radii are located at a few stellar radii, and the temperatures at corotation allow dust survival. Many of the systems are seen at moderate to high inclination. We find that the angular extension of the dusty structure producing the dips is correlated with the stellar period.

Conclusions. Magnetospheric accretion, which causes an accretion column and its base to occult the star, can explain most of the observed light curves. Although compatible with the model, many of the stellar inclination angles are moderate and do not exclude mechanisms other than the occultation by an inner disk warp to account for dipper light curves.

Key words. stars: pre-main sequence – stars: variables: T Tauri, Herbig Ae/Be – protoplanetary disks – accretion, accretion disks – techniques: photometric

1. Introduction

Classical T Tauri stars (CTTSs) are still accreting from their circumstellar disk, and their activity is reflected in their complex photometric variability. Many physical mechanisms have been proposed to explain this variability, such as accretion hotspots, accretion bursts, or occultations by dusty structures in the disk (e.g., [Cody et al. 2014](#); [Alencar et al. 2010](#); [Bouvier et al. 2003](#)). At the next stage of protostellar evolution, weak-lined T Tauri stars (WTTSs) do not show accretion signatures in their spectral lines. Their magnetic field still produces cold spots, which give a sinusoidal modulation to the light curve.

In the past two decades, more attention has been paid to the low-mass star AA Tau. Its light curve showed a constant brightness and narrow quasiperiodic occultations that were less pronounced in the infrared (IR) than in the optical. These observations, combined with spectroscopic and spectropolarimetric data, led to the development of an occultation model. The magnetospheric accretion column would cause a dusty warp in the inner disk to obscure the star when it crosses the line of sight of the observer ([Bouvier et al. 1999, 2003, 2007](#)).

The possibility that CTTSs are still accreting from a circumstellar disk was proposed by [Bertout et al. \(1988\)](#) and had its

roots in the work of [Lynden-Bell & Pringle \(1974\)](#). Although these authors already suggested that accretion might take place along magnetic field lines, the exact role played by the magnetic field in the accretion process was constrained only later. A rotating magnetosphere of a star with a strong magnetic field (approximately of some kG) disrupts the inner disk at a few stellar radii from the star and accretes the material along the closed field lines; the open field lines induce a strong disk wind ([Camenzind 1990](#); [Koenigl 1991](#); [Shu et al. 1994](#)). The most common magnetic field configuration for T Tauri stars is a strong dipole. Depending on the evolutionary status, other magnetic field topologies are possible, but the dipole in most cases remains the dominant component farther away from the star. Moreover, a misalignment of the dipole axis and the stellar rotation axis seems to be very common ([Gregory et al. 2012](#)). When there is such a misalignment, the rotation of the disk provokes a twist in the magnetic field lines, which are dragged in the rotation. The magnetic pressure is not the same in the upper and lower part of the disk, and the normal vector of the inner disk becomes tilted with respect to the rotation axis. This induces a disk warp ([Lai 1999](#); [Terquem & Papaloizou 2000](#)). From the observational point of view, the strong emission lines observed in the spectra of T Tauri stars are related to accretion and not to winds

(Hartmann et al. 1994). Radiative transfer modeling provided observational predictions for magnetospheric accretion (Muzerolle et al. 2001; Kurosawa et al. 2006; Lima et al. 2010).

Magnetohydrodynamical (MHD) simulations confirmed the possibility that magnetospheric accretion might warp the disk (e.g., Romanova et al. 2008, 2013; Romanova & Owocki 2015). In a stable configuration (stable accretion regime), two broad, stable, and symmetric matter streams form from the disk and are accreted as funnel flows onto the stellar surface, producing a hotspot on each hemisphere. In this scenario, the magnetosphere truncates the disk at a few stellar radii close to corotation, where the disk material rotates with $\omega \sim \Omega_*$. The base of the accretion column can host warm dust and be optically thick, which explains the photometric behavior of AA Tau.

After the characterization of AA Tau, additional surveys identified a new class of AA Tau-like YSOs (young stellar objects), the so-called dippers. Dippers have been observed in NGC 2264, Upper Scorpius, ρ Ophiucus, and Orion (e.g., Alencar et al. 2010; Cody et al. 2014; McGinnis et al. 2015; Ansdell et al. 2016a; Cody & Hillenbrand 2018; Morales-Calderón et al. 2011). The occurrence rate of dippers is estimated to be up to 20–30% of CTTSs. As in the case of AA Tau, the light curve exhibits a brightness continuum interrupted by narrow flux dips, which can be aperiodic or quasiperiodic. Quasiperiodic means that while the occurrence of the dips is periodic, their shape and amplitude are not constant over time. The dips are sharp and irregular, their periodicity is in the range of stellar rotation periods of K/M stars, and they last from 1–2 to 4–5 d. The amplitudes can range up to 50–60% in flux.

The common consensus about the origin of dippers is that the occultation is produced by dusty structures in the inner disk. The correlation between the dip depth and the mid-infrared excess at 4.6 μm supports this hypothesis (Ansdell et al. 2016a) as IR excess at this wavelength is a tracer for warm dust at the corotation radius. This makes dippers a powerful tool for studying this region, which is difficult to resolve, yet physically complex. The dusty disk warp model (Bouvier et al. 2007) requires dipper stars to be seen at high inclination, so that the line of sight crosses the base of the accretion column. The generalized magnetospheric accretion model (Bodman et al. 2017) allows also for moderate inclinations. The amplitude and the shape of the dips depends on parameters such as viewing angle, dust opacity, and the tilt between magnetic field and stellar rotation axis. Another possibility are vertical instabilities in the disk, which should be able to endure several rotation cycles. A star with an aligned magnetic field rather accretes via Rayleigh-Taylor (RT) instabilities (e.g., Romanova et al. 2008) in an unstable accretion regime. The so-caused accretion tongues reach the stellar surface at different latitudes and induce a stochastic photometric variability. McGinnis et al. (2015) claimed that this mechanism probably lies at the origin of aperiodic dippers, which appear as stochastic occultations of the stellar photosphere, with smaller amplitudes than periodic dippers.

However, the high occurrence of dippers among YSOs is difficult to reconcile with the condition of a grazing viewing angle on these systems. It was found that the outer disk inclination of dippers can be low or even close to face-on (Ansdell et al. 2020). This either corroborates the possibility of an inner disk that is tilted with respect to the outer disk (e.g., Alencar et al. 2018) or requires other mechanisms that are compatible with lower inclination, such as disk winds (e.g., Bans & Königl 2012).

The Taurus star-forming region hosts a quite young stellar population $\lesssim 3$ Myr (e.g., White & Ghez 2001; Kraus & Hillenbrand 2009) of ~ 400 members (Kenyon et al. 2008) at

a distance of ~ 140 pc (Fleming et al. 2019; Galli et al. 2018). Rebull et al. (2020) presented the global sample of the Taurus region as covered by the K2 C13, with a few additions from C4. This work focuses on the dipper population of the same sample. In Sect. 3 the selection of the dipper sample, the periodicity study, and the stellar parameters are presented. In Sect. 5 the results and the possible scenarios to explain dippers are discussed. Final considerations and future work are presented in Sect. 6.

2. Observations and data reduction

The *Kepler* satellite (Borucki et al. 2010; Haas et al. 2010) was launched in 2009 with the main aim of detecting Earth-like exoplanets. It observed over 170 000 targets simultaneously in its long-cadence mode of 29.4 min. The failure of two reaction wheels led to a substantial change in observing strategy and to a renaming of the mission as K2 (Howell et al. 2014). The spacecraft used its two remaining reaction wheels in tandem with the solar radiation pressure (plus compensatory periodic thruster firings) to control movement in the third dimension. Instead of staring at one field, as the original *Kepler* mission had done, K2 was constrained to view fields in the ecliptic plane for about 70 days at a time (Howell et al. 2014). Within the framework of the K2 mission (2014–2018), 19 fields were observed (Howell et al. 2014). Several discussions of data and reductions of *Kepler* and K2 data are available. In the context of this work, the two most important artifacts to keep in mind are the periodic thruster firings and the relatively low spatial resolution (pixels of $\sim 4 \times 4''$ and the 95% encircled energy diameter of up to 7.5 px). The thruster firings happened every 0.245 days, and so apparent astrophysical periods near this must be scrutinized carefully to ensure that they are not affected by the spacecraft. The low spatial resolution means that source confusion can be an issue, and each source (and light curve) must be inspected individually to assess confusion. Customized apertures are sometimes needed to attempt to mitigate this. The effective observed range of K2 lies between 6 mag $< K_s < 16$ mag (e.g., Rebull et al. 2016). Saturation is not a relevant detection bias in Taurus, which does not host a massive star population. However, deeply embedded low-mass stars are likely to remain undetected with K2.

A few Taurus members were observed in K2 C4 (15 February–24 April 2015), but most of the Taurus members were observed during C13 from 8 March to 27 May 2017¹. We are building on the analysis presented in Rebull et al. (2020). The K2 fields do not cover the entire Taurus cluster, but the stellar properties of the cluster are not thought to vary based on the spatial distribution (see, e.g., Fig. 1 in Rebull et al. 2020). We used light curves from several different data reduction pipelines (also see Rebull et al. 2017). First, the pre-search data conditioning (PDC) version from the Mikulski Archive for Space Telescopes (MAST). Second, a position-detrended version with moving apertures as in Cody & Hillenbrand (2018). Third, the ‘self-flat-fielding’ approach by Vanderburg & Johnson (2014) and the K2SFF pipeline as obtained from MAST. Last, the EVEREST2 pipeline, based on pixel-level decorrelation Luger et al. (2016), as downloaded from MAST.

A comparison of all these light-curve versions allows us to constrain the periodicity (or periodicities) and select the best

¹ https://archive.stsci.edu/files/live/sites/mast/files/home/missions-and-data/k2/_documents/KSCI-19116-003.pdf

Table 1. Spectral types, effective temperatures, and *VJHK* photometry for the presented sample of 22 dippers.

EPIC	2MASS	Name	SpT	Refs.	T_{eff} [K]	A_V [mag]	V	Refs.	J	H	K
246929818	J04465897+1702381	Haro 6-37	K8	1,2	3940	2.1	12.98	7	9.24	7.99	7.31
246942563	J04542368+1709534	St 34	M3	3	3360	0.5	14.59	7	10.69	10.08	9.79
246989752	J04384725+1737260	...	M5.5	1,2	2920 (**)	0.0	12.75	12.11	11.75
247103541	J04363081+1842153	HD 285893	F8	4	6100	0.3	10.01	8	8.76	8.37	7.99
247520207	J04391779+2221034	LkCa 15	K4	5	4492 (***)	0.4	12.14	9	9.42	8.60	8.16
247575958	J04330945+2246487	CFHT Tau 12	M6	1	2860 (**)	3.0	13.15	12.14	11.54
247589612	J04324911+2253027	JH 112 A	K5.5	1,2	4080	2.9	14.44	7	10.24	8.99	8.17
247592463	J04355277+2254231	HP Tau	K4	1,2	4330	3.2	13.78	9	9.55	8.47	7.62
247763883	J04330622+2409339	GH Tau	M2	1,2	3490	0.4	12.87	7	9.11	8.23	7.79
247764745	J04330664+2409549	V807 Tau	K7 (*)	1,2	3970	0.4	11.31	7	8.15	7.36	6.96
247791801	J04333456+2421058	GK Tau	K6.5	1,2	3995	1.0	12.67	9	9.05	8.11	7.47
247792225	J04333405+2421170	GI Tau	M0.4	1,2	3714	1.3	13.39	9	9.34	8.42	7.89
247799571	J04315056+2424180	HK Tau	M1 (*)	1,2	3630	2.4	15.12	7	10.45	9.25	8.59
247805410	J04302961+2426450	FX Tau	M2.2	1,2	3464	1.0	13.39	7	9.39	8.40	7.92
247820821	J04295950+2433078	...	M5	1	2880	0.0	15.97 (****)	10	11.68	10.54	9.81
247885481	J05023985+2459337	...	M4.25	6	3090	0.0	16.04	7	11.78	11.09	10.78
247935061	J04430309+2520187	GO Tau	M2.3	1,2	3451	1.6	14.43	7	10.71	9.78	9.33
248006676	J04404950+2551191	JH 223	M2.8	1,2	3386	1.4	15.66	7	10.75	9.92	9.49
248015397	J04411078+2555116	ITG 34	M5.5	1	2920 (**)	2.2	13.19	12.12	11.45
248029373	J04304425+2601244	DK Tau	K8.5	1,2	3910	0.7	12.58	9	8.72	7.76	7.10
248046139	J04382134+2609137	GM Tau	M5	1,2	2880	2.1	17.83	7	12.80	11.59	10.63
248047443	J04333678+2609492	IS Tau	M0 (*)	1,2	3770	2.4	14.94	7	10.32	9.29	8.64

Notes. *JHK* measurements are from 2MASS. (*)Spectral type by [Esplin & Luhman \(2019\)](#) differs by 0.5 subclasses or more in comparison with [Herczeg & Hillenbrand \(2014\)](#). (**)For spectral types later than M5, the temperature conversion by [Herczeg & Hillenbrand \(2014\)](#) is used. The extrapolation for M6 in [Pecaut & Mamajek \(2013\)](#) would deliver 3038 K. (***) T_{eff} derived spectroscopically by [Alencar et al. \(2018\)](#). (****)The provided amplitude and $\langle V \rangle$ were combined to derive a more representative V_{min} .

References. (1) [Esplin & Luhman \(2019\)](#); (2) [Herczeg & Hillenbrand \(2014\)](#); (3) [Dahm & Lyke \(2011\)](#); (4) [Nesterov et al. \(1995\)](#); (5) [Alencar et al. \(2018\)](#); (6) [Esplin et al. \(2014\)](#); (7) [Lasker et al. \(2008\)](#); (8) [Henden et al. \(2016\)](#); (9) [Grankin et al. \(2007\)](#); (10) [Drake et al. \(2014\)](#).

available periodicity (see [Rebull et al. 2020](#), and references therein) to represent that star's light curve. If the light curve does not present particular issues, the version with moving aperture as in [Cody & Hillenbrand \(2018\)](#) was used by default for consistency. This version was also used for the dipper sample presented in this paper.

As described in [Rebull et al. \(2020\)](#), we started from a more expansive definition of possible Taurus members with K2 light curves, and then weeded it down to 156 members and 23 possible members. The highest-confidence members are those listed in [Luhman \(2018\)](#). We searched for dippers in this set of 156+23 Taurus member light curves.

3. Light-curve analysis

3.1. Identification of dippers

We identified dippers based on a visual inspection of the light curve (see lists in Tables 1 and 2). A common feature in YSOs are sinusoidal patterns, which can be ascribed to cold spots on the stellar photosphere (e.g., [Herbst et al. 1994](#)). Irregular, aperiodic increases in the stellar brightness (bursts) are linked to accretion shocks for T Tauri stars ([Stauffer et al. 2014](#)). Planetary transits and eclipsing binaries do produce dips, but these are strictly periodic and in the first case, have a small amplitude in flux. The criteria for selecting dippers are thus the irregular and sharp shape of the dips, the duration of the dips of up to a few

days, and an amplitude of at least $\sim 10\text{--}60\%$ of the flux. A few examples of dipper light curves are displayed in Fig. 1. The light curves easiest to classify are those in which a stable brightness continuum is interrupted by irregularly shaped dips (e.g., JH 223 in Fig. 1). The bright-faint flux asymmetry is thus high (see, e.g., the M metric in [Cody et al. 2014](#)). The M metric is a useful tool to investigate a large sample of stars. However, it tends to classify as quasiperiodic symmetric (QPS) light curves with irregular dips that do not have a constant brightness continuum. We consider that from a physical point of view, this should not be a striking selection criterion and therefore preferred a manual classification. Dippers with an irregular brightness continuum are CFHT Tau 12 and ITG 34. More symmetric are HK Tau, GH Tau, GM Tau, and EPIC 247820821 (2MASS J04295950+2433078). The last two are more ambiguous, and we differentiated them from spots because of the sharp shape of their dips. We cannot exclude that the dips are superimposed on spots. GI Tau is contaminated by the neighbor GK Tau, and its light curve is complex. However, its own periodicity can be retrieved, and clear dips are visible in the light curve. DK Tau also exhibits a complex light curve. After ~ 25 d of quiescent state, the star becomes a clear dipper. All dipper light curves are shown in Fig. B.1.

In addition to the main dipper sample, two other groups of light curves were taken into account: light curves that show a predominant behavior (e.g., spots, bursts, in Table 2) but also some dips, and low-quality dipper candidates that did not fulfill all of the criteria of the visual inspection and/or were too complex for

Table 2. Additional dippers that exhibit dips in their light curves as secondary variability.

EPIC	2MASS	Name	Type	Period [d]	<i>G</i> [mag]
210725857	J04285053+1844361	...	Sd	2.06	15.19
246859790 (*)	J04440164+1621324	...	Sd	2.16	17.30
247575425	J04331907+2246342	IRAS 04303+2240	Td	7.5	16.09
247584113	J04335200+2250301	CI Tau	db	8.5;	12.15
247585465	J04322415+2251083	...	Bd?	2.48	15.25
247788960	J04323058+2419572	FY Tau	B?d	6.94;	13.77
247810494	J04345542+2428531	AA Tau	d?	...	14.49
247827638 (*)	J04293606+2435556	XEST 13-010	Sd	3.9	14.85
247915927	J04442713+2512164	IRAS 04414+2506	S?d	4.42	15.48
248009353	J04324282+2552314	UZ Tau	Bd	...	12.39
248018164 (*)	J04413882+2556267	Haro 6-33	Td?	...	15.94
248030407 (*)	J04394488+2601527	ITG 15	S?d	3.45	15.00

Notes. The variability type has to be interpreted as: capital letter = dominant variability; d = dipper; s = spot; b = burster; t = long-term trend. The periods are derived with the CLEAN periodogram, and the listed value is the dominant period of the light curve, i.e., of the spot, when present. Only CI Tau and EPIC 247585465 exhibit quasiperiodic dips. The brightness is obtained from the *Gaia* *G* band. (*)Star reported as a dipper by [Rebull et al. \(2020\)](#).

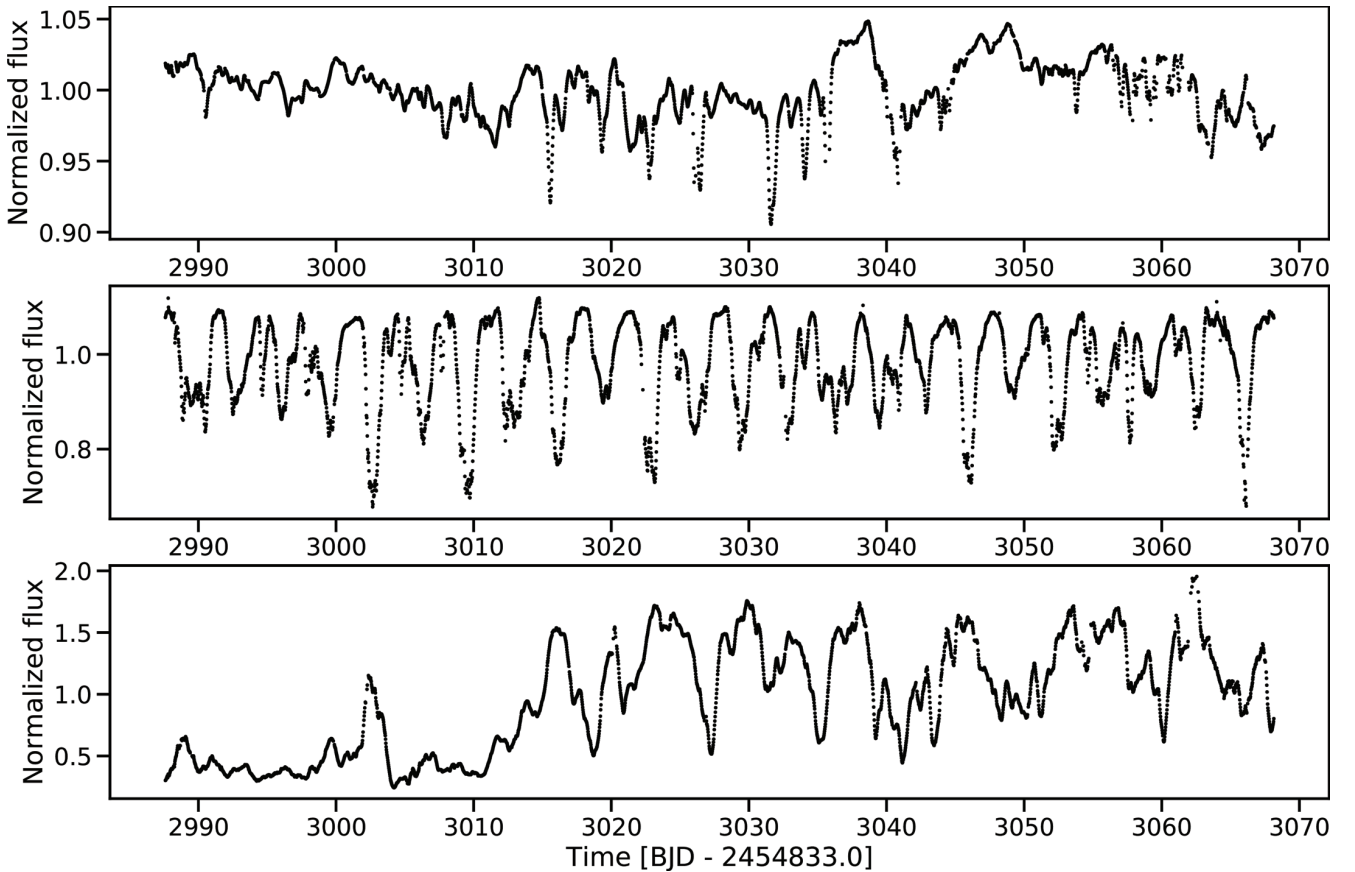


Fig. 1. From top to bottom: example of an aperiodic dipper (HD 285893); a quasiperiodic dipper (JH 223); a dipper with a complex light curve (DK Tau). Dipper light curves are characterized by irregularly shaped fading events, which can last up to a few days.

discerning the different types of their variability (Table 3). In Fig. 2 a few example light curves are shown.

As a result, 22 objects were classified as dippers and 12 were classified as dippers dominated by another type of variability. Almost all of the latter exhibit some aperiodic dips superimposed

on an otherwise variable light curve (Fig. B.2). Eleven additional stars are presented as low-quality candidates in Table 3 and Fig. B.3 and are not further considered in this study. They are rather listed as visual examples of the selection process. The final sample of 34 dippers represents 19% of high-confidence

Table 3. Variable YSOs that are dipper candidates of lower quality.

EPIC	2MASS	Name	Type	Period [d]	<i>G</i> [mag]
210689083	J04313747+1812244	HH 30	t	7.51	...
210690735	J04300399+1813493	UX Tau A+C	t?	3.6;	11.29
210690913	J04313843+1813576	HL Tau	t?
246923113	J04470620+1658428	DR Tau	Bd?	14.71	11.65
247837468	J04293008+2439550	IRAS 04264+2433	?	11.9	...
247923794	J04423769+2515374	DP Tau	t	3.66;	13.51
247992574	J04392090+2545021	GN Tau	t	5.75;	14.56
248017479	J04410826+2556074	ITG 33A	t	6.6;	17.60
248040905	J04295156+2606448	IQ Tau	t	...	13.24
248055184	J04335470+2613275	IT Tau	t	2.74	...
248058354	J04334465+2615005	...	?	...	16.50

Notes. The variability type has to be interpreted as: capital letter = dominant variability; d = dipper; s = spot; b = burster; t = long-term trend. The periods are derived with the CLEAN periodogram and the listed value is the dominant period of the light curve. Most objects in this list are dominated by a long-term trend. The brightness is obtained from the *Gaia G* band.

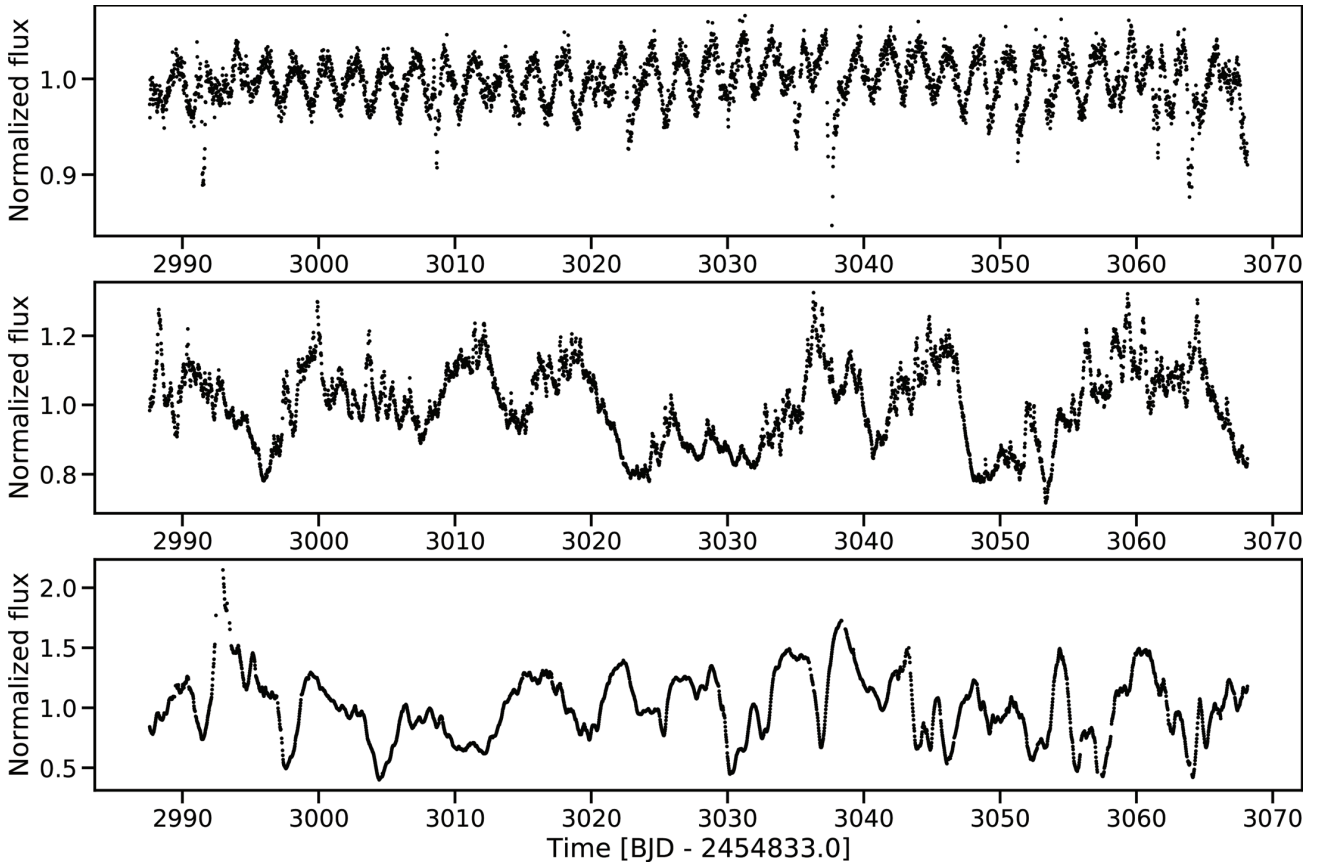


Fig. 2. From top to bottom: a spot-dominated light curve with aperiodic dips (EPIC 246859790); a burst-dominated light curve with dips (CI Tau); a low-quality dipper candidate (IQ Tau). Although dips as described in Fig. 1 are present, the light curve is dominated by another type of variability.

and possible Taurus members (156 + 23 as in Rebull et al. (2020) and 31% of the disked stars (94 + 7 as in Rebull et al. (2020) in this sample.

In addition to the dipper prototype AA Tau (which is now in a faint state and appears in Table 2), Rodriguez et al. (2017) identified five dippers in Taurus-Auriga with KELT light curves, four of which are confirmed in this sample. Rebull et al. (2020) counted 21 dippers in this sample. Sixteen of the dippers analyzed in this study are present in Rebull et al. (2020). Four out

of the 5 further dippers in Rebull et al. (2020) appear here in Table 2. One further light curve (EPIC 247078342) indicated as a dipper in Rebull et al. (2020) is discarded in this study because its shape strongly depends on the reduction pipeline. Our classification is therefore not as strict as in Rebull et al. (2020). Further analysis of the Taurus members sample will be presented in Cody & Hillenbrand (in prep.). As mentioned above, the usage of the M metric or a manual classification can affect the classification for certain stars.

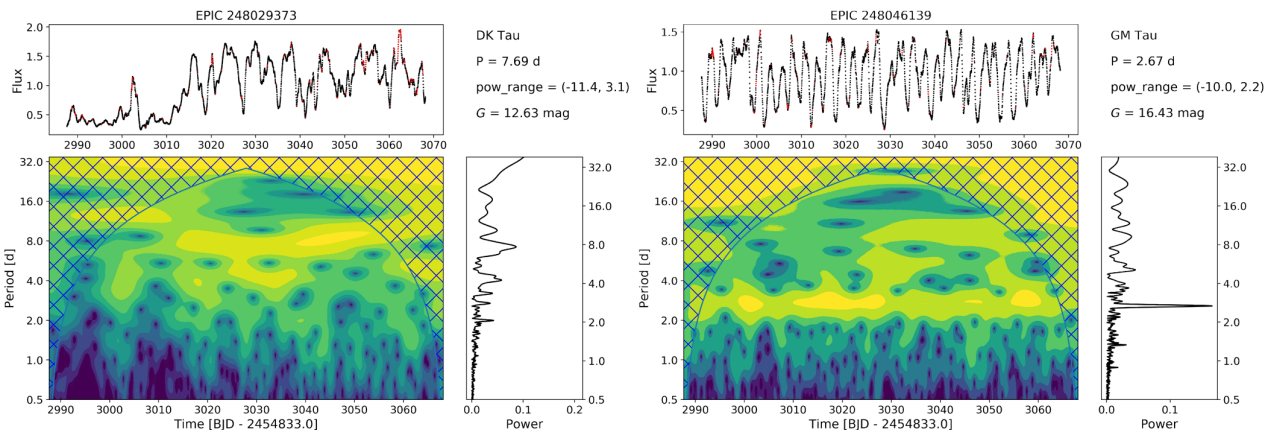


Fig. 3. Different examples of WPS for a time-resolved changing period (DK Tau) and a periodic dipper (GM Tau). *Top panel:* light curves with interpolated points marked in red. *Left panel:* 2D WPS. The crossed lines mark the COI, where edge effects of the wavelet transform become relevant. The power contours extend from low (blue) to high (yellow). The power range and the *Gaia* magnitude are annotated in the upper right corner. *Right panel:* CLEAN periodogram. The logarithmic y -axis with the periods is the same as for the WPS. In the case of DK Tau (*left*), the two peaks in the periodogram at ~ 8 and ~ 10 d can be interpreted as a single period that changes during the observations by means of the WPS. GM Tau displays only one clear period in the WPS and the periodogram. The green stripe at ~ 10 d is just a recurring pattern in the light curve: a deeper dip at $t = 3030, 3040, 3050$ d. This is not a relevant periodicity and does not appear in the periodogram.

3.2. Wavelet analysis of dippers

Dippers can be quasiperiodic or aperiodic, their shape varying from cycle to cycle. Aperiodic narrow dips might appear in an otherwise periodic light curve, or a quasiperiodic dipper might be a transient phenomenon (e.g., McGinnis et al. 2015). Because the variability is irregular, the use of time-resolved period-search algorithms is of high interest.

Common tools used in astronomy such as the Lomb-Scargle periodogram (Lomb 1976; Scargle 1982) and Fourier analysis are not able to deliver information about transient phenomena because they merely resolve the time series in the frequency domain. The windowed Fourier transform (WFT) convolves the signal most commonly with a Gaussian window that is shifted along the signal before the power spectrum is computed. The resulting spectrograms to some extent allow retrieving a time resolution and were applied to dippers by Bodman et al. (2017). However, the width of the window and the time shift cannot be optimized for the entire frequency range, resulting in poor resolution.

When transient phenomena are to be characterized, the wavelet analysis represents a valid alternative because this method allows keeping track of the time variability of a periodic feature by partly losing frequency resolution (see for a summary Torrence & Compo 1998). It can be conceived as a time-resolved WFT with a variable window width that allows recognizing both high- and low-frequency features. A wavelet transform produces a power spectrum after the convolution of the signal and the wavelet, which in most cases is a sort of time-confined sinusoidal wave. We used here the complex Morlet wavelet, which is a complex exponential multiplied by a Gaussian envelope (Grossmann & Morlet 1984). The time and frequency resolution are reached by shifting the wavelet along the time series, then stretching or compressing the wavelet, and repeating the procedure again. This delivers a two-dimensional wavelet power spectrum (WPS), which has a power value for each combination of time and frequency (for more information, see Appendix A).

Wavelet analysis has been successfully applied to a number of phenomena in K2 light curves: stellar rotation (Mathur et al. 2014; García et al. 2014; Bravo et al. 2014), planetary transits,

stellar variability, pulsation, and binaries (Bravo et al. 2014). The implementation in python runs with the package pywt. Because the time series must be evenly sampled for wavelet analysis and some values in the light curve are flagged out during the data reduction, the light curves are linearly interpolated onto even time steps in a preliminary step.

An example of WPS is shown in Fig. 3, while the full atlas of the sample is presented in Appendix E. The x - and y -axis present the linear time and the logarithmic periods (equivalent to the scales, as explained in Appendix A). The contours correspond to the power of the wavelet spectrum, and the region omitted from the cone of influence (COI) is cross-hatched. The contours reach from blue (low power) to yellow (high power). To increase the readability of the plots, the contour plot is saturated at the 99th and third percentile of the power. Moreover, the periodogram and the WPS are cut for the plot at a lower limit of 0.5 d. The WPS is compared to the CLEAN (Roberts et al. 1987) periodogram (to the right of the WPS). For this sample of light curves, this periodogram shows a slightly higher frequency resolution than the Lomb-Scargle periodogram by better resolving close double-peaked periods. The WPS delivers a lower frequency resolution than the periodogram and close peaks are resolved only poorly; on the other hand, it becomes clear when a certain periodicity is present in the time series. High peaks in the periodogram that appear for timescales on the order of one period in the WPS are not real periodicities, but rather parts of the light curve that just highly correlate with the shape of the Morlet wavelet. When two major periodicities are present, the WPS allows us to distinguish which of the two is really predominant in the signal. In case of a changing period, the change can be time-resolved by the WPS, but will appear as several peaks in the periodogram, as is the case for DK Tau (Fig. 3). Depending on the needs of any given light curve, a higher time or frequency resolution can be obtained by changing the central frequency or the bandwidth of the Morlet wavelet (see Appendix A). This does not affect the physical interpretation of the results. Because of the lower frequency resolution of the wavelet transform, it is better to use the period as retrieved from the periodogram. It is possible to project the WPS onto the y -axis and thus average over time to obtain something similar to a periodogram. However, the lower frequency

Table 4. Morphological properties of the dippers.

EPIC	Name	P [d]	σ_P [d]	W [P]	$W_{-\sigma}$ [P]	$W_{+\sigma}$ [P]	A [mag]	$p2p$ [mag]
246929818 ^(a)	Haro 6-37	10.63;	0.72	0.59	0.65	0.50	0.75	1.03
246942563	St 34	5.23;	0.20	0.65 ^(b)	0.59	0.76	0.14	0.33
246989752	...	1.62	0.03	0.22	0.18	0.37	0.16	0.46
247103541	HD 285893	0.05	0.13
247520207	LkCa 15	5.78	0.20	0.64 ^(c)	0.47	0.62	0.54	1.05
247575958	CFHT Tau 12	3.48	0.07	0.59	0.60	0.70	0.23	0.50
247589612	JH 112 A	2.21	0.07	0.20 ^(c)	0.18	0.34	0.11	0.53
247592463	HP Tau	4.33	0.17	0.55 ^(c)	0.51	0.64	0.24	0.65
247763883	GH Tau	2.49	0.06	0.44	0.54	0.48	0.37	0.74
247764745	V807 Tau	4.39	0.12	0.39	0.40	0.35	0.11	0.18
247791801	GK Tau	4.61	0.15	0.43	0.41	0.48	0.62	1.28
247792225	GI Tau	7.13	0.40	0.67 ^(c)	0.34	0.68	0.49	0.97
247799571	HK Tau	3.3	0.07	0.50	0.53	0.44	0.29	0.55
247805410	FX Tau	0.18	0.36
247820821	...	2.38	0.04	0.41	0.43	0.36	1.18	1.77
247885481	...	2.90 ^(d)	0.08	0.60 ^(b)	0.32	0.89	0.05	0.14
247935061	GO Tau	0.17	0.36
248006676 ^(a)	JH 223	3.31	0.09	0.36	0.36	0.39	0.32	0.54
248015397	ITG 34	3.91	0.17	0.51	0.46	0.58	0.53	1.22
248029373 ^(a)	DK Tau	7.69;	0.45	0.57	0.65	0.35	1.08	1.91
248046139	GM Tau	2.67	0.05	0.44	0.49	0.40	1.30	2.00
248047443	IS Tau	7.58	0.41	0.54 ^(c)	0.68	0.43	0.13	0.24

Notes. Columns: the photometric period P , the uncertainty estimated from the Gaussian fitting of the periodogram peak σ_P , the dip width W measured as the FWHM of the folded and binned light curve in units of phase, the dip width estimated considering the binned light curve $\pm\sigma$ of the flux ($W_{-\sigma}$, $W_{+\sigma}$), the dip amplitude with the 90th and 5th flux percentiles A , the peak-to-peak amplitude $p2p$. The stars are detrended before the width was determined, with the exception of those marked ^(a). ^(b)Value discarded because it was not representative of the real dip width. ^(c)Double-peaked dip. ^(d)The peak of the periodogram is at 2.99 d and is linked to a cold spot. A more thorough analysis is needed to retrieve the dipper period at 2.90 d.

resolution of the wavelet transform does not provide any particular advantage for the period determination alone compared to a periodogram.

3.3. Period analysis

Dippers often appear to be quasiperiodic. Following the disk warp model (e.g., [Bouvier et al. 2007](#)), the dusty material obscuring the star must be located close to corotation, which is per definition the region in which circumstellar material rotates with the same angular velocity as the star. [Stauffer et al. \(2015\)](#) and [Rebull et al. \(2018\)](#) identified some light curves that showed both spots and dippers. The overlapping periods of the two phenomena strongly supported the scenario of an inner disk that was rotationally locked to the star because stellar spots follow the stellar rotation. It is thus of interest to discuss the periodicities of dippers compared to stellar rotation.

The variations due to spots are smooth, largely sinusoidal variations. The quasiperiodic dippers produce rather sharp or complex dips, and these events are usually slightly different each time they occur. The distinction between variations originating in spots and dippers can be ambiguous in some unusual cases. Sometimes multiple real periodicities (not harmonics) can show up in the periodogram or in the WPS; in these cases, the physical interpretation of the periodicity can be complicated (see, e.g., discussion in [Rebull et al. 2018, 2020](#)).

In this sample, eight stars exhibit a single clear periodicity (JH 223, EPIC 246989752, CFHT Tau 12, V807 Tau,

GK Tau, HK Tau, GM Tau, and IS Tau), three stars are aperiodic (HD 285893, FX Tau, and GO Tau), and for another three stars, the periodicity is unclear (Haro 6-37, St 34, and DK Tau). Two stars are transient quasiperiodic dippers (JH 112 A and DK Tau). The remaining seven dippers are quasiperiodic, but their light curve or periodogram is more complex than that of the other dippers: LkCa 15, EPIC 247885481, HP Tau, GH Tau, GI Tau, EPIC 247820821, and ITG 34. The periods are listed in Table 4. Those that are uncertain are flagged with a semicolon.

The periods coincide with those published by [Rebull et al. \(2020\)](#), with the exception of that of DK Tau (7.84 d vs. 7.69 d derived here; this small difference is due to the complex periodogram and the usage of two different algorithms). The WPS (Fig. 3) shows that the period increases during the K2 campaign. The periodogram exhibits two peaks at ~ 8 and ~ 10 d. By means of the WPS, they can be interpreted as a single changing period. This could explain why the period of DK Tau is never constrained precisely in the literature (see Appendix D for more details). The stars ITG 34 and GH Tau have a second reported period ([Rebull et al. 2020](#)), which is confirmed here. For GH Tau, a possible third period at 5.09 d is present. An interesting case is EPIC 247885481 (see Sect. 3.3 for a detailed discussion), where the main periodicity of 2.99 d is most probably caused by a spot, while the dips can be folded in phase with a period of 2.90 d. [Rebull et al. \(2020\)](#) reported 2.99 d for the main periodicity, while the dipper period is unresolved both in the periodogram here and in [Rebull et al. \(2020\)](#). In the case of GI Tau, the light curve is contaminated by the neighboring

GK Tau, and the dominant peak in the periodogram is the period of GK Tau. Only the second period is therefore reported as being of GI Tau. EPIC 247820821 shows a second periodicity on the WPS at 7.00 d that does not appear in the periodogram. When folded in phase, the pattern appears to be related to a shift of the minimum of the dip. The periodogram of ITG 34 exhibits several double-peaked periods that cannot be harmonics of each other. It is difficult to recognize a dominant structure in the folded light curve. All the folded light curves are presented in Appendix F. The motions of the *Kepler* satellite might create spurious periods at 0.22, 1.75, and 1.97 d. None of them has been observed here.

A different period for spot and dips? The light curve for EPIC 247885481 (2MASS J05023985+2459337) shows narrow dips superimposed on a sinusoidal variability. The periodogram shows a clear peak at 2.99 d with $\sigma = 0.08$ d, but the folded light curve shows that the period refers to the sinusoidal variation (Fig. 4). The dips can be folded in phase around $P - \sigma$ at ~ 2.90 d. The peak in the periodogram does not appear to have any complex structure.

In order to better study the periodicity, the spot was fit with a sinusoidal wave with a period of 2.99 d (Fig. 4), which was then subtracted from the light curve (Fig. 5). The periodogram before and after the subtraction shows that the main contribution to the periodicity is given by the spot; no substructure appears after the spot subtraction. This can be explained by the fact that the amplitude of the eclipses is very small compared to the noise and that the dip is not clearly present in every period. The shape of the dips is nearly Gaussian, and the dip width is small compared to the period. The residual was fit with a periodic Gaussian pulse such as $f(t) = c + A \sum_{n=-\infty}^{\infty} \exp\left(-\frac{(t-nT-\delta)^2}{2\sigma^2}\right)$, with the period T as a free parameter. The retrieved period is thus 2.90 d for the dips, still very close to $P - \sigma$, and it cannot be confirmed that they are significantly different. Similar conclusions about other stars were reached by Stauffer et al. (2015). Nevertheless, the fact that the dips cannot be folded in phase with the period of the spot is a clear indication that they must be different. The difference between the two periods could be explained by the differential rotation of the stellar surface, assuming that the corotating material is aligned with the equator and the spot is at higher latitude.

3.4. Light-curve morphology

In the following section, the light curve properties of ideal and peculiar dippers are briefly presented and the determination of the dip properties, such as amplitude and width, are explained and discussed.

Ideal dippers. As mentioned in Sects. 1 and 3.1, the main characteristics of dippers are their dips. These are irregular in shape and can either be aperiodic or quasiperiodic. A good example for a quasiperiodic dipper is JH 223 (Fig. 1): The occurrence of the dips is periodic, their shape is irregular, and their amplitude can almost double in two neighboring dips. No other types of variability in form of bursts or other patterns affect the classification. Its period of 3.31 d and the dip duration of ~ 2 d are in range of the rotation periods of CTTSs and of observed dip properties. Aperiodic dippers tend to present either very narrow dips whose shape is rather simple (e.g., Stauffer et al. 2015), which is the case of HD 285893 (Fig. 1), or broad and complex dips.

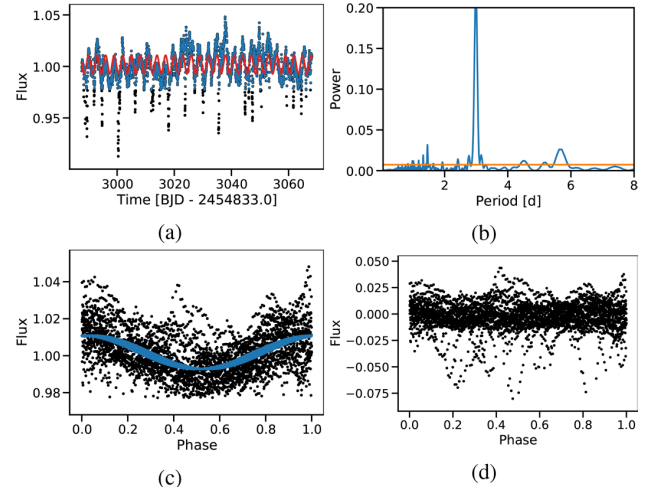


Fig. 4. (a) Light curve of EPIC 247885481. Red: Sinusoidal fit of the flux above the fifth percentile (blue). (b) Periodogram of the star with the FAP level at 0.05 (orange). (c) Light curve above the fifth percentile folded at 2.99 d and sinusoidal fit (blue). (d) Residual light curve after subtraction of the fit as in panels a and c, folded at 2.99 d. The noise is high with respect to the dips, but no evident pattern is present.

Transient dippers. The only clear example of a quasiperiodic and transient dipper in the sample is JH 112 A. The dips have a period of 2.21 d, and if directly linked to the stellar rotation, they are present for a timescale of about ten full rotations. Interestingly, the continuum brightness decreases only as long as the eclipses occur. DK Tau also changes from a fade state to a dipper with a higher brightness continuum, but its light curve is complex, and a strong overall variability has already been observed in former campaigns. The dipper status of quasiperiodic dippers is known to be transient over a few years (e.g., AA Tau), but it is rare to observe a quasiperiodic dipper on such a short timescale. The explanation of a disk warp would imply that the warp significantly changes its height and becomes not visible for the observer after a few rotations, or that the dust in it is completely dissipated on a short timescale.

Double- and multi-peaked dippers. In the sample studied, six periodic dippers exhibit clear double-peaked dips in their light curve: LkCa 15, JH 112 A, HP Tau, GI Tau, HK Tau, and IS Tau (Fig. 6). These double- or multiple-peaked dippers exhibit at least two well-detached dips in the folded light curve (see Appendix F). It should be noted that the dips themselves are in general not Gaussian and have a complex shape. The determination of the dip width for these sources depends on the desired information (the width of the primary peak or the total width of the multi-peaked dip) and is handled in Sect. 3.5. A more detailed description regarding the double dips of individual sources is provided in Appendix D. In the scenario in which a dusty warp occults the star, the constant presence (or absence) of a double dip delivers an indication about the stability and the shape of the warp. In general, it can be remarked that the dips, although periodic, do not occur exactly at the same phase. For HP Tau, the WPS shows that the periodicity slightly varies around a period of 4.33 d. The light curve displays clear shifts of the minima of the dip for different rotation cycles. Moreover, the variations in amplitude of the different dips do not seem correlated to each other. This suggests that either smaller and independent dusty warps occult the star, or that the shape of the dusty structure is highly unstable. A quantitative study of this variation will be object of future work.

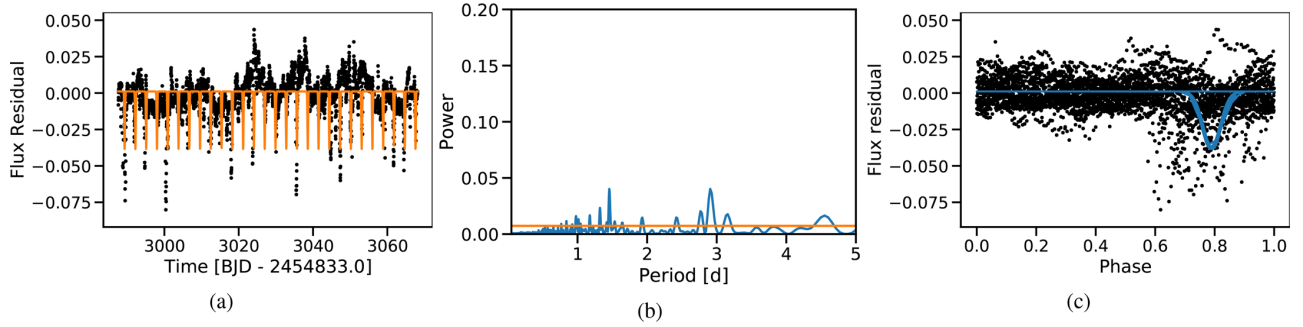


Fig. 5. Fitting with periodic Gaussian pulses (a) of the residual light curve of EPIC 247885481 after the removal of the sinusoidal variability. (b) Periodogram of the residual light curve. The peak is far less evident, but still significant. (c) Residual light curve folded at 2.90 d with the fit Gaussian pulses (blue).

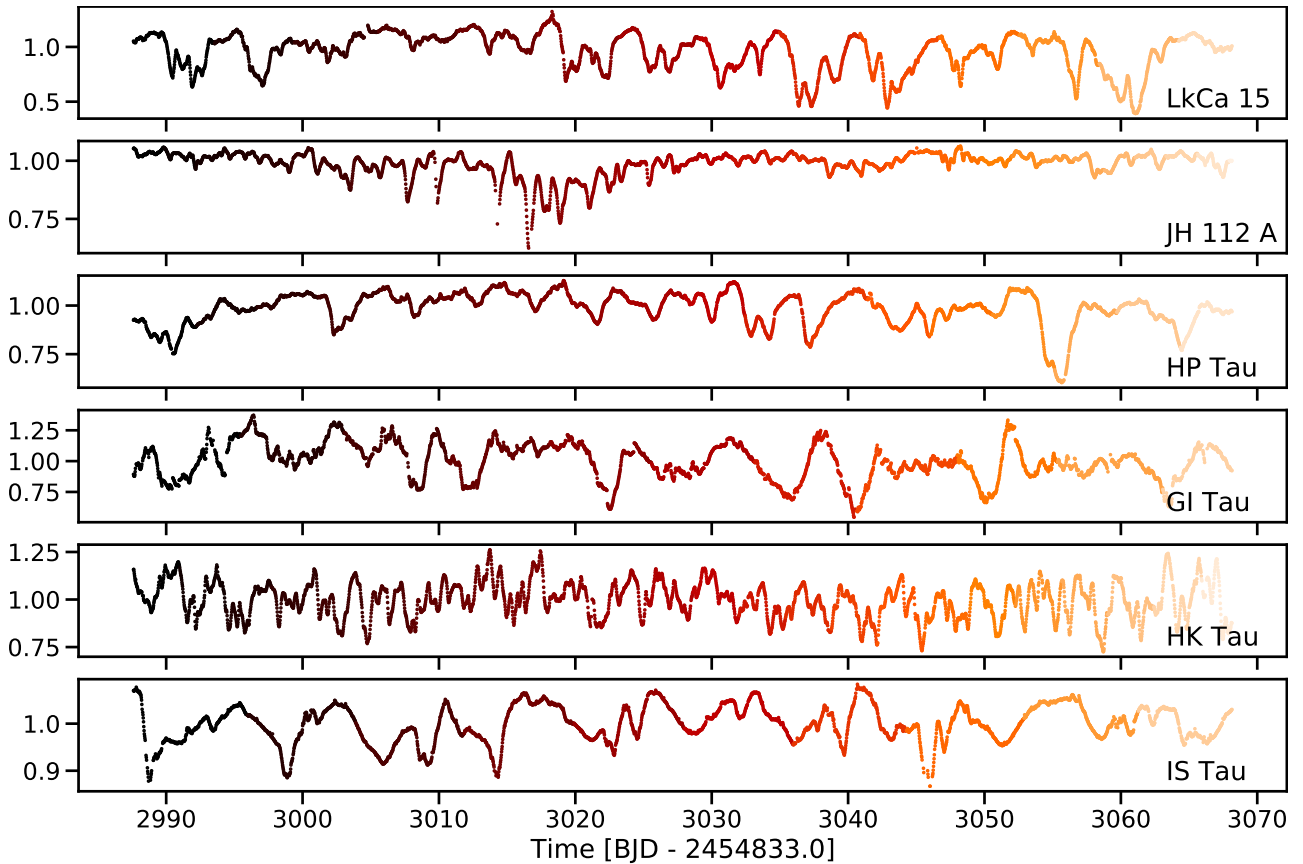


Fig. 6. Light curves of the double-peaked periodic dippers. *Top to bottom:* LkCa 15, JH 112 A, HP Tau, GI Tau, HK Tau, and IS Tau. The color-code is normalized to the length of the observations, one color per phase.

3.5. Dip amplitude and dip width

Among all other sources of variability for YSOs, the long-term trends particularly affect the determination of the dip amplitude because the continuum brightness is unstable. To determine the dip amplitudes, the light curves were therefore detrended using a boxcar filler with a width chosen to be four times the period. This removed the long-term variability and did not interfere with the dips (Fig. 7). For nonperiodic dippers, a standard window of 7 d was chosen. The amplitudes were computed as the difference between the 90th and fifth percentile and peak-to-peak and are listed in Table 4. The light curves of Haro 6-37, JH 223, IS Tau, and DK Tau (for this star, the faint state of the first ~ 30 d has not been included for this and the following analysis) did not need detrending because the continuum brightness is stable.

The detrending was not applied for the study of the periodicity because it might affect the result and interfere with the physical phenomena that cause variability. It is only used in a pragmatic approach to study the dip morphology, without the effect of other stellar variability.

To define an eclipse width, it is useful to bin, that is, to average, the detrended and folded light curve (purple line in the upper panel of Fig. 8). The dip width (black horizontal line in the upper panel of Fig. 8) is then defined at the full width at half maximum (FWHM) of the resulting binned curve. The results are listed in Table 4 and shown in Appendix F. In general, the dip width is about half of the period. The largest dip widths are linked to double- or multi-peaked dippers, with the exception of JH 112 A and HK Tau, which both exhibit a relatively small dip

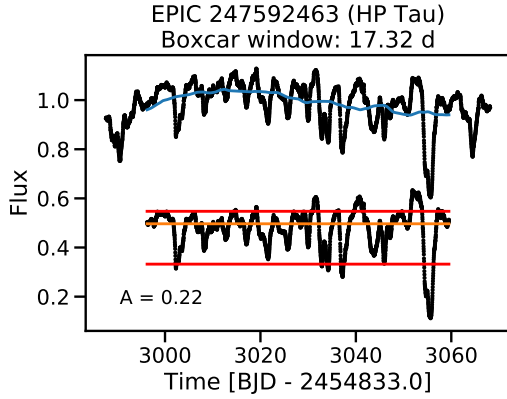


Fig. 7. Determination of the dip amplitude with the example of HP Tau. Top: light-curve detrending of the original data (black) with a boxcar of size $4 \cdot P$. The blue line is the trend. Bottom: detrended light curve. The convolution with a boxcar removes a small part of the data at the edges. Orange line: flux median. Red lines: 90th and fifth percentiles of flux. The usage of flux percentiles allows us to consider the global variability of the light curve.

width ($\lesssim 0.5 P$) and the shortest periods in this group (2.21 and 3.3 d, respectively). The discussion of the correlation between dip width and period is presented in Sect. 5.4.

We estimate an uncertainty on the dip width as follows. For each phase bin, the standard deviation $\sigma(\text{phase})$ of the flux between the different cycles was first computed (purple line in the upper panel of Fig. 8). For every point of the binned light curve, the standard deviation of the phase bin was then added in one case and subtracted in the other (purple line on center and bottom panel in Fig. 8). Finally, the dip width was computed again as FWHM of these modified binned light curves. Upper and lower error bars are defined as difference between the dip width of the modified binned light curve and the original one. Because the shape of the dips may vary strongly after this operation, these error bars can be large.

For double-peaked dippers, the line drawn at the FWHM can cross the binned light curve in more than two points: the error bars $w + \sigma$ and $w - \sigma$ were then chosen to represent the primary peak width and the total width of the dip, which is very large in these cases. This can result in strongly asymmetric error bars (see Sect. 5.4). In Table 4, some width values are flagged because they are not reliable. This can happen when the folded light curve is very noisy and the binned light curve does not show the dips as they can be seen by eye. These plots appear in Fig. F.1.

Another possible representation of the uncertainty on the dip width would be to compute the dip width at different thresholds of the same binned light curve, for example, at 0.3, 0.5 (FWHM), 0.7 of the flux maximum. However, the information about the width of the main dip and the total dip in double-peaked dippers (see, e.g., IS Tau) would be lost.

4. Stellar parameters

Dipper stars are most commonly low-mass T Tauri stars. Their periods of a few days are consistent with the range of rotational periods found in general for young, low-mass stars. There is consensus that the dips in the light curve are caused by dust; in the dusty disk warp scenario, the inner disk warp is located at the corotation radius. Moreover, regardless of the position of the occulting dusty structure, the temperature must be low enough for dust to be able to be present, that is, not to sublimate.

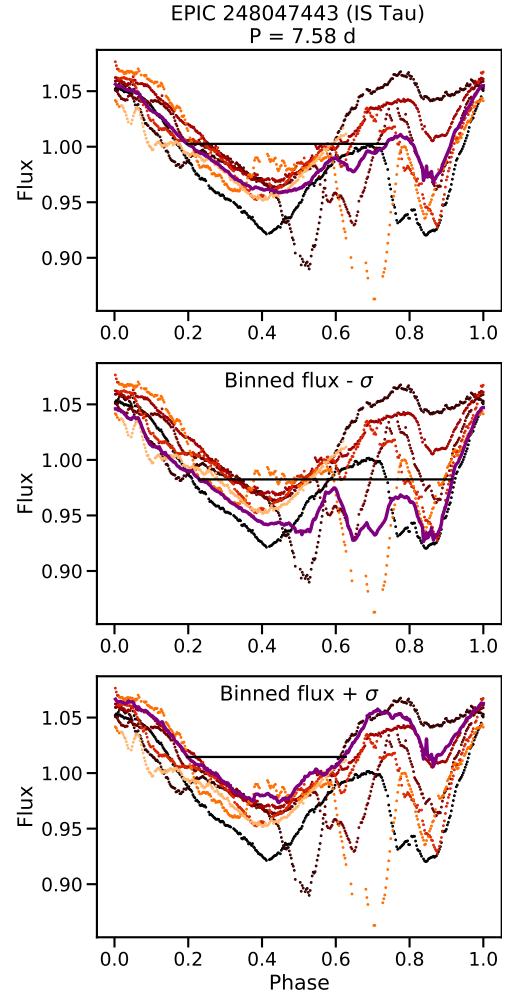


Fig. 8. Dip width measured as the FWHM of the binned light curve (purple line, top). For the folded light curve, each color represents a different cycle. By adding or subtracting the standard deviation of the flux for each phase, it is possible to distinguish between the width of the main dip (bottom) and the double peak (center).

In the following section, the derivation of the different stellar parameters for dipper stars is discussed. In order to verify the conditions and to compute the radius and temperature at corotation, the masses and radii of the star are required. The discussion about each parameter follows in the next paragraphs.

4.1. Effective temperatures and spectral types

Effective temperatures are listed in Table 1 and were derived according to the SpT- T_{eff} conversions of Pecaut & Mamajek (2013). The main sources for the spectral types are Esplin & Luhman (2019) and Herczeg & Hillenbrand (2014), who agree for almost all objects. When spectral subclasses were not explicitly listed in the conversion tables, the value of T_{eff} was linearly interpolated between the two closest subclasses. For spectral types later than M5, the temperature conversions by Herczeg & Hillenbrand (2014) were used.

The uncertainty on T_{eff} follows the uncertainty on the spectral type: for spectral types up to K9, the uncertainty is one spectral subclass; for spectral types between M0 and M4, 0.4 subclasses; and for spectral types later than M4, 0.25 subclasses (Herczeg & Hillenbrand 2014). As a consequence, asymmetric error bars were computed from Pecaut & Mamajek (2013) for an

earlier and later spectral type, respectively. If the later spectral type is missing at the end of the table, a symmetric error bar is produced. The systematic uncertainty linked to the choice of the models of up to 150 K is not taken into account here. A discussion of the consequences on the derived stellar parameters is given in Sect. 5.1.

4.2. VJHK photometry

The light curves of young, accreting stars might be affected by contamination (e.g., by hotspots) in the blue band. Photometry in the *V* and *JHK* bands is therefore preferred. The dipper list was cross-matched with the Two Micron All-Sky Survey (2MASS, [Skrutskie et al. 2006](#)) to obtain *JHK* photometry.

Because a photometric monitoring is the best way to determine the magnitude of variable stars, values reported in the photometric monitoring by [Grankin et al. \(2007\)](#) are preferred for the *V* band, where available. An inspection of the light curves presented for the objects studied here led to the choice of their \bar{V}_m as best estimate for the brightness continuum. However, many of the dipper stars are absent from that collection, and other sources have to be included as well. Three photometric catalogs are common to most sources and include *V*: GSC2.3.2 ([Lasker et al. 2008](#)), NOMAD-1 ([Zacharias et al. 2005](#)), and APASS ([Henden et al. 2016](#))². For individual stars, other additional measurements were retrieved from the literature. All available values for each star were inspected to verify whether any strong inconsistencies existed between the collections. More entries are available in the GSC catalog than in any other collection. If the star was not already reported in [Grankin et al. \(2007\)](#) and there were no particular problems with the photometry, the entry of the GSC catalog was set as *V* value in Table 1, when available.

In the few cases where these single measurements were highly different ($\Delta V > 1$ mag) between the catalogs because of the intrinsic variability of young stars, special attention was given to those stars. One way to assess the plausibility of a *V* band measurement is to verify that it does not lead to a strongly negative extinction. In order to verify that the individually selected visual magnitudes from different sources were self-consistent, the values of *V* were compared with the *Gaia G* ([Gaia Collaboration 2016, 2018](#)) converted into *V*. No offset was found.

4.3. Visual extinction

Most stars in Taurus are subject to at least some reddening. Many stars have moderate or strong infrared excesses, which can affect even the near-IR bands. At the same time, the fainter stars are harder to detect at shorter wavelengths. We therefore calculated the visual extinction by comparing the (*V* – *J*) colors as observed to those for the corresponding spectral type in [Pecaut & Mamajek \(2013\)](#). [Herczeg & Hillenbrand \(2014\)](#) measured a quite high veiling at 7510 Å for some objects in this sample. For those with high veiling, extinction derived with photometry is not as accurate as with spectroscopy. For the stars with $r > 0.1$, the A_V computed by [Herczeg & Hillenbrand \(2014\)](#) from spectroscopy is preferred.

We wished to minimize the risk of inconsistent values that is attached to very few, or just one, photometric measurement. For this reason, the available measurements of A_V in the optical in

the literature were collected and compared (see Table C.1). This allowed us to filter out several clear outliers that are flagged in Table C.1. For stars with lower veiling, the final A_V is an average of the extinction computed here using (*V* – *J*) and the other values in the literature (a comparison of the values we derived and those in the literature is shown in Fig. C.1). The uncertainty was set to the rms of the different values, with a reasonable minimum of 0.3 mag. For measurements of $A_V < 0$, A_V was set to 0 in order to be physical, as was the uncertainty if $A_V \ll 0$.

4.4. Luminosities

The stellar luminosity was computed from the bolometric magnitude M_{bol} as in

$$L_*/L_\odot = 10^{-\frac{M_{\text{bol}} - M_{\text{bol},\odot}}{2.5}}, \quad (1)$$

where $M_{\text{bol},\odot} = 4.25$ mag. Because the brightness and bolometric corrections are mostly available for the *J* band, the bolometric magnitude was derived according to

$$M_{\text{bol}} = m_J - 5 \log(p^{-1}) + 5 - A_J + \text{BC}_J, \quad (2)$$

where m_J is the *J*-band magnitude, p is the parallax (here from *Gaia*), A_J is the extinction in the *J* band, and BC_J is the bolometric correction for the *J* band. The bolometric corrections were retrieved from [Pecaut & Mamajek \(2013\)](#) and interpolated for intermediate spectral types. In case of spectral types later than M5 (not presented in the tables), the BC_J was extrapolated. The computation of A_J from (*J* – *K*) is affected by IR excess. Thus, we preferred to convert A_V into A_J as $\frac{A_J}{A_V} = 0.282$ ([Cardelli et al. 1989](#)).

The *Gaia* parallax was not available for three objects (GH Tau, IS Tau, and FX Tau). We used the distance distributions in Taurus by [Fleming et al. \(2019\)](#) for these stars. FX Tau and GH Tau are located in the B18 cloud, which contains members of the near population at 127.4 ± 3.8 pc. A standard deviation of 7.9 pc was applied as uncertainty for unknown parallaxes. IS Tau lies on the filament L1495, which contains members of both populations. Its luminosity was computed for the two mean distances and is shown with an arrow in Fig. 9. IS Tau appears to more likely be a member of the far population when we assume that it has the same age as the other dippers. In the case of Haro 6-37, the 2MASS measurement in the *J* band is corrupted and no other measurements are available. The visual magnitude and the corresponding BC_V were considered instead.

The procedure for deriving uncertainties on the bolometric correction is the same as for the effective temperature. A major issue for the determination of the luminosity uncertainty is the intrinsic photometric variability of dipper stars, which cannot be included here in absence of an extensive observation campaign. Nevertheless, for stars on their Hayashi tracks, the derivation of the mass depends much more on a precise spectral type than on luminosity (see Fig. 9). The uncertainty on the luminosity affects the derivation of age far more; the isochrones in Fig. 9 accordingly are approximations.

4.5. Masses and radii

In order to derive the mass of the dipper stars in this sample, evolutionary models that reach the lowest end of stellar formation are needed. We therefore preferred the tracks of [Baraffe et al. \(2015\)](#) (Fig. 9) as they include M dwarfs.

² The entries in NOMAD are from the YB6 catalog, which consists of scanned plates and is thus considered a lower-quality source.

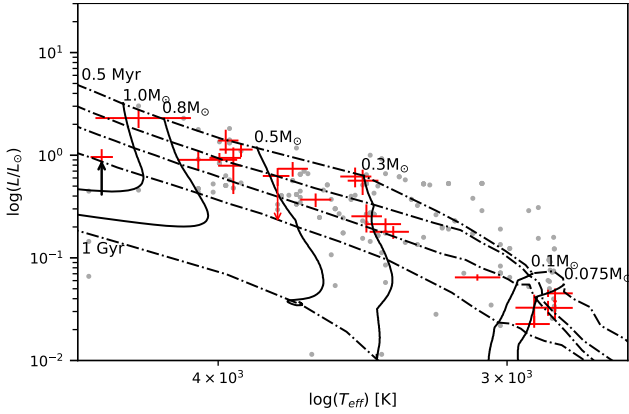


Fig. 9. Evolutionary tracks (solid lines) and isochrones (dashed lines) from Baraffe et al. (2015). The brown dwarf limit lies at $0.073 M_{\odot}$. Isochrones from top to bottom: 0.5, 1, 2, 5 Myr, and 1 Gyr. The red points are the Taurus members classified as dippers, while the gray points are Taurus members as in Herczeg & Hillenbrand (2014). HD 285893 (SpT F8) does not appear in this plot for the sake of readability because its derived T_{eff} is much higher than that of the rest of the sample. The stellar ages scatter around 1 Myr, and with the exception of LkCa15 (marked with a black arrow) and HD 285893, they are on their Hayashi tracks and are still fully convective.

The aim here is to be self-consistent, therefore we derived all masses from the same model. The effective temperature is the dominant term for identifying the corresponding track for this sample. Thus, an identification of the corresponding tracks along the x -axis is the most efficient, with the only exception of the latest M dwarfs, for which the luminosity also plays an important role. Because the tracks are quantized, with a resolution of $0.1 M_{\odot}$ down to $m = 0.2 M_{\odot}$, $0.02 M_{\odot}$ for $0.1 < m \leq 0.2 M_{\odot}$, $0.01 M_{\odot}$ for $m \leq 0.1 M_{\odot}$, the error bars represent the distance between the upper or lower values of the data point and the closest track. The small error bars on the masses listed in Table 5 reflect the small error bars on the effective temperatures. The Hertzsprung-Russell diagram with some of the evolutionary tracks and isochrones is shown in Fig. 9.

The dippers are uniformly distributed around 1 Myr. With the exception of LkCa 15 and HD 285893, the stars identified as dippers have a mass lower than $1 M_{\odot}$, with a few M dwarfs close to the brown dwarf limit of $\sim 0.072 M_{\odot}$. The stars in Herczeg & Hillenbrand (2014) are cross-matched with the members and possible members of Taurus in Rebull et al. (2020) and appear as gray points on the HR diagram. The spectral types are converted into temperatures with the same conversion as we applied to dippers. For spectral types later than K4, the conversion provided by Herczeg & Hillenbrand (2014) exhibits a systematic temperature offset of about +60 K and up to +130 K, while for earlier spectral types, the temperatures proposed by Pecaut & Mamajek (2013) are higher. When several luminosities are provided for a star, the values were averaged in the HR diagram. Because dippers are associated with circumstellar extinction events and their V measurement might have been taken in the fainter state, it might be expected that they are less luminous than non-dipper stars. This does not seem to be the case here. Interestingly, many stars with a mass between 0.1 and $0.3 M_{\odot}$ lie well above the youngest isochrone. On the one hand, this might be an indication of the difficulty of providing precise evolutionary models for stars with a very low mass. On the other hand, for faint and accreting brown dwarfs, the accretion luminosity might dominate the faint stellar luminosity. At the other extreme, with

a $T_{\text{eff}} = 6100$ K and $L = 1.99 L_{\odot}$, HD 285893 almost lies on the ZAMS on the HR diagram. A more detailed discussion is given in the individual notes in Appendix D. This ‘old’ dipper might belong to a recently identified class of debris disk dippers (Gaidos et al. 2019; Tajiri et al. 2020), for which aperiodic extinction events have been attributed to the disruption of planetesimals.

The stellar radii are derived according to the Stefan-Boltzmann law as

$$\frac{R}{R_{\odot}} = \left(\frac{L}{L_{\odot}}\right)^{\frac{1}{2}} \left(\frac{T_{\odot}}{T_{\text{eff}}}\right)^2 \quad (3)$$

and are presented along with the masses in Table 5. The uncertainties on T_{eff} and the luminosity are propagated to the stellar radius.

4.6. Radius and temperature at corotation

In the accretion scenario, the dusty warp that obscures the star is located at corotation. The corotation radius defines the distance from the star at which the material of the Keplerian disk rotates with the same angular velocity as the star. Because in a stable orbit, the gravitational potential of the star is equal to the centrifugal force, the corotation radius is derived as

$$R_{\text{cor}} = \left(\frac{P}{2\pi}\right)^{\frac{2}{3}} (GM_{*})^{\frac{1}{3}}, \quad (4)$$

where P is the stellar period. Considering the simple approximation of no energy transfer between a dust grain situated at R_{cor} and the remaining disk, which reduces the effective irradiation by a factor 4 as in Bouvier et al. (1999), it is possible to derive the temperature at corotation as

$$T_{\text{cor}} = 2^{-\frac{1}{2}} T_{\text{eff}} \left(\frac{R_{*}}{R_{\text{cor}}}\right)^{\frac{1}{2}}. \quad (5)$$

The corotation radii and temperatures computed in this way are listed in Table 5. The corotation radii extend to a few stellar radii, between 2.5 and $9 R_{*}$. The temperatures at corotation are ~ 1000 K, and a few stars reach up to ~ 1500 K. The error bars on this quantity are large because the uncertainties on the stellar radii are about 10–20% for young stars.

4.7. Inclinations

In order to probe the capacity of the magnetospheric accretion model to account for dippers, the angle under which we observe the system is required because dippers cannot be seen close to face-on if the dusty part of the accretion column has to cross the observer’s line of sight to produce dips in the light curve (e.g., McGinnis et al. 2015; Bodman et al. 2017). A more detailed discussion of this point is provided in Sect. 5.1. The stellar inclination is derived according to the formula

$$v \sin i = \sin i \frac{2\pi R_{*}}{P}. \quad (6)$$

The convention we used to define the inclination is 0° for the star seen pole-on and 90° for edge-on. The $v \sin i$ values were retrieved from the literature (see Table 5): the main sources were Nguyen et al. (2012) and Güdel et al. (2007), who retrieved their values for this sample from Rebull et al. (2004).

Table 5. Stellar properties of the dipper sample.

EPIC	Name	L_* [L_\odot]	M_* [M_\odot]	R_* [R_\odot]	R_{cor} [R_*]	T_{cor} [K]	$v \sin i$ [km s^{-1}]	Ref.	i_* [$^\circ$]	$\log \dot{M}_{\text{acc}}$ [$M_\odot \text{ yr}^{-1}$]	Refs.
246929818	Haro 6-37	$0.79^{+0.40}_{-0.37}$	$0.60^{+0.05}_{-0.05}$	$1.91^{+0.54}_{-0.48}$	8.98	930^{+179}_{-158}	12.1 ± 1.2	1	>47	-7.00/-8.12	6,7,8
246942563	St 34	$0.18^{+0.02}_{-0.03}$	$0.25^{+0.05}_{-0.05}$	$1.25^{+0.14}_{-0.13}$	6.38	941^{+118}_{-107}
246989752	...	$0.023^{+0.004}_{-0.002}$	$0.071^{+0.014}_{-0.011}$	$0.59^{+0.08}_{-0.04}$	4.08	1022^{+122}_{-91}
247103541	HD 285893	$1.99^{+0.25}_{-0.25}$	$1.15^{+0.02}_{-0.02}$	$1.26^{+0.08}_{-0.10}$
247520207	LkCa 15	$0.96^{+0.19}_{-0.17}$	$1.12^{+0.01}_{-0.01}$	$1.62^{+0.19}_{-0.18}$	8.69	1077^{+99}_{-95}	13.9 ± 1.2	1	79^{+11}_{-24}	-8.83/-8.87/-9.17	8, 6, 9
247575958	CFHT Tau 12	$0.038^{+0.013}_{-0.013}$	$0.065^{+0.010}_{-0.005}$	$0.79^{+0.14}_{-0.14}$	4.90	913^{+100}_{-112}
247589612	JH 112 A	$0.90^{+0.19}_{-0.17}$	$0.700^{+0.020}_{-0.015}$	$1.90^{+0.28}_{-0.32}$	3.33	1581^{+172}_{-217}
247592463	HP Tau	$2.30^{+0.50}_{-0.46}$	$0.9^{+0.3}_{-0.2}$	$2.70^{+0.53}_{-0.54}$	4.00	1531^{+294}_{-336}	15.4 ± 1.6	2	29^{+11}_{-11}
247763883	GH Tau	$0.62^{+0.14}_{-0.13}$	$0.325^{+0.025}_{-0.025}$	$2.16^{+0.30}_{-0.30}$	2.46	1572^{+166}_{-168}	30.3 ± 0.7	1	44^{+10}_{-10}	-7.92/-8.02/-8.90	7, 10, 6, 8
247764745	V807 Tau	$1.39^{+0.38}_{-0.36}$	$0.60^{+0.05}_{-0.05}$	$2.50^{+0.38}_{-0.38}$	3.81	1437^{+154}_{-161}	13.6 ± 0.7	1	28^{+7}_{-7}	-8.40/<-8.68	8,10
247791801	GK Tau	$0.94^{+0.11}_{-0.10}$	$0.65^{+0.05}_{-0.05}$	$2.03^{+0.16}_{-0.19}$	4.98	1266^{+93}_{-117}	18.7 ± 3.5	2	57^{+23}_{-22}	-8.19	6, 7, 8, 11
247792225	GI Tau	$0.74^{+0.12}_{-0.12}$	$0.45^{+0.05}_{-0.05}$	$2.08^{+0.23}_{-0.23}$	5.75	1095^{+118}_{-118}	12.7 ± 1.9	1	59^{+24}_{-24}	-8.00/-8.02/-8.08	11, 6, 7, 8
247799571	HK Tau	$0.37^{+0.05}_{-0.06}$	$0.40^{+0.05}_{-0.05}$	$1.54^{+0.16}_{-0.16}$	4.47	1214^{+115}_{-115}	21.8 ± 2.5	3	68^{+21}_{-21}	-7.65	12
247805410	FX Tau	$0.56^{+0.16}_{-0.16}$	$0.300^{+0.050}_{-0.025}$	$2.09^{+0.35}_{-0.35}$	9.61 ± 0.19	1	...	-8.65	6,7
247820821	...	$0.045^{+0.004}_{-0.004}$	$0.075^{+0.015}_{-0.003}$	$0.85^{+0.04}_{-0.07}$	3.70	1058^{+39}_{-110}	18.4 ± 1.0	4	>64
247885481	...	$0.065^{+0.005}_{-0.005}$	$0.15^{+0.03}_{-0.03}$	$0.89^{+0.07}_{-0.07}$	5.23	956^{+100}_{-100}
247935061	GO Tau	$0.25^{+0.08}_{-0.08}$	$0.300^{+0.050}_{-0.025}$	$1.41^{+0.26}_{-0.26}$	17.5 ± 9.7	2	...	-7.93/-8.33/-8.42	6,9,8
248006676	JH 223	$0.21^{+0.03}_{-0.03}$	$0.275^{+0.025}_{-0.025}$	$1.34^{+0.14}_{-0.14}$	4.52	1126^{+107}_{-103}
248015397	ITG 34	$0.033^{+0.011}_{-0.010}$	$0.075^{+0.015}_{-0.015}$	$0.71^{+0.15}_{-0.13}$	6.23	827^{+143}_{-128}
248029373	DK Tau	$1.14^{+0.16}_{-0.18}$	$0.55^{+0.05}_{-0.05}$	$2.33^{+0.27}_{-0.24}$	5.78	1150^{+131}_{-112}	17.5 ± 1.2	1	>60	-7.42	6,7,11
248046139	GM Tau	$0.033^{+0.006}_{-0.005}$	$0.065^{+0.015}_{-0.005}$	$0.73^{+0.06}_{-0.09}$	4.49	961^{+60}_{-126}	9.0 ± 2.0	5	41^{+17}_{-15}	-8.60/-8.70	13, 14
248047443	IS Tau	$0.63^{+0.12}_{-0.13}$	$0.50^{+0.05}_{-0.05}$	$1.86^{+0.24}_{-0.23}$	6.93	1013^{+116}_{-110}	-7.91/-8.01	10,8

Notes. Stellar inclinations reported as lower limits have $\sin i > 1$.

References. (1) [Nguyen et al. \(2012\)](#); (2) [Güdel et al. \(2007\)](#); (3) [Hartmann et al. \(1986\)](#); (4) [Kraus et al. \(2017\)](#); (5) [Mohanty et al. \(2005\)](#); (6) [Hartmann et al. \(1998\)](#); (7) [Muzerolle et al. \(1998\)](#); (8) [White & Ghez \(2001\)](#); (9) [Isella et al. \(2009\)](#); (10) [Hartigan & Kenyon \(2003\)](#); (11) [Gullbring et al. \(1998\)](#); (12) [White & Hillenbrand \(2004\)](#); (13) [White & Basri \(2003\)](#); (14) [Herczeg & Hillenbrand \(2008\)](#).

The uncertainty on i grows with $\sin i$, thus higher inclination angles have larger uncertainties. Some stars (Haro 6-37, EPIC 247820821, and DK Tau) exhibit a $\sin i > 1$, which probably indicates that something is amiss with the stellar parameters. In these cases, the minimum inclination angle is indicated as a lower limit. The results are listed in Table 5. For Haro 6-37, the period is uncertain. It is possible that the observed period is not correct or not directly related with the rotation period. For DK Tau, different periods have been reported in the literature because the light curve is complex, and the WPS shows an increasing period during the K2 observations. Because the stellar rotation period is not assumed to vary much, other physical phenomena might affect the dips. For instance, [Grankin et al. \(2007\)](#) reported a long-term variability amplitude of $\Delta V \sim 1.8$ mag for this star, which propagates to any inclination angle between 30° and 90° if taken into account as the uncertainty on V .

4.8. Mass accretion rates and accretion regime

The mass accretion rates of the dippers were collected from the literature, when available (Table 5). They are, in general, on the order of magnitude of $10^{-8} M_\odot \text{ yr}^{-1}$. This is in agreement with the observed mass accretion ranges for T Tauri stars ([Gregory et al. 2006](#)). Exceptions are Haro 6-37, HK Tau, and DK Tau,

which are stronger accretors of about $10^{-7} M_\odot \text{ yr}^{-1}$. LkCa 15 has a very low mass accretion rate for its mass, but it is also a transition object, and a lower mass accretion rate is expected at this stage. In general, quasiperiodic dippers are expected to be generated in a stable accretion regime (see Sect. 5.4) and aperiodic dippers instead in an unstable regime ([McGinnis et al. 2015](#)), which could be caused by a phase of enhanced mass accretion. The complex light curve of DK Tau, one of the strongest accretors, might be an example of unstable accretion. However, for the dipper sample presented in this paper, we found no correlation between mass accretion rate and periodicity.

5. Discussion

Several possible mechanisms for the origin of dippers have been presented in the literature, including dusty disk warps, dusty winds, and disk vortices. In the study of the prototypical dipper AA Tau, [Bouvier et al. \(1999\)](#) proposed that a magnetic dipole, tilted with respect to the stellar rotation axis, might contribute to an inner disk distortion. This can produce a dusty, optically thick disk wall that can account for the photometric variation, if observed at high inclination. This model was further explored by [McGinnis et al. \(2015\)](#), using as free parameters the stellar inclination and location, height, and azimuthal extension of the

dusty wall. In the dipper sample of NGC 2264, which has a similar size as that of Taurus, inclinations down to $\sim 50^\circ$ could be measured, with large uncertainties. [McGinnis et al. \(2015\)](#) were able to fit the light curves with a dusty warp with a mean inclination of $\sim 70^\circ$. Dippers close to edge-on are assumed to be undetectable in photometry because the disk would block the line of sight toward the stellar photosphere.

The first parameter we discuss for the compatibility with the model therefore is the inclination of the star and the disk (Sect. 5.1). For stable accretion, the magnetospheric truncation radius is close to corotation, and the photometric periods of dippers provide evidence for the dusty warp to be located at corotation. One other condition for the validity of the model is thus that the environment at corotation must be cold enough to avoid dust sublimation (Sect. 5.2). It would be helpful to derive the truncation radius to compare it with the corotation radius; unfortunately, not enough precise magnetic field measurements are available for this purpose. [Bodman et al. \(2017\)](#) provided a rough estimate for the mass accretion rate and the magnetic field strength. However, this estimate has a very large uncertainty.

This scenario was challenged by the discovery of dippers seen in millimeter wavelengths in a full range of inclination angles ([Ansdell et al. 2016b, 2020](#)), on which the hypothesis was founded that the inner and outer disk might be misaligned. Binarity can be invoked as a cause of misalignment in a circumbinary disk (e.g., [Facchini et al. 2013, 2018; Franchini et al. 2019](#)). This opens the possibility of finding a dipper with a low outer disk inclination. Nonetheless, the inclination of the inner region must be reasonably high to detect dips. Two examples of well-studied dippers with a misaligned inner disk are LkCa 15 and RX J1604.3-2130 A ([Alencar et al. 2018; Sicilia-Aguilar et al. 2020](#)).

Another way of lifting dust away from the disk midplane is through dusty disk winds. These are spatially more extended than the base of accretion funnel flows, and might shield the stellar brightness at lower viewing angles. Magnetic field lines inclined with respect to the disk symmetry axis ($\theta \geq 30^\circ$) are able to accelerate matter away from the disk. Dust, dragged away with gas, is able to survive in a disk-driven wind at temperatures of several 10^3 K because heating the dust through collisions with gas particles and sputtering is highly inefficient ([Tambovtseva & Grinin 2008](#)). A high mass-accretion rate and strong magnetic field (kG) are required to launch such a disk wind ([Miyake et al. 2016; Labdon et al. 2019](#)), and only the small dust grains are dragged by the wind, while the large-size grains remain in the disk midplane ([Miyake et al. 2016](#)). The resulting floating dust in the disk is able to produce optical fading events and NIR brightening. [Bans & Königl \(2012\)](#) modeled the NIR $3 \mu\text{m}$ bump as produced by absorbed stellar radiation in a dusty wind. However, it seems that such disk winds are observed under a rather high inclination $\sim 70^\circ$ ([Vinković & Čemeljić 2021](#)), much higher than what has been invoked to explain low-inclination dippers (e.g., [Ansdell et al. 2020](#)).

It is also possible to lift dust from the midplane through vortices in the disk that are caused, for example, by Rossby waves. However, the occultations caused in this way would have a very small amplitude and might thus account only for a small fraction of aperiodic dippers ([Stauffer et al. 2015](#)).

5.1. Inclination of star and disk

In this section, we investigate whether the stellar inclination agrees with the inclination of the outer disk and if this is compatible with an AA Tau-like star. For most of the objects considered

here, a moderate to high inclination is clear despite the large error bars.

GH Tau and GM Tau are compatible with an inclination of $\sim 50^\circ$, which is at the lowest end of the magnetospheric accretion scenario. This suggests that the magnetic field axis is highly tilted with respect to the stellar spin axis. In the case of HP Tau and V807 Tau, the proposed dusty warp scenario for the production of dippers fails to explain fading events seen at such a low inclination. We tested whether the photometric variability might significantly affect the estimation of the luminosity and propagate up to the derived stellar inclination. None of these stars shows an amplitude in the K2 light curve that would be large enough to explain the discrepancy. Nevertheless, for HP Tau, a long-term amplitude variation of $\Delta V \sim 1$ mag was reported by [Grankin et al. \(2007\)](#). This can be roughly converted into an upper limit of $i \sim 50^\circ$, which is still at the lowest limit for the magnetospheric accretion model. For V807 Tau, which is a triple system, an overestimation of the brightness of the primary is possible. [Schaefer et al. \(2012\)](#) estimated that V807 A could be 0.5 mag fainter than the total system in the *J* band and fit an extinction of 0 to the system. From these parameters, a higher stellar inclination of 40° can be derived, which is more plausible. This is not sufficient to explain the discrepancy, however. A stellar radius of $\sim 1.5 R_\odot$ would be required to reach an inclination angle of at least 50° .

It is thus more probable that some other phenomenon contributes to the quasiperiodic extinction events for these stars that are inconsistent with a sufficiently high inclination. Dusty disk winds also need high inclination angles to be observable ([Vinković & Čemeljić 2021](#)), and the mass accretion rate of V807 Tau is too low (Table 5). The small amplitude of ~ 0.1 mag might indicate vortices caused by Rossby wave instabilities. However, given the clear periodicity of the light curve, this mechanism can be discarded. Moreover, the almost constant shape of the dips means that the structure occulting the star is probably stable, not very large, optically thick, and it might be that just a small fraction of it is seen by the observer under this low inclination.

One more possibility in the magnetospheric accretion scenario would be that the dust high in the accretion column increases its optical depth immediately before sublimation because evaporation and free-fall timescales are similar ([Nagel & Bouvier 2020](#)). This might imply that an optically thick part of the accretion column could cross the observer's line of sight, thus requiring a lower inclination to see dips.

We compared our dipper sample to inclinations of outer disks that were directly measured at millimeter wavelengths (Table 6). [Akeson & Jensen \(2014\)](#) derived the disk inclination in the image plane by fitting the clean continuum maps with 2D Gaussians. This results in larger error bars than with the methods used by other authors because the continuum map is reconstructed from the visibilities. In general, the inclination of the outer disk is slightly lower than the inclination derived for the inner region, with the exception of DK Tau, which seems strongly misaligned with the outer disk, although this value has to be considered with caution (see Sect. 4).

[Appenzeller & Bertout \(2013\)](#) pointed out that the inclination of CTTs derived from $v \sin i$ are not precise for $i > 30^\circ$ because the uncertainty grows with i . The inclination might also be overestimated when not all line broadening effects are properly considered. For a sample of known CTTs in different regions, i_* and i_{disk} are correlated, but the inclination derived from rotation is 19° higher on average ([Appenzeller & Bertout 2013](#)). This trend is also observed in Taurus for HP Tau, GK Tau,

Table 6. Inclination of the stellar axis i_* from this study compared to observations of the outer disk i_{disk} from the literature.

EPIC	Name	i_* [$^\circ$]	i_{disk} [$^\circ$]	
			(1)	(Other)
246929818	Haro 6-37	>47
246942563	St 34
246989752
247103541	HD 285893
247520207	LkCa 15	79^{+11}_{-24}	...	55 (2); 50^{+4}_{-6} (3)
247575958	CFHT Tau 12
247589612	JH 112 A
247589803	JH 112 B
247592463	HP Tau	29^{+11}_{-11}	$18.3^{+1.2}_{-1.4}$...
247763883	GH Tau	44^{+10}_{-10}
247764745	V807 Tau	28^{+7}_{-7}
247791801	GK Tau	57^{+23}_{-22}	$40.2^{+5.9}_{-6.2}$	73.0^{+59}_{-59} (4); 71^{+5}_{-5} (5)
247792225	GI Tau	59^{+24}_{-24}	$44.0^{+2.0}_{-2.0}$...
247799571	HK Tau	68^{+21}_{-21}	$56.9^{+0.5}_{-0.5}$	46.0^{+29}_{-29} (4); 51^{+2}_{-2} (5); 57.0^{+4}_{-4} (6)
247805410	FX Tau	40^{+4}_{-4} (5)
247820821	...	>64
247885481
247935061	GO Tau	...	$53.9^{+0.5}_{-0.5}$...
248006676	JH 223
248015397	ITG 34
248029373	DK Tau	>60	$12.8^{+2.5}_{-2.8}$	41.0^{+11}_{-11} (4); 20^{+5}_{-5} (5); 27.0^{+9}_{-9} (6)
248046139	GM Tau	41^{+17}_{-15}
248047443	IS Tau

References. (1) Long et al. (2019); (2) van der Marel et al. (2015); (3) Thalmann et al. (2014); (4) Akeson & Jensen (2014); (5) Simon et al. (2017); (6) Harris et al. (2012).

GI Tau, and HK Tau. Nevertheless, the recent observations of misaligned inner disks support the possibility that this systematic also has a physical basis.

Another systematic uncertainty on the stellar inclination is produced by the use of conversion tables between spectral type and effective temperature, which are still not precise for young stars. The use of different conversions can lead to discrepancies of about 150 K, which for a late-type star with $T_{\text{eff}} \sim 3000\text{--}3500$ K means an additional uncertainty of $\sim 5\%$. Propagated to R_* and $\sin i$, this final uncertainty of $\sim 10\%$ corresponds to about 5° for $i_* < 30^\circ$ or 10° for $i_* > 30^\circ$. Thus, the stellar inclinations might be higher than derived by about 10° .

No extreme cases of face-on dippers, as reported by Ansdell et al. (2016b), are observed in this sample. The stellar inclination was derived for 11 dippers (50%), and inclinations of the outer disk are available for 8 (36%) dippers. The dippers for which it was possible to derive a stellar inclination are compatible with the disk warp scenario (thus 9/11), with the exception of HP Tau, whose stellar parameters might be significantly affected by a strong overall photometric variability, and V807 Tau, for which a different scenario is required, even after decomposing the primary and secondary brightness of the system. In general, the stellar inclinations of Taurus dippers are lower than those of dippers in NGC 2264 (McGinnis et al. 2015), for instance.

5.2. Temperature at corotation and dust survival

Given the assumption that dusty material at corotation causes the dips, it is interesting to compare the temperature at

cotation with dust sublimation temperatures in order to confirm or exclude certain characteristics of the dust grains. The sublimation temperature, T_{sub} , of the grains depends on the gas pressure, latent heat, and molecular weight more than on the stellar parameters (Kobayashi et al. 2011). The full range of T_{cor} in Table 5 extends from 800 to 1600 K, with error bars of about 100 K. The only materials able to withstand these temperatures are olivine, pyroxene, and iron (Pollack et al. 1994, see their Table 3). Moreover, the sublimation temperature increases with the gas density; stars with $T_{\text{cor}} > 1400$ K exclude gas densities $< 10^{-8}$ g cm $^{-3}$. The stars with the highest temperatures at corotation in Table 5 can only host dust for even higher gas densities $> 10^{-6}$ g cm $^{-3}$. Because it is currently difficult to resolve the inner disk rim for low-mass YSOs, models for this region have only been developed for intermediate-mass stars (e.g., Isella & Natta 2005; Tannirkulam et al. 2007). It is thus of interest to better constrain these properties for CTTSs in future studies to verify the conditions for dust survival.

Setting a critical temperature for dust $T_{\text{subl}} = 1500$ K, it is possible to derive from Eqs. (5) and (4) the minimum stellar rotation period for a given mass and radius that permits a sufficiently cold environment for dust to survive at corotation as

$$P_{\text{lim}} = 2^{-\frac{1}{2}} \pi \left(\frac{T_{\text{eff}}}{T_{\text{subl}}} \right)^3 R_*^{\frac{3}{2}} (GM_*)^{-\frac{1}{2}}. \quad (7)$$

Figure 10 shows that all periods of dipper stars are well above this limit. For the few stars close to the limit, the condition is satisfied if a $T_{\text{subl}} = 1600$ K is assumed. Previous observations

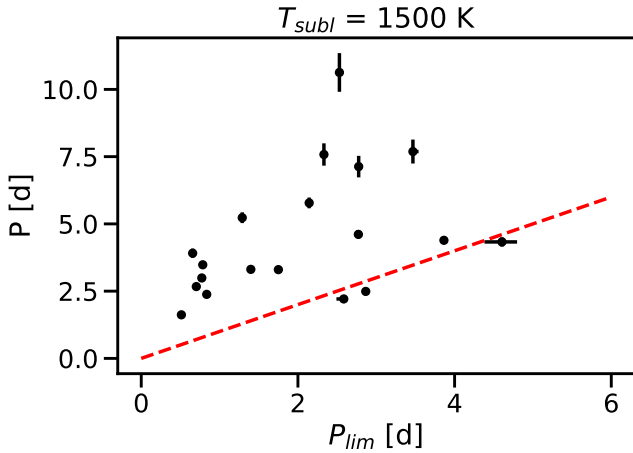


Fig. 10. Period of the dippers in comparison to the minimum rotation period (red line) required for a temperature ≤ 1500 K at corotation. If the star rotates faster, the inner disk is purely gaseous at corotation.

of dippers in ρ Oph and Upper Sco (Bodman et al. 2017) also indicate that it is possible for dust to survive at the corotation radius of dipper stars.

5.3. Dippers in Taurus and in other clusters

The star-forming regions that are known so far to host dippers include NGC 2264, which is 2–3 Myr old (Alencar et al. 2010; Cody et al. 2014; McGinnis et al. 2015; Stauffer et al. 2015), Orion, which is 3 Myr old (Morales-Calderón et al. 2011), ρ Oph and Upper Sco, which are 1 and 10 Myr old, respectively (Ansdell et al. 2016a; Hedges et al. 2018; Cody & Hillenbrand 2018; Rebull et al. 2018), and Taurus (Rebull et al. 2020; Rodríguez et al. 2017). A feature that is shared by all of these regions is the late spectral type, K to M, of the identified dippers. A common explanation for this is the longer pre-main-sequence phase of late-type stars, which allows the disk to be present for a longer time, thus increasing the probability of observing a dipper. Moreover, the lower surface temperature enables dust to be present close to the stellar magnetosphere. In Taurus, as in ρ Oph and Upper Sco, the occurrence of M-type dippers is higher than that of K-type dippers because stars of lower mass always exist in a larger number.

For the fractional rate at which dippers are found among YSOs, the statistics differ from region to region. The main reasons for this are the different counting methods (i.e., fraction of disk-bearing stars vs. all members of the cluster), the different selection techniques, and the target selection process of the survey, which is not necessarily optimized for finding dippers. For ρ Oph and Upper Sco, dippers represent about 20% of disked YSOs (Hedges et al. 2018), which was increased to 30% by Cody & Hillenbrand (2018). These authors also pointed out that in the older Upper Sco, a higher dipper fraction is observed among disked stars. Alencar et al. (2010) claimed that 30–40% of disked stars in NGC 2264 might be dippers, depending on whether a sample of thick or anemic inner disks is considered. This amount was found to be 20% by Cody et al. (2014), who also studied NGC 2264. An exception is Orion, where only 5% of the stars are dippers. This might be due to the photometric accuracy of the survey and a biased target selection (Morales-Calderón et al. 2011), as well as the fact that they did not consider a disked-star sample. In Taurus, considering the additional 12 dippers in Table 2, the occurrence rate is 19% of all the members observed

with K2, and 31% of the members hosting a disk. The ratio of quasiperiodic to aperiodic dippers is about 1:1 for NGC 2264, ρ Oph, and Upper Sco. In Orion, only one-third of the dippers is quasiperiodic. In contrast, most dippers appear to be quasiperiodic in Taurus. The sample analyzed in this study might be unusual in this sense (only 3 aperiodic and 3 uncertain dippers out of 22 in Table 4); it must be noted that for only 2 of the 12 additional dippers in Table 2 the reported periods are most probably linked to quasiperiodic dips. The predominant periodicity in the light curve for the remainder is caused by cold stellar spots, while the extinction events are stochastic. Only 17 out of the 34 presented dippers are strictly quasiperiodic, which brings the ratio to about 1:1. The periods marked as uncertain in Table 4 are not counted as quasiperiodic here.

5.4. Dip width and period

Previous studies investigated whether dip width, dip amplitude, and/or dip width are correlated for dippers. No such correlation has been found so far (e.g., Bodman et al. 2017), except for the class of short-period narrow dips presented by Stauffer et al. (2015). For dip width and amplitude, a dependence would be a constraint on the geometrical properties of the dusty warp as presented by Bouvier et al. (1999). The amplitude of the eclipses depends not only on the viewing angle, but also on the vertical extent of the dusty material occulting the star. On the other hand, the dip width delivers an estimate of its azimuthal extent.

For our sample of Taurus dippers, the quasiperiodic dippers for which it was possible to derive a reliable width are shown in Fig. 11. The data suggest a logarithmic trend of the dip width and the period, with a high scatter due to the intrinsic variability of dippers. It is remarkable that many dippers are obscured $\geq 50\%$ of the time, suggesting that the azimuthal extent of the dusty structure must be larger than 180° around the star. According to the geometrical constraints of a dusty warp, the observed dip width should grow with the inclination. The inclination values listed in Table 6 are represented in Fig. 11 as a color code of the data points. The amplitude of the dips is proportional to the size of the data points as $2\sqrt{\frac{A}{A_{\min}}}$, where A_{\min} is the smallest amplitude of the sample. No correlation is observed within the inclination and the dip width, nor between inclination and dip amplitude. Toward the higher end of the widths, the dip is often double- or multi-peaked, and its shape and position vary from phase to phase. This is the case for HP Tau, LkCa 15, GI Tau, JH 112 A, HK Tau, and IS Tau (see Sect. 3.4). The large error bars on the dip width for these double- or multi-peaked stars reflect the difference between considering the width of the full occultation and the width of the main dip.

Although the dependence can be best described with a logarithmic curve, the size of the sample is too small to draw a solid conclusion on the nature of the best-fitting curve. It is also possible that two different regimes are present, such as a linear trend for short periods, followed by a plateau for longer periods. The two quantities dip width (W) and the natural logarithm of the period ($\ln P$) are correlated with a Pearson correlation coefficient $r = 0.77$ and a p -value of 2.8×10^{-4} . A logarithmic, rather than linear, trend is expected because the star cannot be eclipsing close to 100% of the time, thus flattening the curve for longer periods. The two stars in the lower left corner are crucial for this correlation, however. EPIC 246989752 and JH 112 A (see Fig. F.1 for the dip width) fall in the category of short-duration quasiperiodic dips (Stauffer et al. 2015), with the interesting case of JH 112 A being a transient dipper. The

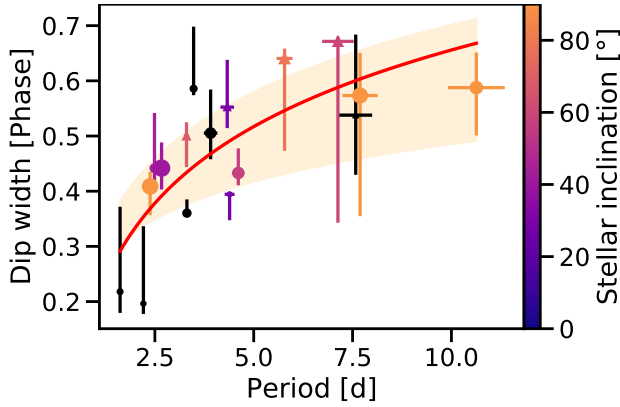


Fig. 11. Dependence of dip width in phase units and period of the quasiperiodic stars in the dipper sample. The error bars on dip width and period correspond to those listed in Table 4. A logarithmic fit $a \log x + b$ is performed just on the data points (red line), and for upper and lower limits of the dip width (orange interval). The double-dipped stars are represented as triangles. The size of the markers is proportional to the square root of the dip amplitude (between 0.05 and 1.3 mag). Two stars for which the dip width derived in this way is not reliable are not represented in this plot. The stellar inclination in degrees is coded as colors of the data points, when available. Although the exact coefficients of the fitting function cannot be constrained from this small sample, W correlates with $\ln P$ with Pearson’s $r = 0.77$. No significant correlation with the dip amplitude can be measured.

derived dip width describes the dip as observed in the folded light curve well. Moreover, the upper error bar is very generous because the binned light curve $+\sigma$ is almost flat. We can therefore exclude that the dip width for these two stars is overestimated. Stauffer et al. (2015) identified a particular class of Gaussian-shaped, narrow, and short-periodic dippers. The definition of “narrow” is set where the ratio of the FWHM of the fit Gaussian and the period is lower than 0.25, while the narrow dippers in NGC 2264 have a FWHM-to-period ratio of 0.15 on average. In Taurus, EPIC 246989752, and JH 112 A would correspond to this category, with a FWHM-to-period ratio of 0.22 and 0.20, respectively. Both exhibit a Gaussian shape. The short-period dippers in NGC 2264 tend to have narrow eclipses for later spectral types (Stauffer et al. 2015). Here, this is true for EPIC 246989752, which is an M dwarf, while JH 112 A has a spectral type of K5.5. We could not find a correlation between dip width and spectral type in the dipper sample.

Another star that can be associated with the population defined by Stauffer et al. (2015) is EPIC 247885481 (Sect. 3.3). It does not appear in Fig. 11 because the width of the dips cannot be constrained reliably in a standardized way. The amplitude is very small compared to the noise, and the dips do not clearly appear in each phase (see Sect. 3.3). The star is an M dwarf and is therefore compatible with the group identified in NGC 2264.

A correlation between R_{cor} and the dip width in units of phase is presented in Fig. 12. Although weaker (Pearson’s $r = 0.63$), a behavior similar to that of Fig. 11 is evident. This is expected because the corotation radius as derived in Eq. (4) is a function of the stellar period. In this case, the correlation is evident even without considering the two data points in the lower left corner, which only argue for a logarithmic instead of a linear dependence.

It is of interest to verify whether this correlation of dip width with period is an implication of existing models and if the observed dip widths are compatible with the mechanisms

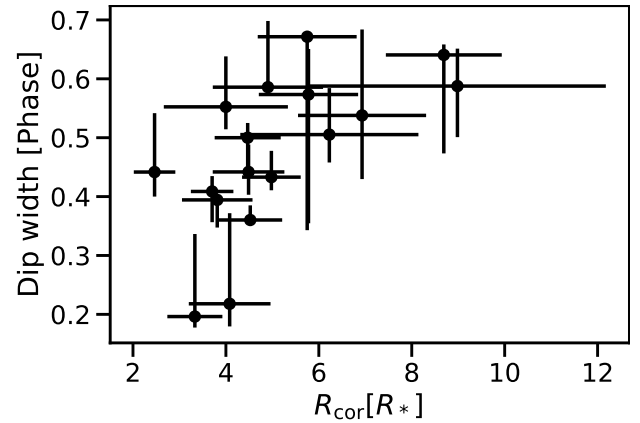


Fig. 12. Dependence of the dip width in units of phase and the corotation radius. Although weaker (Pearson’s $r = 0.63$), a correlation of W and $\ln R_{\text{cor}}$ is also evident here. The lower correlation can be explained by the fact that R_{cor} is a function of both P and M_* .

that have been proposed to explain dippers. In order to generate a quasiperiodic dipper, the most stable configuration of the magnetic field seems to be an inclined dipole in the framework of magnetospheric accretion (Romanova et al. 2013). Two broad, stable, and symmetric matter streams form from the disk and are accreted as funnel flows onto the stellar surface, producing an hotspot in each hemisphere. The observer can see the star obscured either by the dusty warp or even by the funnel flow itself. In this case, the extent of the magnetosphere nearly coincides with the corotation radius, $R_T \approx R_{\text{cor}}$. In case of $R_{\text{cor}} < R_T$, the inner region of the disk rotates with $\omega > \Omega_K$ (where Ω_K is the Keplerian velocity at corotation) and the star is in the propeller regime. The magneto-centrifugal forces lead to the ejection of disk material into an outflow (Romanova & Owocki 2015). During phases of enhanced mass accretion, in which the dipole component of the magnetic field decreases, the disk compresses the magnetosphere and reduces R_T (Romanova et al. 2013). For $R_T < R_{\text{cor}}$, the star is in the accretion regime and the magnetosphere rotates more slowly than the inner disk ($\omega < \Omega_K$). In case of a small or no misalignment between the stellar spin axis and the magnetic moment, the matter from the inner disk accumulates at R_T and the accretion instead occurs through unstable accretion tongues (Romanova et al. 2013), which are taller and thinner than funnel flows that reach the stellar surface close to equator. They can be observable as irregular hotspots in the *UV*. As a result, the light curve is rather stochastic and bursting. An unstable accretion regime has been invoked to explain aperiodic dippers (e.g., McGinnis et al. 2015).

The extent of the corotation radius directly depends on the stellar rotation period. For slow rotators, the corotation radius is located at a larger distance from the star, and the inner disk therefore rotates faster than the star. This facilitates the accretion through instabilities (Romanova et al. 2013; Kulkarni & Romanova 2008).

An observer would expect broad dips to be quasiperiodic because the unstable accretion tongues are rather narrow and tall and would not be able to obscure the star for a significant fraction of time (Romanova et al. 2008). The aperiodic dippers observed in Taurus indeed exhibit rather narrow dips in their light curves.

The quasiperiods observed in dippers might also be linked to a configuration in the accretion regime. In this case, trapped density waves in the inner disk can produce a warp that rotates more slowly than the star and beyond the corotation radius, with

a period that might vary over time. In this case, the simulations show that the inner disk is tilted and also rotates more slowly (Romanova et al. 2013). This could explain the changing, rather long period observed in the WPS of the K2 light curve of DK Tau, which is associated with an outer disk seen at low inclination. However, this would not suffice to explain why the star is obscured in the first part of the light curve. The slowly rotating warp should also have a smaller height than a fast-rotating warp, and DK Tau has an amplitude of 1 mag.

A correlation of period and dip width thus suggests that slow rotators are more probably occulted by more azimuthally extended dusty structures. This aspect has not been directly considered in simulations to date. In the scenario of magnetospheric accretion, this might imply a broader funnel flow for slow rotators.

For T Tauri stars of late spectral type, the internal structure is either fully convective or has small radiative cores (Gregory et al. 2012). The HR diagram of Taurus dippers shows that with the exception of LkCa 15, all stars are on their Hayashi tracks and fully convective. In this case, the magnetic field is expected to be axisymmetric and the dipole component dominates, as is the case for AA Tau.

Vidotto et al. (2014) found a correlation of magnetic flux and rotation period for accreting PMS stars. This implies that stars with a simple magnetic field (i.e., dipole) and with the strongest magnetic fields are also the slowest rotators and truncate the disk at larger distances R_T . The star-disk interaction therefore affects the magnetic field, which in turn affects the stellar rotation. We speculate that the large-scale magnetic field topology might cause the correlation of dip width and period. A stronger magnetic field might have a stabilizing effect on a large warp.

6. Conclusion

We have studied a sample of 179 YSOs in Taurus, which are members or possible members of the cluster (Rebull et al. 2020). We identify a total of 34 dippers, 22 of which are dippers not dominated by another type of variability. This makes up $\sim 20\%$ of the high-confidence and possible Taurus members and $\sim 30\%$ of the disk-bearing Taurus members as observed with K2.

The observations in Taurus highlight again how ephemeral dippers are. A striking example is the dipper prototype AA Tau, which is now in a fainter state and is no longer classified as a quasiperiodic, prototypical dipper. Dipper light curves can persist over timescales of a few years or even a few days. This strongly suggests that the observed occurrence rates are a lower limit to their true occurrence among CTTs.

The ratio of quasiperiodic to aperiodic dippers is 1:1, although most of the dippers studied in detail are quasiperiodic. The large majority of aperiodic dippers observed in Taurus is dominated by another type of variability, mainly that due to cold spots. As found in other surveys, dipper stars are of late spectral type K or M because the lower surface temperature allows dust to survive in the inner disk and create the dips. The dipper stars of the sample are fully convective, low-mass ($< 1 M_\odot$) stars down to the brown dwarf limit, with the presence of a probable debris disk dipper.

Supporting previous dipper surveys, the observed periods are in the range of the rotation periods of low-mass CTTs. In the sample, a transient period, a changing period, and a dipper period very close to the period of a stellar spot are also identified. The temperatures derived at corotation are also compatible with dust survival, and the mass accretion rates are typical for CTTs.

Many of the dippers for which it was possible to derive a stellar inclination are seen at a rather moderate inclination angle, and the outer disk inclination is, when available, slightly lower than the stellar inclination. Whether the stellar inclination is systematically higher than the outer disk inclination cannot be constrained accurately in this small sample, but it would be consistent with recently observed stars with a tilted inner disk.

Magnetospheric accretion is able to explain most but not all Taurus dippers. However, dusty disk winds and Rossby wave instabilities do not seem convincing as explanations for the dippers seen at low inclination in this sample.

A fraction of the quasiperiodic dippers exhibits double or complex dips, whose structure varies with time and whose minima are shifted from one cycle to the next. These examples are worth exploring in a future more precise dynamical analysis.

Finally, a correlation is found between the dip width in units of phase (i.e., the equivalent of the angular extent of the occulting structure) and the rotational period of the dippers. We speculate that this might indicate that the accretion columns of more slowly rotating stars have a larger base, possibly reflecting a different magnetic topology. This dependence needs to be investigated for dippers in other clusters in future work.

Acknowledgements. We wish to thank the anonymous referee for constructive comments which have improved the clarity of this paper, and Didier Fraix-Burnet and Gérard Grégoire for the helpful discussions. This project has received funding from the European Research Council (ERC) under the European Union's Horizon 2020 research and innovation programme (grant agreement No 742095; SPIDI: Star-Planets-Inner Disk-Interactions). Some of the data presented in this paper were obtained from the Mikulski Archive for Space Telescopes (MAST). Support for MAST for non-HST data is provided by the NASA Office of Space Science via grant NNX09AF08G and by other grants and contracts. This research has made use of data products from the Two Micron All-Sky Survey (2MASS), which is a joint project of the University of Massachusetts and the Infrared Processing and Analysis Center, funded by the National Aeronautics and Space Administration and the National Science Foundation. The 2MASS data are served by the NASA/IPAC Infrared Science Archive, which is operated by the Jet Propulsion Laboratory, California Institute of Technology, under contract with the National Aeronautics and Space Administration. This work has made use of data from the European Space Agency (ESA) mission *Gaia* (<https://www.cosmos.esa.int/gaia>), processed by the *Gaia* Data Processing and Analysis Consortium (DPAC, <https://www.cosmos.esa.int/web/gaia/dpac/consortium>). Funding for the DPAC has been provided by national institutions, in particular the institutions participating in the *Gaia* Multilateral Agreement.

References

- Akeson, R. L., & Jensen, E. L. N. 2014, *ApJ*, 784, 62
- Akeson, R. L., Jensen, E. L. N., Carpenter, J., et al. 2019, *ApJ*, 872, 158
- Alencar, S. H. P., Teixeira, P. S., Guimarães, M. M., et al. 2010, *A&A*, 519, A88
- Alencar, S. H. P., Bouvier, J., Donati, J. F., et al. 2018, *A&A*, 620, A195
- Ansdell, M., Gaidos, E., Rappaport, S. A., et al. 2016a, *ApJ*, 816, 69
- Ansdell, M., Gaidos, E., Williams, J. P., et al. 2016b, *MNRAS*, 462, L101
- Ansdell, M., Gaidos, E., Hedges, C., et al. 2020, *MNRAS*, 492, 572
- Appenzeller, I., & Bertout, C. 2013, *A&A*, 558, A83
- Artemenko, S. A., Grankin, K. N., & Petrov, P. P. 2012, *Astron. Lett.*, 38, 783
- Bans, A., & Königl, A. 2012, *ApJ*, 758, 100
- Baraffe, I., Homeier, D., Allard, F., & Chabrier, G. 2015, *A&A*, 577, A42
- Bertout, C., Basri, G., & Bouvier, J. 1988, *ApJ*, 330, 350
- Bodman, E. H. L., Quillen, A. C., Ansdell, M., et al. 2017, *MNRAS*, 470, 202
- Borucki, W. J., Koch, D., Basri, G., et al. 2010, *Science*, 327, 977
- Bouvier, J., Chelli, A., Allain, S., et al. 1999, *A&A*, 349, 619
- Bouvier, J., Grankin, K. N., Alencar, S. H. P., et al. 2003, *A&A*, 409, 169
- Bouvier, J., Alencar, S. H. P., Bouvier, T., et al. 2007, *A&A*, 463, 1017
- Bravo, J. P., Roque, S., Estrela, R., Leão, I. C., & De Medeiros, J. R. 2014, *A&A*, 568, A34
- Camenzind, M. 1990, *Rev. Mod. Astron.*, 3, 234
- Cardelli, J. A., Clayton, G. C., & Mathis, J. S. 1989, *ApJ*, 345, 245
- Cody, A. M., & Hillenbrand, L. A. 2018, *AJ*, 156, 71
- Cody, A. M., Stauffer, J., Baglin, A., et al. 2014, *AJ*, 147, 82
- Dahm, S. E., & Lyke, J. E. 2011, *PASP*, 123, 1383

- Davies, C. L., Gregory, S. G., & Greaves, J. S. 2014, *MNRAS*, **444**, 1157
- Donati, J. F., Bouvier, J., Alencar, S. H., et al. 2019, *MNRAS*, **483**, L1
- Drake, A. J., Graham, M. J., Djorgovski, S. G., et al. 2014, *ApJS*, **213**, 9
- Duchêne, G., Monin, J. L., Bouvier, J., & Ménard, F. 1999, *A&A*, **351**, 954
- Esplin, T. L., & Luhman, K. L. 2019, *AJ*, **158**, 54
- Esplin, T. L., Luhman, K. L., & Mamajek, E. E. 2014, *ApJ*, **784**, 126
- Facchini, S., Lodato, G., & Price, D. J. 2013, *MNRAS*, **433**, 2142
- Facchini, S., Juhász, A., & Lodato, G. 2018, *MNRAS*, **473**, 4459
- Fleming, G. D., Kirk, J. M., Ward-Thompson, D., & Pattle, K. 2019, *ApJ*, submitted [arXiv:1904.06980]
- Franchini, A., Lubow, S. H., & Martin, R. G. 2019, *ApJ*, **880**, L18
- Gaia Collaboration (Prusti, T., et al.) 2016, *A&A*, **595**, A1
- Gaia Collaboration (Brown, A. G. A., et al.) 2018, *A&A*, **616**, A1
- Gaidos, E., Jacobs, T., LaCourse, D., et al. 2019, *MNRAS*, **488**, 4465
- Galli, P. A. B., Loinard, L., Ortiz-Léon, G. N., et al. 2018, *ApJ*, **859**, 33
- García, R. A., Ceillier, T., Salabert, D., et al. 2014, *A&A*, **572**, A34
- Grankin, K. N., Melnikov, S. Y., Bouvier, J., Herbst, W., & Shevchenko, V. S. 2007, *A&A*, **461**, 183
- Gregory, S. G., Jardine, M., Simpson, I., & Donati, J. F. 2006, *MNRAS*, **371**, 999
- Gregory, S. G., Donati, J. F., Morin, J., et al. 2012, *ApJ*, **755**, 97
- Grossmann, A., & Morlet, J. 1984, *SIAM J. Math. Anal.*, **15**, 723
- Güdel, M., Briggs, K. R., Arzner, K., et al. 2007, *A&A*, **468**, 353
- Guieu, S., Pinte, C., Monin, J. L., et al. 2007, *A&A*, **465**, 855
- Gullbring, E., Hartmann, L., Briceño, C., & Calvet, N. 1998, *ApJ*, **492**, 323
- Guo, Z., Herczeg, G. J., Jose, J., et al. 2018, *ApJ*, **852**, 56
- Haas, M. R., Batalha, N. M., Bryson, S. T., et al. 2010, *ApJ*, **713**, L115
- Harris, R. J., Andrews, S. M., Wilner, D. J., & Kraus, A. L. 2012, *ApJ*, **751**, 115
- Hartigan, P., & Kenyon, S. J. 2003, *ApJ*, **583**, 334
- Hartmann, L., & Stauffer, J. R. 1989, *AJ*, **97**, 873
- Hartmann, L., Hewett, R., Stahler, S., & Mathieu, R. D. 1986, *ApJ*, **309**, 275
- Hartmann, L., Hewett, R., & Calvet, N. 1994, *ApJ*, **426**, 669
- Hartmann, L., Calvet, N., Gullbring, E., & D'Alessio, P. 1998, *ApJ*, **495**, 385
- Hartmann, L., Calvet, N., Watson, D. M., et al. 2005, *ApJ*, **628**, L147
- Hedges, C., Hodgkin, S., & Kennedy, G. 2018, *MNRAS*, **476**, 2968
- Henden, A. A., Templeton, M., Terrell, D., et al. 2016, *VizieR Online Data Catalog*: II/336
- Herbst, W., Herbst, D. K., Grossman, E. J., & Weinstein, D. 1994, *AJ*, **108**, 1906
- Herczeg, G. J., & Hillenbrand, L. A. 2008, *ApJ*, **681**, 594
- Herczeg, G. J., & Hillenbrand, L. A. 2014, *ApJ*, **786**, 97
- Howell, S. B., Sobeck, C., Haas, M., et al. 2014, *PASP*, **126**, 398
- Isella, A., & Natta, A. 2005, *A&A*, **438**, 899
- Isella, A., Carpenter, J. M., & Sargent, A. I. 2009, *ApJ*, **701**, 260
- Itoh, Y., Fukagawa, M., Shibai, H., Sumi, T., & Yamamoto, K. 2015, *PASJ*, **67**, 88
- Kenyon, S. J., & Hartmann, L. 1995, *ApJS*, **101**, 117
- Kenyon, S. J., Gómez, M., & Whitney, B. A. 2008, *Low Mass Star Formation in the Taurus-Auriga Clouds*, eds. B. Reipurth (USA: ASP Press), 4, 405
- Kobayashi, H., Kimura, H., Watanabe, S. i., Yamamoto, T., & Müller, S. 2011, *Earth Planets Space*, **63**, 1067
- Koenigl, A. 1991, *ApJ*, **370**, L39
- Kraus, A. L., & Hillenbrand, L. A. 2009, *ApJ*, **703**, 1511
- Kraus, A. L., Ireland, M. J., Martinache, F., & Hillenbrand, L. A. 2011, *ApJ*, **731**, 8
- Kraus, A. L., Ireland, M. J., Hillenbrand, L. A., & Martinache, F. 2012, *ApJ*, **745**, 19
- Kraus, A. L., Herczeg, G. J., Rizzuto, A. C., et al. 2017, *ApJ*, **838**, 150
- Kulkarni, A. K., & Romanova, M. M. 2008, *MNRAS*, **386**, 673
- Kurosawa, R., Harries, T. J., & Symington, N. H. 2006, *MNRAS*, **370**, 580
- Labdon, A., Kraus, S., Davies, C. L., et al. 2019, *A&A*, **627**, A36
- Lai, D. 1999, *ApJ*, **524**, 1030
- Lasker, B. M., Lattanzi, M. G., McLean, B. J., et al. 2008, *AJ*, **136**, 735
- Lima, G. H. R. A., Alencar, S. H. P., Calvet, N., Hartmann, L., & Muzerolle, J. 2010, *A&A*, **522**, A104
- Lomb, N. R. 1976, *Ap&SS*, **39**, 447
- Long, F., Herczeg, G. J., Harsono, D., et al. 2019, *ApJ*, **882**, 49
- Luger, R., Agol, E., Kruse, E., et al. 2016, *AJ*, **152**, 100
- Luhman, K. L. 2018, *AJ*, **156**, 271
- Luhman, K. L., Mamajek, E. E., Shukla, S. J., & Loutrel, N. P. 2017, *AJ*, **153**, 46
- Lynden-Bell, D., & Pringle, J. E. 1974, *MNRAS*, **168**, 603
- Mathur, S., García, R. A., Ballot, J., et al. 2014, *A&A*, **562**, A124
- Mayne, N. J., Harries, T. J., Rowe, J., & Acreman, D. M. 2012, *MNRAS*, **423**, 1775
- McGinnis, P. T., Alencar, S. H. P., Guimarães, M. M., et al. 2015, *A&A*, **577**, A11
- Miyake, T., Suzuki, T. K., & Inutsuka, S.-i. 2016, *ApJ*, **821**, 3
- Mohanty, S., Basri, G., & Jayawardhana, R. 2005, *Astron. Nachr.*, **326**, 891
- Morales-Calderón, M., Stauffer, J. R., Hillenbrand, L. A., et al. 2011, *ApJ*, **733**, 50
- Muzerolle, J., Hartmann, L., & Calvet, N. 1998, *AJ*, **116**, 2965
- Muzerolle, J., Calvet, N., & Hartmann, L. 2001, *ApJ*, **550**, 944
- Nagel, E., & Bouvier, J. 2020, *A&A*, **643**, A157
- Nesterov, V. V., Kuzmin, A. V., Ashimbaeva, N. T., et al. 1995, *A&AS*, **110**, 367
- Nguyen, D. C., Brandeker, A., van Kerkwijk, M. H., & Jayawardhana, R. 2012, *ApJ*, **745**, 119
- Pecaut, M. J., & Mamajek, E. E. 2013, *ApJS*, **208**, 9
- Percy, J. R., Grynko, S., Seneviratne, R., & Herbst, W. 2010, *PASP*, **122**, 753
- Pollack, J. B., Hollenbach, D., Beckwith, S., et al. 1994, *ApJ*, **421**, 615
- Rebull, L. M., Wolff, S. C., & Strom, S. E. 2004, *AJ*, **127**, 1029
- Rebull, L. M., Stauffer, J. R., Bouvier, J., et al. 2016, *AJ*, **152**, 113
- Rebull, L. M., Stauffer, J. R., Hillenbrand, L. A., et al. 2017, *ApJ*, **839**, 92
- Rebull, L. M., Stauffer, J. R., Cody, A. M., et al. 2018, *AJ*, **155**, 196
- Rebull, L. M., Stauffer, J. R., Cody, A. M., et al. 2020, *AJ*, **159**, 273
- Rigliaco, E., Pascucci, I., Duchene, G., et al. 2015, *ApJ*, **801**, 31
- Roberts, D. H., Lehar, J., & Dreher, J. W. 1987, *AJ*, **93**, 968
- Rodriguez, J. E., Ansdell, M., Oelkers, R. J., et al. 2017, *ApJ*, **848**, 97
- Romanova, M. M., & Owocki, S. P. 2015, *Space Sci. Rev.*, **191**, 339
- Romanova, M. M., Kulkarni, A. K., & Lovelace, R. V. E. 2008, *ApJ*, **673**, L171
- Romanova, M. M., Ustyugova, G. V., Koldoba, A. V., & Lovelace, R. V. E. 2013, *MNRAS*, **430**, 699
- Scargle, J. D. 1982, *ApJ*, **263**, 835
- Schaefer, G. H., Prato, L., Simon, M., & Zavala, R. T. 2012, *ApJ*, **756**, 120
- Schaefer, G. H., Prato, L., Simon, M., & Patience, J. 2014, *AJ*, **147**, 157
- Scholz, A., Moore, K., Jayawardhana, R., et al. 2018, *ApJ*, **859**, 153
- Shu, F., Najita, J., Ostriker, E., et al. 1994, *ApJ*, **429**, 781
- Sicilia-Aguilar, A., Manara, C. F., de Boer, J., et al. 2020, *A&A*, **633**, A37
- Simon, M., Guilloteau, S., Di Folco, E., et al. 2017, *ApJ*, **844**, 158
- Skrutskie, M. F., Cutri, R. M., Stiening, R., et al. 2006, *AJ*, **131**, 1163
- Stauffer, J., Cody, A. M., Baglin, A., et al. 2014, *AJ*, **147**, 83
- Stauffer, J., Cody, A. M., McGinnis, P., et al. 2015, *AJ*, **149**, 130
- Strom, K. M., Strom, S. E., Kenyon, S. J., & Hartmann, L. 1988, *AJ*, **95**, 534
- Strom, K. M., Strom, S. E., Edwards, S., Cabrit, S., & Skrutskie, M. F. 1989, *AJ*, **97**, 1451
- Tajiri, T., Kawahara, H., Aizawa, M., et al. 2020, *ApJS*, **251**, 18
- Tambovtseva, L. V., & Grinin, V. P. 2008, *Astron. Lett.*, **34**, 231
- Tannirkulam, A., Harries, T. J., & Monnier, J. D. 2007, *ApJ*, **661**, 374
- Terquem, C., & Papaloizou, J. C. B. 2000, *A&A*, **360**, 1031
- Thalman, C., Mulders, G. D., Hodapp, K., et al. 2014, *A&A*, **566**, A51
- Torrence, C., & Compo, G. P. 1998, *Bull. Am. Meteorol. Soc.*, **79**, 61
- van der Marel, N., van Dishoeck, E. F., Bruderer, S., Pérez, L., & Isella, A. 2015, *A&A*, **579**, A106
- Vanderburg, A., & Johnson, J. A. 2014, *PASP*, **126**, 948
- Vidotto, A. A., Gregory, S. G., Jardine, M., et al. 2014, *MNRAS*, **441**, 2361
- Vinković, D., & Čemeljić, M. 2021, *MNRAS*, **500**, 506
- Watson, D. M., Leisenring, J. M., Furlan, E., et al. 2009, *ApJS*, **180**, 84
- White, R. J., & Basri, G. 2003, *ApJ*, **582**, 1109
- White, R. J., & Ghez, A. M. 2001, *ApJ*, **556**, 265
- White, R. J., & Hillenbrand, L. A. 2004, *ApJ*, **616**, 998
- White, R. J., & Hillenbrand, L. A. 2005, *ApJ*, **621**, L65
- Xiao, H. Y., Covey, K. R., Rebull, L., et al. 2012, *ApJS*, **202**, 7
- Zacharias, N., Monet, D. G., Levine, S. E., et al. 2005, *VizieR Online Data Catalog*: I/297

Appendix A: Wavelets

The Fourier transform (FT) is an extension of the Fourier series, which expresses periodic functions as sums of sinusoids. It decomposes the signal in the frequency domain, and its power spectrum represents each frequency that is present in the original signal. Fourier analysis requires (nearly) evenly sampled data as a condition. Fourier analysis is not able to provide information about the time localization of a given frequency because it has no time resolution in the frequency domain. This is because the sinusoids employed to transform the signal are infinite in time, thus the time information is lost, and only the frequencies are retrieved.

The windowed Fourier transform can help in solving this issue by considering a window (i.e., a slice) of the signal f and transforming only that section, then translating the window along the signal. Given the window $g(t)$, the windowed signal is defined as

$$f_t(s) \equiv g(s - t)f(s). \quad (\text{A.1})$$

Its Fourier transform becomes

$$\mathcal{F}f(\omega, t) = \hat{f}_t(\omega) = \int_{-\infty}^{\infty} ds f_t(s) e^{-i\omega s} = \int_{-\infty}^{\infty} ds f(s) g(s - t) e^{-i\omega s}. \quad (\text{A.2})$$

In physics, $g(t)$ is commonly chosen to be a Gaussian. The window is multiplied with a chop of the signal, transformed separately, and then shifted along the signal. If g is centered in time and frequency, $\hat{f}_t(\omega)$ corresponds to the information of f around time t and frequency ω . The WFT underlies the uncertainty principle: the lower bound for the product of time and frequency resolution is

$$\Delta f \cdot \Delta \tau \geq \frac{1}{4\pi}. \quad (\text{A.3})$$

For this method, the quality of the resulting analysis strongly depends on the chosen size τ of the window function. This determines the time and the frequency resolution a priori and might be inconvenient if both a good time and good frequency resolution are required.

The windowed Fourier transform is constrained by the fixed size of the window, while the Fourier transform delivers no time resolution at all. This issue can be solved by wavelets, by adapting the time-width of the window to the frequency that is to be investigated,

$$\text{CWT}_f(s, \tau) = \frac{1}{\sqrt{s}} \int_{-\infty}^{\infty} f(t) \psi^* \left(\frac{t - \tau}{s} \right) dt, \quad (\text{A.4})$$

where CWT is the continuous wavelet transform. The mother wavelet $\psi(t)$ is in most cases a sinusoidal wave confined in time, stretched and compressed according to the scale s and shifted with a time step τ along the time series. The normalization factor $\frac{1}{\sqrt{s}}$ ensures that the transformed signal has the same energy at each scale. The 2-dimensional wavelet power spectrum (WPS) is produced by a convolution between the wavelet and the signal, which is recomputed for each scale along the time series.

The varying size of the wavelet allows us to identify both high- and low-frequency features in the signal. Both the dis-

crete (DWT) and continuous wavelet transform (CWT) exist; here only the CWT is presented. As for the WFT, the wavelet transform is subject to the uncertainty principle. Based on its shape, a certain wavelet has either a higher time or frequency resolution. Being confined in the time domain results in a broader peak in the frequency domain, which would be a δ -function in the case of the sinusoid of the FT. The complex Morlet wavelet is a good compromise in this respect; moreover, its form is similar to the sought-for signal.

The complex Morlet wavelet used in this work is defined as a superposition of a complex wave and a Gaussian, such as

$$\psi(x) = \frac{1}{\sqrt{\pi T_b}} e^{-\frac{x^2}{T_b}} e^{i2\pi F_c x}, \quad (\text{A.5})$$

where the parameters F_c and T_b are the central frequency and the bandwidth parameter, respectively, and x is a unitless time parameter. This formulation differs from that in [Torrence & Compo \(1998\)](#), as they assumed a Gaussian with unit variance, which can be varied here, and a frequency $\omega_0 = 6$. The advantage of freely setting the bandwidth and the central frequency is that we can customize the time and frequency resolution of the resulting wavelet plot, in order to highlight the position of a periodicity or to focus on the frequencies. A broader Gaussian in the time domain, thus a lower time resolution, is represented by a narrower peak in the frequency domain, translating into higher frequency resolution.

Increasing the bandwidth T_b , that is, the width of the Gaussian, in the time domain decreases the bandwidth in the Fourier domain, that is, delivers a higher frequency resolution by losing time resolution. The central frequency should be close to the frequency of the signal of interest. In order to create an atlas of K2 light curves, the parameters were set to $F_c = 1.0$ and $T_b = 1.5$ as default. For individual cases of interest, these parameters may be changed. In the WPS, a certain scale s corresponds to a frequency F_s as

$$F_s = \frac{F_c}{s \cdot dt}. \quad (\text{A.6})$$

The set of scales of the wavelet transform is equivalent to the custom frequency resolution of a periodogram. They can be set linearly to extend from s_0 to s_{\max} , where s_{\max} corresponds to the longest period of interest according to Eq. (A.6). For a faster and more efficient computation of the WPS, it is better to choose the set of scales according to a power law,

$$s = s_0 2^{j\delta j}, \quad j = 0, 1, \dots, J, \quad \delta j = \frac{\log_2 s_{\max}}{J}. \quad (\text{A.7})$$

Here J is the total number of scales and s_0 should be chosen close to $2dt$.

The cone of influence (COI) defines the range within which the WPS is affected by edge effects, which grow with the scale, as the wavelet is more and more stretched in time. The power spectrum contained in this region should not be regarded as significant. Considering that for the Morlet wavelet the Fourier period λ is almost equivalent to the scale, as $\lambda = 1.03s$ ([Torrence & Compo 1998](#)), the COI is plotted as $\sqrt{2}p$, where p is the period corresponding to a frequency. A central frequency different than 1.0 affects the COI as $\sqrt{2}pF_c$.

Appendix B: Light curves of the dipper sample

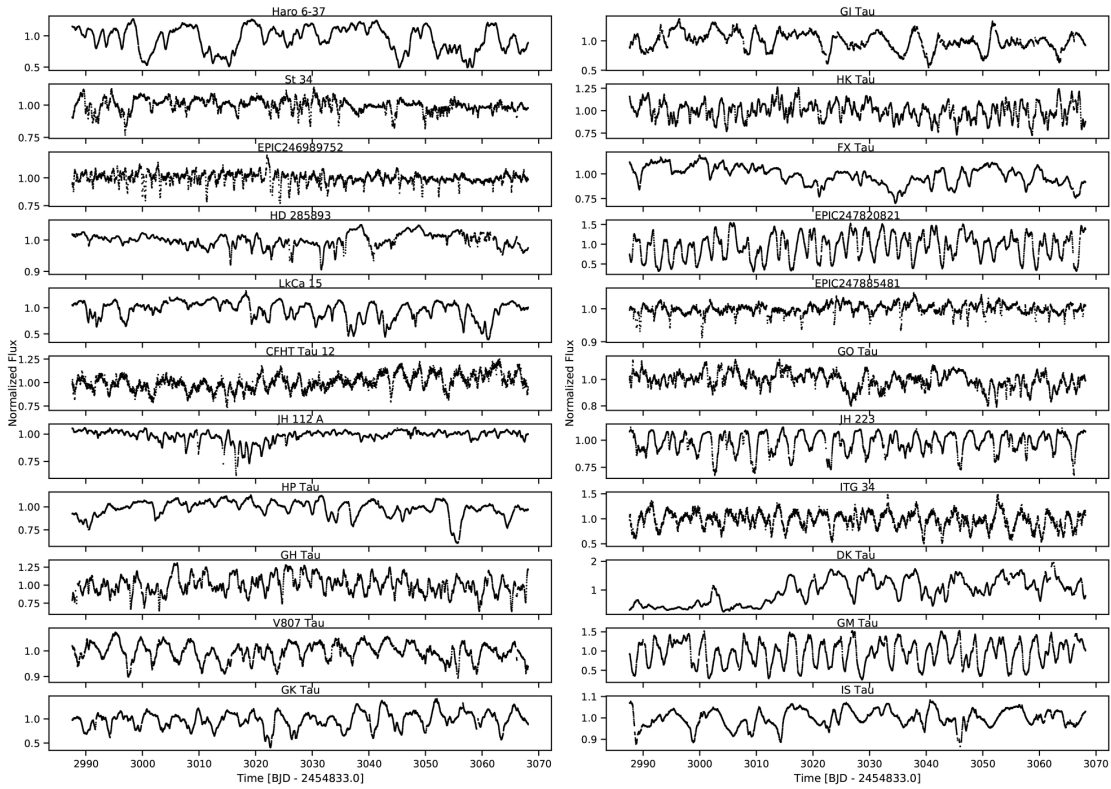


Fig. B.1. Light curves for the dipper sample.

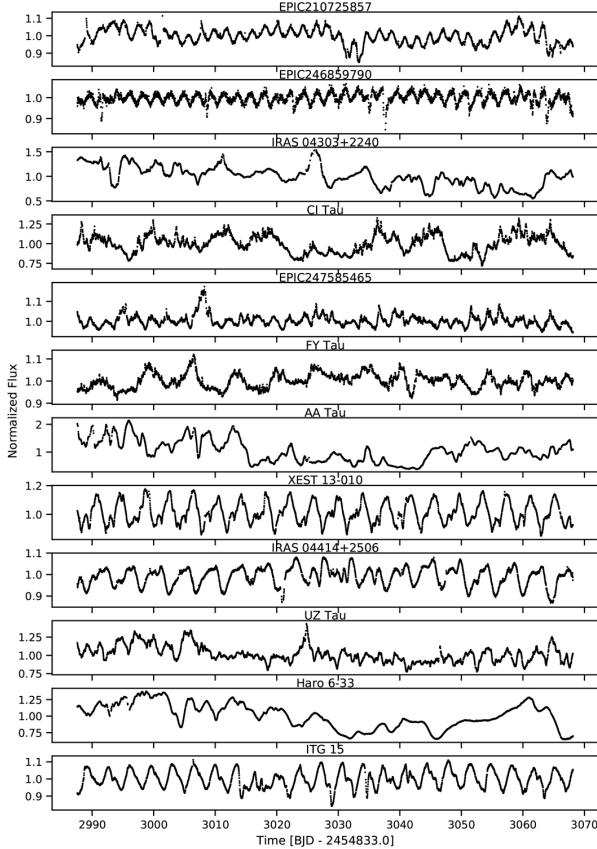


Fig. B.2. Light curves of the additional 12 dippers with another dominant variability in addition to the dips.

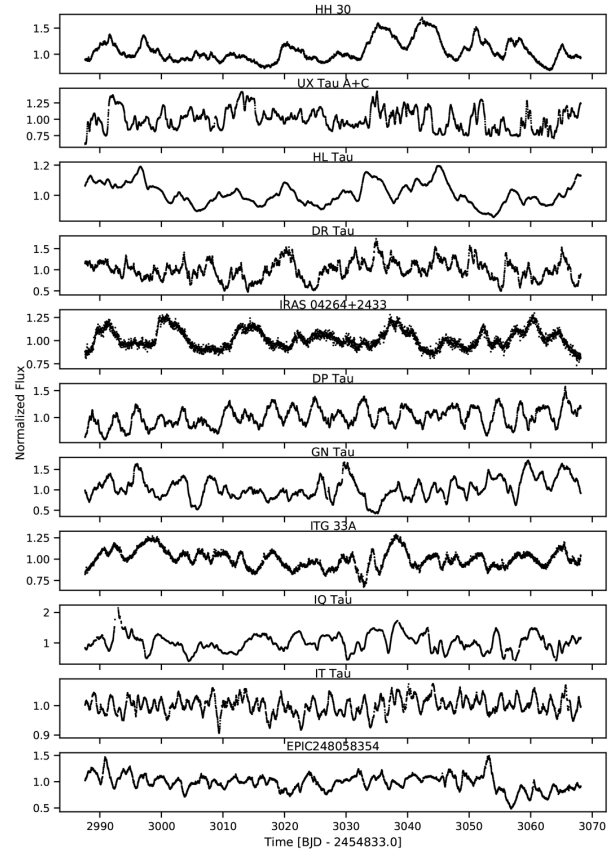


Fig. B.3. Light curves of the 11 low-quality dipper candidates.

Appendix C: Extinction

Table C.1. A_V as measured with $V - J$ compared to the literature.

EPIC	Name	A_V ($V - J$)	r_{7510} ^(a)	A_V ^(a)	A_V ^(b)	A_V ^(c)	A_V ^(d)	A_V ^(e)	A_V ^(f)	A_V ^(g)	A_V ^(h)	A_V ⁽ⁱ⁾	A_V ^(j)	σ_{A_V}
246929818	Haro 6-37	...	0.33	2.05	1.8	...	2.12	2.44	2.1	0.3
246942563	St 34	0.04	0.14	0.5	0.24	0.3 ⁽¹⁾	0.5	0.3
246989752	0.0	0.0	0.3
247103541	HD 285893	0.32	0.3	0.3
247520207	LkCa 15	0.62	0.04	0.3	0.62	0.5	0.3
247575958	CFHT Tau 12	2.64	...	3.44 ⁽²⁾	3.0	0.6
247589612	JH 112 A	2.31	0.0	3.15	3.23	...	2.97	2.9	0.4
247592463	HP Tau	2.81	0.16	3.15	2.3	...	2.26	3.08	3.2	0.3
247763883	GH Tau	0.23	0.0	0.4	0.7	...	0.52	0.25	0.4	0.2
247764745	V807 Tau	0.57	0.05	0.5	2.87 ^(*)	0.03 ⁽³⁾	0.4	0.3
247791801	GK Tau	1.28	0.08	1.35	0.9	0.94	0.87	0.78	1.0	0.2
247792225	GI Tau	1.28	0.04	2.05	0.9	1.34	0.87	1.33	1.3	0.4
247799571	HK Tau	1.95	0.1	2.4	...	2.32	...	3.38	2.4	0.3
247805410	FX Tau	0.50	0.06	0.8	1.1	...	1.08	1.49	1.0	0.4
247820821	...	-1.35	0.0	0.0
247885481	...	-0.43	0.0	0.0	0.0
247935061	GO Tau	0.05 ^(*)	0.09	1.5	1.2	...	1.18	2.44	1.6	0.9
248006676	JH 223	1.59	0.0	1.2	1.4	0.3
248015397	ITG 34	2.6	...	1.77 ⁽²⁾	2.2	0.6
248029373	DK Tau	1.47	0.27	0.7	0.8	1.42	0.76	1.4	0.7	0.3
248046139	GM Tau	-0.28	0.26	2.1	3.54	...	4.34 ⁽²⁾	2.1	0.3
248047443	IS Tau	2.24	0.02	2.55	2.4	0.3

Notes. Only the extinction measured by [Luhman et al. \(2017\)](#) with optical or CTTS methods is reported here. The veiling is measured at 7510 Å by [Herczeg & Hillenbrand \(2014\)](#). ^(*)Value discarded because it is inconsistent with the literature.

References. (a) [Herczeg & Hillenbrand \(2014\)](#); (b) [Strom et al. \(1988\)](#); (c) [Gullbring et al. \(1998\)](#); (d) [Kenyon & Hartmann \(1995\)](#); (e) [Strom et al. \(1989\)](#); (f) [Luhman et al. \(2017\)](#); (g) [Mayne et al. \(2012\)](#); (h) [White & Hillenbrand \(2005\)](#); (i) other refs; (j) this paper; (1) [Hartmann et al. \(2005\)](#); (2) [Guieu et al. \(2007\)](#); (3) [Schaefer et al. \(2012\)](#).

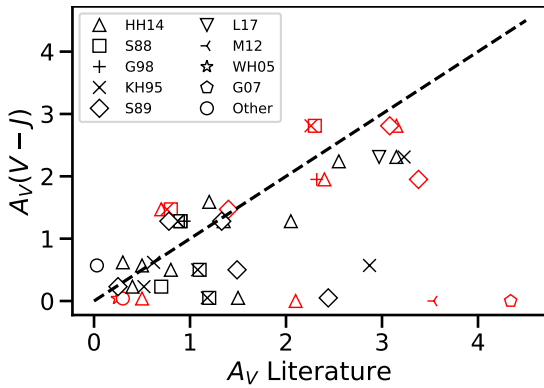


Fig. C.1. Comparison of the A_V derived here from the $(V - J)$ colors compared to the literature values derived also from the optical. References appear in Table C.1. Red points show stars with high veiling. For these, the spectroscopic measurement by [Herczeg & Hillenbrand \(2014\)](#) is preferred. The dashed line represents $A_V(V - J) = A_V(\text{lit})$. The stars with the largest scatter are strongly veiled, and the extinction measured with photometry is less reliable. For GO Tau (four black symbols at the bottom, close to $A_V(V - J) = 0$), the $A_V(V - J)$ value is discarded because it is inconsistent with the literature. Another outlier is the A_V of V807 Tau as measured by KH95; this value is discarded for the same reason.

Table C.1 presents the extinction values computed from $(V - J)$ compared with different A_V from the literature. Using $(J - K)$ leads to an increase in A_V up to a factor 5 because of the infrared excess. The uncertainty on A_V is set as the root-mean-square (rms) of the A_V derived in this study compared with the literature. A minimum reasonable uncertainty of 0.3 mag is applied. Empirically, the uncertainty does not grow with extinction. Figure C.1 shows that veiling affects the derivation of

the extinction from photometry. For stars not affected by veiling, the A_V computed from $(V - J)$ is consistent with optical measurements in the literature.

Appendix D: Notes on individual objects

In the following section, remarks about individual objects are presented. Three stars (St 34, HD 285893, and 2MASSJ05023985+2459337) are possible Taurus members ([Rebull et al. 2020](#)).

HD 285893. According to the HR diagram, the star lies almost on the ZAMS, which means that it is much older than the Taurus population. There are several possibilities to explain this. The star might not be a Taurus member (it is considered a possible member), the spectral type might not be correctly estimated, and/or the star might be seen edge-on, thus its luminosity would be strongly underestimated. The star shows a clear dipper behavior in the light curve, which is unexpected for a spectral type F8 because the higher temperature of the star depletes the inner disk of dust at distances much larger than corotation. The object is poorly studied in the literature and does not appear in more recent spectroscopic surveys. Its behavior appears to be related to the so-called ‘old’ dippers, which can host a debris disk and whose occultations might be caused by disrupting planetesimals ([Gaidos et al. 2019](#); [Tajiri et al. 2020](#)). The dips are narrow, as is commonly the case for aperiodic dippers. The light curve continuum is unstable and aperiodic.

CFHT Tau 12. No binary information has been reported for this star. The star is quasiperiodic (period agrees with [Scholz et al. 2018](#)), but there is no information about $v \sin i$ from which we could derive an inclination. The light curve never reaches a continuum, and no periodicity for this variation can be

derived within the time window of the observations. The shape of the dips clearly distinguishes the dipper phenomenon from spots. The folded light curve is noisy.

2MASSJ04384725+1737260. No companion is known in the literature. The star never clearly reaches the continuum; the periodicity is pretty clear, but some dips seem to be aperiodic (see folded light curve in Fig. F.1). There might also be one or more spots.

2MASSJ04295950+2433078. No binarity is known (Davies et al. 2014). It has a high variability amplitude (0.66 mag). The sinusoidal pattern of the light curve looks rather spot-like, but the star is classified as a dipper based on the irregular shape of the dips. The WPS shows a significant periodicity at ~ 7.5 d, which is much weaker in the periodogram. This might be due to the shape of the light curve, which is well-matched to the Morlet wavelet and is therefore highly correlated. Folded at 7 d, a periodic pattern of several dips appears. A harmonic is excluded.

2MASSJ05023985+2459337. No companion is known in the literature. The light curve exhibits both a spot and a dipper pattern. A dedicated discussion is presented in Sect. 3.3.

ITG 34. is known to be single (Davies et al. 2014; Akeson et al. 2019). The amplitude of the dips is large (0.39 mag). According to the light curve, the star either almost never reaches the continuum level or a few bursts occur during the K2 campaign. The periodogram shows two double-peaked periodicities. The main periodicity is also more stable over time according to the WPS. The second periodicity cannot be a harmonic of the first. The folded light curve is noisy, and no new features emerge when it is folded at a different period. The apparent beat cannot be explained with binarity.

JH 223. is the best example of a quasiperiodic dipper in the sample. The star is a binary with a separation of $2''$. Both components appear to have a disk (Itoh et al. 2015). The star is reported in Kraus et al. (2012) as having a disk, but without evidence for accretion.

IS Tau. is a binary with $0.2''$ separation (Schaefer et al. 2014). It is not known which (or if both) component hosts a disk. Watson et al. (2009) reported a very high mass fraction (80–100%) of crystalline silicates in the inner disk. The light curve is characterized by a combination of broad and narrow eclipses. The strongest periodicity is given by the broad dips. No *Gaia* parallax is available. The star is also located on the L1495 filament of Taurus, which contains members of both the near and the far population (Fleming et al. 2019). In the HR diagram in Fig. 9, the possible luminosity of IS Tau is plotted according to mean distances of 130.6 and 160.2 pc (Fleming et al. 2019). The age is more consistent with that of the remaining sample if IS Tau is a member of the far population. The star shows a double dip; the primary has a larger, quite constant amplitude. For this star, the phase shift of the dips varies more than for other double-peaked dippers.

St 34. is a multiple system (Aab+B) with separation $1.18''$, surrounded by a circumbinary, transitional disk (Rigliaco et al. 2015). The star is reported as SB2 by Akeson et al. (2019). The inner disk appears to be depleted, although some dust is still present (Hartmann et al. 2005). Its membership in the Taurus association is controversial (Hartmann et al. 2005; White & Hillenbrand 2005; Dahm & Lyke 2011). Dahm & Lyke (2011) reported an age for St 34 of ~ 10 Myr. Its lithium depletion (White

& Hillenbrand 2005) would lead to an age of 25 Myr, thus the authors must assume a distance of only 90 pc. In the HR diagram of our study (Fig. 9), the star appears to have an age of 1–2 Myr, given the limitations on the luminosity due to photometric variability. The *Gaia* parallax reports a distance of 143 pc, thus showing that St 34 cannot be a foreground star. Accordingly, the age-derivation based on the lithium depletion timescale apparently does not apply to this star. The light curve is irregular, and a period forest is present in both the periodogram and WPS. The presented period is uncertain. Some contamination might arise from multiplicity.

V807 Tau. is a multiple system (A + Bab) and a separation of $0.3''$ for the wide components, $0.04''$ for the secondary (Schaefer et al. 2012). The *Gaia* distance of V807 Tau is 113 pc, thus it is maybe underestimated. The system is multiple, which means that there might be an issue with the *Gaia* parallax. The star is located in the B18 region of Taurus (Fleming et al. 2019), which has a distance of 110–150 pc. This value has to be considered with caution, but it is not an outlier for this region. Rodriguez et al. (2017) derived a period of 0.809 d, which is inconsistent with K2 data. Schaefer et al. (2012) decomposed the brightness of the single components and obtained a primary star 0.5 mag fainter than the 2MASS J measurement. This leads to a much smaller stellar radius and higher, more plausible stellar inclination. The light curve presents an apparently sinusoidal long-term modulation; moreover, it is unclear if the star reaches its maximum brightness at all. The modulation does not appear to be related to binarity because the binary system has a period of 12 yr. There is only one clear periodicity, and the shape of the dips does not suggest stellar spots.

Haro 6-37. is a triple system. The close binary AB ($0.3''$ Duchêne et al. 1999) is separated from C by $2.6''$ (White & Ghez 2001). The light curve presents unusually broad dips for a dipper with high amplitude (0.5 mag). The periodicity is unclear in the WPS and periodogram. Our luminosity is highly different from that of Herczeg & Hillenbrand (2014) (here $0.8 L_{\odot}$, there $0.07 L_{\odot}$). The derived inclination suggests that the period is either incorrect or that the occultations have another origin.

JH 112 A. is separated from its companion JH 112 B by $6.56''$. JH 112 A is itself a close binary Aa+Ab with a separation of $1.65''$ (Kraus et al. 2011). The star is a transient, quasiperiodic dipper, the dips occur with a period of 2.21 d. The dips are accompanied by a general decrease in brightness; it is not clear if the phenomenon is physical or instrumental. The estimated luminosity is different from that of Herczeg & Hillenbrand (2014). The temperature at corotation is close to 1600 K, thus requiring higher gas densities for dust to survive (Pollack et al. 1994). The star is flagged as a double-peaked dipper. In a few periods, two well-detached peaks are present. The primary peak is always present, and the secondary is strongly variable and sometimes clearly double-peaked.

LkCa15. is a single star (Akeson et al. 2019) that hosts a transition disk. Donati et al. (2019) and Alencar et al. (2018) studied the star in detail. Alencar et al. (2018) confirmed it as a dipper, with a light curve that does not show large changes in its variability over the years (see also Grankin et al. 2007). The K2 light curve shows a variability amplitude of 0.4 mag, in accordance with previous literature. The derived inclination of the inner disks suggests that the inner disk is misaligned with the outer disk ($\sim 50^{\circ}$, see van der Marel et al. 2015; Thalmann et al. 2014). The photometric period is very close to the period derived

from radial velocity and veiling (Alencar et al. 2018), thus supporting the scenario of an inclined warp located at the corotation radius. Donati et al. (2019) reported a slightly lower $v \sin i$ than Alencar et al. (2018). The luminosity we derived ($0.96 \pm 0.18 L_{\odot}$) agrees with theirs ($0.8 \pm 0.15 L_{\odot}$) within the error bars. Nevertheless, the spectroscopically measured T_{eff} is 450 K higher than the conversion by Pecaut & Mamajek (2013). In this analysis, the directly derived temperature by Alencar et al. (2018) is preferred. The K2 light curve folded in phase shows a double-peaked dip that is strongly variable over time. The total width of the eclipsing time for this dipper is therefore very large. The light curve exhibits a long-term trend; it is unclear whether the occultations affect the continuum or if it has other origins. At least two clear peaks with variable depth and occurrence (i.e., position in phase) are always present in the light curve.

GO Tau. The light curve shows an active star in which bursts also occur. This makes it difficult to define a brightness continuum. The period forest in the periodogram results in no clear periodicity in the WPS. This aperiodic dipper includes both very narrow and wider dips. Güdel et al. (2007) derived an upper limit for the rotation period ≤ 3.96 d from $v \sin i$.

HK Tau. is a wide binary with a separation of $2.3''$ (Akeson & Jensen 2014). Both components have disks misaligned with the orbital motion. The light curve does not show a stable continuum. The periodicity is very clear, but the folded light curve is noisy. Some other phenomenon apparently takes place at the stellar surface. Güdel et al. (2007) reported a $v \sin i = 10 \text{ km s}^{-1}$, measured by Hartmann & Stauffer (1989), which would lead to a very low inclination that is inconsistent with both a dipper and the outer disk. We consider this value less reliable than the measurement by Hartmann et al. (1986) because 10 km s^{-1} is the detection limit for $v \sin i$. Instead of being a double-peaked dipper, the star is multi-peaked. The different dips are always present, with a strongly varying amplitude that appears to be uncorrelated between different dips. The Gaussian-shaped tip of the dips is constant, while the dip shapes vary strongly, suggesting that multiple stellar spots might contribute to the photometric variability.

HP Tau. The star does not have a companion (Akeson et al. 2019). Its light curve is quasiperiodic, with strong variations in shape and brightness (up to 0.4 mag). The dips are strongly variable and never appear to be single. The structure of the dips varies from double-peaked to a broad, single peak. Güdel et al. (2007) and Rebull et al. (2004) found in the literature a period of 5.90 d, which disagrees with the K2 period of 4.33 d. The light curve is strongly variable and the periodicity complex; this means that the period might change over time. Its luminosity is probably overestimated ($2.3 L_{\odot}$) and the resulting stellar inclination is very low. It is possible that the stellar parameters cannot be constrained correctly due to the high amplitude of the variability (3 mag in the V band for different surveys). The luminosity disagrees with that derived by Herczeg & Hillenbrand (2014), and the star is also highly veiled.

GH Tau. is separated from its companion by $0.3''$ (Akeson et al. 2019). The light curve is irregular, and it is unclear whether there are two types of eclipses, if the star is bursting, or if there is a long-term variation. The folded light curve is very noisy. Two main periodicities at 2.49 d and 2.94 d are present, although the latter does not show any significant structure. Güdel et al. (2007) indicated a period ≤ 3.57 d derived from $v \sin i$. No *Gaia* parallax was available for this object, but it is located in the B18 group of Taurus (Fleming et al. 2019), with an average distance

of 127.4 pc. The star is the fastest rotator in this sample ($v \sin i = 30 \text{ km s}^{-1}$).

GM Tau. is a single brown dwarf (Akeson et al. 2019) with a transitional disk. The star is a strong accretor and is highly veiled (Herczeg & Hillenbrand 2008, 2014). The sinusoidal light curve does not show a brightness continuum; the star is considered a dipper because of the irregularity of the dips.

FX Tau. is a binary with a separation $0.9''$. Each component hosts a disk (Akeson et al. 2019). This aperiodic dipper has alternating wide and narrow dips. A long-term trend is present in the light curve.

GK Tau. is separated from GI Tau by $13.1''$ (Akeson et al. 2019). It is debated in the literature whether these two stars are physically bound. The star is a clear dipper with high amplitude (0.5 mag). The occultations probably do not allow us to see the brightness continuum. The periodicity is clear, and no other physical phenomena appear to affect the light curve. The period agrees with previous data (Artemenko et al. 2012; Percy et al. 2010; Güdel et al. 2007; Rebull et al. 2004). Percy et al. (2010) found a long-term variability with a timescale of 2500 d for this object.

GI Tau. Guo et al. (2018) reported an uncertain spectral type K5-M0 for this star. We adopted a spectral type of M0.4. The inclination of 60° agrees with the inclination derived here. Guo et al. (2018) linked the 7 d period that we also found to a spot. In their optical monitoring from 2014 to 2016, the folded light curve is clearly sinusoidal, which is far from the observed behavior in the K2 light curve. Guo et al. (2018) observed quasiperiodic dips on timescales that are a multiple of the rotation period. The folded K2 light curve is highly irregular and contaminated by GK Tau. The first peak in the periodogram is a periodicity related to GK Tau and not to GI Tau. The 7.1 d period agrees with previous data (Artemenko et al. 2012; Percy et al. 2010; Güdel et al. 2007; Rebull et al. 2004). Our observed amplitude of 0.4 mag is lower than the variability observed by Guo et al. (2018). The folded light curve suggests that small bursts occurred during the K2 campaign. The star has been classified as dipper, although aperiodic, by Rodriguez et al. (2017). A comparison with the light curve of GK Tau (not shown here), split into each phase according to the period of GI Tau, shows that the dips are highly affected by the neighbor star. Although the intrinsic variability of GI Tau emerges well, it is difficult to describe the behavior of its multiple dips, if there are any. The complexity of the K2 light curve does not allow us to clearly distinguish between the two.

DK Tau. is a binary star with a separation of $2.4''$. Both stars have disks (Akeson et al. 2019; Akeson & Jensen 2014). The light curve exhibits strong variations over long timescales (see Grankin et al. 2007; Rebull et al. 2020, and references therein), and the period varies from one survey to the next. The WPS shows that the period of DK Tau increases from 7.69 d to ~ 10 d during K2 C13, after a fading state in lower brightness. This explains the two different, broad peaks in the periodogram. Percy et al. (2010) and Artemenko et al. (2012) reported a period of 8.18 d, while Rebull et al. (2020) found 7.84 d. The difference can be easily explained for the first with the complexity of the light curve, and for the second, by the use of a different period-finding algorithm in presence of a broad peak. Xiao et al. (2012) reported 4.14 d, which is not consistent with the K2 data. Percy et al. (2010) also derived a long-term timescale of 2000 d for the variability of DK Tau. When the fading state is excluded, the amplitude of the occultations is 0.6 mag.

Appendix E: Wavelet power spectra

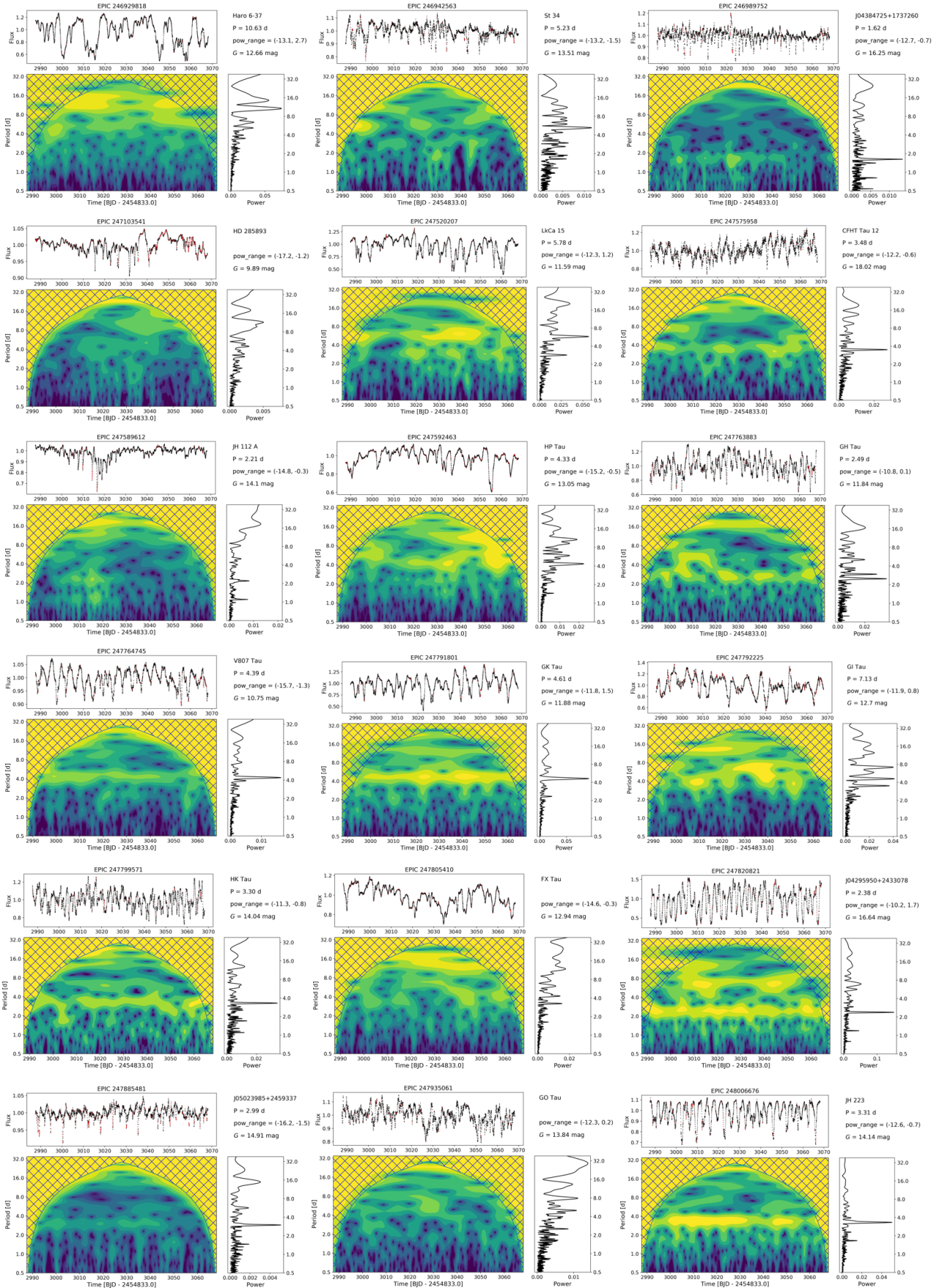


Fig. E.1. Wavelet power spectra of the dipper sample.

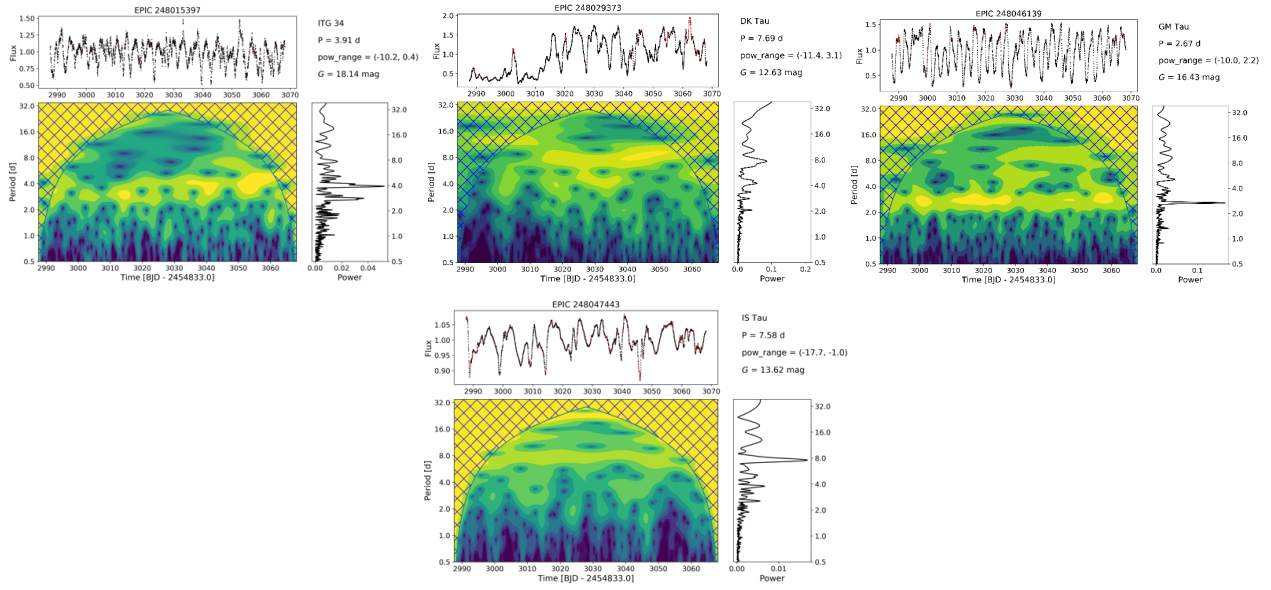


Fig. E.1. continued.

Appendix F: Folded light curves

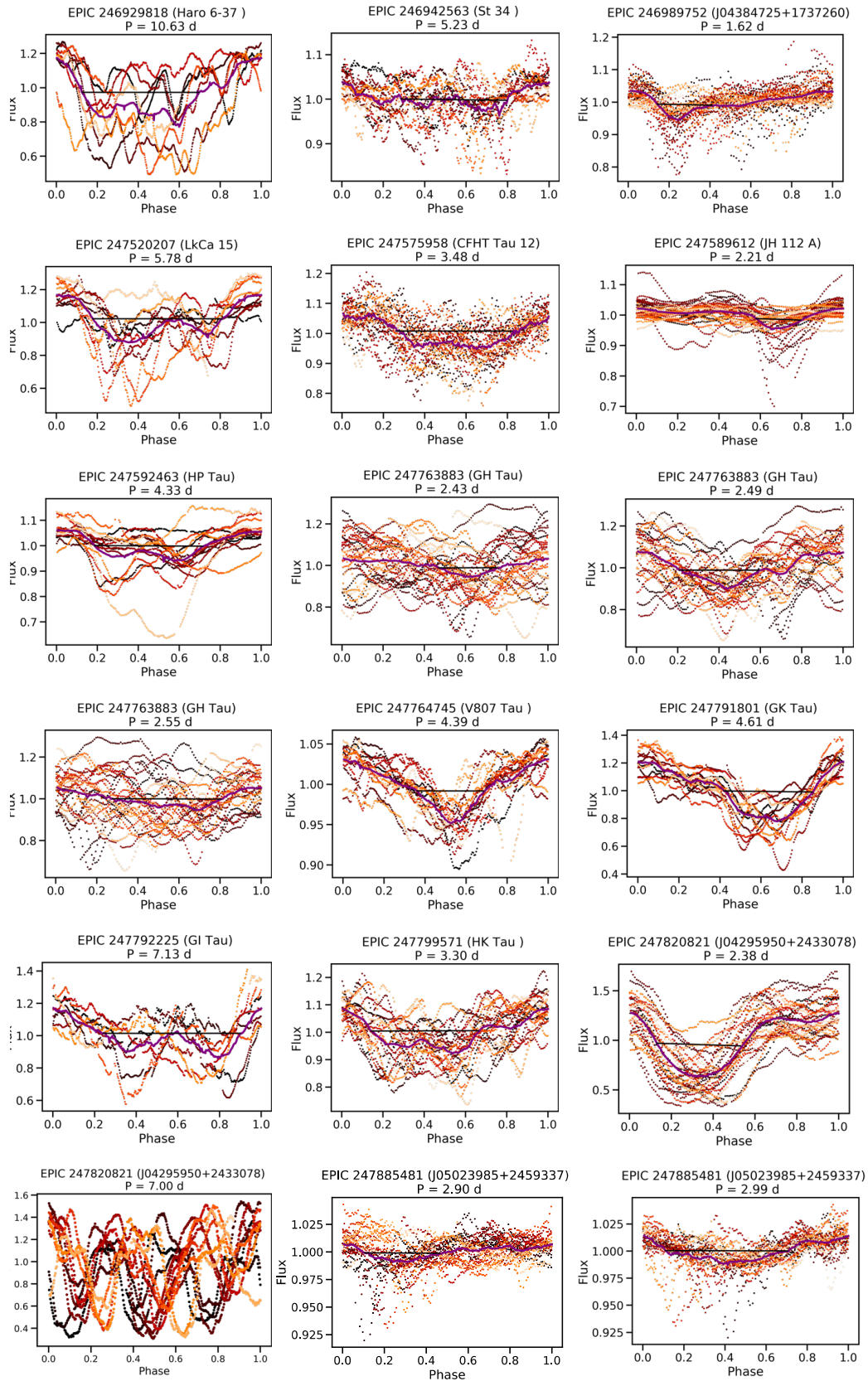


Fig. F.1. Folded light curves of the dipper sample. Every phase has a different color. The purple line shows the binned light curve. The black line represents the automatically determined dip width. For some stars, more than one possible period is shown.

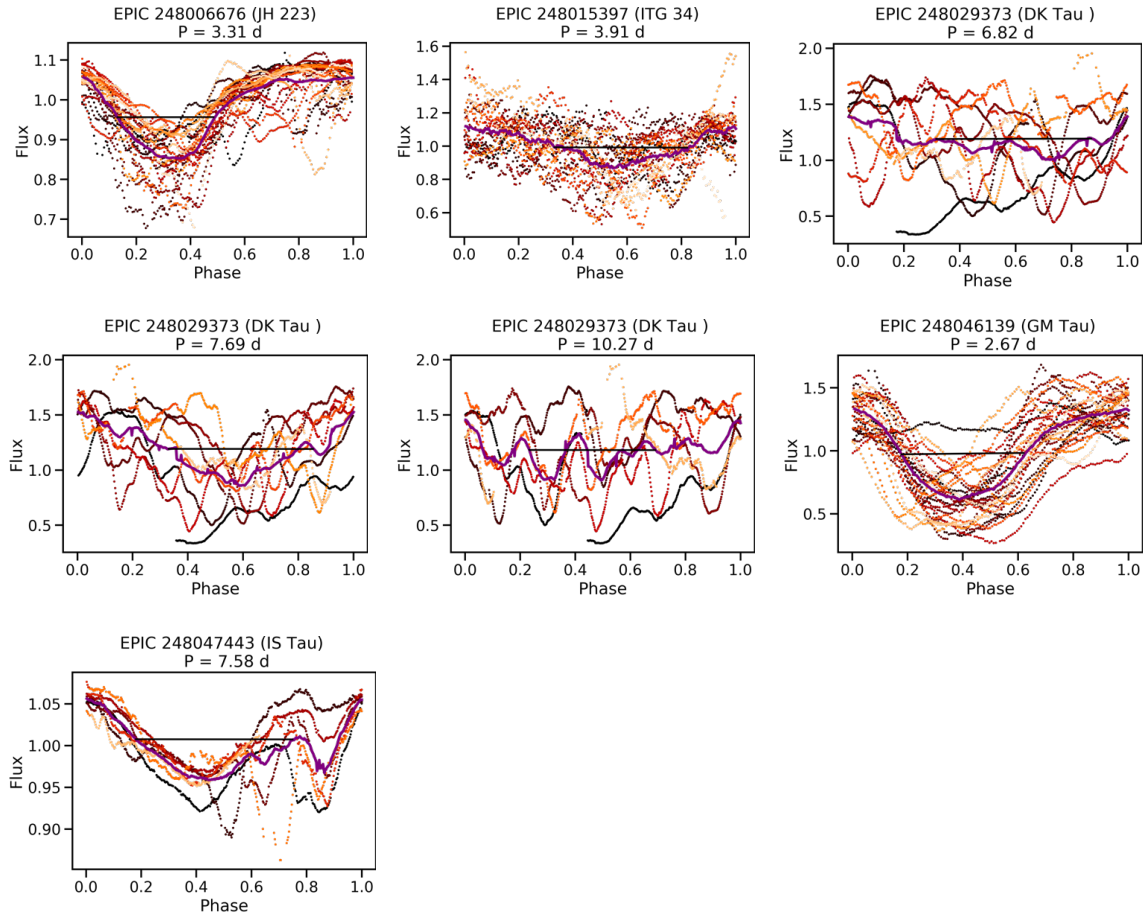


Fig. F.1. continued.

THE DIPPER STAR POPULATION OF TAURUS SEEN WITH K2

Noemi Roggero¹, Jérôme Bouvier¹, Luisa M. Rebull² and Ann Marie Cody³

Abstract. During the evolution of T Tauri stars and the formation of their planetary systems, accretion processes play a key role. However, the more complex interaction at the rim of the inner region of the disk is still not well understood. Some young stars exhibit recurrent, quite irregular flux dips in their photometry (dippers). These can be explained as extinction events by dusty material from the protoplanetary disk, which is finally accreted onto the star. In the magnetospheric accretion scenario, the magnetic field of a young star truncates the disk where the magnetic field pressure is equal to the ram pressure of the accreting material. If the temperature close to this distance is low enough to avoid dust sublimation, dust might be lifted above the disk plane and obscure the star. The dataset for this study consists of K2 light curves (C4 and C13) of the Taurus region, which was observed continuously for ~ 80 days. The stars classified as dippers have spectral types K4-M6, consistent with studies in other regions, and the mass range goes down to the brown dwarf limit. The co-rotation radii can be derived to a few stellar radii, with temperatures at corotation < 1600 K, that indicates that in most cases dust could survive at corotation. Temperatures close to 1600 K give some constraints about the dust composition. Magnetospheric accretion can account for most of the light curves. However, for some dippers, also other phenomena might cause eclipses.

Keywords: protoplanetary disks, stars: pre-main sequence, stars: variables: T Tauri, accretion, accretion disks, techniques: photometric

1 Introduction

Classical T Tauri stars (CTTSs) are low-mass, pre-main-sequence stars. They are $\sim 10^6$ Myr old and are surrounded by a protoplanetary disk, from which they accrete gas and dust in its inner region. The star-disk interaction is regulated by the stellar magnetic field, which truncates the disk at distances < 0.1 AU and drives accretion along the magnetic field lines. CTTSs display a strong variability in both their spectra and their light curves. Many physical mechanisms have been proposed to explain this variability, such as accretion hotspots, accretion bursts, or occultations by dusty structures in the disk (e.g., Cody et al. 2014; Alencar et al. 2010; Bouvier et al. 2003). This talk focuses on a class of variable stars that show dips in their light curve, the so-called ‘dippers’. The dips present an irregular shape and can be quasiperiodic or aperiodic. They are mostly of late spectral type (K to M) and seem to be fairly common among CTTSs, with occurrences of 20% to 40% of young stars. AA Tau was the first dipper studied in detail. Bouvier et al. (1999, 2007) proposed that the magnetic field lines, close to the truncation radius, could lift dust above the disk midplane, and that an observer would see dips in the light curve whenever the dust crossed the line of sight. The temperature in this region must be low enough for the dust to survive at this distance, and the inclination of the system sufficiently high for the observer to look through the dusty structure (Bodman et al. 2017). Photometric observations can thus help to better understand the accretion processes and the inner disk structure on scales that are still challenging to resolve directly with interferometry.

¹ Univ. Grenoble Alpes, CNRS, IPAG, 38000 Grenoble, France

² Infrared Science Archive (IRSA), IPAC, 1200 E. California Blvd., California Institute of Technology, Pasadena, CA 91125, USA

³ SETI Institute, 189 N Bernardo Ave. Suite 200, Mountain View, CA 94043 USA

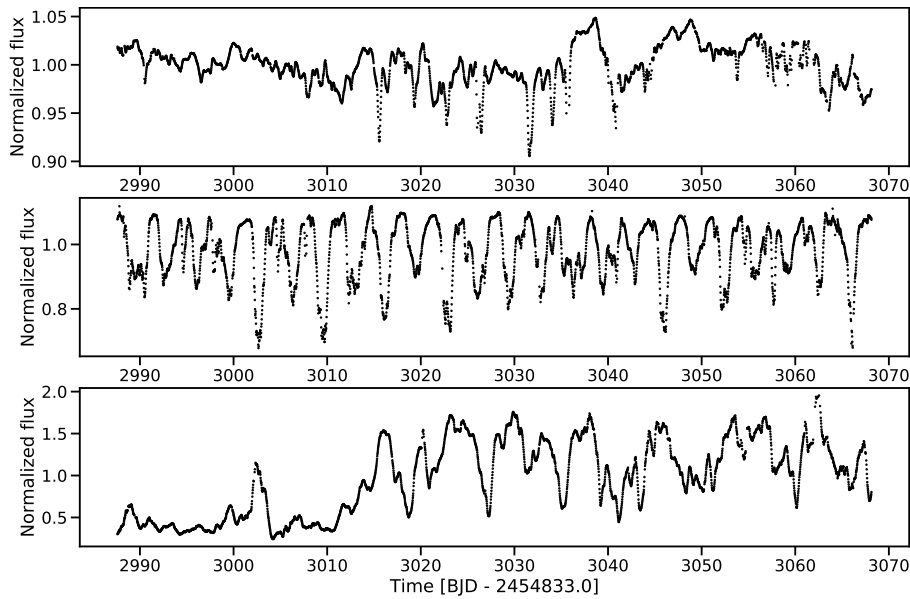


Fig. 1. Examples of an aperiodic dipper (HD 285893, top) a quasiperiodic dipper (JH223, center), and a dipper with a rather complex light curve (DK Tau, bottom).

2 Observations and data reduction

The Taurus region was observed nearly continuously with the Kepler satellite within the framework of the K2 mission (Howell et al. 2014), with a cadence of 29.4 min and a duration of ~ 80 days. The observation campaigns C13 (Mar - May 2017) and C4 (Feb - Apr 2015) delivered light curves for about 900 potential members. K2 data are challenging to reduce and several pipelines are available for this purpose. We compared different reduction pipelines and if the light curve did not present particular issues, we used the version with moving aperture as in Cody & Hillenbrand (2018) as default for consistency. The process to assess the membership of each star to the cluster is explained by Rebull et al. (2020). We attribute a higher-confidence membership to candidates which already appear as members in Luhman (2018). Finally, we searched for dippers in a sample of 156 members plus 23 possible members of Taurus.

3 Results

From the sample of members and possible members of Taurus, we identified 22 dippers, which are studied in more detail, and 12 additional dippers, which are dominated by another type of variability and display mostly aperiodic dips in their light curve (Roggero et al. 2021). This sums up to an occurrence of 20% among Taurus members, and of 30% among disked stars in the sample. This has to be considered as a lower limit to their true occurrence, due to both the observational limits (e.g., the system geometry) and the ephemerality of dippers. A majority of CTTSs might be a dipper at some point of its evolution.

Several properties of dippers are useful to gain information on the inner disk region and the star itself. All possible explanations for dippers converge on a dusty structure at the origin of the dips in the light curve. Thus, dip amplitude and dip width should provide hints on the geometry of this structure. At the same time, several other parameters allow to probe the different models. The hypothesis that the material provoking the occultation is corotating with the star can be probed by studying the dippers' periodicity, and comparing it to the stellar period. The temperature at the corotation radius should be below the dust sublimation temperature (1500 – 1600 K) and the viewing angle of the system can exclude certain dipper models.

3.1 Periodicities

For the aim of studying the periodicities of dippers, we used different algorithms: Lomb-Scargle periodogram (Rebull et al. 2020), CLEAN periodogram and wavelet analysis (Roggero et al. 2021). The latter method opens the possibility of time-resolved frequency analysis. Considering both the dipper sample studied in more detail

and the dippers dominated by another variability (mostly cold stellar spots), the ratio of periodic to aperiodic dippers is of $\sim 1 : 1$. The periods are in the range of a few days, in accordance with the rotation periods of CTTs, supporting the hypothesis of dust at corotation. In the case of the presence of both spots and dips in the light curve, the periods are slightly, yet not significantly different.

3.2 Dips' morphology

We identify dippers based on their light-curve morphology. This type of light curves presents irregularly shaped, sharp dips which can be aperiodic or quasiperiodic in their occurrence (Fig. 1). In order to study the dip morphology, we defined the dip amplitude as difference between the 90th and fifth percentile of flux of the detrended light curve. The amplitude of the dips can be influenced by, for example, the viewing angle, the height and the optical thickness of the dusty structure. We also defined a dip width as full width of half maximum of the detrended, phase-folded and then binned (that is, averaged) light curve (for more details, see Roggero *et al.* 2021). The dip width is a measure of the azimuthal extension of the occulting feature. We investigated whether dip width and dip amplitude correlate, as it might be expected following the model of the dusty disk warp (Bouvier *et al.* 1999), but we could not determine any correlation. However, we found a correlation between the dip width in units of phase and the dips' period, which was not found before (Roggero *et al.* 2021). It appears that the dip width increases with the period. This would imply that slow rotators are surrounded by azimuthally larger dusty warps. We speculate that large-scale magnetic fields might be at the origin of this correlation, by having a stabilizing effect on large warps.

3.3 Stellar parameters

We derived stellar luminosities by using photometric data from the literature, and effective temperatures by means of the conversion tables of Pecaut & Mamajek (2013). The resulting Hertzsprung-Russel diagram is shown in Fig. 2. We used the evolutionary models of Baraffe *et al.* (2015), as they include the lowest stellar masses. Almost all dippers of the sample have masses $< 1 M_{\odot}$, with the lowest ones close to the brown-dwarf limit. Despite the large uncertainties on their age, the stars are spread around the 1 Myr isochrone. These parameters can be used to derive the extent of the corotation radius as in:

$$R_{\text{cor}} = \frac{P^{\frac{2}{3}}}{2\pi} (GM_{*})^{\frac{1}{3}}. \quad (3.1)$$

The corotation radii are located at a few stellar radii, as expected for dippers. We can verify whether dust can survive at this distance from the star with the following approximation:

$$T_{\text{cor}} = 2^{-\frac{1}{2}} T_{\text{eff}} \left(\frac{R_{*}}{R_{\text{cor}}} \right)^{\frac{1}{2}}. \quad (3.2)$$

For all dippers, the temperatures at corotation are below 1600 K, which is considered as an upper limit for dust sublimation. We also derived stellar inclinations following:

$$v \sin i = \sin i \frac{2\pi R_{*}}{P}. \quad (3.3)$$

This parameter is crucial to probe the different models proposed for dippers, as they depend on the viewing angle of the system. In fact, the dusty material has to cross the observer's line of sight in order to produce dips in the light curve; at the same time, dust is not supposed to be present close to the stellar poles. The inner disk wall first proposed by Bouvier *et al.* (1999) for AA Tau requires high inclinations $\sim 70^{\circ}$, while the generalization of the magnetospheric accretion model (Bodman *et al.* 2017) can account, under certain conditions, for inclinations down to $\sim 50^{\circ}$. Dusty disk winds, which have been invoked to explain dippers at low inclination, seem to be observable at rather high inclinations close to $\sim 70^{\circ}$ (Vinković & Čemeljić 2020). The dippers of this sample are seen under moderate to high inclination, thus compatible with the generalized magnetospheric accretion model, but with few exceptions. We also retrieved inclinations of the outer disk from the literature, as observed at mm wavelengths. In general, the star has a higher inclination than the outer disk. This might be due, on one hand, to the high uncertainty on $\sin i$, which grows with the inclination. On the other hand, recent observations point out that misalignments between inner and outer disk might be pretty common among CTTs.

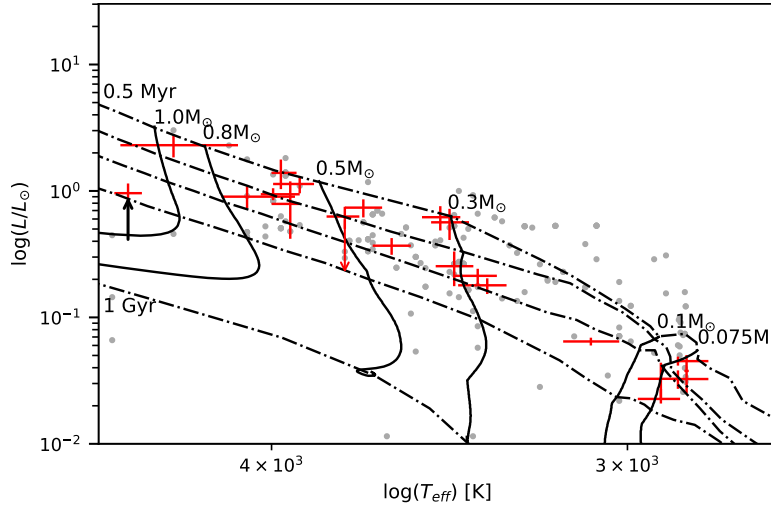


Fig. 2. Hertzsprung-Russell diagram of the studied sample of 22 dippers. The evolutionary tracks (solid lines) and the isochrones (dashed lines) are from Baraffe et al. (2015). Isochrones from top to bottom: 0.5, 1, 2, 5 Myr, and 1 Gyr. The grey points represent other stars in Taurus as in Herczeg & Hillenbrand (2014). For the sake of readability, HD 285893 (spectral type F8) does not appear on this plot. All dippers are scattered around ~ 1 Myr and are fully convective, with the exception of LkCa 15 (indicated with an arrow).

4 Conclusions

We have searched for dippers in a sample of 156 + 23 Taurus members and found 22 dippers, with 12 additional dippers which display a different predominant variability. As a result, around 20% of Taurus members and 30% of disk-bearing stars in Taurus are dippers, as found also in surveys of other star-forming regions. This occurrence is a lower limit, due to the ephemerality of dippers and the observational constraints. The stars analyzed in this study are compatible with the presence of dust at corotation and magnetospheric accretion can account for most, but not all, dipper light curves. Future studies on this dipper sample will consider in more detail the cycle-to-cycle variation of the dips, which might provide a more complete picture of accretion and dust depletion on short time scales.

This project has received funding from the European Research Council (ERC) under the European Union’s Horizon 2020 research and innovation programme (grant agreement No 742095; *SPIDI*: Star-Planets-Inner Disk-Interactions).

References






- Alencar, S. H. P., Teixeira, P. S., Guimarães, M. M., et al. 2010, *A&A*, 519, A88
- Baraffe, I., Homeier, D., Allard, F., & Chabrier, G. 2015, *A&A*, 577, A42
- Bodman, E. H. L., Quillen, A. C., Ansdell, M., et al. 2017, *MNRAS*, 470, 202
- Bouvier, J., Alencar, S. H. P., Bouvier, T., et al. 2007, *A&A*, 463, 1017
- Bouvier, J., Chelli, A., Allain, S., et al. 1999, *A&A*, 349, 619
- Bouvier, J., Grankin, K. N., Alencar, S. H. P., et al. 2003, *A&A*, 409, 169
- Cody, A. M. & Hillenbrand, L. A. 2018, *AJ*, 156, 71
- Cody, A. M., Stauffer, J., Baglin, A., et al. 2014, *AJ*, 147, 82
- Herczeg, G. J. & Hillenbrand, L. A. 2014, *ApJ*, 786, 97
- Howell, S. B., Sobek, C., Haas, M., et al. 2014, *PASP*, 126, 398
- Luhman, K. L. 2018, *AJ*, 156, 271
- Pecaut, M. J. & Mamajek, E. E. 2013, *ApJS*, 208, 9
- Rebull, L. M., Stauffer, J. R., Cody, A. M., et al. 2020, *AJ*, 159, 273
- Roggero, N., Bouvier, J., Rebull, L. M., & Cody, A. M. 2021, *A&A*, 651, A44
- Vinković, D. & Čemeljić, M. 2020, *MNRAS*

B.2 CO-AUTHORED PUBLICATION

This section presents a broad study about the rotation of the young stellar population of Taurus observed with the satellite *K2*, which includes cluster membership, stellar periodicities, morphological classification of the light curves, and disk indicators. In the frame of my PhD thesis, I went through the ~ 200 light curves which built the initial sample provided by the *K2* observations in order to classify by hand the different light curves. I developed wavelet analysis tools and applied them to the entirety of the light curves, in order to better understand complex periodicities and classify them. The further analysis about dipper stars has been published in a different refereed paper, of which I am first author.



Rotation of Low-mass Stars in Taurus with K2

L. M. Rebull¹ , J. R. Stauffer² , A. M. Cody³ , L. A. Hillenbrand⁴, J. Bouvier⁵, N. Roggero⁵ , and T. J. David⁶ 

¹ Infrared Science Archive (IRSA), IPAC, 1200 E. California Blvd., California Institute of Technology, Pasadena, CA 91125, USA; rebull@ipac.caltech.edu

² Spitzer Science Center (SSC), (IPAC), 1200 E. California Blvd., California Institute of Technology, Pasadena, CA 9112, USA

³ Bay Area Environmental Research Institute, 625 2nd St. Ste. 209, Petaluma, CA 94952, USA

⁴ Astronomy Department, California Institute of Technology, Pasadena, CA 91125, USA

⁵ Université de Grenoble, Institut de Planétologie et d'Astrophysique de Grenoble (IPAG), F-38000 Grenoble, France; CNRS, IPAG, F-38000 Grenoble, France

⁶ Center for Computational Astrophysics, Flatiron Institute, New York, NY 10010, USA

Received 2020 February 24; revised 2020 April 7; accepted 2020 April 8; published 2020 May 26

Abstract

We present an analysis of K2 light curves (LCs) from Campaigns 4 and 13 for members of the young (~ 3 Myr) Taurus association, in addition to an older (~ 30 Myr) population of stars that is largely in the foreground of the Taurus molecular clouds. Out of 156 of the highest-confidence Taurus members, we find that 81% are periodic. Our sample of young foreground stars is biased and incomplete, but nearly all stars (37/38) are periodic. The overall distribution of rotation rates as a function of color (a proxy for mass) is similar to that found in other clusters: the slowest rotators are among the early M spectral types, with faster rotation toward both earlier FGK and later M types. The relationship between period and color/mass exhibited by older clusters such as the Pleiades is already in place by Taurus age. The foreground population has very few stars but is consistent with the USCo and Pleiades period distributions. As found in other young clusters, stars with disks rotate on average slower, and few with disks are found rotating faster than ~ 2 days. The overall amplitude of the LCs decreases with age, and higher-mass stars have generally lower amplitudes than lower-mass stars. Stars with disks have on average larger amplitudes than stars without disks, though the physical mechanisms driving the variability and the resulting LC morphologies are also different between these two classes.

Unified Astronomy Thesaurus concepts: [Star formation \(1569\)](#); [Stellar rotation \(1629\)](#); [Starspots \(1572\)](#)

Supporting material: machine-readable tables

1. Introduction

The Taurus-Auriga star-forming region has fundamentally shaped our understanding of how low-mass stars form (see, e.g., Kenyon & Hartmann 1995). At an age of $\lesssim 3$ Myr (e.g., Kraus & Hillenbrand 2009; Luhman 2018) and a distance of ~ 140 pc (e.g., Esplin & Luhman 2017), even the low-mass objects (mid-M to early-L) are bright enough to be well studied. A significant fraction of the members have an infrared (IR) excess indicative of circumstellar disks.

From the earliest studies of the prototype T Tauri and other stars in Taurus, variability was included as a defining characteristic of young stars (Joy 1945). The variability arises from starspots, flares, disk interactions, disk accretion, disk structure occulting the star, and more. NASA's K2 mission (Howell et al. 2014) has recently provided high-quality, long duration (~ 70 days), high cadence (~ 30 minutes) light curves (LCs) for stars in many different clusters. In two of K2's Campaigns (4 and 13), members of the Taurus-Auriga molecular cloud population were included. Those Taurus members, along with the ρ Oph members observed in K2's Campaign 2 (e.g., Rebull et al. 2018), are the youngest cluster stars observed with K2.

Aperiodic variability is expected and common in young stars (see, e.g., Cody et al. 2014; Cody & Hillenbrand 2018). However, when the variability is periodic, we can infer the rotation rate of the star, and hence, we can explore the rotation rates of young stars as a function of stellar mass and disk presence. When combined with comparable observations of other clusters, we can study trends as a function of age. In this paper, we explore the periodic variability of the Taurus members observed with K2. A. M. Cody et al. (2020, in

preparation) will explore the range of LC properties of the disked members.

We have previously published our analysis of the K2 data for the Pleiades (~ 125 Myr; Rebull et al. 2016a, 2016b; Stauffer et al. 2016b; Papers I, II, and III, respectively), Praesepe (~ 790 Myr; Rebull et al. 2017; Paper IV), and Upper Sco/ ρ Oph (~ 8 and ~ 1 Myr; Rebull et al. 2018; Paper V). We have deliberately performed our analyses of these clusters, now including Taurus, in a very homogeneous fashion in order to allow for the best intercomparison of the rotation data across the full age range observed with K2. Upper Sco has less reddening and fewer disks than Taurus; ρ Oph has more reddening than, and a comparable disk fraction to, Taurus. While there are nearly 1000 member stars with periodic LCs in each of the Pleiades, Praesepe, and Upper Sco, there are far fewer stars with suitable K2 data at the youngest ages. In ρ Oph, there are 174 member LCs, 106 ($\sim 60\%$) of which are periodic. There are comparable numbers in Taurus, where there are 156 highest-quality members (see Section 2.2 and Table 1 below), and 81% (127) of those are periodic. In context with the older clusters, Taurus and ρ Oph seem to suffer in comparison, because of fewer stars, more stochastic contributions to the LCs (from disks and accretion, generally yielding a lower fraction of periodic LCs), more reddening and spatial variability in reddening (affecting the scatter in the diagrams), and more uncertainty in membership (yielding a higher contamination rate).

In Section 2, we summarize the data we amassed, including information about the K2 data, literature information, member selection, dereddening, and disk identification. Section 3 begins with period identification and interpretation as well as a

Table 1
Summary of Statistics on Taurus Sample^a

Property	High-confidence Members	Possible Members	~ 3 Myr ^b Members	~ 30 Myr ^c Foreground	NM or Rejected Sources	All Sources
C4	4	3	7	23	131	161
C13	152	22	174	16	513	703
C4 AND C13	0	2	2	1	10	13
C4 OR C13	156	23	179	38	634	851
All	156	23	179	38	634	
Periodic	127 (0.81)	21 (0.91)	148 (0.83)	37 (0.97)	307 (0.48)	
Multi-periodic	32 (0.21)	8 (0.35)	40 (0.22)	12 (0.32)	81 (0.13)	
No IR excess	55 (0.35)	16 (0.70)	71 (0.40)	36 (0.95)	585 (0.92)	
High-conf IR excess	94 (0.60)	7 (0.30)	101 (0.56)	1 (0.03)	35 (0.06)	
Possible IR excess	7 (0.04)	0 (0.00)	7 (0.04)	1 (0.03)	14 (0.02)	
IR excess+periodic	67 (0.43)	5 (0.22)	72 (0.40)	1 (0.03)	8 (0.01)	
IR excess+multi-periodic	11 (0.07)	2 (0.09)	13 (0.07)	0 (0.00)	2 (0.00)	
Burster	22 (0.14)	3 (0.13)	25 (0.14)	0 (0.00)	0 (0.00)	
Burster+IR excess	22 (0.14)	3 (0.13)	25 (0.14)	0 (0.00)	0 (0.00)	
Burster+IR excess+periodic	14 (0.09)	2 (0.09)	16 (0.09)	0 (0.00)	0 (0.00)	
Dipper	18 (0.12)	3 (0.13)	21 (0.12)	0 (0.00)	0 (0.00)	
Dipper+IR excess	18 (0.12)	3 (0.13)	21 (0.12)	0 (0.00)	0 (0.00)	
Dipper+IR excess+periodic	16 (0.10)	2 (0.09)	18 (0.10)	0 (0.00)	0 (0.00)	
Spectral type	151 (0.97)	22 (0.96)	173 (0.97)	26 (0.68)	155 (0.24)	
Gaia parallax	129 (0.83)	20 (0.87)	149 (0.83)	38 (1.00)	558 (0.88)	
IRAC-1	135 (0.87)	4 (0.17)	139 (0.78)	6 (0.16)	168 (0.26)	
WISE-1	156 (1.00)	23 (1.00)	179 (1.00)	38 (1.00)	633 (1.00)	
AKARI 18	39 (0.25)	2 (0.09)	41 (0.23)	0 (0.00)	14 (0.02)	
MIPS-24	98 (0.63)	9 (0.39)	107 (0.60)	12 (0.32)	85 (0.13)	
MIPS-70	40 (0.26)	2 (0.09)	42 (0.23)	0 (0.00)	4 (0.01)	
PACS 70	64 (0.41)	2 (0.09)	66 (0.37)	0 (0.00)	4 (0.01)	
V and K_s measured	57 (0.37)	17 (0.74)	74 (0.41)	22 (0.58)	207 (0.33)	
V from APASS	19 (0.12)	4 (0.17)	23 (0.13)	8 (0.21)	262 (0.41)	
$(V - K_s)$ via Gaia $G - K_s$	36 (0.23)	2 (0.09)	38 (0.21)	5 (0.13)	145 (0.23)	
$(V - K_s)$ via PanSTARRS $g - K_s$	34 (0.22)	0 (0.00)	34 (0.19)	2 (0.05)	13 (0.02)	
SED-interpolated V	10 (0.06)	0 (0.00)	10 (0.06)	1 (0.03)	7 (0.01)	
A_v from JHK_s diagram	31 (0.20)	4 (0.17)	35 (0.20)	9 (0.24)	313 (0.49)	
A_v from spectral type	115 (0.74)	15 (0.65)	130 (0.73)	16 (0.42)	107 (0.17)	
A_v from SED fits	5 (0.03)	4 (0.17)	9 (0.05)	11 (0.29)	25 (0.04)	
Median A_v assigned	5 (0.03)	0 (0.00)	5 (0.03)	2 (0.05)	189 (0.30)	

Notes.

^a Numbers in the table are raw number of stars meeting the stated criterion/criteria, followed by the sample fraction in parentheses.

^b ~ 3 Myr members are the high-confidence (Taurus) member plus the possible (Taurus) member sample.

^c The ~ 30 Myr foreground sample are stars determined in the literature to be young but not kinematically consistent with Taurus membership; these could be members of, e.g., Group 29 (see Section 2.2).

comparison of our periods to those from the literature. This section ends with color–magnitude diagrams (CMD) for the sample. Section 4 discusses the influence of disks on the period distribution. Section 5 presents the distributions of periods and periods against color as a proxy for mass. We also compare Taurus to the rest of the clusters we have analyzed with K2 data (Papers I–V). In Section 6, we characterize the LCs in the same fashion as we did for the other clusters. Finally, we summarize our results in Section 7.

We note explicitly that there are four sets of stars discussed in this paper: (1) highest-quality Taurus members, (2) lower-quality members (in other words, possible Taurus members), (3) a population largely foreground to Taurus that is likely older than Taurus but still young (~ 30 Myr), and (4) nonmembers (NMs). Appendix A contains a detailed description of how we define these categories, with an overview in Section 2.2. When we use the term “members”, we are

referring to the highest-quality plus the possible Taurus members. When we use the term “foreground” (as in “foreground population”), we are referring to the set of stars that are older than Taurus but still relatively young.

2. Data

2.1. K2 Data

Stars in the Taurus Molecular Cloud were observed in two different K2 campaigns, Campaign 4 (C4; 2015 February 7–2015 April 24) and Campaign 13 (C13; 2017 March 8–2017 May 27), with the majority of Taurus members coming from C13; see Figure 1. As in our earlier papers, we start by considering all possible cluster members and then narrow the sample to high-confidence and lower-confidence members (see Section 2.2); results for the likely NMs are listed in the Appendix for reference. There are ~ 850 candidate Taurus

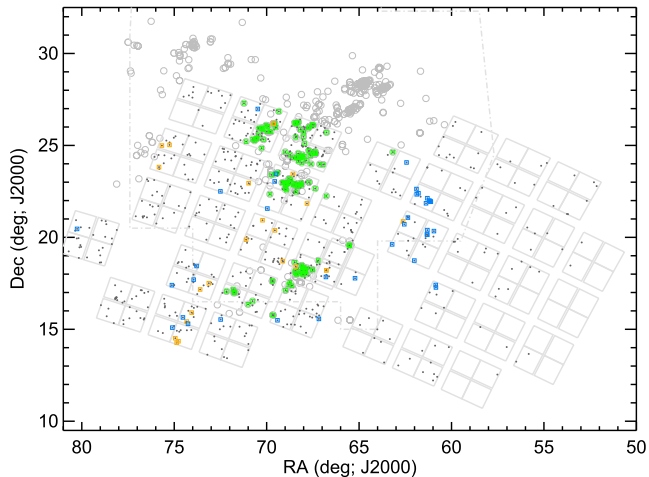


Figure 1. Locations of targets of note projected onto the sky. Small dark gray circles: candidate Taurus members with LCs. Additional green square: highest-quality Taurus members (see Section 2.2 for more on membership). Additional orange: possible Taurus members. Additional blue square: foreground population, e.g., stars determined in the literature to be young but not kinematically consistent with Taurus membership; these could be members of, e.g., Group 29 (see Section 2.2). For context, the large light gray squares are the K2 footprints (C13, left; C4, right), and the small light gray circles are the Taurus members as compiled by Esplin & Luhman (2019). The dashed-dotted line is the polygon considered for potential Taurus members using WISE in Rebull et al. (2011). The K2 observations cover about 30% of the likely Taurus members from Esplin & Luhman (2019).

members with K2 LCs from either campaign and a few with K2 data from both campaigns (see Table 1). All of the LCs used here were observed in the long-cadence (~ 30 minutes cadence) mode.

Our analysis (see Section 2.2 below) focused on the 156 highest-quality Taurus members, 23 possible members, and 38 foreground objects that are young (but likely older than the Taurus molecular cloud population). Figure 1 shows the distribution of these objects with K2 LCs on the sky, in context with other reference points. The area defined as encompassing “Taurus” by, e.g., Esplin & Luhman (2019) goes further north (and east) than the K2 region, such that the K2 observations cover about 30% of the members from Esplin & Luhman (2019). Assuming that there should be no spatial dependence of stellar rotation rate on location in the cluster, there should be no bias in our distribution of periods resulting from the incomplete coverage of the cluster. However, specifically because the K2 region extends over a larger area to the south and west, it encompasses a larger area than has been studied most intensively for potential Taurus members, and enables LC collection from a more dispersed population of candidate young stars.

There are very few stars considered to be Taurus members of any confidence level that have LCs in both the C4 and C13 campaigns. Of these, just two are in the set of possible Taurus members (EPIC 210689309 = AG+18339; EPIC 210689130 = HD 28150), and one is in the foreground population (210662824 = HD 285778). All three of these are periodic in both campaigns. There are an additional 10 field stars with two sets of LCs, and four of them have periods in both campaigns. For all stars in common between C4 and C13 (whether or not they are members), the periods derived separately from both campaigns are the same within $\sim 4\%$ accuracy, suggesting that the effective

astrophysical uncertainty on the periods is likely very low, at least for stars without disks.

Our analysis follows the same approach discussed in our earlier papers (Papers I–V) and is briefly summarized here. For each target, we selected the best (see Paper I) LC from several different available LC versions: (1) the pre-search data conditioning (PDC) version generated by the Kepler project⁷ and obtained from the Mikulski Archive for Space Telescopes (MAST); (2) a version using custom software developed by co-author A.M.C.; (3) the “self-flat-fielding” approach used by Vanderburg & Johnson (2014) and the K2SFF pipeline as obtained from MAST; (4) the LCs from the EVEREST2 pipeline (Luger et al. 2016, 2018), which uses pixel-level decorrelation, as obtained from MAST; and (5) the EVEREST2 pipeline LCs, where large-scale structure is removed via a least-squares (Savitzky–Golay) polynomial smoothing filter (e.g., Press et al. 1992), as implemented in the IDLastro library.⁸ We removed any data points corresponding to thruster firings and any others with bad data flags set in the corresponding data product. Any periodic signals are generally unambiguous and are generally detected in all of the LC versions. The spacecraft slowly drifts and then repositions regularly every 0.245 day, so we particularly scrutinized any detected periods near 0.245 day.

K2 has a relatively large pixel size ($3''.98 \times 3''.98$). To identify sources subject to confusion, we inspected the region around each target with the Finder Chart tool⁹ from NASA’s Infrared Science Archive (IRSA). We also incorporated the diagnostic information provided by the various K2 data reduction pipelines. For those targets where source confusion is a concern, we either took the existing LC most likely to be centered on the target given the diagnostic information provided by the corresponding pipelines or re-reduced the data using the Cody approach but with a small, fixed aperture.

We omitted two of the highest-quality members (see Section 2.2): EPICs 247031436 (HD 28867B; confused with nearby sources) and EPIC 247989931 (2MASS J04412464 +2543530; too faint). For completeness, we note that EPIC 211068851 (HD 26212) is too bright and EPIC 210893410 is too faint, but both are also unlikely to be Taurus or foreground members.

There are a few targets that are either erroneously listed as distinct targets in the EPIC catalog or could be a faint source next to a brighter source; in either case, a good LC cannot be obtained. HL Tau (EPIC 210690913) and XZ Tau AB (EPIC 210690892) are high-quality members and close together in the sky, though resolvable; the XZ Tau binary itself is not resolved. An additional target is listed as EPIC 210690886, but it is too faint and/or close to XZ Tau to measure independently. Given its location, position matching with literature data (see Section 2.3 below) accidentally picks up several matches that should have been matched to XZ Tau AB. As a result, EPIC 210690886 is explicitly removed from our database as effectively a duplicate. DR Tau (EPIC 246923113) is also a high-quality member. EPIC 246923117 is $0''.22$ away from DR Tau and is explicitly removed as effectively a duplicate. EPIC 246926943 is a real though optically faint target near a brighter source. The LC is not easily distinguishable from that of its bright neighbor. This target is listed as an NM as a result.

⁷ <https://keplerscience.arc.nasa.gov/k2-pipeline-release-notes.html>

⁸ <https://idlastro.gsfc.nasa.gov>

⁹ <http://irsa.ipac.caltech.edu/applications/finderchart>

2.2. Membership

2.2.1. Summary

The details of our membership selection process are given in Appendix A. To summarize, we have selected 156 of the “highest-confidence” Taurus members, 23 “possible” Taurus members, and 38 stars that constitute an older (~ 30 Myr) “foreground” population. The highest-confidence members are those objects listed as Taurus members in Esplin & Luhman (2019). The possible members are additional objects selected individually by us from the available literature and Gaia DR2 kinematic data as Taurus members; these are generally more dispersed than the highest-confidence members. The ~ 30 Myr foreground population includes (but is not limited to) members of Group 29 (Oh et al. 2018; Luhman 2018); some stars might potentially belong to Mu Tau (M. Gagne et al. 2020, in preparation; Liu et al. 2020) or possibly Cas-Tau (e.g., Hartmann et al. 1991; de Zeeuw et al. 1999; Luhman 2018; also see the appendix of David et al. 2018 and references therein).

Membership status is used in Table 1 for the sample breakdown and is included in Table 2. The highest-confidence sample is listed as distinct from the possible member sample. The highest-confidence and possible member samples are combined into one sample listed as the ~ 3 Myr member sample. The foreground population is a distinct sample with different kinematics and mean distance, and it is likely significantly older than the Taurus population. For completeness, Table 1 also includes the NM sample. Appendix A.2 lists individually the information on stars in the probable NMs.

Unless explicitly indicated, the subsequent analysis in this paper uses the 156 most confident members (typically colored green in the figures) plus the 23 possible members (typically colored yellow-orange in the figures) as the member sample. The 38 stars in the foreground older population are colored blue in the figures.

2.2.2. Sample Statistics

In general, we expect that Taurus members (in comparison to the NMs) will have a higher fraction of disk indicators, a Gaia DR2 parallax between about 6 and 8 mas, and a high fraction of periodic LCs. In practice, since efforts to determine spectral types have focused on members, we also expect members to have a higher fraction of spectral types in the literature. As can be seen in Table 1, all of this can be found in the Taurus member sample. There is a high fraction of spectral types (Section 2.3), periodic stars (Section 3.1), long-wavelength IR detections, and, therefore, disked stars (Section 2.4) among the members.

The foreground sample, because it is older (~ 30 Myr rather than ~ 3), has a lower fraction of disks (and IR detections). It also has a higher fraction of periodic stars, but this is highly biased, since we started from the set of K2 LCs in C4/C13, not from the set of all possible members of this foreground population (which may extend over more K2 campaigns).

The reddening as determined above (Section 2.5) shows that for the highest-confidence members, the distribution of A_K peaks at ~ 0.1 with a tail to ~ 2 ; both the groups of possible members and the foreground have $A_K < 0.3$, with a peak < 0.05 .

Among our K2 work in older clusters, a very high fraction of the members are periodic—92% in Pleiades (Papers I–II), 87% in Praesepe (Paper IV), and 86% in USco (Paper V). We theorized that the lower fractions in Praesepe and USco may be indicative of NM contamination. In Taurus, 81% of the

highest-quality members stars are periodic; in ρ Oph, only 61% are periodic. Two things are likely contributing to the lower fraction of periodic stars in these youngest clusters. Disk emission affects period determination in that stochastic contributions from the disk make periods harder to find. Additionally, NM contamination is also likely to be a factor. Far more effort has been devoted to determining Taurus membership than membership for ρ Oph, so it is more likely that there is a higher NM contamination rate in ρ Oph. The disk fraction among ρ Oph member stars with a K2 LC is 46%, very similar to the Taurus member sample of $\sim 56\%$ (Table 1); ρ Oph is thought to be younger (~ 1 Myr) than Taurus (~ 3 Myr) and, thus, should have more disks. In both cases, most of the disked stars are also periodic. We suspect that the NM disk-free contamination is higher in ρ Oph than Taurus, at least partially accounting for the relatively low fraction of periodic stars in ρ Oph. In contrast, the membership is likely better in Taurus, and the lower fraction of periodic stars arises primarily from “pollution” of the LC by disk-related effects, making periods harder to find.

We note as well that the lowest-mass Taurus members studied here extend into the brown dwarf regime (see, e.g., Scholz et al. 2018). These mid-M stars represent the youngest, lowest-mass stars with high-quality LCs yet observed.

2.3. Literature Data

The literature on stars in (or around or near) Taurus is rich indeed. Aiming for uniform consistency rather than completeness, rather than scouring the literature for individual photometric measurements, we assembled information on each target from several all-sky or large-scale surveys. We matched by position to each catalog with typical matched positions within an arcsecond.

The optical data came from several catalogs. We searched in Gaia DR1 (Gaia Collaboration et al. 2016) for the G magnitude consistent with our prior analyses, and DR2 (Gaia Collaboration et al. 2018) for the more recent G , R_p , and B_p photometry, in addition to parallaxes and proper motions. The kinematic data provided by Gaia DR2 are particularly useful in identifying members (Section 2.2 includes the Gaia DR2 ID; see Table 1 for fractions of samples with Gaia parallaxes). The distances we used here are those provided by Bailer-Jones et al. (2018). Additional optical data were obtained from the AAVSO Photometric All-Sky Survey (APASS; Henden et al. 2016), specifically, V magnitudes. We used both Pan-STARRS1 (Chambers et al. 2016) and the Sloan Digital Sky Survey (e.g., Ahn et al. 2012) for multiband optical data. Every star here has several optical measurements.

We used infrared data from three all-sky surveys: the Two-Micron All Sky Survey (2MASS; Skrutskie et al. 2006) at J , H , and K_s ; the Widefield Infrared Survey Explorer (WISE; Wright et al. 2010) at 3.5, 4.6, 12, and 22 μm ; and AKARI (Murakami et al. 2007) data at 9, 18, 65, 90, 140, and 160 μm . WISE and AKARI have some similar wavelengths, but they have very different sensitivities. We also used infrared data from two pointed missions (as opposed to all-sky surveys). For the Spitzer Space Telescope (Werner et al. 2004), we started with data from the Spitzer Enhanced Imaging Products (SEIP)¹⁰ at 3.6, 4.5, 5.8, 8, and 24 μm , which aggregates all data from the cryogenic portion of the Spitzer mission. The SEIP only

¹⁰ <http://irsa.ipac.caltech.edu/data/SPITZER/Enhanced/SEIP/overview.html>

Table 2
Contents of Table: Periods and Supporting Data for Taurus Members with K2 Light Curves

Number	Column	Contents
1	EPIC	Number in the Ecliptic Plane Input Catalog (EPIC) for K2
2	Coord	R.A. and decl. (J2000) for target
3	OName	Alternate name for target
4	Gaia	Gaia DR2 ID
5	V mag	V magnitude (in Vega mags), if observed
6	K_s mag	K_s magnitude (in Vega mags), if observed
7	$(V - K_s)_0$	$(V - K_s)$, as directly observed (in Vega mags), if V and K_s exist
8	$(V - K_s)_u$	$(V - K_s)$ used, in Vega mags (observed or inferred; see the text)
9	$E(V - K_s)$	$E(V - K_s)$ adopted for this star (in mags; see Section 2.5)
10	K_s mag0	dereddened $K_{s,0}$ magnitude (in Vega mags), as inferred (see Section 2.5)
11	$(V - K_s)_0$	$(V - K_s)_0$, dereddened $V - K_s$ (in Vega mags), as inferred (see Section 2.5; rounded to nearest 0.1 to emphasize the relatively low accuracy)
12	Uncert	two-digit code denoting origin of $(V - K_s)$ and $(V - K_s)_0$ (see Sections 2.3 and 2.5): First digit (origin of $(V - K_s)$): 1 = V measured directly from the literature (including SIMBAD) and K_s from 2MASS; 2 = V from APASS and K_s from 2MASS; 3 = $(V - K_s)$ inferred from Gaia g and K_s from 2MASS (see Section 2.3); 4 = $(V - K_s)$ inferred from Pan-STARRS1 g and K_s from 2MASS (see Section 2.3); 5 = $(V - K_s)$ inferred from membership work (see Section 2.2; rare); 6 = V inferred from well-populated optical SED and K_s from 2MASS (see Section 2.3); -9 = no measure of $(V - K_s)$. Second digit (origin of $E(V - K_s)$ leading to $(V - K_s)_0$): 1 = dereddening from JHK_s diagram (see Section 2.5); 2 = dereddening back to $(V - K_s)_0$ expected for spectral type; 3 = used median $E(V - K_s) = 0.7$ (see Section 2.5); -9 = no measure of $E(V - K_s)$
13	P1	Primary period, in days (taken to be rotation period in cases where there is >1 period)
14	P2	Secondary period, in days
15	P3	Tertiary period, in days
16	P4	Quaternary period, in days
17	Member	Highest-quality member, possible member, foreground young star (see Section 2.2)
18	IR excess	Whether an IR excess is present or not (see Section 4)
19	IRexStr	Minimum wavelength at which the IR excess is detected or the limit of our knowledge of where there is no excess (see Section 4)
20	Slope	Slope of SED fit to all available detections between 2 and 25 μm
21	Class	SED class (I, flat, II, III)
22	Dip	LC matches dipper characteristics (see Section 6.2)
23	Burst	LC matches burster characteristics (see Section 6.2)
24	Sin/mult	single- or multi-period star
25	dd	LC and power spectrum matches double-dip characteristics (see Section 6.2)
26	ddmove	LC and power spectrum matches moving double-dip characteristics (see Section 6.2)
27	Shape	LC matches shape changer characteristics (see Section 6.2)
28	Beat	LC has beating visible (see Section 6.2)
29	Complex	power spectrum has a complex, structured peak and/or has a wide peak (see Section 6.2)
30	Closep	power spectrum has resolved close peaks (see Section 6.2)
31	Distp	power spectrum has resolved distant peaks (see Section 6.2)
32	Pulse	power spectrum and LC match pulsator characteristics (see Section 6.2)

(This table is available in its entirety in machine-readable form.)

includes objects with high signal-to-noise ratio detections; when flux densities did not appear in the SEIP for our targets, we used catalog data from the Spitzer Taurus project (Rebull et al. 2010) for any bands between 3.6 and 70 μm (note that 70 μm was not included in the SEIP, so all 70 μm data come from the Spitzer Taurus project). Most of the members have a Spitzer counterpart; a relatively low fraction of the NMs have a Spitzer counterpart (see Table 1). Relatively few stars in the sample have a Spitzer/MIPS counterpart at 24 or 70 μm . Herschel data cover a portion of the Taurus region. Analogous to the SEIP, the Herschel Space Observatory (Pilbratt et al. 2010) Highly Processed Data Products for PACS 70, 100, and 160 μm (Marton et al. 2017) incorporate all of the data from the mission. Very few targets have a PACS counterpart, but a higher fraction of the members are detected (a rate that is biased by the observations that targeted known members). K2 generally monitored optically bright stars, thereby selecting against embedded stars bright in the mid- and far-infrared.

In general, there is a steep drop off in counterpart numbers as wavelength increases. Table 1 includes the numbers and fractions of stars in several membership categories (Section 2.2) for several representative infrared bands. However, the fraction of Taurus member stars (not foreground, not NM) that are detected out to long wavelengths is much higher than the fraction of NM stars, as expected—Taurus member stars are more likely to have an IR excess and, thus, be detected in these various infrared data sets.

We used all of these photometric data to assemble a spectral energy distribution (SED) for each target. If the data from one catalog were obviously inconsistent with the rest of the SED, then we removed the data points from that catalog for that source on the assumption that the positional match failed. We also used the IRSA Finder Chart tool (as well as its sister tool, IRSA Viewer) to investigate source mismatches.

Our earlier papers use $(V - K_s)_0$ as a proxy for mass, so to better enable inter-cluster comparisons, we continue to do that here. All of the stars have measured K_s , leaving us to find or

calculate V . A substantial fraction of the targets have measured V magnitudes that we could assemble from the literature above, but several stars still lack V measurements. If a Gaia G magnitude is available (from DR1), then $(V - K_s)$ was interpolated from $(G - K_s)$ as in Paper IV (which used DR1 Gaia data to establish this relationship); we estimate errors on these estimates to be ~ 0.017 – 0.085 mag. For stars redder than $(V - K_s) \sim 5$, the relation from Paper IV is linearly extrapolated to $(V - K_s) \sim 8$. Similarly, if no Gaia G mag is available, but a Pan-STARRS1 g is available, then $(V - K_s)$ can be calibrated via an empirical relation between $(g - K_s)$ and $(V - K_s)$; errors on these estimates are probably comparable to those from Gaia-derived colors. As a last resort, for those stars still missing a V estimate, since the SED is well populated in the optical using literature photometry, a V magnitude is linearly interpolated from the SED. All of the targets thus have a measured or inferred $(V - K_s)$.

Table 2 includes, for the most likely members, possible members, and foreground population (identified in Section 2.2), the relevant supporting photometric data, including the observed or interpolated $(V - K_s)$, plus the periods we derive (in Section 3.1) and the IR excess assessments (Section 2.4). A similar table with all of the likely NMs appears in Appendix A.2.

Most of the Taurus members have spectral types in the literature (Table 1). We assembled spectral types largely from Luhman et al. (2017), Luhman (2018), and Esplin & Luhman (2017, 2019). Some individual sources have spectral types not collected in these papers, and we assigned those spectral types individually based on the literature.

For those stars with spectral types, we used the spectral types as part of the process for identifying disks (see Section 2.4) and determining the best value of reddening (see Section 2.5). For those stars with spectral types, we used a Kurucz–Lejeune (Kurucz 1993; Lejeune et al. 1997) model corresponding to that spectral type and normalized to the data at the J band. We extended a Rayleigh–Jeans line from the longest wavelength model data point to beyond $24 \mu\text{m}$. Using the reddening law from Mathis (1990), we reddened the models for a grid of A_V values, calculated a reduced chi-sq (χ^2_ν) comparing the model to the data at all optical bands (U , if available) through J . We selected the best fit based on the smallest χ^2_ν . These model fits to the SED are not meant to be rigorous but to instead “guide the eye.”

2.4. Disk Indicators

A substantial fraction of the Taurus members have an IR excess, from which we can infer the presence of a circumstellar disk (see summary statistics in Table 1). In the context of this paper (as for Paper V), we wish to have a *complete* list of disks, as opposed to an unbiased list; we identify a star as a disk candidate if it has a plausibly real excess at any IR wavelength (at which we have a detection) in the catalog we assembled. The wavelength at which the IR excess begins is included in Table 2 (and in the Appendix in Table B1 for the NMs).

Because WISE has a lower spatial resolution than Spitzer, we used IRSA’s Finder Chart tool to inspect the WISE images to see if the detections in the catalog reflect what can be seen in the images. Again following Paper V, to identify disks, we looked at the significance of any putative IR excess at 12, 22, and $24 \mu\text{m}$ where available (with χ calculated as described in Paper V), taking into account that for the latest types, the expected photospheric colors may be >0 . We used the

empirical photospheric infrared color $[W1] - [W3]$ as a function of $(V - K_s)_0$ from Paper V. We then assessed the ensemble of information available for all sources (e.g., all points $\geq 2 \mu\text{m}$, the shape of SED, the results of the simple model fit discussed in Section 2.3 above, etc.). For each source, we have an assessment of whether it has a disk, and if so, the shortest wavelength likely contributing to an IR excess.

In this fashion, as for Paper V, we identified unambiguous disk candidates and non-disk candidates (at least, non-disks given the available data, which often extend at least to 12 or $22 \mu\text{m}$), with a few percent of ambiguous (possible) disks noted as such. Table 1 includes the number and sample fraction for each of the relevant samples. More than half of the Taurus members have disks; there is just one high-confidence (and one more possible) disk candidate among the foreground (~ 30 Myr) population. Note that the disk excess criteria are conservative and that the non-disk sample will likely have contamination from weaker (< 5 – 10σ excess) disks. Note also that the lowest-mass bin is likely incomplete in the non-disks due to sensitivity issues (stars with excesses are more likely to be detected at long wavelengths than stars without excesses). While this sample draws from many surveys and wavelengths, in order to be considered at all, there must be an observation in K2, which requires targeting of the source by a human, and therefore, the sample is affected not only by extinction but pixel mask selection.

Independent of the disk candidate status, we performed a simple ordinary least-squares linear fit to all available photometry (with errors, but just detections, not including upper or lower limits) between 2 and $24 \mu\text{m}$, inclusive. In the spirit of Wilking et al. (2001), we define $\alpha = d \log \lambda F_\lambda / d \log \lambda$, where $\alpha > 0.3$ for a Class I, 0.3 to -0.3 for a flat-spectrum source, -0.3 to -1.6 for a Class II, and < -1.6 for a Class III. The slope and the class are both available in Table 2 (and Table B1, where it is assumed that the IR excess is due to a circumstellar disk, which may not be a good assumption).

For completeness, we note two items. First, Table 1 indicates that there are NM with IR excesses. These objects include evolved stars with dusty winds or envelopes, distant Be stars, and a few extragalactic objects (active galactic nuclei, quasi-stellar objects). Second, Tables 2 and B1 indicate the onset of IR excess for each target. Since the IR excess could affect the K_s bands, which could cause an overestimation of A_V in the methods described below, we note that such targets are a minority here; $>80\%$ of the highest-quality members have disks that start at longer than $3 \mu\text{m}$.

2.5. Dereddening

The reddening in the direction of Taurus can be substantial and patchy. As noted above, we obtained spectral types from the literature. In order to deredden the $V - K_s$ colors, we followed the same approach as in Paper V (specifically for ρ Oph), with some modifications.

We can place essentially all of the stars on a $J - H$ versus $H - K_s$ diagram. We can deproject much of the sample back along the reddening law derived by Indebetouw et al. (2005) to the expected JHK_s colors for young stars from Pecaut & Mamajek (2013) or the T Tauri locus from Meyer et al. (1997). Note that there is a discontinuity between the end of the Pecaut & Mamajek relation and the beginning of the T Tauri locus (noted in Meyer et al. 1997 and Paper V); this results in a small gap in the dereddened $(J - K_s)_0$ distribution between ~ 0.9 and

~ 1.0 . The reddening so derived can be converted to $E(V - K_s)$ via $A_K = 0.114A_V$ (Cardelli et al. 1989). This approach worked well for Upper Sco in Paper V, but it did not work as well in ρ Oph, primarily because there is significantly higher reddening. Similarly, there is high reddening toward some of the stars in Taurus, and there is a lot of scatter, even in the NIR colors.

Another approach used in Paper V (and preferred in ρ Oph) was to take the spectral type, compare the observed colors to those expected for that type from Pecaut & Mamajek (2013), and calculate the resultant reddening. Consequently, any distribution of colors for stars dereddened in this fashion will be quantized, because, e.g., all stars of type M1 are assigned to have the same color. Due to the high fraction of spectral types for Taurus members, we can calculate reddening following the above prescription for most of the members.

Because there is patchy reddening and a lot of scatter in the JHK_s diagram (much more than for USco, for example), we took the reddening estimate from the spectral type first. If that value was unphysical (e.g., < 0), then we took the value derived from the JHK_s diagram. Some of those values were still unphysical or insufficient (e.g., $(V - K_s)_0$ was still > 8 or 10). So, for those stars with spectral types, we used the Kurucz–Lejeune model grid fitting described above (Section 2.3) to estimate the reddening in a third way. For several of the foreground population lacking spectral types, the reddening derived from the JHK_s diagram was substantially discrepant from the SED fitting having guessed a spectral type based on the observed $(V - K_s)$. In those cases, we selected the best reddening from the SED fitting. As a fourth and last resort, we assigned a star the modal reddening of $E(V - K_s) \sim 0.46$ determined via the comparison of observed values to that expected from the spectral type for the ensemble.

Table 1 includes the numbers and sample fractions for each of these approaches. The value used for most stars comes from either of the first two approaches (spectral type or JHK_s diagram). For relatively few stars do we have to fall back to the most likely reddening.

The dereddened $(V - K_s)_0$ we used for each object is included in Table 2 for the members and in Appendix A.2 for the NMs. However, to emphasize the net uncertainty, the “vmk0” column in Table 2 has been rounded to the nearest 0.1 mag. The values used in the plots here can be recovered by using the $E(V - K_s)$ (“ev-k”) and $(V - K_s)_{\text{observed}}$ (“vk-used”) columns.

The net errors are hard to quantify after all of these steps. Table 2 (and its analogous Table B1 for NMs) include a two-digit code indicating the origin of the $(V - K_s)$ value and the method by which the $(V - K_s)$ was dereddened to $(V - K_s)_0$ (see Table 2 or B1 for specific definitions). The reddening can be large and a significant source of uncertainty. Via internal comparisons and uncertainties not just on the assumed photospheric colors but also uncertainties in spectral typing, we estimate that the typical uncertainty for Taurus members could be as much as 1 magnitude in $E(V - K_s)$. To quantify this further, for the highest-quality members, we compared the reddening values derived from the JHK_s diagram, from spectral types, and from SED fitting. The reddening derived from the SED is well matched to that from the JHK_s diagram; that from the spectral type has systematic offsets with respect to the others in the sense that the reddening from the spectral types is lower on average but also negative (e.g., unphysical) far more often. In all cases, a Gaussian fit to the distribution of fractional

differences suggests that a scatter of ~ 0.5 mag in $E(V - K_s)$ is typical. Most of the JHK_s measurements come from 2MASS, where the measurements should have been roughly simultaneous for the three bands, so intrinsic variability alone cannot account for the scatter. It is not the case that emission from the disk is affecting the JHK_s , because the K2 sample is biased toward optical sources, and as noted above, most ($> 80\%$) of these disks become apparent at $3.5 \mu\text{m}$ or longer. The large uncertainty in reddening is real but evidently unavoidable.

3. Periods and CMDs

3.1. Finding Periods in the K2 LCs

Our approach for finding periods was identical to that used in Papers I, II, IV, and V. In summary, we used the Lomb–Scargle (Scargle 1982) approach as implemented by the NASA Exoplanet Archive Periodogram Service¹¹ (Akeson et al. 2013). We also used the IRSA Time Series Tool¹², which employs the same underlying code as the Exoplanet Archive service but allows for interactive period selection. We looked for periods between 0.05 and 35 days, with the upper limit being set by roughly half the campaign length. Because the periods are typically unambiguous, false alarm probability (FAP) levels are calculated as exactly zero for most of the periods we present here (and the remaining FAP levels are typically $< 10^{-4}$).

The periods we derive appear in Table 2 for all members and in Appendix A.2 for the NMs.

3.2. Interpretation of Periods

In Papers I, II, and IV, we described in detail the LC and periodogram shapes we observed in the older Pleiades and Praesepe clusters; Paper V included an additional section on the physical interpretation of the LCs of younger stars in USco and ρ Oph. Here, we briefly summarize and refer the reader to those earlier papers for more detail.

Including both C4 and C13, 81% (127 stars) of the highest-confidence Taurus member sample stars have at least one identifiable period in their LC. We retain up to four periods; 32 (21%) have more than one period. Nearly all of the foreground population has at least one period. More than 95% of the sample we focus on here (members of Taurus or belonging to the foreground) have LCs consistent with a surface spot origin. For stars with two (or more) periods that we believe are due to rotation, we plot only one point at the period we believe corresponds to the actual rotation period of the star dominating the $(V - K_s)_0$ measurement. In those cases, particularly among the M stars, where there are two (or more) periods that are not close together, we believe the star to be a likely binary (or other multiple); see Papers II and IV, and Stauffer et al. (2018a).

In a few stars, just two of the possible members, there is a forest of very short period peaks in the periodogram. We take these to be pulsators.

There are seven stars in the entire sample that have little or no IR excess but have periodic LC shapes with scallop shell or flux dip morphologies, which cannot be due to spots or pulsation; see Stauffer et al. (2018b, 2017) for a discussion of these types of LC morphologies. Of these stars, three of

¹¹ <http://exoplanetarchive.ipac.caltech.edu/cgi-bin/Periodogram/nph-simpleupload>

¹² <http://irsa.ipac.caltech.edu/irsaviewer/timeseries>

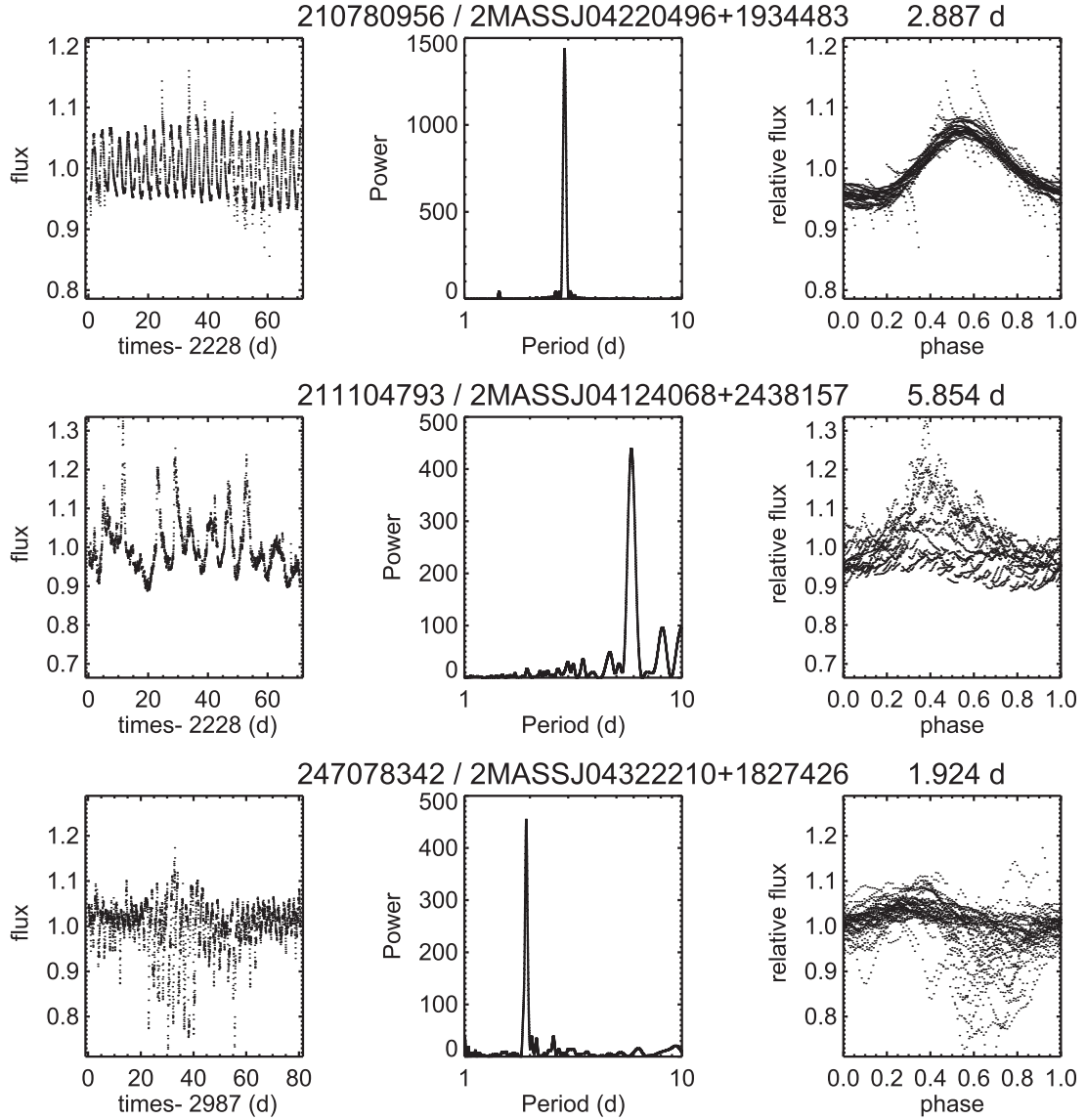


Figure 2. Example Taurus LCs for a single-period sinusoid LC (first row), burster (second row), and dipper (third row). The panels are: best LC, power spectrum, and phased LC for first period. The objects, from top to bottom, are: EPIC 210780956/2MASS J04220496+1934483 (no IR excess; data from C4), EPIC 211104793/2MASS J04124068+2438157 (large IR excess; data from C4), and EPIC 247078342/2MASS J04322210+1827426 (large IR excess; data from C13). All of these targets are confident members of Taurus.

them are highest-quality members (EPIC 246938594, EPIC 246969828 = CI*Melotte25LH19, and EPIC 247794636 = 2MASS J04321786+2422149), three are possible members (EPIC 246676629 = UCAC 4522-000989, 246682490 = UCAC 4522-009859, 247343526 = 2MASS J04405340+2055471), and one is part of the foreground population (EPIC 246776923). Because the primary period in these cases is likely to either be a rotation period or strongly related to a rotation period, these were retained as rotation periods.

As in other young clusters, there are LCs with dipper or burster morphologies (see, Figure 2 and, e.g., Paper V; Cody et al. 2014; Stauffer et al. 2014, 2015, 2016a; Cody & Hillenbrand 2018). All of the LCs we identified as dippers (21 members) or bursters (25 members) also have disks, and all are members of some sort (Table 1). These are identified in the corresponding tables (Table 2 and Appendix A.2). Note that the period we report as the rotation period is often but not always

also the period of the dips/bursts; sometimes the dips/bursts align with the sinusoidal modulation, and sometimes they do not. N. Roggero et al. (2020, in preparation) will explore the dipper population in Taurus.

We categorize “timescales” for LCs that seem to have a repeating pattern, but the pattern does not seem to be due to starspots or other rotation-related phenomena and, therefore, are not taken as periodic; see Appendix B.

3.3. Comparison to Literature Periods

A detailed comparison between periods in the literature (consisting of a few to tens of stars per study) and periods we derive from K2 data is given in Appendix C.

In summary, we conclude that we are recovering most of the periods reported in the literature. The results are a mix of excellent agreement, likely harmonics reported in the literature,

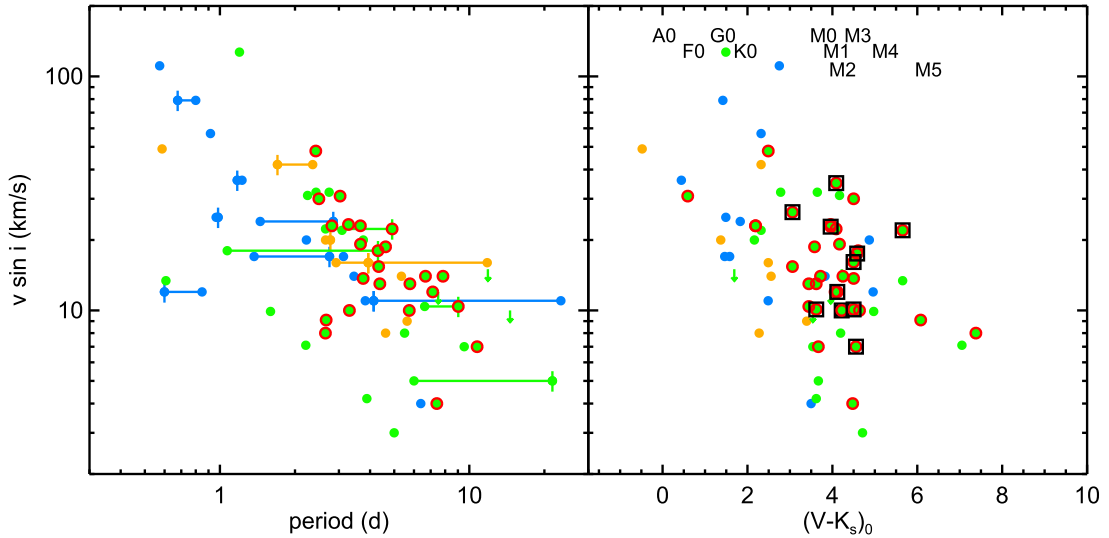


Figure 3. Comparison of periods obtained here to $v \sin i$ from the literature. Left panel: $v \sin i$ (from the literature) vs. period (as derived here). Right panel: $v \sin i$ (from the literature) vs. $(V - K_s)_0$. The colors of the points are as follows: green = highest-confidence member; orange = possible member; and blue = young, foreground population (see Section 2.2), where arrows denote upper limits. An additional red circle around a point denotes a high-confidence disk. In the left panel, the points linked by lines connect the first period (what we have taken as the rotation rate of the star, denoted by a small vertical line) with the fastest and slowest periods available for that star, on the assumption that the $v \sin i$ may not correspond to the first period for those stars with multiple periods. In the right panel, an additional square around a point indicates that we found no period for this star in the K2 data. There is no obvious trend for the stars lacking periods to have systematically higher or lower $v \sin i$ than those with periods.

and, for a few, significant disagreement with the periods derived from the high-quality K2 data.

The study with which we have the most disagreement is the Kilodegree Extremely Little Telescope (KELT) analysis (Rodríguez et al. 2017b), where 19/26 do not match. Our analysis of other clusters in common with KELT produced a much better match in periods. Perhaps this is not surprising, in particular for those stars still actively accreting or where the distribution of spots may be changing on relatively short timescales; changes in the LC shape of an accreting object can reasonably be expected to change on \sim year timescales even though the stellar rotation rate itself does not change on short timescales.

In any event, for each mismatched period, we investigated the prior period and believe that the period(s) we report is/are the correct periods for these stars during the K2 campaign(s).

3.4. Comparison to Literature $v \sin i$

As discussed above in Section 2.2, it is likely that the relatively low fraction of Taurus members with periods in the K2 data is due to disk contributions to the LCs, making periods difficult to extract. To determine whether or not this results in a bias in our derived period (P) distribution, we compared our periods with the projected rotational velocities ($v \sin i$) from the literature. We started with the $v \sin i$ compilations in Rebull et al. (2004) and Güdel et al. (2007) and then added those from Nguyen et al. (2009).

Out of the Taurus members or the foreground population with K2 LCs, there are 51 with $v \sin i$ measurements or limits in the literature. Figure 3 compares the $v \sin i$ and the periods measured here. For stars with multiple measured periods, the measured $v \sin i$ in the literature may not correspond to the period we have taken as the rotation period. Thus, those stars with multiple periods are indicated in the plot. Disks and stars lacking periods in the K2 data are indicated.

In the left panel of Figure 3, we recover the expected relationship in that stars with fast P have large $v \sin i$. Stars with disks lack shorter periods (< 2 days; see Section 4 below). In the right panel of Figure 3, there is no obvious trend for the stars lacking periods to have systematically higher or lower $v \sin i$ than those with periods. We conclude that our sample with periods is not significantly biased by omitting the $\sim 20\%$ of (member) stars (nearly all of which have disks) that do not have periods, and comparisons to other, older clusters should be straightforward.

3.5. CMDs

Figures 4–6 are various versions of the $K_s/(V - K_s)$ CMD for the entire sample with each highlighting the stars of interest: the most likely Taurus members, the possible Taurus members, and the older foreground population. Figure 4 shows the observed CMD, and Figures 5 and 6 show dereddened CMDs. Figures 4 and 5 include apparent and absolute K_s , but not every star has a Gaia distance (see statistics in Table 1), so Figure 6 shows just apparent magnitudes. Figure 6 also distinguishes the periodic from the disked stars. By inspection of these CMDs, we primarily see that reddening is important, and the foreground population is older than the Taurus members.

3.5.1. Taurus Members

The observed CMD (Figure 4) shows a very large scatter for the Taurus members (both high-confidence and possible), most obviously in $(V - K_s)$ color. Correcting for distance alone does not substantially reduce that scatter. (Correcting for distance makes large changes to the scatter of the NMs, and it becomes apparent that many NMs are giants.) When dereddened (Figure 5), the Taurus members (both high-confidence and possible) form a more recognizable cluster sequence, though still with scatter. Some of this scatter arises from uncertainty in the reddening correction, but some is likely intrinsic to the Taurus population. Although we are using K_s , which can be

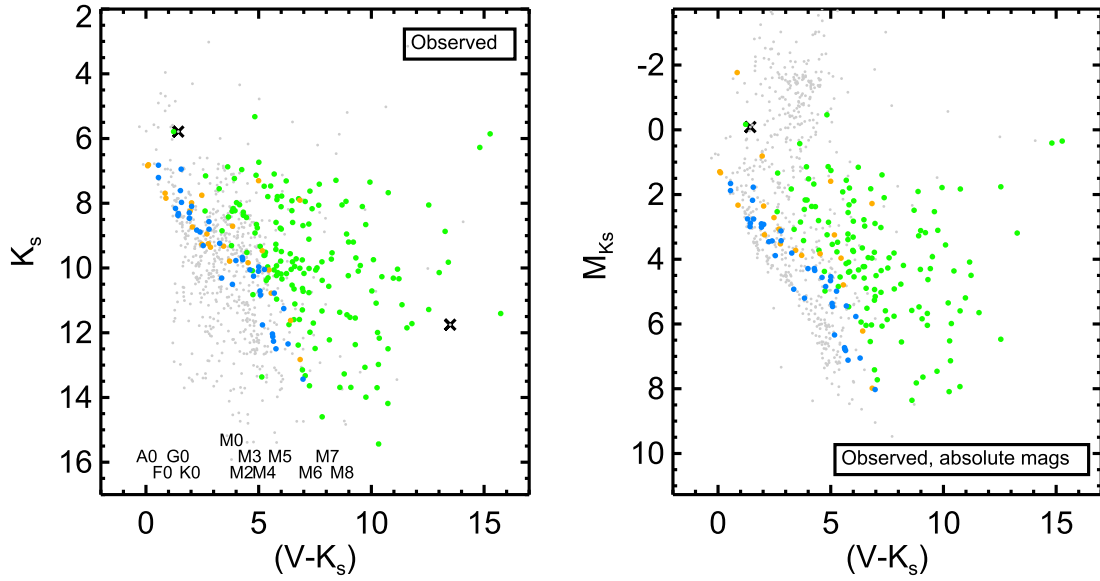


Figure 4. CMDs (K_s vs. $(V - K_s)$) for the sample for which we had or could infer $(V - K_s)$ as described in the text (Section 2.3). In both plots, the colors are as follows: green shows highest-quality members; orange shows possible members; blue shows the foreground population; and gray shows those in the initial sample of candidate members (see Section 2.2). Points shown as \times are too bright or too faint to yield periods from their LCs. Approximate spectral types for each $(V - K_s)$ color are given in the first plot. Left panel: observed values. Note that Taurus members (highest-quality) are often highly reddened, and the foreground population has a considerably lower range of observed colors. Right panel: observed values but shifted for each object for which we had a Gaia DR2 distance (Section 2.3, sample fractions in Table 1) to convert the y-axis to absolute K_s . In these observed CMDs, the members have a large dispersion toward the red. The foreground population is relatively well-behaved. The NM background includes a lot of giants, as revealed in the right-panel CMD using absolute magnitudes.

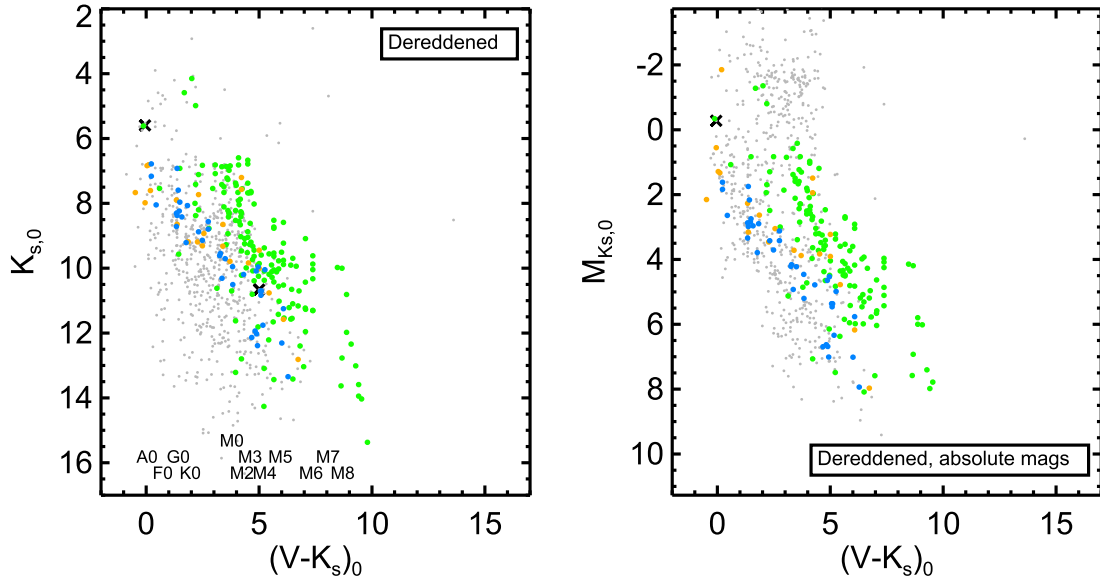


Figure 5. Dereddened CMDs ($K_{s,0}$ vs. $(V - K_{s,0})$) for the sample. The notation is the same as in Figure 4, and note that the range on the x-axis is the same as that in Figure 4 as well. Left panel: dereddened (Section 2.5), observed values; right panel: dereddened absolute values. Correcting for reddening brings most of the stars bluer, and the change is large for many of the Taurus member stars in particular. The Taurus members are in a cluster sequence, but it is not as tight a relationship as in the older clusters (Papers I or IV) because the stars are so young. Some quantization can be seen as a result of the dereddening approach for some stars with spectral types (see Section 2.5). Little change occurs for the foreground population, as they are less subject to reddening than the Taurus members. They are lower in the CMD than the Taurus population, indicating that they are older.

affected by circumstellar disks, because this sample is defined by, and thus biased toward, targets with K2 LCs, those stars with disks substantial enough to significantly affect K_s are generally also those that are so embedded as to not have a K2 LC. Table 2 (and its NM counterpart Table B1) includes an indication of where the IR excess starts, if an IR excess is

detected. Less than 20% of the highest-quality member are likely to have their K_s value affected by disk excesses.

The relative lack of highest-confidence members toward the higher masses ($(V - K_s)_0 \lesssim 4$) noted in Section 2.2 is apparent; many of the possible members (and for that matter, foreground population; see below) do fall in this color range.

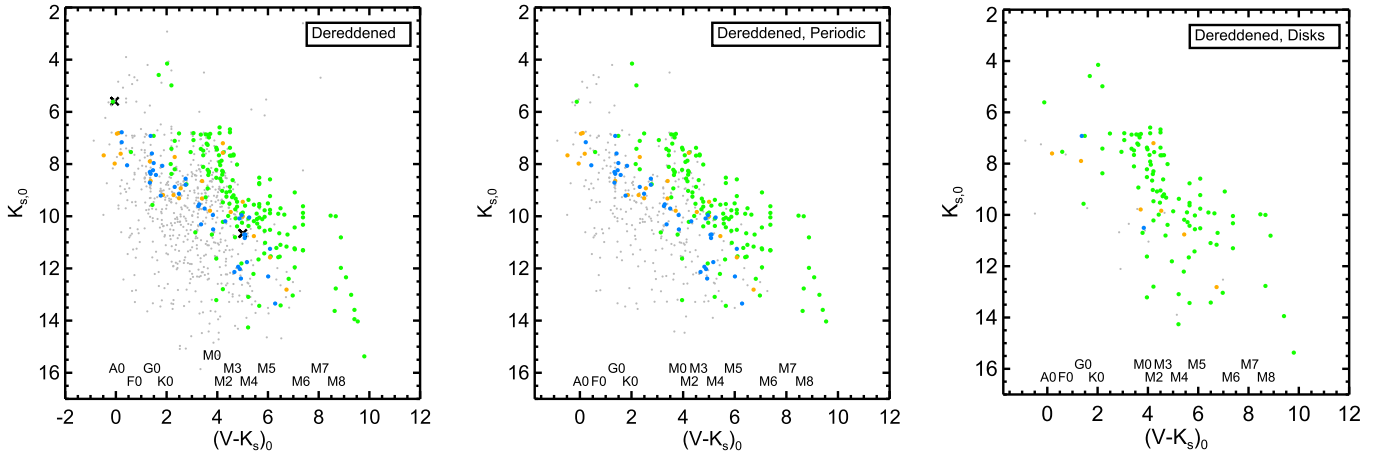


Figure 6. Dereddened CMDs ($K_{s,0}$ vs. $(V - K_s)_0$) for the sample. The notation is the same as in Figures 4 or 5, but now the x -axis is adjusted to encompass the smaller range of dereddened member $(V - K_s)_0$. Left panel: $K_{s,0}$ vs. $(V - K_s)_0$ for the sample (same as the left panel Figure 5; repeated here to show with the same y -axis as the other plots in this figure). Middle panel: $K_{s,0}$ vs. $(V - K_s)_0$ for the periodic subsample. Right panel: $K_{s,0}$ vs. $(V - K_s)_0$ for the subsample with circumstellar disks (IR excess). The periodic sample and the sample with disks are more dominated by Taurus members; nearly all of the foreground population have periods, and just two have disks.

Figure 6 highlights the periodic and disked samples in the dereddened CMD. (See statistics in Table 1.) Because a high fraction of the members (high-confidence and possible) are periodic, most of the Taurus stars appearing in the dereddened CMD also appear in the dereddened CMD of stars with periods. Because a lower fraction of the NMs have periods, many NMs do not appear in the CMD of stars with periods; in general, if a target has a period, it is more likely to be young. Similarly, a high fraction of the disked population are also members (most often members of Taurus, as opposed to the foreground population).

3.5.2. Foreground Population

In contrast to the Taurus members in Figure 4, there is not very much scatter in the foreground population’s observed CMD; these stars, on average, have low extinction. The foreground sample is in front of most of the gas and dust associated with Taurus, so this tight cluster sequence is not surprising. In both Figures 4 and 5, the foreground population is also clearly lower in the CMD than most of the Taurus members (from either confidence level), indicating that this foreground population is older than that of Taurus.

In Figure 6, the periodic subsample retains all but one of the stars considered part of the foreground population. The fact that they have measurable periods means they likely have big spots and thus are likely young, but they are not Taurus members (see Section 2.2). Just two of the foreground population have a disk (one possible disk, one unambiguous disk); this low disk fraction is another indication that the foreground population is older than the Taurus members.

4. Disks and Rotation

Paper V presented LCs from USco that provide direct evidence for disk locking, with a striking clumping of disked stars near ~ 2 days, particularly for the later spectral types. Figure 7 shows period (P) versus IR excess ($[3.5]-[12]$), for ρ Oph (~ 1 Myr; data from Paper V) and Taurus (~ 3 Myr; just the highest-quality member sample). There are comparable numbers of stars in these two clusters and likely comparable uncertainties leading to $(V - K_s)_0$, though we believe that we

have done a slightly better job of dereddening in Taurus than in ρ Oph (see Section 2.5). Uncertainties in P should be low, and reddening should not significantly affect the $[3.5]-[12]$ excess, but reddening will affect which bins (which panel in the plot) encompass which targets.

The relationship between P and color seen in USco (Paper V) is not nearly so convincing in ρ Oph. However, in Taurus, the relationship is clearer; the disked stars are clumped near ~ 2 days, and there are very few stars that both rotate more quickly than ~ 2 days and have disks. Taurus resembles USco more than ρ Oph, which makes sense, as Taurus is older than ρ Oph (and younger than USco). Moreover, ρ Oph may be too young for disk locking to dominate (e.g., Hartmann 2002). As noted above, Figure 3 also suggests that the stars with disks rotate more slowly.

More detailed statistical tests reinforce what is seen by eye. For USco, all statistical tests find significant differences (Kolmogorov–Smirnov $[K-S]$ and Anderson–Darling for just the period distributions; 2D two-sided $K-S$ for the full distribution of P versus $(V - K_s)_0$). For the other two clusters, the disked and non-disked star samples are small enough that the results are just not as clear. In ρ Oph, the 2D distributions that are most significantly different are for $2 < (V - K_s)_0 < 4$ (the upper right panel), but there are only four non-disked stars, so this is not a very robust result. In Taurus, the P distribution alone for the non-disked sample is close to that for the disked stars; there is a clumping of the black points near $\sim 3-5$ days, which is most apparent in the $2 < (V - K_s)_0 < 4$ bin (the upper right panel of Figure 7). The 1D P distributions are the most different for the $(V - K_s)_0 < 2$ sample, but there are very few stars. The 2D distributions are significantly distinct between the disked and non-disked populations in each panel, but more ambiguously than for USco. (USco 2D $K-S$ for the $5 < (V - K_s)_0 < 7.5$ bin has a probability of $\sim 2 \times 10^{-20}$ that they come from the same parent population; the same test for the same Taurus bin is ~ 0.001 . The same test for the same color range but for ρ Oph is just 0.23.)

We conclude that, within the constraints of the relatively small number of stars and the uncertainty in $(V - K_s)_0$, there is some evidence that disks affect the rotation rate distribution in Taurus. The distribution of rotation rates versus color in Taurus

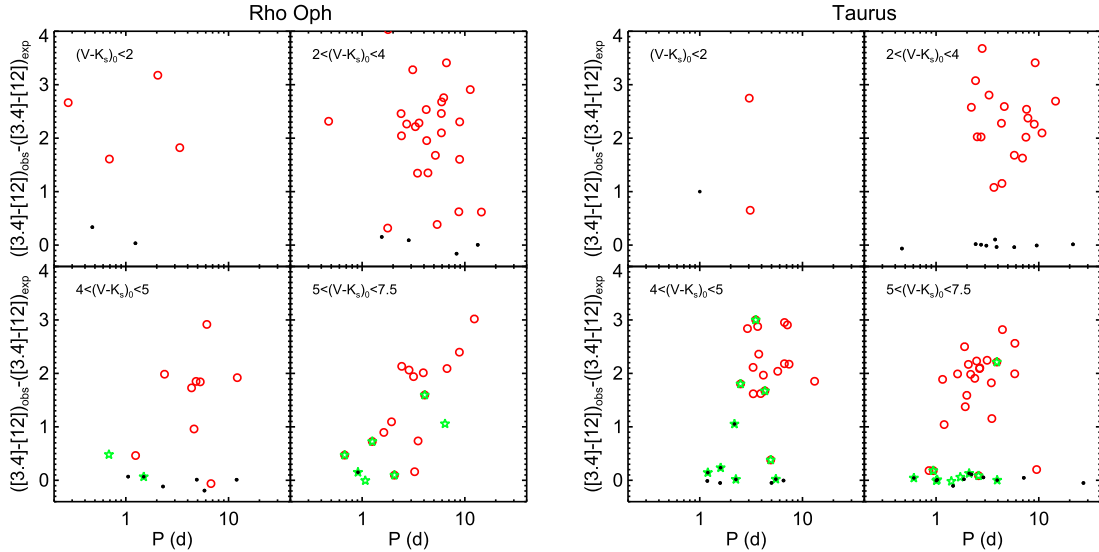


Figure 7. Observed $[3.4]–[12]$ minus the expected photospheric $[3.4]–[12]$ (see Section 2.4) vs. P for stars in ρ Oph (left panels) and Taurus (right panels; highest-confidence members only), differentiating between the high-confidence disked stars (red, open circles) and the high-confidence non-disked stars (small black dots). M stars are shown in the bottom panels; the left bottom panel, $4 < (V - K_s)_0 < 5$, is roughly M0–M3, and the right bottom panel, $5 < (V - K_s)_0 < 7.5$, is roughly M4–M5. An additional green star in these panels denotes that it has more than one period (and is not tagged a pulsator), e.g., a likely binary; see the text. The relationship in ρ Oph is far less clear than that in USco, because there is far more uncertainty in $(V - K_s)_0$, and there are far fewer stars in comparison to USco. Although uncertainty in $(V - K_s)_0$ and far fewer stars also affect Taurus, the relationship in Taurus more clearly resembles that in USco than in ρ Oph; Taurus is older than ρ Oph and younger than USco.

more closely resembles that from USco than that from ρ Oph. We note also that there seem to be few binaries with disks in the lower-mass bin in Taurus, but with the relatively few stars available, it is hard to assess the significance of this in comparison to the other clusters.

We also note that all but one of the highest-confidence Taurus members that lack a period from K2 also have disks, supporting the idea that stochastic contributions from the disk can make periods harder to find.

5. Period–Color Distributions

In this section, we investigate P as a function of $(V - K_s)_0$ and put Taurus (and the foreground population) in context with the other clusters we have studied with K2 data. As in our other K2 rotation papers, for stars with more than one period, we have taken the first period and the measured $(V - K_s)_0$ as representative of the same star (likely the primary if it is a multiple); both the assumed $(V - K_s)_0$ and first period are listed in Table 2. Even if the star is a designated multiple identified from additional periods and position in the CMD, we do not include subsidiary companions separately in this analysis. Additionally, as before, we assume that the stars in these three clusters represent snapshots in time of the same population (see Coker et al. 2016).

5.1. Distribution of P versus $(V - K_s)_0$

Figure 8 shows P versus $(V - K_s)_0$. The left panel has the foreground older population; the others have both the highest-confidence members and the possible members. Overall, the slowest rotators are found in the early M stars and the fastest rotators are found in both the highest masses, A stars and F stars, and in the lowest masses we have here, mid-M stars. Despite the far fewer stars available from the foreground population, it can be seen, on average, that they are rotating more quickly than the (younger) Taurus members, consistent

with their older ages. The disked stars are, on average, rotating more slowly than the disk-free Taurus members, consistent with disk locking (see Section 4 above). The latest M stars in Taurus are the youngest M stars yet studied with high-quality LCs.

Figure 9 puts the P versus $(V - K_s)_0$ for Taurus and the foreground population in context with the other young clusters that have periods we derived from K2 LCs: ρ Oph (~ 1 Myr; Paper V), USco (~ 8 Myr; Paper V), Pleiades (~ 125 Myr; Papers I–III), and Praesepe (~ 790 Myr; Paper IV).

There are relatively few stars in Taurus (and even fewer foreground stars) in comparison with the older clusters. The shortest periods in all of these clusters are on the order of hours and are limited by breakup (see discussion in Paper V). The longest periods found in the youngest clusters are those of early M stars and are ~ 10 – 20 days; there are many periods longer than ~ 10 days in Praesepe, encompassing K and early M stars. At older ages, there are two well-defined sequences: rotation period increasing (slower rotation) to lower mass for FGK stars, and a second sequence where rotation period decreases sharply (faster rotation) as mass decreases among the M dwarfs. These two trends (particularly the latter) appear to already be in place by Taurus’s age (~ 3 Myr). For higher-mass stars ($(V - K_s)_0 \lesssim 3$), the trend is for higher masses to have faster rotation rates (smaller P), and lower masses to have slower rotation rates, although there are very few stars available. For low-mass ($(V - K_s)_0 \gtrsim 3$) stars, there are shorter periods at lower masses. Such trends are harder to see in the ρ Oph sample, perhaps because of larger uncertainties in the colors (due to larger and more variable reddening). It does seem to be there in the Taurus foreground sample as well (~ 30 Myr). There is an apparent decrease in the range of periods at a given color/mass as a function of age; this is at least partially (perhaps completely) due to the larger uncertainties in the inferred colors at younger ages. The $(V - K_s)_0$ colors are more uncertain in the youngest clusters due to the larger

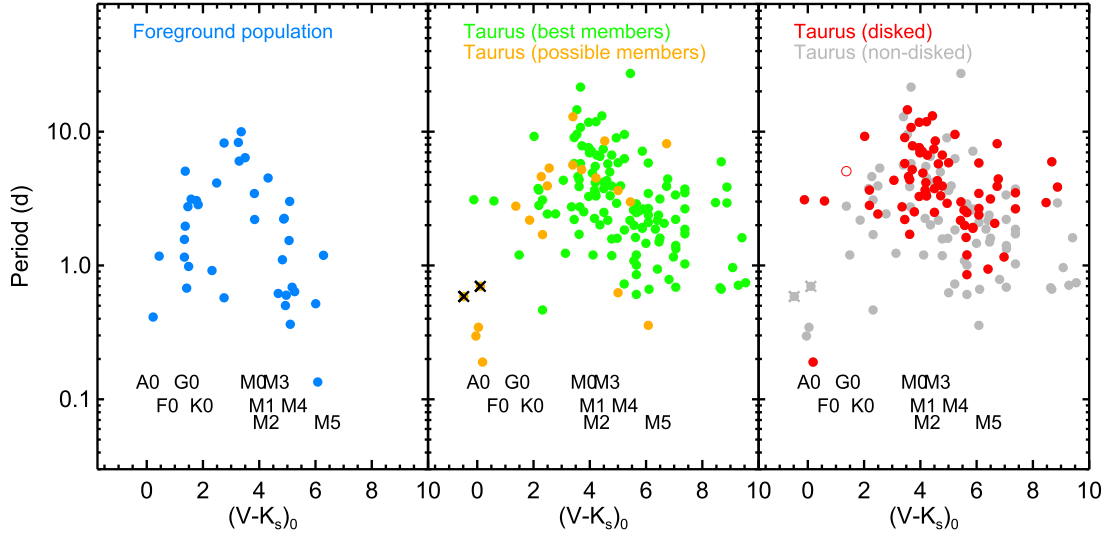


Figure 8. P vs. $(V - K_s)_0$. Left panel: (blue) foreground population. Middle panel: green = highest-quality Taurus members; orange = lower-confidence Taurus members; an additional \times denotes stars that we believe to be pulsators. Right panel: red is disked, and gray is non-disked, for best and possible Taurus members (the single high-confidence disk among the foreground population is a hollow red circle). Approximate spectral types are indicated for reference. The slowest rotators are found in the early M stars; fast rotators are found in the A, F, and G stars and in the mid-M stars, the latest type we have here. Stars from the foreground population, on average, rotate more quickly than the younger Taurus members. Stars with disks, on average, rotate more slowly than stars without disks.

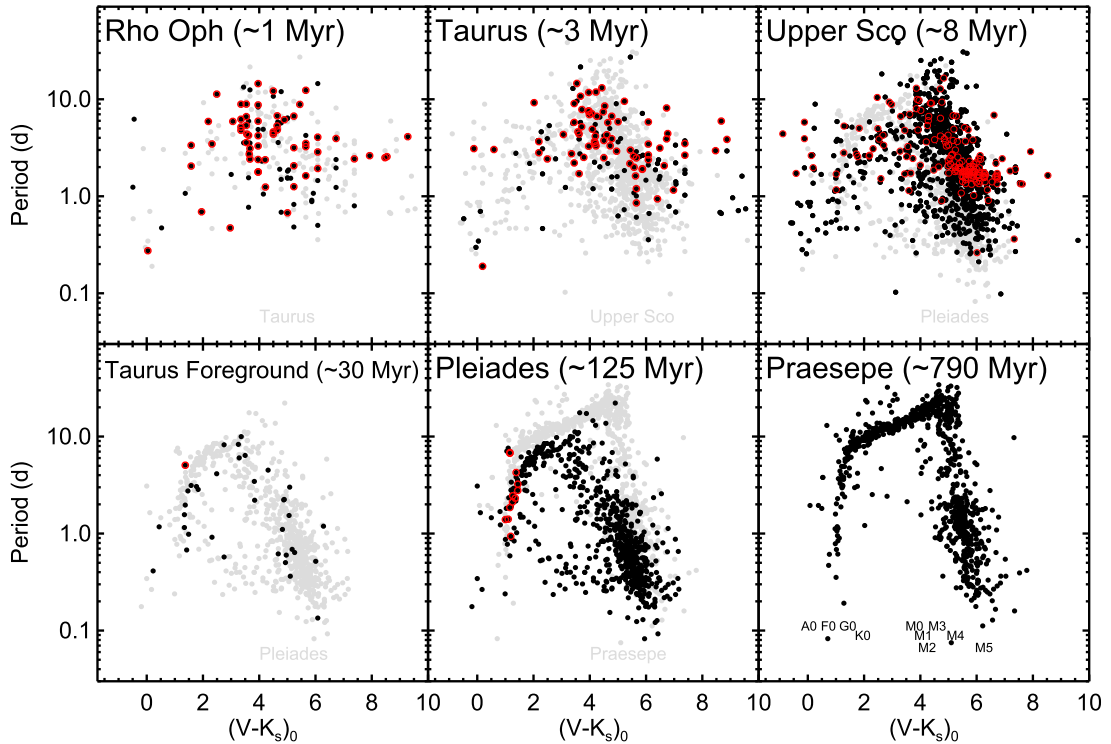


Figure 9. P vs. $(V - K_s)_0$ for stars in Taurus and the foreground population (“Taurus Foreground”) in context with the other clusters with K2 periods. In each panel, the black dots are members, and the gray dots are members from the next panel—e.g., the Taurus sample has the USco sample in gray beneath it to aid in comparison between clusters. (The Pleiades appears for comparison in both USco and the Taurus foreground because the foreground population is just too sparse to provide meaningful comparisons to USco.) Additional red circles denote circumstellar disks; note that the Pleiades disks are all debris disks, while most of the disks in USco and all of those in Taurus and ρ Oph are primordial disks. Upper left panel: ρ Oph (~ 1 Myr, from Paper V); upper center panel: Taurus (~ 3 Myr); upper right panel: USco (~ 8 Myr, from Paper V); lower left panel: Taurus foreground (~ 30 Myr); lower center panel: Pleiades (125 Myr, from Papers I–III); lower right panel: Praesepe (~ 790 Myr, Paper IV). Approximate spectral types are indicated for reference in the Praesepe panel. Errors on colors are conservatively estimated to be ~ 1 mag for ρ Oph and Taurus, ~ 0.4 mag for USco and the Taurus foreground, and smaller than the points for the Pleiades and Praesepe. Recall that the apparent quantization of some stars’ $(V - K_s)_0$ (most apparent in ρ Oph and some Taurus) is a result of our dereddening to the expected $(V - K_s)$ color for that spectral type when that method of dereddening was the best option (see Section 2.5). The Taurus distribution has a lot of scatter but is starting to resemble the USco distribution. The (sparse) Taurus foreground distribution is consistent with the Pleiades distribution.

extinction corrections, possibly the influence on K_s from the disk (this is relatively rare in this sample), and possibly due to variable extinction or accretion (and the non-simultaneity of the observed or inferred V and measured K_s). The Taurus distribution is not as organized as USco, but it is also not as disorganized as ρ Oph. The Taurus distribution is starting to resemble the USco distribution, but it still has a lot of scatter, particularly in the M stars, more like ρ Oph. The Taurus foreground distribution is sparse indeed but consistent with the Pleiades distribution.

The influence of disks can be seen in Figure 9; the top panels show all primordial disks, and the “pile-up” at ~ 2 days is obvious in USco but less so in the younger clusters (see Section 4 above). The disks in the Pleiades are all debris disks; the debris disk sample is likely incomplete among the M stars in Pleiades and Praesepe, since the more subtle IR excesses indicative of debris disks are harder to find among the fainter stars.

6. Linkages to Analysis in Papers I–V

Although the high-quality K2 data enable us to derive reliable periods for active young stars, the presence of disks makes a difference in the rotation rates and the LC shapes in clusters younger than ~ 10 Myr. There are some similarities between the LCs we find in Taurus (and the foreground population) and LCs in the other clusters. In this section, we provide an assessment of the properties of the Taurus LCs in the same fashion as our other papers.

6.1. Amplitudes

We included in Papers I (Pleiades) and IV (Praesepe) information about the variability amplitude, where we define amplitude as the difference in magnitude between the 10th and the 90th percentile of the flux distribution for a given LC. We did not include such a discussion in Paper V (USco and ρ Oph) because the systematics in that campaign (C2) were large and hard to manage (e.g., the fraction of the variability due to the instrument or due to the star is hard to determine). In most cases, however, the amplitudes we measured for the “best” LC for the periodic sources in USco and ρ Oph are probably usable in the ensemble, especially given the relatively large uncertainty in $(V - K_s)_0$. The instrumental systematics in the Taurus campaigns are much lower than that in C2, so here again, the amplitudes are probably due primarily to the astrophysical source.

Figure 10 shows the amplitudes of periodic variability (10th to 90th percentiles) as a function of color and period for our K2 young clusters. As in Figure 9, the echoes of structures seen in the older and more populated cluster plots can be seen in the younger clusters. The average LC amplitude decreases with cluster age.

Stars with primordial disks have larger amplitudes, on average, though disked and non-disked stars both have a wide range of amplitudes in the youngest three clusters (ρ Oph, Taurus, and USco). The variability amplitudes for the Taurus disked stars primarily measure the larger amplitude variability due to accretion bursts (“bursters”) or variable extinction (“dippers”). The variability amplitudes for the non-disked stars (and for the low-mass stars in the older clusters in Figure C1) primarily measure non-axisymmetrically distributed spots as they rotate into and out of our line of sight.

The earliest spectral type stars sampled here (A and F stars) have lower amplitudes, on average, than their same-age counterparts among the G, K, and M stars. This makes sense since the A and F stars are expected to have substantially less fractional spot coverage than the G, K, and M stars at any given age.

We expected that longer period rotators might have lower amplitudes on average, due to lower levels of activity. That is very roughly the case at the ages of Praesepe and perhaps Pleiades; it might be the case at the age of USco, and it seems to not be the case for disk-free younger stars.

There is obvious substructure seen in the amplitude distribution against color or period in Praesepe (and more subtle echoes of it in the Pleiades) as a function of $(V - K_s)_0$, some of which may be selection effects in that the longest periods may require larger amplitudes for detection (Paper IV). The substructure seen in the amplitude distribution in the Pleiades and Praesepe is not obvious in the clusters < 100 Myr—perhaps the behavior is not yet organized enough, or there are not enough stars for comparison. That lack of structure could be explained in the $(V - K_s)_0$ plot by invoking the likely large uncertainties in $(V - K_s)_0$ for the young clusters, but the uncertainty in P is likely small, so the relative lack of substructure in the distributions as a function of P for the younger stars is likely real, though greatly complicated by the range of masses included at any given P (or amplitude).

6.2. LC and Periodogram Categories

In Papers II, IV, and V, we classified the LC and periodogram morphologies for the Pleiades, Praesepe, USco, and ρ Oph; see these references for discussion of the classes (e.g., double-dip, scallop, etc.). Table 3 includes statistics on these classifications for all of the clusters, now including Taurus.

A high fraction of the Taurus stars are periodic, 83%. As for nearly all of the other clusters, $\sim 70\%$ of the periodic Taurus members have only one period; about 30% of the periodic sample has at least two real periods. The Taurus foreground has different proportions, but it is likely biased/incomplete.

There are some aspects of the periodic LC morphologies that are common between the clusters and others that show signs of evolution with stellar age. Specifically:

1. The fraction of double-dip stars falls substantially between Praesepe and ρ Oph. Assuming that the rate at which we find double-dip characteristics increases as rotation period decreases (e.g., Basri & Nguyen 2018), this makes sense since Praesepe is, on average, rotating much more slowly than ρ Oph.
2. LCs of the scallop shell morphology (and related categories) continue to be rare but much more common among the younger clusters. None have disks. We note that Zhan et al. (2019) find scallop shell stars at ~ 40 Myr, but there are very few by ~ 125 Myr, the age of the Pleiades.
3. LC categories suggestive of complicated spot occurrence and evolution (beater, complex peak) seem harder to find in clusters with a higher disk fraction. In contrast, shape changers (which could arise from spot/spot group

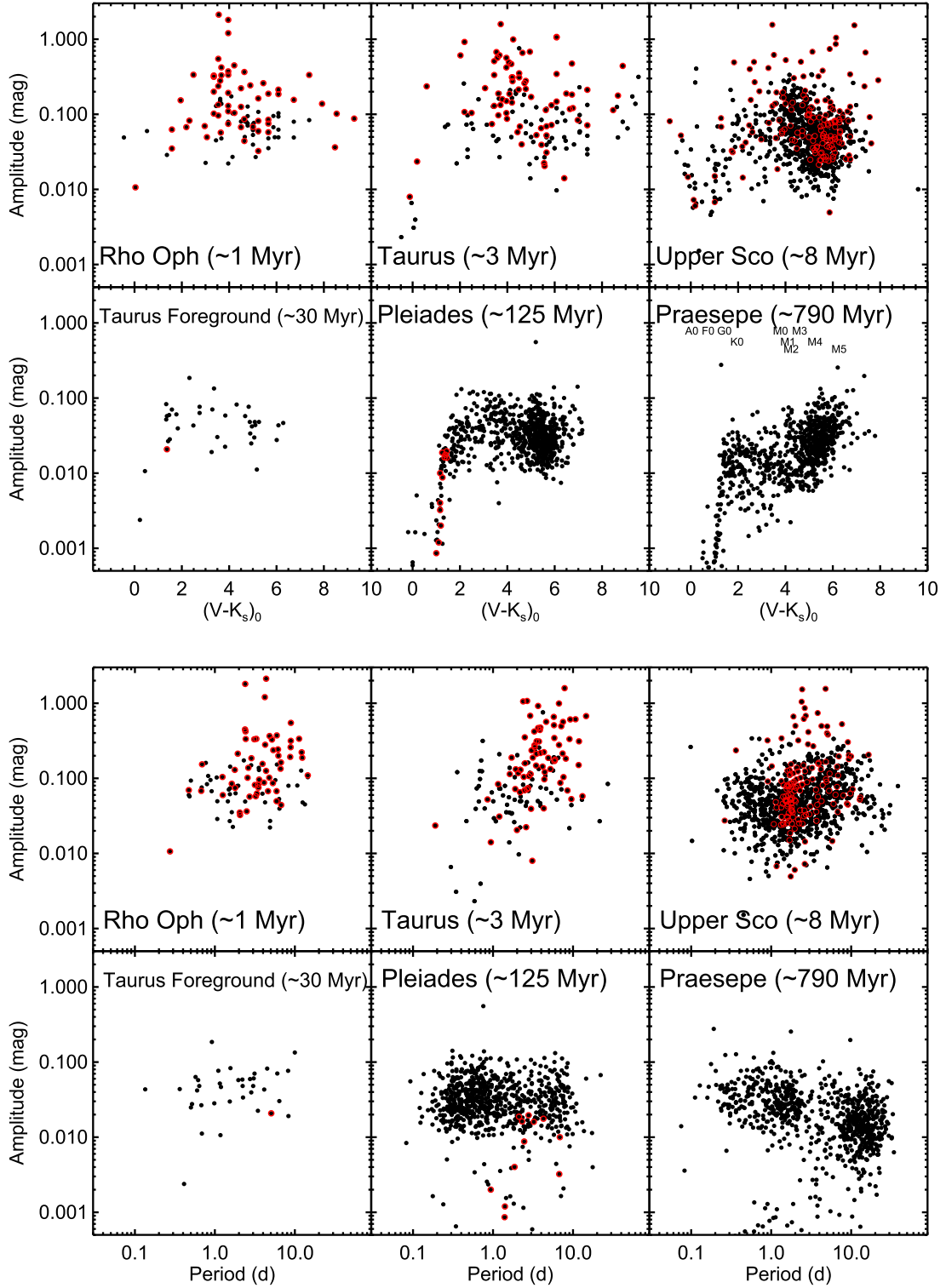


Figure 10. Amplitude (10th to 90th percentiles) in magnitudes as a function of $(V - K_s)_0$ (top panels) or period in days (bottom panels) for the same clusters as in Figure 9; an additional red circle indicates a disk. Note that the same y-range is used for each panel; the overall average amplitude decreases with cluster age, as expected. The average amplitude for stars with disks is larger than that for stars without disks. There is substructure in the older clusters that is not obvious in the younger clusters. See the text for discussion.

emergence/evolution or from disk influence) are more common in clusters with a higher disk fraction.

4. Resolved distant peaks (which are most likely binaries, either real or apparent) occur at comparable rates across all clusters. Pulsators are rare in all clusters, which is

unsurprising, at least in the stellar mass range where our studies are focused.

5. Dippers and bursters only occur in clusters that still have primordial disks, consistent with our physical interpretation of these phenomena as interactions with gas/dust disks. The

Table 3
Star/LC/Periodogram Categories^a

Category	Praesepe			Pleiades				Tau F ⁺ gnd			USco				Taurus				ρ Oph			
	(1) ^b	(2) ^c	(3) ^d	(1) ^b	(2) ^c	(3) ^d	(4) ^e	(1) ^b	(2) ^c	(3) ^d	(1) ^b	(2) ^c	(3) ^d	(4) ^e	(1) ^b	(2) ^c	(3) ^d	(4) ^e	(1) ^b	(2) ^c	(3) ^d	(4) ^e
Member LCs	938	1.00	...	826	1.00	38	1.00	...	1136	1.00	179	1.00	174	1.00
Periodic	819	0.87	1.00	759	0.92	1.00	1.00	37	0.97	1.00	974	0.86	1.00	0.81	148	0.83	1.00	0.71	106	0.61	1.00	0.73
Single period	674	0.72	0.82	598	0.72	0.79	0.50	25	0.66	0.68	756	0.67	0.78	0.68	108	0.60	0.73	0.58	85	0.49	0.80	0.61
Multi-period	145	0.15	0.18	161	0.19	0.21	0.50	12	0.32	0.32	218	0.19	0.22	0.12	40	0.22	0.27	0.13	21	0.12	0.20	0.11
Double-dip	163	0.17	0.20	107	0.13	0.14	0.25	6	0.16	0.16	133	0.12	0.14	0.09	12	0.07	0.08	0.05	6	0.03	0.06	0.04
Moving double-dip	121	0.13	0.15	31	0.04	0.04	0.17	5	0.13	0.14	32	0.03	0.03	0.02	5	0.03	0.03	0.01
Shape changer	297	0.32	0.36	114	0.14	0.15	0.25	16	0.42	0.43	277	0.24	0.28	0.43	83	0.46	0.55	0.58	47	0.27	0.44	0.45
Scallop/clouds? ^f	5	0.01	0.01	...	1	0.03	0.03	28	0.02	0.03	...	6	0.03	0.04	0.00
Beater	77	0.08	0.09	136	0.16	0.18	0.75	7	0.18	0.19	107	0.09	0.11	0.03	18	0.10	0.12	0.05	10	0.06	0.09	0.06
Complex peak	68	0.07	0.08	89	0.11	0.12	0.42	2	0.05	0.05	8	0.01	0.01	...	6	0.03	0.04	0.02
Resolved, close peaks	71	0.08	0.09	127	0.15	0.17	0.42	9	0.24	0.24	151	0.13	0.16	0.08	25	0.14	0.17	0.07	12	0.07	0.11	0.04
Resolved, distant peaks	77	0.08	0.09	39	0.05	0.05	0.17	5	0.13	0.14	85	0.07	0.09	0.05	18	0.10	0.12	0.06	9	0.05	0.08	0.08
Pulsator	17	0.02	0.02	8	0.01	0.01	0.00	13	0.01	0.01	0.01	2	0.01	0.01
Disk	12	0.01	0.02	1.00	208	0.18	0.17	1.00	101	0.56	0.49	1.00	80	0.46	0.55	1.00
Dipper ^g	66	0.06	0.06	0.31	21	0.12	0.12	0.21	17	0.10	0.15	0.20
Burster ^g	24	0.02	0.01	0.11	25	0.14	0.11	0.25	13	0.07	0.08	0.16

Notes.

^a This table has been updated to reflect slightly new classifications in a few cases for stars in clusters that we have already published, and one error—the total sample listed in the analogous table in the Pleiades paper erroneously included just the best members as the total sample, but the rest of that table incorporated both the best plus “ok” members. The numbers in the present paper are correct.

^b Total number of stars in the (sub)sample; for Taurus, it is the combination of the highest-quality and possible members. Examples for Praesepe: there are 938 members and 819 periodic members.

^c Sample fraction (fraction of the given type), out of the members. Examples for Praesepe: 87% of the members are periodic; 72% of the members are single-period.

^d Periodic sample fraction (fraction of the given type), out of the periodic members. Examples for Praesepe: 82% of the periodic members are single-period; 18% of the periodic members are multi-periodic.

^e Disked sample fraction (fraction of the given type), out of the disked members. Note that this column does not appear for those clusters without disks. Examples for Pleiades: 100% of the disked member stars are periodic; 50% of the disked member stars are single-period; 25% of the disked member stars are double-dip.

^f Described in Papers I–V sometimes as “orbiting clouds?”, Stauffer et al. (2017, 2018a) categorized scallops, persistent flux dips, and transient flux dip stars. Here, we simply use the term “scallop” to include all three LC categories (Stauffer et al. 2017, 2018a).

^g Some objects are tagged burster or dipper but not periodic. The fraction of the periodic sample that is burster or dipper is correct, for the periodic subsample.

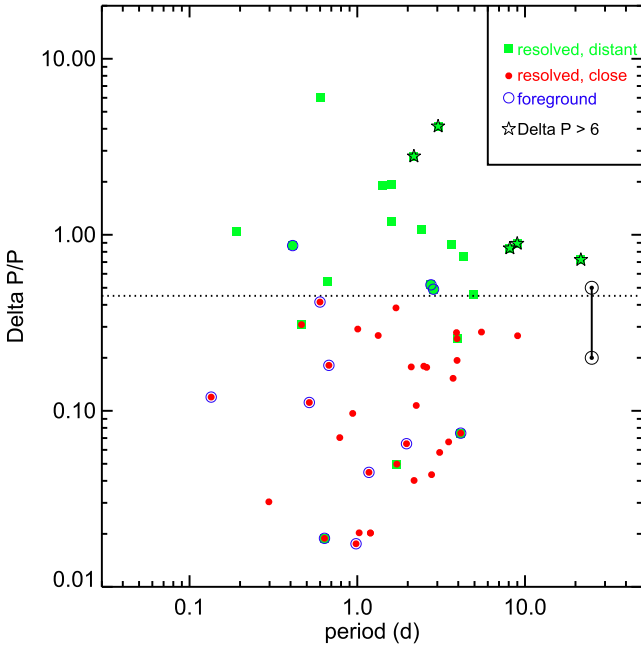


Figure 11. Plot of $\Delta P/P_1$ vs. P for stars that are multi-periodic and with resolved distant peaks (green squares) and resolved close peaks (red dots) for high-confidence and possible members. An additional black star indicates that $|\Delta P| > 6$ days. An additional blue circle means the star is from the older foreground population. The range of possible values for the Sun is included for reference (\odot); if one takes as ΔP the range of periods measured where sunspots occur, $\Delta P/P_1 \sim 0.1$ – 0.2 , but if one takes the full range of ΔP , equator to pole, $\Delta P/P_1 \sim 0.5$. The dotted line is at $\Delta P/P_1 = 0.45$ and denotes the boundary between close and distant resolved peaks. There are far fewer structures in this diagram as compared to that for the Pleiades; it is possible that there are not enough complete cycles in the ~ 70 days campaign for extraction of clear multiple periods, or the disk influence on the LCs complicates derivation of the periods.

vast majority of dippers and bursters are also disked stars; a few have little or no IR excess, though they could still have gas disks depleted in dust.

6.3. ΔP Distributions

As for the other clusters, we calculated the $\Delta P/P_{\text{rot}}$ metric for stars with resolved multi-period peaks; see Figure 11. This metric $\Delta P/P_{\text{rot}}$ is defined by taking the closest peak to the P_{rot} , subtracting the smaller from the larger, and dividing by the P_{rot} . For well-separated peaks and/or M stars (see Paper V and Stauffer et al. 2018a), it is very likely that the two periods are two independent periods of two components of a binary system.

The distribution in Taurus, like that for USco/ ρ Oph (Paper V) and Praesepe (Paper IV), has relatively little structure as compared to that for the Pleiades (Paper II). Here, as noted in Paper V, the ~ 70 days K2 campaigns are not quite long enough to capture multiple complete cycles in order to be able to resolve two close periods. If the phasing of the two periods is favorable, we can resolve the two periods, but if the phasing is not “lucky”, ~ 70 days is not long enough to distinguish the periods.

7. Summary and Conclusions

We have presented the K2 LCs and periods derived from them for the Taurus star-forming region. We have LCs for about 30% of the highest-confidence Taurus members in the

literature; most of the Taurus members are north of the region observed by K2. However, because the K2 region extends over a larger area, it enables the study not only of bona fide Taurus molecular cloud members, but also of a somewhat older, more dispersed population of candidate young stars.

We followed the methodology used in our earlier Papers I–V and find, again, that cluster membership is one of the most difficult parts of our analysis. We distributed all plausible candidate members of Taurus that were observed by K2 among four bins—highest-quality members, possible members, a population of stars in front of the Taurus members (“foreground”) that are likely about three times older than Taurus members, and NMs. We retain, for further analysis, a sample consisting of the highest-quality members and the possible members. Dereddening is also challenging and likely contributes uncertainty to the $(V - K_s)_0$ colors. We used IR data to identify stars with disks. We classified the LCs according to the classes we identified in Papers I–V. We retained up to four periods for each star.

We find slightly more than 80% of the Taurus members to be periodic; the foreground population is highly biased/incomplete, but nearly all of the foreground population is also periodic.

We find that the periods from our analysis are generally well matched to those from the (substantial) previous literature, except for possibly the KELT analysis (Rodriguez et al. 2017a). Our periods are also consistent with the available literature $v \sin i$ values, and our analysis suggests that there is no substantial bias in our sample introduced by our inability to get periods from stars with a high level of stochastic contributions (from, e.g., a disk or accretion).

Despite the relatively paucity of stars with K2 LCs and derived periods in Taurus (as compared to USco), similar relationships between rotation rate and disk presence are found in Taurus. Especially for the M stars, the periods are clumped near ~ 2 days, and there are very few stars that both have disks and rotate faster than ~ 2 days.

The latest M stars in Taurus are the youngest M stars thus far studied with high-quality LCs, extending into the brown dwarf regime.

The overall distribution of rotation rates as a function of color (as a proxy for mass) in Taurus, and in the foreground population, is similar to that found in other clusters: the slowest rotators are in the early M stars, and both the higher masses and lower masses are the fastest rotators. The member distribution looks similar to that from ρ Oph and USco (Paper V), suggesting that the distribution (particularly for M stars) is already in place by the age of Taurus (~ 3 Myr). The slightly older (~ 30 Myr) foreground population has very few stars but is consistent with the USco and Pleiades distributions.

The LC amplitude distribution as a function of $(V - K_s)_0$ or period has trends and substructure, not all of which are easy to interpret. The overall amplitude goes down as clusters age. Higher-mass stars have lower amplitudes than lower-mass stars; however, there is a selection effect in that the amplitudes of the faintest stars have to be larger to be detected. Stars with primordial disks have, on average, larger amplitudes, though the mechanisms driving the variability are different than for stars without disks. Interpretation of additional structure in these distributions is much less clear.

As for many of the other young clusters observed by K2, about 70% of the periodic members have just one period

detected, and about 30% of the periodic members have more than one period. Scallop shell/orbiting dust cloud stars are still rare; there are just seven in the sample discussed here (one from the foreground and six from Taurus). LC categories that we have interpreted as spot/spot group changes (emergence/evolution), namely beaters and complex peaks, seem harder to find in clusters with many primordial disks. Shape changers, which could be from spot/spot group changes or from disk interactions and/or accretion, are more common in clusters with a higher disk fraction. Dippers and bursters are only found in clusters with primordial disks; most of these specific objects have obvious dusty disks.

A. M. Cody et al. (2020, in preparation) will explore the range of LC properties of the disked members of Taurus. N. Roggero et al. (2020, in preparation) will explore the dipper population in Taurus.

Some of the data presented in this paper were obtained from the Mikulski Archive for Space Telescopes (MAST). Support for MAST for non-HST data is provided by the NASA Office of Space Science via grant NNX09AF08G and by other grants and contracts. This paper includes data collected by the Kepler mission. Funding for the Kepler mission is provided by the NASA Science Mission directorate. This research has made use of the NASA/IPAC Infrared Science Archive (IRSA), which is operated by the Jet Propulsion Laboratory, California Institute of Technology, under contract with the National Aeronautics and Space Administration. This research has made use of NASA's Astrophysics Data System (ADS) Abstract Service, and of the SIMBAD database, operated at CDS, Strasbourg, France. This research has made use of data products from the Two-Micron All-Sky Survey (2MASS), which is a joint project of the University of Massachusetts and the Infrared Processing and Analysis Center, funded by the National Aeronautics and Space Administration and the National Science Foundation. The 2MASS data are served by the NASA/IPAC Infrared Science Archive, which is operated by the Jet Propulsion Laboratory, California Institute of Technology, under contract with the National Aeronautics and Space Administration. This publication makes use of data products from the Widefield Infrared Survey Explorer, which is a joint project of the University of California, Los Angeles, and the Jet Propulsion Laboratory/California Institute of Technology, funded by the National Aeronautics and Space Administration.

Facilities: 2MASS, WISE, IRSA, Exoplanet Archive.

Appendix A Membership

A.1. Members

Despite the fact that Taurus is close (~ 140 pc) and has been studied for decades, membership is still controversial. Recent literature combines years of prior data collection with the Gaia DR2 data in an attempt to create a complete list of members (e.g., Luhman et al. 2017; Luhman 2018; Esplin & Luhman 2019; Galli et al. 2019; and references therein). Numerous approaches have sought a dispersed population of young stars (e.g., Wichmann et al. 1996; Slesnick et al. 2006; Rebull et al. 2010; Rebull et al. 2011; Kraus et al. 2017; and references therein). The net result is persistently confusing in the literature, with a subset of stars that most authors agree must be members, stars where membership evidence is mixed, and

still other stars where evidence is both mixed and controversial, particularly those having several indications of youth but with distinct motions and/or distances that are apparently inconsistent with membership.

In the context of this paper, we needed to find the sample of member stars that also had K2 LCs. It is important to note three important selection effects. First, K2 LCs were only downloaded for targets submitted in advance, so completeness is limited by the submitted list of targets. Second, the K2 observations did not cover all of the sky encompassing the least controversial Taurus members (see Figure 1, in addition to discussion below). Third, since it observed in optical bands, K2 effectively selected against those Taurus members that are so embedded as to attenuate the optical data (see discussion below and Section 2.4).

Based on our experience with the other K2 clusters that we previously analyzed (Papers I–V), we knew that we had to start with an overly generous list of possible members; by starting with an expansive set, we could analyze all of the LCs in the same way, at the same time (thus reducing biases in the analysis). Subsequent membership modifications implemented late in the process then become trivial to implement.

We assembled a list of 851 EPIC-numbered targets with LCs (e.g., targets submitted in advance that had actually been observed) that could be members of Taurus with data in either of the Taurus-relevant K2 campaigns (C4 and C13). These targets originated from any of the 64 different K2 GO programs that mention in their abstract studying young stars or members of Taurus. These programs did not necessarily perform complete and thorough vetting of possible targets prior to target submission (we note that both C4 and C13 predate Gaia DR2); observers just included targets that could be Taurus members, so we likewise included them in our initial target list assembly.

We proceeded with the analysis of those ~ 850 LCs in parallel with membership assessment efforts. For most of these targets (see Section 2.3 and Table 1), there are Gaia DR2 and 2MASS data. We explored a variety of parameter spaces such as vector point diagrams and CMDs. While this process was underway, Luhman (2018) was published, with similar subgroups as we had identified, but with a much more complete analysis than we had accomplished to that point. Subsequently, Esplin & Luhman (2019) and Galli et al. (2019) were published, again presenting lists of members based primarily on Gaia DR2 data. These recent analyses include all of the least controversial Taurus members. We made the decision to adopt the intersection of those targets with K2 LCs and those in Esplin & Luhman (2019) as the *highest-quality members*.

Note that the regions of sky encompassed by Luhman (2018), Esplin & Luhman (2019), and Galli et al. (2019) are significantly different than the region of sky observed by K2 in the two campaigns including Taurus members (Figure 1). The K2 observations cover about 30% of the Taurus members from Esplin & Luhman (2019), and the K2 observations also encompass a much larger region of the sky to the south of where the membership work was focused. Moreover, the Esplin & Luhman (2019) member list seems to have very few higher-mass G and K stars.¹³ Since that mass range proved interesting for the rotation rate distribution in Papers I–V, we wanted to be

¹³ A similar G star deficit was noted also by Tokovinin & Briceño (2020) in the context of the USco membership determined by Luhman and collaborators.

sure that we had that region of parameter space well-represented here.

As a result of the larger areal coverage and the G star deficit, we sought to reassess membership for stars with K2 LCs that were not already in the highest-quality members, in particular, stars meeting those criteria. We investigated the literature for each possible additional target in question, as well as the Gaia DR2 data. In most cases, a star had several or many papers in the literature citing it as a suspected Taurus member, and it had DR2 data consistent with belonging to Taurus, or it had very few references suggesting membership and usually DR2 data inconsistent with membership. The *less likely (lower-confidence) members* include targets added by our own additional star-by-star inspections, including a few from Galli et al. (2019) or Kraus et al. (2017) that were not in Esplin & Luhman (2019).

In this process, we realized that there was a subset of stars that had indications of youth but distances and/or motions incompatible with Taurus membership; these include those “controversial” members mentioned above. Many of these targets are listed in Luhman (2018) as Group 29 members (see also Oh et al. 2018). Some appear in the literature as possible members of Mu Tau (M. Gagne et al. 2020, in preparation; Liu et al. 2020) or possibly Cas-Tau (e.g., Hartmann et al. 1991; de Zeeuw et al. 1999; Luhman 2018; also see appendix of David et al. 2018). Analyses to date of this population in the literature suggest that they are ~ 30 Myr (e.g., Kraus et al. 2017). Our list of *Taurus foreground* stars are primarily those Group 29 members, plus targets added by our own additional star-by-star inspections that might very well be Mu Tau or Cas-Tau members (see also Stauffer et al. 2020).

Much of the supporting non-survey data available in the literature (Section 2.3) is biased toward those least controversial members, and those targets nearby in projected distance. For example, a high fraction of the highest-confidence members have a Spitzer and/or Herschel counterpart

(Sections 2.3 and 2.4; Table 1) because those pointed missions targeted the most well-known members. Circularly, the most reliable members also are more likely to have an IR excess and, thus, be detected in various IR data sets. Similarly, we expect members to be young and significantly spotted and, therefore, periodic more often, which is the case (Section 3.1).

A.2. Nonmembers

After extracting the members (of any sort) out of the ~ 850 in our initial sample, we are left with ~ 630 nominal NMs. Among this nominal NM sample, there is an anomalously high fraction of apparent IR excesses and an anomalously high periodic fraction (Table 1). Looking at the distribution of Gaia distances from Bailer-Jones et al. (2018), many are nominally at ~ 140 pc, more than would be expected for a randomly selected set of field stars. We suspect that we have been somewhat conservative in identifying members, and that some (perhaps several) legitimate members are left in the NM sample. Moreover, the set of stars with K2 LCs is biased toward objects appearing in the literature as young, which makes the entire K2 sample different than any random selection of stars.

For these NMs, we performed much of the same analysis as for our members, but they were largely ignored in the discussion in the rest of the paper. We include results from these additional stars here, should they be of use to future investigators. We provide the NMs in Table A1, which has the same contents as in Table 2 above (except for the columns on cluster membership and dippers/bursters, none of which are found among the NMs). Note that the Gaia DR2 ID is provided for easily matching parallaxes and proper motions. We focused on the analysis of the members, and as such, some of the NMs may not have been vetted as closely as the member sample.

Table A1
Periods and Supporting Data for Taurus Likely Nonmembers with K2 Light Curves

Number	Label	Contents
1	EPIC	Number in the Ecliptic Plane Input Catalog (EPIC) for K2
2	Coord	R.A. and decl. (J2000) for target
3	OName	Alternate name for target
4	Gaia	Gaia DR2 ID
5	V mag	V magnitude (in Vega mags), if observed
6	Ks mag	K _s magnitude (in Vega mags), if observed
7	(V - K _s) _o	(V - K _s), as directly observed (in Vega mags), if V and K _s exist
8	(V - K _s) _u	(V - K _s) used, in Vega mags (observed or inferred; see the text)
9	E(V - K _s)	E(V - K _s) adopted for this star (in mags; see Section 2.5)
10	K _s mag ₀	dereddened K _{s,0} magnitude (in Vega mags), as inferred (see Section 2.5)
11	(V - K _s) ₀	(V - K _s) ₀ , dereddened V - K _s (in Vega mags), as inferred (see Section 2.5; rounded to nearest 0.1 to emphasize the relatively low accuracy)
12	Uncert	two-digit code denoting the origin of (V - K _s) and (V - K _s) ₀ (see Sections 2.3 and 2.5): First digit (origin of (V - K _s)): 1 = V measured directly from the literature (including SIMBAD) and K _s from 2MASS; 2 = V from APASS and K _s from 2MASS; 3 = (V - K _s) inferred from Gaia g and K _s from 2MASS (see Section 2.3); 4 = (V - K _s) inferred from Pan-STARRS1 g and K _s from 2MASS (see Section 2.3); 5 = (V - K _s) inferred from membership work (see Section 2.2; rare); 6 = V inferred from well-populated optical SED and K _s from 2MASS (see Section 2.3); -9 = no measure of (V - K _s). Second digit (origin of E(V - K _s) leading to (V - K _s) ₀): 1 = dereddening from JHK _s diagram (see Section 2.5); 2 = dereddening back to (V - K _s) ₀ expected for spectral type; 3 = used median E(V - K _s) = 0.7 (see Section 2.5); -9 = no measure of E(V - K _s)
13	P1	Primary period, in days (taken to be rotation period in cases where there is >1 period)
14	P2	Secondary period, in days
15	P3	Tertiary period, in days
16	P4	Quaternary period, in days
17	IR excess	Whether an IR excess is present or not (see Section 4)
18	IRexStr	Minimum wavelength at which the IR excess is detected or the limit of our knowledge of where there is no excess (see Section 4)
19	Slope	Slope of SED fit to all available detections between 2 and 25 μm
20	Class	SED class (I, flat, II, III)
21	Sin/mult	single or multi-period star
22	dd	LC and power spectrum matches double-dip characteristics (see Section 6.2)
23	ddmove	LC and power spectrum matches moving double-dip characteristics (see Section 6.2)
24	Shape	LC matches shape changer characteristics (see Section 6.2)
25	Beat	LC has beating visible (see Section 6.2)
26	Complex	power spectrum has a complex, structured peak and/or has a wide peak (see Section 6.2)
27	Closep	power spectrum has resolved close peaks (see Section 6.2)
28	Distp	power spectrum has resolved distant peaks (see Section 6.2)
29	Pulse	power spectrum and LC match pulsator characteristics (see Section 6.2)

(This table is available in its entirety in machine-readable form.)

Table B1
Lists of Objects with Timescales

EPIC	Other Name	Membership	Timescale
210552148	LP415-113	NM	~35
210666196	...	NM	~15
210683818	HBC 393	Mem	~25
210716897	RXJ 0426.3+1836	NM	~38 ^a
246835564	...	NM	~28
247122185	...	NM	~35
247532735	V*V1108 Tau	NM	~15
247575425	IRAS 04303+2240	Mem	~7.5
247590222	IRAS 04302+2247	Mem	~25
247805410	V*FX Tau	Mem	~11.6
247820507	[RRA 2004]Haro 6-10VLA1	Mem	~13.6
247946210	IRASF 04570+2520	NM	~35
247961728	V*V414 Tau	NM	~35
248019700	SS Ttau 044325.1+255706	NM	~23
248049475	V*DO Tau	Mem	~16
248054085	SSTtau 044453.1+261257	NM	~16.5

Note.

^a This star has an additional real, shorter period, which we take to be the rotation period.

Appendix B Timescales

As in Papers I–V, some LCs have some repeated patterns that we cannot identify with certainty as a rotation period. These “timescales” tend to be longer than most of the rotation periods. Sometimes, there is not enough data to go >1 complete cycle. Table B1 summarizes the timescales for the stars out of the entire ensemble. Note that some also appear in the list of periodic stars but with a shorter period that we believe to be the rotation period; the longer-term variability is unlikely to be rotation.

Appendix C Comparison to Literature Periods

In this appendix section, we compare periods for stars in common between our study and several literature studies, regardless of whether or not the stars are currently thought to be Taurus members or not. Specific stars are listed in Table C1.

Rebull et al. (2004) collected periods from the then-current literature for many young stars, including stars in Taurus. There are 27 stars in common between the literature compilation in Rebull et al. (2004) and the present study, but only 23 of them are periodic in both studies; see Figure C1. Most (17) of them match periods to within a fractional difference of 10%, leaving six that do not match. In three cases (EPIC 210690735 = UX Tau), 247592463 = HP Tau, 248029373 = DK Tau), the LC is complex enough that it could explain the different period obtained in the literature. For EPIC 210670948, the period compiled in Rebull et al. (2004; citing Preibisch & Smith 1997) does not match other literature nor the K2 period, and we conclude that it is wrong. For 246770655, the period from the literature matches our secondary period (though the primary period appears in the Figure). In the last case, EPIC 247034775 (V1076 Tau), the literature reports conflicting values. Rebull et al. (2004) recorded the period as 6.2 days, apparently originally from Grankin (1993), and that is what appears in Figure C1 and Table C2. Grankin (1997) reports that the period of 9.91 days from Grankin (1994) “is more credible.” The K2

data yield $P = 9.5412$ days, supporting the longer period; there is no ~ 6 days period in the K2 data.

Grankin et al. (2007) presented periods for 39 stars in Taurus obtained as part of the ROTOR program at Mount Maidanak Observatory. Eighteen of those stars also have K2 LCs that we determine to be periodic (four more are not periodic in K2). Most (12) of these stars do not have the same periods in the K2 data. Five of them have very different periods, and five more are plausibly harmonics; see Figure C1. As part of this same ROTOR project, Artemenko et al. (2012) published several additional periods. Of the seven new stars in common, all of them have complex LCs. Only four have periods we derived from the K2 data; three of them match very well, and the fourth may be a harmonic.

As part of the XMM-Newton Extended Survey of the Taurus Molecular Cloud (XEST; Güdel et al. 2007) and the Spitzer Taurus survey (Rebull et al. 2010), an extensive survey of the literature at that time was made, and a list of periods assembled to which we can compare. There are 40 stars in common with our study, only 29 of which are periodic in both studies. However, most of those are curiously listed as limits on the period in Güdel et al. (2007) see Figure C1. For those stars with secure periods, there is a good match, eight of the nine are well within 10%.

Xiao et al. (2012) used the Trans-Atlantic Exoplanet Survey (TrES) to monitor L1495, a portion of the Taurus molecular cloud. Only three stars are in common between the studies: EPICs 247822311 (WK 812), 248029373 (DK Tau), and 248040905 (IQ Tau). EPIC 248029373 is the only one where the periods are not effectively identical. We obtain 7.84 days where Xiao et al. report 4.094 days, which is not consistent with our data. However, the K2 LC is complex and it is plausible that another campaign at a different time may obtain a longer period.

Rigon et al. (2017) used The Wide Angle Search for Planets (WASP) to probe the long-term variability of stars largely in Taurus-Auriga. Only two stars are in common, AA Tau (EPIC 247810494; also see below) and VO Tau (EPIC 248049475). Rigon et al. report period ranges, and we do not find periods for either one. For the first one, they report a 58 and a 5 day period; other literature report 8–13 days periods. For the latter, they report 5–6, 24, and 6–7 days. We see both of these stars as irregular bursters during the K2 window and cannot determine a period; we would not be sensitive to periods longer than ~ 35 days in any case.

Rodriguez et al. (2017a) used the KELT to find rotation periods (and dippers) in Taurus. Separately, the KELT LC for EPIC 248180268 = HD 283782 = V1334 Tau appeared in Rodriguez et al. (2017b); since there is a period reported there that came from KELT data, we include this period here. In total, there are 33 stars in common between us, 26 of which are periodic in both studies. Only seven match periods to within 10%; see Figure C1. A few more have periods in KELT comparable to our secondary or tertiary period; see Table C2. For each of the stars in common, the LCs were investigated in detail, and the KELT period could not be recovered in most cases. We find that a few stars appear as irregular bursters (at least during the K2 epoch), so perhaps it is not surprising in those cases that the periods are so different. There is no clear reason why the rest of the stars are not recovered at the same periods. However, many of the KELT LCs that do not match are of very low amplitude, and the KELT LCs cover a very

Table C1
Comparison to Literature Periods (All in Units of Days)

EPIC	Other Name	Rebull +04	Grankin +07	Artemenko +12	Güdel +07	Xiao +17	Rodriguez +17b	Scholz +18	Hambálek +19	P_1	P_2	P_3	P_4	Match?	Notes
210631263	HD 285372	0.573	0.5733	y	...
210662824	HD 285778	2.74	2.736	2.7503	1.3713	y	...
210670948	[FK 83] LDN155151	1.2	2.43	2.4282	y/n	Match with Güdel+ but not Rebull+.
210674635	2MASS J04312405 +1800215	<6.29	2.2098	n	True that P_{here} is $<P_{\text{XEST}}$, but 2.2 days really clear in K2, and nothing at ~ 6 days.
210683818	HBC 393	<3.82	n	At best, K2 data suggest a 20–25 days timescale; there is not anything near 3.8 days.
210689130	HD 28150	...	0.696	0.6981	y	...
210690598	EM*LkHA358	<6.8	3.5045	3.7378	n	True that P_{here} is $<P_{\text{XEST}}$, but ~ 3 days really clear in K2, and nothing at ~ 7 days.
210690735	V*UX Tau	2.7	3.6584	n	No match with Rebull+ from either period. However, K2 LC power spectrum suggests ~ 2 days at another time may be plausible.
210690892	XZ Tau AB	2.6	...	3.24	2.6	n	No period in K2.
210690913	V*HL Tau	<7.21	n	There is a 7.7 days peak in the K2 data but it does not phase well; a 24 days period is more plausible in the K2 data.
210698143	2MASS J04311578 +1820072	<7.66	1.5954	3.4961	n	True that P_{here} is $<P_{\text{XEST}}$, but periods really clear in K2, and nothing at ~ 7 days.
210698281	V*V827 Tau	3.75	3.75	3.7582	y	...
210699801	EM*LkHA267	<5.67	4.3047	1.07	n	True that P_{here} is $<P_{\text{XEST}}$, but periods clear in K2 and nothing at ~ 5.6 days.
210767482	HD 284418	14.81	15.3682	y	\sim match
210777988	V*T Tau	2.8	2.8	2.8116	y	...
210792668	1.168	n	No period in K2.
210805120	V*V1196 Tau	3.02	y	No period in K2.
210818897	V*V1298 Tau	...	2.86	2.885	2.8484	1.4508	y	...
210881343	0.736	6.4388	2.7789	n	No period near 0.7 in K2 data.
210977750	2MASS J04073502 +2237394	...	0.816	0.1346	0.1507	n	No period near 0.8 in K2 data.
211104793	2MASS J04124068 +2438157	...	5.58	5.8543	y	...

Table C1
(Continued)

EPIC	Other Name	Rebull +04	Grankin +07	Artemenko +12	Güdel +07	Xiao +17	Rodríguez +17b	Scholz +18	Hambálek +19	P_1	P_2	P_3	P_4	Match?	Notes
211182143	1.961	n	No period in K2.
246695532	V*V1840Ori	...	1.231	5.343	n	There is a peak near 1.5 days in one and only one of the data reductions (K2SFF); we suspect that this period may correspond to one of the other targets near 246695532.
246760205	HD 286179	3.33	3.14	3.1297	y	...
246770655	WDS J04573 +1524AB	2.39	2.412	1.7013	2.3551	y	~match with our P_2
246798563	V*V1326 Tau	...	2.54	2.5385	y	...
246802680	HD 285957	3.07	3.055	3.0868	y	...
246815623	V*V1351 Tau	...	5.64	5.6313	y	...
246825172	V*V1353 Tau	...	0.884	7.6307	n	No period near 0.9 days in K2 data.
246923113	V*DR Tau	2.8	14.5698	n	No period near 2.8 days in K2 data.
246977631	V*V1346 Tau	...	0.829	4.6167	n	No period near 0.8 days in K2 data.
247031423	HD 28867	<2	3.0978	3.2775	n	No match even with the inequality; perhaps Güdel + found a harmonic?
247032616	V*V826 Tau	3.7	3.7	3.8829	y	...
247034775	V*V1076 Tau	6.2	9.5412	n	No period near 6 days in K2 data, but 6 days may not be real; 9.91 days from Grankin (1994) is a better match to the K2 data.
247047380	V*DM Tau	<6.74	...	DM	7.4081	n	Not a match, but the K2 LC has potentially many periods in it, including near 6 days.
247051861	2MASS J04321606 +1812464	<7.84	2.6496	n	True that P_{here} is $<P_{\text{XEST}}$, but ~3 days really clear in K2, and nothing at ~8 days.
247076294	HD 31281	0.791	0.6771	0.7999	y	Hambalek+ found our P_2 .
247119725	[WKS 96]42	1.31	4.175	n	No period near 1.3 days in K2 data.
247126197	HD 285840	1.55	1.548	1.5461	y	...
247139505	LP 415-183	...	1.41	18.3841	n	No period near 1.4 days in K2 data.
247225984	V*V1333 Tau	12.594	12.9213	y	...
247280905	V*V1325 Tau	...	2.96	2.935	3.9332	2.9233	11.7995	...	y	Others match our P_2 .
247303990	1.46	0.5498	0.793	n	Complicated K2 LC, with several strong peaks, but

Table C1
(Continued)

EPIC	Other Name	Rebull +04	Grankin +07	Artemenko +12	Güdel +07	Xiao +17	Rodríguez +17b	Scholz +18	Hambálek +19	P_1	P_2	P_3	P_4	Match?	Notes
247360583	2MASS J04564525 +2035116	...	1.079	0.4389	n	none of them are at ~ 1.5 days, and none of them are harmonics of 1.5 days.
247454835	2MASS J05064662 +2104296	1.593	...	2.688	2.7733	2.653	y/n	Rodríguez+ is the outlier.
247520207	HD 284496	2.71	5.765	5.7795	y	...
247528573	EM'LkCa15	5.85	0.517	n	No period in K2.
247539775	2MASS J04464475 +2224508	n	Very, very clear period in K2, not near 0.5 or 11 days.
247548866	V*V1341 Tau	...	0.478	11.198	0.9165	n	...
247575425	[BLH 2002] KPNO-Tau8	0.69	...	0.6878	y	...
247575958	IRAS 04303+2240	<5.23	n	Complicated K2 LC power spectrum suggests $\sim 5.x$ days at another time may be plausible.
247584113	2MASS J04330945 +2246487 CI Tau	3.51	...	3.4916	y	...
247585953	2MASS J04340717 +2251227	1.177	2.9775	5.3517	1.4534	...	n	More P in literature are 8.9891, 16.10 (Johns-Krull et al. 2016). ~ 9 days is thought to be period of planet, which is recovered; nothing near 16 days in K2, but LC complicated. More P in literature (based on this K2 LC) is ~ 6.6 and ~ 9 , for star and planet, respectively (Biddle et al. 2018).
247591534	2MASS J04355760 +2253574	1.16	...	1.1984	y	No period near 1.7 days in K2 data.
247592103	CoKuHP TauG2	1.2	1.2	...	5.798	1.1978	1.222	y/n	...
247592463	V*HP Tau	5.9	5.9	4.3307	n	Rodríguez+ is the outlier. Complex K2 LC, could explain mismatch.
247592919	Haro 6-28	<3.98	n	Complex K2 LC, no clear periods.
247594260	V*V1335 Tau	...	3.762	3.766	3.7998	y	...
247599080	IRAS 04295+2251	<1.48	1.7081	n	...

Table C1
(Continued)

EPIC	Other Name	Rebull +04	Grankin +07	Artemenko +12	Güdel +07	Xiao +17	Rodríguez +17b	Scholz +18	Hambálek +19	P_1	P_2	P_3	P_4	Match?	Notes
247600777	2MASS J04363893 +2258119	0.96	...	0.9645	y	No match even with the inequality; K2 LC is low SNR.
247604448	2MASS J04361038 +2259560	2.91	...	2.933	y	...
247609913	V*V1117 Tau	1.184	6.3887	n	No period near 1.2 days in K2 data.
247630187	2MASS J04350850 +2311398	1.5	...	1.4981	y	...
247739445	2MASS J04302365 +2359129	1.61	...	1.6119	y	...
247748412	2MASS J04322329 +2403013	3.37	...	3.3643	y	...
247763883	V*GH Tau	<3.57	2.4937	2.9408	n	True that P_{here} is $<P_{\text{XEST}}$; K2 LC power spectrum suggests a longer period at another time may be plausible.
247764745	V*V807 Tau	0.809	4.3784	n	No period near 0.8 days in K2 data.
247776236	HD 28975	0.957	4.353	n	No period near 0.9 days in K2 data.
247781229	HD 28819	0.516	0.6086	0.2849	n	K2 LC power spectrum suggests that ~ 0.5 days at another time may be plausible.
247791556	2MASS J04330197 +2421000	<4.67	1.03	...	1.0261	1.0469	n	True that P_{here} is $<P_{\text{XEST}}$; nothing near 4.6 days in K2.
247791801	V*GK Tau	4.6	...	4.61	4.6	4.6165	y	...
247792225	V*GI Tau	7.2	...	7.09	7.2	7.1334	y	...
247795097	V*V928 Tau	<7.45	2.2468	2.4876	n	True that P_{here} is $<P_{\text{XEST}}$; K2 periods very clear and nothing near 7 days.
247799571	V*HK Tau	<8.86	3.3056	n	True that P_{here} is $<P_{\text{XEST}}$; K2 LC power spectrum suggests a longer period at another time may be plausible.
247804500		0.929	n	No period in K2.

Table C1
(Continued)

EPIC	Other Name	Rebull +04	Grankin +07	Artemenko +12	Güdel +07	Xiao +17	Rodríguez +17b	Scholz +18	Hambálek +19	P_1	P_2	P_3	P_4	Match?	Notes
247805410	2MASS J04352474 +2426218 V*FX Tau	<12.34	n	Complicated K2 LC power spectrum suggests a longer period at another time may be plausible.
247810494	V*AA Tau	8.22	...	8.19	8.22	...	13.613	y/n	Rigon et al. (2017) reports 58.5 days. No period in K2, but LC has a lot of structure, suggesting that periodic behavior at another time may be plausible.
247810751	Haro 6-13	<7.3	3.2778	n	True that P_{here} is $<P_{\text{XEST}}$; K2 LC power spectrum suggests a longer period at another time may be plausible.
247820507	[RRA 2004] Haro 6-10VLA1	<5.63	n	No match even with the inequality; K2 LC power spectrum suggests a shorter period at another time may be plausible.
247822311	WK 812	2.75	2.75	2.747	2.743	2.7412	y	...
247837468	IRAS 04264+2433	<1.52	11.8717	n	No match even with the inequality; K2 LC power spectrum suggests a shorter period at another time may be plausible.
247843485	V*ZZ Tau	1.311	4.1609	n	No period near 1.3 days in K2 data.
247864498	V*TW Tau	5.6	0.844	5.5013	7.0425	y/n	Rodríguez+ is the outlier.
247915927	IRAS	4.48	...	4.43	y	...
247923794	S04414+2506 V*DP Tau	<2.76	3.6623	n	No match even with the inequality; K2 LC power spectrum suggests a shorter period at another time may be plausible.
247935061	V*GO Tau	<3.96	n	No period in K2, but LC has a lot of structure, suggesting that periodic behavior at another time may be plausible.
247941378	V*V999 Tau	<2.25	...	23.935	4.9052	2.6515	n	...

Table C1
(Continued)

EPIC	Other Name	Rebull +04	Grankin +07	Artemenko +12	Güdel +07	Xiao +17	Rodríguez +17b	Scholz +18	Hambálek +19	P_1	P_2	P_3	P_4	Match?	Notes
247941613	V ⁺ V1000 Tau	23.935	2.1764	8.2537	n	Two K2 periods are very clear, neither consistent with prior observations.
247941930	EM ⁺ LkHA332	<4.9	...	23.935	n	Complex K2 LC, could explain mismatch.
247950452	2MASS J04334291 +2526470	0.73	...	0.7269	y	Complex K2 LC, could be plausible at another time.
247953586	2MASS J04320329 +2528078	2.39	...	2.3765	y	...
247968420	2MASS J04414825 +2534304	2.9	...	2.9144	y	...
247986526	DF Tau AB	7.2	...	7.18	16.504	n	Complex K2 LC, could be plausible at another time.
247991214	2MASS J04390396 +2544264	3.3	...	3.1401	y	...
247992574	V ⁺ GN Tau	<11.8	5.7452	n	True that P_{here} is $<P_{\text{XEST}}$; LC has a lot of structure, suggesting that a different period at another time may be plausible.
248009353	UZ Tau AB	<4.9	3.7527	n	True that P_{here} is $<P_{\text{XEST}}$; LC has a lot of structure, suggesting that a different period at another time may be plausible.
248010721	HD 283707	0.967	n	No period in K2.
248014510	HD 283809	20.121	1.653	1.4033	0.9651	2.3834	n	No period near 20 days in K2 data.
248018164	Haro 6-33	<2.13	n	No period in K2, but LC has a lot of structure, suggesting that periodic behavior at another time may be plausible.
248018652	[BLH 2002] KPNO-Tau7	1.18	...	1.1572	y	...
248019693	XEST02-040	...	3.12	1.4708	n	Strong EB in K2 data, no P at 3 days.
248023915	2MASS J04380083 +2558572	2	...	0.6644	1.0263	n	No period near 2 days in K2 data.
248029373	DK Tau AB	8.4	...	8.18	...	4.094	7.8414	n	...

Table C1
(Continued)

EPIC	Other Name	Rebull +04	Grankin +07	Artemenko +12	Güdel +07	Xiao +17	Rodríguez +17b	Scholz +18	Hambálek +19	P_1	P_2	P_3	P_4	Match?	Notes
248029954	2MASS J04394748 +2601407	2.9	...	2.9502	y	Complex K2 LC, could explain mismatch. ...
248040905	V ¹ Q Tau	6.25	6.25	6.902	1.18	6.6721	y/n	Rodríguez+ is the outlier.
248045033	TYC 1833- 575-1	0.952	2.6393	n	No period near 0.9 days in K2 data.
248049475	V ¹ DO Tau	0.961	n	Rigon et al. (2017) reports 5–6, 24, 6–7, 17, 35 days. No period in K2, but LC has a lot of structure, suggesting that periodic behavior at another time may be plausible.
248055184	IT Tau A	2.751	2.7434	y	...
248060724	[BLH 2002] KPNO-Tau14	1.86	...	1.8637	y	...
248145565	HD 283798	...	0.6	0.965	...	0.987	0.9831	0.9658	y/n	Grankin+ is the outlier.
248175684	V ¹ V1328 Tau	0.601	1.5287	3.8492	n	No period near 0.6 days in K2 data.
248180268	HD 283782	0.321	...	0.87	0.465	0.3214	2.0182	...	n	No period near 0.8 days in K2 data; Rodríguez+ matches our P_2 .
248245414	0.921	n	No period near 0.9 days in K2 data.
248248731	2.43	n	No period near 2 days in K2 data.

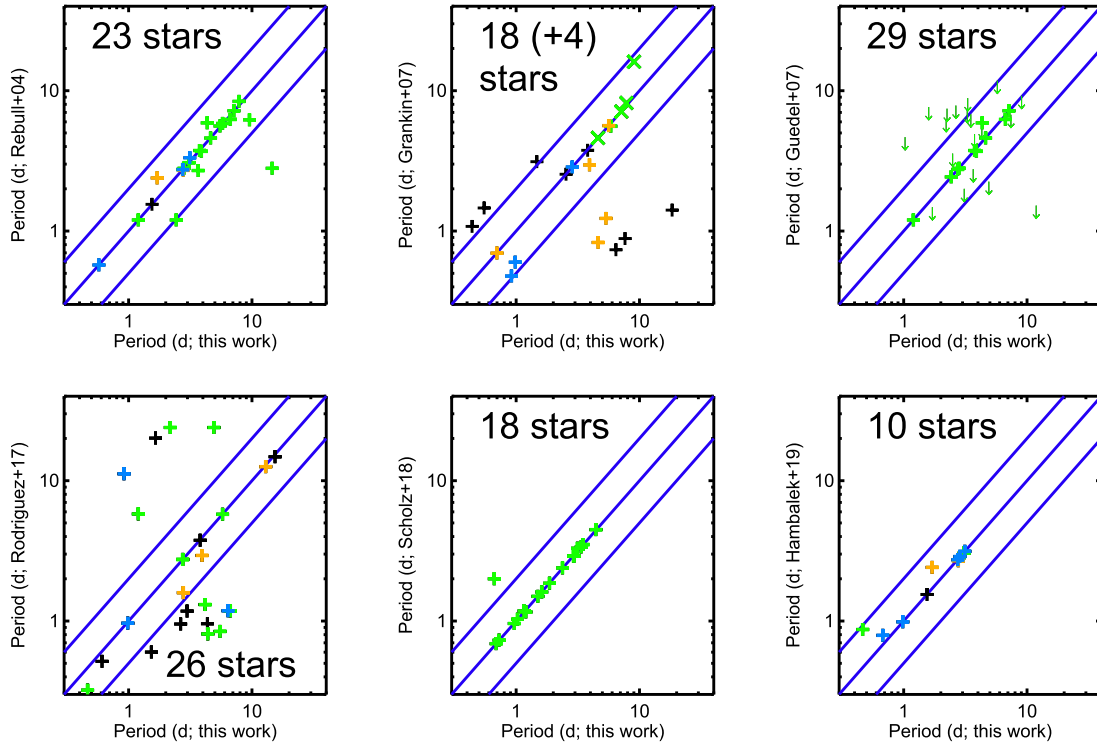


Figure C1. Comparison of periods obtained here to periods obtained in the literature. The colors of the points are as follows: green = highest-confidence member; orange = possible member; blue = young, foreground object; and black = likely NM (see Section 2.2). From the upper left to lower right panels: Rebull et al. (2004), literature compilation, 23 periodic stars in common; Grankin et al. (2007), 18 periodic stars in common, with four more (shown as \times) from Artemenko et al. (2012), Güdel et al. (2007), literature compilation, 29 periodic stars in common; Rodríguez et al. (2017a), KELT, 26 periodic stars in common; Scholz et al. (2018), K2, 18 stars in common; Hambálek et al. (2019), SuperWASP/NSVS/K2, 10 stars in common. The dark blue lines are at one-to-one, $P/2$, and $2P$. (Xiao et al. 2012 has only three stars in common and so is not plotted; see the text and Table C2. Rigon et al. (2017) reports period ranges and so is not plotted here.) Most of the periods match well (see the text for much more discussion).

long time baseline, so if, say, periods are appearing/disappearing at different latitudes under the assumption of surface differential rotation, the rotation period may appear to change over the KELT baseline, making it harder to determine. For the LCs we have, our periods are correct, though some of the LCs are complex. (We note that our recovery rate between K2 and KELT was much higher in our earlier K2 papers.)

More recently, Scholz et al. (2018) used some of the same K2 data as we are using to explore the rotation rates of brown dwarfs in Taurus, and there are 18 stars in common. The periods are all recovered well, except that of EPIC 248023915 (2MASS J04380083+2558572), where the period reported in Scholz et al. is about twice the second period we obtain; we suspect they found an alias rather than the true period.

Most recently, Hambálek et al. (2019) used SuperWASP, the Northern Sky Variability Survey (NSVS), and K2 to study 20 weak-lined T Tauri stars in Taurus; there are 12 stars in common, 10 of which are periodic in both studies. Most of the stars are well matched; see Figure C1. There are three stars where we report two K2 periods, and Hambálek et al. find the period we identified as the second period: EPICs 247076294, 248180268, and 246770655. In the case of 247076294, the two K2 periods are so close to each other that the difference does not stand out in the plot, but the Hambálek et al. period matches the second K2 period.

AA Tau (EPIC 247810494) is somewhat of a special case. It has been the subject of numerous, intensive studies (e.g., Bouvier et al. 1999, 2007; Donati et al. 2010; and references therein). Those studies identified AA Tau as having a period of

8.22 days and defining the class of “dippers” among disk-bearing stars regularly occulted by disk matter close to the star. There is no evidence for an ~ 8 days period in the K2 data; in fact, we find no significant periodicity at all. Additionally, we find no obvious dipper signatures during this campaign; particularly in the first half of the campaign, the LC shares more characteristics with bursters than with dippers. Substantial variation has been noted in this system before (e.g., Bouvier et al. 2003, 2013). The dipper character of the LC as well as the 8.2 days period seen in ground-based LCs for decades disappeared altogether as the star underwent a major dimming event in recent years (Bouvier et al. 2013), a state from which it has not yet recovered.

ORCID iDs

L. M. Rebull <https://orcid.org/0000-0001-6381-515X>
 J. R. Stauffer <https://orcid.org/0000-0003-3595-7382>
 A. M. Cody <https://orcid.org/0000-0002-3656-6706>
 N. Roggero <https://orcid.org/0000-0003-4370-086X>
 T. J. David <https://orcid.org/0000-0001-6534-6246>

References

- Ahn, C. P., Alexandroff, R., & Allende Prieto, C. 2012, *ApJS*, 203, 21
 Akeson, R., Chen, X., Ciardi, D., et al. 2013, *PASP*, 125, 989
 Artemenko, S., Grankin, K., & Petrov, P. 2012, *AstL*, 38, 783
 Bailer-Jones, C., Rybizki, J., Foesneau, M., Mantelet, G., & Andrae, R. 2018, *AJ*, 156, 58
 Basri, G., & Nguyen, H. 2018, *ApJ*, 863, 190

- Biddle, L., Johns-Krull, C., Llama, J., Prato, L., & Skiff, B. 2018, *ApJL*, **853**, L34
- Bouvier, J., Alencar, S., Bouvier, T., et al. 2007, *A&A*, **463**, 1017
- Bouvier, J., Chelli, A., Allain, S., et al. 1999, *A&A*, **349**, 619
- Bouvier, J., Grangin, K., Alencar, S., et al. 2003, *A&A*, **409**, 169
- Bouvier, J., Grankin, K., Ellerbroek, L., Bouy, H., & Barrado, D. 2013, *A&A*, **557**, 77
- Cardelli, J., Clayton, G., & Mathis, J. 1989, *ApJ*, **345**, 245
- Chambers, K., Magnier, E., Metcalf, N., et al. 2016, arXiv:1612.05560
- Cody, A. M., & Hillenbrand, L. A. 2018, *AJ*, **156**, 71
- Cody, A. M., Stauffer, J., Baglin, A., et al. 2014, *AJ*, **147**, 82
- Coker, C., Pinsonneault, M., & Terndrup, D. 2016, *ApJ*, **833**, 122
- David, T., Mamajek, E., Vanderburg, A., et al. 2018, *AJ*, **156**, 302
- de Zeeuw, P., Hoogerwerf, R., de Bruijne, J., Brown, A., & Blaauw, A. 1999, *AJ*, **117**, 354
- Donati, J.-F., Skelly, M., Bouvier, J., et al. 2010, *MNRAS*, **409**, 1347
- Esplin, T. L., & Luhman, K. L. 2017, *AJ*, **154**, 134
- Esplin, T. L., & Luhman, K. L. 2019, *AJ*, **158**, 54
- Gaia Collaboration, Brown, A., Vallenari, A., et al. 2016, *A&A*, **595**, A2
- Gaia Collaboration, Brown, A., Vallenari, A., et al. 2018, *A&A*, **616**, A1
- Galli, P. A. B., Loinard, L., Bouy, H., et al. 2019, *A&A*, **630**, A137
- Grankin, K. N. 1993, *IBVS*, **3823**, 1
- Grankin, K. N. 1994, *IBVS*, **4042**, 1
- Grankin, K. N. 1997, *AstL*, **23**, 615
- Grankin, K. N., Artemenko, S. A., & Melnikov, S. Y. 2007, *IBVS*, **5752**, 1
- Güdel, M., Briggs, K., Arzner, K., et al. 2007, *A&A*, **468**, 353
- Hambálek, L., Vaňko, M., Paunzen, E., et al. 2019, *MNRAS*, **483**, 1642
- Hartmann, L. 2002, *ApJL*, **566**, L29
- Hartmann, L., Jones, B., Stauffer, J., & Kenyon, S. 1991, *AJ*, **101**, 1050
- Henden, A., Templeton, M., Terrell, D., et al. 2016, *yCat*, **2336**, 0
- Howell, S., et al. 2014, *PASP*, **126**, 398
- Indebetouw, R., Mathis, J., Babler, B., et al. 2005, *ApJ*, **619**, 931
- Johns-Krull, C. M., McLane, J. N., Prato, L., et al. 2016, *ApJ*, **826**, 206
- Joy, A. H. 1945, *ApJ*, **102**, 168
- Kenyon, S., & Hartmann, L. 1995, *ApJS*, **101**, 117
- Kraus, A., Herczeg, G., Rizzuto, A., et al. 2017, *ApJ*, **838**, 150
- Kraus, A., & Hillenbrand, L. 2009, *ApJ*, **704**, 531
- Kurucz, R. 1993, *yCat*, **6039**, 0
- Lejeune, T., Cuisinier, F., & Buser, R. 1997, *A&AS*, **125**, 229
- Liu, J., Fang, M., & Liu, C. 2020, *AJ*, **159**, 3
- Luger, R., Agol, E., Kruse, E., et al. 2016, *AJ*, **152**, 100
- Luger, R., Kruse, E., Foreman-Mackey, D., Agol, E., & Saunders, N. 2018, *AJ*, **156**, 99
- Luhman, K. 2018, *AJ*, **156**, 271
- Luhman, K., Mamajek, E., Shukla, S., & Loutrel, N. 2017, *AJ*, **153**, 46
- Marton, G., Calzoletti, L., Perez Garcia, A., et al. 2017, Explanatory Supplement, https://irsa.ipac.caltech.edu/data/Herschel/PPSC/docs/HPPSC_ExplanatorySupplement.pdf
- Mathis, J. 1990, *ARA&A*, **28**, 37
- Meyer, M., Calvet, N., & Hillenbrand, L. 1997, *AJ*, **114**, 288
- Murakami, H., Baba, H., Barthel, P., et al. 2007, *PASJ*, **59**, 369
- Nguyen, D. C., Jayawardhana, R., van Kerkwijk, M. H., et al. 2009, *ApJ*, **695**, 1648
- Oh, S., Price-Whelan, A. M., Hogg, D. W., Morton, T. D., & Spergel, D. N. 2018, *AJ*, **153**, 257
- Pecaut, M., & Mamajek, E. 2013, *ApJS*, **208**, 9
- Pilbratt, G., Riedinger, J., Passvogel, T., et al. 2010, *A&A*, **518**, L1
- Preibisch, T., & Smith, M. D. 1997, *A&A*, **322**, 825
- Press, W., Teukolsky, S., Vetterling, W., & Flannery, B. 1992, Numerical Recipes in C (Cambridge: Cambridge Univ. Press)
- Rebull, L. M., Koenig, X. P., Padgett, D. L., et al. 2011, *ApJS*, **196**, 4
- Rebull, L., Padgett, D., McCabe, C.-E., et al. 2010, *ApJS*, **186**, 259
- Rebull, L., Stauffer, J., Bouvier, J., et al. 2016a, *AJ*, **152**, 114
- Rebull, L., Stauffer, J., Cody, A., et al. 2016b, *AJ*, **152**, 113
- Rebull, L., Stauffer, J., Cody, A. M., et al. 2018, *AJ*, **155**, 196
- Rebull, L., Stauffer, J., Hillenbrand, L., et al. 2017, *ApJ*, **839**, 92
- Rebull, L., Wolff, S. C., & Strom, S. E. 2004, *AJ*, **127**, 1029
- Rigon, L., Scholz, A., Anderson, D., & West, R. 2017, *MNRAS*, **465**, 3889
- Rodriguez, J., Ansdell, M., Oelkers, R., et al. 2017a, *ApJ*, **848**, 91
- Rodriguez, J., Zhou, G., Cargile, P., et al. 2017b, *ApJ*, **836**, 209
- Scargle, J. D. 1982, *ApJ*, **263**, 835
- Scholz, A., Moore, K., Jayawardhana, R., et al. 2018, *ApJ*, **859**, 153
- Skrutskie, M., Cutri, R. M., Stiening, R., et al. 2006, *AJ*, **131**, 1163
- Slesnick, C., Carpenter, J., & Hillebrand, L. 2006, *AJ*, **131**, 3016
- Stauffer, J., Barrado, D., David, T., et al. 2020, *AJ*, in press
- Stauffer, J., Cody, A. M., Baglin, A., et al. 2014, *AJ*, **147**, 83
- Stauffer, J., Cody, A. M., McGinnis, P., et al. 2015, *AJ*, **149**, 130
- Stauffer, J., Cody, A. M., Rebull, L., et al. 2016a, *AJ*, **151**, 60
- Stauffer, J., Collier Cameron, A., Jardine, M., et al. 2017, *AJ*, **153**, 152
- Stauffer, J., Rebull, L., Bouvier, J., et al. 2016b, *AJ*, **152**, 142
- Stauffer, J., Rebull, L., Cody, A. M., et al. 2018a, *AJ*, **156**, 275
- Stauffer, J., Rebull, L., David, T., et al. 2018b, *AJ*, **155**, 152
- Tokovinin, A., & Briceño, C. 2020, *AJ*, **159**, 15
- Vanderburg, A., & Johnson, J. 2014, *PASP*, **126**, 948
- Werner, M., Roellig, T., Low, F., et al. 2004, *ApJS*, **154**, 1
- Wichmann, R., Krautter, J., Schmitt, J., et al. 1996, *A&A*, **312**, 439
- Wilking, B., Bontemps, S., Schuler, R., Greene, T., & André, P. 2001, *ApJ*, **551**, 357
- Wright, E., Eisenhardt, P. R. M., Mainzer, A. K., et al. 2010, *AJ*, **140**, 1868
- Xiao, H. Y., Covey, K. R., Rebull, L. M., et al. 2012, *ApJS*, **202**, 7
- Zhan, Z., Guenther, M., Rappaport, S., et al. 2019, *ApJ*, **876**, 127

BIBLIOGRAPHY

- ALMA Partnership, C. L. Brogan, L. M. Pérez, et al. (July 2015). “The 2014 ALMA Long Baseline Campaign: First Results from High Angular Resolution Observations toward the HL Tau Region.” In: *ApJ* 808.1, L3, p. L3. DOI: [10.1088/2041-8205/808/1/L3](https://doi.org/10.1088/2041-8205/808/1/L3). arXiv: [1503.02649](https://arxiv.org/abs/1503.02649) [astro-ph.SR].
- Adams, F. C. and F. H. Shu (Sept. 1986). “Infrared Spectra of Rotating Protostars.” In: *ApJ* 308, p. 836. DOI: [10.1086/164555](https://doi.org/10.1086/164555).
- Adams, Fred C., Charles J. Lada, and Frank H. Shu (Jan. 1987). “Spectral Evolution of Young Stellar Objects.” In: *ApJ* 312, p. 788. DOI: [10.1086/164924](https://doi.org/10.1086/164924).
- Aguiar-Conraria, Luís and Maria Joana Soares (2010). *The Continuous Wavelet Transform: A Primer*. NIPE Working Papers 23/2010. NIPE - Universidade do Minho. URL: <https://EconPapers.repec.org/RePEc:nip:nipewp:23/2010>.
- Akeson, R. L. and E. L. N. Jensen (Mar. 2014). “Circumstellar Disks around Binary Stars in Taurus.” In: *ApJ* 784.1, 62, p. 62. DOI: [10.1088/0004-637X/784/1/62](https://doi.org/10.1088/0004-637X/784/1/62). arXiv: [1402.5363](https://arxiv.org/abs/1402.5363) [astro-ph.SR].
- Akeson, Rachel L., Eric L. N. Jensen, John Carpenter, Luca Ricci, Stefan Laos, Natasha F. Nogueira, and Emma M. Suen-Lewis (2019). “Resolved Young Binary Systems and Their Disks.” In: *ApJ* 872.2, 158, p. 158. DOI: [10.3847/1538-4357/aaff6a](https://doi.org/10.3847/1538-4357/aaff6a). arXiv: [1901.05029](https://arxiv.org/abs/1901.05029) [astro-ph.SR].
- Alencar, S. H. P., P. S. Teixeira, M. M. Guimarães, P. T. McGinnis, J. F. Gameiro, J. Bouvier, S. Aigrain, E. Flaccomio, and F. Favata (2010). “Accretion dynamics and disk evolution in NGC 2264: a study based on CoRoT photometric observations.” In: *A&A* 519, A88, A88. DOI: [10.1051/0004-6361/201014184](https://doi.org/10.1051/0004-6361/201014184). arXiv: [1005.4384](https://arxiv.org/abs/1005.4384) [astro-ph.SR].
- Alencar, S. H. P., J. Bouvier, J. F. Donati, et al. (Dec. 2018). “Inner disk structure of the classical T Tauri star LkCa 15.” In: *A&A* 620, A195, A195. DOI: [10.1051/0004-6361/201834263](https://doi.org/10.1051/0004-6361/201834263). arXiv: [1811.04806](https://arxiv.org/abs/1811.04806) [astro-ph.SR].
- Ambartsumian, V. A. (1947). *The evolution of stars and astrophysics*.
- Andre, P., D. Ward-Thompson, and M. Barsony (May 2000). “From Prestellar Cores to Protostars: the Initial Conditions of Star Formation.” In: *Protostars and Planets IV*. Ed. by V. Mannings, A. P. Boss, and S. S. Russell, p. 59. arXiv: [astro-ph/9903284](https://arxiv.org/abs/astro-ph/9903284) [astro-ph].
- Andrews, Sean M. and Jonathan P. Williams (Dec. 2007). “A Submillimeter View of Circumstellar Dust Disks in ρ Ophiuchi.” In: *ApJ* 671.2, pp. 1800–1812. DOI: [10.1086/522885](https://doi.org/10.1086/522885). arXiv: [0708.4185](https://arxiv.org/abs/0708.4185) [astro-ph].
- Ansdell, M., E. Gaidos, J. P. Williams, G. Kennedy, M. C. Wyatt, D. M. LaCourse, T. L. Jacobs, and A. W. Mann (2016a). “Dipper discs not inclined towards edge-on orbits.” In: *MNRAS* 462.1, pp. L101–L105. DOI: [10.1093/mnrasl/slw140](https://doi.org/10.1093/mnrasl/slw140). arXiv: [1607.03115](https://arxiv.org/abs/1607.03115) [astro-ph.EP].
- Ansdell, M., E. Gaidos, S. A. Rappaport, et al. (2016b). “Young “Dipper” Stars in Upper Sco and Oph Observed by K2.” In: *ApJ* 816.2, 69, p. 69. DOI: [10.3847/0004-637X/816/2/69](https://doi.org/10.3847/0004-637X/816/2/69). arXiv: [1510.08853](https://arxiv.org/abs/1510.08853) [astro-ph.EP].
- Ansdell, M., E. Gaidos, C. Hedges, et al. (Feb. 2020). “Are inner disc misalignments common? ALMA reveals an isotropic outer disc inclination distribution for young dipper stars.” In: *MNRAS* 492.1, pp. 572–588. DOI: [10.1093/mnras/stz3361](https://doi.org/10.1093/mnras/stz3361). arXiv: [1912.01610](https://arxiv.org/abs/1912.01610) [astro-ph.EP].
- Anthonioz, F., F. Ménard, C. Pinte, et al. (Jan. 2015). “The VLTI/PIONIER near-infrared interferometric survey of southern T Tauri stars. I. First results.” In: *A&A* 574, A41, A41. DOI: [10.1051/0004-6361/201424520](https://doi.org/10.1051/0004-6361/201424520). arXiv: [1412.1052](https://arxiv.org/abs/1412.1052) [astro-ph.SR].
- Appenzeller, Immo and Claude Bertout (2013). “Inclination effects in T Tauri star spectra.” In: *Astronomy & Astrophysics* 558, A83. ISSN: 1432-0746. DOI: [10.1051/0004-6361/201322160](https://doi.org/10.1051/0004-6361/201322160). URL: <http://dx.doi.org/10.1051/0004-6361/201322160>.
- Artemenko, S. A., K. N. Grankin, and P. P. Petrov (2012). “Rotation effects in classical T Tauri stars.” In: *Astronomy Letters* 38.12, pp. 783–792. DOI: [10.1134/S1063773712110011](https://doi.org/10.1134/S1063773712110011). arXiv: [1301.2493](https://arxiv.org/abs/1301.2493) [astro-ph.SR].

- Auchère, F., C. Froment, K. Bocchialini, E. Buchlin, and J. Solomon (July 2016). “On the Fourier and Wavelet Analysis of Coronal Time Series.” In: *ApJ* 825.2, 110, p. 110. DOI: [10.3847/0004-637X/825/2/110](https://doi.org/10.3847/0004-637X/825/2/110). arXiv: [1606.05251](https://arxiv.org/abs/1606.05251) [astro-ph.SR].
- Balog, Zoltan, László L. Kiss, József Vinkó, G. H. Rieke, James Muzerolle, András Gáspár, Erick T. Young, and Nadya Gorlova (June 2009). “Spitzer/IRAC-MIPS Survey of NGC 2451A AND B: Debris Disks at 50-80 Million Years.” In: *ApJ* 698.2, pp. 1989–2013. DOI: [10.1088/0004-637X/698/2/1989](https://doi.org/10.1088/0004-637X/698/2/1989). arXiv: [0904.2608](https://arxiv.org/abs/0904.2608) [astro-ph.SR].
- Bans, Alissa and Ariele Königl (Oct. 2012). “A Disk-wind Model for the Near-infrared Excess Emission in Protostars.” In: *ApJ* 758.2, 100, p. 100. DOI: [10.1088/0004-637X/758/2/100](https://doi.org/10.1088/0004-637X/758/2/100). arXiv: [1207.1508](https://arxiv.org/abs/1207.1508) [astro-ph.SR].
- Baraffe, Isabelle, Derek Homeier, France Allard, and Gilles Chabrier (May 2015). “New evolutionary models for pre-main sequence and main sequence low-mass stars down to the hydrogen-burning limit.” In: *A&A* 577, A42, A42. DOI: [10.1051/0004-6361/201425481](https://doi.org/10.1051/0004-6361/201425481). arXiv: [1503.04107](https://arxiv.org/abs/1503.04107) [astro-ph.SR].
- Bayo, A., C. Rodrigo, D. Barrado Y Navascués, E. Solano, R. Gutiérrez, M. Morales-Calderón, and F. Allard (Dec. 2008). “VOSA: virtual observatory SED analyzer. An application to the Collinder 69 open cluster.” In: *A&A* 492.1, pp. 277–287. DOI: [10.1051/0004-6361:200810395](https://doi.org/10.1051/0004-6361:200810395). arXiv: [0808.0270](https://arxiv.org/abs/0808.0270) [astro-ph].
- Benisty, M., A. Juhasz, A. Boccaletti, et al. (June 2015). “Asymmetric features in the protoplanetary disk MWC 758.” In: *A&A* 578, L6, p. L6. DOI: [10.1051/0004-6361/201526011](https://doi.org/10.1051/0004-6361/201526011). arXiv: [1505.05325](https://arxiv.org/abs/1505.05325) [astro-ph.SR].
- Bertout, Claude, Gibor Basri, and Jerome Bouvier (July 1988). “Accretion Disks around T Tauri Stars.” In: *ApJ* 330, p. 350. DOI: [10.1086/166476](https://doi.org/10.1086/166476).
- Bessell, M. S. (Oct. 1979). “UBVRI photometry II: the Cousins VRI system, its temperature and absolute flux calibration, and relevance for two-dimensional photometry.” In: *PASP* 91, pp. 589–607. DOI: [10.1086/130542](https://doi.org/10.1086/130542).
- Bessolaz, N., C. Zanni, J. Ferreira, R. Keppens, and J. Bouvier (Jan. 2008). “Accretion funnels onto weakly magnetized young stars.” In: *A&A* 478.1, pp. 155–162. DOI: [10.1051/0004-6361:20078328](https://doi.org/10.1051/0004-6361:20078328). arXiv: [0712.2921](https://arxiv.org/abs/0712.2921) [astro-ph].
- Blandford, R. D. and D. G. Payne (June 1982). “Hydromagnetic flows from accretion disks and the production of radio jets.” In: *MNRAS* 199, pp. 883–903. DOI: [10.1093/mnras/199.4.883](https://doi.org/10.1093/mnras/199.4.883).
- Blinova, A. A., M. M. Romanova, and R. V. E. Lovelace (July 2016). “Boundary between stable and unstable regimes of accretion. Ordered and chaotic unstable regimes.” In: *MNRAS* 459.3, pp. 2354–2369. DOI: [10.1093/mnras/stw786](https://doi.org/10.1093/mnras/stw786). arXiv: [1501.01948](https://arxiv.org/abs/1501.01948) [astro-ph.SR].
- Bodman, Eva H. L., Alice C. Quillen, Megan Ansdell, Michael Hippke, Tabettha S. Boyajian, Eric E. Mamajek, Eric G. Blackman, Aaron Rizzuto, and Joel H. Kastner (2017). “Dippers and dusty disc edges: new diagnostics and comparison to model predictions.” In: *MNRAS* 470.1, pp. 202–223. DOI: [10.1093/mnras/stx1034](https://doi.org/10.1093/mnras/stx1034). arXiv: [1605.03985](https://arxiv.org/abs/1605.03985) [astro-ph.SR].
- Borucki, William J., David Koch, Gibor Basri, et al. (2010). “Kepler Planet-Detection Mission: Introduction and First Results.” In: *Science* 327.5968, pp. 977–980. ISSN: 0036-8075. DOI: [10.1126/science.1185402](https://doi.org/10.1126/science.1185402). eprint: <https://science.sciencemag.org/content/327/5968/977.full.pdf>. URL: <https://science.sciencemag.org/content/327/5968/977>.
- Bouvier, J., E. Covino, O. Kovo, E. L. Martin, J. M. Matthews, L. Terranegra, and S. C. Beck (July 1995). “COYOTES II: SPOT properties and the origin of photometric period variations in T Tauri stars.” In: *A&A* 299, p. 89.
- Bouvier, J., A. Chelli, S. Allain, et al. (1999). “Magnetospheric accretion onto the T Tauri star AA Tauri. I. Constraints from multisite spectrophotometric monitoring.” In: *A&A* 349, pp. 619–635.
- Bouvier, J., K. N. Grankin, S. H. P. Alencar, et al. (2003). “Eclipses by circumstellar material in the T Tauri star AA Tau. II. Evidence for non-stationary magnetospheric accretion.” In: *A&A* 409, pp. 169–192. DOI: [10.1051/0004-6361:20030938](https://doi.org/10.1051/0004-6361:20030938). arXiv: [astro-ph/0306551](https://arxiv.org/abs/astro-ph/0306551) [astro-ph].
- Bouvier, J., S. H. P. Alencar, T. J. Harries, C. M. Johns-Krull, and M. M. Romanova (Jan. 2007a). “Magnetospheric Accretion in Classical T Tauri Stars.” In: *Protostars and Planets V*. Ed. by Bo Reipurth, David Jewitt, and Klaus Keil, p. 479. arXiv: [astro-ph/0603498](https://arxiv.org/abs/astro-ph/0603498) [astro-ph].

- Bouvier, J., S. H. P. Alencar, T. Bouvier, et al. (2007b). "Magnetospheric accretion-ejection processes in the classical T Tauri star AA Tauri." In: *A&A* 463.3, pp. 1017–1028. DOI: [10.1051/0004-6361:20066021](https://doi.org/10.1051/0004-6361:20066021). arXiv: [astro-ph/0611787](https://arxiv.org/abs/astro-ph/0611787) [astro-ph].
- Bouvier, J., K. Grankin, L. E. Ellerbroek, H. Bouy, and D. Barrado (Sept. 2013). "AA Tauri's sudden and long-lasting deepening: enhanced extinction by its circumstellar disk." In: *A&A* 557, A77, A77. DOI: [10.1051/0004-6361/201321389](https://doi.org/10.1051/0004-6361/201321389). arXiv: [1304.1487](https://arxiv.org/abs/1304.1487) [astro-ph.SR].
- Bouvier, J., K. Perraut, J. B. Le Bouquin, G. Duvert, C. Dougados, W. Brandner, M. Benisty, J. P. Berger, and E. Alécian (Apr. 2020). "Probing the magnetospheric accretion region of the young pre-transitional disk system DoAr 44 using VLTI/GRAVITY." In: *A&A* 636, A108, A108. DOI: [10.1051/0004-6361/202037611](https://doi.org/10.1051/0004-6361/202037611). arXiv: [2004.00848](https://arxiv.org/abs/2004.00848) [astro-ph.SR].
- Bravo, J. P., S. Roque, R. Estrela, I. C. Leão, and J. R. De Medeiros (Aug. 2014). "Wavelets: a powerful tool for studying rotation, activity, and pulsation in Kepler and CoRoT stellar light curves." In: *A&A* 568, A34, A34. DOI: [10.1051/0004-6361/201323032](https://doi.org/10.1051/0004-6361/201323032). arXiv: [1407.1084](https://arxiv.org/abs/1407.1084) [astro-ph.IM].
- Cabrit, S. (Jan. 2002). "Constraints on accretion-ejection structures in young stars." In: *EAS Publications Series*. Ed. by Jerome Bouvier and Jean-Paul Zahn. Vol. 3. EAS Publications Series, pp. 147–182. DOI: [10.1051/eas:2002049](https://doi.org/10.1051/eas:2002049).
- Cabrit, Sylvie, Suzan Edwards, Stephen E. Strom, and Karen M. Strom (May 1990). "Forbidden-Line Emission and Infrared Excesses in T Tauri Stars: Evidence for Accretion-driven Mass Loss?" In: *ApJ* 354, p. 687. DOI: [10.1086/168725](https://doi.org/10.1086/168725).
- Calvet, Nuria and Erik Gullbring (Dec. 1998). "The Structure and Emission of the Accretion Shock in T Tauri Stars." In: *ApJ* 509.2, pp. 802–818. DOI: [10.1086/306527](https://doi.org/10.1086/306527).
- Calvet, Nuria, James Muzerolle, César Briceño, Jesus Hernández, Lee Hartmann, José Luis Saucedo, and Karl D. Gordon (Sept. 2004). "The Mass Accretion Rates of Intermediate-Mass T Tauri Stars." In: *AJ* 128.3, pp. 1294–1318. DOI: [10.1086/422733](https://doi.org/10.1086/422733).
- Camenzind, M. (Jan. 1990). "Magnetized Disk-Winds and the Origin of Bipolar Outflows." In: *Reviews in Modern Astronomy* 3, pp. 234–265. DOI: [10.1007/978-3-642-76238-3_17](https://doi.org/10.1007/978-3-642-76238-3_17).
- Cardelli, Jason A., Geoffrey C. Clayton, and John S. Mathis (Oct. 1989). "The Relationship between Infrared, Optical, and Ultraviolet Extinction." In: *ApJ* 345, p. 245. DOI: [10.1086/167900](https://doi.org/10.1086/167900).
- Chabrier, G., I. Baraffe, F. Allard, and P. Hauschildt (Oct. 2000). "Evolutionary Models for Very Low-Mass Stars and Brown Dwarfs with Dusty Atmospheres." In: *ApJ* 542.1, pp. 464–472. DOI: [10.1086/309513](https://doi.org/10.1086/309513). arXiv: [astro-ph/0005557](https://arxiv.org/abs/astro-ph/0005557) [astro-ph].
- Chiang, E. I. and P. Goldreich (Nov. 1997). "Spectral Energy Distributions of T Tauri Stars with Passive Circumstellar Disks." In: *ApJ* 490.1, pp. 368–376. DOI: [10.1086/304869](https://doi.org/10.1086/304869). arXiv: [astro-ph/9706042](https://arxiv.org/abs/astro-ph/9706042) [astro-ph].
- Chini, R., V. H. Hoffmeister, A. Nasser, O. Stahl, and H. Zinnecker (Aug. 2012). "A spectroscopic survey on the multiplicity of high-mass stars." In: *MNRAS* 424, pp. 1925–1929. DOI: [10.1111/j.1365-2966.2012.21317.x](https://doi.org/10.1111/j.1365-2966.2012.21317.x). arXiv: [1205.5238](https://arxiv.org/abs/1205.5238) [astro-ph.SR].
- Chun-Lin, L. (2010). *A Tutorial of the Wavelet Transform*. URL: <http://disp.ee.ntu.edu.tw/tutorial/WaveletTutorial.pdf>.
- Cody, Ann Marie and Lynne A. Hillenbrand (Aug. 2018). "The Many-faceted Light Curves of Young Disk-bearing Stars in Upper Sco – Oph Observed by K2 Campaign 2." In: *AJ* 156.2, 71, p. 71. DOI: [10.3847/1538-3881/aacead](https://doi.org/10.3847/1538-3881/aacead). arXiv: [1802.06409](https://arxiv.org/abs/1802.06409) [astro-ph.SR].
- Cody, Ann Marie, John Stauffer, Annie Baglin, et al. (Apr. 2014). "CSI 2264: Simultaneous Optical and Infrared Light Curves of Young Disk-bearing Stars in NGC 2264 with CoRoT and Spitzer—Evidence for Multiple Origins of Variability." In: *AJ* 147.4, 82, p. 82. DOI: [10.1088/0004-6256/147/4/82](https://doi.org/10.1088/0004-6256/147/4/82). arXiv: [1401.6582](https://arxiv.org/abs/1401.6582) [astro-ph.SR].
- Cohen, M. (Jan. 1973). "Infra-red observations of young stars - II. T Tauri stars and the Orion population." In: *MNRAS* 161, p. 97. DOI: [10.1093/mnras/161.1.97](https://doi.org/10.1093/mnras/161.1.97).
- Cohen, M. and L. V. Kuhi (Dec. 1979). "Observational studies of pre-main-sequence evolution." In: *ApJS* 41, pp. 743–843. DOI: [10.1086/190641](https://doi.org/10.1086/190641).
- Colavita, M., R. Akeson, P. Wizinowich, et al. (Aug. 2003). "Observations of DG Tauri with the Keck Interferometer." In: *ApJ* 592.2, pp. L83–L86. DOI: [10.1086/377704](https://doi.org/10.1086/377704). arXiv: [astro-ph/0307051](https://arxiv.org/abs/astro-ph/0307051) [astro-ph].

- Collier Cameron, A. and C. G. Campbell (July 1993). "Rotational evolution of magnetic T Tauri stars with accretion discs." In: *A&A* 274, p. 309.
- Currie, Thayne, Christian Marois, Lucas Cieza, et al. (2019). "No Clear, Direct Evidence for Multiple Protoplanets Orbiting LkCa 15: LkCa 15 bcd are Likely Inner Disk Signals." In: *The Astrophysical Journal* 877.1, p. L3. DOI: [10.3847/2041-8213/ab1b42](https://doi.org/10.3847/2041-8213/ab1b42). URL: <https://doi.org/10.3847/2041-8213/ab1b42>.
- Dahm, S. E. (2008). "The Young Cluster and Star Forming Region NGC 2264." In: *Handbook of Star Forming Regions, Volume I*. Ed. by B. Reipurth. Vol. 4, p. 966.
- Dahm, S. E. and J. E. Lyke (2011). "The Low-Mass Companion to the Lithium-Depleted, Spectroscopic Binary HBC 425 (St 34)." In: *PASP* 123.910, p. 1383. DOI: [10.1086/663724](https://doi.org/10.1086/663724). arXiv: [1111.2081](https://arxiv.org/abs/1111.2081) [astro-ph.SR].
- Daubechies, I., ed. (1992). *Ten lectures on wavelets*.
- Daubechies, Ingrid (Sept. 1990). "The wavelet transform, time-frequency localization and signal analysis." In: *IEEE Transactions on Information Theory* 36, pp. 961–1005.
- David, Trevor J., Erik A. Petigura, Rodrigo Luger, Daniel Foreman-Mackey, John H. Livingston, Eric E. Mamajek, and Lynne A. Hillenbrand (Nov. 2019). "Four Newborn Planets Transiting the Young Solar Analog V1298 Tau." In: *ApJ* 885.1, L12, p. L12. DOI: [10.3847/2041-8213/ab4c99](https://doi.org/10.3847/2041-8213/ab4c99). arXiv: [1910.04563](https://arxiv.org/abs/1910.04563) [astro-ph.EP].
- Davies, Claire L., Scott G. Gregory, and Jane S. Greaves (Oct. 2014). "Accretion discs as regulators of stellar angular momentum evolution in the ONC and Taurus-Auriga." In: *MNRAS* 444.2, pp. 1157–1176. DOI: [10.1093/mnras/stu1488](https://doi.org/10.1093/mnras/stu1488). arXiv: [1407.6212](https://arxiv.org/abs/1407.6212) [astro-ph.SR].
- Dipierro, Giovanni, Daniel Price, Guillaume Laibe, Kieran Hirsh, Alice Cerioli, and Giuseppe Lodato (Aug. 2015). "On planet formation in HL Tau." In: *Monthly Notices of the Royal Astronomical Society: Letters* 453.1, pp. L73–L77. ISSN: 1745-3925. DOI: [10.1093/mnrasl/slv105](https://doi.org/10.1093/mnrasl/slv105). eprint: <https://academic.oup.com/mnrasl/article-pdf/453/1/L73/3057747/slv105.pdf>. URL: <https://doi.org/10.1093/mnrasl/slv105>.
- Donati, J. F., S. G. Gregory, S. H. P. Alencar, et al. (Oct. 2011). "The large-scale magnetic field and poleward mass accretion of the classical T Tauri star TW Hya." In: *MNRAS* 417.1, pp. 472–487. DOI: [10.1111/j.1365-2966.2011.19288.x](https://doi.org/10.1111/j.1365-2966.2011.19288.x). arXiv: [1106.4162](https://arxiv.org/abs/1106.4162) [astro-ph.SR].
- Donati, J. F., J. Bouvier, S. H. Alencar, et al. (Feb. 2019). "The magnetic propeller accretion regime of LkCa 15." In: *MNRAS* 483.1, pp. L1–L5. DOI: [10.1093/mnrasl/sly207](https://doi.org/10.1093/mnrasl/sly207). arXiv: [1811.04810](https://arxiv.org/abs/1811.04810) [astro-ph.SR].
- Drake, A. J., M. J. Graham, S. G. Djorgovski, et al. (July 2014). "The Catalina Surveys Periodic Variable Star Catalog." In: *ApJS* 213.1, 9, p. 9. DOI: [10.1088/0067-0049/213/1/9](https://doi.org/10.1088/0067-0049/213/1/9). arXiv: [1405.4290](https://arxiv.org/abs/1405.4290) [astro-ph.SR].
- Duchêne, G., J. L. Monin, J. Bouvier, and F. Ménard (Nov. 1999). "Accretion in Taurus PMS binaries: a spectroscopic study." In: *A&A* 351, pp. 954–962. arXiv: [astro-ph/9909378](https://arxiv.org/abs/astro-ph/9909378) [astro-ph].
- Duchêne, Gaspard and Adam Kraus (Aug. 2013). "Stellar Multiplicity." In: *ARA&A* 51.1, pp. 269–310. DOI: [10.1146/annurev-astro-081710-102602](https://doi.org/10.1146/annurev-astro-081710-102602). arXiv: [1303.3028](https://arxiv.org/abs/1303.3028) [astro-ph.SR].
- Dullemond, C. P., C. Dominik, and A. Natta (Oct. 2001). "Passive Irradiated Circumstellar Disks with an Inner Hole." In: *ApJ* 560.2, pp. 957–969. DOI: [10.1086/323057](https://doi.org/10.1086/323057). arXiv: [astro-ph/0106470](https://arxiv.org/abs/astro-ph/0106470) [astro-ph].
- Dullemond, Cornelis P. (Nov. 2010). "Evolution of protoplanetary disks." In: *Highlights of Astronomy* 15, pp. 736–737. DOI: [10.1017/S1743921310011269](https://doi.org/10.1017/S1743921310011269).
- Eisenhauer, Frank (July 2019). "GRAVITY+: Towards faint science." In: *The Very Large Telescope in 2030*, p. 30. DOI: [10.5281/zenodo.4697646](https://doi.org/10.5281/zenodo.4697646).
- Eisner, J. A., L. A. Hillenbrand, R. J. White, J. S. Bloom, R. L. Akeson, and C. H. Blake (2007). "Near-Infrared Interferometric, Spectroscopic, and Photometric Monitoring of T Tauri Inner Disks." In: *The Astrophysical Journal* 669.2, pp. 1072–1084. DOI: [10.1086/521874](https://doi.org/10.1086/521874). URL: <https://doi.org/10.1086/521874>.
- Eisner, J. A., J. D. Monnier, J. Woillez, R. L. Akeson, R. Millan-Gabet, J. R. Graham, L. A. Hillenbrand, J. U. Pott, S. Ragland, and P. Wizinowich (Aug. 2010). "Spatially and Spectrally Resolved Hydrogen

- Gas within 0.1 AU of T Tauri and Herbig Ae/Be Stars." In: *ApJ* 718.2, pp. 774–794. DOI: [10.1088/0004-637X/718/2/774](https://doi.org/10.1088/0004-637X/718/2/774). arXiv: [1006.1651](https://arxiv.org/abs/1006.1651) [astro-ph.GA].
- Esplin, T. L. and K. L. Luhman (2019). "A Survey for New Members of Taurus from Stellar to Planetary Masses." In: *AJ* 158.2, 54, p. 54. DOI: [10.3847/1538-3881/ab2594](https://doi.org/10.3847/1538-3881/ab2594). arXiv: [1907.00055](https://arxiv.org/abs/1907.00055) [astro-ph.SR].
- Esplin, T. L., K. L. Luhman, and E. E. Mamajek (2014). "A WISE Survey of Circumstellar Disks in Taurus." In: *ApJ* 784.2, 126, p. 126. DOI: [10.1088/0004-637X/784/2/126](https://doi.org/10.1088/0004-637X/784/2/126). arXiv: [1402.4705](https://arxiv.org/abs/1402.4705) [astro-ph.SR].
- Evans Neal J., II, Michael M. Dunham, Jes K. Jørgensen, et al. (Apr. 2009). "The Spitzer c2d Legacy Results: Star-Formation Rates and Efficiencies; Evolution and Lifetimes." In: *ApJS* 181.2, pp. 321–350. DOI: [10.1088/0067-0049/181/2/321](https://doi.org/10.1088/0067-0049/181/2/321). arXiv: [0811.1059](https://arxiv.org/abs/0811.1059) [astro-ph].
- Facchini, Stefano, Giuseppe Lodato, and Daniel J. Price (Aug. 2013). "Wave-like warp propagation in circumbinary discs - I. Analytic theory and numerical simulations." In: *MNRAS* 433.3, pp. 2142–2156. DOI: [10.1093/mnras/stt877](https://doi.org/10.1093/mnras/stt877). arXiv: [1306.4331](https://arxiv.org/abs/1306.4331) [astro-ph.SR].
- Facchini, Stefano, Attila Juhász, and Giuseppe Lodato (Feb. 2018). "Signatures of broken protoplanetary discs in scattered light and in sub-millimetre observations." In: *MNRAS* 473.4, pp. 4459–4475. DOI: [10.1093/mnras/stx2523](https://doi.org/10.1093/mnras/stx2523). arXiv: [1709.08369](https://arxiv.org/abs/1709.08369) [astro-ph.SR].
- Farge, M. (1992). "Wavelet transforms and their applications to turbulence." In: *Annual Review of Fluid Mechanics* 24, pp. 395–457. DOI: [10.1146/annurev.fl.24.010192.002143](https://doi.org/10.1146/annurev.fl.24.010192.002143).
- Feiden, Gregory A. (Sept. 2016). "Magnetic inhibition of convection and the fundamental properties of low-mass stars. III. A consistent 10 Myr age for the Upper Scorpius OB association." In: *A&A* 593, A99, A99. DOI: [10.1051/0004-6361/201527613](https://doi.org/10.1051/0004-6361/201527613). arXiv: [1604.08036](https://arxiv.org/abs/1604.08036) [astro-ph.SR].
- Ferreira, J., P. O. Petrucci, G. Henri, L. Saugé, and G. Pelletier (Mar. 2006). "A unified accretion-ejection paradigm for black hole X-ray binaries. I. The dynamical constituents." In: *A&A* 447.3, pp. 813–825. DOI: [10.1051/0004-6361:20052689](https://doi.org/10.1051/0004-6361:20052689). arXiv: [astro-ph/0511123](https://arxiv.org/abs/astro-ph/0511123) [astro-ph].
- Flaherty, K. M., J. Muzerolle, G. Rieke, R. Gutermuth, Z. Balog, W. Herbst, S. T. Megeath, and M. Kun (Mar. 2012). "Infrared Variability of Evolved Protoplanetary Disks: Evidence for Scale Height Variations in the Inner Disk." In: *ApJ* 748.1, 71, p. 71. DOI: [10.1088/0004-637X/748/1/71](https://doi.org/10.1088/0004-637X/748/1/71). arXiv: [1202.1553](https://arxiv.org/abs/1202.1553) [astro-ph.GA].
- Fleming, Graham D., Jason Matthew Kirk, Derek Ward-Thompson, and Kate Pattle (2019). "Revealing the Two 'Horns' of Taurus with GAIA DR2." In: *arXiv e-prints*, arXiv:1904.06980, arXiv:1904.06980. arXiv: [1904.06980](https://arxiv.org/abs/1904.06980) [astro-ph.SR].
- Gaia Collaboration, T. Prusti, J. H. J. de Bruijne, et al. (Nov. 2016). "The Gaia mission." In: *A&A* 595, A1, A1. DOI: [10.1051/0004-6361/201629272](https://doi.org/10.1051/0004-6361/201629272). arXiv: [1609.04153](https://arxiv.org/abs/1609.04153) [astro-ph.IM].
- Gaia Collaboration, A. G. A. Brown, A. Vallenari, et al. (Aug. 2018). "Gaia Data Release 2. Summary of the contents and survey properties." In: *A&A* 616, A1, A1. DOI: [10.1051/0004-6361/201833051](https://doi.org/10.1051/0004-6361/201833051). arXiv: [1804.09365](https://arxiv.org/abs/1804.09365) [astro-ph.GA].
- Gaidos, E., T. Jacobs, D. LaCourse, et al. (Oct. 2019). "Planetesimals around stars with TESS (PAST) - I. Transient dimming of a binary solar analogue at the end of the planet accretion era." In: *MNRAS* 488.4, pp. 4465–4476. DOI: [10.1093/mnras/stz1942](https://doi.org/10.1093/mnras/stz1942). arXiv: [1907.02476](https://arxiv.org/abs/1907.02476) [astro-ph.EP].
- Galli, Daniele, Susana Lizano, Frank H. Shu, and Anthony Allen (Aug. 2006). "Gravitational Collapse of Magnetized Clouds. I. Ideal Magnetohydrodynamic Accretion Flow." In: *ApJ* 647.1, pp. 374–381. DOI: [10.1086/505257](https://doi.org/10.1086/505257). arXiv: [astro-ph/0604573](https://arxiv.org/abs/astro-ph/0604573) [astro-ph].
- Galli, Phillip A. B., Laurent Loinard, Gisela N. Ortiz-Léon, et al. (2018). "The Gould's Belt Distances Survey (GOBELINS). IV. Distance, Depth, and Kinematics of the Taurus Star-forming Region." In: *ApJ* 859.1, 33, p. 33. DOI: [10.3847/1538-4357/aabf91](https://doi.org/10.3847/1538-4357/aabf91). arXiv: [1805.09357](https://arxiv.org/abs/1805.09357) [astro-ph.SR].
- Gao, R. X. and R. Yan (2011). *Wavelets. Theory and Applications for Manufacturing*. 1st ed. Springer US. ISBN: 978-1-4419-1544-3. DOI: [10.1007/978-1-4419-1545-0](https://doi.org/10.1007/978-1-4419-1545-0).
- García, R. A., T. Ceillier, D. Salabert, et al. (Dec. 2014). "Rotation and magnetism of Kepler pulsating solar-like stars. Towards asteroseismically calibrated age-rotation relations." In: *A&A* 572, A34, A34. DOI: [10.1051/0004-6361/201423888](https://doi.org/10.1051/0004-6361/201423888). arXiv: [1403.7155](https://arxiv.org/abs/1403.7155) [astro-ph.SR].
- Ghosh, P. and F. K. Lamb (July 1978). "Disk accretion by magnetic neutron stars." In: *ApJ* 223, pp. L83–L87. DOI: [10.1086/182734](https://doi.org/10.1086/182734).

- Ghosh, P. and F. K. Lamb (Aug. 1979a). “Accretion by rotating magnetic neutron stars. II. Radial and vertical structure of the transition zone in disk accretion.” In: *ApJ* 232, pp. 259–276. DOI: [10.1086/157285](https://doi.org/10.1086/157285).
- (Nov. 1979b). “Accretion by rotating magnetic neutron stars. III. Accretion torques and period changes in pulsating X-ray sources.” In: *ApJ* 234, pp. 296–316. DOI: [10.1086/157498](https://doi.org/10.1086/157498).
- Grankin, K. N., S. Yu. Melnikov, J. Bouvier, W. Herbst, and V. S. Shevchenko (2007). “Results of the ROTOR-program. I. The long-term photometric variability of classical T Tauri stars.” In: *A&A* 461.1, pp. 183–195. DOI: [10.1051/0004-6361:20065489](https://doi.org/10.1051/0004-6361:20065489). arXiv: [astro-ph/0611028](https://arxiv.org/abs/astro-ph/0611028) [astro-ph].
- Gravity Collaboration, R. Abuter, M. Accardo, et al. (June 2017). “First light for GRAVITY: Phase referencing optical interferometry for the Very Large Telescope Interferometer.” In: *A&A* 602, A94, A94. DOI: [10.1051/0004-6361/201730838](https://doi.org/10.1051/0004-6361/201730838). arXiv: [1705.02345](https://arxiv.org/abs/1705.02345) [astro-ph.IM].
- Gravity Collaboration, Y. I. Bouvarour, K. Perraut, et al. (Oct. 2020). “The GRAVITY young stellar object survey. III. The dusty disk of RY Lup.” In: *A&A* 642, A162, A162. DOI: [10.1051/0004-6361/202038249](https://doi.org/10.1051/0004-6361/202038249). arXiv: [2008.08527](https://arxiv.org/abs/2008.08527) [astro-ph.SR].
- Gregory, S. G., M. Jardine, I. Simpson, and J. F. Donati (Sept. 2006). “Mass accretion on to T Tauri stars.” In: *MNRAS* 371.2, pp. 999–1013. DOI: [10.1111/j.1365-2966.2006.10734.x](https://doi.org/10.1111/j.1365-2966.2006.10734.x). arXiv: [astro-ph/0606682](https://arxiv.org/abs/astro-ph/0606682) [astro-ph].
- Gregory, S. G., J. F. Donati, J. Morin, G. A. J. Hussain, N. J. Mayne, L. A. Hillenbrand, and M. Jardine (Aug. 2012). “Can We Predict the Global Magnetic Topology of a Pre-main-sequence Star from Its Position in the Hertzsprung-Russell Diagram?” In: *ApJ* 755.2, 97, p. 97. DOI: [10.1088/0004-637X/755/2/97](https://doi.org/10.1088/0004-637X/755/2/97). arXiv: [1206.5238](https://arxiv.org/abs/1206.5238) [astro-ph.SR].
- Grossmann, A. and J. Morlet (1984). “Decomposition of Hardy Functions into Square Integrable Wavelets of Constant Shape.” In: *SIAM Journal on Mathematical Analysis* 15.4, pp. 723–736. DOI: [10.1137/0515056](https://doi.org/10.1137/0515056). eprint: <https://doi.org/10.1137/0515056>. URL: <https://doi.org/10.1137/0515056>.
- Güdel, M., K. R. Briggs, K. Arzner, et al. (June 2007). “The XMM-Newton extended survey of the Taurus molecular cloud (XEST).” In: *A&A* 468.2, pp. 353–377. DOI: [10.1051/0004-6361:20065724](https://doi.org/10.1051/0004-6361:20065724). arXiv: [astro-ph/0609160](https://arxiv.org/abs/astro-ph/0609160) [astro-ph].
- Guieu, S., C. Pinte, J. L. Monin, et al. (2007). “On the circum(sub)stellar environment of brown dwarfs in Taurus.” In: *A&A* 465.3, pp. 855–864. DOI: [10.1051/0004-6361:20066140](https://doi.org/10.1051/0004-6361:20066140). arXiv: [astro-ph/0701251](https://arxiv.org/abs/astro-ph/0701251) [astro-ph].
- Gullbring, Erik, Lee Hartmann, Cesar Briceño, and Nuria Calvet (Jan. 1998). “Disk Accretion Rates for T Tauri Stars.” In: *ApJ* 492.1, pp. 323–341. DOI: [10.1086/305032](https://doi.org/10.1086/305032).
- Guo, Zhen, Gregory J. Herczeg, Jessy Jose, et al. (Jan. 2018). “Star-Disk Interactions in Multiband Photometric Monitoring of the Classical T Tauri Star GI Tau.” In: *ApJ* 852.1, 56, p. 56. DOI: [10.3847/1538-4357/aa9e52](https://doi.org/10.3847/1538-4357/aa9e52). arXiv: [1711.08652](https://arxiv.org/abs/1711.08652) [astro-ph.SR].
- Haas, Michael R., Natalie M. Batalha, Steve T. Bryson, et al. (2010). “Kepler Science Operations.” In: *ApJ* 713.2, pp. L115–L119. DOI: [10.1088/2041-8205/713/2/L115](https://doi.org/10.1088/2041-8205/713/2/L115). arXiv: [1001.0437](https://arxiv.org/abs/1001.0437) [astro-ph.EP].
- Haisch Karl E., Jr., Elizabeth A. Lada, and Charles J. Lada (June 2001). “Disk Frequencies and Lifetimes in Young Clusters.” In: *ApJ* 553.2, pp. L153–L156. DOI: [10.1086/320685](https://doi.org/10.1086/320685). arXiv: [astro-ph/0104347](https://arxiv.org/abs/astro-ph/0104347) [astro-ph].
- Harris, Robert J., Sean M. Andrews, David J. Wilner, and Adam L. Kraus (June 2012). “A Resolved Census of Millimeter Emission from Taurus Multiple Star Systems.” In: *ApJ* 751.2, 115, p. 115. DOI: [10.1088/0004-637X/751/2/115](https://doi.org/10.1088/0004-637X/751/2/115). arXiv: [1203.6353](https://arxiv.org/abs/1203.6353) [astro-ph.SR].
- Hartigan, Patrick and Scott J. Kenyon (Jan. 2003). “A Spectroscopic Survey of Subarcsecond Binaries in the Taurus-Auriga Dark Cloud with the Hubble Space Telescope.” In: *ApJ* 583.1, pp. 334–357. DOI: [10.1086/345293](https://doi.org/10.1086/345293). arXiv: [astro-ph/0209608](https://arxiv.org/abs/astro-ph/0209608) [astro-ph].
- Hartmann, J. (May 1904). “Investigations on the spectrum and orbit of delta Orionis.” In: *ApJ* 19, pp. 268–286. DOI: [10.1086/141112](https://doi.org/10.1086/141112).
- Hartmann, L. and J. R. Stauffer (Mar. 1989). “Additional Measurements of Pre-Main-Sequence Stellar Rotation.” In: *AJ* 97, p. 873. DOI: [10.1086/115033](https://doi.org/10.1086/115033).
- Hartmann, L., R. Hewett, S. Stahler, and R. D. Mathieu (Oct. 1986). “Rotational and Radial Velocities of T Tauri Stars.” In: *ApJ* 309, p. 275. DOI: [10.1086/164599](https://doi.org/10.1086/164599).

- Hartmann, Lee, Robert Hewett, and Nuria Calvet (May 1994). "Magnetospheric Accretion Models for T Tauri Stars. I. Balmer Line Profiles without Rotation." In: *ApJ* 426, p. 669. DOI: [10.1086/174104](https://doi.org/10.1086/174104).
- Hartmann, Lee, Nuria Calvet, Erik Gullbring, and Paola D'Alessio (Mar. 1998). "Accretion and the Evolution of T Tauri Disks." In: *ApJ* 495.1, pp. 385–400. DOI: [10.1086/305277](https://doi.org/10.1086/305277).
- Hartmann, Lee, Nuria Calvet, Dan M. Watson, et al. (2005). "The Accretion Disk of the Lithium-depleted Young Binary *St 34*." In: *ApJ* 628.2, pp. L147–L150. DOI: [10.1086/432756](https://doi.org/10.1086/432756).
- Hartmann, Lee, Gregory Herczeg, and Nuria Calvet (Sept. 2016). "Accretion onto Pre-Main-Sequence Stars." In: *ARA&A* 54, pp. 135–180. DOI: [10.1146/annurev-astro-081915-023347](https://doi.org/10.1146/annurev-astro-081915-023347).
- Hayashi, C. (Jan. 1961). "Stellar evolution in early phases of gravitational contraction." In: *PASJ* 13, pp. 450–452.
- Hedges, Christina, Simon Hodgkin, and Grant Kennedy (May 2018). "Discovery of new dipper stars with K2: a window into the inner disc region of T Tauri stars." In: *MNRAS* 476.3, pp. 2968–2998. DOI: [10.1093/mnras/sty328](https://doi.org/10.1093/mnras/sty328). arXiv: [1802.00409](https://arxiv.org/abs/1802.00409) [astro-ph.SR].
- Henden, A. A., M. Templeton, D. Terrell, T. C. Smith, S. Levine, and D. Welch (Jan. 2016). "VizieR Online Data Catalog: AAVSO Photometric All Sky Survey (APASS) DR9 (Henden+, 2016)." In: *VizieR Online Data Catalog*, II/336, pp. II/336.
- Herbig, George H. (Dec. 1952). "Emission-line Stars in Galactic Nebulosities." In: *JRASC* 46, p. 222.
- Herbst, W., D. K. Herbst, E. J. Grossman, and D. Weinstein (Nov. 1994). "Catalogue of UBVRI Photometry of T Tauri Stars and Analysis of the Causes of Their Variability." In: *AJ* 108, p. 1906. DOI: [10.1086/117204](https://doi.org/10.1086/117204).
- Herczeg, Gregory J. and Lynne A. Hillenbrand (July 2008). "UV Excess Measures of Accretion onto Young Very Low Mass Stars and Brown Dwarfs." In: *ApJ* 681.1, pp. 594–625. DOI: [10.1086/586728](https://doi.org/10.1086/586728). arXiv: [0801.3525](https://arxiv.org/abs/0801.3525) [astro-ph].
- (2014). "An Optical Spectroscopic Study of T Tauri Stars. I. Photospheric Properties." In: *ApJ* 786.2, 97, p. 97. DOI: [10.1088/0004-637X/786/2/97](https://doi.org/10.1088/0004-637X/786/2/97). arXiv: [1403.1675](https://arxiv.org/abs/1403.1675) [astro-ph.SR].
- Hillenbrand, Lynne A., Stephen E. Strom, Frederick J. Vrba, and Jocelyn Keene (Oct. 1992). "Herbig Ae/Be Stars: Intermediate-Mass Stars Surrounded by Massive Circumstellar Accretion Disks." In: *ApJ* 397, p. 613. DOI: [10.1086/171819](https://doi.org/10.1086/171819).
- Holman, Matthew J., Daniel C. Fabrycky, Darin Ragozzine, et al. (Oct. 2010). "Kepler-9: A System of Multiple Planets Transiting a Sun-Like Star, Confirmed by Timing Variations." In: *Science* 330.6000, p. 51. DOI: [10.1126/science.1195778](https://doi.org/10.1126/science.1195778).
- Howell, Steve B., Charlie Sobeck, Michael Haas, et al. (2014). "The K2 Mission: Characterization and Early Results." In: *PASP* 126.938, p. 398. DOI: [10.1086/676406](https://doi.org/10.1086/676406). arXiv: [1402.5163](https://arxiv.org/abs/1402.5163) [astro-ph.IM].
- Hoyle, F. (Nov. 1953). "On the Fragmentation of Gas Clouds Into Galaxies and Stars." In: *ApJ* 118, p. 513. DOI: [10.1086/145780](https://doi.org/10.1086/145780).
- Huang, Jane, Sean M. Andrews, Cornelis P. Dullemond, et al. (Dec. 2018a). "The Disk Substructures at High Angular Resolution Project (DSHARP). II. Characteristics of Annular Substructures." In: *ApJ* 869.2, L42, p. L42. DOI: [10.3847/2041-8213/aaf740](https://doi.org/10.3847/2041-8213/aaf740). arXiv: [1812.04041](https://arxiv.org/abs/1812.04041) [astro-ph.EP].
- Huang, Jane, Sean M. Andrews, Laura M. Pérez, et al. (Dec. 2018b). "The Disk Substructures at High Angular Resolution Project (DSHARP). III. Spiral Structures in the Millimeter Continuum of the Elias 27, IM Lup, and WaOph 6 Disks." In: *ApJ* 869.2, L43, p. L43. DOI: [10.3847/2041-8213/aaf7a0](https://doi.org/10.3847/2041-8213/aaf7a0). arXiv: [1812.04193](https://arxiv.org/abs/1812.04193) [astro-ph.SR].
- Isella, A. and A. Natta (Aug. 2005). "The shape of the inner rim in proto-planetary disks." In: *A&A* 438.3, pp. 899–907. DOI: [10.1051/0004-6361:20052773](https://doi.org/10.1051/0004-6361:20052773). arXiv: [astro-ph/0503635](https://arxiv.org/abs/astro-ph/0503635) [astro-ph].
- Isella, Andrea, John M. Carpenter, and Anneila I. Sargent (Aug. 2009). "Structure and Evolution of Pre-main-sequence Circumstellar Disks." In: *ApJ* 701.1, pp. 260–282. DOI: [10.1088/0004-637X/701/1/260](https://doi.org/10.1088/0004-637X/701/1/260). arXiv: [0906.2227](https://arxiv.org/abs/0906.2227) [astro-ph.SR].
- Itoh, Yusuke, Misato Fukagawa, Hiroshi Shibai, Takahiro Sumi, and Kodai Yamamoto (Oct. 2015). "Study of infrared excess from circumstellar disks in binaries with Spitzer/IRAC." In: *PASJ* 67.5, 88, p. 88. DOI: [10.1093/pasj/psv071](https://doi.org/10.1093/pasj/psv071). arXiv: [1508.05595](https://arxiv.org/abs/1508.05595) [astro-ph.SR].
- Joy, Alfred H. (Sept. 1945). "T Tauri Variable Stars." In: *ApJ* 102, p. 168. DOI: [10.1086/144749](https://doi.org/10.1086/144749).
- (Nov. 1949). "Bright-Line Stars among the Taurus Dark Clouds." In: *ApJ* 110, p. 424. DOI: [10.1086/145217](https://doi.org/10.1086/145217).

- Kaiser, G. (2011). *A Friendly Guide to Wavelets*. 1st ed. Birkhäuser Basel. ISBN: 978-0-8176-8110-4. DOI: [10.1007/978-0-8176-8111-1](https://doi.org/10.1007/978-0-8176-8111-1).
- Kennedy, G. M. and M. C. Wyatt (Aug. 2013). “The bright end of the exo-Zodi luminosity function: disc evolution and implications for exo-Earth detectability.” In: *MNRAS* 433.3, pp. 2334–2356. DOI: [10.1093/mnras/stt900](https://doi.org/10.1093/mnras/stt900).
- Kenyon, S. J. and L. Hartmann (Dec. 1987). “Spectral Energy Distributions of T Tauri Stars: Disk Flaring and Limits on Accretion.” In: *ApJ* 323, p. 714. DOI: [10.1086/165866](https://doi.org/10.1086/165866).
- Kenyon, S. J., M. Gómez, and B. A. Whitney (2008). “Low Mass Star Formation in the Taurus-Auriga Clouds.” In: *Handbook of Star Forming Regions, Volume I*. Ed. by B. Reipurth. Vol. 4, p. 405.
- Kenyon, Scott J. and Lee Hartmann (Nov. 1995). “Pre-Main-Sequence Evolution in the Taurus-Auriga Molecular Cloud.” In: *ApJS* 101, p. 117. DOI: [10.1086/192235](https://doi.org/10.1086/192235).
- Keppler, M., M. Benisty, A. Müller, et al. (Sept. 2018). “Discovery of a planetary-mass companion within the gap of the transition disk around PDS 70.” In: *A&A* 617, A44, A44. DOI: [10.1051/0004-6361/201832957](https://doi.org/10.1051/0004-6361/201832957). arXiv: [1806.11568](https://arxiv.org/abs/1806.11568) [astro-ph.EP].
- Kholopov, P. N. (1951). In: *Peremennyye Zvezdy* 8.83.
- Kippenhahn, R., A. Weigert, and A. Weiss (2012). *Stellar Structure and Evolution*. 2nd ed. Astronomy and Astrophysics Library. Springer-Verlag Berlin Heidelberg.
- Kobayashi, H., H. Kimura, S. i. Watanabe, T. Yamamoto, and S. Müller (Oct. 2011). “Sublimation temperature of circumstellar dust particles and its importance for dust ring formation.” In: *Earth, Planets, and Space* 63.10, pp. 1067–1075. DOI: [10.5047/eps.2011.03.012](https://doi.org/10.5047/eps.2011.03.012). arXiv: [1104.5627](https://arxiv.org/abs/1104.5627) [astro-ph.EP].
- Koenigl, Arieh (Mar. 1991). “Disk Accretion onto Magnetic T Tauri Stars.” In: *ApJ* 370, p. L39. DOI: [10.1086/185972](https://doi.org/10.1086/185972).
- Kraus, Adam L. and Lynne A. Hillenbrand (2009). “Unusually Wide Binaries: Are They Wide or Unusual?” In: *ApJ* 703.2, pp. 1511–1530. DOI: [10.1088/0004-637X/703/2/1511](https://doi.org/10.1088/0004-637X/703/2/1511). arXiv: [0908.1385](https://arxiv.org/abs/0908.1385) [astro-ph.SR].
- Kraus, Adam L., Michael J. Ireland, Frantz Martinache, and Lynne A. Hillenbrand (Apr. 2011). “Mapping the Shores of the Brown Dwarf Desert. II. Multiple Star Formation in Taurus-Auriga.” In: *ApJ* 731.1, 8, p. 8. DOI: [10.1088/0004-637X/731/1/8](https://doi.org/10.1088/0004-637X/731/1/8). arXiv: [1101.4016](https://arxiv.org/abs/1101.4016) [astro-ph.SR].
- Kraus, Adam L., Michael J. Ireland, Lynne A. Hillenbrand, and Frantz Martinache (Jan. 2012). “The Role of Multiplicity in Disk Evolution and Planet Formation.” In: *ApJ* 745.1, 19, p. 19. DOI: [10.1088/0004-637X/745/1/19](https://doi.org/10.1088/0004-637X/745/1/19). arXiv: [1109.4141](https://arxiv.org/abs/1109.4141) [astro-ph.EP].
- Kraus, Adam L., Gregory J. Herczeg, Aaron C. Rizzuto, Andrew W. Mann, Catherine L. Slesnick, John M. Carpenter, Lynne A. Hillenbrand, and Eric E. Mamajek (Apr. 2017). “The Greater Taurus-Auriga Ecosystem. I. There is a Distributed Older Population.” In: *ApJ* 838.2, 150, p. 150. DOI: [10.3847/1538-4357/aa62a0](https://doi.org/10.3847/1538-4357/aa62a0). arXiv: [1702.04341](https://arxiv.org/abs/1702.04341) [astro-ph.SR].
- Kulkarni, A. K. and M. M. Romanova (May 2008). “Accretion to magnetized stars through the Rayleigh-Taylor instability: global 3D simulations.” In: *MNRAS* 386.2, pp. 673–687. DOI: [10.1111/j.1365-2966.2008.13094.x](https://doi.org/10.1111/j.1365-2966.2008.13094.x). arXiv: [0802.1759](https://arxiv.org/abs/0802.1759) [astro-ph].
- Kurosawa, Ryuichi, Tim J. Harries, and Neil H. Symington (Aug. 2006). “On the formation of H α line emission around classical T Tauri stars.” In: *MNRAS* 370.2, pp. 580–596. DOI: [10.1111/j.1365-2966.2006.10527.x](https://doi.org/10.1111/j.1365-2966.2006.10527.x). arXiv: [astro-ph/0605234](https://arxiv.org/abs/astro-ph/0605234) [astro-ph].
- Kurosawa, Ryuichi, M. M. Romanova, and T. J. Harries (Oct. 2011). “Multidimensional models of hydrogen and helium emission line profiles for classical T Tauri stars: method, tests and examples.” In: *MNRAS* 416.4, pp. 2623–2639. DOI: [10.1111/j.1365-2966.2011.19216.x](https://doi.org/10.1111/j.1365-2966.2011.19216.x). arXiv: [1102.0828](https://arxiv.org/abs/1102.0828) [astro-ph.SR].
- Labdon, Aaron, Stefan Kraus, Claire L. Davies, et al. (July 2019). “Dusty disk winds at the sublimation rim of the highly inclined, low mass young stellar object SU Aurigae.” In: *A&A* 627, A36, A36. DOI: [10.1051/0004-6361/201935331](https://doi.org/10.1051/0004-6361/201935331). arXiv: [1905.11907](https://arxiv.org/abs/1905.11907) [astro-ph.EP].
- Lada, C. J. and B. A. Wilking (Dec. 1984). “The nature of the embedded population in the rho Ophiuchi dark cloud : mid-infrared observations.” In: *ApJ* 287, pp. 610–621. DOI: [10.1086/162719](https://doi.org/10.1086/162719).
- Lai, Dong (Oct. 1999). “Magnetically Driven Warping, Precession, and Resonances in Accretion Disks.” In: *ApJ* 524.2, pp. 1030–1047. DOI: [10.1086/307850](https://doi.org/10.1086/307850). arXiv: [astro-ph/9904110](https://arxiv.org/abs/astro-ph/9904110) [astro-ph].

- Lamzin, S. A. (Mar. 1995). "On the structure of the accretion shock wave in the case of young stars." In: *A&A* 295, pp. L20–L22.
- Lasker, Barry M., Mario G. Lattanzi, Brian J. McLean, et al. (Aug. 2008). "The Second-Generation Guide Star Catalog: Description and Properties." In: *AJ* 136.2, pp. 735–766. DOI: [10.1088/0004-6256/136/2/735](https://doi.org/10.1088/0004-6256/136/2/735). arXiv: [0807.2522](https://arxiv.org/abs/0807.2522) [astro-ph].
- Lee, Gregory R., Ralf Gommers, Filip Waselewski, Kai Wohlfahrt, and Aaron O'Leary (2019). "Py-Wavelets: A Python package for wavelet analysis." In: *Journal of Open Source Software* 4.36, p. 1237. DOI: [10.21105/joss.01237](https://doi.org/10.21105/joss.01237). URL: <https://doi.org/10.21105/joss.01237>.
- Lima, G. H. R. A., S. H. P. Alencar, N. Calvet, L. Hartmann, and J. Muzerolle (Nov. 2010). "Modeling the H α line emission around classical T Tauri stars using magnetospheric accretion and disk wind models." In: *A&A* 522, A104, A104. DOI: [10.1051/0004-6361/201014490](https://doi.org/10.1051/0004-6361/201014490). arXiv: [1007.3976](https://arxiv.org/abs/1007.3976) [astro-ph.SR].
- Liner, C. (2010). "An overview of wavelet transform concepts and applications." In: URL: <http://www.agl.uh.edu/pdf/reports/liner-wavelet.pdf>.
- Liu, Haoyu Baobab, Antoine Mérand, Joel D. Green, et al. (Oct. 2019). "Diagnosing 0.1-10 au Scale Morphology of the FU Ori Disk Using ALMA and VLTI/GRAVITY." In: *ApJ* 884.1, 97, p. 97. DOI: [10.3847/1538-4357/ab391c](https://doi.org/10.3847/1538-4357/ab391c). arXiv: [1908.02981](https://arxiv.org/abs/1908.02981) [astro-ph.SR].
- Loinard, Laurent, Rosa M. Torres, Amy J. Mioduszewski, and Luis F. Rodríguez (Mar. 2008). "A Preliminary VLBA Distance to the Core of Ophiuchus, with an Accuracy of 4%." In: *ApJ* 675.1, p. L29. DOI: [10.1086/529548](https://doi.org/10.1086/529548). arXiv: [0801.2192](https://arxiv.org/abs/0801.2192) [astro-ph].
- Lomb, N. R. (Feb. 1976). "Least-squares frequency analysis of unequally spaced data." In: *Ap&SS* 39, pp. 447–462. DOI: [10.1007/BF00648343](https://doi.org/10.1007/BF00648343).
- Long, Feng, Paola Pinilla, Gregory J. Herczeg, et al. (Dec. 2018). "Gaps and Rings in an ALMA Survey of Disks in the Taurus Star-forming Region." In: *ApJ* 869.1, 17, p. 17. DOI: [10.3847/1538-4357/aae8e1](https://doi.org/10.3847/1538-4357/aae8e1). arXiv: [1810.06044](https://arxiv.org/abs/1810.06044) [astro-ph.SR].
- Long, Feng, Gregory J. Herczeg, Daniel Harsono, et al. (Sept. 2019). "Compact Disks in a High-resolution ALMA Survey of Dust Structures in the Taurus Molecular Cloud." In: *ApJ* 882.1, 49, p. 49. DOI: [10.3847/1538-4357/ab2d2d](https://doi.org/10.3847/1538-4357/ab2d2d). arXiv: [1906.10809](https://arxiv.org/abs/1906.10809) [astro-ph.SR].
- Long, M., M. M. Romanova, and R. V. E. Lovelace (Dec. 2005). "Locking of the Rotation of Disk-Accreting Magnetized Stars." In: *ApJ* 634.2, pp. 1214–1222. DOI: [10.1086/497000](https://doi.org/10.1086/497000). arXiv: [astro-ph/0510659](https://arxiv.org/abs/astro-ph/0510659) [astro-ph].
- Lucy, L. B. (Apr. 1999). "Computing radiative equilibria with Monte Carlo techniques." In: *A&A* 344, pp. 282–288.
- Luger, Rodrigo, Eric Agol, Ethan Kruse, Rory Barnes, Andrew Becker, Daniel Foreman-Mackey, and Drake Deming (2016). "EVEREST: Pixel Level Decorrelation of K2 Light Curves." In: *AJ* 152.4, 100, p. 100. DOI: [10.3847/0004-6256/152/4/100](https://doi.org/10.3847/0004-6256/152/4/100). arXiv: [1607.00524](https://arxiv.org/abs/1607.00524) [astro-ph.EP].
- Luhman, K. L. (Dec. 2018). "The Stellar Membership of the Taurus Star-forming Region." In: *AJ* 156.6, 271, p. 271. DOI: [10.3847/1538-3881/aae831](https://doi.org/10.3847/1538-3881/aae831). arXiv: [1811.01359](https://arxiv.org/abs/1811.01359) [astro-ph.SR].
- Luhman, K. L., E. E. Mamajek, S. J. Shukla, and N. P. Loutrel (Jan. 2017). "A Survey for New Members of the Taurus Star-forming Region with the Sloan Digital Sky Survey." In: *AJ* 153.1, 46, p. 46. DOI: [10.3847/1538-3881/153/1/46](https://doi.org/10.3847/1538-3881/153/1/46). arXiv: [1610.09412](https://arxiv.org/abs/1610.09412) [astro-ph.GA].
- Lynden-Bell, D. and J. E. Pringle (Sept. 1974). "The evolution of viscous discs and the origin of the nebular variables." In: *MNRAS* 168, pp. 603–637. DOI: [10.1093/mnras/168.3.603](https://doi.org/10.1093/mnras/168.3.603).
- Lyra, Wladimir and Min-Kai Lin (Sept. 2013). "Steady State Dust Distributions in Disk Vortices: Observational Predictions and Applications to Transitional Disks." In: *ApJ* 775.1, 17, p. 17. DOI: [10.1088/0004-637X/775/1/17](https://doi.org/10.1088/0004-637X/775/1/17). arXiv: [1307.3770](https://arxiv.org/abs/1307.3770) [astro-ph.EP].
- Lyra, Wladimir and Mordecai-Mark Mac Low (Sept. 2012). "Rossby Wave Instability at Dead Zone Boundaries in Three-dimensional Resistive Magnetohydrodynamical Global Models of Protoplanetary Disks." In: *ApJ* 756.1, 62, p. 62. DOI: [10.1088/0004-637X/756/1/62](https://doi.org/10.1088/0004-637X/756/1/62). arXiv: [1204.5711](https://arxiv.org/abs/1204.5711) [astro-ph.EP].
- Mathur, S., R. A. García, J. Ballot, T. Ceillier, D. Salabert, T. S. Metcalfe, C. Régulo, A. Jiménez, and S. Bloemen (Feb. 2014). "Magnetic activity of F stars observed by Kepler." In: *A&A* 562, A124, A124. DOI: [10.1051/0004-6361/201322707](https://doi.org/10.1051/0004-6361/201322707). arXiv: [1312.6997](https://arxiv.org/abs/1312.6997) [astro-ph.SR].

- Mayama, Satoshi, Eiji Akiyama, Olja Panić, et al. (Nov. 2018). “ALMA Reveals a Misaligned Inner Gas Disk inside the Large Cavity of a Transitional Disk.” In: *ApJ* 868.1, L3, p. L3. DOI: [10.3847/2041-8213/aae88b](https://doi.org/10.3847/2041-8213/aae88b). arXiv: [1810.06941](https://arxiv.org/abs/1810.06941) [astro-ph.EP].
- Mayne, N. J., Tim J. Harries, John Rowe, and David M. Acreman (June 2012). “Bayesian fitting of Taurus brown dwarf spectral energy distributions.” In: *MNRAS* 423.2, pp. 1775–1804. DOI: [10.1111/j.1365-2966.2012.20999.x](https://doi.org/10.1111/j.1365-2966.2012.20999.x). arXiv: [1203.6657](https://arxiv.org/abs/1203.6657) [astro-ph.SR].
- McGinnis, P. T., S. H. P. Alencar, M. M. Guimarães, et al. (2015). “CSI 2264: Probing the inner disks of AA Tauri-like systems in NGC 2264.” In: *Astronomy and Astrophysics* 577, A11, A11. DOI: [10.1051/0004-6361/201425475](https://doi.org/10.1051/0004-6361/201425475). arXiv: [1502.07692](https://arxiv.org/abs/1502.07692) [astro-ph.SR].
- Ménard, F. (1989). PhD Thesis. Université de Montreal.
- Mendoza V., Eugenio E. (Mar. 1966). “Infrared Photometry of T Tauri Stars and Related Objects.” In: *ApJ* 143, p. 1010. DOI: [10.1086/148584](https://doi.org/10.1086/148584).
- (Mar. 1968). “Infrared Excesses in T Tauri Stars and Related Objects.” In: *ApJ* 151, p. 977. DOI: [10.1086/149497](https://doi.org/10.1086/149497).
- Meyer, Michael R., Nuria Calvet, and Lynne A. Hillenbrand (July 1997). “Intrinsic Near-Infrared Excesses of T Tauri Stars: Understanding the Classical T Tauri Star Locus.” In: *AJ* 114, pp. 288–300. DOI: [10.1086/118474](https://doi.org/10.1086/118474).
- Miyake, Tomoya, Takeru K. Suzuki, and Shu-ichiro Inutsuka (Apr. 2016). “Dust Dynamics in Protoplanetary Disk Winds Driven by Magnetorotational Turbulence: A Mechanism for Floating Dust Grains with Characteristic Sizes.” In: *ApJ* 821.1, 3, p. 3. DOI: [10.3847/0004-637X/821/1/3](https://doi.org/10.3847/0004-637X/821/1/3). arXiv: [1505.03704](https://arxiv.org/abs/1505.03704) [astro-ph.EP].
- Mohanty, S., G. Basri, and R. Jayawardhana (Dec. 2005). “Accretion in brown dwarfs down to nearly planetary masses.” In: *Astronomische Nachrichten* 326.10, pp. 891–894. DOI: [10.1002/asna.200510450](https://doi.org/10.1002/asna.200510450).
- Morales-Calderón, M., J. R. Stauffer, L. A. Hillenbrand, et al. (2011). “Ysovar: The First Sensitive, Wide-area, Mid-infrared Photometric Monitoring of the Orion Nebula Cluster.” In: *ApJ* 733.1, 50, p. 50. DOI: [10.1088/0004-637X/733/1/50](https://doi.org/10.1088/0004-637X/733/1/50). arXiv: [1103.5238](https://arxiv.org/abs/1103.5238) [astro-ph.SR].
- Muzerolle, James, Lee Hartmann, and Nuria Calvet (Dec. 1998). “A Brgamma Probe of Disk Accretion in T Tauri Stars and Embedded Young Stellar Objects.” In: *AJ* 116.6, pp. 2965–2974. DOI: [10.1086/300636](https://doi.org/10.1086/300636).
- Muzerolle, James, Nuria Calvet, and Lee Hartmann (Apr. 2001). “Emission-Line Diagnostics of T Tauri Magnetospheric Accretion. II. Improved Model Tests and Insights into Accretion Physics.” In: *ApJ* 550.2, pp. 944–961. DOI: [10.1086/319779](https://doi.org/10.1086/319779).
- Muzerolle, James, Nuria Calvet, Lee Hartmann, and Paola D’Alessio (Nov. 2003). “Unveiling the Inner Disk Structure of T Tauri Stars.” In: *ApJ* 597.2, pp. L149–L152. DOI: [10.1086/379921](https://doi.org/10.1086/379921). arXiv: [astro-ph/0310067](https://arxiv.org/abs/astro-ph/0310067) [astro-ph].
- Nagel, E. and J. Bouvier (Nov. 2020). “The dipper light curve of V715 Persei: is there dust in the magnetosphere?” In: *A&A* 643, A157, A157. DOI: [10.1051/0004-6361/202038594](https://doi.org/10.1051/0004-6361/202038594). arXiv: [2010.05973](https://arxiv.org/abs/2010.05973) [astro-ph.SR].
- Nesterov, V. V., A. V. Kuzmin, N. T. Ashimbaeva, A. A. Volchkov, S. Röser, and U. Bastian (1995). “The Henry Draper Extension Charts: A catalogue of accurate positions, proper motions, magnitudes and spectral types of 86933 stars.” In: *A&AS* 110, p. 367.
- Nguyen, Duy Cuong, Alexis Brandeker, Marten H. van Kerkwijk, and Ray Jayawardhana (Feb. 2012). “Close Companions to Young Stars. I. A Large Spectroscopic Survey in Chamaeleon I and Taurus-Auriga.” In: *ApJ* 745.2, 119, p. 119. DOI: [10.1088/0004-637X/745/2/119](https://doi.org/10.1088/0004-637X/745/2/119). arXiv: [1112.0002](https://arxiv.org/abs/1112.0002) [astro-ph.SR].
- Oh, Semyeong, Adrian M. Price-Whelan, David W. Hogg, Timothy D. Morton, and David N. Spergel (June 2017). “Comoving Stars in Gaia DR1: An Abundance of Very Wide Separation Comoving Pairs.” In: *AJ* 153.6, 257, p. 257. DOI: [10.3847/1538-3881/aa6ffd](https://doi.org/10.3847/1538-3881/aa6ffd). arXiv: [1612.02440](https://arxiv.org/abs/1612.02440) [astro-ph.SR].
- Pantolmos, G., C. Zanni, and J. Bouvier (Nov. 2020). “Magnetic torques on T Tauri stars: Accreting versus non-accreting systems.” In: *A&A* 643, A129, A129. DOI: [10.1051/0004-6361/202038569](https://doi.org/10.1051/0004-6361/202038569). arXiv: [2009.00940](https://arxiv.org/abs/2009.00940) [astro-ph.SR].

- Pecaut, Mark J. and Eric E. Mamajek (2013). "Intrinsic Colors, Temperatures, and Bolometric Corrections of Pre-main-sequence Stars." In: *ApJS* 208.1, 9, p. 9. DOI: [10.1088/0067-0049/208/1/9](https://doi.org/10.1088/0067-0049/208/1/9). arXiv: [1307.2657](https://arxiv.org/abs/1307.2657) [astro-ph.SR].
- Pecaut, Mark J., Eric E. Mamajek, and Eric J. Bubar (Feb. 2012). "A Revised Age for Upper Scorpius and the Star Formation History among the F-type Members of the Scorpius-Centaurus OB Association." In: *ApJ* 746.2, 154, p. 154. DOI: [10.1088/0004-637X/746/2/154](https://doi.org/10.1088/0004-637X/746/2/154). arXiv: [1112.1695](https://arxiv.org/abs/1112.1695) [astro-ph.SR].
- Percy, John R. (2007). *Understanding Variable Stars*.
- Percy, John R., Sergiy Grynko, Rajiv Seneviratne, and William Herbst (July 2010). "Self-Correlation Analysis of the Photometric Variability of T Tauri Stars. II. A Survey." In: *PASP* 122.893, p. 753. DOI: [10.1086/654826](https://doi.org/10.1086/654826).
- Pinte, C., F. Ménard, G. Duchêne, and P. Bastien (Dec. 2006). "Monte Carlo radiative transfer in protoplanetary disks." In: *A&A* 459.3, pp. 797–804. DOI: [10.1051/0004-6361:20053275](https://doi.org/10.1051/0004-6361:20053275). arXiv: [astro-ph/0606550](https://arxiv.org/abs/astro-ph/0606550) [astro-ph].
- Pinte, C., T. J. Harries, M. Min, A. M. Watson, C. P. Dullemond, P. Woitke, F. Ménard, and M. C. Durán-Rojas (May 2009). "Benchmark problems for continuum radiative transfer. High optical depths, anisotropic scattering, and polarisation." In: *A&A* 498.3, pp. 967–980. DOI: [10.1051/0004-6361/200811555](https://doi.org/10.1051/0004-6361/200811555). arXiv: [0903.1231](https://arxiv.org/abs/0903.1231) [astro-ph.SR].
- Pinte, C., G. van der Plas, F. Ménard, et al. (Aug. 2019). "Kinematic detection of a planet carving a gap in a protoplanetary disk." In: *Nature Astronomy* 3, pp. 1109–1114. DOI: [10.1038/s41550-019-0852-6](https://doi.org/10.1038/s41550-019-0852-6). arXiv: [1907.02538](https://arxiv.org/abs/1907.02538) [astro-ph.SR].
- Pollack, James B., David Hollenbach, Steven Beckwith, Damon P. Simonelli, Ted Roush, and Wesley Fong (1994). "Composition and Radiative Properties of Grains in Molecular Clouds and Accretion Disks." In: *ApJ* 421, p. 615. DOI: [10.1086/173677](https://doi.org/10.1086/173677).
- Pouilly, K., J. Bouvier, E. Alecian, S. H. P. Alencar, A. M. Cody, J. F. Donati, K. Grankin, L. Rebull, and C. P. Folsom (Dec. 2021). "Beyond the dips of V807 Tau, a spectropolarimetric study of a dipper's magnetosphere." In: *A&A* 656, A50, A50. DOI: [10.1051/0004-6361/202140850](https://doi.org/10.1051/0004-6361/202140850). arXiv: [2109.10589](https://arxiv.org/abs/2109.10589) [astro-ph.SR].
- Ray, T. P. and J. Ferreira (Dec. 2021). "Jets from young stars." In: *New A Rev.* 93, 101615, p. 101615. DOI: [10.1016/j.newar.2021.101615](https://doi.org/10.1016/j.newar.2021.101615). arXiv: [2009.00547](https://arxiv.org/abs/2009.00547) [astro-ph.SR].
- Ray, T., C. Dougados, F. Bacciotti, J. Eisloffel, and A. Chrysostomou (Jan. 2007). "Toward Resolving the Outflow Engine: An Observational Perspective." In: *Protostars and Planets V*. Ed. by Bo Reipurth, David Jewitt, and Klaus Keil, p. 231. arXiv: [astro-ph/0605597](https://arxiv.org/abs/astro-ph/0605597) [astro-ph].
- Rebull, L. M., S. C. Wolff, and S. E. Strom (Feb. 2004). "Stellar Rotation in Young Clusters: The First 4 Million Years." In: *AJ* 127.2, pp. 1029–1051. DOI: [10.1086/380931](https://doi.org/10.1086/380931).
- Rebull, L. M., J. R. Stauffer, J. Bouvier, et al. (Nov. 2016a). "Rotation in the Pleiades with K2. I. Data and First Results." In: *AJ* 152.5, 113, p. 113. DOI: [10.3847/0004-6256/152/5/113](https://doi.org/10.3847/0004-6256/152/5/113). arXiv: [1606.00052](https://arxiv.org/abs/1606.00052) [astro-ph.SR].
- Rebull, L. M., J. R. Stauffer, J. Bouvier, et al. (Nov. 2016b). "Rotation in the Pleiades with K2. II. Multiperiod Stars." In: *AJ* 152.5, 114, p. 114. DOI: [10.3847/0004-6256/152/5/114](https://doi.org/10.3847/0004-6256/152/5/114). arXiv: [1606.00055](https://arxiv.org/abs/1606.00055) [astro-ph.SR].
- Rebull, L. M., J. R. Stauffer, L. A. Hillenbrand, A. M. Cody, J. Bouvier, D. R. Soderblom, M. Pinsonneault, and L. Hebb (2017). "Rotation of Late-type Stars in Praesepe with K2." In: *ApJ* 839.2, 92, p. 92. DOI: [10.3847/1538-4357/aa6aa4](https://doi.org/10.3847/1538-4357/aa6aa4). arXiv: [1703.07031](https://arxiv.org/abs/1703.07031) [astro-ph.SR].
- Rebull, L. M., J. R. Stauffer, A. M. Cody, L. A. Hillenbrand, T. J. David, and M. Pinsonneault (May 2018). "Rotation of Low-mass Stars in Upper Scorpius and ρ Ophiuchus with K2." In: *AJ* 155.5, 196, p. 196. DOI: [10.3847/1538-3881/aab605](https://doi.org/10.3847/1538-3881/aab605). arXiv: [1803.04440](https://arxiv.org/abs/1803.04440) [astro-ph.SR].
- Rebull, L. M., J. R. Stauffer, A. M. Cody, L. A. Hillenbrand, J. Bouvier, N. Roggero, and T. J. David (June 2020). "Rotation of Low-mass Stars in Taurus with K2." In: *AJ* 159.6, 273, p. 273. DOI: [10.3847/1538-3881/ab893c](https://doi.org/10.3847/1538-3881/ab893c). arXiv: [2004.04236](https://arxiv.org/abs/2004.04236) [astro-ph.SR].
- Reggiani, M., M. Robberto, N. Da Rio, M. R. Meyer, D. R. Soderblom, and L. Ricci (Oct. 2011). "Quantitative evidence of an intrinsic luminosity spread in the Orion nebula cluster." In: *A&A* 534, A83, A83. DOI: [10.1051/0004-6361/201116946](https://doi.org/10.1051/0004-6361/201116946). arXiv: [1108.1015](https://arxiv.org/abs/1108.1015) [astro-ph.GA].

- Rigliaco, Elisabetta, I. Pascucci, G. Duchene, et al. (Mar. 2015). "Probing Stellar Accretion with Mid-infrared Hydrogen Lines." In: *ApJ* 801.1, 31, p. 31. DOI: [10.1088/0004-637X/801/1/31](https://doi.org/10.1088/0004-637X/801/1/31). arXiv: [1501.06210](https://arxiv.org/abs/1501.06210) [astro-ph.SR].
- Roberts, D. H., J. Lehar, and J. W. Dreher (1987). "Time series analysis with CLEAN. I. Derivation of a spectrum." In: *AJ* 93, pp. 968–989. DOI: [10.1086/114383](https://doi.org/10.1086/114383).
- Robitaille, J.-F., G. Joncas, and M.-A. Miville-Deschênes (May 2014). "Multiscale analysis of Galactic dust emission using complex wavelet transforms - I. Separation of Gaussian and non-Gaussian fluctuations in Herschel observations." In: *MNRAS* 440, pp. 2726–2741. DOI: [10.1093/mnras/stu375](https://doi.org/10.1093/mnras/stu375).
- Rodriguez, Joseph E., Megan Ansdell, Ryan J. Oelkers, et al. (Oct. 2017). "Identification of Young Stellar Variables with KELT for K2. I. Taurus Dippers and Rotators." In: *ApJ* 848.2, 97, p. 97. DOI: [10.3847/1538-4357/aa8c78](https://doi.org/10.3847/1538-4357/aa8c78). arXiv: [1703.02522](https://arxiv.org/abs/1703.02522) [astro-ph.SR].
- Roggero, Noemi, Jérôme Bouvier, Luisa M. Rebull, and Ann Marie Cody (2021). "The dipper population of Taurus seen with K2." In: *A&A* 651, A44, A44. DOI: <https://doi.org/10.1051/0004-6361/202140646>. arXiv: [2106.02064](https://arxiv.org/abs/2106.02064) [astro-ph.SR].
- Romanova, M. M., G. V. Ustyugova, A. V. Koldoba, and R. V. E. Lovelace (Mar. 2013). "Warps, bending and density waves excited by rotating magnetized stars: results of global 3D MHD simulations." In: *MNRAS* 430.1, pp. 699–724. DOI: [10.1093/mnras/sts670](https://doi.org/10.1093/mnras/sts670). arXiv: [1209.1161](https://arxiv.org/abs/1209.1161) [astro-ph.SR].
- Romanova, Marina M. and Stanley P. Owocki (Oct. 2015). "Accretion, Outflows, and Winds of Magnetized Stars." In: *Space Sci. Rev.* 191.1-4, pp. 339–389. DOI: [10.1007/s11214-015-0200-9](https://doi.org/10.1007/s11214-015-0200-9). arXiv: [1605.04979](https://arxiv.org/abs/1605.04979) [astro-ph.SR].
- Romanova, Marina M., Akshay K. Kulkarni, and Richard V. E. Lovelace (Feb. 2008). "Unstable Disk Accretion onto Magnetized Stars: First Global Three-dimensional Magnetohydrodynamic Simulations." In: *ApJ* 673.2, p. L171. DOI: [10.1086/527298](https://doi.org/10.1086/527298). arXiv: [0711.0418](https://arxiv.org/abs/0711.0418) [astro-ph].
- Rydgren, A. E., S. E. Strom, and K. M. Strom (Mar. 1976). "The nature of the objects of Joy: a study of the T Tauri phenomenon." In: *ApJS* 30, pp. 307–336. DOI: [10.1086/190364](https://doi.org/10.1086/190364).
- Rydgren, A. E., J. T. Schmelz, and F. J. Vrba (May 1982). "Evidence for a characteristic maximum temperature in the circumstellar dust associated with T Tau stars." In: *ApJ* 256, pp. 168–176. DOI: [10.1086/159894](https://doi.org/10.1086/159894).
- Sallum, S., K. B. Follette, J. A. Eisner, et al. (Nov. 2015). "Accreting protoplanets in the LkCa 15 transition disk." In: *Nature* 527.7578, pp. 342–344. DOI: [10.1038/nature15761](https://doi.org/10.1038/nature15761). arXiv: [1511.07456](https://arxiv.org/abs/1511.07456) [astro-ph.EP].
- Sana, H., J.-B. Le Bouquin, S. Lacour, et al. (Nov. 2014). "Southern Massive Stars at High Angular Resolution: Observational Campaign and Companion Detection." In: *ApJS* 215, 15, p. 15. DOI: [10.1088/0067-0049/215/1/15](https://doi.org/10.1088/0067-0049/215/1/15). arXiv: [1409.6304](https://arxiv.org/abs/1409.6304) [astro-ph.SR].
- Scargle, J. D. (Dec. 1982). "Studies in astronomical time series analysis. II - Statistical aspects of spectral analysis of unevenly spaced data." In: *ApJ* 263, pp. 835–853. DOI: [10.1086/160554](https://doi.org/10.1086/160554).
- Schaefer, G. H., L. Prato, M. Simon, and R. T. Zavala (Sept. 2012). "Orbit and Stellar Properties of the Young Triple V807 Tau." In: *ApJ* 756.2, 120, p. 120. DOI: [10.1088/0004-637X/756/2/120](https://doi.org/10.1088/0004-637X/756/2/120). arXiv: [1207.7037](https://arxiv.org/abs/1207.7037) [astro-ph.SR].
- Schaefer, G. H., L. Prato, M. Simon, and J. Patience (June 2014). "Orbital Motion in Pre-main Sequence Binaries." In: *AJ* 147.6, 157, p. 157. DOI: [10.1088/0004-6256/147/6/157](https://doi.org/10.1088/0004-6256/147/6/157). arXiv: [1405.0225](https://arxiv.org/abs/1405.0225) [astro-ph.SR].
- Scholz, Aleks, Keavin Moore, Ray Jayawardhana, Suzanne Aigrain, Dawn Peterson, and Beate Stelzer (June 2018). "A Universal Spin-Mass Relation for Brown Dwarfs and Planets." In: *ApJ* 859.2, 153, p. 153. DOI: [10.3847/1538-4357/aabfbc](https://doi.org/10.3847/1538-4357/aabfbc). arXiv: [1804.07380](https://arxiv.org/abs/1804.07380) [astro-ph.EP].
- Shakura, N. I. and R. A. Sunyaev (June 1973). "Reprint of 1973A&A....24..337S. Black holes in binary systems. Observational appearance." In: *A&A* 500, pp. 33–51.
- Shu, Frank, Joan Najita, Eve Ostriker, Frank Wilkin, Steven Ruden, and Susana Lizano (July 1994). "Magnetocentrally Driven Flows from Young Stars and Disks. I. A Generalized Model." In: *ApJ* 429, p. 781. DOI: [10.1086/174363](https://doi.org/10.1086/174363).
- Sicilia-Aguilar, A., C. F. Manara, J. de Boer, M. Benisty, P. Pinilla, and J. Bouvier (Jan. 2020). "Time-resolved photometry of the young dipper RX J1604.3-2130A. Unveiling the structure and mass

- transport through the innermost disk." In: *A&A* 633, A37, A37. DOI: [10.1051/0004-6361/201936565](https://doi.org/10.1051/0004-6361/201936565). arXiv: [1911.04938](https://arxiv.org/abs/1911.04938) [astro-ph.SR].
- Siess, L., E. Dufour, and M. Forestini (June 2000). "An internet server for pre-main sequence tracks of low- and intermediate-mass stars." In: *A&A* 358, pp. 593–599. arXiv: [astro-ph/0003477](https://arxiv.org/abs/astro-ph/0003477) [astro-ph].
- Simon, M., S. Guilloteau, E. Di Folco, et al. (Aug. 2017). "Dynamical Masses of Low-mass Stars in the Taurus and Ophiuchus Star-forming Regions." In: *ApJ* 844.2, 158, p. 158. DOI: [10.3847/1538-4357/aa78f1](https://doi.org/10.3847/1538-4357/aa78f1). arXiv: [1706.03505](https://arxiv.org/abs/1706.03505) [astro-ph.SR].
- Skrutskie, M. F., R. M. Cutri, R. Stiening, et al. (Feb. 2006). "The Two Micron All Sky Survey (2MASS)." In: *AJ* 131.2, pp. 1163–1183. DOI: [10.1086/498708](https://doi.org/10.1086/498708).
- Smak, J. (May 1964). "On the colors of T Tau stars and related objects." In: *ApJ* 139, p. 1095. DOI: [10.1086/147851](https://doi.org/10.1086/147851).
- Sota, A., J. Maíz Apellániz, N. I. Morrell, R. H. Barbá, N. R. Walborn, R. C. Gamen, J. I. Arias, and E. J. Alfaro (Mar. 2014). "The Galactic O-Star Spectroscopic Survey (GOSSS). II. Bright Southern Stars." In: *ApJS* 211, 10, p. 10. DOI: [10.1088/0067-0049/211/1/10](https://doi.org/10.1088/0067-0049/211/1/10). arXiv: [1312.6222](https://arxiv.org/abs/1312.6222) [astro-ph.GA].
- Sousa, A. P., J. Bouvier, S. H. P. Alencar, et al. (May 2021). "Star-disk interaction in the T Tauri star V2129 Ophiuchi: An evolving accretion-ejection structure." In: *A&A* 649, A68, A68. DOI: [10.1051/0004-6361/202140346](https://doi.org/10.1051/0004-6361/202140346). arXiv: [2103.16383](https://arxiv.org/abs/2103.16383) [astro-ph.SR].
- Stahler, S. W., F. H. Shu, and R. E. Taam (Oct. 1980). "The evolution of protostars. I - Global formulation and results." In: *ApJ* 241, pp. 637–654. DOI: [10.1086/158377](https://doi.org/10.1086/158377).
- Stahler, Steven W. and Francesco Palla (2004). *The Formation of Stars*.
- Stauffer, John, Ann Marie Cody, Annie Baglin, et al. (Apr. 2014). "CSI 2264: Characterizing Accretion-burst Dominated Light Curves for Young Stars in NGC 2264." In: *AJ* 147.4, 83, p. 83. DOI: [10.1088/0004-6256/147/4/83](https://doi.org/10.1088/0004-6256/147/4/83). arXiv: [1401.6600](https://arxiv.org/abs/1401.6600) [astro-ph.SR].
- Stauffer, John, Ann Marie Cody, Pauline McGinnis, et al. (Apr. 2015). "CSI 2264: Characterizing Young Stars in NGC 2264 With Short-Duration Periodic Flux Dips in Their Light Curves." In: *AJ* 149.4, 130, p. 130. DOI: [10.1088/0004-6256/149/4/130](https://doi.org/10.1088/0004-6256/149/4/130). arXiv: [1501.06609](https://arxiv.org/abs/1501.06609) [astro-ph.SR].
- Stauffer, John, Luisa Rebull, Jerome Bouvier, et al. (Nov. 2016). "Rotation in the Pleiades with K2. III. Speculations on Origins and Evolution." In: *AJ* 152.5, 115, p. 115. DOI: [10.3847/0004-6256/152/5/115](https://doi.org/10.3847/0004-6256/152/5/115). arXiv: [1606.00057](https://arxiv.org/abs/1606.00057) [astro-ph.SR].
- Stolker, T., C. Dominik, H. Avenhaus, et al. (Nov. 2016). "Shadows cast on the transition disk of HD 135344B. Multiwavelength VLT/SPHERE polarimetric differential imaging." In: *A&A* 595, A113, A113. DOI: [10.1051/0004-6361/201528039](https://doi.org/10.1051/0004-6361/201528039). arXiv: [1603.00481](https://arxiv.org/abs/1603.00481) [astro-ph.EP].
- Strom, Karen M., Stephen E. Strom, Scott J. Kenyon, and Lee Hartmann (Feb. 1988). "Luminosity Excesses in Low-Mass Young Stellar Objects: A Statistical Study." In: *AJ* 95, p. 534. DOI: [10.1086/114653](https://doi.org/10.1086/114653).
- Strom, Karen M., Stephen E. Strom, Suzan Edwards, Sylvie Cabrit, and Michael F. Skrutskie (May 1989). "Circumstellar Material Associated with Solar-Type Pre-Main-Sequence Stars: A Possible Constraint on the Timescale for Planet Building." In: *AJ* 97, p. 1451. DOI: [10.1086/115085](https://doi.org/10.1086/115085).
- Tajiri, Tomoyuki, Hajime Kawahara, Masataka Aizawa, et al. (2020). *Dippers from the TESS Full-Frame Images I: The Results of the first 1 year data and Discovery of A Runaway dipper*. arXiv: [2009.12830](https://arxiv.org/abs/2009.12830) [astro-ph.EP].
- Tambovtseva, L. V. and V. P. Grinin (Apr. 2008). "Dust in the disk winds from young stars as a source of the circumstellar extinction." In: *Astronomy Letters* 34.4, pp. 231–240. DOI: [10.1134/S1063773708040026](https://doi.org/10.1134/S1063773708040026). arXiv: [0801.2236](https://arxiv.org/abs/0801.2236) [astro-ph].
- Tannirkulam, A., T. J. Harries, and J. D. Monnier (May 2007). "The Inner Rim of YSO Disks: Effects of Dust Grain Evolution." In: *ApJ* 661.1, pp. 374–384. DOI: [10.1086/513265](https://doi.org/10.1086/513265). arXiv: [astro-ph/0702044](https://arxiv.org/abs/astro-ph/0702044) [astro-ph].
- Terquem, C. and J. C. B. Papaloizou (Aug. 2000). "The response of an accretion disc to an inclined dipole with application to AA Tau." In: *A&A* 360, pp. 1031–1042. arXiv: [astro-ph/0006113](https://arxiv.org/abs/astro-ph/0006113) [astro-ph].
- Thalmann, C., G. D. Mulders, K. Hodapp, et al. (June 2014). "The architecture of the LkCa 15 transitional disk revealed by high-contrast imaging." In: *A&A* 566, A51, A51. DOI: [10.1051/0004-6361/201322915](https://doi.org/10.1051/0004-6361/201322915). arXiv: [1402.1766](https://arxiv.org/abs/1402.1766) [astro-ph.SR].

- Thalmann, C., M. Janson, A. Garufi, et al. (2016). “RESOLVING THE PLANET-HOSTING INNER REGIONS OF THE LkCa 15 DISK.” In: *The Astrophysical Journal* 828.2, p. L17. DOI: [10.3847/2041-8205/828/2/L17](https://doi.org/10.3847/2041-8205/828/2/L17). URL: <https://doi.org/10.3847/2041-8205/828/2/L17>.
- Torrence, Christopher and Gilbert P. Compo (1998). “A Practical Guide to Wavelet Analysis.” In: *Bulletin of the American Meteorological Society* 79.1, pp. 61–78.
- VanderPlas, Jacob T. (May 2018). “Understanding the Lomb-Scargle Periodogram.” In: *ApJS* 236.1, 16, p. 16. DOI: [10.3847/1538-4365/aab766](https://doi.org/10.3847/1538-4365/aab766). arXiv: [1703.09824](https://arxiv.org/abs/1703.09824) [astro-ph.IM].
- Vanderburg, Andrew and John Asher Johnson (2014). “A Technique for Extracting Highly Precise Photometry for the Two-Wheeled Kepler Mission.” In: *PASP* 126.944, p. 948. DOI: [10.1086/678764](https://doi.org/10.1086/678764). arXiv: [1408.3853](https://arxiv.org/abs/1408.3853) [astro-ph.IM].
- Varsavsky, Carlos M. (Sept. 1960). “The Gravitational Contraction Times of Stars in Very Young Clusters.” In: *ApJ* 132, p. 354. DOI: [10.1086/146934](https://doi.org/10.1086/146934).
- Venuti, L., J. Bouvier, E. Flaccomio, et al. (Oct. 2014). “Mapping accretion and its variability in the young open cluster NGC 2264: a study based on u-band photometry.” In: *A&A* 570, A82, A82. DOI: [10.1051/0004-6361/201423776](https://doi.org/10.1051/0004-6361/201423776). arXiv: [1408.0432](https://arxiv.org/abs/1408.0432) [astro-ph.SR].
- Vidotto, A. A., S. G. Gregory, M. Jardine, et al. (July 2014). “Stellar magnetism: empirical trends with age and rotation.” In: *MNRAS* 441.3, pp. 2361–2374. DOI: [10.1093/mnras/stu728](https://doi.org/10.1093/mnras/stu728). arXiv: [1404.2733](https://arxiv.org/abs/1404.2733) [astro-ph.SR].
- Vinković, Dejan and Miljenko Čemljić (Oct. 2020). “Inner dusty regions of protoplanetary discs - II. Dust dynamics driven by radiation pressure and disc winds.” In: *MNRAS*. DOI: [10.1093/mnras/staa3272](https://doi.org/10.1093/mnras/staa3272). arXiv: [2010.09384](https://arxiv.org/abs/2010.09384) [astro-ph.EP].
- Vural, J., A. Kreplin, S. Kraus, G. Weigelt, T. Driebe, M. Benisty, M. Dugué, F. Massi, J. L. Monin, and M. Vannier (July 2012). “Revealing the inner circumstellar disk of the T Tauri star S Coronae Australis N using the VLTI.” In: *A&A* 543, A162, A162. DOI: [10.1051/0004-6361/201218892](https://doi.org/10.1051/0004-6361/201218892). arXiv: [1207.2467](https://arxiv.org/abs/1207.2467) [astro-ph.SR].
- Watson, Dan M., Jarron M. Leisenring, Elise Furlan, et al. (Jan. 2009). “Crystalline Silicates and Dust Processing in the Protoplanetary Disks of the Taurus Young Cluster.” In: *ApJS* 180.1, pp. 84–101. DOI: [10.1088/0067-0049/180/1/84](https://doi.org/10.1088/0067-0049/180/1/84). arXiv: [0704.1518](https://arxiv.org/abs/0704.1518) [astro-ph].
- White, R. J. and A. M. Ghez (2001). “Observational Constraints on the Formation and Evolution of Binary Stars.” In: *ApJ* 556.1, pp. 265–295. DOI: [10.1086/321542](https://doi.org/10.1086/321542). arXiv: [astro-ph/0103098](https://arxiv.org/abs/astro-ph/0103098) [astro-ph].
- White, Russel J. and Gibor Basri (Jan. 2003). “Very Low Mass Stars and Brown Dwarfs in Taurus-Auriga.” In: *ApJ* 582.2, pp. 1109–1122. DOI: [10.1086/344673](https://doi.org/10.1086/344673). arXiv: [astro-ph/0209164](https://arxiv.org/abs/astro-ph/0209164) [astro-ph].
- White, Russel J. and Lynne A. Hillenbrand (Dec. 2004). “On the Evolutionary Status of Class I Stars and Herbig-Haro Energy Sources in Taurus-Auriga.” In: *ApJ* 616.2, pp. 998–1032. DOI: [10.1086/425115](https://doi.org/10.1086/425115). arXiv: [astro-ph/0408244](https://arxiv.org/abs/astro-ph/0408244) [astro-ph].
- (2005). “A Long-lived Accretion Disk around a Lithium-depleted Binary T Tauri Star.” In: *ApJ* 621.1, pp. L65–L68. DOI: [10.1086/428752](https://doi.org/10.1086/428752). arXiv: [astro-ph/0501307](https://arxiv.org/abs/astro-ph/0501307) [astro-ph].
- Williams, Jonathan P. and Lucas A. Cieza (Sept. 2011). “Protoplanetary Disks and Their Evolution.” In: *ARA&A* 49.1, pp. 67–117. DOI: [10.1146/annurev-astro-081710-102548](https://doi.org/10.1146/annurev-astro-081710-102548). arXiv: [1103.0556](https://arxiv.org/abs/1103.0556) [astro-ph.GA].
- Xiao, Hong Yu, Kevin R. Covey, Luisa Rebull, David Charbonneau, Georgi Mandushev, Francis O’Donovan, Catherine Slesnick, and James P. Lloyd (Sept. 2012). “A Census of Rotation and Variability in L1495: A Uniform Analysis of Trans-atlantic Exoplanet Survey Light Curves for Pre-main-sequence Stars in Taurus.” In: *ApJS* 202.1, 7, p. 7. DOI: [10.1088/0067-0049/202/1/7](https://doi.org/10.1088/0067-0049/202/1/7).
- Yakovlev, A. S. (2005). *Window Fourier and Wavelet Transforms. Properties and Applications of Wavelets*. URL: http://wwwmayr.in.tum.de/konferenzen/Jass05/courses/2/Yakovlev/Yakovlev_paper.pdf.
- Zacharias, N., D. G. Monet, S. E. Levine, S. E. Urban, R. Gaume, and G. L. Wycoff (Nov. 2005). “VizieR Online Data Catalog: NOMAD Catalog (Zacharias+ 2005).” In: *VizieR Online Data Catalog*, I/297, pp. I/297.
- Zanni, C. and J. Ferreira (Dec. 2009). “MHD simulations of accretion onto a dipolar magnetosphere. I. Accretion curtains and the disk-locking paradigm.” In: *A&A* 508.3, pp. 1117–1133. DOI: [10.1051/0004-6361/200912879](https://doi.org/10.1051/0004-6361/200912879).

- (Feb. 2013). “MHD simulations of accretion onto a dipolar magnetosphere. II. Magnetospheric ejections and stellar spin-down.” In: *A&A* 550, A99, A99. DOI: [10.1051/0004-6361/201220168](https://doi.org/10.1051/0004-6361/201220168). arXiv: [1211.4844](https://arxiv.org/abs/1211.4844) [astro-ph.SR].
- de Lira, S. R., J. P. Bravo, I. C. Leão, A. D. da Costa, B. L. Canto Martins, D. B. de Freitas, and J. R. De Medeiros (Apr. 2019). “A wavelet analysis of photometric variability in Kepler white dwarf stars.” In: *MNRAS* 484.3, pp. 3935–3940. DOI: [10.1093/mnras/stz122](https://doi.org/10.1093/mnras/stz122). arXiv: [1901.05384](https://arxiv.org/abs/1901.05384) [astro-ph.SR].
- de Zeeuw, P. T., R. Hoogerwerf, J. H. J. de Bruijne, A. G. A. Brown, and A. Blaauw (Jan. 1999). “A HIPPARCOS Census of the Nearby OB Associations.” In: *AJ* 117.1, pp. 354–399. DOI: [10.1086/300682](https://doi.org/10.1086/300682). arXiv: [astro-ph/9809227](https://arxiv.org/abs/astro-ph/9809227) [astro-ph].
- van der Marel, N., E. F. van Dishoeck, S. Bruderer, L. Pérez, and A. Isella (July 2015). “Gas density drops inside dust cavities of transitional disks around young stars observed with ALMA.” In: *A&A* 579, A106, A106. DOI: [10.1051/0004-6361/201525658](https://doi.org/10.1051/0004-6361/201525658). arXiv: [1504.03927](https://arxiv.org/abs/1504.03927) [astro-ph.EP].